BEILSTEIN JOURNAL OF NANOTECHNOLOGY

Molecular assemblies on surfaces – towards physical and electronic decoupling of organic molecules

Edited by Sabine Maier and Meike Stöhr

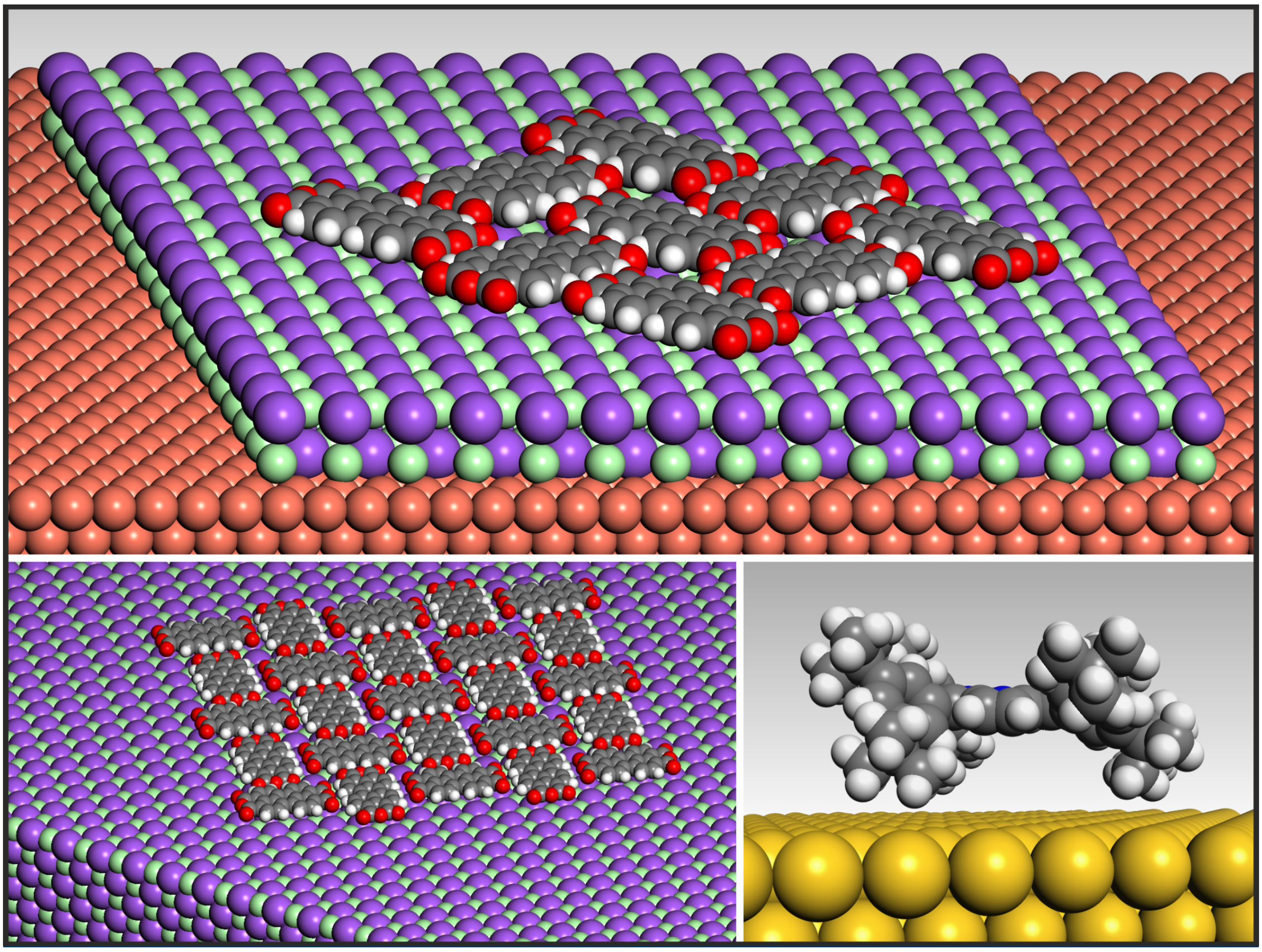

Imprint

Beilstein Journal of Nanotechnology
www.bjnano.org
ISSN 2190-4286
Email: journals-support@beilstein-institut.de

The *Beilstein Journal of Nanotechnology* is published by the Beilstein-Institut zur Förderung der Chemischen Wissenschaften.

Beilstein-Institut zur Förderung der
Chemischen Wissenschaften
Trakehner Straße 7–9
60487 Frankfurt am Main
Germany
www.beilstein-institut.de

Cover image description: Physical and electronic decoupling of organic molecules can be achieved via thin insulating films, bulk insulators or functionalizing them with bulky groups.

BEILSTEIN JOURNAL OF NANOTECHNOLOGY

Molecular assemblies on surfaces: towards physical and electronic decoupling of organic molecules

Sabine Maier*[1] and Meike Stöhr*[2]

Editorial

Open Access

Address:
[1]Department of Physics, Friedrich-Alexander-Universität Erlangen-Nürnberg, Erwin-Rommel-Str. 1, 91058 Erlangen, Germany and [2]Zernike Institute for Advanced Materials, University of Groningen, Nijenborgh 4, 9747 AG Groningen, Netherlands

Email:
Sabine Maier* - sabine.maier@fau.de; Meike Stöhr* - m.a.stohr@rug.nl

* Corresponding author

Keywords:
decoupling layer; molecular self-assembly; scanning probe microscopy; surface science

Beilstein J. Nanotechnol. **2021,** *12,* 950–956.
https://doi.org/10.3762/bjnano.12.71

Received: 29 July 2021
Accepted: 04 August 2021
Published: 23 August 2021

This article is part of the thematic issue "Molecular assemblies on surfaces – towards physical and electronic decoupling of organic molecules".

Editor-in-Chief: T. Schimmel

Over the past two decades, organic molecules adsorbed on atomically defined metal surfaces have been intensively studied to obtain an in-depth understanding of their self-assembly behavior, on-surface reactivity, as well as their structural and electronic properties [1-6]. An important aspect to unravel their potential use in electronic and optoelectronic devices is how their functionality can be preserved when adsorbed on surfaces. Unfortunately, the (strong) interaction of the molecules with the metallic surface, for example, due to hybridization of molecular states with electronic bands from the metallic substrate, often alters the electronic properties of the molecules and, moreover, can even turn off their sought-after functionality. As a result of the (strong) interaction, the molecular scaffolds can also become distorted, electronic states may be significantly broadened and shifted, and vibronic states may even be quenched. Decoupling strategies offer unique opportunities to reduce these (strong) interactions. In the following, recent progress to decouple both single molecules and molecular assemblies physically and electronically from a (strongly) interacting support is briefly reviewed.

The molecule–substrate decoupling can either be achieved by suitable molecular design or manipulation of the molecular building blocks, or passivation of the substrate. Molecular engineering approaches include rigid spacers added to the molecular core [7-10] or specially designed double-decker molecules [11] to maintain the active part of the molecule sufficiently high above the surface to prevent it from interacting with the latter. Alternatively, molecular/oligomeric structures can be attached to the tip of a scanning probe microscope and mechanically lifted from the metallic surface such that they hang freely between metal contacts. This manipulation technique allows for measuring, amongst others, the electronic conductance, magnetic properties, reversible switching, and electroluminescence of free-standing molecules [12-16]. Physical decoupling strategies involving the design or manipulation of the molecular building block significantly limit the selection of building blocks and often hinder probing molecular properties with intramolecular resolution. Therefore, modifications of the substrate, for instance by adding or intercalating a decoupling layer, are often the better choice. In the best case, these interfacial layers have a large bandgap to prevent a hybridization with molecular states as well as with the metallic/semiconducting substrate. All the strategies for physical and electronic decoupling have been developed in view of fundamental studies as well as application in devices.

Ultrathin semiconducting or insulating decoupling layers can be epitaxially grown as mono- and multilayers on many metallic substrates by either physical or chemical vapor deposition. Among others, ultrathin dielectric layers of either alkali halides (e.g., NaCl [17]) or metal oxides (e.g., MgO [18], Al_2O_3 [19], and CuO [20]), or nitrides (CuN [21]) have been shown to be beneficial for successfully reducing or even completely switching off the unwanted interaction between the metal substrate and the organic building blocks. Recently, two-dimensional (2D) materials, including hexagonal boron nitride (*h*BN) [22,23], graphene [24-27], and MoS_2 [28], have emerged as monatomically thin decoupling layers. Van der Waals 2D materials are generally well suited due to their chemical inertness and the low density of states near the Fermi level. However, the electronic decoupling efficiency also depends on the electronic structure of the 2D material. Sometimes, only molecular states in the bandgap of the 2D material can be decoupled. Moreover, ultrathin organic spacer layers can efficiently electronically decouple further organic layers from a metal surface. The decoupling strategy with organic layers relies on both an increased separation between the organic layer of interest and the metal as well as the different electronic gaps of the organic interface layer and following ones [29-32]. Additional concepts to weaken adsorbate–surface interactions involve the post-deposition intercalation of atomic species such as iodine [33].

For semiconductors, for example, bare silicon or germanium, electronic decoupling of molecules can be achieved by either the growth of ultrathin dielectric layers on top of the surface [34,35] or a chemical modification of the surface to saturate the dangling bonds. In surface-science-based studies, for the latter approach hydrogenation of semiconductor surfaces is frequently applied as effective passivation against chemisorption of adsorbates [36-39], while also B deposition was shown to result in effective passivation of the Si surface [40,41]. In particular for electronic devices, oxidized semiconductor surfaces (e.g., silicon dioxide layers formed on bare silicon) are mostly used as substrates for fabricating devices [42].

Most of these ultrathin interfacial layers significantly reduce both the molecular adsorption energy and the hybridization of molecular states with the electronic bands in metals and semiconductors. However, charge transport is not completely inhibited, and electrons can still tunnel from the metal through these decoupling layers to the organic molecules and vice versa. This has the great advantage that these systems can still be examined by scanning tunneling microscopy (STM) and spectroscopy (STS), which gives insight into structural and electronic properties of individual molecules. For applications such vertical tunneling through the interfacial layers can be undesirable since it prevents the current from flowing across electrode–molecule–electrode junctions [43] or leads to the charging of physisorbed molecules on top of such layers [18]. Hence, ultrathin insulating layers are often not sufficient to truly electronically insulate molecular structures. For this, the usage of either thicker insulating films (mostly alkali halides) or bulk insulators is required.

For studying molecules on bulk insulators, ionic crystals (e.g., KBr, NaCl, CaF_2, and calcite) have mostly served as model systems. To a lesser extent, metal oxides have also been used, for which defects and charging often pose additional challenges [44-46]. On electronically insulating surfaces, non-contact atomic force microscopy (AFM) is the method of choice to study molecular assemblies and individual molecules in real space. Molecular adsorption and self-assembly are significantly altered compared to metals due to an often weak interaction between organics and bulk insulators. In contrast to face-on adsorption on metals, a tilted and edge-on adsorption becomes possible for planar aromatic molecules on bulk insulators. Due to lowered diffusion barrier and adsorption energy, the two-dimensional molecular layers can be affected by dewetting and may change into three-dimensional clusters [47]. In return, the reduced molecule–surface interaction on insulating films or bulk insulators can stabilize highly reactive molecules, offering unique opportunities for the bottom-up assembly of novel carbon-based materials using on-surface chemistry [48,49]. However, the significantly reduced catalytic activity on non-metallic substrates requires exploring alternative reaction mechanisms beyond thermal activation, for example, photon-induced reactions [46,49-51] or electron-induced reactions by electrons from a probe tip [52,53].

In the following, we would like to highlight a few examples for physical properties and built-in functionalities of molecular systems, which were successfully accessed by employing one of the decoupling strategies mentioned above. Electronic decoupling significantly increases the lifetime of excited molecular states and improves the effective energy resolution (down to a few millielectronvolts) of molecular resonances observed in tunneling spectroscopy since the hybridization of molecular states with the ones of the metallic/semiconducting support is prevented. Thereby, it became feasible to investigate molecular orbitals [17], observe and switch the charge state of individual molecules [54-59], and resolve individual vibronic states in single molecules and molecular assemblies [23,28,60,61]. Similarly, the lack of electronic states around the Fermi level in a superconductor was used to preserve electronic properties in adsorbed molecules. For example, the spin relaxation in magnetic molecules was suppressed on a superconducting surface, which then resulted in a significant enhancement of the excited-state spin lifetimes [62]. Concerning optical properties, successful decoupling made the examination of fluorescence from both single molecules and molecular assemblies feasible by tunneling electron excitation [19,63-66]. Also, sub-molecularly resolved Raman images were successfully demonstrated [67]. Additionally, electroluminescence was reported for suspended molecular wires between a metallic surface and the tip of a scanning tunneling microscope [14]. Moreover, the decoupling brings considerable benefits for surface-supported molecular switches, in particular for preserving reversible switching capabilities [68,69], but also conformational [9,10,70], tautomeric [71], and charge state switching could be shown [56].

This Thematic Issue highlights recent experimental and theoretical developments in realizing and understanding physically and electronically decoupled single molecules and molecular assemblies on surfaces. Several decoupling strategies at the solid–vacuum and solid–liquid interface were explored to elucidate structural, electronic, vibronic, and chemical properties of decoupled molecular structures.

Physical decoupling by molecular design often relies on non-planar adsorbates with bulky spacer groups, which can adopt various conformations. From a theoretical point of view, finding the energetically most stable conformational structure can be challenging and costly because conventional atomistic simulations are often limited to the partial exploration of the potential energy landscape due to the complexity of the system. Recently developed structure search methods that combine machine learning with density functional theory provide the possibility of reliable structure identification of non-planar molecules, as demonstrated for the example of (1*S*)-camphor on Cu(111) [72]. Such computational tools become relevant for molecules with bulky spacer groups since they are very valuable for predicting and interpreting the structural and conformational properties as well as the decoupling of such molecules on surfaces.

With an appropriate molecular design, the built-in functionality of the active part of the molecule can be preserved upon adsorption on a surface. An example of the preservation of catalytic properties is demonstrated for the redox behavior of manganese porphyrins at the solid–liquid interface. Redox reactions at the axial ligands attached to the metal center of the porphyrin were observed regardless of the type of surface (highly oriented pyrolytic graphite (HOPG) and Au surfaces were used), solvent (1-phenyloctane and *n*-tetradecane) and tip material (Pt/Ir, Au, and W), which indicates that the ligands have to be decoupled from the substrates [73].

Suitable functionalization of molecules is another concept to vary their adsorption strength on metal substrates. For instance, partial fluorination of pentacene molecules decreased the adsorption strength on strongly interacting substrates such as Cu [74] but did not result in notable effects on Ag(111) [75]. Although this decoupling concept is only practical on Cu, the fluorination significantly changed the molecular multilayer growth on Ag(111) and led to a physical decoupling with a nearly bulk crystalline structure for the fluorinated pentacene.

Two articles within this Thematic Issue discuss structural templating effects at the solid–liquid interface by systematically looking at the influence of organic decoupling layers. Reynaerts et al. [76] investigated the suitability of long-chain alkanes as physical decoupling layers from a graphite surface. The occurrence of the same polymorphs for 4-tetradecyloxybenzoic acid assemblies in the presence and absence of the long-chain alkane buffer layer indicated that the influence of the substrate could not solely explain the self-assembled structures. However, the alkane buffer layer provided the possibility to monitor the STM-induced nucleation, growth, and ripening of self-assembled monolayers in a more controlled fashion. Söngen et al. [77] provide insight into the interaction of organic molecules with bulk insulators by discussing the adsorption of ethanol on both calcite and magnesite using three-dimensional AFM experiments. Although molecules adsorbed on bulk insulators are electronically decoupled, molecular self-assemblies can experience a substrate templating effect due to the presence of heterogeneous adsorption sites. Therefore, Söngen et al. [77] found on bulk calcite and magnesite that the first ethanol layer arranges in a laterally ordered way due to ionic interactions, where ethanol adopts well-defined adsorption positions on the carbonate surface. In contrast, the following layers lack this order as they reside on ethanol layers. Hence, they experience a physical decoupling due to the changing chemical environment.

Next, we outline articles that use 2D materials and ultrathin dielectric layers as decoupling layers. While on the one hand, molecular functionalization is a powerful approach to tune the electronic and optical properties of 2D materials, in particular for many practical applications [78], 2D materials, on the other hand, offer an alternative way for decoupling molecular structures from metal substrates [24]. 2D van der Waals materials are generally inert and therefore, are potentially well suited for physical decoupling of molecular structures. However, moiré patterns present due to the lattice mismatch between 2D material and its substrate might serve as structural templates for molecular adsorption and self-assembly [79-82]. The electronic decoupling depends on the electronic properties of the 2D materials as they can be insulators, semiconductors, semimetals, or metals [83].

Rothe et al. [84] demonstrated that semimetallic graphene is an appropriate buffer layer for the physical and chemical decoupling of rubrene from Pt(111). The strong molecule–surface interaction on Pt(111) is expressed by hit-and-stick adsorption due to a substantial diffusion barrier. In contrast, on graphene/Pt(111) the growth of molecular domains is facilitated. Electronically, the width of the highest occupied molecular orbital (HOMO) resonance is reduced by a factor of ten on graphene/Pt(111) compared to bare Pt(111) due to a reduction of the molecule–surface hybridization. The significantly reduced resonance width allowed for resolving vibronic states in both frontier orbitals on graphene/Pt(111) by STS.

The semiconducting 2D material MoS_2 may act as a decoupling layer for molecules from the underlying metal substrate if the molecular resonances lie within the MoS_2 bandgap. Hence, Yousofnejad et al. [85] found using MoS_2 on Ag(111) as substrate that the HOMO of tetracyanoquinodimethane (TNCQ) is not decoupled because it is located in the MoS_2 valence band, while the lowest unoccupied molecular orbital narrows but still suffers from lifetime broadening because it is situated at the conduction band onset of MoS_2. Despite this, the vibronic states of the transiently negatively charged TCNQ could be resolved by STS.

*h*BN is an insulator and has therefore been widely used to decouple organic molecules from metal substrates. Three articles within this Thematic Issue successfully employed *h*BN to investigate the pristine properties of particular molecules. Schaal et al. [86] showed that *h*BN on Ni(111) electronically decoupled tetraphenyldibenzoperiflanthene such that the molecular vibronic progression was observable by in situ differential reflectance spectroscopy, which is otherwise only achieved for multilayers on the bare Ni. On *h*BN/Cu(111), Zimmermann et al. [87] could visualize the molecular orbitals of pyrene derivatives by STM at the submolecular level, while Brülke et al. [88] measured the fluorescence of monolayer perylenetetracarboxylic dianhydride (PTCDA), which is quenched on bare Cu(111) and would require three molecular decoupling layers to be probed on Cu(111). In all three studies using *h*BN, ordered molecular films were observed. The decoupling even allowed for the formation of complex self-assemblies such as kagome lattices by tuning the number and position of the substituents of the pyrenes derivatives [87].

Metal oxide thin films on top of metal substrates are another interesting class of ultrathin interfacial layers to decouple organic molecules and to enable the study of their electronic properties without the contribution of the underlying metal substrate. Hurdax et al. reported that both charged and neutral species of sexiphenyl can co-exist on thin dielectric MgO films on Ag(100) [89]. Due to the changed work function of the substrate, charging of the adsorbates is enabled by electron tunneling. The charge transfer strongly influences the molecular conformation by planarizing the carbon backbone as well as the self-assembly. Hurdax et al. [89] suggested that work function measurements before and after the adsorption of molecules should give insight into the electronic and physical decoupling. It should be noted that metal oxide thin films feature heterogeneous adsorption sites, which can lead to the anchoring of organic molecules having specific functional groups. Hence, the interplay of the potential energy landscape of the substrate and the intermolecular interactions steers the self-assembly in such systems. Xiang et al. [90] studied these aspects for the self-assembly of porphyrin derivatives on cobalt oxide films on top of Ir(100). While the unfunctionalized diphenylporphyrin self-assembled on the bilayer film but not on the two-bilayer film, the opposite observation was made for cyanotetraphenylporphyrin.

Physical decoupling of molecules from a semiconducting substrate is discussed for the example of both insulating CaF_2 thin films on Si(111) [91] and hydrogen passivation of Ge(001) surfaces [92]. In the first case, three scenarios were compared: PTCDA on Si, on a thin CaF_2, and on a thicker CaF_2 layer. While isolated PTCDA molecules were pinned to defects on Si and also on the thin CaF_2 layer, PTCDA was physically decoupled via the thicker CaF_2 films and self-assembled into small islands. For FePc on H-passivated Ge(001), efficient physical decoupling facilitated the growth of large islands with upright oriented molecules, similar to their arrangement in molecular crystals.

In summary, the articles collected in this Thematic Issue highlight recent experimental and theoretical developments in the atomic- and molecular-scale understanding of physically and electronically decoupled single molecules and molecular assemblies on surfaces. Over the last decade, significant progress in this field led to a manifold of decoupling strategies for single molecules and surface-supported molecular architectures. Decoupling strategies are highly relevant to preserve the intrinsic structural, electronic, and optical properties of the molecules for performing insightful fundamental surface-science-based studies on them and, thus, play a crucial role in designing new molecule-based electronic and optoelectronic devices.

Sabine Maier and Meike Stöhr

Erlangen and Groningen, July 2021

Acknowledgements

We would like to thank all the authors for their interest in this Thematic Issue and their excellent contributions. We also wish to acknowledge the Beilstein-Institut editorial team for their excellent support and the editorial board for the opportunity to publish this Thematic Issue.

ORCID® iDs

Sabine Maier - https://orcid.org/0000-0001-9589-6855
Meike Stöhr - https://orcid.org/0000-0002-1478-6118

References

1. Elemans, J. A. A. W.; Lei, S.; De Feyter, S. *Angew. Chem., Int. Ed.* **2009,** *48,* 7298–7332. doi:10.1002/anie.200806339
2. Barth, J. V. *Annu. Rev. Phys. Chem.* **2007,** *58,* 375–407. doi:10.1146/annurev.physchem.56.092503.141259
3. Held, P. A.; Fuchs, H.; Studer, A. *Chem. – Eur. J.* **2017,** *23,* 5874–5892. doi:10.1002/chem.201604047
4. Grill, L.; Hecht, S. *Nat. Chem.* **2020,** *12,* 115–130. doi:10.1038/s41557-019-0392-9
5. Clair, S.; de Oteyza, D. G. *Chem. Rev.* **2019,** *119,* 4717–4776. doi:10.1021/acs.chemrev.8b00601
6. Lei, S.; De Feyter, S. *Top. Curr. Chem.* **2008,** *285,* 269–312. doi:10.1007/128_2007_23
7. Langlais, V. J.; Schlittler, R. R.; Tang, H.; Gourdon, A.; Joachim, C.; Gimzewski, J. K. *Phys. Rev. Lett.* **1999,** *83,* 2809–2812. doi:10.1103/physrevlett.83.2809
8. Jung, T. A.; Schlittler, R. R.; Gimzewski, J. K.; Tang, H.; Joachim, C. *Science* **1996,** *271,* 181–184. doi:10.1126/science.271.5246.181
9. Alemani, M.; Peters, M. V.; Hecht, S.; Rieder, K.-H.; Moresco, F.; Grill, L. *J. Am. Chem. Soc.* **2006,** *128,* 14446–14447. doi:10.1021/ja065449s
10. Comstock, M. J.; Levy, N.; Kirakosian, A.; Cho, J.; Lauterwasser, F.; Harvey, J. H.; Strubbe, D. A.; Fréchet, J. M. J.; Trauner, D.; Louie, S. G.; Crommie, M. F. *Phys. Rev. Lett.* **2007,** *99,* 038301. doi:10.1103/physrevlett.99.038301
11. Matino, F.; Schull, G.; Köhler, F.; Gabutti, S.; Mayor, M.; Berndt, R. *Proc. Natl. Acad. Sci. U. S. A.* **2011,** *108,* 961. doi:10.1073/pnas.1006661107
12. Lafferentz, L.; Ample, F.; Yu, H.; Hecht, S.; Joachim, C.; Grill, L. *Science* **2009,** *323,* 1193–1197. doi:10.1126/science.1168255
13. Temirov, R.; Lassise, A.; Anders, F. B.; Tautz, F. S. *Nanotechnology* **2008,** *19,* 065401. doi:10.1088/0957-4484/19/6/065401
14. Reecht, G.; Scheurer, F.; Speisser, V.; Dappe, Y. J.; Mathevet, F.; Schull, G. *Phys. Rev. Lett.* **2014,** *112,* 047403. doi:10.1103/physrevlett.112.047403
15. Reecht, G.; Lotze, C.; Sysoiev, D.; Huhn, T.; Franke, K. J. *ACS Nano* **2016,** *10,* 10555–10562. doi:10.1021/acsnano.6b06559
16. Aradhya, S. V.; Venkataraman, L. *Nat. Nanotechnol.* **2013,** *8,* 399–410. doi:10.1038/nnano.2013.91
17. Repp, J.; Meyer, G.; Stojković, S. M.; Gourdon, A.; Joachim, C. *Phys. Rev. Lett.* **2005,** *94,* 026803. doi:10.1103/physrevlett.94.026803
18. Hollerer, M.; Lüftner, D.; Hurdax, P.; Ules, T.; Soubatch, S.; Tautz, F. S.; Koller, G.; Puschnig, P.; Sterrer, M.; Ramsey, M. G. *ACS Nano* **2017,** *11,* 6252–6260. doi:10.1021/acsnano.7b02449
19. Qiu, X. H.; Nazin, G. V.; Ho, W. *Science* **2003,** *299,* 542. doi:10.1126/science.1078675
20. Yang, X.; Krieger, I.; Lüftner, D.; Weiß, S.; Heepenstrick, T.; Hollerer, M.; Hurdax, P.; Koller, G.; Sokolowski, M.; Puschnig, P.; Ramsey, M. G.; Tautz, F. S.; Soubatch, S. *Chem. Commun.* **2018,** *54,* 9039–9042. doi:10.1039/c8cc03334j
21. Miyamachi, T.; Gruber, M.; Davesne, V.; Bowen, M.; Boukari, S.; Joly, L.; Scheurer, F.; Rogez, G.; Yamada, T. K.; Ohresser, P.; Beaurepaire, E.; Wulfhekel, W. *Nat. Commun.* **2012,** *3,* 938. doi:10.1038/ncomms1940
22. Auwärter, W. *Surf. Sci. Rep.* **2019,** *74,* 1–95. doi:10.1016/j.surfrep.2018.10.001
23. Schulz, F.; Drost, R.; Hämäläinen, S. K.; Liljeroth, P. *ACS Nano* **2013,** *7,* 11121–11128. doi:10.1021/nn404840h
24. Kumar, A.; Banerjee, K.; Liljeroth, P. *Nanotechnology* **2017,** *28,* 082001. doi:10.1088/1361-6528/aa564f
25. MacLeod, J. M.; Rosei, F. *Small* **2014,** *10,* 1038–1049. doi:10.1002/smll.201301982
26. Kong, L.; Enders, A.; Rahman, T. S.; Dowben, P. A. *J. Phys.: Condens. Matter* **2014,** *26,* 443001. doi:10.1088/0953-8984/26/44/443001
27. Riss, A.; Wickenburg, S.; Tan, L. Z.; Tsai, H.-Z.; Kim, Y.; Lu, J.; Bradley, A. J.; Ugeda, M. M.; Meaker, K. L.; Watanabe, K.; Taniguchi, T.; Zettl, A.; Fischer, F. R.; Louie, S. G.; Crommie, M. F. *ACS Nano* **2014,** *8,* 5395–5401. doi:10.1021/nn501459v
28. Krane, N.; Lotze, C.; Reecht, G.; Zhang, L.; Briseno, A. L.; Franke, K. J. *ACS Nano* **2018,** *12,* 11698–11703. doi:10.1021/acsnano.8b07414
29. Forker, R.; Kasemann, D.; Dienel, T.; Wagner, C.; Franke, R.; Müllen, K.; Fritz, T. *Adv. Mater. (Weinheim, Ger.)* **2008,** *20,* 4450–4454. doi:10.1002/adma.200801112
30. Wang, Q.; Franco-Cañellas, A.; Ji, P.; Bürker, C.; Wang, R.-B.; Broch, K.; Thakur, P. K.; Lee, T.-L.; Zhang, H.; Gerlach, A.; Chi, L.; Duhm, S.; Schreiber, F. *J. Phys. Chem. C* **2018,** *122,* 9480–9490. doi:10.1021/acs.jpcc.8b01529
31. Franke, K. J.; Schulze, G.; Henningsen, N.; Fernández-Torrente, I.; Pascual, J. I.; Zarwell, S.; Rück-Braun, K.; Cobian, M.; Lorente, N. *Phys. Rev. Lett.* **2008,** *100,* 036807. doi:10.1103/physrevlett.100.036807
32. Liu, Z.; Sun, K.; Li, X.; Li, L.; Zhang, H.; Chi, L. *J. Phys. Chem. Lett.* **2019,** *10,* 4297–4302. doi:10.1021/acs.jpclett.9b01167
33. Rastgoo-Lahrood, A.; Björk, J.; Lischka, M.; Eichhorn, J.; Kloft, S.; Fritton, M.; Strunskus, T.; Samanta, D.; Schmittel, M.; Heckl, W. M.; Lackinger, M. *Angew. Chem., Int. Ed.* **2016,** *55,* 7650–7654. doi:10.1002/anie.201600684
34. Duverger, E.; Boyer, A.-G.; Sauriat-Dorizon, H.; Sonnet, P.; Stephan, R.; Hanf, M.-C.; Riedel, D. *ACS Appl. Mater. Interfaces* **2020,** *12,* 29661–29670. doi:10.1021/acsami.0c06631
35. Chiaravalloti, F.; Dujardin, G.; Riedel, D. *J. Phys.: Condens. Matter* **2015,** *27,* 054006. doi:10.1088/0953-8984/27/5/054006
36. Bellec, A.; Ample, F.; Riedel, D.; Dujardin, G.; Joachim, C. *Nano Lett.* **2009,** *9,* 144–147. doi:10.1021/nl802688g

37. Godlewski, S.; Kolmer, M.; Kawai, H.; Such, B.; Zuzak, R.; Saeys, M.; de Mendoza, P.; Echavarren, A. M.; Joachim, C.; Szymonski, M. *ACS Nano* **2013,** *7,* 10105–10111. doi:10.1021/nn404254y
38. Uder, B.; Ludwig, C.; Petersen, J.; Gompf, B.; Eisenmenger, W. *Z. Phys. B: Condens. Matter* **1995,** *97,* 389–390. doi:10.1007/bf01317220
39. Gruyters, M.; Pingel, T.; Gopakumar, T. G.; Néel, N.; Schütt, C.; Köhler, F.; Herges, R.; Berndt, R. *J. Phys. Chem. C* **2012,** *116,* 20882–20886. doi:10.1021/jp3058433
40. Lyo, I.-W.; Kaxiras, E.; Avouris, P. *Phys. Rev. Lett.* **1989,** *63,* 1261–1264. doi:10.1103/physrevlett.63.1261
41. Makoudi, Y.; Palmino, F.; Duverger, E.; Arab, M.; Chérioux, F.; Ramseyer, C.; Therrien, B.; Tschan, M. J.-L.; Süss-Fink, G. *Phys. Rev. Lett.* **2008,** *100,* 076405. doi:10.1103/physrevlett.100.076405
42. Vilan, A.; Cahen, D. *Chem. Rev.* **2017,** *117,* 4624–4666. doi:10.1021/acs.chemrev.6b00746
43. Bombis, C.; Ample, F.; Lafferentz, L.; Yu, H.; Hecht, S.; Joachim, C.; Grill, L. *Angew. Chem., Int. Ed.* **2009,** *48,* 9966–9970. doi:10.1002/anie.200904645
44. Hoffmann-Vogel, R. *Rep. Prog. Phys.* **2018,** *81,* 016501. doi:10.1088/1361-6633/aa8fda
45. Rahe, P.; Kittelmann, M.; Neff, J. L.; Nimmrich, M.; Reichling, M.; Maass, P.; Kühnle, A. *Adv. Mater. (Weinheim, Ger.)* **2013,** *25,* 3948–3956. doi:10.1002/adma.201300604
46. Richter, A.; Floris, A.; Bechstein, R.; Kantorovich, L.; Kühnle, A. *J. Phys.: Condens. Matter* **2018,** *30,* 133001. doi:10.1088/1361-648x/aab0b9
47. Burke, S. A.; Topple, J. M.; Grütter, P. *J. Phys.: Condens. Matter* **2009,** *21,* 423101. doi:10.1088/0953-8984/21/42/423101
48. Kaiser, K.; Scriven, L. M.; Schulz, F.; Gawel, P.; Gross, L.; Anderson, H. L. *Science* **2019,** *365,* 1299–1301. doi:10.1126/science.aay1914
49. Para, F.; Bocquet, F.; Nony, L.; Loppacher, C.; Féron, M.; Cherioux, F.; Gao, D. Z.; Federici Canova, F.; Watkins, M. B. *Nat. Chem.* **2018,** *10,* 1112–1117. doi:10.1038/s41557-018-0120-x
50. Palmino, F.; Loppacher, C.; Chérioux, F. *ChemPhysChem* **2019,** *20,* 2271–2280. doi:10.1002/cphc.201900312
51. Lindner, R.; Rahe, P.; Kittelmann, M.; Gourdon, A.; Bechstein, R.; Kühnle, A. *Angew. Chem., Int. Ed.* **2014,** *53,* 7952–7955. doi:10.1002/anie.201309128
52. Pavliček, N.; Gross, L. *Nat. Rev. Chem.* **2017,** *1,* 0005. doi:10.1038/s41570-016-0005
53. Gross, L.; Schuler, B.; Pavliček, N.; Fatayer, S.; Majzik, Z.; Moll, N.; Peña, D.; Meyer, G. *Angew. Chem., Int. Ed.* **2018,** *57,* 3888–3908. doi:10.1002/anie.201703509
54. Wu, S. W.; Ogawa, N.; Ho, W. *Science* **2006,** *312,* 1362. doi:10.1126/science.1124881
55. Swart, I.; Sonnleitner, T.; Repp, J. *Nano Lett.* **2011,** *11,* 1580–1584. doi:10.1021/nl104452x
56. Fatayer, S.; Albrecht, F.; Zhang, Y.; Urbonas, D.; Peña, D.; Moll, N.; Gross, L. *Science* **2019,** *365,* 142. doi:10.1126/science.aax5895
57. Patera, L. L.; Queck, F.; Scheuerer, P.; Repp, J. *Nature* **2019,** *566,* 245–248. doi:10.1038/s41586-019-0910-3
58. Heim, T.; Lmimouni, K.; Vuillaume, D. *Nano Lett.* **2004,** *4,* 2145–2150. doi:10.1021/nl0487673
59. Rahe, P.; Steele, R. P.; Williams, C. C. *Nano Lett.* **2016,** *16,* 911–916. doi:10.1021/acs.nanolett.5b03725
60. Qiu, X. H.; Nazin, G. V.; Ho, W. *Phys. Rev. Lett.* **2004,** *92,* 206102. doi:10.1103/physrevlett.92.206102
61. Mehler, A.; Néel, N.; Kröger, J. *J. Phys. Chem. Lett.* **2020,** *11,* 5204–5211. doi:10.1021/acs.jpclett.0c01320
62. Heinrich, B. W.; Braun, L.; Pascual, J. I.; Franke, K. J. *Nat. Phys.* **2013,** *9,* 765–768. doi:10.1038/nphys2794
63. Ćavar, E.; Blüm, M.-C.; Pivetta, M.; Patthey, F.; Chergui, M.; Schneider, W.-D. *Phys. Rev. Lett.* **2005,** *95,* 196102. doi:10.1103/physrevlett.95.196102
64. Zhu, S.-E.; Kuang, Y.-M.; Geng, F.; Zhu, J.-Z.; Wang, C.-Z.; Yu, Y.-J.; Luo, Y.; Xiao, Y.; Liu, K.-Q.; Meng, Q.-S.; Zhang, L.; Jiang, S.; Zhang, Y.; Wang, G.-W.; Dong, Z.-C.; Hou, J. G. *J. Am. Chem. Soc.* **2013,** *135,* 15794–15800. doi:10.1021/ja4048569
65. Chen, C.; Chu, P.; Bobisch, C. A.; Mills, D. L.; Ho, W. *Phys. Rev. Lett.* **2010,** *105,* 217402. doi:10.1103/physrevlett.105.217402
66. Kabakchiev, A.; Kuhnke, K.; Lutz, T.; Kern, K. *ChemPhysChem* **2010,** *11,* 3412–3416. doi:10.1002/cphc.201000531
67. Jaculbia, R. B.; Imada, H.; Miwa, K.; Iwasa, T.; Takenaka, M.; Yang, B.; Kazuma, E.; Hayazawa, N.; Taketsugu, T.; Kim, Y. *Nat. Nanotechnol.* **2020,** *15,* 105–110. doi:10.1038/s41565-019-0614-8
68. Zhang, J. L.; Zhong, J. Q.; Lin, J. D.; Hu, W. P.; Wu, K.; Xu, G. Q.; Wee, A. T. S.; Chen, W. *Chem. Soc. Rev.* **2015,** *44,* 2998–3022. doi:10.1039/c4cs00377b
69. van der Molen, S. J.; Liljeroth, P. *J. Phys.: Condens. Matter* **2010,** *22,* 133001. doi:10.1088/0953-8984/22/13/133001
70. Qiu, X. H.; Nazin, G. V.; Ho, W. *Phys. Rev. Lett.* **2004,** *93,* 196806. doi:10.1103/physrevlett.93.196806
71. Liljeroth, P.; Repp, J.; Meyer, G. *Science* **2007,** *317,* 1203. doi:10.1126/science.1144366
72. Järvi, J.; Rinke, P.; Todorović, M. *Beilstein J. Nanotechnol.* **2020,** *11,* 1577–1589. doi:10.3762/bjnano.11.140
73. Habets, T.; Speller, S.; Elemans, J. A. A. W. *Beilstein J. Nanotechnol.* **2020,** *11,* 1264–1271. doi:10.3762/bjnano.11.110
74. Koch, N.; Gerlach, A.; Duhm, S.; Glowatzki, H.; Heimel, G.; Vollmer, A.; Sakamoto, Y.; Suzuki, T.; Zegenhagen, J.; Rabe, J. P.; Schreiber, F. *J. Am. Chem. Soc.* **2008,** *130,* 7300–7304. doi:10.1021/ja800286k
75. Wang, Q.; Chen, M.-T.; Franco-Cañellas, A.; Shen, B.; Geiger, T.; Bettinger, H. F.; Schreiber, F.; Salzmann, I.; Gerlach, A.; Duhm, S. *Beilstein J. Nanotechnol.* **2020,** *11,* 1361–1370. doi:10.3762/bjnano.11.120
76. Reynaerts, R.; Mali, K. S.; De Feyter, S. *Beilstein J. Nanotechnol.* **2020,** *11,* 1291–1302. doi:10.3762/bjnano.11.113
77. Söngen, H.; Jaques, Y. M.; Spijker, P.; Marutschke, C.; Klassen, S.; Hermes, I.; Bechstein, R.; Zivanovic, L.; Tracey, J.; Foster, A. S.; Kühnle, A. *Beilstein J. Nanotechnol.* **2020,** *11,* 891–898. doi:10.3762/bjnano.11.74
78. Daukiya, L.; Seibel, J.; De Feyter, S. *Adv. Phys.: X* **2019,** *4,* 1625723. doi:10.1080/23746149.2019.1625723
79. Cui, X.; Troadec, C.; Wee, A. T. S.; Huang, Y. L. *ACS Omega* **2018,** *3,* 3285–3293. doi:10.1021/acsomega.8b00014
80. Zhang, H. G.; Sun, J. T.; Low, T.; Zhang, L. Z.; Pan, Y.; Liu, Q.; Mao, J. H.; Zhou, H. T.; Guo, H. M.; Du, S. X.; Guinea, F.; Gao, H.-J. *Phys. Rev. B* **2011,** *84,* 245436. doi:10.1103/physrevb.84.245436
81. Mao, J.; Zhang, H.; Jiang, Y.; Pan, Y.; Gao, M.; Xiao, W.; Gao, H.-J. *J. Am. Chem. Soc.* **2009,** *131,* 14136–14137. doi:10.1021/ja904907z
82. Maccariello, D.; Garnica, M.; Niño, M. A.; Navío, C.; Perna, P.; Barja, S.; Vázquez de Parga, A. L.; Miranda, R. *Chem. Mater.* **2014,** *26,* 2883–2890. doi:10.1021/cm5005467
83. Miró, P.; Audiffred, M.; Heine, T. *Chem. Soc. Rev.* **2014,** *43,* 6537–6554. doi:10.1039/c4cs00102h
84. Rothe, K.; Mehler, A.; Néel, N.; Kröger, J. *Beilstein J. Nanotechnol.* **2020,** *11,* 1157–1167. doi:10.3762/bjnano.11.100

85. Yousofnejad, A.; Reecht, G.; Krane, N.; Lotze, C.; Franke, K. J. *Beilstein J. Nanotechnol.* **2020,** *11,* 1062–1071. doi:10.3762/bjnano.11.91
86. Schaal, M.; Aihara, T.; Gruenewald, M.; Otto, F.; Domke, J.; Forker, R.; Yoshida, H.; Fritz, T. *Beilstein J. Nanotechnol.* **2020,** *11,* 1168–1177. doi:10.3762/bjnano.11.101
87. Zimmermann, D. M.; Seufert, K.; Đorđević, L.; Hoh, T.; Joshi, S.; Marangoni, T.; Bonifazi, D.; Auwärter, W. *Beilstein J. Nanotechnol.* **2020,** *11,* 1470–1483. doi:10.3762/bjnano.11.130
88. Brülke, C.; Bauer, O.; Sokolowski, M. M. *Beilstein J. Nanotechnol.* **2020,** *11,* 1663–1684. doi:10.3762/bjnano.11.149
89. Hurdax, P.; Hollerer, M.; Egger, L.; Koller, G.; Yang, X.; Haags, A.; Soubatch, S.; Tautz, F. S.; Richter, M.; Gottwald, A.; Puschnig, P.; Sterrer, M.; Ramsey, M. G. *Beilstein J. Nanotechnol.* **2020,** *11,* 1492–1503. doi:10.3762/bjnano.11.132
90. Xiang, F.; Schmitt, T.; Raschmann, M.; Schneider, M. A. *Beilstein J. Nanotechnol.* **2020,** *11,* 1516–1524. doi:10.3762/bjnano.11.134
91. Rahe, P. *Beilstein J. Nanotechnol.* **2020,** *11,* 1615–1622. doi:10.3762/bjnano.11.144
92. Zuzak, R.; Szymonski, M.; Godlewski, S. *Beilstein J. Nanotechnol.* **2021,** *12,* 232–241. doi:10.3762/bjnano.12.19

License and Terms

BEILSTEIN JOURNAL OF NANOTECHNOLOGY

Three-dimensional solvation structure of ethanol on carbonate minerals

Hagen Söngen[1,2,3], Ygor Morais Jaques[4], Peter Spijker[4], Christoph Marutschke[2], Stefanie Klassen[2], Ilka Hermes[2], Ralf Bechstein[1,2], Lidija Zivanovic[4], John Tracey[4], Adam S. Foster[3,4,5] and Angelika Kühnle*[1,2,3]

Full Research Paper

Open Access

Address:
[1]Physical Chemistry I, Faculty of Chemistry, Bielefeld University, Universitätsstraße 25, 33615 Bielefeld, Germany, [2]Institute of Physical Chemistry, Johannes Gutenberg University Mainz, Duesbergweg 10 - 14, 55099 Mainz, Germany, [3]Graduate School Materials Science in Mainz, Staudingerweg 9, 55128 Mainz, Germany, [4]Department of Applied Physics, Aalto University, Helsinki FI-00076, Finland and [5]WPI Nano Life Science Institute (WPI-NanoLSI), Kanazawa University, Kakumamachi, Kanazawa 920-1192, Japan

Email:
Angelika Kühnle* - kuehnle@uni-bielefeld.de

* Corresponding author

Keywords:
3D AFM; calcite; ethanol; magnesite; MD simulation; solvation structure

Beilstein J. Nanotechnol. **2020,** *11,* 891–898.
doi:10.3762/bjnano.11.74

Received: 13 March 2020
Accepted: 13 May 2020
Published: 10 June 2020

This article is part of the thematic issue "Molecular assemblies on surfaces – towards physical and electronic decoupling of organic molecules".

Guest Editor: S. Maier

Abstract

Calcite and magnesite are important mineral constituents of the earth's crust. In aqueous environments, these carbonates typically expose their most stable cleavage plane, the (10.4) surface. It is known that these surfaces interact with a large variety of organic molecules, which can result in surface restructuring. This process is decisive for the formation of biominerals. With the development of 3D atomic force microscopy (AFM) it is now possible to image solid–liquid interfaces with unprecedented molecular resolution. However, the majority of 3D AFM studies have been focused on the arrangement of water at carbonate surfaces. Here, we present an analysis of the assembly of ethanol – an organic molecule with a single hydroxy group – at the calcite and magnesite (10.4) surfaces by using high-resolution 3D AFM and molecular dynamics (MD) simulations. Within a single AFM data set we are able to resolve both the first laterally ordered solvation layer of ethanol on the calcite surface as well as the following solvation layers that show no lateral order. Our experimental results are in excellent agreement with MD simulations. The qualitative difference in the lateral order can be understood by the differing chemical environment: While the first layer adopts specific binding positions on the ionic carbonate surface, the second layer resides on top of the organic ethyl layer. A comparison of calcite and magnesite reveals a qualitatively similar ethanol arrangement on both carbonates, indicating the general nature of this finding.

Introduction

Sedimentary rocks including the minerals calcite and magnesite are abundant constituents of the earth's crust and their interaction with the environment is relevant for a wide range of geological processes, such as dissolution and weathering. Moreover, calcite plays a prominent role in many industrial processes, for example, incrustation inhibition and desalination. As any interaction between a mineral and its environment takes place at the interface, the interfacial structure is of fundamental importance for gaining molecular-level understanding of the mineral reactivity. In the presence of water, the hydration structure at the interface needs to be known. With the advent of high-resolution 3D atomic force microscopy (AFM) [1], the hydration structure of many interfaces has been studied, including the aqueous interface of mica [2] calcite [3,4] dolomite [5,6] and organic crystals [7]. However, while the majority of 3D AFM works have concentrated on water, comparatively fewer experimental studies exist addressing the interfacial arrangement of other solvent molecules [8-10]. This is unfortunate given the relevance of the interaction between organic molecules and carbonate surfaces, for example, in the field of biomineralization [11]. Moreover, by changing the solvent molecule, fundamental understanding can be gained when comparing the influence of systematically changed functional groups. Here, we focus on the arrangement of ethanol molecules as they have an OH group in common with water but differ in their properties due to their hydrocarbon chain.

The calcite–ethanol interface has been investigated theoretically by using both density functional theory (DFT) [12,13] and molecular dynamics (MD) simulations [14-17]. It has been found that ethanol molecules strongly bind towards calcite (10.4) terraces – even stronger than water [12,14,16,17]. Ethanol molecules bind towards calcite with their hydroxy group placed in between a surface calcium ion and a surface carbonate: The oxygen of the hydroxy group binds towards a calcium ion, while the hydrogen of the hydroxy group binds towards a carbonate group, which is similar to the bonding configuration of an isolated ethanol molecule on calcite obtained with DFT calculations [13]. Consequently, the hydrocarbon chains of the ethanol molecules point away from the surface. This results in one ethanol molecule per $CaCO_3$ at the calcite (10.4) surface. The ordered first layer of ethanol molecules above the calcite surface is followed by a region of low ethanol density, which has been referred to as a gap [15,17]. Beyond the gap, ethanol again arranges in vertical layers with a vertical distance of approximately 0.5 nm. In contrast to the first layer, however, it has been calculated that both the lateral order and the orientational order of the ethanol molecules in the upper layers is significantly less pronounced. Thus, these theoretical studies predict that ethanol molecules at the calcite interface exhibit very different binding configurations depending in which layer they are.

Only isolated aspects of the above-mentioned theoretical studies have been confirmed experimentally. With lateral AFM images, the calcite (10.4) surface has been laterally resolved in ethanol at the atomic scale [18]. The observed periodicity matched the surface unit cell dimensions. However, from lateral AFM images it is not straightforward to determine at which vertical distance the tip was scanned above the surface. Therefore, it remains unclear whether the observed lateral structure corresponds to the first ordered layer of ethanol on calcite or the calcite surface itself.

The vertical structure of ethanol on calcite has been investigated in a combined X-ray reflectivity and MD study [15]. As a result, ethanol was found to form layers above the calcite surface. However, due to the lack of lateral resolution in the X-ray reflectivity measurements, no experimental information on the lateral order within the first layer has been obtained to date. Furthermore, no information on the interfacial orientation and binding configuration has been collected experimentally.

Here, we report on high-resolution 3D AFM data that reveals both the lateral and the vertical solvation structure at the calcite–ethanol interface in a single data set. By comparison with existing literature and MD simulations, we can assign the single laterally ordered layer to the first solvation layer. This first layer is fundamentally different from the following layers as the ethanol molecules adopt specific adsorption positions on the carbonate surface. In contrast, the second layer then resides on top of the less well-defined layer of ethyl groups. For the magnesite–ethanol interface, we find a remarkably similar solvation structure as for the calcite–ethanol interface in both the AFM data and the MD simulations. This latter result confirms the general nature of our findings.

Results and Discussion

AFM results

A vertical slice of the frequency shift ($\Delta\nu_{\mathrm{exc}}$) obtained at the calcite (10.4)–ethanol interface is shown in Figure 1a. The average over all data shown in the slice is given as a vertical profile (i.e., as function of the z-piezo displacement z_{p}) in Figure 1b. The corresponding data for the magnesite-ethanol interface is shown in a similar fashion in the second row of Figure 1 (panels c and d).

In both cases, the frequency shift exhibits local minima and maxima. Close to the surface (at the bottom), laterally alternating local maxima with a periodicity of approximately 0.3 nm

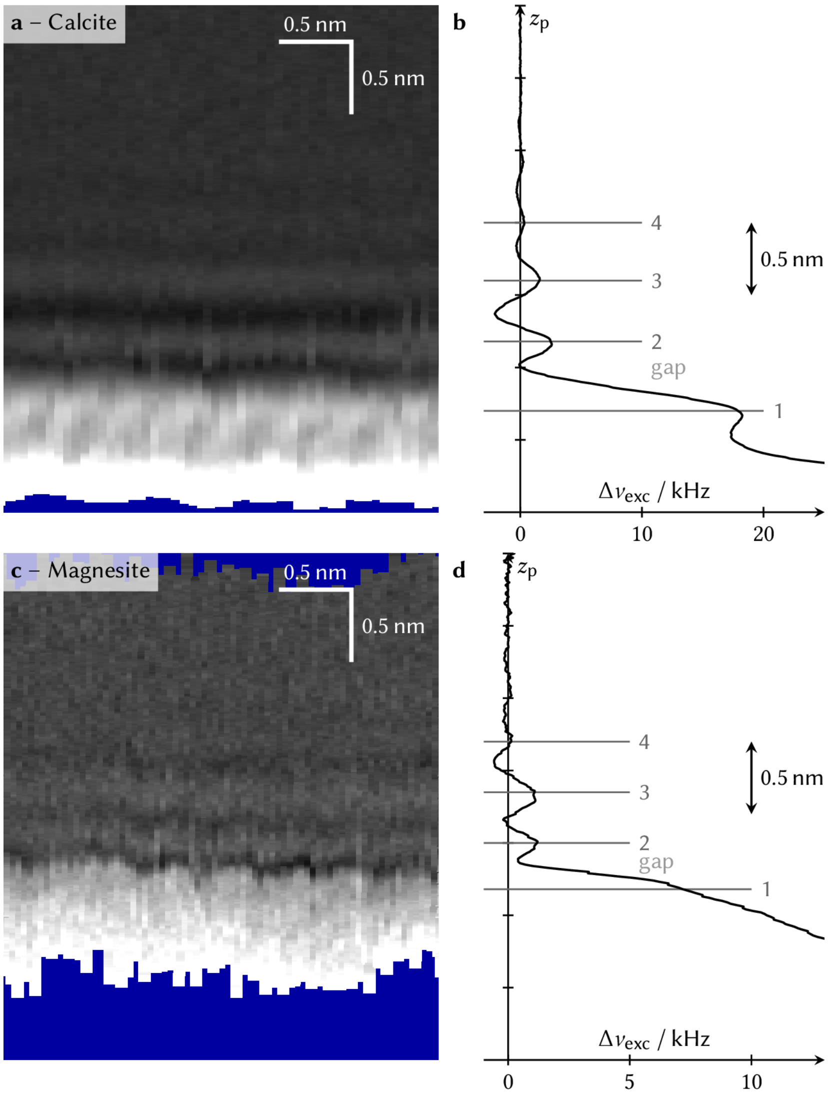

Figure 1: Vertical slice of the frequency shift at the calcite–ethanol interface (a) and at the magnesite–ethanol interface (c). The graphs on the right (b) and (d) show the average of all profiles shown in the slice. In all cases, the frequency is shown as a function of the *z*-piezo displacement z_p. The black/white color scale ranges from approximately −5 kHz to 27 kHz for calcite and from approximately −5 kHz to 15 kHz for magnesite. The vertical scale bar in (a) and (c) equally applies to the profiles in (b) and (d).

can be observed. Note that due to lateral drift, it is not possible to quantify the lateral distance of the first-layer ethanol molecules with a precision that would allow discrimination between the different surface unit cell sizes of calcite and magnesite. Nevertheless, it appears very reasonable to assign this lateral structure to the ordered first layer of ethanol molecules. We note that the data of calcite and magnesite differ slightly when the tip is closer to the surface than the gap. While in the case of calcite a clear maximum (labelled 1 in Figure 1) is seen, the same feature appears to be a saddle point rather than a maximum in the case of magnesite. At this short tip–sample distance, the solvent–tip approximation [19,20] alone cannot explain the data, but instead the chemical nature and macroscopic shape of the tip plays a crucial role. Hence, the observed difference is likely due to the different tips used in the experiments.

The experimental data shows further layers above the first layer. In sharp contrast to the first layer, no lateral structure is visible in the upper layers. A precise determination of the absolute distances of the layers requires a precise calibration of the *z*-piezo movement, which is lacking for the presented data set. However, the comparison with previous images containing step edges allows determination of the vertical layer-to-layer distances that are in the order of 0.5 nm. This experimentally obtained layer-to-layer distance is in good agreement with the above-cited previous calculations of ethanol interfaces.

Moreover, observing no order in the upper layers fits well to the MD simulations from previous theoretical studies, which do not indicate significant lateral order in the layers above the first layer for the calcite–ethanol interface [14-17]. This finding is similar to what has been observed before for the solvation structure of 2-propanol on calcite (10.4) [3]. Also, for the latter work, lateral order was observed in the first layer only. Comparing the results obtained on calcite and magnesite reveals some minor differences that are within the variations typically seen for different tips. Thus, our experimental findings suggest these findings to be equally valid for the magnesite–ethanol interface.

MD simulation results

To allow for consistent comparisons between our experimental data and simulations, we performed MD simulations of both the calcite–ethanol and the magnesite–ethanol interface. In Figure 2 we present vertical slices and density profiles of both the calcite–ethanol (Figure 2a and 2b) and the magnesite–ethanol (Figure 2c and 2d) interface showing the atomic positions of the ethanol molecules throughout the production run of the simulation.

In the graphs in Figure 2b and 2d, the atomic number density profiles for ethanol–carbon, hydroxy–oxygen and

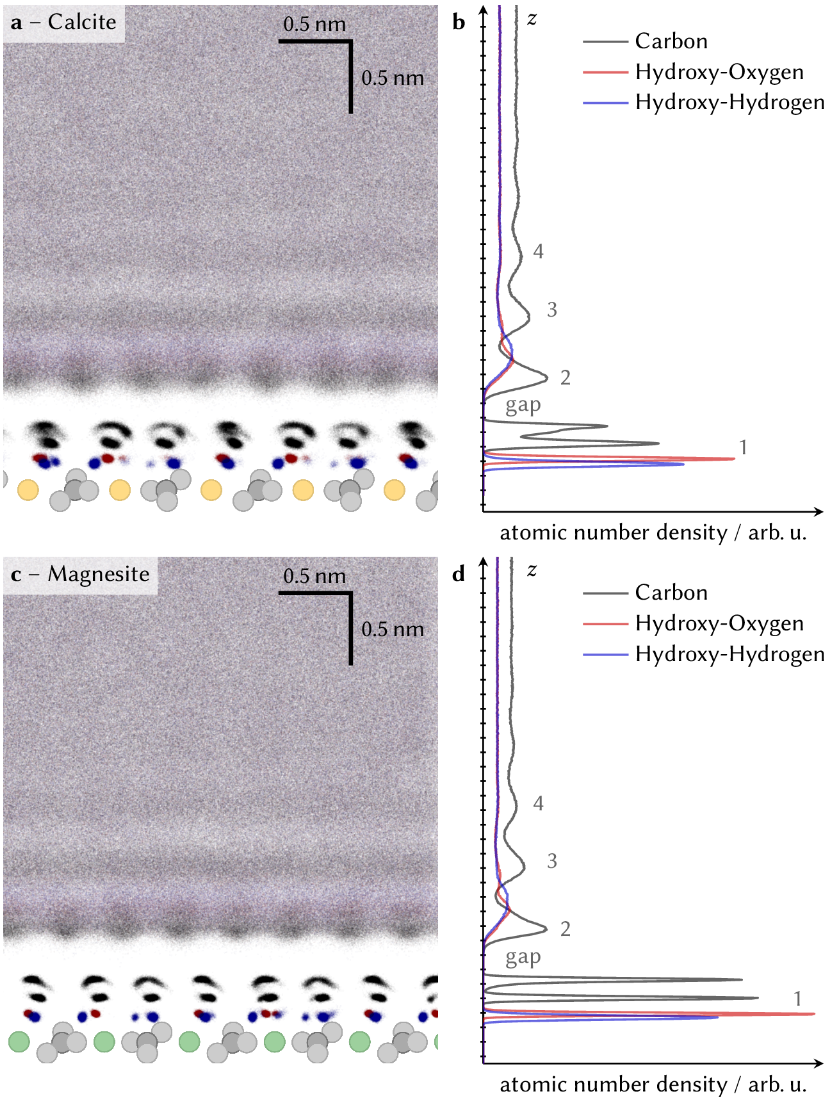

Figure 2: Vertical slices showing the atomic positions of ethanol–carbon (black), hydroxy–oxygen (red) and hydroxy–hydrogen (blue) at the (a) calcite–ethanol and (c) magnesite–ethanol interface. The graphs were created by drawing a semi-transparent dot for each atom at each time step of the simulation. The surfaces are represented by the carbonate groups (grey) and calcium (yellow) and magnesium (green) spheres, respectively. (b and d) Corresponding averaged density profiles are shown in the graphs to the right.

hydroxy–hydrogen atoms averaged from the data presented in the slice are shown. The density maxima for the hydroxy atoms directly above the surface (at small z) indicate that the hydroxy group is oriented with the hydrogen towards the surface. The two distinguishable peaks for the carbon atoms following at larger distance from the surface show that the hydrocarbon chains of the molecules are all aligned perpendicular to the surface, pointing away from it. All atomic number density profiles show a pronounced minimum after this first layer of ethanol molecules on top of the calcite surface, the so-called "gap". At larger distances from the surface, a second solvation layer can be identified by a peak in each of the atomic number density profiles. All three peaks in the second layer (carbon, oxygen, hydrogen) are significantly broader compared to the first layer. In sharp contrast to the first solvation layer, where the hydroxy group is oriented towards the surface, ethanol in the second layer shows only a very weak orientational preference (there is a slight preference for the OH to point away from the surface).

Even broader peaks can be recognized in the profiles at larger distances from the surface, which is indicative of a faint third, fourth, etc. layer. From the MD simulation, we obtain a layer-to-layer distance of approximately 0.5 nm, which fits well with the experimental AFM data.

To further investigate the lateral order in the first layer, we show the lateral hydroxy–oxygen density within the first solvation layer, superimposed on a lateral view of the calcite and magnesite surfaces in Figure 3. The hydrogen and oxygen positions at the calcite–ethanol interface are given in Figure 3a,

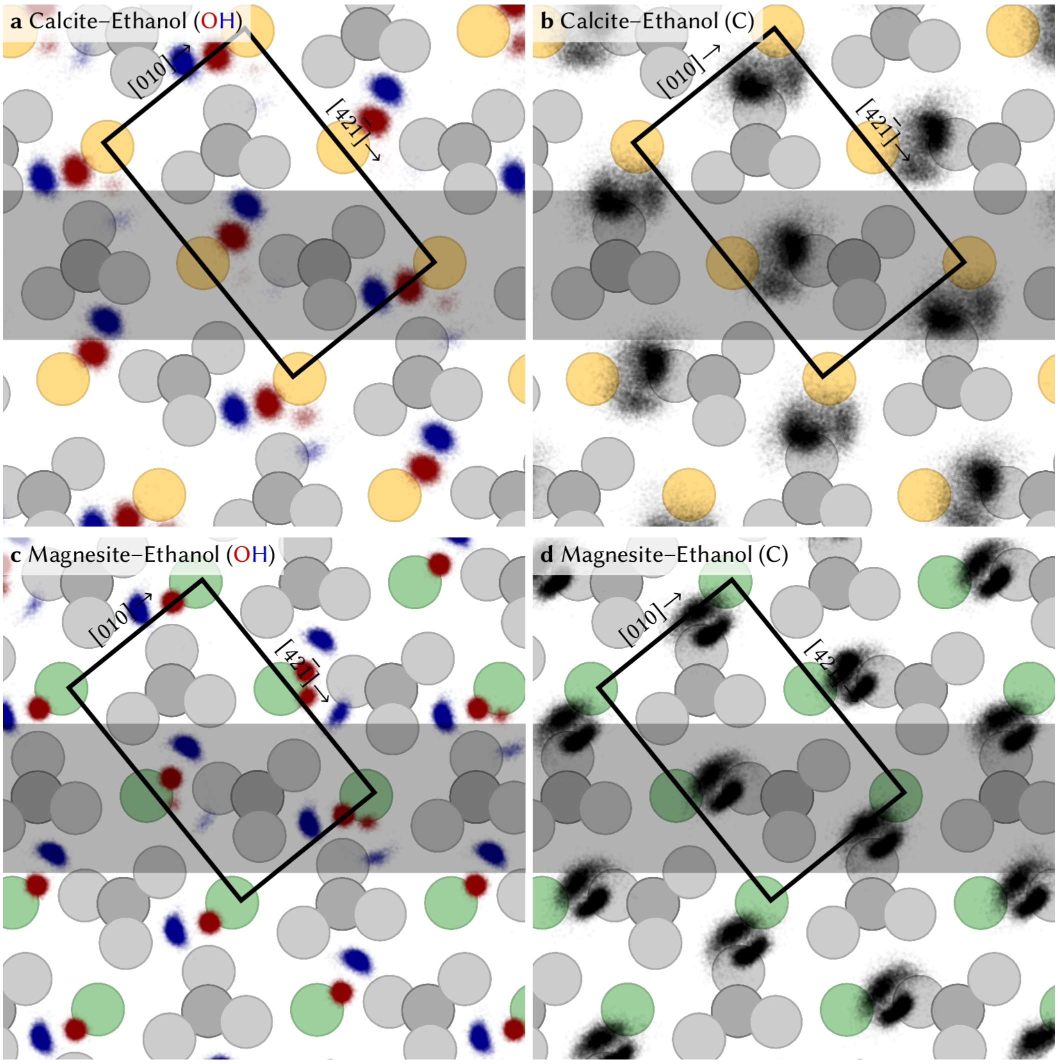

Figure 3: Top view showing the position of all hydroxy–oxygen (red) and hydroxy–hydrogen (blue) atoms on (a) calcite and (c) magnesite as well as the position of all carbon atoms (black) of ethanol molecules within the first layer on (b) calcite and (d) magnesite in each simulation time step. The grey overlay indicates the area used for the vertical slice in Figure 2. The positions of the surface atoms are indicated by grey, yellow and green spheres, representing atoms from the carbonate groups, as well as calcium and magnesium atoms, respectively.

while the positions of all carbon atoms in the first layer are shown in Figure 3b. The respective information for the magnesite–ethanol interface is presented in Figure 3c and Figure 3d. The OH-oxygen is preferably located in between a calcium and a carbonate ion. This is in accordance with the previous MD simulations [14-17], which have shown that ethanol arranges in a ordered first layer above calcite, where one ethanol molecule binds towards one $CaCO_3$ unit. The oxygen is closer to the cation (Ca/Mg) and the hydrogen creates a hydrogen bond with a protruding oxygen of a carbonate group. During the time of the simulation (10 ns), all ethanol molecules in the first layer exhibit a highly confined lateral position, which fits to the observed lateral order. In rare cases, we observed that some of the hydrogens from the OH group switch the hydrogen bond back and forth to a neighboring carbonate group within a very similar distance during the simulation run, which we further discuss in Supporting Information File 1.

To compare the MD simulations with the AFM data, we use the well-established “solvent–tip approximation” [19,20]. We note that it is relevant to discuss whether this approximation holds true for ethanol as well. However, in this work, we assume that a single ethanol molecule probes the solvation structure. In this model, the frequency shift modulation is approximately proportional to the solvent density. This model has worked well in previous works with the solvent water [10], even in the case of defects [21].

There is excellent qualitative agreement between the experimentally obtained frequency shift data (Figure 1) and the atomic density data from the MD simulations (Figure 2). The AFM data confirms the laterally alternating minima and maxima within the first layer and the oscillatory vertical density profile predicted by the MD simulations.

Conclusion

We combined high-resolution 3D AFM with MD simulations to characterize the solvation structure of ethanol above calcite and magnesite (10.4) surfaces. For the calcite surface, our high-resolution AFM data revealed a layered structure. In the first layer, a lateral structure is visible in the data. The layers above the first layer, however, do not show any lateral structure.

Therefore, the experimental data indicate that ethanol molecules form a single laterally ordered layer directly above the calcite surface, which fits perfectly to the MD simulation data. This finding can be understood by the different chemical environment. While the first layer adopts well-defined adsorption positions on the carbonate surface, the following layers only reside on ethanol layers with clear consequences for the lateral order. For a structurally very similar system, namely the magnesite–ethanol system, we find that both the AFM data as well as the MD data are similar to the calcite data. This latter result indicates that the finding made here is of general nature.

Experimental and Theoretical Methods

Atomic force microscopy

For the AFM experiments we used a modified commercial atomic force microscope [22] with custom photothermal cantilever excitation [23] and a custom three-dimensional scanning and data acquisition mode [24] in the frequency-modulation mode [25]. The quantities given in this work are labelled as introduced in [26]. After cleaving calcite (Korth Kristalle, Germany) and magnesite (SurfaceNet, Germany) in air, ethanol (Sigma Aldrich, article number 32205, purity ≥ 99.8%) was injected in the liquid cell. Since the ethanol was exposed to air during the measurement, it constantly evaporates, making it necessary to repeatedly inject ethanol during a measurement session. Cantilevers of type TAP300 GB-G were used. The acquisition time for each vertical slice (trace and retrace) of a 3D map was 10 s and the frequency of the (approach and retract) z-modulation was 10 Hz, corresponding to 50 approach and 50 retract curves per vertical slice. For typical operation parameters, we refer to our earlier work [5,24,26].

While we show frequency shift data in the main text, we include a detailed discussion on the static deflection in Supporting Information File 1, where we also discuss the robustness and reproducibility of the AFM results.

Molecular dynamics simulations

We employed molecular dynamics simulations to model both calcite and magnesite with their (10.4) surface exposed as a nine layer crystal with three surface unit cells in the $[42\bar{1}]$ direction and six surface unit cells in the [010] direction. Each crystal was first centered in the simulation box. The vertical box size (in z-direction) was then increased up to 15 nm in order to place ethanol molecules on both exposed (10.4) surfaces, thus ensuring bulk properties of the solvent far away from the surface. The obtained systems, composed of 1620 crystal atoms and 800 ethanol molecules, are charge neutral and periodic in all three directions. The surface unit cell of the simulated crystal measured $0.81 \times 0.49\ \mathrm{nm}^2$ for calcite and $0.73 \times 0.46\ \mathrm{nm}^2$ for magnesite.

We first performed an energy minimization of the system with conjugated gradients [27,28] to ensure that the atoms from either ethanol or mineral were in an initially stable configuration. After that, an equilibration of 0.5 ns in an NVT ensemble was performed, followed by 5 ns equilibration in an NPT ensemble and another 2 ns in a NVT ensemble. The production run was performed after that in an NVT simulation of 10 ns.

Temperature control in NVT and NPT ensembles was set to 300 K, using the Nosé–Hoover scheme [29-31] with five thermostat chains. In the NPT ensemble, pressure control was set to 1 atm using Nosé–Hoover barostats [29]. Electrostatics were calculated with the particle-particle-particle-mesh method [32].

In order to prevent drift of the entire system, the carbon atoms in the crystal middle layer were kept fixed during the dynamics. A time step of 1 fs was used for the integration of the equation of motion, ensuring proper energy conservation.

The output data was collected every 1 ps during the production run, providing enough statistics for all required analysis. MD simulations were performed in Lammps code [33]. The analysis was performed using the Python library MDAnalysis [34,35].

Calcite and magnesite were described by the force-field developed in [36,37]. It has been shown in previous calcite studies that this force field successfully describes all the calcite properties. Ethanol was described by the CHARMM General Force Field (CGenFF) [38,39]. The cross-terms between the minerals and ethanol were obtained through Lorentz–Berthelot combination rules [40].

Supporting Information

Supporting Information File 1

Additional information.
[https://www.beilstein-journals.org/bjnano/content/supplementary/2190-4286-11-74-S1.pdf]

Acknowledgements

Parts of this work were conducted within the doctoral thesis of H.S.

Funding

H.S. was a recipient of a DFG-funded position through the Excellence Initiative by the Graduate School Materials Science in Mainz (GSC 266). A.K. gratefully acknowledges financial support by the German Research Foundation (DFG) through Grant No. KU1980/7-1. P.S., L.Z. and A.S.F. have been supported by the Academy of Finland through its Centres of Excellence Program (project no. 915804) and acknowledge the use of the computational resources provided by the Aalto Science-IT project and CSC, Helsinki for computational resources. Y.M.J. and A.S.F. were supported by the Academy of Finland (project no. 314862). The collaboration between the groups of A.S.F. and A.K. was funded through travel grants from the Academy of Finland (PSINAS, project no. 11285128) and the Deutscher Akademischer Austausch Dienst (PSINAS, project no. 57161955).

ORCID® iDs

Ygor Morais Jaques - https://orcid.org/0000-0003-0114-9854
Peter Spijker - https://orcid.org/0000-0003-2538-1981
Christoph Marutschke - https://orcid.org/0000-0002-4810-6918
Ilka Hermes - https://orcid.org/0000-0001-5659-1290
Adam S. Foster - https://orcid.org/0000-0001-5371-5905
Angelika Kühnle - https://orcid.org/0000-0003-1214-1006

References

1. Fukuma, T.; Garcia, R. *ACS Nano* **2018,** *12,* 11785–11797. doi:10.1021/acsnano.8b07216
2. Fukuma, T.; Ueda, Y.; Yoshioka, S.; Asakawa, H. *Phys. Rev. Lett.* **2010,** *104,* 016101. doi:10.1103/physrevlett.104.016101
3. Imada, H.; Kimura, K.; Onishi, H. *Langmuir* **2013,** *29,* 10744–10751. doi:10.1021/la402090w
4. Fukuma, T.; Reischl, B.; Kobayashi, N.; Spijker, P.; Canova, F. F.; Miyazawa, K.; Foster, A. S. *Phys. Rev. B* **2015,** *92,* 155412. doi:10.1103/physrevb.92.155412
5. Söngen, H.; Marutschke, C.; Spijker, P.; Holmgren, E.; Hermes, I.; Bechstein, R.; Klassen, S.; Tracey, J.; Foster, A. S.; Kühnle, A. *Langmuir* **2017,** *33,* 125–129. doi:10.1021/acs.langmuir.6b03814
6. Reischl, B.; Raiteri, P.; Gale, J. D.; Rohl, A. L. *J. Phys. Chem. C* **2019,** *123,* 14985–14992. doi:10.1021/acs.jpcc.9b00939
7. Nishioka, R.; Hiasa, T.; Kimura, K.; Onishi, H. *J. Phys. Chem. C* **2013,** *117,* 2939–2943. doi:10.1021/jp3117424
8. Hiasa, T.; Kimura, K.; Onishi, H. *Colloids Surf., A* **2012,** *396,* 203–207. doi:10.1016/j.colsurfa.2011.12.073
9. Minato, T.; Araki, Y.; Umeda, K.; Yamanaka, T.; Okazaki, K.-i.; Onishi, H.; Abe, T.; Ogumi, Z. *J. Chem. Phys.* **2017,** *147,* 124701. doi:10.1063/1.4996226
10. Hirayama, T.; Kawamura, R.; Fujino, K.; Matsuoka, T.; Komiya, H.; Onishi, H. *Langmuir* **2017,** *33,* 10492–10500. doi:10.1021/acs.langmuir.7b02528
11. Nudelman, F.; Sommerdijk, N. A. J. M. *Angew. Chem., Int. Ed.* **2012,** *51,* 6582–6596. doi:10.1002/anie.201106715
12. Andersson, M. P.; Stipp, S. L. S. *J. Phys. Chem. C* **2012,** *116,* 18779–18787. doi:10.1021/jp304671k
13. Ataman, E.; Andersson, M. P.; Ceccato, M.; Bovet, N.; Stipp, S. L. S. *J. Phys. Chem. C* **2016,** *120,* 16586–16596. doi:10.1021/acs.jpcc.6b01349
14. Cooke, D. J.; Gray, R. J.; Sand, K. K.; Stipp, S. L. S.; Elliott, J. A. *Langmuir* **2010,** *26,* 14520–14529. doi:10.1021/la100670k
15. Pasarín, I. S.; Yang, M.; Bovet, N.; Glyvradal, M.; Nielsen, M. M.; Bohr, J.; Feidenhans'l, R.; Stipp, S. L. S. *Langmuir* **2012,** *28,* 2545–2550. doi:10.1021/la2021758
16. Sand, K. K.; Yang, M.; Makovicky, E.; Cooke, D. J.; Hassenkam, T.; Bechgaard, K.; Stipp, S. L. S. *Langmuir* **2010,** *26,* 15239–15247. doi:10.1021/la101136j
17. Bovet, N.; Yang, M.; Javadi, M. S.; Stipp, S. L. S. *Phys. Chem. Chem. Phys.* **2015,** *17,* 3490–3496. doi:10.1039/c4cp05235h

18. Sand, K. K.; Stipp, S. L. S.; Hassenkam, T.; Yang, M.; Cooke, D.; Makovicky, E. *Mineral. Mag.* **2008,** *72,* 353–357. doi:10.1180/minmag.2008.072.1.353
19. Amano, K.-i.; Suzuki, K.; Fukuma, T.; Takahashi, O.; Onishi, H. *J. Chem. Phys.* **2013,** *139,* 224710. doi:10.1063/1.4839775
20. Watkins, M.; Reischl, B. *J. Chem. Phys.* **2013,** *138,* 154703. doi:10.1063/1.4800770
21. Söngen, H.; Reischl, B.; Miyata, K.; Bechstein, R.; Raiteri, P.; Rohl, A. L.; Gale, J. D.; Fukuma, T.; Kühnle, A. *Phys. Rev. Lett.* **2018,** *120,* 116101. doi:10.1103/physrevlett.120.116101
22. Rode, S.; Stark, R.; Lübbe, J.; Tröger, L.; Schütte, J.; Umeda, K.; Kobayashi, K.; Yamada, H.; Kühnle, A. *Rev. Sci. Instrum.* **2011,** *82,* 073703. doi:10.1063/1.3606399
23. Adam, H.; Rode, S.; Schreiber, M.; Kobayashi, K.; Yamada, H.; Kühnle, A. *Rev. Sci. Instrum.* **2014,** *85,* 023703. doi:10.1063/1.4864084
24. Söngen, H.; Nalbach, M.; Adam, H.; Kühnle, A. *Rev. Sci. Instrum.* **2016,** *87,* 063704. doi:10.1063/1.4952954
25. Albrecht, T. R.; Grütter, P.; Horne, D.; Rugar, D. *J. Appl. Phys.* **1991,** *69,* 668–673. doi:10.1063/1.347347
26. Söngen, H.; Bechstein, R.; Kühnle, A. *J. Phys.: Condens. Matter* **2017,** *29,* 274001. doi:10.1088/1361-648x/aa6f8b
27. Reid, J. K. *SIAM J. Numer. Anal.* **1972,** *9,* 325–332. doi:10.1137/0709032
28. Hestenes, M. R.; Stiefel, E. *J. Res. Natl. Bur. Stand. (U. S.)* **1952,** *49,* 409–436. doi:10.6028/jres.049.044
29. Shinoda, W.; Shiga, M.; Mikami, M. *Phys. Rev. B* **2004,** *69,* 134103. doi:10.1103/physrevb.69.134103
30. Nosé, S. *J. Chem. Phys.* **1984,** *81,* 511–519. doi:10.1063/1.447334
31. Hoover, W. G. *Phys. Rev. A* **1985,** *31,* 1695–1697. doi:10.1103/physreva.31.1695
32. Hockney, R. W.; Eastwood, J. W. *Computer Simulation Using Particles;* CRC Press: Boca Raton, FL, USA, 1988; p 540. doi:10.1201/9781439822050
33. Plimpton, S. *J. Comput. Phys.* **1995,** *117,* 1–19. doi:10.1006/jcph.1995.1039
34. Gowers, R. J.; Linke, M.; Barnoud, J.; Reddy, T. J. E.; Melo, M. N.; Seyler, S. L.; Domanski, J.; Dotson, D. L.; Buchoux, S.; Kenney, I. M.; Beckstein, O. MDAnalysis: A Python Package for the Rapid Analysis of Molecular Dynamics Simulations. In *Proceedings of the 15th Python in Science Conference,* Scientific computing with Python, Austin, Texas, July 11–17, 2016; pp 98–105. doi:10.25080/majora-629e541a-00e
35. Michaud-Agrawal, N.; Denning, E. J.; Woolf, T. B.; Beckstein, O. *J. Comput. Chem.* **2011,** *32,* 2319–2327. doi:10.1002/jcc.21787
36. Raiteri, P.; Demichelis, R.; Gale, J. D. *J. Phys. Chem. C* **2015,** *119,* 24447–24458. doi:10.1021/acs.jpcc.5b07532
37. Silvestri, A.; Budi, A.; Ataman, E.; Olsson, M. H. M.; Andersson, M. P.; Stipp, S. L. S.; Gale, J. D.; Raiteri, P. *J. Phys. Chem. C* **2017,** *121,* 24025–24035. doi:10.1021/acs.jpcc.7b06700
38. Vanommeslaeghe, K.; Hatcher, E.; Acharya, C.; Kundu, S.; Zhong, S.; Shim, J.; Darian, E.; Guvench, O.; Lopes, P.; Vorobyov, I.; Mackerell, A. D., Jr. *J. Comput. Chem.* **2010,** *31,* 671–690. doi:10.1002/jcc.21367
39. Yu, W.; He, X.; Vanommeslaeghe, K.; MacKerell, A. D., Jr. *J. Comput. Chem.* **2012,** *33,* 2451–2468. doi:10.1002/jcc.23067
40. Lorentz, H. A. *Ann. Phys. (Berlin, Ger.)* **1881,** *248,* 127–136. doi:10.1002/andp.18812480110

License and Terms

The definitive version of this article is the electronic one which can be found at:
doi:10.3762/bjnano.11.74

BEILSTEIN JOURNAL OF NANOTECHNOLOGY

Monolayers of MoS_2 on Ag(111) as decoupling layers for organic molecules: resolution of electronic and vibronic states of TCNQ

Asieh Yousofnejad, Gaël Reecht*, Nils Krane, Christian Lotze and Katharina J. Franke

Full Research Paper

Open Access

Address:
Fachbereich Physik, Freie Universität Berlin, Arnimallee 14, 14195
Berlin, Germany

Email:
Gaël Reecht* - greecht@zedat.fu-berlin.de

* Corresponding author

Keywords:
decoupling layer; molybdenum disulfide (MoS_2); scanning tunneling microscopy, tetracyanoquinodimethane (TCNQ); vibronic states

Beilstein J. Nanotechnol. **2020,** *11,* 1062–1071.
doi:10.3762/bjnano.11.91

Received: 15 April 2020
Accepted: 03 July 2020
Published: 20 July 2020

This article is part of the thematic issue "Molecular assemblies on surfaces – towards physical and electronic decoupling of organic molecules".

Guest Editor: S. Maier

Abstract

The electronic structure of molecules on metal surfaces is largely determined by hybridization and screening by the substrate electrons. As a result, the energy levels are significantly broadened and molecular properties, such as vibrations are hidden within the spectral line shapes. Insertion of thin decoupling layers reduces the line widths and may give access to the resolution of electronic and vibronic states of an almost isolated molecule. Here, we use scanning tunneling microscopy and spectroscopy to show that a single layer of MoS_2 on Ag(111) exhibits a semiconducting bandgap, which may prevent molecular states from strong interactions with the metal substrate. We show that the lowest unoccupied molecular orbital (LUMO) of tetracyanoquinodimethane (TCNQ) molecules is significantly narrower than on the bare substrate and that it is accompanied by a characteristic satellite structure. Employing simple calculations within the Franck–Condon model, we reveal their vibronic origin and identify the modes with strong electron–phonon coupling.

Introduction

When molecules are adsorbed on metal surfaces, their electronic states are strongly perturbed by hybridization, charge transfer and screening [1-4]. These effects lead to a broadening and shift of the molecular resonances [5]. Often the molecular functionality is also lost due to these interactions [6]. However, addressing individual molecules in devices or by single-molecule spectroscopy as offered in a scanning tunneling microscope, requires a metal electrode. To (partially) preserve the molecular properties the molecule–electrode coupling has to be properly designed. An elegant way is to clamp the molecule between electrodes via single-atom bonds at opposing sites of the molecule while the molecule is freely hanging between the electrodes [7-10]. While these configurations give access to important transport properties [11-13], they do not allow for imaging molecular properties with intramolecular resolution [14]. The latter requires the molecules to be flat lying on a surface. To decouple such flat-lying molecules from a metal, thin insulating layers have been engineered, ranging from ionic salts [15,16], over oxides [17-19], nitrides [20], and molecular layers [21,22] to 2D materials, such as graphene [23,24], and hexagonal boron nitride [25].

The most recent development of decoupling layers made use of the in situ fabrication of single layers of transition metal dichalcogenides on metal surfaces. A monolayer of MoS_2 on Au(111) provided very narrow molecular resonances, close to the thermal resolution limit at 4.6 K [26]. The exquisite decoupling efficiency has been ascribed to a combination of its rather large thickness of three atomic layers, its electronic bandgap, and its non-ionic nature. Together, these properties prohibited fast electronic relaxations into the metal and coupling to phonons, which otherwise led to lifetime broadening [27,28].

The electronic properties of MoS_2 on a metal surface are not the same as those of a free-standing monolayer. Both theory and experiment have found considerable hybridization of electronic states at the interface [29]. As a consequence, the bandgap is narrowed. Instead of the predicted bandgap of 2.8 eV of the free-standing layer [30,31], the bandgap of the hybrid structure amounts to only approx. 1.7 eV [29]. Interestingly, the states at the K point are much less affected than the states at the Γ point. Hence, the system remains promising for optoelectronic devices with selective access to the spin–orbit-split bands at K and K' by circularly polarized light [32].

The potential as decoupling layer for molecules may become even more appealing by the fact that monolayers of transition metal dichalcogenides can be grown in situ on different metal surfaces, where the precise hybridization and band alignment depend on the nature of the substrate [33]. One may thus envision tuning the bandgap alignment for decoupling either the lowest unoccupied (LUMO) or the highest occupied molecular orbital (HOMO) of the molecules.

While MoS_2 on Au(111) has already been established as an outstanding decoupling layer [26], we will now explore this potential for MoS_2 on a Ag(111) surface. In agreement with the band modifications of WS_2 on Au(111) and Ag(111), we find that the bandgap remains almost the same, albeit shifted to lower energies [33]. As a test molecule we chose tetracyanoquinodimethane (TCNQ). Due to its electron-accepting character, this choice will allow us to detect a negative ion resonance within the bandgap of MoS_2. We will show that the LUMO is indeed decoupled from the metallic substrate as we can detect a narrow line width followed by a satellite structure. We can reproduce this fine structure by simulating the vibronic states of the gas-phase molecule.

Results and Discussion

We have grown monolayer islands of MoS_2 on an atomically clean Ag(111) surface, which had been exposed to sputtering–annealing cycles under ultrahigh vacuum before. The growth procedure was adapted from that of MoS_2 on Au(111) [34,35], with Mo deposition on the surface in a H_2S atmosphere of $5 \cdot 10^{-5}$ mbar, while the sample is annealed to 800 K. TCNQ molecules were deposited on the as-prepared sample held at 230 K. The sample was then cooled down and transferred to the scanning tunneling microscope (STM). All measurements were performed at 4.6 K. Differential conductance (dI/dV) maps and spectra were recorded with a lock-in amplifier at modulation frequencies of 812–921 Hz, with the amplitudes given in the figure captions.

Characterization of single-layer MoS_2 on Ag(111)

Figure 1a presents an STM image of the Ag(111) surface after the growth of MoS_2 as described above. We observe islands with tens to hundreds of nanometer diameter and of 2.3 ± 0.2 Å apparent height (inset of Figure 1). The apparent height is much smaller than the layer distance in bulk MoS_2 [36] due to electronic structure effects, but in agreement with a single layer of MoS_2 on a metal surface [34]. The islands exhibit a characteristic hexagonal pattern reflecting a moiré structure, which results from the lattice mismatch between the Ag(111) surface and MoS_2 (Figure 1b). Areas with large apparent height correspond to domains in which the S atoms sit on top of Ag atoms, whereas the lower areas represent two different hollow sites (fcc or hcp stacking) of the S atoms on the Ag lattice. The most abundant moiré periodicity amounts to approx. 3.3 ± 0.1 nm. This value is similar to the one observed for MoS_2 on Au(111) [29,32,34,37].

Given the similar lattice constants of Au (4.08 Å) and Ag (4.09 Å), a locking into a similar superstructure at the metal–MoS_2 interface is not surprising. However, occasionally, we also observe moiré patterns with lattice constants of 3.6 ± 0.1 and 3.0 ± 0.1 nm, and different angles between MoS_2 and the Ag(111) lattice. This indicates shallow energetic minima of the lattice orientations. Atomically resolved STM images (Figure 1c) reveal the expected S–S distance of 3.15 Å in the top layer [36,39-41].

For an efficient decoupling of a molecule from the substrate, the interlayer must provide an electronic bandgap. As the moiré

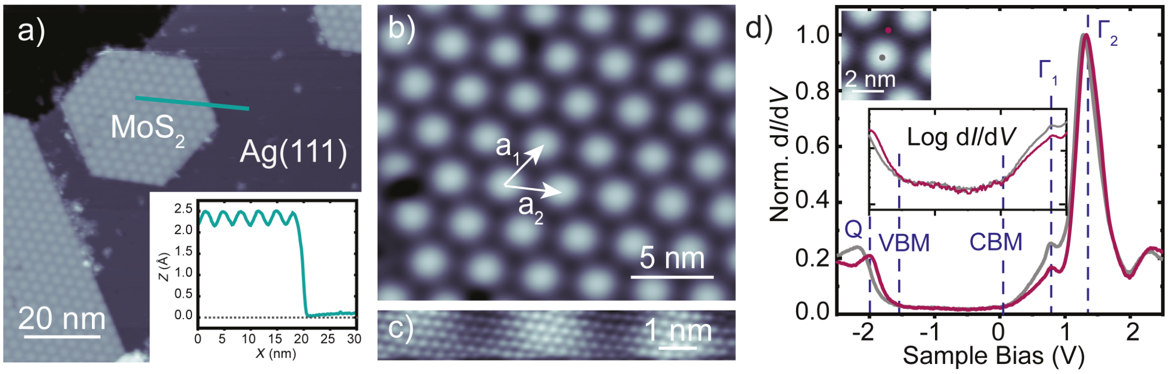

Figure 1: a) STM topography of MoS_2 on Ag(111) recorded at $V = 1.2$ V, $I = 20$ pA. Inset: Line profile of a monolayer MoS_2 island along the green line. b) Close-up view on the moiré structure. c) Atomically resolved terminating S layer ($V = 5$ mV, $I = 1$ nA). d) Constant-height dI/dV spectra of MoS_2/Ag(111) recorded on a top and on a hollow region of the moiré structure as shown on the inserted STM topography (feedback opened at $V = 2.5$ V, $I = 0.5$ nA, $V_{mod} = 10$ mV). The inset shows the gap region of MoS_2/Ag(111) on a logarithmic scale. We identify the valence band maximum (VBM) and the conduction band minimum (CBM) as the changes of the slope of the dI/dV signal. Dashed lines indicate the CBM at approx. 0.05 V and the VBM at approx. −1.55 V. The strong features in the dI/dV spectra are associated to the onset of specific bands, which are labeled by Q, Γ_1 and Γ_2 according to their location in the Brillouin zone. The assignment follows that in [38].

pattern bears a topographic and an electronic modulation [38], we investigate the differential conductance (dI/dV) spectra on different locations (Figure 1d). We first examine the spectrum on the top site of the moiré structure. We observe a gap in the density of states, which is flanked by an onset of conductance at approx. −1.55 V and approx. +0.05 V (marked by dashed lines labeled VBM or CBM, which have been determined from a logarithmically scaled plot). Additionally, there are pronounced peaks at approx. 0.77 V and approx. 1.28 V. First, we note that the observed bandgap is significantly smaller than the 2.8 eV bandgap of a single layer of free-standing MoS_2 [30,31]. This indicates a strong hybridization of the electronic states of the MoS_2 layer and the Ag substrate. Second, we note that the spectral features are similar to those observed for single-layer MoS_2 on Au(111) [29,35,38]. For direct comparison, we plot the spectra on the top sites of the MoS_2 moiré on Au(111) and Ag(111) in Figure 2a. At negative bias voltage, the onsets of conductance are essentially the same, while the features at positive bias voltage appear approx. 140 mV closer to the Fermi level on Ag(111) than on Au(111).

Before discussing the differences between the layers on Au(111) and Ag(111), we investigate the effect of the different stacking at the interface on the electronic properties. The spectrum of a hollow site on Ag(111) shows a shift of the features at negative bias voltage by about approx. 130 mV towards the Fermi level (E_F), whereas the peaks at positive bias undergo a much smaller shift (approx. 50 mV) away from E_F (Figure 1d). On Au(111), there are also variations between hollow and top sites, with the strongest shift at negative bias voltage (Figure 2).

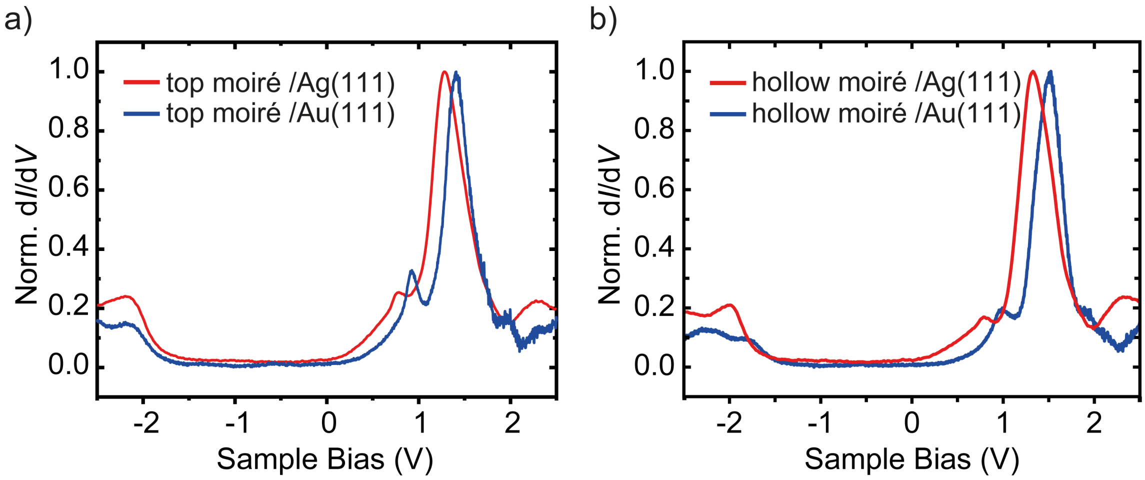

Figure 2: Constant-height dI/dV spectra recorded (a) on a top and (b) on a hollow site of the moiré structure of MoS_2 on Ag(111) (red curves) and on Au(111) (blue curves). Feedback opened at $V = 2.5$ V, $I = 0.5$ nA, $V_{mod} = 10$ mV (all spectra, except for hollow site on Au(111): $V_{mod} = 5$ mV).

To understand the differences between the substrate and the local sites, we first discuss the origin of the spectroscopic features. Based on the similarity of the spectral shapes on Au(111) and Ag(111), we tentatively assign the strong peaks at approx. 0.8 V (labeled as Γ_1) and approx. 1.3 V (labeled as Γ_2) (values averaged over the different moiré sites) to bands at the $\overline{\Gamma}$ point [38]. More precisely, the peak at Γ_2 has been assigned to bands at Γ, which are also present in free-standing MoS_2, but are broadened due to hybridization with the substrate. The peak at Γ_1 has been observed in tunneling spectra of MoS_2 on Au(111), but has not been found in calculations. It has been interpreted as a hybrid metal–MoS_2 or an interface state [38]. The conduction band minimum, which is expected to lie at the $\overline{K}$ point for quasi free-standing as well as metal-supported single-layer MoS_2 [29,42-44], is hardly visible in the tunneling spectra due to the rapid decay of the tunneling constant with $k_\parallel$ [38,45]. The same applies to the valence band maximum, such that the strongest feature in the tunneling spectra at −2 V arises from bands close to the $\overline{Q}$ point [38].

Comparison of spectra on the moiré hollow sites suggest a rigid shift of the conduction bands between the MoS_2 bands on Ag and Au. In a very simple interpretation, this agrees with the lower work function of Ag than that of Au. A down-shift of the conduction band structure by approx. 280 meV has been observed by photoemission of WS_2 on Au(111) and Ag(111) [33]. Angle-resolved measurements further showed that the shift also included band distortions, such that bands at Q were crossing E_F (instead of at K). The band distortion was explained by hybridization of the WS_2 bands with the Ag substrate [33]. As our dI/dV signal is not sensitive to $k_\parallel$, we would not be able to detect band distortions in the MoS_2–Ag system. However, the clear shift of the states at Γ can be easily understood by hybridization of S-derived states of mainly out-of-plane character with Ag states in analogy to [29].

In the occupied states, the bands on the hollow site follow the same trend of a down-shift, suggesting that the states near $\overline{Q}$ are equally affected by hybridization with Ag states [33]. In contrast, the tunneling spectra on the top sites, seem to coincide for Au and Ag substrates. We also note that the tunneling conductance close to the $\overline{Q}$ point is the most sensitive to the precise location on the moiré pattern. Hence, we suggest that this site is most strongly affected by screening effects, which may vary on the different substrates [46] and partially compensate for hybridization effects.

Electronic properties of TCNQ molecules on MoS_2 on Ag(111)

Deposition of TCNQ molecules (structure shown in Figure 3a) on the sample held at 230 K leads to large densely packed molecular islands on the MoS_2 areas (Figure 3b). The large size and high degree of order of these islands reflects a low diffusion barrier on the MoS_2 substrate. The moiré pattern of MoS_2 remains intact and visible through the molecular monolayer. High-resolution STM images recorded at 0.8 V (Figure 3c) allow for the resolution of the individual molecules and their arrangement. Each TCNQ molecule appears with back-to-back double U-shapes separated by a nodal plane. As will be discussed later, and based on previous work on TCNQ [5,23], this appearance can be associated to the spatial distribution of the lowest unoccupied molecular orbital (LUMO). The molecular arrangement can be described by the lattice vectors $a_1 = 0.9 \pm 0.1$ nm, $a_2 = 1.0 \pm 0.1$ nm and the angle (96 ± 2)° (see model in Figure 3c). This structure is stabilized by dipole–dipole interactions between the cyano endgroups and the quinone center of neighboring molecules. This assembly is very similar to typical self-assembled TCNQ islands on weakly interacting substrates [5,23,47-49]. When measured at a lower bias voltage (e.g., at $V = 0.2$ V in Figure 4a), the molecules appear with featureless elliptical shape, reflecting only the topographic extent of the molecules.

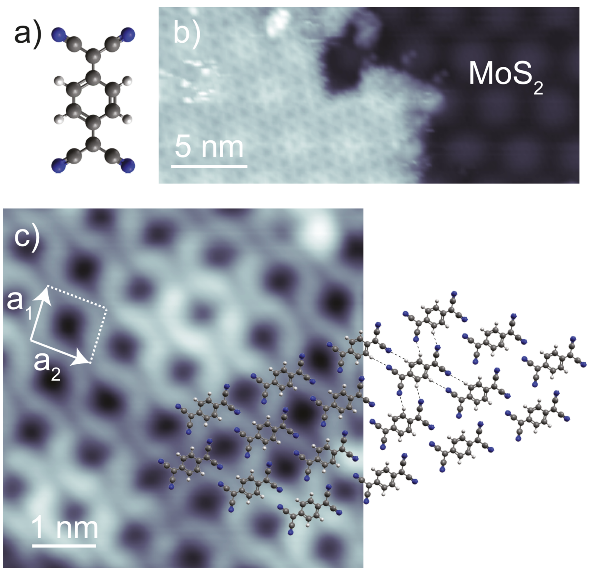

Figure 3: a) Stick-and-ball model of TCNQ. Gray, blue, and white spheres represent C, N, and H atoms, respectively. b) STM topography of a TCNQ molecular island on MoS_2/Ag(111) recorded at $V = 1$ V, $I = 10$ pA. c) STM topography of a TCNQ island on MoS_2/Ag(111) recorded at $V = 0.8$ V, $I = 200$ pA, with superimposed molecular models suggesting intermolecular dipole–dipole interactions (dashed lines). White arrows represent the unit cell of the self-organized TCNQ domain with lattice vectors $a_1 = 0.9 \pm 0.10$ nm and $a_2 = 1.0 \pm 0.10$ nm and the angle between them of (96 ± 2)°.

The strong bias-voltage dependence of the TCNQ molecules on the MoS_2 layer promises energetically well separated molecular states. To investigate these properties in more detail, we re-

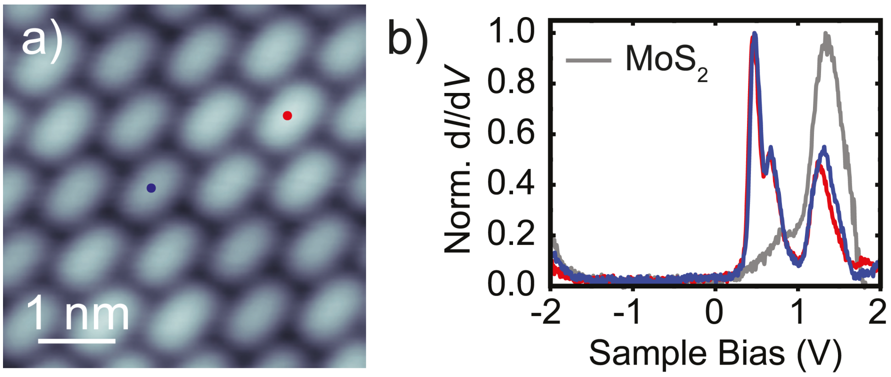

Figure 4: a) STM topography of a self-assembled TCNQ island on MoS_2/Ag(111), recorded at V = 0.2 V, I = 20 pA. b) dI/dV spectra acquired on TCNQ molecules within the island in panel a, with the precise location marked by colored dots. The gray spectrum was recorded on a bare MoS_2 layer for reference. Feedback opened at V = 2 V, I = 100 pA, with V_{mod} =20 mV.

corded dI/dV spectra on top of the molecules (Figure 4b). These show two main resonances at approx. 0.47 V and approx. 0.64 V. Another peak at approx. 1.3 V matches the Γ resonance of the bare MoS_2 layer. At negative bias voltage, we observe an onset of conductance at approx. −1.8 V. The dI/dV spectra thus show that the STM image in Figure 4a was recorded within the energy gap of the molecule, which explains the featureless shape. In order to determine the origin of each of the resonances, we recorded constant-height dI/dV maps at their corresponding energies (Figure 5).

For the first resonance at positive bias voltage (470 mV, Figure 5a), we observe the same double U-shape, separated by a nodal plane, which we used in Figure 3 for the identification of the molecular arrangement. The dI/dV map at 640 mV exhibits the same shape, suggesting the same orbital as its origin. At 1.3 V, the molecules do not show any characteristic feature (Figure 5c). Finally, Figure 5d presents a conductance map at −2 V associated with the onset of conductance observed at negative bias voltage for spectra on the molecule. Here, the dI/dV signal is rather blurred, but we remark that it is more

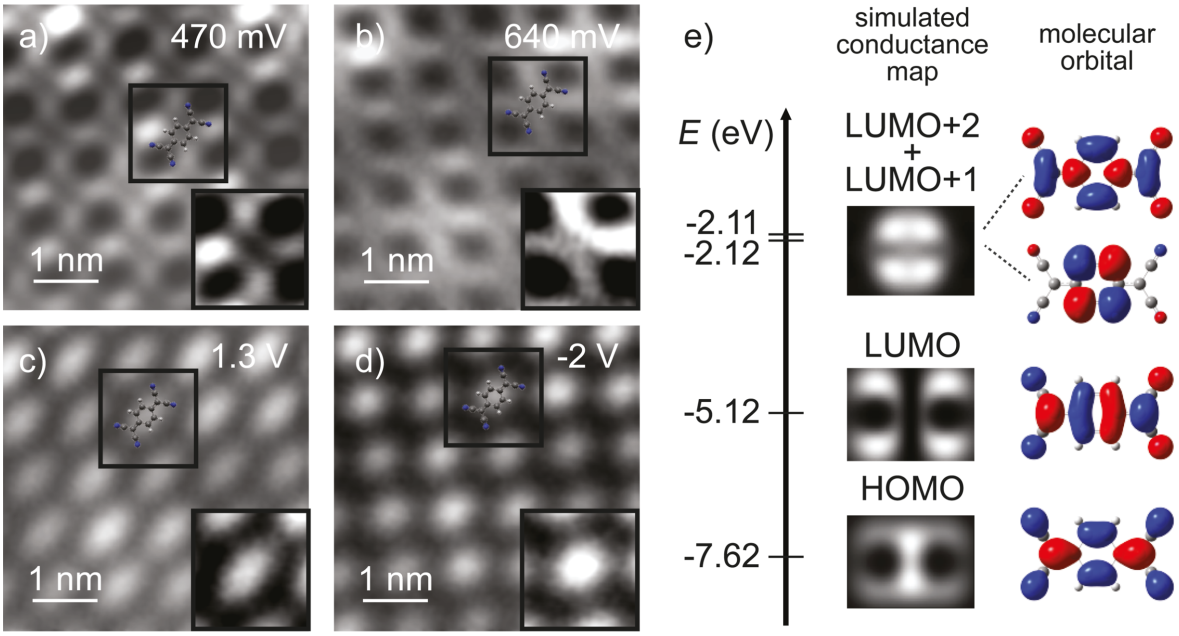

Figure 5: a–d) Constant-height dI/dV maps of a TCNQ island on MoS_2 recorded at the resonance energies derived in Figure 4b. Feedback opened in panels (a–c) V = 2 V, I = 100 pA and (d) V = −2 V, I = 30 pA on the center of the molecule with V_{mod} = 20 mV. Close-up images with enhanced contrast on one molecule are shown as inset for each map. e) Energy-level diagram of TCNQ determined from gas-phase DFT calculations (left). The isosurfaces of the frontier molecular orbitals are shown on the right. These have been used to calculate the tunneling matrix element M_{ts} with an s-wave tip at a tip–molecule distance of 7.5 Å, work function of 5 eV. The map of the spatial distribution of $|M_{ts}|^2$ is shown in the middle panel.

localized in the center of the molecule as compared to the elliptical shape in Figure 5c.

For the identification of molecular orbitals, it is often sufficient to compare the dI/dV maps with the shape of the gas-phase molecular orbitals. Using this method, the U-shaped features have previously been associated to the LUMO of TCNQ [5,23,49]. Here, we corroborate this assignment by simulating constant-height dI/dV maps of a free, flat-lying molecule. We first calculated the gas-phase electronic structure using density functional theory (DFT) calculations with the B3PW91 functional and the 6-31g(d,p) basis set as implemented in the Gaussian 09 package [50]. The isodensity contour plots of the highest occupied molecular orbital (HOMO) and some of the lowest unoccupied orbitals are shown in Figure 5e, right panel. The HOMO/LUMO can be unambiguously distinguished by the absence/presence of a nodal plane at the center of the quinone backbone. For direct comparison with the dI/dV maps, we calculate the tunneling matrix element between an s-wave tip and the spatially resolved molecular wave function across the molecule [51]. The maps of the square of the tunneling matrix element are depicted in Figure 5e next to the corresponding molecular orbitals. Because LUMO+1 and LUMO+2 are quasi-degenerate, we used the sum of their wave functions for the calculations of the tunneling matrix elements. As expected, the nodal planes of the molecular orbitals dominate the simulated dI/dV maps and can be taken as a robust signature for molecular orbital identification. Additionally, the simulated maps reveal that the dI/dV intensity is not directly proportional to the isosurface density. For instance, there is hardly any intensity within the U shapes of the TCNQ LUMO, and the HOMO is mainly localized at the very center of the quinone moiety. We note that the simulated maps were obtained at a tip–molecule distance (center of the s-wave tip to center of the molecule) of 7.5 Å. This value was chosen because it represents reasonable tunneling conditions in experiments. However, variation of the tip height by (±2 Å) does not have any influence on the observation of the main features within the map (i.e., nodal planes, or intensity maxima) [52].

Comparison with the experimental constant-height dI/dV maps, now allows for an unambiguous identification of the origin of the molecular resonances. As suggested previously, the resonance at 0.47 V can be derived from the LUMO with the double U-shape being in very good agreement with the calculations of the tunneling matrix element. The very same signatures in the conductance map at 0.64 V suggest that this resonance stems from the LUMO as well. The DFT calculations show that the LUMO is non-degenerate. Hence, we can exclude a substrate-induced lifting of the degeneracy. The energy difference of only 170 meV between the two resonances lies within the typical vibrational energies of organic molecules and may, thus, be indicative of a vibronic peak. We will elucidate this point further below.

The dI/dV map at 1.3 V essentially shows the same elliptical shapes of the molecules as the STM image recorded in the electronic gap (Figure 4a). Our DFT calculations suggest that the next higher unoccupied orbitals lie 3 eV above the LUMO and show a pattern of nodal planes that are absent in the experiment. Additionally, given the energy similar to that of the MoS_2 bands, this resonance is probably not associated to the molecular layer, but to direct tunneling into the MoS_2 states.

The assignment of the orbital origin at negative bias voltage bears some intricacies, because the experimental map lacks characteristic nodal planes. The reduced spatial resolution is most probably caused by the overlap with density of states of the substrate as we are approaching the onset of the valence band of MoS_2. One may suggest that the stronger localization of dI/dV intensity toward the quinone center is in agreement with the large tunneling matrix element of the HOMO at the center of the molecule. This assignment may be enforced by the coincidence of the observed molecular energy gap of TCNQ with the DFT-derived gap. However, DFT is known to underestimate HOMO–LUMO gaps. Although this effect may be compensated by the screening properties of the substrate, we refrain from a definite assignment. In any case, our data clearly shows that the HOMO is at or within the conduction band of MoS_2.

By comparison with simulations, we thus arrive at a clear identification of the energy level alignment. Most notably, we find that the LUMO-derived resonance lies close to, but above, the Fermi level of the substrate, whereas the HOMO is far below. This leaves the molecule in a neutral state with a negligible amount of charge transfer, despite the electron accepting character of TCNQ. Nonetheless, its electron affinity of approx. 3.4 eV [53,54] is consistent with the LUMO alignment just above E_F when considering the work function of MoS_2/Ag(111) of 4.7 eV [55]. We found small shifts of the LUMO onsets by at most 50 mV between the spectra of TCNQ molecules lying at the top or hollow sites of the moiré structure of MoS_2. These shifts correspond to the moiré-induced shifts in unoccupied states of the MoS_2 layer and thus only reflect the different screening properties from the substrate. In turn, we do not observe any modification of the electronic structure of MoS_2. This indicates weak interactions of the molecules all along the MoS_2 layer.

Importantly, the resonance at 470 mV has a rather narrow width of approx. 100 mV. This is significantly smaller than resonances typically observed on metal surfaces, where strong hybridization effects lead to widths of the order of approx. 500 meV [5,48]. The narrow width thus reflects that MoS_2 acts as a decoupling layer from the metal substrate. However, this resonance width is broader than what has been observed for the HOMO resonance of other organic molecules on MoS_2 on Au(111) [26,52,56]. In contrast to those cases, where the HOMO lay well inside the electronic gap of MoS_2, the LUMO of TCNQ is located right at the onset of the conduction band. This provides relaxation pathways for electrons tunneling into the LUMO, though still significantly less than on the bare metal.

Vibronic excitations of TCNQ on MoS_2 on Ag(111)

Having shown that the resonances at 470 and 640 mV originate both from the LUMO of TCNQ, we now turn to a more detailed analysis. A close-up view of the spectral range with these peaks is shown in the bottom panel of Figure 6b with the LUMO-derived peak at 470 mV shifted to zero energy and its peak height being normalized. The satellite structure is reminiscent of vibronic sidebands, which occur due to the simultaneous excitation of a vibrational mode upon charging [22,25,57-61]. The sidepeaks should thus obey the same symmetry as the parent orbital state [62-64]. In the simplest case, these

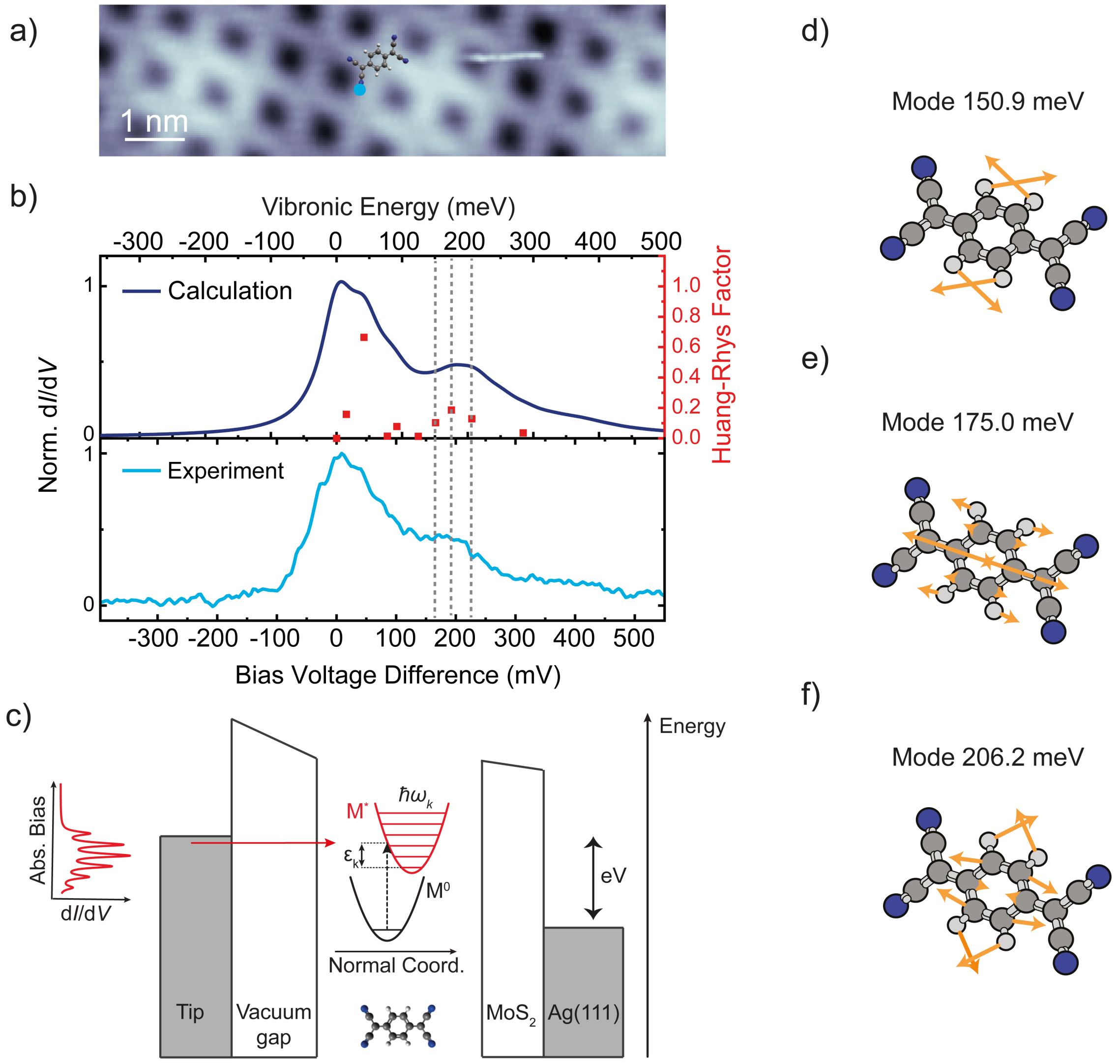

Figure 6: a) STM topography image of a TCNQ island recorded at V = 1 V, I = 10 pA. b) Simulated (top panel) and experimental (bottom panel) dI/dV spectra at the position indicated by the blue dot in panel (a) with feedback opened at V = 2 V, I = 100 pA, with V_{mod} = 10 mV. The simulated spectrum is obtained from DFT calculations for all vibrational modes of the $TCNQ^-$ molecule with a Huang–Rhys factor higher than 0.01 (dots associated with the right axis). A Lorentzian peak of 60 meV broadening is applied to all of these modes. c) Schematic representation of electron transport through a TCNQ molecule adsorbed on MoS_2/Ag(111): singly charged $TCNQ^-$ is formed upon injecting an electron into a vibronic state of an unoccupied molecular electronic level. d–f) Visualization of the vibrational modes contributing to the satellite peak. The orange arrows represent the displacement of the atoms involved in these vibrations.

excitations can be described within the Franck–Condon model (see sketch in Figure 6c). When probing the LUMO in tunneling spectroscopy, the molecule is transiently negatively charged. Within the Born–Oppenheimer approximation, this process is described by a vertical transition in the energy level diagram from the ground state M^0 to the excited state M^*. Upon charging, the molecule undergoes a geometric distortion, captured by the shift of the potential energy curve of the excited state. Vertical transitions allow for probing many vibronic states, with the intensities given by a Poisson distribution,

$$I_{kn} = e^{-S_k} \frac{S_k^n}{n!},$$

with S_k being the Huang–Rhys factor of the vibrational mode k and n its harmonics. The Huang–Rhys factor is determined by the relaxation energy ε_k of a vibrational mode when charging the molecule as

$$S_k = \frac{\varepsilon_k}{\hbar\omega_k}.$$

From the DFT calculations of the TCNQ molecule, we determine all vibrational eigenmodes in the negatively charged state and also derive the Huang–Rhys factors S_k [26]. The latter are plotted in the upper panel of Figure 6b (dots, right axis). Applying to each of the vibronic states a Lorentzian peak with a full width at half maximum of 60 meV and intensity proportional to the Poisson distribution, as described above, leads to the simulated Franck–Condon spectrum in the upper panel of Figure 6b. This spectrum closely resembles the experimental one and, therefore, nicely reflects the nature of the satellite structure. We note that the bias voltage axis (bottom panel) is scaled by 10% compared to the energy axis (top panel) to account for the voltage drop across the MoS_2 layer [65]. We now realize that the peak at approx. 640 meV consists of three vibrational modes (at 151, 175, and 206 meV) exhibiting a large Huang–Rhys factor. These modes correspond to in-plane breathing modes of TCNQ (see schemes in Figure 6d–f), which are particularly sensitive to charging. Additionally, a mode at 40 meV has a large Huang–Rhys factor. The excitation of this mode is not energetically well separated from the elastic onset of the LUMO in experiment. However, this mode contributes to an asymmetric line shape, which can be realized by comparing the low-energy flank to the high-energy fall-off of the first resonance. The low-energy side can be fitted by a Voigt profile and suggests a lifetime broadening of 55 ± 15 meV. This is, however, insufficient for a peak separation from the mode at 40 meV.

We further note that the experimental spectrum was taken on a cyano group, where no nodal planes exist in the LUMO, as their presence may lead to vibration-assisted tunneling in addition to the bare Franck–Condon excitation [52].

Conclusion

We have shown that a single layer of MoS_2 may act as a decoupling layer for molecules from the underlying metal surface, if the molecular resonances lie within the semiconducting bandgap of MoS_2. MoS_2 on Au(111) and Ag(111) exhibit very similar gap structures, but are shifted in energy according to the different work functions of the metal. Though this is not the only reason for the band modifications [33], we suggest that such considerations may help when searching for appropriate decoupling layers for specific molecules. We have challenged the decoupling properties of MoS_2/Ag(111) for TCNQ molecules. These exhibit their LUMO resonance just at the conduction band onset of MoS_2, whereas the HOMO lies within the valence band. Hence, the HOMO is not decoupled from the substrate, and also the LUMO suffers considerable lifetime broadening as compared to resonances, which would be well separated from the onsets of the MoS_2 bands. The lifetime broadening of 55 ± 15 meV can be translated into a lifetime of approx. 6 fs of the excited state. This is almost one order of magnitude longer than on the bare metal surface, where the hot electron vanishes into the bulk on ultrafast timescales, but an order of magnitude shorter than for molecular resonances well separated from the band onsets [26,52,56]. Yet, the increase in the lifetime of the excited state allowed us to resolve vibronic states of the transiently negatively charged TCNQ molecule albeit only up to approx. 200 meV above the LUMO resonance, where contributions of MoS_2 bands at Γ become strong. Our simulations reproduce the experimental satellite structure of the LUMO very well, although the experimental width prevented us from resolving the individual modes.

Acknowledgements

We acknowledge discussions with S. Trishin and J. R. Simon.

Funding

A. Yousofnejad acknowledges a scholarship from the Claussen–Simon Stiftung. This work was supported by the Deutsche Forschungsgemeinschaft (DFG) - project number 182087777 - SFB 951 (A14), and project number 328545488 - TRR 227 (B05).

ORCID® iDs

Asieh Yousofnejad - https://orcid.org/0000-0002-7275-0228
Gaël Reecht - https://orcid.org/0000-0001-5036-7271
Christian Lotze - https://orcid.org/0000-0001-6847-5676
Katharina J. Franke - https://orcid.org/0000-0001-9416-023X

Preprint

A non-peer-reviewed version of this article has been previously published as a preprint https://arxiv.org/abs/2006.12154

References

1. Lu, X.; Grobis, M.; Khoo, K. H.; Louie, S. G.; Crommie, M. F. *Phys. Rev. B* **2004,** *70,* 115418. doi:10.1103/physrevb.70.115418
2. Thygesen, K. S.; Rubio, A. *Phys. Rev. Lett.* **2009,** *102,* 046802. doi:10.1103/physrevlett.102.046802
3. Braun, S.; Salaneck, W. R.; Fahlman, M. *Adv. Mater. (Weinheim, Ger.)* **2009,** *21,* 1450–1472. doi:10.1002/adma.200802893
4. Tautz, F. S. *Prog. Surf. Sci.* **2007,** *82,* 479–520. doi:10.1016/j.progsurf.2007.09.001
5. Torrente, I. F.; Franke, K. J.; Pascual, J. I. *Int. J. Mass Spectrom.* **2008,** *277,* 269–273. doi:10.1016/j.ijms.2008.07.013
6. Tegeder, P. *J. Phys.: Condens. Matter* **2012,** *24,* 394001. doi:10.1088/0953-8984/24/39/394001
7. Reed, M. A.; Zhou, C.; Muller, C. J.; Burgin, T. P.; Tour, J. M. *Science* **1997,** *278,* 252–254. doi:10.1126/science.278.5336.252
8. Reichert, J.; Ochs, R.; Beckmann, D.; Weber, H. B.; Mayor, M.; v. Löhneysen, H. *Phys. Rev. Lett.* **2002,** *88,* 176804. doi:10.1103/physrevlett.88.176804
9. Venkataraman, L.; Klare, J. E.; Tam, I. W.; Nuckolls, C.; Hybertsen, M. S.; Steigerwald, M. L. *Nano Lett.* **2006,** *6,* 458–462. doi:10.1021/nl052373+
10. Lafferentz, L.; Ample, F.; Yu, H.; Hecht, S.; Joachim, C.; Grill, L. *Science* **2009,** *323,* 1193–1197. doi:10.1126/science.1168255
11. Nitzan, A.; Ratner, M. A. *Science* **2003,** *300,* 1384–1389. doi:10.1126/science.1081572
12. Tao, N. J. *Nat. Nanotechnol.* **2006,** *1,* 173–181. doi:10.1038/nnano.2006.130
13. Aradhya, S. V.; Venkataraman, L. *Nat. Nanotechnol.* **2013,** *8,* 399–410. doi:10.1038/nnano.2013.91
14. Reecht, G.; Lotze, C.; Sysoiev, D.; Huhn, T.; Franke, K. J. *ACS Nano* **2016,** *10,* 10555–10562. doi:10.1021/acsnano.6b06559
15. Repp, J.; Meyer, G.; Stojković, S. M.; Gourdon, A.; Joachim, C. *Phys. Rev. Lett.* **2005,** *94,* 026803. doi:10.1103/physrevlett.94.026803
16. Liljeroth, P.; Repp, J.; Meyer, G. *Science* **2007,** *317,* 1203–1206. doi:10.1126/science.1144366
17. Qiu, X. H.; Nazin, G. V.; Ho, W. *Science* **2003,** *299,* 542–546. doi:10.1126/science.1078675
18. Heinrich, A. J.; Gupta, J. A.; Lutz, C. P.; Eigler, D. M. *Science* **2004,** *306,* 466–469. doi:10.1126/science.1101077
19. Rau, I. G.; Baumann, S.; Rusponi, S.; Donati, F.; Stepanow, S.; Gragnaniello, L.; Dreiser, J.; Piamonteze, C.; Nolting, F.; Gangopadhyay, S.; Albertini, O. R.; Macfarlane, R. M.; Lutz, C. P.; Jones, B. A.; Gambardella, P.; Heinrich, A. J.; Brune, H. *Science* **2014,** *344,* 988–992. doi:10.1126/science.1252841
20. Hirjibehedin, C. F.; Lutz, C. P.; Heinrich, A. J. *Science* **2006,** *312,* 1021–1024. doi:10.1126/science.1125398
21. Franke, K. J.; Schulze, G.; Henningsen, N.; Fernández-Torrente, I.; Pascual, J. I.; Zarwell, S.; Rück-Braun, K.; Cobian, M.; Lorente, N. *Phys. Rev. Lett.* **2008,** *100,* 036807. doi:10.1103/physrevlett.100.036807
22. Matino, F.; Schull, G.; Köhler, F.; Gabutti, S.; Mayor, M.; Berndt, R. *Proc. Natl. Acad. Sci. U. S. A.* **2011,** *108,* 961–964. doi:10.1073/pnas.1006661107
23. Garnica, M.; Stradi, D.; Barja, S.; Calleja, F.; Díaz, C.; Alcamí, M.; Martín, N.; Vázquez de Parga, A. L.; Martín, F.; Miranda, R. *Nat. Phys.* **2013,** *9,* 368–374. doi:10.1038/nphys2610
24. Riss, A.; Wickenburg, S.; Tan, L. Z.; Tsai, H.-Z.; Kim, Y.; Lu, J.; Bradley, A. J.; Ugeda, M. M.; Meaker, K. L.; Watanabe, K.; Taniguchi, T.; Zettl, A.; Fischer, F. R.; Louie, S. G.; Crommie, M. F. *ACS Nano* **2014,** *8,* 5395–5401. doi:10.1021/nn501459v
25. Schulz, F.; Drost, R.; Hämäläinen, S. K.; Liljeroth, P. *ACS Nano* **2013,** *7,* 11121–11128. doi:10.1021/nn404840h
26. Krane, N.; Lotze, C.; Reecht, G.; Zhang, L.; Briseno, A. L.; Franke, K. J. *ACS Nano* **2018,** *12,* 11698–11703. doi:10.1021/acsnano.8b07414
27. Repp, J.; Meyer, G.; Paavilainen, S.; Olsson, F. E.; Persson, M. *Phys. Rev. Lett.* **2005,** *95,* 225503. doi:10.1103/physrevlett.95.225503
28. Fatayer, S.; Schuler, B.; Steurer, W.; Scivetti, I.; Repp, J.; Gross, L.; Persson, M.; Meyer, G. *Nat. Nanotechnol.* **2018,** *13,* 376–380. doi:10.1038/s41565-018-0087-1
29. Bruix, A.; Miwa, J. A.; Hauptmann, N.; Wegner, D.; Ulstrup, S.; Grønborg, S. S.; Sanders, C. E.; Dendzik, M.; Grubišić Čabo, A.; Bianchi, M.; Lauritsen, J. V.; Khajetoorians, A. A.; Hammer, B.; Hofmann, P. *Phys. Rev. B* **2016,** *93,* 165422. doi:10.1103/physrevb.93.165422
30. Cheiwchanchamnangij, T.; Lambrecht, W. R. L. *Phys. Rev. B* **2012,** *85,* 205302. doi:10.1103/physrevb.85.205302
31. Qiu, D. Y.; da Jornada, F. H.; Louie, S. G. *Phys. Rev. Lett.* **2013,** *111,* 216805. doi:10.1103/physrevlett.111.216805
32. Bana, H.; Travaglia, E.; Bignardi, L.; Lacovig, P.; Sanders, C. E.; Dendzik, M.; Michiardi, M.; Bianchi, M.; Lizzit, D.; Presel, F.; De Angelis, D.; Apostol, N.; Kumar Das, P.; Fujii, J.; Vobornik, I.; Larciprete, R.; Baraldi, A.; Hofmann, P.; Lizzit, S. *2D Mater.* **2018,** *5,* 035012. doi:10.1088/2053-1583/aabb74
33. Dendzik, M.; Bruix, A.; Michiardi, M.; Ngankeu, A. S.; Bianchi, M.; Miwa, J. A.; Hammer, B.; Hofmann, P.; Sanders, C. E. *Phys. Rev. B* **2017,** *96,* 235440. doi:10.1103/physrevb.96.235440
34. Grønborg, S. S.; Ulstrup, S.; Bianchi, M.; Dendzik, M.; Sanders, C. E.; Lauritsen, J. V.; Hofmann, P.; Miwa, J. A. *Langmuir* **2015,** *31,* 9700–9706. doi:10.1021/acs.langmuir.5b02533
35. Krane, N.; Lotze, C.; Läger, J. M.; Reecht, G.; Franke, K. J. *Nano Lett.* **2016,** *16,* 5163–5168. doi:10.1021/acs.nanolett.6b02101
36. Wakabayashi, N.; Smith, H. G.; Nicklow, R. M. *Phys. Rev. B* **1975,** *12,* 659–663. doi:10.1103/physrevb.12.659
37. Sørensen, S. G.; Füchtbauer, H. G.; Tuxen, A. K.; Walton, A. S.; Lauritsen, J. V. *ACS Nano* **2014,** *8,* 6788–6796. doi:10.1021/nn502812n
38. Krane, N.; Lotze, C.; Franke, K. J. *Surf. Sci.* **2018,** *678,* 136–142. doi:10.1016/j.susc.2018.03.015
39. Bronsema, K. D.; De Boer, J. L.; Jellinek, F. *Z. Anorg. Allg. Chem.* **1986,** *540,* 15–17. doi:10.1002/zaac.19865400904
40. Schumacher, A.; Scandella, L.; Kruse, N.; Prins, R. *Surf. Sci.* **1993,** *289,* L595–L598. doi:10.1016/0039-6028(93)90875-k
41. Helveg, S.; Lauritsen, J. V.; Lægsgaard, E.; Stensgaard, I.; Nørskov, J. K.; Clausen, B. S.; Topsøe, H.; Besenbacher, F. *Phys. Rev. Lett.* **2000,** *84,* 951–954. doi:10.1103/physrevlett.84.951
42. Mak, K. F.; Lee, C.; Hone, J.; Shan, J.; Heinz, T. F. *Phys. Rev. Lett.* **2010,** *105,* 136805. doi:10.1103/physrevlett.105.136805
43. Splendiani, A.; Sun, L.; Zhang, Y.; Li, T.; Kim, J.; Chim, C.-Y.; Galli, G.; Wang, F. *Nano Lett.* **2010,** *10,* 1271–1275. doi:10.1021/nl903868w
44. Miwa, J. A.; Ulstrup, S.; Sørensen, S. G.; Dendzik, M.; Čabo, A. G.; Bianchi, M.; Lauritsen, J. V.; Hofmann, P. *Phys. Rev. Lett.* **2015,** *114,* 046802. doi:10.1103/physrevlett.114.046802

45. Zhang, C.; Chen, Y.; Johnson, A.; Li, M.-Y.; Li, L.-J.; Mende, P. C.; Feenstra, R. M.; Shih, C.-K. *Nano Lett.* **2015,** *15,* 6494–6500. doi:10.1021/acs.nanolett.5b01968
46. Rösner, M.; Steinke, C.; Lorke, M.; Gies, C.; Jahnke, F.; Wehling, T. O. *Nano Lett.* **2016,** *16,* 2322–2327. doi:10.1021/acs.nanolett.5b05009
47. Barja, S.; Garnica, M.; Hinarejos, J. J.; Vázquez de Parga, A. L.; Martín, N.; Miranda, R. *Chem. Commun.* **2010,** *46,* 8198–8200. doi:10.1039/c0cc02675a
48. Park, C.; Rojas, G. A.; Jeon, S.; Kelly, S. J.; Smith, S. C.; Sumpter, B. G.; Yoon, M.; Maksymovych, P. *Phys. Rev. B* **2014,** *90,* 125432. doi:10.1103/physrevb.90.125432
49. Pham, V. D.; Ghosh, S.; Joucken, F.; Pelaez-Fernandez, M.; Repain, V.; Chacon, C.; Bellec, A.; Girard, Y.; Sporken, R.; Rousset, S.; Dappe, Y. J.; Narasimhan, S.; Lagoute, J. *npj 2D Mater. Appl.* **2019,** *3,* 5. doi:10.1038/s41699-019-0087-5
50. *Gaussian 09,* Revision D.01; Gaussian, Inc.: Wallingford, CT, USA, 2009.
51. Bardeen, J. *Phys. Rev. Lett.* **1961,** *6,* 57–59. doi:10.1103/physrevlett.6.57
52. Reecht, G.; Krane, N.; Lotze, C.; Zhang, L.; Briseno, A. L.; Franke, K. J. *Phys. Rev. Lett.* **2020,** *124,* 116804. doi:10.1103/physrevlett.124.116804
53. Milián, B.; Pou-Amérigo, R.; Viruela, R.; Ortı, E. *Chem. Phys. Lett.* **2004,** *391,* 148–151. doi:10.1016/j.cplett.2004.04.102
54. Zhu, G.-Z.; Wang, L.-S. *J. Chem. Phys.* **2015,** *143,* 221102. doi:10.1063/1.4937761
55. Zhong, H.; Quhe, R.; Wang, Y.; Ni, Z.; Ye, M.; Song, Z.; Pan, Y.; Yang, J.; Yang, L.; Lei, M.; Shi, J.; Lu, J. *Sci. Rep.* **2016,** *6,* 21786. doi:10.1038/srep21786
56. Reecht, G.; Krane, N.; Lotze, C.; Franke, K. J. *ACS Nano* **2019,** *13,* 7031–7035. doi:10.1021/acsnano.9b02117
57. Qiu, X. H.; Nazin, G. V.; Ho, W. *Phys. Rev. Lett.* **2004,** *92,* 206102. doi:10.1103/physrevlett.92.206102
58. Pradhan, N. A.; Liu, N.; Ho, W. *J. Phys. Chem. B* **2005,** *109,* 8513–8518. doi:10.1021/jp045289b
59. Nazin, G. V.; Wu, S. W.; Ho, W. *Proc. Natl. Acad. Sci. U. S. A.* **2005,** *102,* 8832–8837. doi:10.1073/pnas.0501171102
60. Frederiksen, T.; Franke, K. J.; Arnau, A.; Schulze, G.; Pascual, J. I.; Lorente, N. *Phys. Rev. B* **2008,** *78,* 233401. doi:10.1103/physrevb.78.233401
61. Wickenburg, S.; Lu, J.; Lischner, J.; Tsai, H.-Z.; Omrani, A. A.; Riss, A.; Karrasch, C.; Bradley, A.; Jung, H. S.; Khajeh, R.; Wong, D.; Watanabe, K.; Taniguchi, T.; Zettl, A.; Neto, A. H. C.; Louie, S. G.; Crommie, M. F. *Nat. Commun.* **2016,** *7,* 13553. doi:10.1038/ncomms13553
62. Huan, Q.; Jiang, Y.; Zhang, Y. Y.; Ham, U.; Ho, W. *J. Chem. Phys.* **2011,** *135,* 014705. doi:10.1063/1.3598958
63. Schwarz, F.; Wang, Y. F.; Hofer, W. A.; Berndt, R.; Runge, E.; Kröger, J. *J. Phys. Chem. C* **2015,** *119,* 15716–15722. doi:10.1021/acs.jpcc.5b03392
64. Mehler, A.; Néel, N.; Bocquet, M.-L.; Kröger, J. *J. Phys.: Condens. Matter* **2019,** *31,* 065001. doi:10.1088/1361-648x/aaf54c
65. Krane, N.; Lotze, C.; Bogdanoff, N.; Reecht, G.; Zhang, L.; Briseno, A. L.; Franke, K. J. *Phys. Rev. B* **2019,** *100,* 035410. doi:10.1103/physrevb.100.035410

License and Terms

The definitive version of this article is the electronic one which can be found at:
doi:10.3762/bjnano.11.91

BEILSTEIN JOURNAL OF NANOTECHNOLOGY

Scanning tunneling microscopy and spectroscopy of rubrene on clean and graphene-covered metal surfaces

Karl Rothe, Alexander Mehler, Nicolas Néel* and Jörg Kröger

Full Research Paper

Open Access

Address:
Institut für Physik, Technische Universität Ilmenau, D-98693 Ilmenau, Germany

Email:
Nicolas Néel* - nicolas.neel@tu-ilmenau.de

* Corresponding author

Keywords:
graphene; metal surfaces; molecular superstructures; rubrene; scanning tunneling microscopy; scanning tunneling spectroscopy; vibronic states

Beilstein J. Nanotechnol. **2020,** *11,* 1157–1167.
doi:10.3762/bjnano.11.100

Received: 27 March 2020
Accepted: 23 July 2020
Published: 03 August 2020

This article is part of the thematic issue "Molecular assemblies on surfaces – towards physical and electronic decoupling of organic molecules".

Guest Editor: S. Maier

Abstract

Rubrene ($C_{42}H_{28}$) was adsorbed with submonolayer coverage on Pt(111), Au(111), and graphene-covered Pt(111). Adsorption phases and vibronic properties of $C_{42}H_{28}$ consistently reflect the progressive reduction of the molecule–substrate hybridization. Separate $C_{42}H_{28}$ clusters are observed on Pt(111) as well as broad molecular resonances. On Au(111) and graphene-covered Pt(111) compact molecular islands with similar unit cells of the superstructure characterize the adsorption phase. The highest occupied molecular orbital of $C_{42}H_{28}$ on Au(111) exhibits weak vibronic progression while unoccupied molecular resonances appear with a broad line shape. In contrast, vibronic subbands are present for both frontier orbitals of $C_{42}H_{28}$ on graphene. They are due to different molecular vibrational quanta with distinct Huang–Rhys factors.

Introduction

Two-dimensional materials are emerging as monatomically thin buffer layers (BLs) on metal surfaces, i.e., as intermediate films that efficiently reduce the hybridization of an adsorbate with the metallic substrate. The minimization of the adsorbate–substrate coupling is motivated by the desire to preserve genuine properties of the free atom or molecule even after adsorption. For instance, adsorption on a BL often retains the sharp electronic and vibrational energy levels that are characteristic for the atom or molecule vacuum state and that would inevitably be broadened or even quenched upon adsorption on the metal surface. Narrow molecular resonances on surfaces are desirable because they increase the residence time of injected charge at the adsorbate, which is favorable for, e.g., energy conversion processes or the observation of vibronic progression [1].

Structural aspects of adsorption on the prominent two-dimensional materials graphene [2] and hexagonal boron nitride (h-BN) [3] have been studied in detail. In contrast, vibrational spectroscopy at the single-molecule level is scarce. Scanning tunneling spectroscopy (STS) of vibronic levels of 1,3,5-tris(2,2-dicyanovinyl)benzene on graphene-covered h-BN on SiO_2 [4], of cobalt phthalocyanine molecules on graphene-covered SiO_2/Si samples [5] as well as on h-BN-covered Ir(111) [6], of conjugated oligohenylenes on h-BN-covered Cu(111) [7], of manganese phthalocyanine on h-BN-covered Rh(111) [8], and of 5,10,15,20-tetraphenylbisbenz[5,6]indendo[1,2,3-*cd*:1′,2′,3′-*lm*]perylene on graphene-covered Ir(111) [9] have been reported so far. In these studies molecular orbitals, the highest occupied molecular orbital (HOMO) or the lowest unoccupied molecular orbital (LUMO), appear with spectroscopic fine structure in differential conductance (dI/dV, I: tunneling current, V: bias voltage) data, which is assigned to vibronic progression induced by a single group of molecular vibrations with similar quantum energies. Another type of two-dimensional materials is represented by single layers of transition metal dichalcogenides. A single layer of MoS_2 on Au(111) has recently been used to electronically decouple 2,5-bis(3-dodecylthiophen-2-yl)thieno[3,2-*b*]thiophene from the metal surface [10]. A rich vibronic fine structure was observed in the HOMO spectroscopic signature induced by several fundamental vibrational modes of the molecule together with their higher harmonics and combination vibrations.

In the work presented here, 5,6,11,12-tetraphenyltetracene (rubrene, $C_{42}H_{28}$, Figure 1) was adsorbed on different surfaces, namely Pt(111), Au(111), and graphene on Pt(111), in order to demonstrate a gradual reduction of the $C_{42}H_{28}$–surface hybridization. The choice of the molecule and substrate surfaces was motivated as follows. $C_{42}H_{28}$ is a polycyclic aromatic hydrocarbon (Figure 1a) with an extended system of delocalized π electrons. In the gas phase, intramolecular steric hindrance [11,12] causes the phenyl groups to rotate around their σ bonds, out of the tetracene backbone plane (Figure 1b). The molecule therefore adopts a lander configuration that supposedly is beneficial to the electronic decoupling of its backbone from the substrate it is adsorbed to. Moreover, a twisted tetracene backbone (Figure 1c) is energetically more favorable than its planar, i.e., nontwisted, geometry (Figure 1b) for the vacuum state of $C_{42}H_{28}$ [13,14]. Upon adsorption of the molecule, the backbone may even be tilted with respect to the surface plane, i.e., it encloses a finite angle with the surface and, thus, deviates from a parallel adsorption [15]. From a more general point of view, $C_{42}H_{28}$ has gained in importance for its suitability in light-emitting diodes [16] and organic field-effect transistors [17]. As substrate surfaces, Pt(111) and Au(111) were chosen for their different electronic structure around the Fermi level. Pt(111) exhibits a high density of d states close to the Fermi energy (E_F) [18,19], while Au(111) is characterized by a surface-projected gap of sp-derived electron states [20]. Graphene on Pt(111) exhibits a considerable distance of 330 pm from the metal surface [21], which implies a weak graphene–metal hybridization. Adsorbates on graphene-covered Pt(111) are therefore expected to be well decoupled from the metal substrate.

After adsorption of $C_{42}H_{28}$ on Pt(111) scanning tunneling microscopy (STM) images reveal the occurrence of separate molecular clusters and very broad molecular resonances in STS data, which is attributed to an elevated $C_{42}H_{28}$–Pt interaction. On Au(111) the observations are compatible with a reduced hybridization since compact molecular islands with a regular superstructure form and vibronic progression of the HOMO dI/dV spectroscopic signature is visible. Unoccupied molecular orbitals, however, appear as broad and merged resonances without indication of a vibronic fine structure. The molecular superstructure on graphene is similar to the assembly on Au(111), albeit with a lower molecule surface density, and dI/dV data exhibit vibronic progression in both frontier orbitals, which

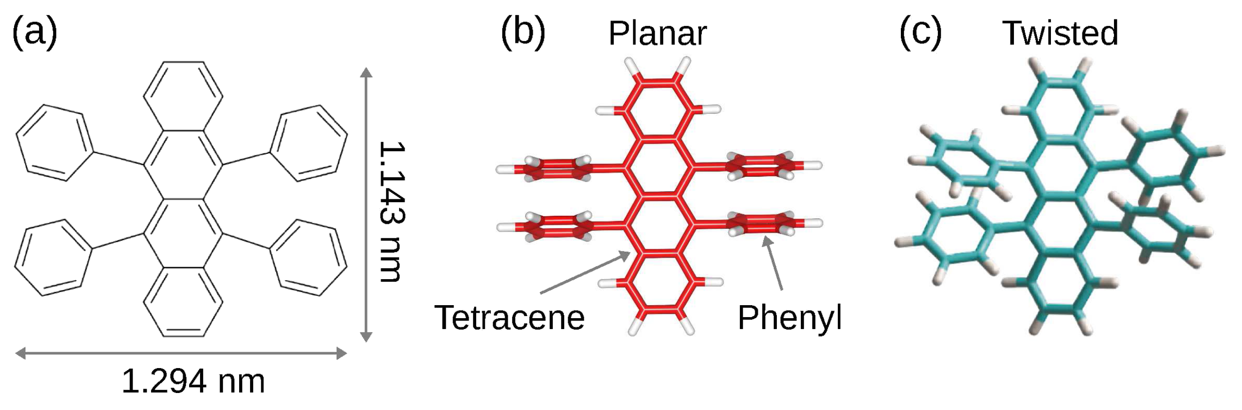

Figure 1: (a) Skeletal formula of $C_{42}H_{28}$ including dimensions. (b) Sketch of the planar molecular configuration. (c) Sketch of the twisted molecular configuration. Adapted with permission from [22], copyright (2008) American Chemical Society.

reflects the effective separation of $C_{42}H_{28}$ from the metal surface.

Experimental

The experiments were performed with an STM operated in ultrahigh vacuum (10^{-9} Pa) and at low temperature (Pt(111) and graphene-covered Pt(111) at 5 K, Au(111) at 78 K). Pt(111) and Au(111) surfaces were cleaned by Ar^+ ion bombardment and annealing. Graphene was epitaxially grown on Pt(111) by exposing the heated (1300 K) surface to the molecular precursor C_2H_4 (purity 99.9%) at a partial pressure of 10^{-4} Pa for 120 s [23]. $C_{42}H_{28}$ molecules were sublimated from a powder (purity 98%), deposited in a heated (500 K) W crucible and directed towards the sample surface at room temperature. Molecular coverages below the closed single molecular layer are estimated from STM images as the percentage of the covered surface area. All STM images were recorded at constant current with the bias voltage applied to the sample. Constant-height dI/dV data were acquired with a lock-in amplifier by sinusoidally modulating the bias voltage (5 mV_{rms}, 750 Hz) and measuring the first harmonic of the current response of the tunneling barrier.

Results and Discussion

Pt(111)–$C_{42}H_{28}$

Figure 2a shows an overview STM image of $C_{42}H_{28}$ on Pt(111) at a coverage of approx. 20%. Well separated molecules or clusters of molecules can be discerned on the terrace without evidence for island formation or decoration of substrate step edges. These observations are indicative of an effectively reduced surface diffusion after adsorption, which lowers the mobility of adsorbed molecules and, thus, the formation of large molecular islands. The close-up view in Figure 2b shows that $C_{42}H_{28}$ molecules exhibit a submolecular structure consisting of two bright lobes separated by a central line with dim contrast. Some molecules even exhibit three lobes (Figure 2c). The two bright lobes of $C_{42}H_{28}$ in Figure 2b are assigned to one pair of phenyl groups each, while the dim line is attributed to the tetracene backbone (Figure 1). The two opposite pairs of phenyl groups appear with different contrast. Considering geometric properties alone, these microscopic observations contradict the twisted configuration of the molecule (Figure 1c) where one diagonal pair of phenyl groups would appear higher than the other. Such a configuration was indeed observed for a closed monolayer of $C_{42}H_{28}$ on Ag(100) [24]. However, it is difficult to infer geometric heights from STM images due to variations in the local density of states. Moreover, the elevated hybridization of $C_{42}H_{28}$ with Pt(111) is likely to distort the relaxed vacuum configuration of the molecule. A comparison of experimental data with simulated STM images would allow for further insight into the actual adsorption geometry; however, this is out of the scope of this work. The absence of individually resolved $C_{42}H_{28}$ phenyl groups on Pt(111) may be ascribed to the aforementioned elevated hybridization of the molecular and the substrate electronic structure, possibly mediated by the high density of Pt d bands at E_F [18,19]. In such cases, submolecular motifs are often suppressed.

Before corroborating the suggestion of elevated molecule–substrate coupling by STS data the occurrence of chiral molecular species shall be discussed. The close-up STM image in Figure 2c shows adsorbed $C_{42}H_{28}$ molecules that appear with three rather than two lobes. Moreover, numbering the brightest to the dimmest lobe with **1**, **2**, and **3** reveals that two senses of rotation, clockwise (*R*) and anticlockwise (*L*), occur. In agreement with previous findings for $C_{42}H_{28}$ on Au(111) [25,26], the three lobes reflect a tilted molecular backbone. Lobes **1** and **2** are assigned to one pair of phenyl groups each, similar to the as-

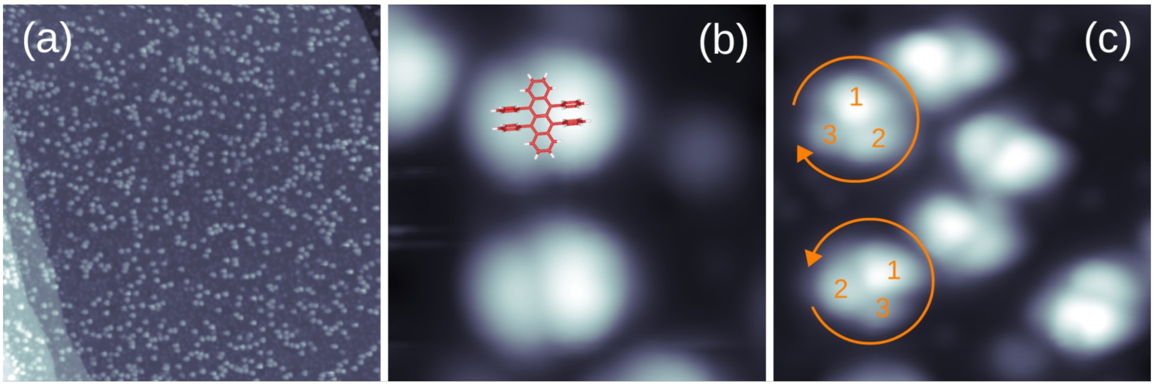

Figure 2: (a) STM image of $C_{42}H_{28}$ molecules on Pt(111) (bias voltage: 1 V, tunneling current: 100 pA, size: 150 × 150 nm^2). (b) Close-up view of $C_{42}H_{28}$ with twisted configuration of the backbone 1 V, 100 pA, 5 × 5 nm^2). The attached molecule sketch is to scale. (c) Close-up view of $C_{42}H_{28}$ with twisted and tilted configuration of the backbone (1 V, 100 pA, 7.1 × 7.1 nm^2). **1**, **2**, and **3** number the brightest to the dimmest lobe and reveal the two rotational senses.

signment for molecules appearing with two lobes only. Lobe **3** is due to one end of the tetracene backbone that likely adopts an inclined adsorption geometry, i.e., encloses a finite angle with the Pt(111) surface plane. In the case of $C_{42}H_{28}$ on Au(111) this angle was determined as approx. 38° by near-edge X-ray absorption fine structure spectroscopy [15]. The observed chirality, R-$C_{42}H_{28}$ and L-$C_{42}H_{28}$, therefore results from the left or right pair of phenyl groups of a twisted $C_{42}H_{28}$ molecule being closer to the surface. On Au(111) the formation of homochiral clusters led to remarkable supramolecular assemblies [25-27], which, however, are not present on Pt(111).

The presumably elevated $C_{42}H_{28}$–Pt(111) hybridization is corroborated by dI/dV spectra of the molecule. Figure 3 shows spectra recorded above intramolecular sites that approximately correspond to one phenyl group of the opposite lobes. The bottom spectrum was acquired atop the dim lobe of the molecule showing a peak at approx. −1.6 V and a rather broad feature at approx. 1.0 V. In contrast, dI/dV spectra recorded atop the bright lobe (top spectrum in Figure 3) only exhibit a broad peak at approx. −1.3 V and no further peak-like signature up to 2 V. Both spectra do not exhibit a clear-cut gap region, i.e., a bias voltage range with nearly vanishing dI/dV signal. These observations reflect the strong hybridization of $C_{42}H_{28}$ with the Pt(111) surface and hamper the meaningful determination of a HOMO–LUMO gap width. Moreover, the spectra of Figure 3 emphasize that a bright (dim) contrast does not necessarily imply a high (low) geometrical distance. The bright lobe of the molecule exhibits a dI/dV spectrum with a single broad orbital feature, which indicates its elevated hybridization with the metal surface rather than its greater distance from the surface.

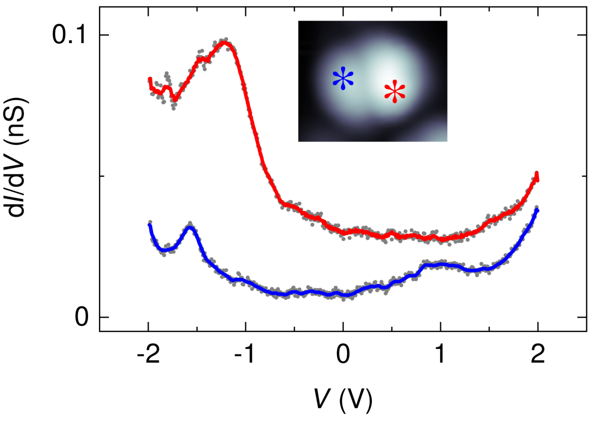

Figure 3: Spectra of dI/dV (dots) recorded above the different lobes of $C_{42}H_{28}$ on Pt(111) (feedback loop parameters prior to spectroscopy: 2.5 V, 100 pA). The solid lines represent smoothed data. The bottom (top) spectrum was acquired atop the left (right) lobe of the molecule as indicated in the inset. Inset: STM image of a single $C_{42}H_{28}$ molecule on Pt(111) (1 V, 100 pA, 3 × 2.5 nm^2) with asterisks marking the positions of spectroscopy.

Au(111)–$C_{42}H_{28}$

Figure 4a shows an overview STM image of $C_{42}H_{28}$ on Au(111) at a surface coverage of approx. 50%. The molecules form well-ordered large islands. In addition to the regular arrangement of $C_{42}H_{28}$, The STM image reveals a periodic pattern of stripes, which are due to the $22 \times \sqrt{3}$ (or herringbone) reconstruction of Au(111) [28-30]. It consists of adjacent surface regions with alternating hexagonal close-packed (hcp) and face-centered cubic (fcc) stacking of Au(111) atom planes. These domains are separated by discommensuration lines (or soliton walls), which are visible as stripes with increased apparent height in Figure 4a. By measuring the width of hcp and fcc stacking domains on clean and $C_{42}H_{28}$-covered Au(111) we find that $C_{42}H_{28}$ adsorption leaves the surface reconstruction invariant. In addition, step edges of the Au(111) surface are decorated with molecules (inset to Figure 4a). These topographic data univocally hint at an enhanced $C_{42}H_{28}$ mobility after adsorption compared to the situation on Pt(111) (vide supra). The STM data presented in Figure 4a reveal an additional periodic modulation of the apparent height along the discommensuration lines, which will be discussed below.

The close-up STM image of a molecular island (Figure 4b) enables the resolution of individual molecules and the unit cell of the molecular superstructure. For negative bias voltages a single $C_{42}H_{28}$ molecule exhibits four lobes, which are attributed to the four phenyl groups. The superimposed molecule sketch visualizes this assignment. For some molecules the apparent height of all four phenyl groups is similar, while others exhibit a pair of diagonal phenyl groups appearing higher than the other pair, similar to previous findings on Ag(100) [24]. This observation is compatible with the presence of a mixture of molecules adsorbing with either a planar, i.e., all phenyl groups appear with similar heights, or a twisted, i.e., with different apparent heights for diagonal pairs of phenyl groups, tetracene backbone. The STM images do not indicate the presence of a tilted backbone. Therefore, the molecules adopt a nonchiral adsorption configuration, which contrasts the findings on Pt(111) (vide supra) and previously reported results for Au(111) [15,25-27]. In its crystalline phase the $C_{42}H_{28}$ molecule may indeed adopt the planar configuration of its tetracene backbone owing to a large cohesive energy that overcompensates through intermolecular hybridization the energy cost for planarization [13,31]. Flat $C_{42}H_{28}$ molecules were previously reported for monolayers on Au(111) [32], while on Bi(001) a coexistence of twisted and planar $C_{42}H_{28}$ was observed [33].

The unit cell of the superstructure is spanned by the lattice vectors **a** and **b** with $\mathbf{a} \parallel \langle 11\bar{2} \rangle$ (crystallographic direction of soliton walls), $|\mathbf{a}|$ = 1.15 ± 0.10 nm, $|\mathbf{b}|$ = 1.30 ± 0.10 nm,

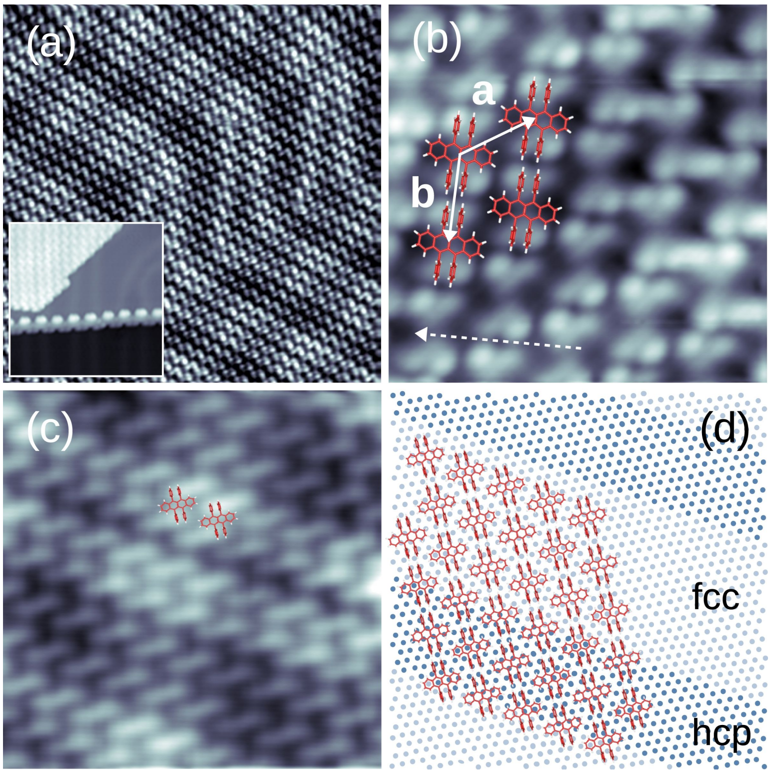

Figure 4: (a) STM image of $C_{42}H_{28}$ molecules on Au(111) (−0.8 V, 50 pA, 30 × 30 nm^2). Inset: STM image of a Au(111) step edge decorated in a zigzag manner with $C_{42}H_{28}$ molecules on the top and bottom terrace (−2 V, 50 pA, 19 × 19 nm^2). (b) Close-up view of a molecular island (−0.65 V, 100 pA, 5 × 5 nm^2). Sketches of $C_{42}H_{28}$ (to scale) are superimposed to facilitate the identification of individual molecules. The unit cell vectors **a** and **b** of the $C_{42}H_{28}$ lattice are indicated as arrows. The dashed arrow marks a $\langle 1\bar{1}0\rangle$ compact direction of Au(111). (c) Close-up STM image, which emphasizes the Au(111) reconstruction lines together with an additional periodic modulation of the apparent height along these lines (1 V, 50 pA, 10 × 10 nm^2). (d) Sketch of suggested $C_{42}H_{28}$ adsorption on Au(111) with molecular rows being aligned with the separation of the fcc (bright dots) and hcp (dark dots) stacking domains of the surface reconstruction.

$\measuredangle(\mathbf{a},\mathbf{b}) = (124 \pm 5)°$, giving rise to a molecule surface density of approx. 0.67 nm^{-2}. The tetracene backbone is oriented along a $\langle 1\bar{1}0\rangle$ crystallographic direction of Au(111). In [32] a similar superstructure with planar $C_{42}H_{28}$ backbones oriented parallel to the Au(111) surface was reported. In that work a multilayer $C_{42}H_{28}$ film was deposited at room temperature and subsequently annealed to achieve a monolayer coverage. Different superstructures of $C_{42}H_{28}$ with twisted and tilted backbones were presented in [25-27,34] for Au(111) and in [35] for Bi(111). In these reports, the deposition of molecules was performed at 5 K [25-27,34] and 100 K [35] with subsequent annealing at room temperature [25-27,34] and 350 K [35]. Therefore, deposition at low temperature seems to favor the adsorption with twisted and tilted backbones, possibly due to an initial high density of small island with chiral molecules, while the subsequent annealing preserves the twisted and tilted configuration of the molecular backbone and leads to homochiral domains. The twisted configuration of the molecular backbone of $C_{42}H_{28}$ is not limited to low-temperature depositions. It was likewise observed for room-temperature deposition on low-index Cu surfaces [22,36] and Ag(100) [24].

The STM image in Figure 4c shows the influence of the $22 \times \sqrt{3}$ Au(111) reconstruction on the $C_{42}H_{28}$ assembly. Evidently, the molecular superstructure matches the period of the reconstruction, which is reflected by the alignment of molecule rows with the discommensuration lines. A single row of $C_{42}H_{28}$ occupies the top of the soliton walls and the narrow hcp stacking domain, while three rows of $C_{42}H_{28}$ reside atop the wider fcc surface regions (confer the sketch in Figure 4d for an illustration). Additionally, Figure 4c unveils a modulation of the apparent height along the discommensuration lines with a corrugation of approx. 9 pm, which is smaller than the approx. 26 pm modulation induced by the Au(111) reconstruction. As Figure 4d shows, nearly equivalent adsorption sites are occupied by the $C_{42}H_{28}$ molecules every 4**a** along the discommensuration lines. Therefore, the additional periodic pattern is due to a moiré effect along the soliton walls. A similar matching of the molecular superstructure with the Au(111) reconstruction was previously reported for $C_{64}H_{36}$ [37].

Next, spectroscopic results obtained for $C_{42}H_{28}$ on Au(111) will be discussed. An overview spectrum is presented in

Figure 5a where a peak-like signature is visible at approx. −0.67 V, which is assigned to the HOMO. The sharp line shape of the HOMO is in accordance with a theoretical work [34], which demonstrated a very low hybridization of the HOMO with the Au(111) electronic states. At positive bias voltage an increase of d*I*/d*V* for $V \geq 1$ V is visible, probably due to the LUMO. Figure 5c shows a d*I*/d*V* spectrum in a higher bias voltage range of unoccupied states. The presented data were normalized by taking the exponential transmission factor of the tunneling barrier into account [38]. The normalized d*I*/d*V* data show a peak at approx. 2.3 V. Due to the considerably broad onset of d*I*/d*V* data starting from approx. 1 V it is difficult to unambiguously assign this peak to the LUMO or LUMO+1. Much wider unoccupied molecular resonances have been observed, too, in pump–probe photoemission experiments on thin $C_{42}H_{28}$ films adsorbed on highly oriented pyrolithic graphite and traced to the elevated molecule–substrate hybridization with a concomitant reduced lifetime of electrons injected into the LUMO [39]. Due to the absence of peaked orbital signatures a HOMO–LUMO gap width is hard to estimate. In a previous report, constant-current d*I*/d*V* data were presented for $C_{42}H_{28}$ on Au(111) and a HOMO–LUMO gap exceeding 3 eV was extracted [25]. A direct comparison to the spectroscopic data presented here is hampered due to the different spectroscopy mode applied and due to the presence of various molecular conformers [25] that were not observed in our experiments with a different preparation.

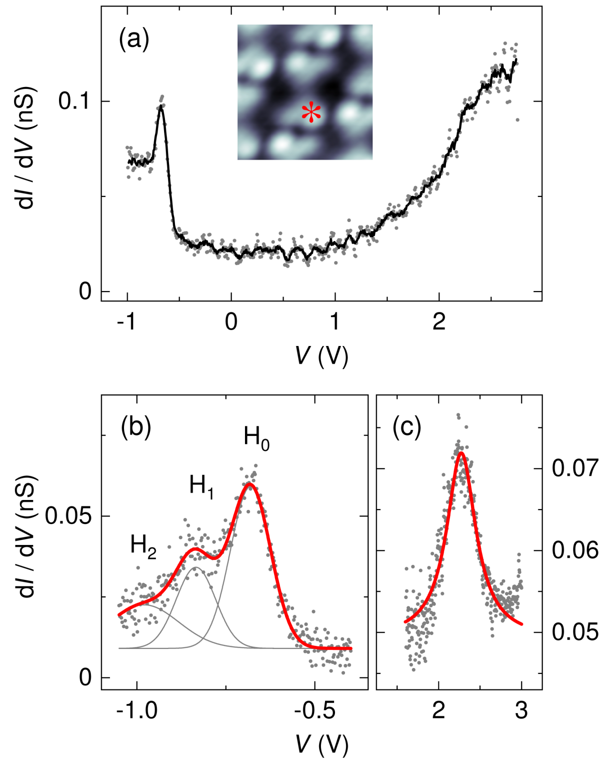

Figure 5: (a) Spectrum of d*I*/d*V* (dots) recorded above a $C_{42}H_{28}$ phenyl group on Au(111) with the spectroscopic signature of the HOMO appearing at approx. −0.67 V (feedback loop parameters: −1 V, 50 pA). The solid line represents smoothed data. Inset: STM image of a single $C_{42}H_{28}$ molecule on Au(111) (−0.65 V, 100 nA, 2 × 2 nm^2) with the asterisk marking the position of spectroscopy. (b) Close-up view of the HOMO (H_0) vibronic fine structure (feedback loop parameters: −1 V, 50 pA). The presented data (dots) are normalized [38]. Vibronic side bands are labeled H_1 and H_2. The thick solid line represents a fit of three Lorentzian line shapes (thin gray lines) and a constant background to the data. (c) Normalized d*I*/d*V* data (dots) showing a peaked unoccupied molecular orbital at approx. 2.3 V (feedback loop parameters: 3 V, 50 pA). The solid line represents the fit of a Lorentzian line shape and a constant background to the data.

Using an increased bias voltage sampling in the HOMO spectral region exhibits d*I*/d*V* data with spectroscopic fine structure (Figure 5b). Three Lorentzian line shapes were superimposed to fit the normalized [38] data using a least-squares fit routine that adjusts the positions, widths and heights of the Lorentzian peaks. Aside from the peak labeled H_0, which is attributed to the spectroscopic signature of the $C_{42}H_{28}$ HOMO, additional peaks H_1 and H_2 are observed. While the peak height of H_2 is weak, its inclusion in the fit was necessary to closely describe the d*I*/d*V* data. The separations H_0–H_1 and H_1–H_2 are nearly identical, 160 ± 10 mV, which hints at vibronic progression due to a group of molecular vibrational modes with energies $h\nu \approx 160$ meV (*h*: Planck constant, ν: vibrational frequency). In vibronic progression the molecule is electronically and vibrationally excited from its ground state by an attached charge, i.e., hole or electron. Here, $C_{42}H_{28}$ is transiently charged by the extraction of an electron from the HOMO in the course of the tunneling process. Therefore, the peak labeled H_0 in Figure 5 reflects the vibrational ground state of positively charged $C_{42}H_{28}$. If the energy of the tunneling electron is sufficiently large then vibrationally excited states of the transiently charged $C_{42}H_{28}$ may be reached, which appear as the satellite peaks H_1 and H_2 to H_0. This resonant transition from a molecular ground state to an electronically and vibrationally excited state is described within the Franck–Condon picture [40]. In particular, the peak heights $I_{\nu,n}$ of the vibronic subbands resulting from transitions of the vibrational ground state of neutral $C_{42}H_{28}$ to the *n*-th vibrationally excited and transiently charged $C_{42}H_{28}$ obey a Poisson distribution,

$$I_{\nu,n} = \frac{S_\nu^n}{n!} \cdot \exp\left(-S_\nu\right), \tag{1}$$

where n is the vibrational quantum number and S_ν is the Huang–Rhys factor, which determines the coupling of the hole or electron to the vibrational quantum with energy $h\nu$. The Huang–Rhys factor can be expressed as

$$S_\nu = \frac{\varepsilon_\nu}{h\nu}, \tag{2}$$

where ε_ν denotes the relaxation energy of the vibration when charging the molecule [10,41]. Comparing the peak height of the orbital signature (I_0) with the first vibronic subband ($I_{\nu,1}$) enables direct access to the Huang–Rhys factor via

$$S_\nu = \frac{I_{\nu,1}}{I_0}. \qquad (3)$$

For the $C_{42}H_{28}$ HOMO on Au(111) a Huang–Rhys factor of approx. 0.5 can be extracted from dI/dV data (Figure 5b) for the vibrational mode with $h\nu \approx 160$ meV.

The energy of the vibrational mode is in good agreement with one of the three $C_{42}H_{28}$ vibrations that were previously determined on a theoretical basis to exhibit a particularly strong Holstein coupling to the HOMO of $C_{42}H_{28}$ embedded in a molecular crystal [42]. Generally speaking, the Holstein coupling describes the local interaction of a charge carrier with a molecular vibration [40] and may therefore be relevant to identify vibrational quanta that induce vibronic progression of a molecular orbital. In the particular case considered here, the charge carrier is a tunneling electron extracted from the $C_{42}H_{28}$ HOMO and may efficiently couple to the Holstein mode reported previously [42]. The calculated mode in question has an energy of 1349 cm^{-1} ≈ 167 meV and mainly consists of stretching vibrations of the tetracene skeleton where the HOMO is mostly localized [43,44].

Graphene–$C_{42}H_{28}$

An STM image of $C_{42}H_{28}$ on graphene-covered Pt(111) at approx. 50% coverage is presented in Figure 6a. It shows an ordered molecular island adjacent to clean graphene, which exhibits a moiré pattern (inset to Figure 6a). The unit cell of the regular molecular superstructure can be inferred from the close-up view in Figure 6b. The lattice vectors are **a** and **b** with **b** || $\langle 11\bar{2}0\rangle$ (crystallographic direction of the graphene lattice, marked by the dashed line in Figure 6b), |**a**| = 1.40 ± 0.10 nm, |**b**| = 1.70 ± 0.10 nm and $\measuredangle(\mathbf{a},\mathbf{b}) = (125 \pm 5)°$. While the unit cell geometry is nearly identical to the one of $C_{42}H_{28}$ on Au(111), the surface density of $C_{42}H_{28}$ on graphene is approx. 0.51 nm^{-2} and, thus, lower than that observed on Au(111). The lower molecule density may tentatively be explained by a molecular superstructure that is formed owing to the optimization of the intermolecular coupling. This might be facilitated by very low energy barriers, which are even lower than those observed for $C_{42}H_{28}$ on Au(111), for translational and rotational degrees of freedom. A template effect of graphene or a moiré lattice on the molecular assembly was not identified. Merely the orientation of the tetracene backbone perpendicular to a $\langle 11\bar{2}0\rangle$ graphene crystallographic direction was observed. A finite residual coupling of the molecule to graphene-covered Pt(111) is likewise indicated by the comparison of the superstructure in Figure 6 with the one obtained for a thicker $C_{42}H_{28}$ film on graphene-covered SiC(0001) [45]. In the latter work a smaller unit cell was reported with individual $C_{42}H_{28}$ molecules appearing uniformly in STM images. It is likely that the difference to the superstructure depicted in Figure 6 results from an efficiently decoupled molecule residing on top of a molecular film deposited on nearly free graphene on SiC(0001).

Similar to observations on Pt(111), $C_{42}H_{28}$ molecules on graphene appear with two or three lobes in STM images, which are labeled α and β in Figure 6b. The two lobes at opposite sites of a dim separating line, which is assigned to the tetracene backbone, are attributed to the two phenyl groups, while the

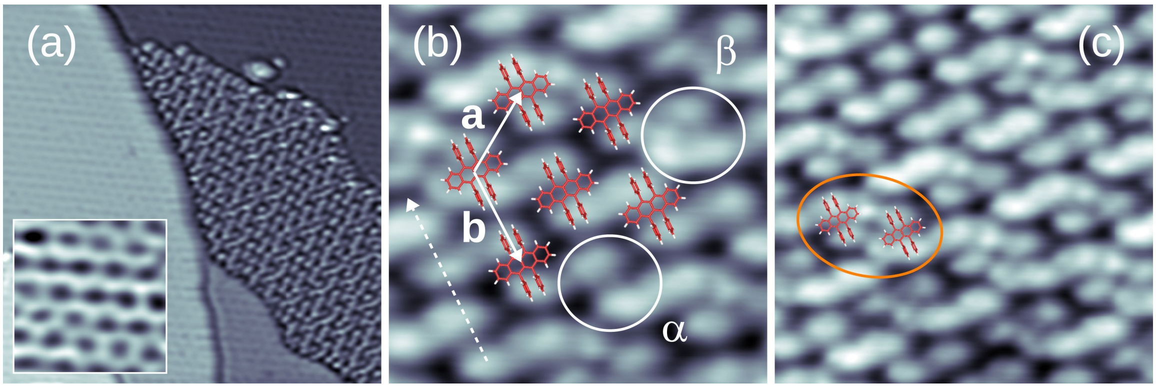

Figure 6: (a) STM image of $C_{42}H_{28}$ molecules on graphene-covered Pt(111) (2 V, 100 pA, 34 × 34 nm^2). Inset: Close-up view of clean graphene with moiré pattern (5 × 5 nm^2). (b) Close-up view of a molecular island (2 V, 20 pA, 6 × 6 nm^2). Molecular sketches (to scale) of the $C_{42}H_{28}$ molecules are superimposed. The unit cell vectors **a** and **b** of the $C_{42}H_{28}$ lattice are indicated as arrows. The dashed arrow marks a $\langle 11\bar{2}0\rangle$ crystallographic direction of graphene. Molecules with planar (α) and twisted as well as tilted (β) configuration are encircled. (c) Close-up view of molecular rows of molecules with twisted and tilted configuration (2 V, 20 pA, 8.3 × 8.3 nm^2). The ellipse indicates a pair of molecules with twisted and tilted configuration.

third lobe at one end of the dim line is caused by the tilting of the backbone. Therefore, α-$C_{42}H_{28}$ on graphene has an apparently planar tetracene moiety, while β-$C_{42}H_{28}$ exhibits a tilted and possibly twisted backbone. Very often, rows of β-$C_{42}H_{28}$ are observed within the compact $C_{42}H_{28}$ island (Figure 6c). Inside the row, pairs of β-molecules orient the upward tilted part of their tetracene backbone towards each other. The coexistence of different $C_{42}H_{28}$ configurations was previously reported for a variety of surfaces [25,35,36] and is not specific to graphene.

Spectroscopy data corroborate the weak hybridization of $C_{42}H_{28}$ with the graphene-covered Pt(111) surface. Figure 7a shows a spectrum of d*I*/d*V* acquired atop a $C_{42}H_{28}$ molecule embedded in a molecular island. The spectroscopic signatures of HOMO and LUMO are visible at, respectively, approx. −0.87 and approx. 0.92 V. The molecular resonance widths are smaller than those observed on the other surfaces; in particular, the LUMO exhibits a narrow line shape.

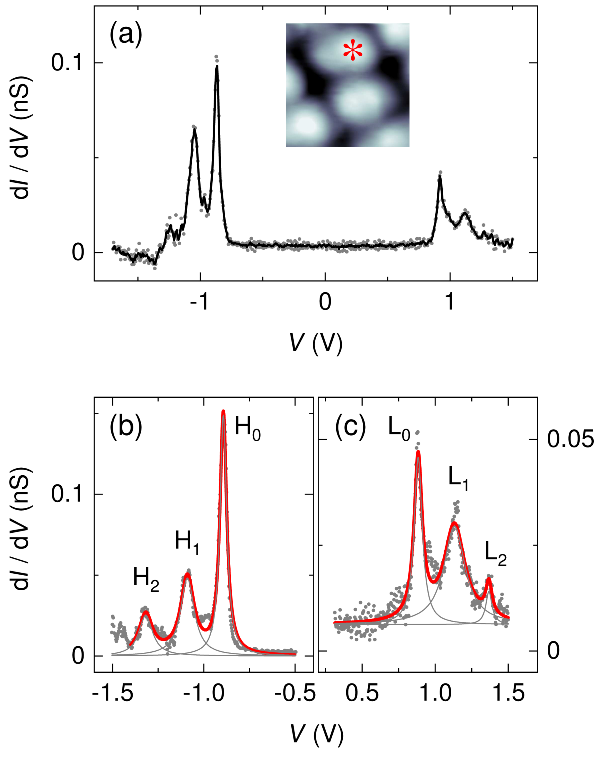

Figure 7: (a) Spectrum of d*I*/d*V* (dots) recorded above a $C_{42}H_{28}$ phenyl group on graphene-covered Pt(111) (feedback loop parameters: −1.5 V, 15 pA). The solid line represents smoothed data. Inset: STM image of a single $C_{42}H_{28}$ molecule on graphene-covered Pt(111) (2 V, 20 pA, 2 × 2 nm^2) with an asterisk marking the position of spectroscopy. (b) Close-up d*I*/d*V* spectrum (dots) of the HOMO (H_0) spectral fine structure (H_1, H_2) (feedback loop parameters: −1.5 V, 30 pA). The thick solid line represents a fit of three Lorentzian line shapes (thin gray lines) and a constant background to the data. (c) Like (b), for the LUMO (L_0) with vibronic fine structure (L_1, L_2) (feedback loop parameters: 1.5 V, 20 pA).

Before analyzing the vibronic subbands of the molecular resonances we remark that the HOMO–LUMO gap width defined as the difference between LUMO and HOMO energy varies between approx. 1.6 eV and approx. 1.8 eV, depending on the individual molecule. The approx. 0.2 eV variation of the gap width is due to changes in the LUMO energy since the HOMO resonance essentially retains its energy at approx. −0.87 eV. Assuming that $C_{42}H_{28}$ is weakly coupled to the substrate, its orbital energies are expected to be aligned with the vacuum level [46] and, thus, susceptible to local changes in the work function. Site-specific work functions are indeed present on the moiré lattice of graphene. For instance, graphene-covered Ir(111), which may serve as a reference for graphene on Pt(111) owing to the comparably low hybridization of graphene with the two metal surfaces, exhibits work function changes of the order of 0.1 eV [47]. In the experiments presented here, the LUMO experiences changes in its energy while the HOMO is essentially pinned, which at first sight contradicts the alignment of the orbitals with the vacuum level. However, $C_{42}H_{28}$ is an electron donor and has the propensity to transfer negative charge to the substrate, which could in principle reduce or compensate the work-function-induced shift of the HOMO. A similar behavior was previously reported for $C_{64}H_{36}$ adsorbed on h-BN-covered Ru(0001) [48]. Intermolecular couplings [49] that were previously shown to induce strong orbital energy shifts due to different local molecular environments are unlikely to cause the LUMO energy variation because the molecular superstructure in the present case is regular. Moreover, a shift of the LUMO peak due to the electric field between tip and surface [50,51] can likewise be excluded due to the magnitude of the effect and the similar tip–molecule distances in the experiment.

Vibronic fine structure is visible in the two frontier orbitals giving rise to vibronic subbands of the HOMO, H_1 and H_2, with equidistant spacings of 180 ± 10 mV, and for the LUMO, L_1 and L_2, with equidistant spacings of 220 ± 10 mV. In order to clearly see the vibronic transitions in the HOMO and LUMO spectroscopic signatures, close-up views with increased bias voltage sampling are presented in Figure 7b for the HOMO and in Figure 7c for the LUMO. The raw d*I*/d*V* data were fit by the superposition of three individual Lorentzian line shapes (thin lines) on a constant background. Therefore, different groups of vibrational modes participate in the vibronic progression of the different frontier orbitals. Within the uncertainty margin the vibrational quantum with energy $h\nu_1 \approx 180$ meV is most likely the same mode as that observed for $C_{42}H_{28}$ on Au(111) and corresponds to the vibrational mode with large Holstein coupling (vide supra). The second vibrational quantum with energy $h\nu_2 \approx 220$ meV is likely to coincide with the $C_{42}H_{28}$ vibration with energy 1594 $cm^{-1} \approx 200$ meV, which was likewise predicted to exhibit an elevated Holstein coupling [42]. The calculations [42] were performed for the HOMO alone. However, both vibronic excitations mainly involve tetracene stretching vibrations and both the HOMO and the LUMO are close to the tetracene backbone [43,44]. Therefore, vibronic progression induced by one of these vibrational modes is likely to occur in the LUMO as well. The exact displacement patterns of the modes at 1349 cm^{-1} and 1594 cm^{-1} differ [42]. The different symmetries of the displacement patterns may explain why the 1349 cm^{-1} (1594 cm^{-1}) mode couples particularly well to the HOMO (LUMO). It has recently been shown that matching symmetries of vibrational and electronic states are favorable for the occurrence of vibronic progression [9]. Using Equation 3, the Huang–Rhys factor for vibronic progression of the HOMO (LUMO) is approx. 0.4 (approx. 0.6).

Comparison

Topographic and spectroscopic data of $C_{42}H_{28}$ on Pt(111), Au(111) and graphene-covered Pt(111) consistently show the progressive reduction of the molecule–substrate interaction. The hit-and-stick adsorption of $C_{42}H_{28}$ on Pt(111) indicates a strong suppression of the $C_{42}H_{28}$ mobility after adsorption. Molecular orbitals leave weak and broad signatures in dI/dV spectra.

Using the same preparation parameters for $C_{42}H_{28}$ deposition on Au(111) as on Pt(111) leads to island growth with a regular superstructure. The crystalline adsorption phase unravels that low energy barriers for translation and rotation of the molecule exist because the individual $C_{42}H_{28}$ molecules can optimize the coupling to adjacent molecules. A finite adsorbate–substrate interaction is reflected by the presence of a molecular superstructure that matches the period of the Au(111) reconstruction. However, the HOMO resonance width has decreased by a factor of three compared to its width on Pt(111). Even vibronic progression due to a group of molecular vibrations with an energy of approx. 160 meV and a Huang–Rhys factor of approx. 0.5 is visible in the HOMO spectral line shape, which for molecules adsorbed on metal surfaces is exceptional. Unoccupied molecular orbitals, in contrast, are weak and broad with no indication of vibronic progression.

The most effective reduction of the $C_{42}H_{28}$–metal hybridization is achieved by adsorption of $C_{42}H_{28}$ on graphene-covered Pt(111). The unit cell of the molecular superstructure is similar to the one observed on Au(111), albeit with a lower molecule surface density and with no additional moiré pattern. Compared to direct adsorption on Pt(111) the HOMO resonance width of $C_{42}H_{28}$ on graphene-covered Pt(111) is reduced by more than a factor of ten. Likewise, the LUMO appears as a sharply peaked signature in dI/dV spectroscopy. Different groups of $C_{42}H_{28}$ vibrational quanta induce vibronic progression of the frontier orbitals. The HOMO exhibits vibronic fine structure due to vibrations with $h\nu_1 \approx 180$ meV and a Huang–Rhys factor of $S_{\nu_1} \approx 0.4$, while the LUMO shows vibronic side bands due to molecular vibrational quanta with $h\nu_2 \approx 220$ meV and $S_{\nu_2} \approx 0.6$.

Conclusion

Using the hydrocarbon molecule $C_{42}H_{28}$ the progressive reduction of the molecule–surface hybridization can be achieved by using inert metal substrates, Au rather than Pt, and by introducing a two-dimensional material, e.g., graphene, as a buffer layer between the adsorbed molecule and the metal. The degree of decoupling can be judged by the molecule assembly after adsorption, the spectral line width of molecular resonances and the occurrence of vibronic progression. The most effective reduction of residual $C_{42}H_{28}$–metal hybridization was achieved here by adsorption on graphene-covered Pt(111). On this surface $C_{42}H_{28}$ exhibits vibronic progression in both frontier orbitals, induced by different molecular vibrational quanta and with different Huang–Rhys factors. Consequently, graphene represents an appropriate buffer layer for exploring electronic and vibronic properties at the single-molecule level.

Funding

Financial support by the Deutsche Forschungsgemeinschaft through Grant No. KR 2912/12-1 is acknowledged.

ORCID® iDs

Karl Rothe - https://orcid.org/0000-0001-6672-398X
Alexander Mehler - https://orcid.org/0000-0001-5329-1698
Nicolas Néel - https://orcid.org/0000-0003-0498-9138
Jörg Kröger - https://orcid.org/0000-0002-6452-5864

References

1. Qiu, X. H.; Nazin, G. V.; Ho, W. *Phys. Rev. Lett.* **2004,** *92,* 206102. doi:10.1103/physrevlett.92.206102
2. Kong, L.; Enders, A.; Rahman, T. S.; Dowben, P. A. *J. Phys.: Condens. Matter* **2014,** *26,* 443001. doi:10.1088/0953-8984/26/44/443001
3. Auwärter, W. *Surf. Sci. Rep.* **2019,** *74,* 1–95. doi:10.1016/j.surfrep.2018.10.001
4. Riss, A.; Wickenburg, S.; Tan, L. Z.; Tsai, H.-Z.; Kim, Y.; Lu, J.; Bradley, A. J.; Ugeda, M. M.; Meaker, K. L.; Watanabe, K.; Taniguchi, T.; Zettl, A.; Fischer, F. R.; Louie, S. G.; Crommie, M. F. *ACS Nano* **2014,** *8,* 5395–5401. doi:10.1021/nn501459v
5. Bouvron, S.; Maurand, R.; Graf, A.; Erler, P.; Gragnaniello, L.; Skripnik, M.; Wiedmann, D.; Engesser, C.; Nef, C.; Fu, W.; Schönenberger, C.; Pauly, F.; Fonin, M. *Nanoscale* **2018,** *10,* 1487–1493. doi:10.1039/c7nr06860c
6. Schulz, F.; Drost, R.; Hämäläinen, S. K.; Liljeroth, P. *ACS Nano* **2013,** *7,* 11121–11128. doi:10.1021/nn404840h
7. Palma, C.-A.; Joshi, S.; Hoh, T.; Ecija, D.; Barth, J. V.; Auwärter, W. *Nano Lett.* **2015,** *15,* 2242–2248. doi:10.1021/nl503956p

8. Liu, L.; Dienel, T.; Widmer, R.; Gröning, O. *ACS Nano* **2015,** *9,* 10125–10132. doi:10.1021/acsnano.5b03741
9. Mehler, A.; Néel, N.; Bocquet, M.-L.; Kröger, J. *J. Phys.: Condens. Matter* **2019,** *31,* 065001. doi:10.1088/1361-648x/aaf54c
10. Krane, N.; Lotze, C.; Reecht, G.; Zhang, L.; Briseno, A. L.; Franke, K. J. *ACS Nano* **2018,** *12,* 11698–11703. doi:10.1021/acsnano.8b07414
11. Sato, N.; Seki, K.; Inokuchi, H. *J. Chem. Soc., Faraday Trans. 2* **1981,** *77,* 1621–1633. doi:10.1039/f29817701621
12. Biedermann, P. U.; Levy, A.; Stezowski, J. J.; Agranat, I. *Chirality* **1995,** *7,* 199–205. doi:10.1002/chir.530070404
13. Kytka, M.; Gisslen, L.; Gerlach, A.; Heinemeyer, U.; Kováč, J.; Scholz, R.; Schreiber, F. *J. Chem. Phys.* **2009,** *130,* 214507. doi:10.1063/1.3147009
14. Park, S.-W.; Choi, J.-M.; Lee, K. H.; Yeom, H. W.; Im, S.; Lee, Y. K. *J. Phys. Chem. B* **2010,** *114,* 5661–5665. doi:10.1021/jp910459p
15. Käfer, D.; Ruppel, L.; Witte, G.; Wöll, C. *Phys. Rev. Lett.* **2005,** *95,* 166602. doi:10.1103/physrevlett.95.166602
16. Zhang, Z.-l.; Jiang, X.-y.; Xu, S.-h.; Nagatomo, T.; Omoto, O. *Synth. Met.* **1997,** *91,* 131–132. doi:10.1016/s0379-6779(98)80073-8
17. Sundar, V. C.; Zaumseil, J.; Podzorov, V.; Menard, E.; Willett, R. L.; Someya, T.; Gershenson, M. E.; Rogers, J. A. *Science* **2004,** *303,* 1644–1646. doi:10.1126/science.1094196
18. Kokalj, A.; Causà, M. *J. Phys.: Condens. Matter* **1999,** *11,* 7463–7480. doi:10.1088/0953-8984/11/39/304
19. Baud, S.; Ramseyer, C.; Bihlmayer, G.; Blügel, S.; Barreteau, C.; Desjonquères, M. C.; Spanjaard, D.; Bernstein, N. *Phys. Rev. B* **2004,** *70,* 235423. doi:10.1103/physrevb.70.235423
20. Reinert, F.; Nicolay, G.; Schmidt, S.; Ehm, D.; Hüfner, S. *Phys. Rev. B* **2001,** *63,* 115415. doi:10.1103/physrevb.63.115415
21. Sutter, P.; Sadowski, J. T.; Sutter, E. *Phys. Rev. B* **2009,** *80,* 245411. doi:10.1103/physrevb.80.245411
22. Miwa, J. A.; Cicoira, F.; Bedwani, S.; Lipton-Duffin, J.; Perepichka, D. F.; Rochefort, A.; Rosei, F. *J. Phys. Chem. C* **2008,** *112,* 10214–10221. doi:10.1021/jp802762q
23. Hattab, H.; N'Diaye, A. T.; Wall, D.; Jnawali, G.; Coraux, J.; Busse, C.; van Gastel, R.; Poelsema, B.; Michely, T.; Meyer zu Heringdorf, F.-J.; Horn-von Hoegen, M. *Appl. Phys. Lett.* **2011,** *98,* 141903. doi:10.1063/1.3548546
24. Viereck, J.; Rangan, S.; Häberle, P.; Galoppini, E.; Douglas, C. J.; Bartynski, R. A. *J. Phys. Chem. C* **2019,** *123,* 14382–14390. doi:10.1021/acs.jpcc.9b01659
25. Blüm, M.-C.; Pivetta, M.; Patthey, F.; Schneider, W.-D. *Phys. Rev. B* **2006,** *73,* 195409. doi:10.1103/physrevb.73.195409
26. Pivetta, M.; Blüm, M.-C.; Patthey, F.; Schneider, W.-D. *ChemPhysChem* **2010,** *11,* 1558–1569. doi:10.1002/cphc.200900846
27. Blüm, M.-C.; Ćavar, E.; Pivetta, M.; Patthey, F.; Schneider, W.-D. *Angew. Chem., Int. Ed.* **2005,** *44,* 5334–5337. doi:10.1002/anie.200501467
28. Wöll, C.; Chiang, S.; Wilson, R. J.; Lippel, P. H. *Phys. Rev. B* **1989,** *39,* 7988–7991. doi:10.1103/physrevb.39.7988
29. Barth, J. V.; Brune, H.; Ertl, G.; Behm, R. J. *Phys. Rev. B* **1990,** *42,* 9307–9318. doi:10.1103/physrevb.42.9307
30. Hanke, F.; Björk, J. *Phys. Rev. B* **2013,** *87,* 235422. doi:10.1103/physrevb.87.235422
31. Jurchescu, O. D.; Meetsma, A.; Palstra, T. T. M. *Acta Crystallogr., Sect. B: Struct. Sci.* **2006,** *62,* 330–334. doi:10.1107/s0108768106003053
32. Wang, L.; Kong, H.; Chen, X.; Du, X.; Chen, F.; Liu, X.; Wang, H. *Appl. Phys. Lett.* **2009,** *95,* 093102. doi:10.1063/1.3213563
33. Lan, M.; Xiong, Z.-H.; Li, G.-Q.; Shao, T.-N.; Xie, J.-L.; Yang, X.-F.; Wang, J.-Z.; Liu, Y. *Phys. Rev. B* **2011,** *83,* 195322. doi:10.1103/physrevb.83.195322
34. Tomba, G.; Stengel, M.; Schneider, W.-D.; Baldereschi, A.; De Vita, A. *ACS Nano* **2010,** *4,* 7545–7551. doi:10.1021/nn101884p
35. Sun, K.; Lan, M.; Wang, J.-Z. *Phys. Chem. Chem. Phys.* **2015,** *17,* 26220–26224. doi:10.1039/c5cp04608d
36. Miwa, J. A.; Cicoira, F.; Lipton-Duffin, J.; Perepichka, D. F.; Santato, C.; Rosei, F. *Nanotechnology* **2008,** *19,* 424021. doi:10.1088/0957-4484/19/42/424021
37. Mehler, A.; Kirchhuebel, T.; Néel, N.; Sojka, F.; Forker, R.; Fritz, T.; Kröger, J. *Langmuir* **2017,** *33,* 6978–6984. doi:10.1021/acs.langmuir.7b00306
38. Ziegler, M.; Néel, N.; Sperl, A.; Kröger, J.; Berndt, R. *Phys. Rev. B* **2009,** *80,* 125402. doi:10.1103/physrevb.80.125402
39. Ueba, T.; Yamada, T.; Munakata, T. *J. Chem. Phys.* **2016,** *145,* 214703. doi:10.1063/1.4968847
40. Coropceanu, V.; Cornil, J.; da Silva Filho, D. A.; Olivier, Y.; Silbey, R.; Brédas, J.-L. *Chem. Rev.* **2007,** *107,* 926–952. doi:10.1021/cr050140x
41. Repp, J.; Meyer, G.; Paavilainen, S.; Olsson, F. E.; Persson, M. *Phys. Rev. Lett.* **2005,** *95,* 225503. doi:10.1103/physrevlett.95.225503
42. Girlando, A.; Grisanti, L.; Masino, M.; Bilotti, I.; Brillante, A.; Della Valle, R. G.; Venuti, E. *Phys. Rev. B* **2010,** *82,* 035208. doi:10.1103/physrevb.82.035208
43. Ueba, T.; Terawaki, R.; Morikawa, T.; Kitagawa, Y.; Okumura, M.; Yamada, T.; Kato, H. S.; Munakata, T. *J. Phys. Chem. C* **2013,** *117,* 20098–20103. doi:10.1021/jp407933m
44. da Silva Filho, D. A.; Kim, E.-G.; Brédas, J.-L. *Adv. Mater. (Weinheim, Ger.)* **2005,** *17,* 1072–1076. doi:10.1002/adma.200401866
45. Udhardt, C.; Forker, R.; Gruenewald, M.; Watanabe, Y.; Yamada, T.; Ueba, T.; Munakata, T.; Fritz, T. *Thin Solid Films* **2016,** *598,* 271–275. doi:10.1016/j.tsf.2015.12.023
46. Ishii, H.; Sugiyama, K.; Ito, E.; Seki, K. *Adv. Mater. (Weinheim, Ger.)* **1999,** *11,* 605–625. doi:10.1002/(sici)1521-4095(199906)11:8<605::aid-adma605>3.0.co;2-q
47. Altenburg, S. J.; Berndt, R. *New J. Phys.* **2014,** *16,* 053036. doi:10.1088/1367-2630/16/5/053036
48. Mehler, A.; Néel, N.; Kröger, J. *J. Vac. Sci. Technol., A* **2019,** *37,* 061404. doi:10.1116/1.5125486
49. Kröger, J.; Jensen, H.; Berndt, R.; Rurali, R.; Lorente, N. *Chem. Phys. Lett.* **2007,** *438,* 249–253. doi:10.1016/j.cplett.2007.03.001
50. Limot, L.; Maroutian, T.; Johansson, P.; Berndt, R. *Phys. Rev. Lett.* **2003,** *91,* 196801. doi:10.1103/physrevlett.91.196801
51. Kröger, J.; Limot, L.; Jensen, H.; Berndt, R.; Johansson, P. *Phys. Rev. B* **2004,** *70,* 033401. doi:10.1103/physrevb.70.033401

License and Terms

BEILSTEIN JOURNAL OF NANOTECHNOLOGY

Hybridization vs decoupling: influence of an h-BN interlayer on the physical properties of a lander-type molecule on Ni(111)

Maximilian Schaal[1], Takumi Aihara[2], Marco Gruenewald[1], Felix Otto[1], Jari Domke[1], Roman Forker[1], Hiroyuki Yoshida[2,3] and Torsten Fritz*[1]

Full Research Paper

Open Access

Address:
[1]Institute of Solid State Physics, Friedrich Schiller University Jena, Helmholtzweg 5, 07743 Jena, Germany, [2]Graduate School of Engineering, Chiba University, 1-33, Yayoi-cho, Inage-ku, Chiba 263-8522, Japan and [3]Molecular Chirality Research Center, Chiba University, 1-33, Yayoi-cho, Inage-ku, Chiba 263-8522, Japan

Email:
Torsten Fritz* - torsten.fritz@uni-jena.de

* Corresponding author

Keywords:
buried interface; decoupling; hexagonal boron nitride; hybridization; tetraphenyldibenzoperiflanthene (DBP); two-dimensional materials

Beilstein J. Nanotechnol. **2020,** *11,* 1168–1177.
doi:10.3762/bjnano.11.101

Received: 14 April 2020
Accepted: 08 July 2020
Published: 04 August 2020

This article is part of the thematic issue "Molecular assemblies on surfaces – towards physical and electronic decoupling of organic molecules".

Guest Editor: M. Stöhr

Abstract

2D materials such as hexagonal boron nitride (h-BN) are widely used to decouple organic molecules from metal substrates. Nevertheless, there are also indications in the literature for a significant hybridization, which results in a perturbation of the intrinsic molecular properties. In this work we study the electronic and optical properties as well as the lateral structure of tetraphenyldibenzoperiflanthene (DBP) on Ni(111) with and without an atomically thin h-BN interlayer to investigate its possible decoupling effect. To this end, we use in situ differential reflectance spectroscopy as an established method to distinguish between hybridized and decoupled molecules. By inserting an h-BN interlayer we fabricate a buried interface and show that the DBP molecules are well decoupled from the Ni(111) surface. Furthermore, a highly ordered DBP monolayer is obtained on h-BN/Ni(111) by depositing the molecules at a substrate temperature of 170 °C. The structural results are obtained by quantitative low-energy electron diffraction and low-temperature scanning tunneling microscopy. Finally, the investigation of the valence band structure by ultraviolet photoelectron spectroscopy shows that the low work function of h-BN/Ni(111) further decreases after the DBP deposition. For this reason, the h-BN-passivated Ni(111) surface may serve as potential n-type contact for future molecular electronic devices.

Introduction

The interfaces between organic molecules and metal contacts play a crucial role in the design of new molecular electronic devices since they affect the charge carrier injection and therefore the device efficiency. An important process to consider is the electronic interaction of organic molecules that are in direct contact with the metal, i.e., the interaction of frontier orbitals with the bands of the metal substrate, which results in changes of the intrinsic optical and electronic properties of the adsorbed molecule. This process is referred to as hybridization, which may be accompanied by the reduction of the HOMO–LUMO gap, the change of the energy-level alignment, and even charge transfer [1,2]. Some applications, however, require to preserve the intrinsic properties of the molecules such as the typically rather narrow optical absorption and/or emission bands. To achieve this, one needs to electronically decouple the molecules from the substrate, which can be achieved through different ways such as the usage of wide-band-gap insulator thin films (e.g., oxides, alkali halides) [3,4], a molecular spacer layer [5,6], or sp^2-hybridized two-dimensional interlayers (e.g., graphene and hexagonal boron nitride (h-BN)) [7,8]. The advantageous properties of an h-BN monolayer on metal single crystals are the high crystal quality, chemical inertness and the wide band gap of approx. 6 eV, which apparently renders h-BN a promising candidate for the decoupling of highly ordered molecular films [9,10].

However, indications for a significant hybridization of organic molecules on h-BN/Cu(111) were found recently [11,12]. This raises the question under which specific conditions an h-BN monolayer is sufficient to efficiently decouple organic molecules. Until now only a few publications exist which are concerned with this issue [13-16].

In this work we report on the decoupling process by a direct comparison of tetraphenyldibenzoperiflanthene (DBP) adsorbed on Ni(111) with and without an h-BN interlayer. The latter is known to form a commensurate overlayer in which nitrogen and boron atoms occupy top and fcc hollow adsorption sites, respectively [17]. For this reason, h-BN on Ni(111) exhibits an atomically flat morphology [18,19]. DBP is a promising molecule in the field of organic electronics, for example, as an electron donor [20-23] or acceptor [24] in organic photovoltaic applications, and as a dopant in organic light emitting diodes [25].

For our comprehensive study we utilized differential reflectance spectroscopy (DRS), low-energy electron diffraction (LEED), low-temperature scanning tunneling microscopy (LT-STM), as well as photoelectron spectroscopy (PES). Our results reveal that DBP on h-BN/Ni(111) is well decoupled from the metal substrate Ni(111). Furthermore, it was possible to obtain large domains of highly ordered molecules by depositing at an elevated substrate temperature of 170 °C.

Results and Discussion

Optical spectroscopy

Figure 1 shows the comparison of the differential reflectance (DR) spectra (definition see Experimental section) of DBP on bare Ni(111) as well as of DBP on h-BN/Ni(111) grown at substrate temperatures T_{sub} of 25 °C and 170 °C, respectively. For DBP on Ni(111) deposited at a substrate temperature of 25 °C we observe rather broad and featureless DR spectra at the beginning of the deposition. Such broad spectra are indicative of a strong electronic interaction of first-layer molecules with the Ni(111) substrate. A similar broadening was observed for

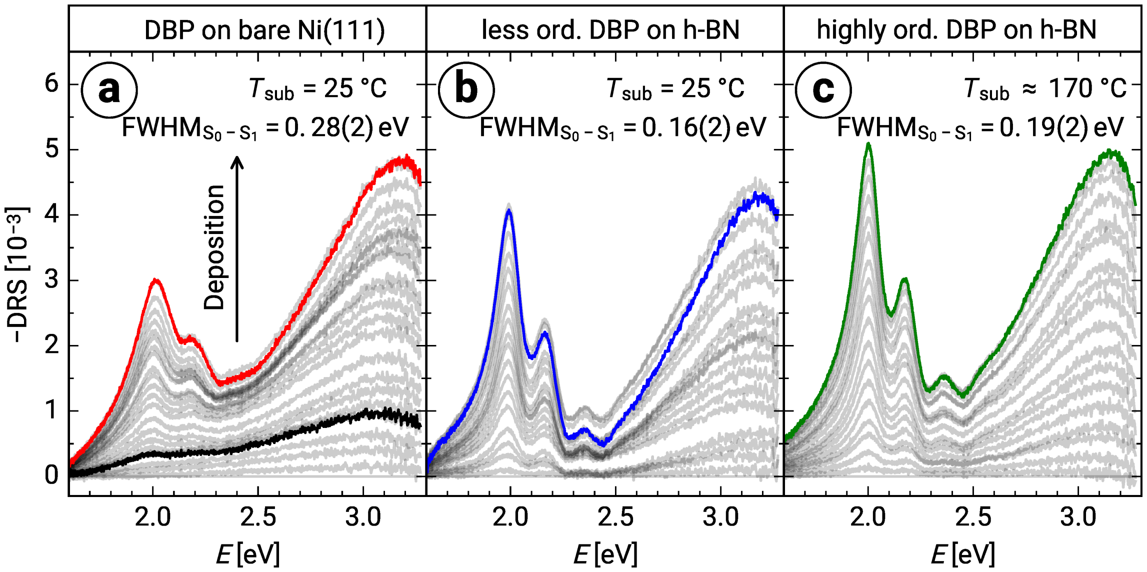

Figure 1: Film-thickness dependent evolution of the DR spectra of (a) DBP on bare Ni(111) as well as of DBP on h-BN/Ni(111) deposited at (b) room temperature and at (c) approx. 170 °C. Colored spectra correspond to a film thickness of 1 MLE. The black spectrum (about 0.25 MLE) is representative of the strong electronic interaction between first-layer molecules and Ni(111). The full widths at half-maximum of the $S_0 \rightarrow S_1$ transitions were determined by a fit of a Voigt function in combination with a linear background.

DBP on Ag(111), where a mixing of the molecular frontier orbitals with the metal bands of the substrate was concluded [26]. After about 0.25 monolayer equivalents (MLE, definition see section "Sample preparation" below), which is marked by a black line in Figure 1, distinct molecular features emerge at about 2.0 and 2.2 eV. We assign these to the $S_0 \rightarrow S_1$ transition and the corresponding vibronic progression of DBP [27]. This indicates an electronic decoupling of the molecules from Ni(111) due to the beginning adsorption already in the second (or higher) layer(s). Further, the somewhat larger peak widths, as compared to the spectra of DBP on mica [25], might be an inhomogeneous broadening effect caused by a higher degree of rotational disorder in the DBP film on Ni(111), compared to DBP on mica [26].

In contrast, the DR spectra of both DBP layers on h-BN/Ni(111) grown at different substrate temperatures show directly the formation of a molecular fingerprint, which is considerably narrower than that of DBP on bare Ni(111) (see full widths at half-maximum (FWHM) of the $S_0 \rightarrow S_1$ transitions in Figure 1) and in very good agreement with the DR spectra of DBP on inert mica [26]. Consequently, h-BN efficiently decouples the molecules deposited on top from the underlying Ni(111) resulting in a monomer-like behavior.

Furthermore, we extracted the optical constants from the DRS measurements of both DBP layers on h-BN/Ni(111). The numerical algorithm is described in [28]. In the following, we will focus on the imaginary part of the dielectric function (ε'') only, which is depicted in Figure 2, as this physical quantity is indicative of the optical absorption. The comparison between DBP deposited at substrate temperatures of 25 °C and 170 °C shows larger ε'' values and a slight shift towards higher energies by 15 meV for the latter. Both could be explained by a slightly different packing motif with also different packing densities. The optical gap of DBP adsorbed on h-BN/Ni(111) was determined by the maximum of the absorption peak of the $S_0 \rightarrow S_1$ transition (marked as black dashed lines in Figure 2). Therefore, we obtained values of 2.020(5) and 2.035(5) eV for DBP deposited at substrate temperatures of 25 °C and 170 °C, respectively. The determination of the optical constants of DBP on bare Ni(111) was not possible because of the superposition of the spectra of hybridized molecules and aggregates.

For molecules on top of the first layer the absorption features start to shift to higher energies followed by the formation of a new optical species at lower energies (LE species) as illustrated in Supporting Information File 1, Figure S1. While the shift can be explained by a different dielectric environment of second-layer DBP molecules compared with those in the first layer, the new optical species can be clearly assigned to the fingerprint of DBP aggregates. The similarity of the spectral fingerprints of the monomers in the first and aggregates in higher layers is notable, but can be rationalized by the expected weak excitonic coupling due to the lander-type geometry of DBP. Beside excitonic coupling, also conformational changes may play a role as found for the chemically similar rubrene on highly oriented pyrolytic graphite (HOPG) [29]. Our interpretation of the

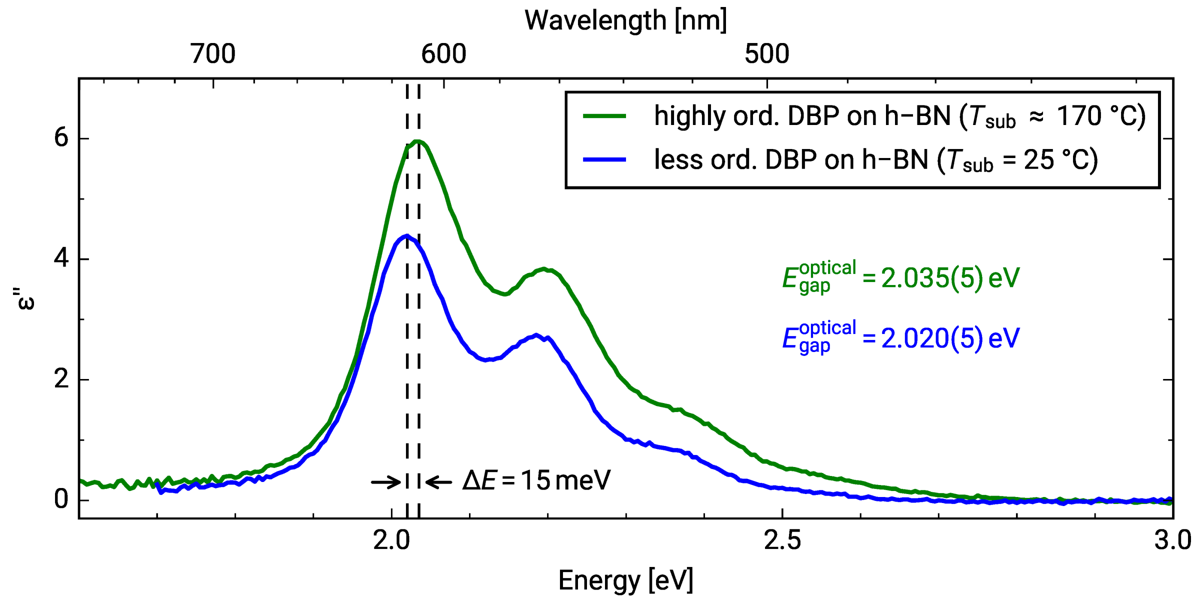

Figure 2: Imaginary part of the dielectric function obtained from the differential reflectance spectra of 1 MLE DBP on h-BN/Ni(111) (blue: substrate temperature = 25 °C, green: substrate temperature approx. 170 °C). Black dashed lines mark the spectral position of the $S_0 \rightarrow S_1$ transition.

optical spectra is further supported by LT-STM measurements (see Supporting Information File 1, Figure S2) which show a completely filled monolayer as well as molecular clusters on top of the first layer.

Lateral structure

In this section we discuss the impact of the h-BN interlayer on the lateral structure of DBP. The LEED measurement of DBP on bare Ni(111) (not shown) exhibits no molecular diffraction pattern, merely a diffuse background is formed upon deposition of DBP. We suggest that the strong interaction of DBP with Ni(111), presumably via the localized d bands, causes a drastic decrease of the mobility of the molecules hindering the highly ordered assembly of the molecules due to a hit-and-stick adsorption. Such a behavior was also observed for one monolayer of pentacene on Ni(111) [30].

In contrast, the LEED measurement of DBP on h-BN/Ni(111) deposited at a substrate temperature of 25 °C shows a ring-like diffraction pattern (see Supporting Information File 1, Figure S3) which can be explained by randomly oriented molecular domains or by a lattice gas or liquid-like phase [31]. A change of the LEED pattern due to a post-growth annealing process in a temperature range from 100 °C to 300 °C was not visible. In fact, at a temperature of 300 °C the desorption of DBP molecules was observed by a decrease of the C 1s intensity measured by XPS (not shown). Therefore, we conclude that a post-growth annealing process does not lead to an increase of the lateral order.

However, a highly ordered film was achieved by depositing at a substrate temperature of 170 °C. The LEED image in Figure 3a shows the corresponding diffraction pattern induced by a highly ordered molecular film. For this reason, we labeled this sample as highly ordered DBP layer. The DBP layer that was deposited at a substrate temperature of 25 °C, on the other hand, is labeled as less ordered DBP layer. An increase of the crystal quality of the DBP thin film grown at a substrate temperature higher than 90 °C was also reported by Zhou et al. [32]. The distinct LEED pattern of the highly ordered DBP layer makes it possible to apply a quantitative analysis by means of a LEED simulation that is numerically fitted to the diffraction pattern. The resulting simulation is shown in Figure 3 as yellow circles overlaid with the LEED image. The corresponding epitaxy matrix as well as the lattice parameters are summarized in Table 1.

We used the projection method proposed by Forker et al. to identify possible coincidences of the adsorbate and the substrate lattice [35]. We find more than one possible coincidence within the error margin of the epitaxy matrix. However, we can exclude higher-order commensurate (HOC) and point-on-line (POL) coincidences with a substrate order lower than four. By tendency, the higher the substrate order, the lower is the epitaxial energy gain and therefore the probability of the coincidence [35,36]. In the case of highly ordered DBP on h-BN/Ni(111), suitable coincidences with the lowest substrate orders are the on-line coincidences (1, 2), (−1, −2), (−2, 1), and (2, −1).

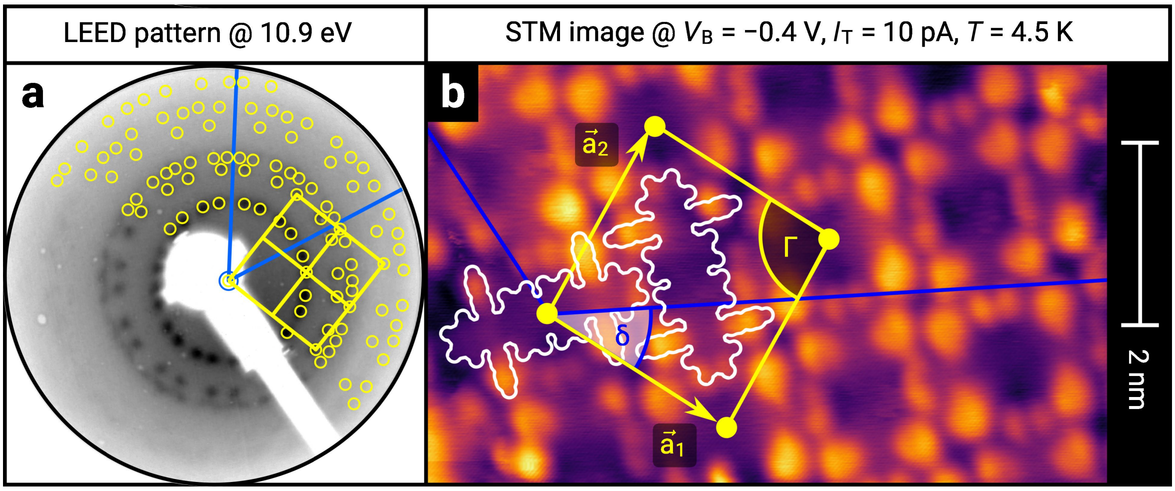

Figure 3: (a) LEED image (logarithmic intensity scale, contrast inverted) of the highly ordered DBP layer on h-BN/Ni(111) grown at a substrate temperature of 170 °C. Half of the LEED image is superimposed by the LEED simulation. Yellow points and lines correspond to the reciprocal lattice of the DBP structure including symmetry equivalents (rotational and mirror domains). Blue lines indicate two primitive reciprocal lattice directions of the substrate. (b) LT-STM image of the same sample, superimposed by the real-space structure of the molecular lattice (marked in yellow) as well as the contours of the two molecules in the unit cell. Blue lines indicate the direction of the primitive lattice vectors of the substrate. The lattice parameters are summarized in Table 1.

Table 1: Comparison of the lattice parameters obtained by our LEED analysis with reference data of DBP on Au(111) (1 MLE) [33] and on Ag(111) (1.3 MLE) [34]. The angle Γ is defined between the lattice vectors of the adsorbate $\vec{a}_1$ and $\vec{a}_2$. The angle between the adsorbate lattice vector $\vec{a}_1$ and the direction of the substrate lattice vector $\vec{s}_1$ is labeled with δ. Before each epitaxy matrix a prefactor along with its margin of error indicates the absolute scaling uncertainty of the analyzed LEED image. Please note that the epitaxy matrix of DBP on Au(111) and on Ag(111) deviates from the matrix of DBP on h-BN/Ni(111) because of different lattice constants of the substrate as well as slightly different lattice parameters of the adsorbate. We used the acronyms POL and LOL (for point-on-line and line-on-line epitaxy) to characterize the type of epitaxy. The uncertainty of the numerical fitting procedure is given in parentheses behind each value and refers to the last significant digits.

Substrates	$\lvert\vec{a}_1\rvert$ [Å]	$\lvert\vec{a}_2\rvert$ [Å]	Γ [°]	δ [°]	Epitaxy matrix & type
h-BN/Ni(111) [this work]	22.8(4)	23.1(5)	90.1(5)	36.1(4)	$1.00(1)\cdot\begin{pmatrix} 4.28(7) & -6.23(7) \\ 9.80(7) & 8.67(7) \end{pmatrix}$ LOL
Au(111) [33]	21.0(3)	23.8(4)	90.2(4)	45.0(3)	$1.00(5)\cdot\begin{pmatrix} 8.14(4) & 5.96(5) \\ -2.51(4) & 6.72(6) \end{pmatrix}$ LOL
Ag(111) [34]	20.5(1)	23.2(1)	90.4(1)	−14.1(1)	$1.00(4)\cdot\begin{pmatrix} 5.90(1) & -2.00(1) \\ 6.40(1) & 9.00(1) \end{pmatrix}$ POL

A comparison with reported lateral structures of DBP on Ag(111) [34] and Au(111) [33] shows very similar adsorbate lattice parameters except for the unit cell rotation with respect to the primitive substrate vector $\vec{s}_1$ (see Table 1). For this reason, we find that the molecules adopt a similar herringbone arrangement (rectangular unit cell with a basis of two molecules with different azimuthal orientation) on h-BN/Ni(111). This structural model was verified by the LT-STM measurement shown in Figure 3b. We superimposed the STM image by the contours of the two molecules in the unit cell as well as the adsorbate lattice as determined by LEED. A DBP molecule is characterized by four bright protrusions, which correspond to the phenyl substituents oriented nearly perpendicular to the aromatic backbone and two smaller double lobes which correspond to the bisbenz[5,6]indeno end groups [26].

The large-area LT-STM measurement shown in Supporting Information File 1, Figure S2 reveals highly ordered molecular domains with defects at the domain boundaries as well as clusters of molecules on top of the first DBP layer. The fast Fourier transform (FFT) of that STM image resembles the LEED simulation of the molecular lattice (considering eight symmetry equivalent domains only), which supports our structural model.

Valence band structure and work function change

The ultraviolet photoelectron spectroscopy (UPS) measurements of the DBP films on Ni(111) and h-BN/Ni(111) are depicted in Figure 4. We use the notation proposed by Kirchhuebel et al. to assign spectroscopic features to the underlying molecular orbitals, taking into consideration the probing process [37]. Within this notation, each feature is ascribed to the involved molecular orbital with the probing process being characterized by the initial state as subscript and the final state as a superscript. For example, a single-photon photoionization (UPS measurement) describes a transition from the neutral ground state (0) to a positively charged state (+1), namely a cation state. In the case of the HOMO, HOMO-1 and HOMO-2, the notations H_0^{+1}, $(\mathrm{H}-1)_0^{+1}$, and $(\mathrm{H}-2)_0^{+1}$ are used, respectively.

The comparison of the different UP spectra shows very broad features for DBP on the bare Ni(111) surface, which in turn renders an identification of the underlying orbitals very difficult. The UPS features of DBP on h-BN/Ni(111), on the other hand, are much sharper and shifted to higher binding energies. The reduction of the line width can be explained by an increase of the structural order, which was already discussed in the last section, as well as by a decrease in hybridization. Probable reasons for the shift of the molecular orbitals to higher binding energies are the work function change as well as the less efficient photo hole screening compared to DBP on bare Ni(111). The adsorption of DBP molecules on the bare Ni(111) surface results in a reduction of the work function from 5.27(2) to 4.17(2) eV. The h-BN layer on Ni(111) causes an even more drastic decrease of the substrate work function to 3.55(2) eV. The subsequent adsorption of DBP on the h-BN interlayer slightly reduces the work function to 3.52(2)/3.45(2) eV (less ordered/highly ordered). The drastic work function reduction for DBP on bare Ni(111) as well as h-BN on Ni(111) results from the strong adsorbate–substrate interaction (hybridization). In contrast, the push-back effect is presumably responsible for the small work function change caused by the adsorption of DBP on h-BN/Ni(111). Furthermore, we determined the adiabatic and vertical ionization energy as distance of the onset and the peak maximum of the HOMO-derived feature to the vacuum level, respectively [38]. Therefore, we used Gaussian fits of the UP spectra in Figure 4. Table 2 summarizes the determined work functions and ionization energies.

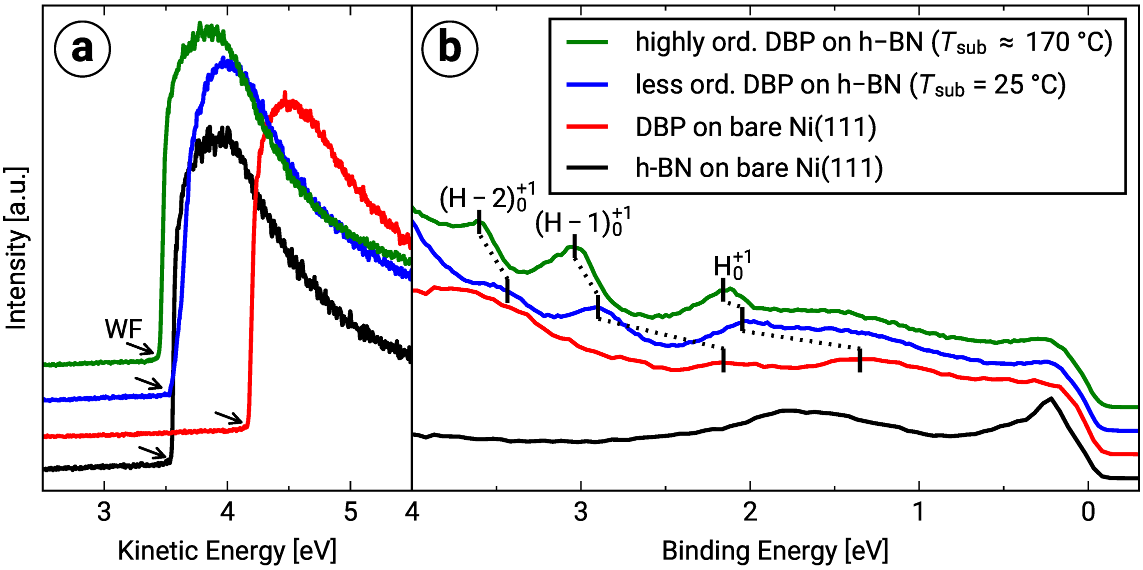

Figure 4: (a) Secondary electron cut-off (SECO) of DBP on bare Ni(111) (approx. 1.0 MLE), on h-BN/Ni(111) (less ordered (approx. 1.0 MLE) and highly ordered (approx. 1.6 MLE)), and of bare h-BN/Ni(111). The kinetic energy onset of the SECO, which corresponds to the work function is marked by black arrows. (b) Corresponding ultraviolet photoelectron spectra at a polar angle of 70°. The positions of the HOMO (H_0^{+1}), HOMO-1 ($(H-1)_0^{+1}$) and HOMO-2 ($(H-2)_0^{+1}$) are marked by vertical black lines.

Table 2: Overview of the work function (WF), adiabatic ionization energy (IE_a), and vertical ionization energy (IE_v) for DBP on bare Ni(111) (approx. 1.0 MLE) and DBP on h-BN/Ni(111) (less ordered (approx. 1.0 MLE) and highly ordered (approx. 1.6 MLE)). The uncertainty of the numerical fit is given in parentheses behind each value and refers to the last significant digits. The determination of the adiabatic ionization energy for DBP on bare Ni(111) was not possible because of the overlap of the very broad HOMO-derived feature with the Ni 3d bands.

	H_0^{+1} [eV]	WF [eV]	IE_a [eV]	IE_v [eV]
DBP on Ni(111)	1.35(5)	4.17(2)	–	5.52(7)
less ordered DBP on h-BN/Ni(111)	2.05(1)	3.52(2)	5.26(4)	5.57(3)
highly ordered DBP on h-BN/Ni(111)	2.16(1)	3.45(2)	5.36(4)	5.61(3)

In contrast to Fermi level pinning, where binding energy shifts are not correlated to the work function change, we suggest that the vacuum level alignment is responsible for the energy level alignment since the work function change is sufficient to explain the binding energy shifts of the molecular orbitals. This is a further indication of the weak molecule–substrate interaction and therefore the efficient electronic decoupling of the DBP molecules by the h-BN layer [39,40].

Furthermore, the low work function of h-BN/Ni(111) has quite interesting consequences for possible applications in molecular electronic devices. Low work function metals such as Al, Ca or Ba are typically used to achieve a low electron injection barrier, which is necessary to build high-performance n-type organic semiconductors [41]. However, these substrates suffer from a high chemical reactivity (prone to oxidation) and a strong hybridization with the organic molecules [41]. In contrast to these traditional low work function materials, h-BN on Ni(111) is chemically inert, and we showed that organic molecules like DBP are decoupled from the metal surface which makes this system a promising n-type contact for molecular electronics.

Core level spectroscopy

Finally, we investigated the chemical structure by means of X-ray photoelectron spectroscopy (XPS) at normal emission. In Figure 5 the N 1s, the C 1s and the B 1s spectra for DBP on bare Ni(111) as well as on h-BN/Ni(111) and bare h-BN/Ni(111) are presented. The analysis of the peak positions and intensities was realized by fitting asymmetric pseudo-Voigt functions [42] in the case of the N 1s and the B 1s levels and symmetric pseudo-Voigt functions in the case of the C 1s levels in combination with an active Shirley background [43]. The peak positions of each core level are summarized in Table 3.

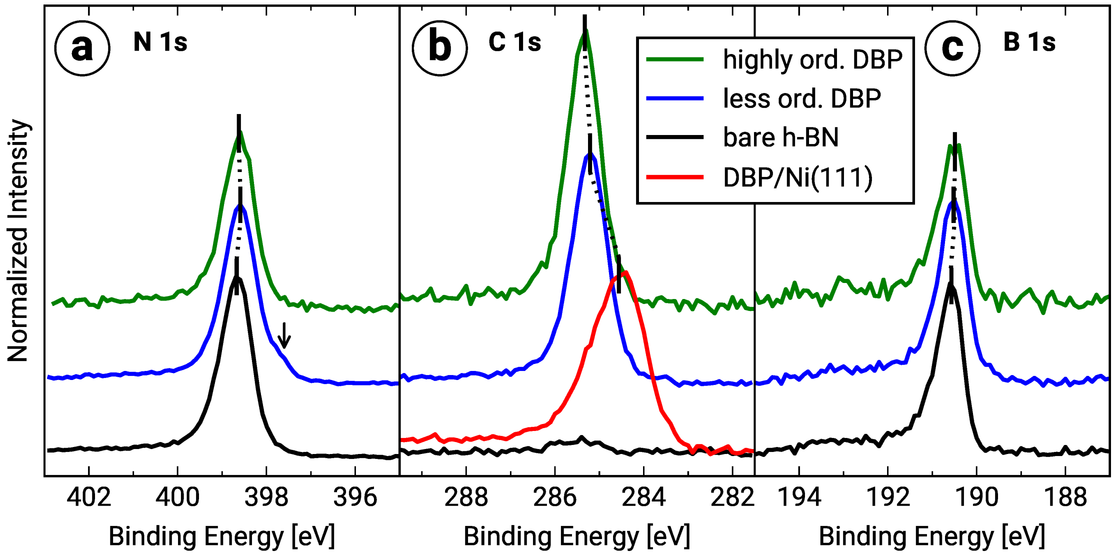

Figure 5: (a) N 1s, (b) C 1s, and (c) B 1s X-ray photoelectron spectra of DBP on bare Ni(111) (approx. 1.0 MLE) as well as of h-BN on Ni(111), and of DBP on h-BN/Ni(111) (less ordered (approx. 1.0 MLE) and highly ordered (approx. 1.6 MLE)). The intensity is normalized to the peak maxima of the N 1s core levels and corrected according to the photoionization cross sections of Yeh and Lindau [44]. For each spectrum the binding energy of the core level is marked by vertical black lines. The black arrow points to an unassigned second component of the N 1s level of the less ordered DBP layer on h-BN/Ni(111).

Table 3: Overview of the binding energies (BE) of the N 1s, C 1s and B 1s core levels for DBP on bare Ni(111) (approx. 1.0 MLE) as well as h-BN on Ni(111) and DBP on h-BN/Ni(111) (less ordered (approx. 1.0 MLE) and highly ordered (approx. 1.6 MLE)). The uncertainty of the numerical fitting procedure is given in parentheses behind each value and refers to the last significant digits.

BE [eV]	N 1s	C 1s	B 1s
DBP on Ni(111)	–	284.56(1)	–
h-BN on Ni(111)	398.67(1)	–	190.58(1)
less ordered DBP on h-BN/Ni(111)	398.59(1)	285.21(1)	190.50(1)
highly ordered DBP on h-BN/Ni(111)	398.62(1)	285.33(1)	190.49(1)

The comparison of the C 1s level of DBP on bare Ni(111) with DBP on h-BN/Ni(111) shows that the peak positions are shifted against each other, and the line width of the latter is significantly reduced. The binding energy shift is consistent with vacuum level alignment (see section "Valence band structure and work function change" above). The origin of the more pronounced broadening as well as the asymmetric line shape [45] of the C 1s level in the case of DBP on bare Ni(111) may stem from a variety of different adsorption configurations (chemical environments) due to disorder and the strong hybridization. We also observed a slight binding-energy shift of the N 1s and B 1s levels after the DBP adsorption, which shows that the DBP molecules also slightly influence the properties of the h-BN interlayer. Furthermore, a small new component at the low binding energy side of the N 1s level (at approx. 397.6 eV) of the less ordered DBP layer is visible. We suggest that the new component may originate from the chemical bonding of the DBP molecules to the nitrogen atoms of the h-BN interlayer, which possibly reduces the molecular mobility. This additional diffusion barrier thus hampers the molecular self-assembly and can be overcome by a higher substrate temperature during the film growth, which agrees with our structural findings above.

Conclusion

To summarize, we investigated the influence of an h-BN interlayer on the optical, structural and electronic properties of DBP on Ni(111). By inserting the h-BN layer, we fabricated a buried interface, and a monomer-like behavior was observed by means of DRS instead of a strong hybridization, which occurs on the bare metal substrate. Therefore, we conclude that one h-BN layer is sufficient to decouple the DBP molecules from the Ni(111) substrate. This statement is supported by the vacuum level alignment of the frontier orbitals, which was concluded from our UPS data. The investigation of the chemical structure by means of XPS revealed that the DBP adsorption also mildly influences the h-BN interlayer. A notable improvement of the lateral order was achieved by depositing DBP at a substrate temperature of 170 °C. The LEED measurement showed a clear diffraction pattern proving the high ordering of the DBP monolayer. By means of the combination of the quantitative LEED analysis and the LT-STM measurements, we concluded that the DBP molecules adopt a herringbone structure similar to DBP on Ag(111) and Au(111). Furthermore, we observed that the low work function of h-BN/Ni(111) decreases upon DBP deposition down to a value of 3.45(2) eV for the highly ordered DBP layer on h-BN/Ni(111). Therefore, h-BN on Ni(111) can potentially be used as n-type contact in molecular electronic devices with the advantage to minimize the metal–organic hybridization.

Experimental

Sample preparation

The Ni(111) single crystal (MaTecK GmbH, Germany, purity 99.99%) was prepared by several cycles of Ar^+ sputtering at room temperature and annealing at 800 °C. The h-BN layer was grown by thermal dehydrogenation of borazine molecules at a substrate temperature of 800 °C similar to [19]. We purchased borazine from Katchem Ltd. (Czech Republic) with a specified purity of >98%. The quality of the h-BN layer was checked by XPS and LEED. DBP raw material was purchased from Luminescence Technology Corp (Lumtec, Taiwan) with a specified purity of >99%. To remove remaining impurities we applied two cycles of temperature gradient sublimation according to [46]. The growth of the DBP films was achieved by deposition from an effusion cell at approx. 330 °C in ultrahigh vacuum. The layer thicknesses of the DBP films were determined based on DRS [28]. We use the unit monolayer equivalent (MLE) as defined and calibrated in detail in the Supporting Information File 1, Figure S1. Initially, the DRS signal accumulates rather uniformly for an increasing amount of deposited molecules on the substrate surface. Beginning at a certain threshold the DRS signal exhibits a noticeable blueshift (Supporting Information File 1, Figure S1), and we use this sudden change for our definition of 1 MLE. This spectral shift as well as the subsequent emergence of a new component in the spectra is attributed to DBP adsorbing in the second layer. We emphasize that this definition of 1 MLE does not necessarily imply that the substrate surface is entirely covered with densely packed molecular domains. Yet, we also refer to our large-area STM images (Supporting Information File 1, Figure S2), which confirm a close-packed DBP wetting layer as well as DBP clusters on top for a nominal film thickness of about 1.6 MLE. Hence, there is little discrepancy between 1 MLE, defined via DRS, and a fully covered substrate surface.

Experimental methods

All experiments were performed in ultrahigh vacuum with a base pressure in the range of 10^{-10} mbar. The adsorption of the DBP molecules was monitored by in situ DRS utilizing a 100 W halogen tungsten lamp, a blazed-grating monochromator (Acton Research SpectraPro SP2156), and a thermoelectrically cooled charge-coupled device (CCD) (Princeton Instruments PIXIS 100BR eXcelon/UV) [28,47,48]. The experimental setup is described in detail in [28]. The DRS signal is defined as:

$$\mathrm{DRS}(E,d)=\frac{R(E,d)-R(E,0)}{R(E,d)}, \qquad (1)$$

where $R(E, 0)$ and $R(E, d)$ are the reflectance spectra of the bare substrate and the DBP covered substrate, respectively, and d being the film thickness. Each reflectance spectrum was accumulated over 30 s to increase the signal-to-noise ratio. Furthermore, we used the difference of consecutive reflectance spectra to calculate the ΔDRS intensity using the following formula:

$$\Delta\mathrm{DRS}(E,d_\mathrm{i})=\frac{R(E,d_\mathrm{i})-R(E,d_\mathrm{i-1})}{R(E,d_\mathrm{i})} \qquad (2)$$
$$d_\mathrm{i}-d_\mathrm{i-1}\ \ldots \quad \text{thickness increment}$$

The lateral structure of the DBP films was investigated in reciprocal space using an Omicron MCP-LEED (MCP2-SPECTALEED) and in real space by LT-STM using a JT-STM/AFM (SPECS Surface Nano Analysis GmbH) with a tungsten tip operated at 4.5 K. We used the non-commercial software LEEDCal [49] for the distortion correction of the LEED images and the commercial software LEEDLab [50] for the quantitative LEED analysis. The LT-STM images were only modified by a mean plane subtraction. The electronic properties were investigated by PES with monochromatized Al Kα (SPECS Focus 500, $E_\mathrm{excitation}$ = 1486.71 eV), monochromatized and p-polarized He Iα (SPECS UVLS-600, $E_\mathrm{excitation}$ = 21.22 eV) radiation, and a SPECS PHOIBOS 150 hemispherical electron analyzer equipped with a 3D delay line detector (SPECS DLD4040-150). The energy resolutions of the UPS and XPS measurements were determined to be approx. 10 meV and approx. 0.55 eV, respectively. For the determination of the work function we used a bias voltage of approx. −9 V to shift the secondary electron cut-off.

Supporting Information

Supporting Information File 1

Additional experimental results.
[https://www.beilstein-journals.org/bjnano/content/supplementary/2190-4286-11-101-S1.pdf]

Funding

This project was funded by the Deutsche Forschungsgemeinschaft (DFG) through project numbers FR 875/16-1 and FR 875/19-1 and by the Futaba Research Grant Program of the Futaba Foundation. In addition, we thank the international student exchange program of Chiba University for funding the stay of T. A. at Jena University.

ORCID® iDs

Maximilian Schaal - https://orcid.org/0000-0003-4533-1666
Marco Gruenewald - https://orcid.org/0000-0003-1545-7831
Felix Otto - https://orcid.org/0000-0002-2327-5950
Jari Domke - https://orcid.org/0000-0001-9339-0711
Roman Forker - https://orcid.org/0000-0003-0969-9180
Hiroyuki Yoshida - https://orcid.org/0000-0002-8889-324X
Torsten Fritz - https://orcid.org/0000-0001-6904-1909

References

1. Duhm, S.; Gerlach, A.; Salzmann, I.; Bröker, B.; Johnson, R. L.; Schreiber, F.; Koch, N. *Org. Electron.* **2008,** *9,* 111–118. doi:10.1016/j.orgel.2007.10.004
2. Koch, N. *J. Phys.: Condens. Matter* **2008,** *20,* 184008. doi:10.1088/0953-8984/20/18/184008
3. Yang, X.; Krieger, I.; Lüftner, D.; Weiß, S.; Heepenstrick, T.; Hollerer, M.; Hurdax, P.; Koller, G.; Sokolowski, M.; Puschnig, P.; Ramsey, M. G.; Tautz, F. S.; Soubatch, S. *Chem. Commun.* **2018,** *54,* 9039–9042. doi:10.1039/c8cc03334j
4. Xu, C.; Que, Y.; Zhuang, Y.; Lin, Z.; Wu, X.; Wang, K.; Xiao, X. *J. Phys. Chem. B* **2018,** *122,* 601–611. doi:10.1021/acs.jpcb.7b05140
5. Forker, R.; Kasemann, D.; Dienel, T.; Wagner, C.; Franke, R.; Müllen, K.; Fritz, T. *Adv. Mater. (Weinheim, Ger.)* **2008,** *20,* 4450–4454. doi:10.1002/adma.200801112
6. Wang, Q.; Franco-Cañellas, A.; Ji, P.; Bürker, C.; Wang, R.-B.; Broch, K.; Thakur, P. K.; Lee, T.-L.; Zhang, H.; Gerlach, A.; Chi, L.; Duhm, S.; Schreiber, F. *J. Phys. Chem. C* **2018,** *122,* 9480–9490. doi:10.1021/acs.jpcc.8b01529
7. Martínez-Galera, A. J.; Nicoara, N.; Martínez, J. I.; Dappe, Y. J.; Ortega, J.; Gómez-Rodríguez, J. M. *J. Phys. Chem. C* **2014,** *118,* 12782–12788. doi:10.1021/jp500768y
8. Forker, R.; Dienel, T.; Krause, A.; Gruenewald, M.; Meissner, M.; Kirchhuebel, T.; Gröning, O.; Fritz, T. *Phys. Rev. B* **2016,** *93,* 165426. doi:10.1103/physrevb.93.165426
9. Auwärter, W. *Surf. Sci. Rep.* **2019,** *74,* 1–95. doi:10.1016/j.surfrep.2018.10.001
10. Kratzer, M.; Matkovic, A.; Teichert, C. *J. Phys. D: Appl. Phys.* **2019,** *52,* 383001. doi:10.1088/1361-6463/ab29cb
11. Wang, M.; Kim, M.; Odkhuu, D.; Park, N.; Lee, J.; Jang, W.-J.; Kahng, S.-J.; Ruoff, R. S.; Song, Y. J.; Lee, S. *ACS Nano* **2014,** *8,* 5478–5483. doi:10.1021/nn501837c
12. Jang, S. K.; Youn, J.; Song, Y. J.; Lee, S. *Sci. Rep.* **2016,** *6,* 30449. doi:10.1038/srep30449
13. Brülke, C.; Heepenstrick, T.; Krieger, I.; Wolff, B.; Yang, X.; Shamsaddinlou, A.; Weiß, S.; Bocquet, F. C.; Tautz, F. S.; Soubatch, S.; Sokolowski, M. *Phys. Rev. B* **2019,** *99,* 121404. doi:10.1103/physrevb.99.121404
14. Schwarz, M.; Duncan, D. A.; Garnica, M.; Ducke, J.; Deimel, P. S.; Thakur, P. K.; Lee, T.-L.; Allegretti, F.; Auwärter, W. *Nanoscale* **2018,** *10,* 21971–21977. doi:10.1039/c8nr06387g
15. Mehler, A.; Néel, N.; Kröger, J. *J. Vac. Sci. Technol., A* **2019,** *37,* 061404. doi:10.1116/1.5125486
16. Matković, A.; Genser, J.; Kratzer, M.; Lüftner, D.; Chen, Z.; Siri, O.; Puschnig, P.; Becker, C.; Teichert, C. *Adv. Funct. Mater.* **2019,** *29,* 1903816. doi:10.1002/adfm.201903816
17. Sun, X.; Pratt, A.; Li, Z. Y.; Ohtomo, M.; Sakai, S.; Yamauchi, Y. *J. Appl. Phys.* **2014,** *115,* 17C117. doi:10.1063/1.4866237
18. Auwärter, W.; Kreutz, T. J.; Greber, T.; Osterwalder, J. *Surf. Sci.* **1999,** *429,* 229–236. doi:10.1016/s0039-6028(99)00381-7
19. Preobrajenski, A. B.; Vinogradov, A. S.; Mårtensson, N. *Phys. Rev. B* **2004,** *70,* 165404. doi:10.1103/physrevb.70.165404
20. Hirade, M.; Nakanotani, H.; Yahiro, M.; Adachi, C. *ACS Appl. Mater. Interfaces* **2011,** *3,* 80–83. doi:10.1021/am100915s
21. Xiao, X.; Zimmerman, J. D.; Lassiter, B. E.; Bergemann, K. J.; Forrest, S. R. *Appl. Phys. Lett.* **2013,** *102,* 073302. doi:10.1063/1.4793195
22. Zheng, Y.-q.; Potscavage, W. J., Jr.; Komino, T.; Hirade, M.; Adachi, J.; Adachi, C. *Appl. Phys. Lett.* **2013,** *102,* 143304. doi:10.1063/1.4801647
23. Chen, C.-W.; Huang, Z.-Y.; Lin, Y.-M.; Huang, W.-C.; Chen, Y.-H.; Strzalka, J.; Chang, A. Y.; Schaller, R. D.; Lee, C.-K.; Pao, C.-W.; Lin, H.-W. *Phys. Chem. Chem. Phys.* **2014,** *16,* 8852–8864. doi:10.1039/c3cp55385j
24. Bartynski, A. N.; Grob, S.; Linderl, T.; Gruber, M.; Brütting, W.; Thompson, M. E. *J. Phys. Chem. C* **2016,** *120,* 19027–19034. doi:10.1021/acs.jpcc.6b06302
25. Nakanotani, H.; Higuchi, T.; Furukawa, T.; Masui, K.; Morimoto, K.; Numata, M.; Tanaka, H.; Sagara, Y.; Yasuda, T.; Adachi, C. *Nat. Commun.* **2014,** *5,* 4016. doi:10.1038/ncomms5016
26. Otto, F.; Kirchhuebel, T.; Baby, A.; Sojka, F.; Fratesi, G.; Fritz, T.; Forker, R. *J. Phys. Chem. C* **2020,** *124,* 4114–4127. doi:10.1021/acs.jpcc.9b10560
27. Debad, J. D.; Morris, J. C.; Lynch, V.; Magnus, P.; Bard, A. J. *J. Am. Chem. Soc.* **1996,** *118,* 2374–2379. doi:10.1021/ja9537888
28. Forker, R.; Gruenewald, M.; Fritz, T. *Annu. Rep. Prog. Chem., Sect. C: Phys. Chem.* **2012,** *108,* 34–68. doi:10.1039/c2pc90002e
29. Udhardt, C.; Forker, R.; Gruenewald, M.; Watanabe, Y.; Yamada, T.; Ueba, T.; Munakata, T.; Fritz, T. *Thin Solid Films* **2016,** *598,* 271–275. doi:10.1016/j.tsf.2015.12.023
30. Dinca, L. E.; De Marchi, F.; MacLeod, J. M.; Lipton-Duffin, J.; Gatti, R.; Ma, D.; Perepichka, D. F.; Rosei, F. *Nanoscale* **2015,** *7,* 3263–3269. doi:10.1039/c4nr07057g
31. Bischoff, F.; Seufert, K.; Auwärter, W.; Joshi, S.; Vijayaraghavan, S.; Écija, D.; Diller, K.; Papageorgiou, A. C.; Fischer, S.; Allegretti, F.; Duncan, D. A.; Klappenberger, F.; Blobner, F.; Han, R.; Barth, J. V. *ACS Nano* **2013,** *7,* 3139–3149. doi:10.1021/nn305487c
32. Zhou, Y.; Taima, T.; Shibata, Y.; Miyadera, T.; Yamanari, T.; Yoshida, Y. *Sol. Energy Mater. Sol. Cells* **2011,** *95,* 2861–2866. doi:10.1016/j.solmat.2011.06.001
33. Mehler, A.; Kirchhuebel, T.; Néel, N.; Sojka, F.; Forker, R.; Fritz, T.; Kröger, J. *Langmuir* **2017,** *33,* 6978–6984. doi:10.1021/acs.langmuir.7b00306
34. Kirchhuebel, T.; Gruenewald, M.; Sojka, F.; Kera, S.; Bussolotti, F.; Ueba, T.; Ueno, N.; Rouillé, G.; Forker, R.; Fritz, T. *Langmuir* **2016,** *32,* 1981–1987. doi:10.1021/acs.langmuir.5b04069
35. Forker, R.; Meissner, M.; Fritz, T. *Soft Matter* **2017,** *13,* 1748–1758. doi:10.1039/c6sm02688e

36. Wagner, C.; Forker, R.; Fritz, T. *J. Phys. Chem. Lett.* **2012,** *3,* 419–424. doi:10.1021/jz2015605
37. Kirchhuebel, T.; Monti, O. L. A.; Munakata, T.; Kera, S.; Forker, R.; Fritz, T. *Phys. Chem. Chem. Phys.* **2019,** *21,* 12730–12747. doi:10.1039/c8cp07318j
38. Ivanov, M. V.; Wang, D.; Zhang, D.; Rathore, R.; Reid, S. A. *Phys. Chem. Chem. Phys.* **2018,** *20,* 25615–25622. doi:10.1039/c8cp02936a
39. Braun, S.; Salaneck, W. R.; Fahlman, M. *Adv. Mater. (Weinheim, Ger.)* **2009,** *21,* 1450–1472. doi:10.1002/adma.200802893
40. Otero, R.; Vázquez de Parga, A. L.; Gallego, J. M. *Surf. Sci. Rep.* **2017,** *72,* 105–145. doi:10.1016/j.surfrep.2017.03.001
41. Quinn, J. T. E.; Zhu, J.; Li, X.; Wang, J.; Li, Y. *J. Mater. Chem. C* **2017,** *5,* 8654–8681. doi:10.1039/c7tc01680h
42. Schmid, M.; Steinrück, H.-P.; Gottfried, J. M. *Surf. Interface Anal.* **2014,** *46,* 505–511. doi:10.1002/sia.5521
43. Herrera-Gomez, A.; Bravo-Sanchez, M.; Ceballos-Sanchez, O.; Vazquez-Lepe, M. O. *Surf. Interface Anal.* **2014,** *46,* 897–905. doi:10.1002/sia.5453
44. Yeh, J. J.; Lindau, I. *At. Data Nucl. Data Tables* **1985,** *32,* 1–155. doi:10.1016/0092-640x(85)90016-6
45. Klein, B. P.; van der Heijden, N. J.; Kachel, S. R.; Franke, M.; Krug, C. K.; Greulich, K. K.; Ruppenthal, L.; Müller, P.; Rosenow, P.; Parhizkar, S.; Bocquet, F. C.; Schmid, M.; Hieringer, W.; Maurer, R. J.; Tonner, R.; Kumpf, C.; Swart, I.; Gottfried, J. M. *Phys. Rev. X* **2019,** *9,* 011030. doi:10.1103/physrevx.9.011030
46. Levin, A. A.; Leisegang, T.; Forker, R.; Koch, M.; Meyer, D. C.; Fritz, T. *Cryst. Res. Technol.* **2010,** *45,* 439–448. doi:10.1002/crat.200900730
47. McIntyre, J. D. E.; Aspnes, D. E. *Surf. Sci.* **1971,** *24,* 417–434. doi:10.1016/0039-6028(71)90272-x
48. Sun, L. D.; Hohage, M.; Zeppenfeld, P.; Berkebile, S.; Koller, G.; Netzer, F. P.; Ramsey, M. G. *Appl. Phys. Lett.* **2006,** *88,* 121913. doi:10.1063/1.2189014
49. Sojka, F.; Meissner, M.; Zwick, C.; Forker, R.; Fritz, T. *Rev. Sci. Instrum.* **2013,** *84,* 015111. doi:10.1063/1.4774110
50. *LEEDLab,* v 1.2; Fritz & Sojka GbR, 2018, https://fritz-sojka-gbr.de.

License and Terms

The definitive version of this article is the electronic one which can be found at:
doi:10.3762/bjnano.11.101

BEILSTEIN JOURNAL OF NANOTECHNOLOGY

Role of redox-active axial ligands of metal porphyrins adsorbed at solid–liquid interfaces in a liquid-STM setup

Thomas Habets[1], Sylvia Speller[2,3] and Johannes A. A. W. Elemans*[1]

Full Research Paper

Open Access

Address:
[1]Radboud University, Institute for Molecules and Materials (IMM), 6525 AJ Nijmegen, Netherlands, [2]University of Rostock, Institute of Physics, Albert-Einstein-Straße 23, 18059 Rostock, Germany and [3]University of Rostock, Department Life, Light, Matter, Albert-Einstein-Straße 25, 18059 Rostock, Germany

Email:
Johannes A. A. W. Elemans* - J.Elemans@science.ru.nl

* Corresponding author

Keywords:
manganese; porphyrins; redox reactions; scanning tunneling microscopy; solid–liquid interface

Beilstein J. Nanotechnol. **2020,** *11,* 1264–1271.
https://doi.org/10.3762/bjnano.11.110

Received: 15 April 2020
Accepted: 30 July 2020
Published: 24 August 2020

This article is part of the thematic issue "Molecular assemblies on surfaces – towards physical and electronic decoupling of organic molecules".

Guest Editor: M. Stöhr

Abstract

In a liquid-STM setup environment, the redox behavior of manganese porphyrins was studied at various solid–liquid interfaces. In the presence of a solution of Mn(III)Cl porphyrins in 1-phenyloctane, which was placed at a conductive surface, large and constant additional currents relative to a set tunneling current were observed, which varied with the magnitude of the applied bias voltage. These currents occurred regardless of the type of surface (HOPG or Au(111)) or tip material (PtIr, Au or W). The additional currents were ascribed to the occurrence of redox reactions in which chloride is oxidized to chlorine and the Mn(III) center of the porphyrin moiety is reduced to Mn(II). The resulting Mn(II) porphyrin products were identified by UV–vis analysis of the liquid phase. For solutions of Mn(III) porphyrins with non-redox active acetate instead of chloride axial ligands, the currents remained absent.

Introduction

Manganese(III) porphyrins are well-known catalysts for the epoxidation of alkenes [1-4]. The manganese center of the porphyrin moiety serves as a coordination site for an oxygen atom, which subsequently is inserted into the double bond of the alkene. A variety of oxygen donors can be used to oxidize the manganese center to an active manganese-oxo (Mn=O) species, such as iodosylbenzene, hypochlorite and hydrogen peroxide. The use of the environmentally most benign oxidant, molecular oxygen (O_2), is also possible, but comes with a drawback. To be able to generate an Mn=O complex, the Mn(III) porphyrin first needs to be reduced to a Mn(II) porphyrin, which can subsequently coordinate to O_2 and activate it for splitting of the O–O bond. To accomplish this, generally a co-reductor (e.g., isobutyric aldehyde [3,5,6]) is included in the catalytic system in order to facilitate the first reduction step.

Previously, our group has investigated the catalytic properties of manganese porphyrins at the single-molecule level, employing scanning tunneling microscopy (STM) [7-9]. Since our aim was to stay as close as possible to the laboratory conditions at which catalysis takes place (typically in an organic solvent under ambient conditions), we carried out our STM studies at a solid–liquid interface at room temperature. We found that while the porphyrin catalyst **MnTUPCl** (tetrakis-*meso*-undecylporphyrin manganese(III) chloride, Figure 1a) is fully inert in *n*-tetradecane solution, it becomes catalytically active in the epoxidation of alkenes when it is adsorbed at the interface of a Au(111) substrate and an *n*-tetradecane solution of the compound [7]. From real-time topographic signature changes in the STM images (Figure 1c), combined with optical reflectance spectroscopy, it was concluded that Mn=O complexes were readily formed in the presence of O_2 gas. This was a surprising result, since a chemical co-reductor was absent. It turned out that a sufficiently negatively biased surface was responsible for the reduction of the metal centers of the porphyrin moieties from Mn(III) to Mn(II), which activated them to coordinate and dissociate O_2.

Although these STM studies provided fundamentally new insights into reactivity at the single-molecule scale, some mechanistic aspects still remained unclear. For instance, the reduction of the Mn(III) porphyrin to a Mn(II) porphyrin also involves the dissociation of the axially coordinating Cl ligand from the metal center, and it is as yet unclear what the fate of this ligand is. In the catalysis study with **MnTUPCl** at the Au(111) surface, two possible mechanisms were proposed [7]: (i) A surface gold atom coordinates to the manganese center of **MnTUPCl** in an axial ligand-like fashion, inducing a chlorine radical to dissociate, thereby reducing the Mn(III) center to Mn(II), or (ii) the surface actively reduces **MnTUPCl** by donating an electron, followed by dissociation of a chloride anion.

In this paper, we investigate in more detail the role of the axially coordinating Cl ligand of **MnTUPCl** at a solid–liquid interface in a liquid-STM setup. By systematically varying the experimental conditions in terms of type of substrate, solvent, solute, and concentration of the solute, we will demonstrate that the ligand can in fact be involved in redox processes in the liquid-STM setup.

Results and Discussion

One of the possible mechanisms for axial ligand dissociation mentioned in the introduction was the direct attachment of a gold atom to the manganese center of **MnTUPCl**, coming from the Au(111) surface below. As a first experiment we therefore decided to also investigate with STM the behavior of **MnTUPCl** at a HOPG surface instead of a Au(111) surface, since in that case no direct metal atom coordination from the substrate is possible. To our surprise we found a strong influence of the solvent on the success of imaging the molecules with STM. When *n*-tetradecane was used as the solvent, monolayers of **MnTUPCl** readily formed on Au(111) (Figure 1c), while poorly organized and dynamic layers were formed on HOPG (not shown). When, however, 1-phenyloctane, a broadly applied aromatic solvent in liquid-STM studies, was used, it was impossible to image the surface or adsorbed molecules regardless of the used surface, due to the occurrence of a large additional increase in measured tunneling current. While the imaging of monolayers of **MnTUPCl** and other metal porphyrins based on the TUP-ligand generally requires a tunneling set

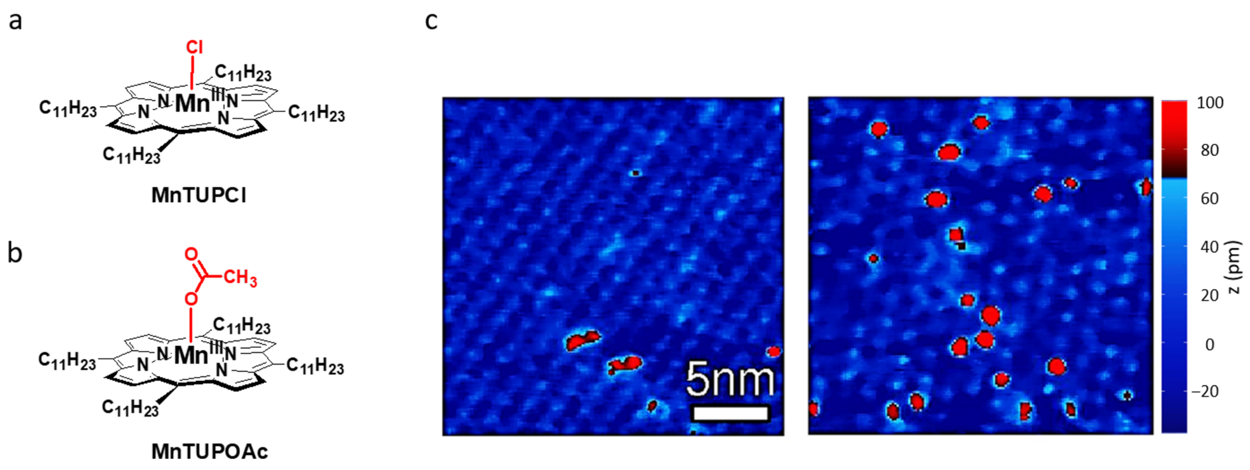

Figure 1: (a) Molecular structure of **MnTUPCl**. (b) Molecular structure of **MnTUPOAc**. (c) STM images of a monolayer of **MnTUPCl** at a Au(111)–*n*-tetradecane interface; the light blue spots are the native **MnTUPCl** molecules, the red spots their respective Mn=O complexes; left image: in argon atmosphere, a few Mn=O species are present; right image: in oxygen atmosphere, more Mn=O species have been formed. The color bar on the right indicates apparent heights. The STM images were adapted from our previous work [7].

current of less than 5 pA [7,10-13], now additional currents of several tens of picoamperes were present. Remarkably, the additional currents were never observed in experiments with analogous porphyrins with a copper(II) or cobalt(II) center [10,11]. In the following, we will investigate the redox behavior of **MnTUPCl** at the solid–liquid interface in more detail.

It is well-established that during and after the addition of solutions of molecules to the sample surface in an STM setup, the observed current between the tip and sample can increase. This increase may, for example, be the result of a mechanical disturbance made to the system upon adding the liquid, the presence of ions in the solution, and/or polarization of the solution or solutes therein. In most cases the additional current is of the order of the noise level of the STM (approx. 1 pA), or at least significantly smaller than the applied tunneling current. However, after the addition of a 1-phenyloctane solution of **MnTUPCl** ($c = 1 \times 10^{-4}$ M), significant currents with a magnitude of about 50 pA were measured between the $Pt_{90}Ir_{10}$ tip and the HOPG sample. The magnitude of the additional current increased with an increasing concentration of the compound, or with an increasing magnitude of the bias voltage. Over a time of minutes to hours, the additional current decayed somewhat, but not to zero. In order to qualify the behavior of the additional current, we slightly adjusted our STM setup. Conventionally, we added with a syringe a small droplet (5–10 µL) of solution to a sample of HOPG, which was contained around the tip and at the surface because of the surface tension of the droplet. In our modified setup, we used a liquid cell to contain a larger and well-defined volume of solution at the sample surface, ensuring that the concentration of the solutes remains stable during the sometimes prolonged measurements. During the experiments the voltage difference between the tip and sample surface was varied using the STM controller, while the current and the applied voltage were recorded using a data logger. The quantitative behavior of solutions of **MnTUPCl** at the surface of the STM setup did not change by using this modification, in the sense that the magnitude of the current still increased with the concentration and the magnitude of the bias voltage. After the addition of 350 µL of a 1-phenyloctane solution of **MnTUPCl** (c = 1 x 10^{-4} M) to the modified STM setup, currents of 40 ± 20 pA were measured between the tip and the HOPG sample (at a bias voltage of 0 mV). This current remained even when the tip was manually retracted far out of tunneling range (tip sample distance: 12 ± 2 µm), while still staying in contact with the solution.

Next, the dependency of the observed current upon systematic variation of the bias voltage was monitored (black trace in Figure 2a). The observed dependency of the current on the concentration of the solutions at a set bias voltage of −2 V is plotted in Figure 2b. In a reference experiment under the same conditions, pure 1-phenyloctane displayed current changes of only 1–2 pA, independent of changes in bias voltage (not shown). This observation implies that it is not exclusively the solvent that is responsible for the current. The observed behavior can have different causes. For example, due to the polarization of the solvent and/or the solutes therein, a current may flow from the tip to the sample or vice versa. Such a polarization may be triggered by a voltage change. However, it can be expected that when the voltage after the change remains constant, after a certain time a new equilibrium will be reached in which

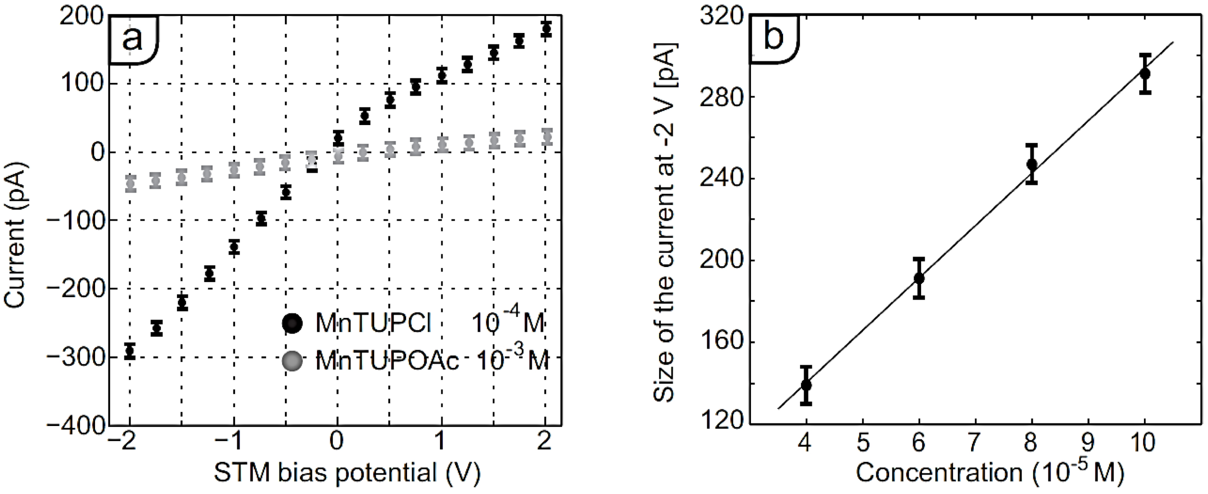

Figure 2: (a) Bias voltage dependence of the measured current in the STM setup at the interface of HOPG and a solution in 1-phenyloctane of **MnTUPCl** ($c = 1 \times 10^{-4}$ M, black) and of **MnTUPOAc** ($c = 1 \times 10^{-3}$ M, grey). (b) Concentration dependence of the measured current in the STM setup at a bias voltage of −2 V of **MnTUPCl** at the same interface ($c = 1 \times 10^{-4}$ M); the line is a linear fit through the data points. Both graphs show the average ±1 S.D. of 1000 measurements recorded within a time span of 1.5 min.

the flow of charges has died out and the additional current decays to zero. In the case of the experiments with **MnTUPCl**, however, such a decay was never observed, and the current remained relatively stable as a function of the time. Alternatively, the current may be a result of the formation and presence of conducting assemblies of π-stacked porphyrins. However, in this case an exponential decay of the conductance would be expected with an increasing distance between the tip and sample [14], which again was not observed for solutions of **MnTUPCl**. The variations in the additional current did not increase when the tip–sample separation distance was varied between 5 and 20 µm (20 µm was the physical limit of the setup). Therefore, it is considered to be unlikely that the observed current is a result of conducting assemblies of π-stacked porphyrins connecting the tip with the HOPG surface.

The observed current may also be caused by reduction or oxidation reactions of the solutes at the tip and at the sample surface. Such reactions would result in so-called Faradaic currents between the tip and the sample. In the case of **MnTUPCl**, the following redox reactions at the tip or sample surface can be envisaged:

$$2\mathbf{Mn(III)TUPCl} + 2e^- \rightarrow 2\mathbf{Mn(II)TUP} + 2Cl^- \quad (1)$$

$$2Cl^- \rightarrow Cl_2 + 2e^- \quad (2)$$

We base these proposed reactions on the fact that the manganese center can be reduced from (III) to (II) [15,16], results from previous work that the substrates in an STM setup act as electrodes at which manganese porphyrins can be reduced [6-8], and the fact that also cobalt porphyrins can accept electrons from a HOPG surface in a liquid-STM setup [17,18]. While we have demonstrated that these redox reactions do not occur spontaneously in solutions of **MnTUPCl** in, e.g., a glass test tube [7], they do occur in the STM setup when two electrically connected conductive surfaces (tip and sample) are present. This suggests that adsorption of the molecules to these surfaces indeed activates their reactivity. Our proposal of redox reactions is supported by the observation that the magnitude of the current increases with an increasing concentration of **Mn(III)TUPCl** in the supernatant solution. Typically, Faradaic currents depend linearly on the concentration of the redox-active species, and Figure 2b indeed shows a linear dependence of the observed currents on the used concentration of **Mn(III)TUPCl**. Based on the proposed one-electron process, the measured currents of up to 300 pA agree with a reaction rate of 3×10^{-15} mol/s. The solutions applied to the surface contain about 3.5×10^{-8} mol of **MnTUPCl**, which is a sufficient amount to sustain the reactions for weeks, at least in principle. However, since we propose that the reduction of the manganese porphyrins takes place when they are adsorbed to the negatively biased electrode, their adsorption–desorption process must be dynamic. Once **Mn(II)TUP** complexes are formed, they must be able to desorb and replaced by molecules of **Mn(III)TUPCl** from the supernatant solution so that the reduction reactions can continue. Given the fact that the molecules of **MnTUPCl** are adsorbed to the interface via relatively weak physisorption interactions, such dynamics are likely.

In the proposed redox reactions, the chloride ligands, which are axially coordinated to the manganese centers, play an essential role in generating the observed currents. First, they dissociate when the manganese center is reduced. We propose that the ions are subsequently solvated by the 1-phenyloctane solvent and migrate to the other electrode (vide infra). Second, in a counter reaction they are oxidized to chlorine gas. No net current would be observed if one of the two processes would not occur. In order to check the proposed role of the chloride ions, an analogous porphyrin containing an acetate instead of a chloride axial ligand was synthesized (**MnTUPOAc**, Figure 1a). The acetate ligand cannot act as a reductor, and as a consequence a similar current as observed in the case of **MnTUPCl** should not occur. The currents measured upon the addition of 350 µL of a 1-phenyloctane solution of **MnTUPOAc** ($c = 1 \times 10^{-3}$ mM) to the modified STM setup are shown in gray in Figure 2a. Even at a ten times higher concentration of **MnTUPOAc** than that of **MnTUPCl** in the previously discussed experiments, the measured currents stayed between −50 ± 10 and +30 ± 10 pA upon variation of the bias voltage between −2 and +2 V, respectively. Similar results were obtained when a 350 µL 1-phenyloctane solution of **CuTUP** [10] ($c = 1 \times 10^{-3}$ mM), a closely related metal porphyrin without an axial ligand coordinated to the metal center, was used. Both observations support the proposed essential role of the chloride counterion for the redox reactivity of **MnTUPCl**.

To investigate the influence of the nature of the used electrodes, we varied the sample surfaces (HOPG and Au(111)) and the tip material ($Pt_{90}Ir_{10}$, Au and W). A summary of these experiments is given in Table 1. Additional currents were observed on both used surfaces (Au(111) and HOPG), and with all the used tip materials. The differences in observed currents for different systems demonstrate the complexity of characterizing redox reactions with a two-probe system (tip and sample) in a non-conducting liquid. Obviously, such a setup is not the perfect design for experiments to investigate redox behavior, but it is worthwhile to consider what its shortcomings are. It can be expected that the rates of the reactions in Equation 1 and Equation 2 depend, among other factors, on the surface at which the reactions occur [19]. This specific surface effect is highlighted by the observation that the magnitude of the observed currents

Table 1: Measured currents (in pA) between the tip and the sample in the modified liquid-STM setup as a function of the applied bias voltage (V_{bias}). Porphyrin concentrations were 1 × 10^{-4} M, except for **MnTUPOAc** and **CuTUP** where a concentration of 1 × 10^{-3} M was used. Numbers between brackets indicate uncertainties (±1 S.D.).

			V_{bias}		
substrate	solute	Tip	−2 V	0 V	2 V
solvent: 1-phenyloctane					
HOPG	**MnTUPCl**	PtIr	−1470 (130)	110 (17)	1710 (50)
HOPG	**MnTUPOAc**	PtIr	−50 (10)	−10 (10)	30 (5)
Au(111)	**MnTUPCl**	PtIr	−660 (80)	200 (20)	910 (30)
HOPG	**MnTUPCl**	Au	−770 (90)	230 (30)	1110 (40)
Au(111)	**MnTUPCl**	Au	−870 (90)	190 (30)	1190 (60)
HOPG	**MnTUPCl**	W	−700 (40)	40 (10)	700 (20)
HOPG	**CuTUP**	PtIr	−20 (3)	9.8 (5)	37 (2)
HOPG	none	PtIr	−7.8 (4)	−9.4 (4)	−9.6 (3)
solvent: *n*-tetradecane					
HOPG	**MnTUPCl**	PtIr	−11 (9)	−3 (9)	5 (9)
HOPG	none	PtIr	−10 (8)	−10 (9)	−10 (8)
Au(111)	**MnTUPCl**	PtIr	−7 (9)	−2 (8)	3 (9)
Au(111)	none	PtIr	−11 (8)	−11 (9)	−11 (8)

is typically not mirrored when the sign of the applied bias voltage is switched (Table 1), indicating that when the two redox reactions occur at different sample electrodes this gives rise to different reaction rates. First, only the overall potential difference between the tip and the sample is known. The potential drops from the surfaces to the solution are governed by the material of the surface and structural properties of the interface, the type and polarizability of the solvent, the solutes (and their concentration), the presence of ions in the solvent, and a possible assembly of solutes at the interface. Furthermore, the reaction rates are determined by the chemical and electronic state of the sample surface, ion concentrations in the solution, and the availability of possible reaction intermediates. Most of these complications may be eliminated by adding a third, reference electrode to the setup and by using a conducting electrolyte (so that it turns into a so-called electrochemical (EC) STM [20,21]). At the same time, the absence of an electrolyte, which typically contains a high concentration of added salts, allows us to pinpoint the behavior of the axial ligand of our catalyst in the non-polar liquid in which also our catalysis studies were carried out. Still, our system shows several of the characteristics of a conventional electrochemical cell. Apart from the bias dependency of the reaction rate (both in terms of size and sign), also higher concentrations of the redox-active species lead to higher reaction rates, which points at increased dynamic exchange of the redox-active species at the sample and tip electrodes. Furthermore, the proposed transport of chloride ions through the 1-phenyloctane solvent basically makes it an electrolyte, albeit an unconventional one.

Assuming that the observed additional currents are caused by the proposed redox reactions (Equation 1 and Equation 2), **Mn(II)TUP** is generated, which may dissociate from the solid–liquid interface and dissolve in the supernatant solution. To investigate changes in supernatant composition during the STM experiments, ex situ UV–vis spectroscopy measurements were carried out. UV–vis spectra of supernatant solutions from different experiments in the modified STM setup using **MnTUPCl** and **MnTUPOAc** are depicted in Figure 3. The solid traces represent solutions that had been in the modified STM setup for four days, with the tip out of tunnel range and at a bias voltage of −2 V. The dashed traces (absorption value manually offset by 0.3 AU) are from reference solutions of the same composition, which were left to stand in an unsealed test tube next to the STM setup for the same four days. All used concentrations were 1 × 10^{-4} M.

The UV–vis spectra of the sample and reference solutions of **MnTUPOAc** (Figure 3b) are nearly identical, showing the characteristic strong Soret band at 481 nm and Q-bands at 604 and 640 nm. In contrast, the UV–vis spectra of the sample and reference solutions of **MnTUPCl** (Figure 3a) show that the chemical composition of the solution that was in the STM setup had clearly changed. Both spectra show a Soret band at 478 nm,

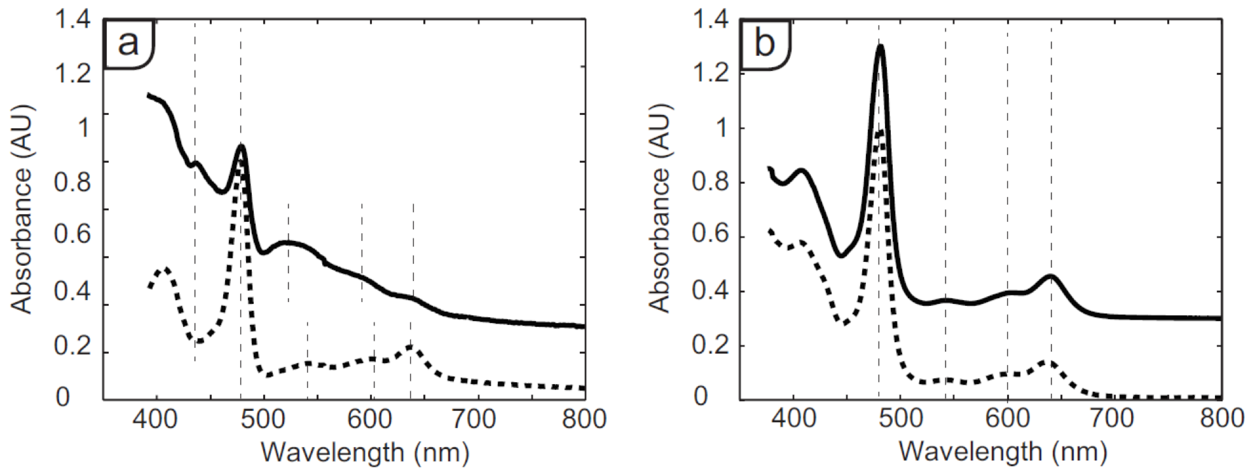

Figure 3: UV–vis spectra of sample (solid traces) and reference solutions (dashed traces of (a) **MnTUPCl** and (b) **MnTUPOAc** in 1-phenyloctane. The locations of main bands are indicated by narrow dashed vertical lines.

but in the spectrum of the sample solution a small, new band has emerged at 437 nm. Also the first Q-band has blueshifted by 21 nm, and a larger background absorbance is observed. These spectral changes indicate that the molecules of **MnTUPCl** are reactive in the STM setup under the influence of the bias voltage.

Following our hypotheses described above, the solution might also contain molecules of **Mn(II)TUP**. A blue shift of the Soret band from 478 to 437 nm is indeed in line with a one-electron reduction of the porphyrin Mn(III) center to Mn(II) [22,23]. However, since this species is highly reactive to oxidation by air, other changes in the UV–vis spectrum may additionally be caused by the formation of oxidation products of **Mn(II)TUP**. Because the spectrum is quite broad and no clear other bands can be recognized, it is at this stage difficult to draw conclusions about the identity of these products.

The occurrence of the additional currents appeared to depend on the nature and polarity of the solvent. When a solution of **MnTUPCl** in the non-aromatic and less polar solvent *n*-tetradecane was subjected to a bias voltage in the modified STM setup, no significant additional currents were observed compared to reference experiments in which the porphyrins were absent (Table 1). This does not directly imply that the redox reactions in Equation 1 and Equation 2 do not occur under these conditions; the redox reaction rates may be very low, i.e., below 2.5×10^7 e^-/s (comparable with a current of approx. 4 pA), and not exceed the noise level of the STM setup. Possible aspects that could cause the difference in observed current between solutions of **MnTUPCl** in 1-phenyloctane and *n*-tetradecane are: (i) a better solubility of chloride ions and/or **Mn(II)TUP** species in 1-phenyloctane compared to *n*-tetradecane, and (ii) a difference in dielectric constants of the used solvents, which are 2.26 and 2.03, respectively. A different dielectric constant may lead to a different potential decay at the interfaces, which in turn may influence the reaction rates. However, since the difference in dielectric constant between the two solvents is small, we propose the first explanation as being more likely. An enhanced solubility of the ions in the aromatic solvent 1-phenyloctane may be the result of attractive anion–π interactions [24].

Conclusion

MnTUPCl dissolved in 1-phenyloctane and placed in a tunnel junction yields high additional currents. We attribute them to Faradaic currents and put forward two possible explanations for the reduction of the manganese centers of the molecules of **MnTUPCl** at the Au(111)–*n*-tetradecane interface in a liquid-STM, i.e., the coordination of a gold atom from the top-most gold layer to **MnTUPCl** in an axial ligand-like fashion, or an active reduction as the result of the donation of an electron from the gold surface to the **MnTUPCl**. In this work it was shown that the use of the aromatic solvent 1-phenyloctane was accompanied by the emergence of large additional currents in the STM setup. These currents are in line with the occurrence of redox reactions at the two electrodes (surface and tip), in which chloride axial ligands dissociate upon reduction of the manganese centers at one electrode, after which the chloride ions are oxidized to chlorine gas at the other electrode. These reactions are supported by several observations: (i) The observed additional currents are stable as a function of the time and depend linearly on the applied **MnTUPCl** concentration in the supernatant solution, which would be expected for the proposed redox reactivity; (ii) when one of the redox partners was eliminated, i.e., by replacing the chloride axial ligand of the Mn(III) porphyrin by a redox-inert acetate ligand

(**MnTUPOAc**), no such additional currents are observed; (iii) ex situ UV–vis spectra of the supernatant solution significantly changed over time, indicating reactivity in the modified STM setup and the formation of Mn(II) porphyrin, which is one of the expected products of the proposed redox reactions.

Since apparently the axial ligand of Mn(III) porphyrins can play an essential role in the redox behavior of these compounds at a solid–liquid interface in a liquid-STM setup, our future research will be focused on the variation of these ligands and their role for the use of the metal porphyrins in catalysis. In particular, we intend to study with liquid-STM the catalytic properties of **MnTUPOAc** in the epoxidation of alkenes, and compare its performance to that of **MnTUPCl** under the same conditions.

Experimental

Materials and methods

All commercially obtained chemicals were used without further purification unless stated otherwise. The purity of 1-phenyloctane, the solvent in which the additional currents were observed, was confirmed by ^{1}H NMR spectroscopy; moreover, the currents were observed in multiple batches of this solvent, of two different suppliers (ACROS Organics or Sigma-Aldrich), independent whether it was vacuum-distilled prior to use or used as received. For TLC analysis, TLC silicagel 60 F254 (Merck, Burlington, MA, USA) and for column chromatography silica gel 0.035–0.070 mm, (Acros, Branchburg, N.J., USA) was used. MALDI-TOF mass spectra were measured in reflective mode with dithranol as a matrix on a Bruker Microflex LRF MALDI-TOF mass spectrometer (Bruker, Billerica, MA, USA). UV–vis spectra were recorded on a Varian Cary 50 UV–vis spectrophotometer.

Syntheses

Synthesis of MnTUPOCl and CuTUP

Compounds **MnTUPCl** [7] and **CuTUP** [10] were synthesized according to literature procedures.

Synthesis of MnTUPOAc

A solution of the free ligand **TUP** [7] (50 mg, 0.054 mmol) and $Mn(OAc)_2 \cdot 4H_2O$ (52 mg, 0.21 mmol) in argon-purged DMF (5 mL) was stirred and heated at reflux under argon for 3 h. After cooling, the solvent was evaporated and the residue was re-dissolved in CH_2Cl_2 (20 mL). The solution was extracted with water (2 × 50 mL) and then concentrated to a volume of 5 mL. An equal volume of a saturated aqueous NaOAc solution was added and the mixture was vigorously stirred open to air for 16 h. The product in the organic layer was subsequently purified by column chromatography (silica 60H, eluent CH_2Cl_2/MeOH 9:1, v/v) to yield **MnTUPOAc** (48 mg, 86%) as a dark green solid. MALDI-TOFMS *m*/*z* 979 $[M–OAc]^+$; UV–vis (CH_2Cl_2) λ/nm (log(ε/$M^{-1}cm^{-1}$)): 397 (4.52), 375 (4.60), 481 (4.95), 548 (3.35), 604 (3.56), 640 (4.01).

Experiments in the liquid-STM setup

A solution of a porphyrin compound was dissolved in an appropriate solvent (see text) and applied to a freshly cleaved HOPG substrate (10 × 10 mm^2, NT-MDT, ZYB) or Au(111) film (10 × 10 mm^2 with a thickness of 200 nm evaporated on freshly cleaved muscovite mica) which was mounted into a liquid-cell in a custom-built liquid-STM setup [7]. The STM-tip (mechanically cut) was immersed in a typical volume of 350 μL of the solution. The used concentrations of porphyrin varied between 1×10^{-4} and 1×10^{-3} M and are mentioned at the relevant experiments in the main text. The STM measurements were performed in constant-current mode using an Omicron Scala SPM controller. All experiments were performed in the thermostatted environment (21.5 ± 0.5 °C) of the NanoLab Nijmegen.

Acknowledgements

The work described in this paper is part of the Ph.D. thesis of T. Habets (ISBN: 978-94-028-1437-8).

Funding

We acknowledge funding by the Council for the Chemical Sciences of the Netherlands Organisation for Scientific Research (ECHO grant 700.57.023 and VIDI grant 700.58.423) and the European Research Council (ERC Starting Grant NANOCAT–259064). S.S. acknowledges the collaborative research center 1270 of the German Physical Society.

ORCID® iDs

Johannes A. A. W. Elemans - https://orcid.org/0000-0003-3825-7218

References

1. Meunier, B. *Chem. Rev.* **1992,** *92,* 1411–1456. doi:10.1021/cr00014a008
2. Rose, E.; Andrioletti, B.; Zrig, S.; Quelquejeu-Ethève, M. *Chem. Soc. Rev.* **2005,** *34,* 573–583. doi:10.1039/b405679p
3. Bernar, I.; Rutjes, F. P. J. T.; Elemans, J. A. A. W.; Nolte, R. J. M. *Catalysts* **2019,** *9,* 195. doi:10.3390/catal9020195
4. Nodzewska, A.; Wadolowska, A.; Watkinson, M. *Coord. Chem. Rev.* **2019,** *382,* 181–216. doi:10.1016/j.ccr.2018.12.004
5. de Torres, M.; van Hameren, R.; Nolte, R. J. M.; Rowan, A. E.; Elemans, J. A. A. W. *Chem. Commun.* **2013,** *49,* 10787–10789. doi:10.1039/c3cc45608k
6. Zhou, X.; Ji, H. *Chem. Eng. J.* **2010,** *156,* 411–417. doi:10.1016/j.cej.2009.10.066
7. Hulsken, B.; Van Hameren, R.; Gerritsen, J. W.; Khoury, T.; Thordarson, P.; Crossley, M. J.; Rowan, A. E.; Nolte, R. J. M.; Elemans, J. A. A. W.; Speller, S. *Nat. Nanotechnol.* **2007,** *2,* 285–289. doi:10.1038/nnano.2007.106

8. den Boer, D.; Li, M.; Habets, T.; Iavicoli, P.; Rowan, A. E.; Nolte, R. J. M.; Speller, S.; Amabilino, D. B.; De Feyter, S.; Elemans, J. A. A. W. *Nat. Chem.* **2013,** *5,* 621–627. doi:10.1038/nchem.1667
9. Li, M.; den Boer, D.; Iavicoli, P.; Adisoejoso, J.; Uji-i, H.; Van der Auweraer, M.; Amabilino, D. B.; Elemans, J. A. A. W.; De Feyter, S. *J. Am. Chem. Soc.* **2014,** *136,* 17418–17421. doi:10.1021/ja510930z
10. Coenen, M. J. J.; Cremers, M.; den Boer, D.; van den Bruele, F. J.; Khoury, T.; Sintic, M.; Crossley, M. J.; van Enckevort, W. J. P.; Hendriksen, B. L. M.; Elemans, J. A. A. W.; Speller, S. *Chem. Commun.* **2011,** *47,* 9666–9668. doi:10.1039/c1cc12569a
11. Coenen, M. J. J.; den Boer, D.; van den Bruele, F. J.; Habets, T.; Timmers, K. A. A. M.; van der Maas, M.; Khoury, T.; Panduwinata, D.; Crossley, M. J.; Reimers, J. R.; van Enckevort, W. J. P.; Hendriksen, B. L. M.; Elemans, J. A. A. W.; Speller, S. *Phys. Chem. Chem. Phys.* **2013,** *15,* 12451–12458. doi:10.1039/c3cp50829c
12. Reimers, J. R.; Panduwinata, D.; Visser, J.; Chin, Y.; Tang, C.; Goerigk, L.; Ford, M. J.; Sintic, M.; Sum, T.-J.; Coenen, M. J. J.; Hendriksen, B. L. M.; Elemans, J. A. A. W.; Hush, N. S.; Crossley, M. J. *Proc. Natl. Acad. Sci. U. S. A.* **2015,** *112,* E6101–E6110. doi:10.1073/pnas.1516984112
13. Reimers, J. R.; Panduwinata, D.; Visser, J.; Chin, Y.; Tang, C.; Goerigk, L.; Ford, M. J.; Baker, M.; Sum, T. J.; Coenen, M. J. J.; Hendriksen, B. L. M.; Elemans, J. A. A. W.; Hush, N. S.; Crossley, M. J. *J. Phys. Chem. C* **2016,** *120,* 1739–1748. doi:10.1021/acs.jpcc.5b11621
14. Lafferentz, L.; Ample, F.; Yu, H.; Hecht, S.; Joachim, C.; Grill, L. *Science* **2009,** *323,* 1193–1197. doi:10.1126/science.1168255
15. Giraudeau, A.; Callot, H. J.; Jordan, J.; Ezhar, I.; Gross, M. *J. Am. Chem. Soc.* **1979,** *101,* 3857–3862. doi:10.1021/ja00508a024
16. He, Y.; Borguet, E. *Angew. Chem., Int. Ed.* **2007,** *46,* 6098–6101. doi:10.1002/anie.200603822
17. Friesen, B. A.; Bhattarai, A.; Mazur, U.; Hipps, K. W. *J. Am. Chem. Soc.* **2012,** *134,* 14897–14904. doi:10.1021/ja304431b
18. Hipps, K. W.; Mazur, U. *Langmuir* **2018,** *34,* 3–17. doi:10.1021/acs.langmuir.7b02672
19. Bard, A.; Faulkner, L. *Electrochemical Methods: Fundamentals and Applications;* John Wiley & Sons, 2000.
20. Itaya, K. *Prog. Surf. Sci.* **1998,** *58,* 121–247. doi:10.1016/s0079-6816(98)00022-7
21. Liang, Y.; Pfisterer, J. H. K.; McLaughlin, D.; Csoklich, C.; Seidl, L.; Bandarenka, A. S.; Schneider, O. *Small Methods* **2019,** *3,* 1800387. doi:10.1002/smtd.201800387
22. Reed, C. A.; Kouba, J. K.; Grimes, C. J.; Cheung, S. K. *Inorg. Chem.* **1978,** *17,* 2666–2670. doi:10.1021/ic50187a057
23. Harriman, A.; Porter, G. *J. Chem. Soc., Faraday Trans. 2* **1979,** *75,* 1543–1552. doi:10.1039/f29797501543
24. Schottel, B. L.; Chifotides, H. T.; Dunbar, K. R. *Chem. Soc. Rev.* **2008,** *37,* 68–83. doi:10.1039/b614208g

License and Terms

BEILSTEIN JOURNAL OF NANOTECHNOLOGY

Growth of a self-assembled monolayer decoupled from the substrate: nucleation on-command using buffer layers

Robby Reynaerts, Kunal S. Mali* and Steven De Feyter*

Full Research Paper

Address:
Department of Chemistry, Division of Molecular Imaging and Photonics, KU Leuven, Celestijnenlaan 200F, B-3001 Leuven, Belgium

Email:
Kunal S. Mali* - kunal.mali@kuleuven.be; Steven De Feyter* - steven.defeyter@kuleuven.be

* Corresponding author

Keywords:
benzoic acid; nucleation; self-assembly; solution–solid interface; substrate effect

Beilstein J. Nanotechnol. **2020,** *11,* 1291–1302.
https://doi.org/10.3762/bjnano.11.113

Received: 13 May 2020
Accepted: 12 August 2020
Published: 01 September 2020

This article is part of the thematic issue "Molecular assemblies on surfaces – towards physical and electronic decoupling of organic molecules".

Guest Editor: M. Stöhr

Abstract

Structural polymorphism is ubiquitous in physisorbed self-assembled monolayers formed at the solution–solid interface. One of the ways to influence network formation at this interface is to physically decouple the self-assembled monolayer from the underlying substrate thereby removing the influence of the substrate lattice, if any. Here we show a systematic exploration of self-assembly of a typical building block, namely 4-tetradecyloxybenzoic acid at the 1-phenyloctane–graphite interface in the presence and in the absence of a buffer layer formed by a long chain alkane, namely *n*-pentacontane. Using scanning tunneling microscopy (STM), three different structural polymorphs were identified for 4-tetradecyloxybenzoic acid at the 1-phenyloctane–graphite interface. Surprisingly, the same three structures were formed on top of the buffer layer, albeit at different concentrations. Systematic variation of experimental parameters did not lead to any new network in the presence of the buffer layer. We discovered that the self-assembly on top of the buffer layer allows better control over the nanoscale manipulation of the self-assembled networks. Using the influence of the STM tip, we could initiate the nucleation of small isolated domains of the benzoic acid on-command in a reproducible fashion. Such controlled nucleation experiments hold promise for studying fundamental processes inherent to the assembly process on surfaces.

Introduction

The ability of some molecules to crystalize in more than one type of packing – a property widely known as crystal polymorphism – is not limited to the realm of bulk (3D) crystals but also extends to the 2D world of physisorbed self-assembled monolayers [1-4]. In fact, observation of multiple polymorphic networks, especially for organic monolayers formed at the solution–solid interface, is a more of routine occurrence than an exception. Such structurally diverse monolayers are typically formed on solid substrates such as highly oriented pyrolytic graphite (HOPG), graphene, and metals such as Cu, Ag and Au and have been characterized using scanning probe methods, especially scanning tunneling microscopy (STM) [2]. While the formation of structurally diverse crystalline monolayers provides exciting opportunities for surface modification and also for investigating crystal engineering in 2D [5], predicting 2D polymorphism is often nontrivial. The understanding of this already enigmatic process is further impaired by the nature of the solution–solid interface. A number of factors such as the temperature [6-9], the solvent [10-15], the substrate [16-18] and the concentration of the building block in solution [19-24] are known to influence network formation at the solution–solid interface.

One of the unconventional ways to influence the structure formation at the solution–solid interface involves the use of buffer layers. Such buffer layers typically comprise of monolayers formed by long chain alkanes [25-27] or alkane derivatives such as fatty acids [28-30] or alkylamines [31], especially when graphite is used as the substrate. The rationale here is that given the strong influence of the substrate lattice on the adsorption as well as the self-assembly of typical organic molecules, insertion of another layer in between the assembling building block and the substrate would allow the formation of an alternative polymorph that would not be obtained otherwise. In line with this strategy, self-assembled buffer layers of *n*-pentacontane (***n*-C$_{50}$**) have been used to obtain a previously unknown polymorph of hexakis(*n*-dodecyl)-*peri*-hexabenzocoronene (**HBC-C$_{12}$**) which was not formed when the assembly process was carried out at the *n*-tetradecane–HOPG interface without the buffer layer [26]. Buffer layers of ***n*-C$_{50}$** have also been used to 'select' certain polymorphs of a Fréchet dendron based on the symmetry of the underlying alkane layer [27]. Buffer layers of tetratriacontane [25] and tridecylamine [31] were used to template the self-assembly of copper phthalocyanine. Room temperature STM measurements revealed that the adsorption as well as the diffusion of clusters of CuPc molecules was strongly influenced by the symmetry and the structure of the buffer layers. Notably, no self-assembly was observed when CuPc solutions were directly deposited on the HOPG substrate highlighting the role of buffer layers in stabilizing the self-assembled networks [25,31].

Besides their use for influencing structure formation by acting as a physical barrier between the substrate and the assembling moiety, buffer layers are also widely used to study intrinsic electronic properties of functional organic systems such as organic semiconductors [32,33] and films of 1D/2D polymers [34-37] via electronic decoupling. Alkane buffer layers have been employed as efficient electronic decoupling platforms for studying the intrinsic electronic properties of graphene and fullerenes [38]. Apart from alkane derivatives, inorganic systems such as chemisorbed iodine layers [34-37], and ultrathin layers of KCl [39], NaCl [40], CuN [41] and oxides [32,42] have been used. Typically, the ultrathin films of these wide band gap materials act as insulating layers while still allowing electron tunneling through them. Chemisorbed iodine layers have been used as passivating layers on metals such as Au for achieving controlled electrochemical polymerization of thiophene to produce polythiophene nanowires with tunable lengths [36,37].

In the context of their use for controlling surface architectures, insertion of the buffer layers between the assembling moiety and the solid substrate affects the assembly process via the following major avenues: (1) The buffer layers, in principle, offer a new substrate with a different, often lower, symmetry. (2) The buffer layer has a different lattice constant compared to the solid substrate. (3) The adsorption enthalpy of the assembling moiety on the buffer layer is often different (lower) on the buffer layer compared to that on the solid substrate. These factors may lead to different adsorption conformation for initial single molecule adsorption coupled with higher orientational freedom and significantly different (often reduced) lateral corrugation barriers for molecular diffusion on buffer layers compared to that on pristine unmodified solid substrates. The result could be a selection of a polymorph that is otherwise not obtained under 'normal' experimental conditions. The decoupling effects could be significant especially for organic building blocks substituted with long alkyl chains because the soft-epitaxy of such chains with the graphite lattice is well established [43-45].

In this contribution, we present a systematic, curiosity-driven study of the self-assembly of a relatively simple building block, namely 4-tetradecyloxybenzoic acid (**BA-OC$_{14}$**, Figure 1a), with and without ***n*-C$_{50}$** (Figure 1b) buffer layers at the 1-phenyloctane–HOPG interface. Our previous investigation into the assembly behavior of this building block revealed that it forms structurally complex monolayers at the 1-phenyloctane–HOPG interface. Despite its simple molecular structure, the networks of **BA-OC$_{14}$** consist of a dense arrangement of hydrogen bonded dimers wherein the molecular columns show periodic kinks along the column axis after every three dimers. The origin of this relatively complex packing was thought to be the specific registry of the alkoxy chains with the substrate lattice that does not allow parallel and straight row packing of dimers due to the steric hindrance of the bulky phenyl groups. The result is a tilted arrangement of the **BA-OC$_{14}$** dimers that show periodic kinks that were thought to arise to maintain the specific registry with the substrate lattice [45]. Considering that the self-assembled network formed by **BA-OC$_{14}$** at the 1-phenyloctane–HOPG interface could possibly represent a substrate lattice-controlled assembly, we set out to address the following questions: (1) Will **BA-OC$_{14}$** form a similar network structure on top of a ***n*-C$_{50}$** buffer layer? (2) Would the self-assembly of **BA-OC$_{14}$** atop the ***n*-C$_{50}$** buffer layer lead to the formation of another polymorph? (3) Does the assembly atop such buffer layers provide better control over our ability to monitor/manipulate dynamic assembly processes? The results and discussion provided below delve into some of these aspects.

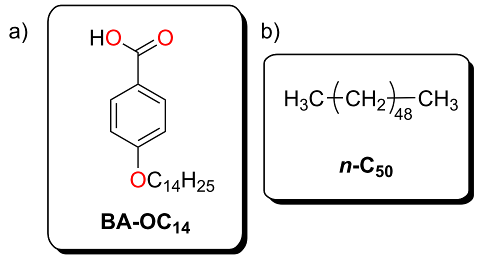

Figure 1: Molecular structures of (a) 4-tetradecyloxybenzoic acid (**BA-OC$_{14}$**) and (b) *n*-pentacontane (***n*-C$_{50}$**) used in this study. Monolayers of ***n*-C$_{50}$** were used as buffer layers to physically decouple the monolayers formed by **BA-OC$_{14}$** from the underlying graphite substrate.

Results and Discussion

Self-assembly of **BA-OC$_{14}$** without buffer layer

The famous and somewhat provocative quote of McCrone that, "… every compound has different polymorphic forms, and that, in general, the number of forms known for that compound is proportional to the time and money spent in research on that compound." [46] also applies to on-surface 2D assembly of building blocks. In fact, it is not unusual to observe multiple complex polymorphs for a building block with a seemingly simple molecular structure as demonstrated by the assembly of 4-octadecyloxybenzamide, which was found to form six different network structures [19]. Thus, before carrying out self-assembly experiments with ***n*-C$_{50}$** buffer layers, we systematically studied the concentration dependence of **BA-OC$_{14}$** assembly to comprehensively identify the different structures formed by **BA-OC$_{14}$** at the 1-phenyloctane–HOPG interface. With this exercise, we can have reasonable confidence that any 'new' polymorph observed atop buffer layers is indeed a new structure and is not formed as a consequence of slight changes in the solution concentration and thus is also observed in the absence of the buffer layer. To this effect, the concentration dependence of self-assembly was examined within the concentration range of 7.7×10^{-4} M to 4.0×10^{-5} M. For concentrations below 4.0×10^{-5} M, no self-assembly was observed.

Figure 2 shows large-scale and high-resolution STM images of the different polymorphs of **BA-OC$_{14}$** observed at the 1-phenyloctane–HOPG interface together with the proposed molecular models. Polymorph A (Figure 2a,d) is formed exclusively within the concentration range of 7.7×10^{-4} M to 1.9×10^{-4} M. This network has been reported by us earlier [45]. The high-resolution image provided in Figure 2d shows that the lamellar structure consists of bright blobs corresponding to the benzene rings flanked on either side by relatively darker regions which arise due to the tetradecyloxy chains. The benzene rings always appear in pairs indicating formation of hydrogen bonded dimers. Each lamella shows regular kinks along the lamella propagation direction. The kinks appear after every three hydrogen bonded dimers and the next three dimers are shifted with respect to the previous triplet of dimers (highlighted in red and green color, Figure 2g). The tetradecyloxy chains are oriented at ≈60° with respect to the column axis and are always aligned along one of the main symmetry axes of the graphite lattice. The tetradecyloxy chains in the neighboring lamellae are arranged in a tail-to-tail fashion without any interdigitation. The lamellae make an angle of ≈8° with respect to the nearest symmetry axis of graphite. The unit cell parameters of the network are provided in Table 1 and match with those reported by us earlier [45].

Lowering the concentration to 9×10^{-5} M lead to the formation of two additional networks at the 1-phenyloctane–HOPG interface. Although polymorph A remains the dominant network on the surface with the highest surface coverage (≈60%), another network with a significantly different unit cell (Figure 2b,e and Table 1) was observed. This network, referred hereon as polymorph B, lacks the peculiar bright-dark contrast observed in the STM images of polymorph A. Figure 2e,h shows a high-resolution STM image of polymorph B and the corresponding molecular model, respectively. It can be readily noticed that **BA-OC$_{14}$** molecules still form dimers but the molecules are stacked antiparallel to each other. The dimers show a shift in the propagation direction after every four (parallel) dimers which can be noticed from the proposed molecular model (red and green circles, Figure 2h). Due to this shift, the two (parallel) dimers with a different propagation direction are closer to each other. The molecular model also reveals that the space between four benzene rings may host a molecule of solvent adsorbed edge-on (black arrow, Figure 2h) with respect to the surface. The collection of such four benzene rings together with the co-adsorbed molecule of 1-phenyloctane is often imaged as a single bright feature in large-scale STM images (as evident

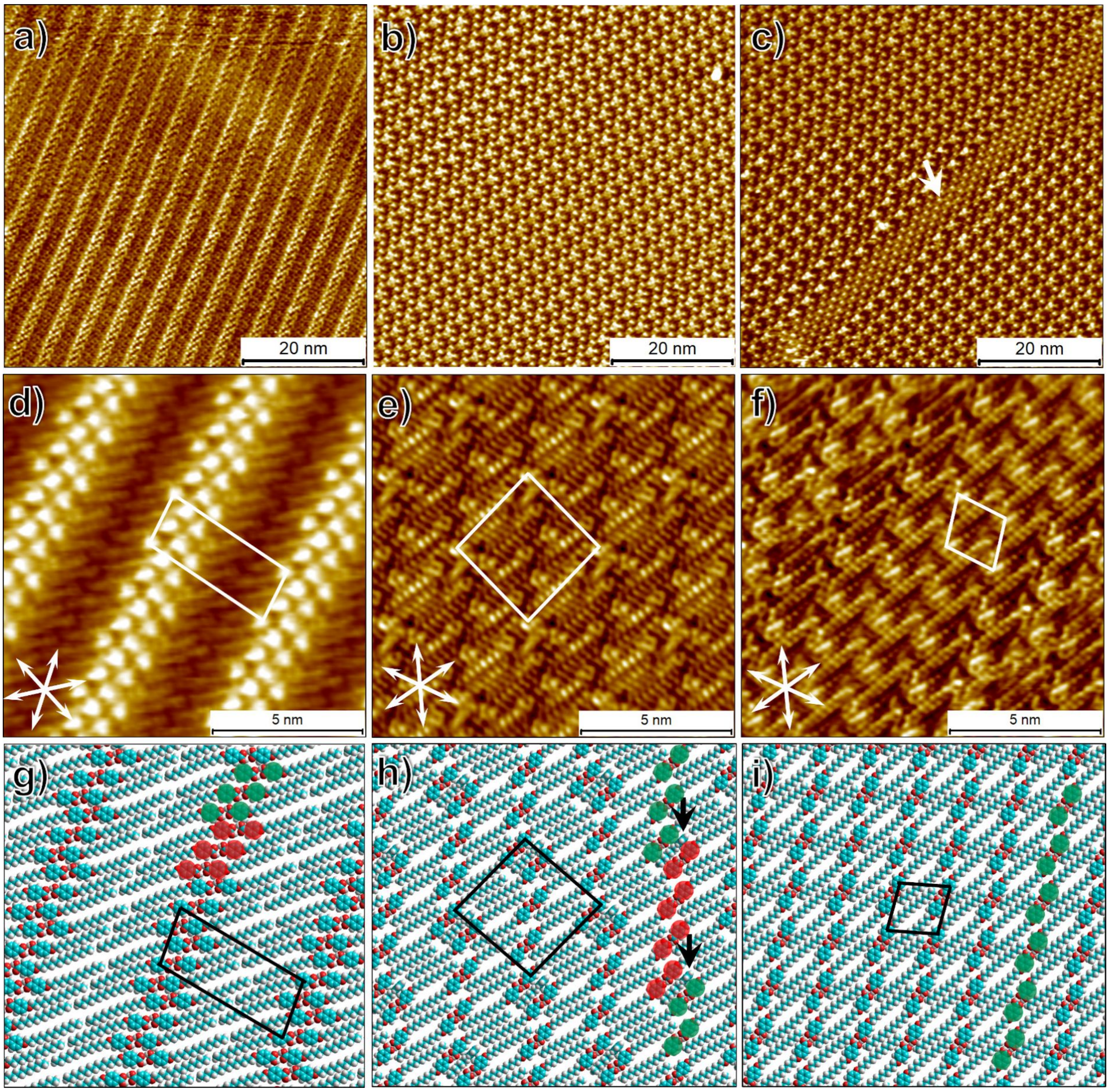

Figure 2: STM images of concentration dependent polymorphs of **BA-OC$_{14}$** formed at the 1-phenyloctane–HOPG interface. (a,b,c) Large scale STM images of polymorph A, B and C, respectively. (d,e,f) High-resolution STM images of polymorph A, B and C, respectively. The white double-headed arrows at the lower left corner of the image represent the three symmetry axes of the graphite lattice. (g,h,i) Molecular models for polymorph A, B and C, respectively. Imaging conditions: (a) I_{set} = 70 pA, V_{bias} = −1.55 V; (b,c) I_{set} = 140 pA, V_{bias} = 0.55 V; (d) I_{set} = 50 pA, V = −1.85 V; (e,f) I_{set} = 140 pA, V_{bias} = 0.55 V. For additional data, see Figures S1 and S2 in Supporting Information File 1.

from Figure 2b). At 9 × 10^{-5} M, the surface coverage of polymorph B was found to be ≈39%.

At 9 × 10^{-5} M, another network, polymorph C, is observed that only slightly differs from polymorph B, and has the lowest surface coverage (≈5%). Polymorph C (white arrow, Figure 2c) tends to appear on the edges of the domains of polymorph B and can be identified by its distinct STM contrast compared to that of polymorph B. Figure 2f,i shows the high-resolution STM image and the proposed molecular model for polymorph C, respectively. It is evident that the network consists of antiparallel dimers similar to those observed in the case of polymorph B, however, the dimers do not show a shift in the propagation direction (green circles, Figure 2i). Polymorph C, despite its low surface coverage was found to be stable to STM scanning and did not transform into other structures within the typical time frame of STM experiments. At concentrations lower than 9 × 10^{-5} M no self-assembly was observed indicating that the concentration limit for **BA-OC$_{14}$** assembly under these conditions is reached.

Table 1: Unit cell parameters for the benzoic acid polymorphs (A, B and C) observed in this study together with those of ***n*-C$_{50}$** buffer layer. *D*$_1$ and *D*$_2$ are the molecular densities of the different polymorphs observed on HOPG and atop ***n*-C$_{50}$** buffer layer, respectively. θ$_1$ and θ$_2$ are the percentage surface coverages of the respective polymorphs at [**BA-OC$_{14}$**] = 9 × 10^{-5} M (on HOPG) and [**BA-OC$_{14}$**] = 3.8 × 10^{-4} M (***n*-C$_{50}$** buffer layer), respectively.

	Unit cell (HOPG)			*D*$_1$ (molecules/ nm^2)	θ$_1$ (%)	Unit cell (***n*-C$_{50}$** buffer layer)			*D*$_2$ (molecules/ nm^2)	θ$_2$ (%)
	a (nm)	b (nm)	α (°)			a (nm)	b (nm)	α (°)		
A	1.8 ± 0.1	4.4 ± 0.1	81.0 ± 2.7°	0.74	60	1.8 ± 0.1	4.6 ± 0.1	77.9 ± 2.4°	0.71	50
B	3.4 ± 0.1	3.4 ± 0.1	86.9 ± 1.3°	0.68	39	3.6 ± 0.2	3.4 ± 0.1	88.2 ± 4.9°	0.65	49
C	1.7 ± 0.1	1.6 ± 0.1	79.6 ± 1.0 °	0.71	1	1.5 ± 0.1	2.0 ± 0.2	83.6 ± 2.7°	0.68	1
***n*-C$_{50}$**	6.6 ± 0.1	0.5 ± 0.1	90.0 ± 2.0°	–	–	–	–	–	–	–

Self-assembly of BA-OC$_{14}$ with *n*-C$_{50}$ buffer layer

Having confirmed the possibility of the formation of three different polymorphs of **BA-OC$_{14}$** at the 1-phenyloctane–HOPG interface, we turned our attention to the buffer layer experiments. In order to minimize the influence of the domain borders of the buffer layers on the nucleation and the growth of the **BA-OC14** domains, we first optimized the deposition conditions in order to obtain large domains of ***n*-C$_{50}$**. Specifically, we targeted domain sizes of ≥250 nm × 250 nm by carrying out systematic concentration-dependent measurements since lower solution concentrations are known to favor large domain sizes. Annealing of the samples was also carried out. We noticed that at lower solution concentrations, the ***n*-C$_{50}$** monolayers exhibit a highly dynamic behavior with significant reorganization of domains upon repeated scanning with the STM tip (Figure S3 in Supporting Information File 1). Figure 3a,b shows a typical high-resolution STM image of the ***n*-C$_{50}$** buffer layer together with the proposed molecular model for the assembly. ***n*-C$_{50}$** monolayers consist of a lamellar structure in which the alkane molecules are fully extended and are oriented at 90° with respect to the lamella axis. This monolayer structure is identical to that reported earlier [26].

After thoroughly understanding and optimization of the self-assembly behavior of **BA-OC$_{14}$** and ***n*-C$_{50}$** at the 1-phenyloctane–HOPG interface, we moved on to the self-assembly experiments with the buffer layer. Although the buffer layer experiments described below were carried out using sequential deposition of solutions of ***n*-C$_{50}$** and **BA-OC$_{14}$** (in that sequence), we stress that the outcome of the experiments remained the same when carried out using premixed solutions of the two components. Typically, a drop of 1 × 10^{-5} M solution of ***n*-C$_{50}$** was first applied onto a freshly cleaved HOPG surface and the surface was imaged using STM to ensure full coverage of the ***n*-C$_{50}$** monolayer. After this, a drop of **BA-OC$_{14}$** solution was applied and the imaging was resumed. Note that while choosing the concentration of **BA-OC$_{14}$**, the dilution effect arising from the mixing ***n*-C$_{50}$** solution already present on the HOPG surface was taken into account (approxi-

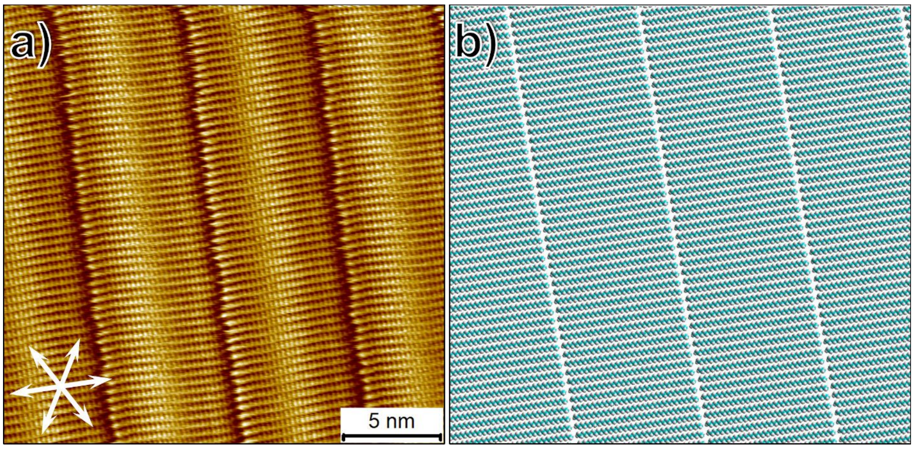

Figure 3: (a) High-resolution STM image of the ***n*-C$_{50}$** monolayer formed at the 1-phenyloctane–HOPG interface. The white double-headed arrows at the lower left corner of the image represent the three symmetry axes of the graphite lattice. (b) Molecular model for the ***n*-C$_{50}$** monolayer. Imaging conditions: I_{set} = 200 pA, V_{bias} = −0.8 V.

mately 50% dilution, since equal volumes of the two solutions were used). Similar precaution was exercised when the premixed solutions were prepared. For **BA-OC$_{14}$** the chosen concentration was the one where its self-assembly behavior on bare HOPG is fully known. Thus, a **BA-OC$_{14}$** concentration of 3.8×10^{-4} M was selected because the net concentration after mixing is $\approx 1.9 \times 10^{-4}$ M where polymorph A was observed at the bare HOPG–1-phenyloctane interface. For ***n*-C$_{50}$**, the chosen optimal concentration was 0.01 mM, because at this concentration we observed reasonably high-average domain size and relatively low dynamics within the ***n*-C$_{50}$** monolayer.

Figure 4a–c shows a representative large scale STM image of the HOPG surface upon addition of a 3.8×10^{-4} M **BA-OC$_{14}$** solution onto the HOPG surface covered with the ***n*-C$_{50}$** monolayer. Surprisingly, the large-scale images reveal networks of **BA-OC$_{14}$** adsorbed atop the ***n*-C$_{50}$** buffer layer that are reminiscent of the ones observed on bare HOPG in the absence of the buffer layer. At this concentration of **BA-OC$_{14}$** ($\approx 1.9 \times 10^{-4}$ M), we could observe all the three polymorphs atop the ***n*-C$_{50}$** buffer layer whereas only polymorph A was formed in the absence of the buffer layer. High-resolution STM images were recorded for scrutinizing the self-assembled networks further and to determine the unit cell parameters of the three polymorphs. Figure 4d–f shows high-resolution STM images which reveal that the three structures formed atop the ***n*-C$_{50}$** buffer layer are exactly the same as those observed when formed directly on top of the HOPG substrate. The unit cell parameters obtained for the structures formed on the buffer layer are comparable to those formed at the 1-phenyloctane–HOPG interface (Table 1).

A notable feature of the high-resolution STM images presented in Figure 4d–f is that the alkyl chains of the **BA-OC$_{14}$** molecules within the monolayers formed on top of the buffer layer still appear to be in registry with the graphite symmetry axes. This begs a question whether the **BA-OC$_{14}$** is indeed formed on the top of the buffer layer? To confirm the bilayer formation

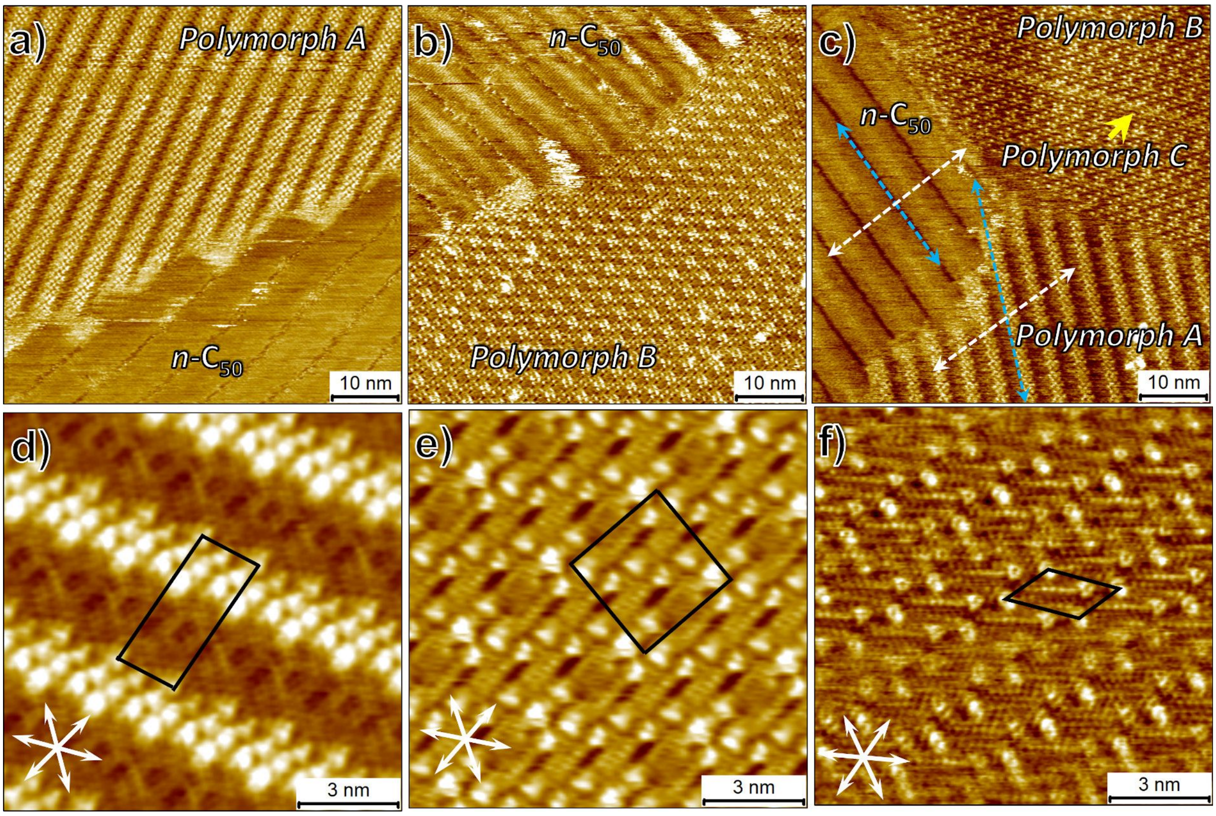

Figure 4: Self-assembled monolayers of **BA-OC$_{14}$** formed on top of the ***n*-C$_{50}$** buffer layer at the 1-phenyloctane–HOPG interface. The experiment was carried out using sequential deposition of the two solutions [**BA-OC$_{14}$**] = 3.8×10^{-4} M, [***n*-C$_{50}$**] = 1.0×10^{-5} M. (a–c) Representative large scale STM images showing the formation of polymorph A and polymorph B atop the ***n*-C$_{50}$** buffer layer. (d–f) Representative high-resolution images showing the structure of the polymorph A and polymorph B atop the ***n*-C$_{50}$** buffer layer. The white double-headed arrows at the lower left corner of the image represent the three symmetry axes of the graphite lattice. Imaging conditions: (a) I_{set} = 120 pA, V_{bias} = −1.2 V; (b) I_{set} = 110 pA, V_{bias} = −1.45 V; (c) I_{set} = 140 pA, V_{bias} = −0.45 V; (d) I_{set} = 20 pA, V_{bias} = −0.17 V; (e) I_{set} = 110 pA, V_{bias} = −1.45 V; (f) I_{set} = 190 pA, V_{bias} = −0.4 V. For additional large-scale images, see Figure S4 in Supporting Information File 1.

and to rule out phase separation of the two components in 2D, we reversed the sequence of solution deposition. Thus, the solution of **BA-OC$_{14}$** was added to the bare HOPG substrate first and the monolayer formed (polymorph A) was imaged for a few hours to ascertain full surface coverage. In the second step, ***n*****-C$_{50}$** solution was added to the surface and the STM imaging was resumed. This experiment revealed that ***n*****-C$_{50}$** completely removed the **BA-OC$_{14}$** monolayer thus confirming that **BA-OC$_{14}$** does not compete with ***n*****-C$_{50}$** for adsorption on the HOPG surface thereby also justifying its choice as the buffer layer. Furthermore, certain STM images clearly showed the ***n*****-C$_{50}$** lamellae running underneath the **BA-OC$_{14}$** monolayer as displayed in Figure 5a–c. The superposition of the STM contrast of the two columns is visible in the STM image which would not be possible if the two monolayers were adsorbed side-by-side on the HOPG surface (see also Figure S5 in Supporting Information File 1). Last but not the least, the controlled nucleation experiments described below, also confirm the formation of the **BA-OC$_{14}$** islands on top of the buffer layer. The registry of the alkyl chains of **BA-OC$_{14}$** with the graphite lattice can be understood by considering the orientation of the **BA-OC$_{14}$** islands with respect to the ***n*****-C$_{50}$** lamellae. As depicted in the large scale STM image provided in Figure 4c, the lamellae of polymorph A are often oriented at approximately 30° with respect to the ***n*****-C$_{50}$** lamellae (blue dashed arrows). Given that the alkyl chains of **BA-OC$_{14}$** are oriented at an angle of 60° with respect to its lamella axis, it can be easily deduced that they are aligned along the ***n*****-C$_{50}$** molecular axis as highlighted by the white dashed arrows which indicate the long molecular axes of the ***n*****-C$_{50}$** and the **BA-OC$_{14}$** molecules (also see Figure S6 in Supporting Information File 1). However, we also discovered that in a few cases the two molecules are not always aligned as is the case in Figure 5a–c.

For ***n*****-C$_{50}$**, the chosen optimal concentration was 1.0×10^{-4} M, because at this concentration we observed reasonably high average domain size and relatively low dynamics within the ***n*****-C$_{50}$** monolayer. Lowering the concentration of **BA-OC$_{14}$** further (range $\approx 1.9 \times 10^{-4}$ M to 9×10^{-5} M) while keeping the same concentration of ***n*****-C$_{50}$** led to exclusive formation of polymorph A. Large domains of the polymorph A were observed with very little real-time spontaneous nucleation of domains.

Considering the original goal, our pursuit for new 2D polymorphs of **BA-OC$_{14}$** atop the ***n*****-C$_{50}$** buffer layer did not yield positive results. This also casts a doubt on the extent of the influence of the substrate lattice on the assembly of alkoxybenzoic acids as originally proposed by us [45]. While the observation of similar polymorphs on top of the buffer layer does not necessarily rule out the role of substrate lattice on the assembly, it is certainly not the sole explanation for the peculiar network structure of polymorph A. At this juncture, we believe that the

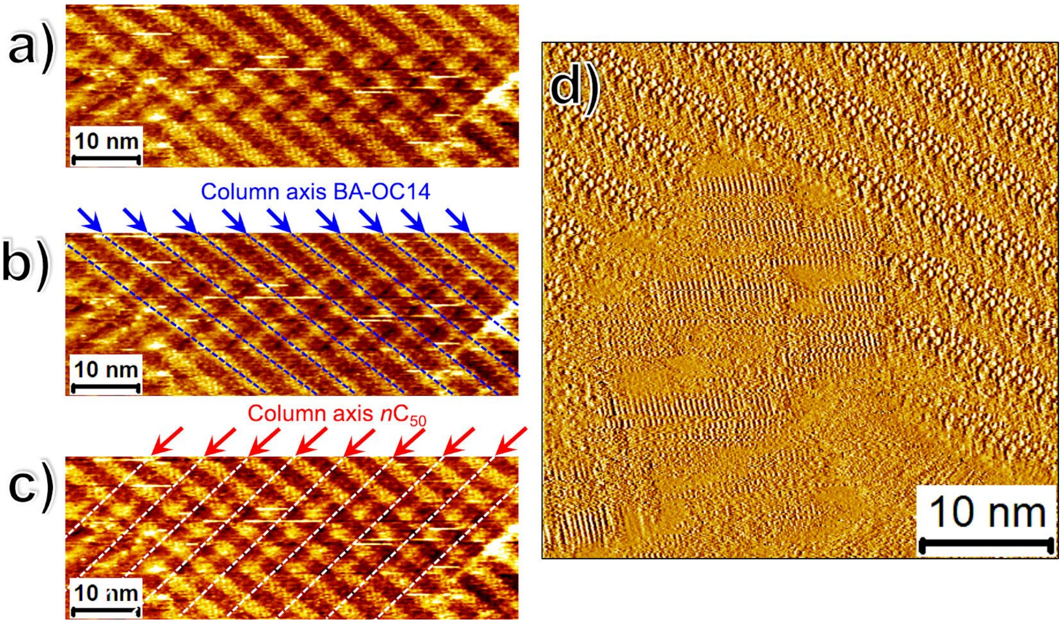

Figure 5: (a) STM image showing the superposition of the ***n*****-C$_{50}$** lamellae with those of **BA-OC$_{14}$** confirming the bilayer structure of the system. Panels (b) and (c) show the same STM image with colored markers to aid the eye to identify the superimposed STM contrast arising from the columns of benzoic acid (blue dotted lines) and those of pentacontane (white dotted lines) running underneath. For the corresponding large-scale image see Figure S5 in Supporting Information File 1. Imaging conditions: I_{set} = 130 pA, V_{bias} = −0.65 V. (b) STM current image showing the alignment of the chains of the tetradecyloxy chains of **BA-OC$_{14}$** with the long axes of ***n*****-C$_{50}$** molecules. Imaging conditions: I_{set} = 90 pA, V_{bias} = −0.17 V.

formation of the characteristic kinked lamellae in the case of 4-alkoxybenzoic acids is a result of a tendency to achieve close-packed assemblies together with the contribution of various other factors, the influence of the substrate lattice being possibly one of them. We have recently reported on similar behavior in the case of brominated alkoxybenzenes where a brick-wall type structure was ascribed to a tendency to form close packed networks since the formation of kinks/fractures within the monolayer allowed higher packing densities in the monolayers [47].

While studying the self-assembly of **BA-OC$_{14}$** on the buffer layers, we discovered a number of interesting aspects of this peculiar interface. As anticipated, the mobility of **BA-OC$_{14}$** on the buffer layers was significantly higher than that at the 1-phenyloctane–HOPG interface. It was possible to observe the nucleation, the growth as well as the desorption of molecular domains (see Figure S7 in the Supporting Information File 1) which was otherwise not possible for monolayers adsorbed directly on the graphite surface. In the following section we describe our attempts to observe such dynamic phenomena and to induce nucleation of **BA-OC$_{14}$** domains using the STM tip.

STM tip-induced nucleation on-command atop ***n*-C$_{50}$** buffer layer

During the course of this investigation, we uncovered that it is possible to enforce the nucleation of small **BA-OC$_{14}$** islands on the buffer layers using the STM tip. Such “on-command” nucleation was achieved using two different stimuli, namely by applying short voltage pulses to the STM tip and by scanning the surface of the buffer layer at higher than normal tunneling currents (Figure 6a). Application of voltage pulses to the STM tip while imaging the ***n*-C$_{50}$** buffer layer (containing **BA-OC$_{14}$** in the supernatant) lead to nucleation of small islands of polymorph A of **BA-OC$_{14}$**. The domain size was typically around 20 × 20 nm. These domains were found to either grow or shrink upon subsequent STM imaging of the same area. Figure 6b–e shows one such pulse-induced on-command nucleation event. A voltage pulse with a magnitude of −4.2 V lasting 1 ms was applied onto an ‘empty’ region of the ***n*-C$_{50}$** buffer layer (marked by an arrow in Figure 6c) which did not have any adsorbed domain of **BA-OC$_{14}$**. A **BA-OC$_{14}$** domain can be seen to appear right after the voltage pulse was applied (white arrow, Figure 6c) and was found to grow in the subsequent scans (white arrows, Figure 6d,e). Such pulse-induced nucleation was possible to carry out by selecting any area of the buffer layer which did not have a **BA-OC$_{14}$** domain. We also systematically examined the influence of the magnitude and the duration of the voltage pulse on the nucleation events. This exercise revealed that a pulse width of 1 ms and a minimum required pulse height of −3.3 V was necessary for inducing the nucleation of **BA-OC$_{14}$** domains. The outcome of the pulse-induced nucleation experiment remained the same irrespective of the sign of the pulse.

Scanning small areas of the ***n*-C$_{50}$** buffer layer (with **BA-OC$_{14}$** supernatant) at higher tunneling currents and lower bias (typically −0.05 V and 0.5 nA) provided better control over the on-command nucleation process. These parameters are used for obtaining the resolution at which the graphite lattice is visible. Figure 6f shows an STM image of the buffer layer. The area highlighted by the square (30 nm × 30 nm) was scanned using the aforementioned parameters. In the subsequent scan, the parameters were changed to normal imaging parameters and the size of the scan was restored to the original (zoomed out). The subsequent scan presented in Figure 6g reveals the presence of a small domain of **BA-OC$_{14}$** in the area scanned at the different tunneling parameters. It can also be noticed that the lamellae of the new domain follow the same registry conditions (≈30° with respect to the column axis of ***n*-C$_{50}$**) as described earlier. This means that the tetradecyloxy chains of **BA-OC$_{14}$** are aligned with the alkane molecules underneath. We note that the ‘nucleation on command’ experiments always furnished polymorph A.

Quite naturally, one could suspect that the observed nucleation occurs on top of the graphite surface, because under the scanning parameters used, the STM tip is pushed very close to the substrate allowing possible removal of the buffer layer. If this was the case, one would observe gradual removal of the nucleated domain of **BA-OC$_{14}$** by ***n*-C$_{50}$** molecules. This was not observed. In fact, in some cases, after inducing the nucleation in this fashion, the newly formed **BA-OC$_{14}$** domain was found to grow rapidly (Figure S8 in Supporting Information File 1). If this would happen in a hypothetical scenario where the **BA-OC$_{14}$** domain nucleated directly on HOPG, it would require the displacement of ***n*-C$_{50}$** molecules by **BA-OC$_{14}$** molecules which was never observed during the independent control experiments. Similar to the pulse-induced process, the scanning-induced nucleation could also be stimulated a number of times although in some instances (minority cases) no nucleation of **BA-OC$_{14}$** domain was observed.

So, what is the mechanism behind the on-command nucleation of **BA-OC$_{14}$** on the buffer layers? We propose that the stimuli provided, namely scanning at higher currents and the voltage pulsing, removes the residual layer of ***n*-C$_{50}$** molecules interacting with the monolayer of ***n*-C$_{50}$** adsorbed on the surface. Given that the concentration of ***n*-C$_{50}$** in solution is well above than that required to form a monolayer, it is not unreasonable to consider that there exist excess molecules of ***n*-C$_{50}$** that interact

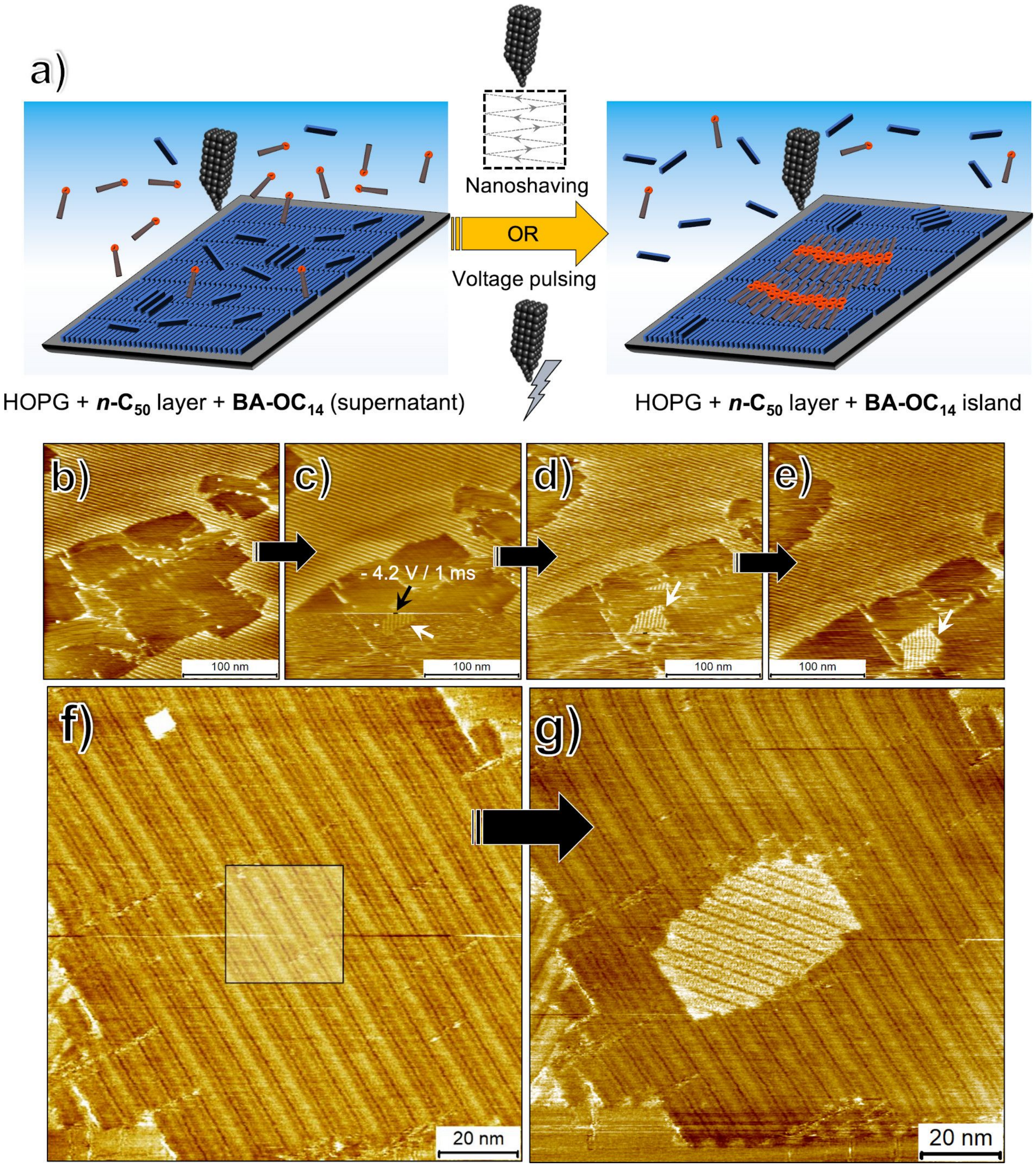

Figure 6: On-command nucleation of **BA-OC$_{14}$** islands on top of the ***n*-C$_{50}$** buffer layer. (a) Schematic for the STM-induced nucleation process. (b–e) Sequential STM images where the nucleation of **BA-OC$_{14}$** islands was achieved using application of voltage pulses to the STM tip. The black arrow in (c) shows the point at which a −4.2 V (1 ms) pulse was applied to the STM tip. The white arrow shows the island of **BA-OC$_{14}$** that nucleated immediately after the pulse. As evident in panels (d,e) this island grew in subsequent scans. (f,g) Sequential STM images showing nucleation on-command by bringing the STM tip closer to the surface and scanning at high tunneling current. The square highlighted in (f) was scanned at −0.05 V and 0.5 nA. After this, the original image size was restored by zooming out. As evident from (g) a new island of **BA-OC$_{14}$** is nucleated approximately in the area which was manipulated in the previous scan. Imaging conditions: (b–e) I_{set} = 130 pA, V_{bias} = −1.3 V; (f,g) I_{set} = 140 pA, V_{bias} = −0.7 V.

with the preformed buffer layer. ‘Blasting’ the surface of the buffer layer with a voltage pulse or ‘sweeping’ it by bringing the tip closer to the surface removes these excess ***n*-C$_{50}$** molecules thereby allowing the nucleation of **BA-OC$_{14}$** islands which then subsequently grow. The observed relative concentration dependency of nucleation and growth also suggests that a higher ***n*-$\mathbf{C_{50}}$** concentration 'blocks' the nucleation of **BA-$\mathbf{OC_{14}}$** on top of the buffer layer.

Conclusion

New structures, whether in bulk or on surfaces, are found as long as one keeps looking for them by continuously adjusting experimental conditions that affect (2D) crystallization. Keeping this generally accepted perception in mind, we had set out to alter an important factor that is known to influence self-assembly on solid surfaces, namely the influence of the substrate lattice. We used a monolayer of ***n*-$\mathbf{C_{50}}$** as a 'new' substrate for the self-assembly of **BA-$\mathbf{OC_{14}}$** at the solution–solid interface and anticipated that, given the different lattice constant of the ***n*-$\mathbf{C_{50}}$** layer compared to graphite, we would create possibilities for the formation of new polymorph(s). The self-assembly experiments using the buffer layer however revealed that **BA-$\mathbf{OC_{14}}$** forms the same structural polymorphs in the presence and in the absence of the buffer layer. This indicates that the peculiar network formation, at least in the case of polymorph A, cannot be solely explained by the influence of the substrate lattice. We hypothesize that in the case of alkoxybenzoic acids, a tendency to form close-packed networks supersedes other factors.

The buffer layer however provided a unique platform for self-assembly experiments where the nucleation, growth and ripening of the self-assembled monolayer could be monitored in a more controlled fashion compared to that on the surface of HOPG. The on-command nucleation demonstrated here is an exciting approach to study nucleation of typical systems with precise control on the size and shape of the domains that can be formed using the STM tip. This approach holds a promise as a new platform for investigating elementary stages of self-assembly processes. Despite the lack of discovery of new polymorphs in the present case, the buffer layer strategy could prove fruitful towards identification of new structures in future.

Experimental

***n*-$\mathbf{C_{50}}$** was obtained from Sigma-Aldrich (purity ≥97%) and used without further purification. **BA-$\mathbf{OC_{14}}$** was synthesized using a protocol previously reported by us [45]. Stock solutions of ***n*-$\mathbf{C_{50}}$** (1.0×10^{-3} M) and **BA-$\mathbf{OC_{14}}$** (7.7×10^{-4} M) were prepared by dissolving appropriate amounts of solid materials in 1-phenyloctane (Sigma-Aldrich, >99%). The stock solutions were diluted further with 1-phenyoctane to make concentration series. All STM experiments were performed at room temperature (21–23 °C) using a PicoLE or a PicoSPM (Agilent) machine operating in constant-current mode with the tip immersed in the supernatant liquid. STM tips were prepared by mechanically cutting a Pt/Ir wire (80%/20%, diameter 0.2 mm). Prior to imaging, a drop of solution was placed onto a freshly cleaved surface of highly oriented pyrolytic graphite (HOPG, grade ZYB, Advanced Ceramics Inc., Cleveland, USA). For experiments involving the ***n*-$\mathbf{C_{50}}$** buffer layer, both sequential deposition and premixing protocols were used. For sequential deposition, a solution of ***n*-$\mathbf{C_{50}}$** was first applied to a freshly cleaved graphite surface. The STM imaging was carried out to ensure full surface coverage of the buffer layer. After this, a drop of **BA-$\mathbf{OC_{14}}$** solution was applied and the imaging was resumed. The STM experiments were repeated in 2–3 sessions using different tips to check for reproducibility and to avoid experimental artefacts, if any. For voltage pulsing experiments described here, the pulses were applied during the line scan. Each voltage pulse was applied to the substrate after retracting the STM tip at a certain distance (around 1 nm) from the surface. The feedback loop was turned off to maintain the separation between the tip and the sample during the period of voltage pulse in order to avoid the tip crash onto the surface. The software used for STM imaging does not log the tunneling current reached during each pulse. For analysis purposes, recording of a monolayer image was followed by imaging the graphite substrate underneath it under the same experimental conditions, except for increasing the current and lowering the bias. The images were corrected for drift via Scanning Probe Image Processor (SPIP) software (Image Metrology ApS), using the recorded graphite images for calibration purposes, allowing a more accurate unit cell determination. The unit cell parameters were determined by examining at least 4 images and only the average values are reported. The images are Gaussian filtered and/or correlation averaged. The imaging parameters are indicated in the figure caption: tunneling current (I_{set}), and sample bias (V_{bias}). The molecular models were built using HyperchemTM 8.0.1 program.

Supporting Information

Supporting Information File 1

Additional STM data.
[https://www.beilstein-journals.org/bjnano/content/supplementary/2190-4286-11-113-S1.pdf]

Acknowledgements

We thank Prof. Koen Binnemans (Department of Chemistry, KU Leuven) for kindly providing the sample of 4-alkoxybenzoic acid used in this study and Dr. Lander Verstraete for providing the high-resolution STM image of the ***n*-$\mathbf{C_{50}}$** monolayer.

Funding

This work is financially supported by the Fund of Scientific Research − Flanders (FWO), in part by FWO under EOS

30489208, and KU Leuven Research Fund (C14/15/053 and C14/19/079).

ORCID® iDs

Kunal S. Mali - https://orcid.org/0000-0002-9938-6446
Steven De Feyter - https://orcid.org/0000-0002-0909-9292

References

1. Desiraju, G. R. *J. Am. Chem. Soc.* **2013,** *135,* 9952–9967. doi:10.1021/ja403264c
2. Goronzy, D. P.; Ebrahimi, M.; Rosei, F.; Arramel; Fang, Y.; De Feyter, S.; Tait, S. L.; Wang, C.; Beton, P. H.; Wee, A. T. S.; Weiss, P. S.; Perepichka, D. F. *ACS Nano* **2018,** *12,* 7445–7481. doi:10.1021/acsnano.8b03513
3. Lackinger, M.; Heckl, W. M. *Langmuir* **2009,** *25,* 11307–11321. doi:10.1021/la900785f
4. Tahara, K.; Lei, S.; Adisoejoso, J.; De Feyter, S.; Tobe, Y. *Chem. Commun.* **2010,** *46,* 8507–8525. doi:10.1039/c0cc02780d
5. Mali, K. S.; Pearce, N.; De Feyter, S.; Champness, N. R. *Chem. Soc. Rev.* **2017,** *46,* 2520–2542. doi:10.1039/c7cs00113d
6. Gutzler, R.; Sirtl, T.; Dienstmaier, J. F.; Mahata, K.; Heckl, W. M.; Schmittel, M.; Lackinger, M. *J. Am. Chem. Soc.* **2010,** *132,* 5084–5090. doi:10.1021/ja908919r
7. Blunt, M. O.; Adisoejoso, J.; Tahara, K.; Katayama, K.; Van der Auweraer, M.; Tobe, Y.; De Feyter, S. *J. Am. Chem. Soc.* **2013,** *135,* 12068–12075. doi:10.1021/ja405585s
8. Marie, C.; Silly, F.; Tortech, L.; Müllen, K.; Fichou, D. *ACS Nano* **2010,** *4,* 1288–1292. doi:10.1021/nn901717k
9. Bellec, A.; Arrigoni, C.; Schull, G.; Douillard, L.; Fiorini-Debuisschert, C.; Mathevet, F.; Kreher, D.; Attias, A.-J.; Charra, F. *J. Chem. Phys.* **2011,** *134,* 124702. doi:10.1063/1.3569132
10. Kampschulte, L.; Lackinger, M.; Maier, A.-K.; Kishore, R. S. K.; Griessl, S.; Schmittel, M.; Heckl, W. M. *J. Phys. Chem. B* **2006,** *110,* 10829–10836. doi:10.1021/jp057553m
11. Takami, T.; Mazur, U.; Hipps, K. W. *J. Phys. Chem. C* **2009,** *113,* 17479–17483. doi:10.1021/jp905223b
12. Zhang, X.; Chen, T.; Chen, Q.; Deng, G.-J.; Fan, Q.-H.; Wan, L.-J. *Chem. – Eur. J.* **2009,** *15,* 9669–9673. doi:10.1002/chem.200901618
13. Lackinger, M.; Griessl, S.; Heckl, W. M.; Hietschold, M.; Flynn, G. W. *Langmuir* **2005,** *21,* 4984–4988. doi:10.1021/la0467640
14. Ochs, O.; Hocke, M.; Spitzer, S.; Heckl, W. M.; Martsinovich, N.; Lackinger, M. *Chem. Mater.* **2020,** *32,* 5057–5065. doi:10.1021/acs.chemmater.0c00827
15. Wang, S.; Zhao, F.; Luo, S.; Geng, Y.; Zeng, Q.; Wang, C. *Phys. Chem. Chem. Phys.* **2015,** *17,* 12350–12355. doi:10.1039/c5cp00531k
16. Balandina, T.; Tahara, K.; Sändig, N.; Blunt, M. O.; Adisoejoso, J.; Lei, S.; Zerbetto, F.; Tobe, Y.; De Feyter, S. *ACS Nano* **2012,** *6,* 8381–8389. doi:10.1021/nn303144r
17. Katsonis, N.; Marchenko, A.; Fichou, D. *J. Am. Chem. Soc.* **2003,** *125,* 13682–13683. doi:10.1021/ja0375737
18. Kudernac, T.; Sändig, N.; Fernandez Landaluce, T.; van Wees, B. J.; Rudolf, P.; Katsonis, N.; Zerbetto, F.; Feringa, B. L. *J. Am. Chem. Soc.* **2009,** *131,* 15655–15659. doi:10.1021/ja901718q
19. Ahn, S.; Matzger, A. J. *J. Am. Chem. Soc.* **2010,** *132,* 11364–11371. doi:10.1021/ja105039s
20. Lei, S.; Tahara, K.; De Schryver, F. C.; Van der Auweraer, M.; Tobe, Y.; De Feyter, S. *Angew. Chem., Int. Ed.* **2008,** *47,* 2964–2968. doi:10.1002/anie.200705322
21. Adisoejoso, J.; Tahara, K.; Lei, S.; Szabelski, P.; Rżysko, W.; Inukai, K.; Blunt, M. O.; Tobe, Y.; De Feyter, S. *ACS Nano* **2012,** *6,* 897–903. doi:10.1021/nn204398m
22. Shen, X.; Wei, X.; Tan, P.; Yu, Y.; Yang, B.; Gong, Z.; Zhang, H.; Lin, H.; Li, Y.; Li, Q.; Xie, Y.; Chi, L. *Small* **2015,** *11,* 2284–2290. doi:10.1002/smll.201402645
23. Cometto, F. P.; Kern, K.; Lingenfelder, M. *ACS Nano* **2015,** *9,* 5544–5550. doi:10.1021/acsnano.5b01658
24. Miao, X.; Xu, L.; Cui, L.; Deng, W. *Phys. Chem. Chem. Phys.* **2014,** *16,* 12544–12553. doi:10.1039/c4cp00871e
25. Xu, B.; Yin, S.; Wang, C.; Qiu, X.; Zeng, Q.; Bai, C. *J. Phys. Chem. B* **2000,** *104,* 10502–10505. doi:10.1021/jp001618y
26. Piot, L.; Marchenko, A.; Wu, J.; Müllen, K.; Fichou, D. *J. Am. Chem. Soc.* **2005,** *127,* 16245–16250. doi:10.1021/ja0548844
27. Rohr, C.; Balbás Gambra, M.; Gruber, K.; Höhl, C.; Malarek, M. S.; Scherer, L. J.; Constable, E. C.; Franosch, T.; Hermann, B. A. *Chem. Commun.* **2011,** *47,* 1800–1802. doi:10.1039/c0cc03603j
28. Li, Y.; Liu, L.; Subramani, R.; Pan, Y.; Liu, B.; Yang, Y.; Wang, C.; Mamdouh, W.; Besenbacher, F.; Dong, M. *Chem. Commun.* **2011,** *47,* 9155–9157. doi:10.1039/c1cc11443c
29. Lei, S. B.; Wang, C.; Yin, S. X.; Wang, H. N.; Xi, F.; Liu, H. W.; Xu, B.; Wan, L. J.; Bai, C. L. *J. Phys. Chem. B* **2001,** *105,* 10838–10841. doi:10.1021/jp0105701
30. Lei, S. B.; Wang, C.; Yin, S. X.; Xu, Q. M.; Bai, C. L. *Surf. Interface Anal.* **2001,** *32,* 253–255. doi:10.1002/sia.1048
31. Lei, S.; Wang, C.; Wan, L.; Bai, C. *J. Phys. Chem. B* **2004,** *108,* 1173–1175. doi:10.1021/jp037457q
32. Yang, X.; Krieger, I.; Lüftner, D.; Weiß, S.; Heepenstrick, T.; Hollerer, M.; Hurdax, P.; Koller, G.; Sokolowski, M.; Puschnig, P.; Ramsey, M. G.; Tautz, F. S.; Soubatch, S. *Chem. Commun.* **2018,** *54,* 9039–9042. doi:10.1039/c8cc03334j
33. Forker, R.; Kasemann, D.; Dienel, T.; Wagner, C.; Franke, R.; Müllen, K.; Fritz, T. *Adv. Mater. (Weinheim, Ger.)* **2008,** *20,* 4450–4454. doi:10.1002/adma.200801112
34. Rastgoo-Lahrood, A.; Björk, J.; Lischka, M.; Eichhorn, J.; Kloft, S.; Fritton, M.; Strunskus, T.; Samanta, D.; Schmittel, M.; Heckl, W. M.; Lackinger, M. *Angew. Chem., Int. Ed.* **2016,** *55,* 7650–7654. doi:10.1002/anie.201600684
35. Rastgoo-Lahrood, A.; Lischka, M.; Eichhorn, J.; Samanta, D.; Schmittel, M.; Heckl, W. M.; Lackinger, M. *Nanoscale* **2017,** *9,* 4995–5001. doi:10.1039/c7nr00705a
36. Sakaguchi, H.; Matsumura, H.; Gong, H.; Abouelwafa, A. M. *Science* **2005,** *310,* 1002–1006. doi:10.1126/science.1117990
37. Sakaguchi, H.; Matsumura, H.; Gong, H. *Nat. Mater.* **2004,** *3,* 551–557. doi:10.1038/nmat1176
38. Nirmalraj, P.; Thompson, D.; Molina-Ontoria, A.; Sousa, M.; Martín, N.; Gotsmann, B.; Riel, H. *Nat. Mater.* **2014,** *13,* 947–953. doi:10.1038/nmat4060
39. Neff, J. L.; Götzen, J.; Li, E.; Marz, M.; Hoffmann-Vogel, R. *Beilstein J. Nanotechnol.* **2012,** *3,* 186–191. doi:10.3762/bjnano.3.20
40. Repp, J.; Meyer, G.; Paavilainen, S.; Olsson, F. E.; Persson, M. *Science* **2006,** *312,* 1196–1199. doi:10.1126/science.1126073
41. Hirjibehedin, C. F.; Lutz, C. P.; Heinrich, A. J. *Science* **2006,** *312,* 1021–1024. doi:10.1126/science.1125398

42. Rau, I. G.; Baumann, S.; Rusponi, S.; Donati, F.; Stepanow, S.; Gragnaniello, L.; Dreiser, J.; Piamonteze, C.; Nolting, F.; Gangopadhyay, S.; Albertini, O. R.; Macfarlane, R. M.; Lutz, C. P.; Jones, B. A.; Gambardella, P.; Heinrich, A. J.; Brune, H. *Science* **2014,** *344,* 988–992. doi:10.1126/science.1252841
43. Groszek, A. J. *Proc. R. Soc. London, Ser. A* **1970,** *314,* 473–498. doi:10.1098/rspa.1970.0019
44. Ilan, B.; Florio, G. M.; Hybertsen, M. S.; Berne, B. J.; Flynn, G. W. *Nano Lett.* **2008,** *8,* 3160–3165. doi:10.1021/nl8014186
45. Mali, K. S.; Lava, K.; Binnemans, K.; De Feyter, S. *Chem. – Eur. J.* **2010,** *16,* 14447–14458. doi:10.1002/chem.201001653
46. McCrone, W. C. Polymorphism. In *Physics and Chemistry of the Organic Solid State;* Fox, D.; Labels, M. M.; Weissberger, M., Eds.; Wiley Interscience: New York, NY, USA, 1965; Vol. 11, pp 725–767.
47. Mukherjee, A.; Sanz-Matias, A.; Velpula, G.; Waghray, D.; Ivasenko, O.; Bilbao, N.; Harvey, J. N.; Mali, K. S.; De Feyter, S. *Chem. Sci.* **2019,** *10,* 3881–3891. doi:10.1039/c8sc04499f

License and Terms

The definitive version of this article is the electronic one which can be found at:
https://doi.org/10.3762/bjnano.11.113

BEILSTEIN JOURNAL OF NANOTECHNOLOGY

Impact of fluorination on interface energetics and growth of pentacene on Ag(111)

Qi Wang[1], Meng-Ting Chen[2], Antoni Franco-Cañellas[1], Bin Shen[3], Thomas Geiger[3], Holger F. Bettinger[3], Frank Schreiber[1], Ingo Salzmann[4], Alexander Gerlach[*1] and Steffen Duhm[*2]

Full Research Paper

Open Access

Address:
[1]Institut für Angewandte Physik, Universität Tübingen, Auf der Morgenstelle 10, 72076 Tübingen, Germany, [2]Institute of Functional Nano & Soft Materials (FUNSOM), Jiangsu Key Laboratory for Carbon-Based Functional Materials & Devices and Joint International Research Laboratory of Carbon-Based Functional Materials and Devices, Soochow University, Suzhou 215123, People's Republic of China, [3]Institut für Organische Chemie, Universität Tübingen, Auf der Morgenstelle 18, 72076 Tübingen, Germany and [4]Department of Physics, Department of Chemistry & Biochemistry, Concordia University, 7141 Sherbrooke St. West, Montreal, Quebec H4B 1R6, Canada

Email:
Alexander Gerlach* - alexander.gerlach@uni-tuebingen.de;
Steffen Duhm* - duhm@suda.edu.cn

* Corresponding author

Keywords:
decoupling; fluorination; metal–organic interfaces; organic pi-conjugated molecules; X-ray standing wave technique

Beilstein J. Nanotechnol. **2020,** *11,* 1361–1370.
https://doi.org/10.3762/bjnano.11.120

Received: 10 April 2020
Accepted: 19 August 2020
Published: 08 September 2020

This article is part of the thematic issue "Molecular assemblies on surfaces – towards physical and electronic decoupling of organic molecules".

Guest Editor: M. Stöhr

Abstract

We studied the structural and electronic properties of 2,3,9,10-tetrafluoropentacene (F4PEN) on Ag(111) via X-ray standing waves (XSW), low-energy electron diffraction (LEED) as well as ultraviolet and X-ray photoelectron spectroscopy (UPS and XPS). XSW revealed that the adsorption distances of F4PEN in (sub)monolayers on Ag(111) were 3.00 Å for carbon atoms and 3.05 Å for fluorine atoms. The F4PEN monolayer was essentially lying on Ag(111), and multilayers adopted π-stacking. Our study shed light not only on the F4PEN–Ag(111) interface but also on the fundamental adsorption behavior of fluorinated pentacene derivatives on metals in the context of interface energetics and growth mode.

Introduction

The performance of organic (opto)electronic devices is strongly affected by the energy level alignment at the various interfaces in such devices [1-3]. Fluorination is a viable way to change the ionization energies (IEs) of organic semiconductor thin films [4-6], which are an important parameter for energy level alignment [7,8]. Moreover, at organic–metal interfaces, fluorination is believed to decrease the coupling strength between the substrate and the adsorbate [9-11]. However, at such interfaces, vertical adsorption heights [12,13], interface dipoles (vacuum level shifts) [9,14] and consequently the energy level alignment [15-17] are affected by fluorination. Furthermore, fluorination can change the molecular multilayer growth [18-21], which in turn affects the IEs. Overall, predicting the impact of fluorination on the energetics at organic–metal interfaces still remains a challenge.

In this context, pentacene (PEN) and perfluorinated pentacene (PFP) are frequently-studied model compounds [9,18,22-35]. PEN and PFP have almost identical optical gaps in thin films (1.85 eV and 1.75 eV, respectively) [36,37], and the experimental gas phase IEs (measured by UPS) are 6.59 eV [38] and 7.50 eV [39], respectively. This trend of the IEs is also found for thin films comprised of PEN or PFP with a flat-lying (long and short molecular axes parallel to the substrate) orientation, which have IEs (in monolayers on graphite) of 5.65 eV and 6.20 eV, respectively [25,26]. The decrease in the IE is due to solid state polarization, which is a general phenomenon for molecular thin films [40-44]. However, in thin films comprised of molecules in a standing orientation on SiO_2 (long molecular axis perpendicular to the substrate), the IE of PEN decreases to 4.90 eV and the IE of PFP increases to 6.65 eV [45]. The opposite trend of the orientation dependency of the IEs has its origin in the strongly polar C–F bonds of PFP [5,27], which reverse the intramolecular quadrupole moment of PEN and PFP [46]. The collective influence of these quadrupoles in turn affects the potential energy, and thus the IEs of the thin films, an effect that is likewise termed electrostatic contribution polarization [11,44].

Perfluorination does not impact the orientation of PEN and PFP in the contact layer with clean metals, where both compounds are lying flat [9,30,31,47-52]. On Au(111), the coupling strength of both monolayers with the substrate is rather similar and physisorptive [29,53]. On Cu(111), PFP shows a behavior close to physisorption [9], although the coupling strength might be slightly stronger than with Au(111) [54]. PEN on Cu(111), however, is strongly chemisorbed, involving a partial filling of the former lowest unoccupied molecular orbital (LUMO) by a charge transfer from the substrate [9,28]. This can be explained by the repulsive interaction of the fluorine atoms with the substrate, which leads to much larger vertical adsorption heights of PFP compared to PEN in monolayers on Cu(111) [9]. Ag(111) represents an intermediate case [55] with weak chemisorption of PEN [28,51] and physisorption of PFP [50]. Multilayers of PEN adopt a herringbone arrangement on virtually all substrates [47,56-59], whereas PFP multilayers exhibit π-stacking [18,56]. The different multilayer packing motifs of PEN and PFP can again be explained by electrostatic intramolecular interactions [18].

Overall, the influence of perfluorination on the multilayer growth and on the interfacial coupling of pentacene on clean metal surfaces is understood to a large extent. However, the impact of partial fluorination is less well studied, and thus we explored thin films of partially fluorinated PEN, namely 2,3,9,10-tetrafluoropentacene (F4PEN) [46,60,61]. F4PEN physisorbs on Au(111) [62] and chemisorbs on Cu(111), involving interfacial charge transfer and strong molecular distortions [63]. Here, we investigated the coupling with Ag(111) as we expected this to be an interesting intermediate case. We determined the vertical adsorption heights of F4PEN (sub)monolayers on Ag(111) employing the XSW technique [64-67]. The lateral order in the monolayer was determined by LEED. Possible chemical interactions between F4PEN and the substrate were studied by XPS. The energy level alignment was investigated by UPS. Furthermore, we compared the adsorption behavior of F4PEN on Ag(111) with that of PEN and PFP on the same substrate to understand the influence of fluorine substitution on the interfacial electronic structure of prototypical pentacene derivatives at organic–metal interfaces.

Results

The determination of the vertical adsorption heights of F4PEN in (sub)monolayers on Ag(111) relied on high-resolution core level spectra, which are shown in Figure 1 (additional XPS spectra are shown in Supporting Information File 1, Figure S1). Following the assignment of the F4PEN core levels on Cu(111) [63], the C 1s peak centered at 287.29 eV binding energy (BE) was assigned to the carbon atoms bound to the fluorine atoms (C–F), and the main peak centered at 284.88 eV BE was assigned to the carbon atoms in the backbone of F4PEN (C–C). In addition, at the low-BE edge a small tail attributed to the carbon atoms bound to the substrate (C–Ag) belonged to the broken C–F bonds due to the dehalogenation reaction [63,68]. The symmetric F 1s peak was centered at 687.47 eV BE. Figure 1 shows the photoelectron yield (Y_p), i.e., the photoemission intensity of the core-levels as a function of the photon energy, which allowed to determine the coherent position (P_H) and the coherent fraction (f_H) of the adsorbate atoms [66,69]. The former gave the adsorption distance in terms of the lattice spacing of the silver substrate: $d_H = d_0(n + P_H)$ (typical precision < 0.05 Å), with n being an integer. The coherent fraction $0 \le f_H \le 1$ describes the degree of vertical order of the adsorbate atoms, with $f_H = 0$ for a completely disordered system and $f_H = 1$ for all probed adsorbate atoms having the same adsorption distance. XSW measurements were performed for two (sub)monolayer coverages of F4PEN on Ag(111), yielding essentially the same results (the data for higher coverage is

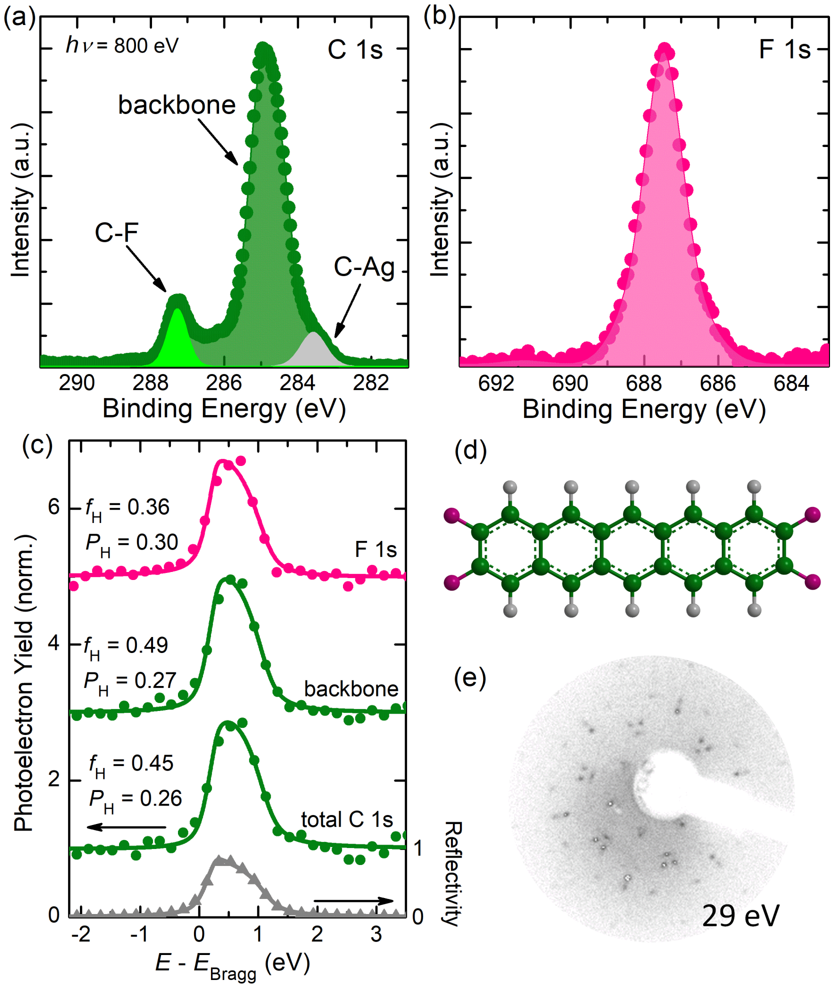

Figure 1: (a) C 1s and (b) F 1s core levels of F4PEN in monolayers on Ag(111) measured at DLS. (c) Reflectivity and photoelectron yield (Y_p) as a function of the photon energy (*hu*) relative to the Bragg energy (E_{Bragg} = 2630 eV) for a (sub)monolayer (<2 Å) F4PEN thin film on Ag(111). For each element, the coherent position (P_H) and the coherent fraction (f_H) are given. (d) Chemical structure of F4PEN. (e) LEED pattern for F4PEN on Ag(111) with a nominal thickness of 4 Å, measured at 295 K with a beam energy of 29 eV. The LEED pattern is almost the same as for PEN on Cu(111) [28].

shown in Supporting Information File 1, Figure S2). F4PEN adsorbed in an essentially planar geometry, with averaged vertical adsorption distances of around 3.00 Å for carbon and fluorine atoms. The adsorption distances are summarized in Table 1, together with literature values for PEN and PFP. In general, the adsorption distance of F4PEN in (sub)monolayers on Ag(111) was similar to that of PEN and PFP on the same substrate.

Table 1: Summary of the element-specific vertical adsorption heights (d_H/Å) of (fluorinated) pentacene in (sub)monolayers on Ag(111) measured with the XSW technique. A low coverage indicates the submonolayer (<2 Å) and a high coverage indicates an almost closed monolayer (≈3 Å). The values for PEN and PFP are taken from [51] and [50], respectively.

coverage	element	PEN	F4PEN			PFP
		d_H	f_H	P_H	d_H	d_H
low	C	2.98	0.49	0.27	3.00 ± 0.03	3.16
	F	–	0.36	0.30	3.05 ± 0.02	3.16
high	C	3.12	0.37	0.26	2.97 ± 0.02	–
	F	–	0.45	0.24	2.93 ± 0.01	–

Turning from vertical to lateral order, the LEED pattern of F4PEN on Ag(111) is shown in Figure 1e. At a nominal thickness of 4 Å, F4PEN is well-ordered, in contrast to PEN on the same substrate, which is disordered at room temperature for the same thickness [28,31,52]. Interestingly, the LEED pattern of F4PEN on Ag(111) was virtually identical to those of PEN on Cu(111) [28]. Increasing the coverage to nominally 48 Å did not significantly change the LEED image (see Supporting Information File 1, Figure S3). This indicated that increasing the coverage does not change the lateral order at the contact layer and pointed towards Stranski–Krastanov growth (island on wetting layer) [70] since the signal from the interface was visible even when a nominal coverages corresponding to several layers was deposited. Stranski–Krastanov growth has been suggested for F4PEN on Cu(111) [63], and furthermore was supported by thickness-dependent XPS, where the relative intensity barely changed as the nominal F4PEN thickness increased from 8 to 48 Å (for the spectra see Supporting Information File 1, Figure S4). Furthermore, a rigid shift of the C 1s and F 1s core levels of around 0.2 eV to a higher BE could be observed for a nominal thickness from 2 to 48 Å. This shift could be attributed to the screening effect (also often called the mirror force effect), which is commonly observed in photoemission data of organic thin films on metal substrates [71-73]. The absence of nonrigid shifts of the core level peaks between the mono- and multilayer coverage, which usually occur in the case of chemisorption [74-77], pointed to a weak interfacial coupling.

Figure 2a shows the UPS data for the valence band region of stepwise deposited F4PEN on Ag(111). For a nominal thickness of 1 Å, two peaks that could be assigned to the HOMO and HOMO−1 levels of F4PEN were visible. The low BE onset of the HOMO-derived peak was located at a 1.56 eV BE. For a thicknesses of 4 Å and larger, a third peak emerged at the high BE shoulder of the HOMO-derived peak. Interestingly, the maxima of these two peaks did not change with an increasing coverage (as highlighted by the vertical lines in Figure 2a). However, the HOMO-derived peak broadened, and for a nominal thickness of 48 Å, its onset was at 1.51 eV BE. The HOMO−1-derived peak also broadened, but its maximum showed a shift to higher BE with increasing coverage. This shift was essentially parallel to that of a deeper-lying valence electron feature (centered at around a 10 eV BE, the spectra are shown in Supporting Information File 1, Figure S5) and to that of the core levels. Possible reasons why the HOMO level did not show the screening effect and the origins of the third peak will be discussed below.

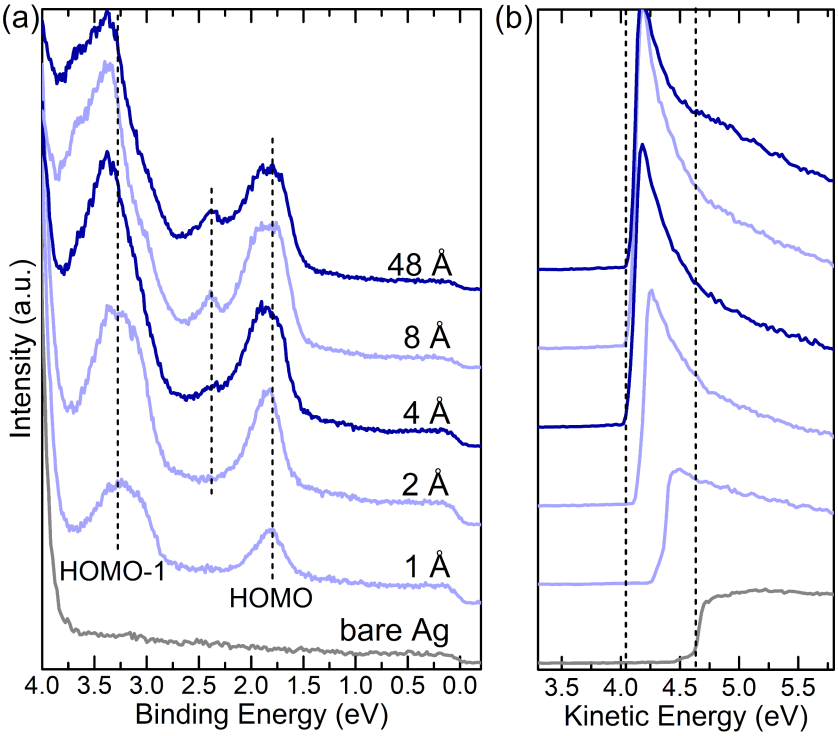

Figure 2: Valence band (a) and secondary electron region (b) of the UPS spectra of F4PEN on Ag(111). In (a), the nominal mass thickness is denoted.

The secondary electron cut-off (SECO) spectra (Figure 2b) allowed to determine the VL position above the Fermi level (E_F), which was reduced from an initial value of 4.62 eV [i.e., the work function of clean Ag(111)] to 4.05 eV for a nominal F4PEN thickness of 4 Å and stayed essentially constant when increasing the coverage. The VL decrease of 0.57 eV was rather similar to that of PEN or PFP thin films on the same substrate [28,50] and could be mainly attributed to the so-called push-back effect, i.e., the reduction of the surface dipole part of the metal work function [78] by the mere presence of the molecular adsorbate [73,79,80]. The VL and the HOMO onset gave the IE, which decreased from 5.87 eV for the monolayer (4 Å) to 5.56 eV for the multilayer (48 Å).

Discussion

Figure 3 summarizes the experimental results of F4PEN thin films on Ag(111) and compares them with those of PEN and PFP thin films on the same substrate. Notably, the valence band spectra were almost identical for the monolayer coverages. In all cases, the HOMO-derived peak was centered at 1.85 eV, while the peak centered at a higher BE (≈3.00 eV) was identified as the HOMO−1-derived peak. In addition, the vertical adsorption geometries were rather similar (Table 1), and no obvious distortions became evident for the fluorinated compounds, which drew the picture of lying molecules (PEN, F4PEN, and PFP) in monolayers on Ag(111). The carbon atoms of PFP [50] exhibited a slightly larger adsorption distance compared to PEN (low coverage) [51] and F4PEN. The increase in d_H for PEN by raising the coverage was explained by a vertical ordering due to intermolecular interactions [51]. The small coverage-dependent changes of F4PEN showed an opposite trend, but the change in the vertical adsorption heights of the carbon atoms was only 0.02 Å, i.e., within the experimental uncertainty. In particular, the fluorine atoms showed a difference in the adsorption distance of $\Delta d_H = 0.10$ Å. For the higher coverage (see Supporting Information File 1, Figure S2), the fluorine atoms were apparently located below the carbon atoms. However, such a behavior would be rather unusual as for F4PEN as well as for PFP on Cu(111), an upward bending of the fluorine atoms was observed [9,63] and is also expected due to the repulsive interaction of the fluorine atoms with the metal surface [81]. Moreover, also for related peripherally fluorinated molecules on the (111) surfaces of coinage metals, a downward bending of the fluorine atoms has never been observed [64]. In particular, this holds for PFP on Ag(111) [50] and F_{16}CuPc on the same substrate [82]. Taking into account the error bar of our measurements, a lying adsorption geometry will be considered in the following. For a higher coverage, F4PEN adsorbed at a lower position than PEN, which seemed to be at odds with the expected decrease of the organic–metal coupling strength by fluorination. However, also the carbon atoms of F4PEN on Cu(111) have smaller vertical adsorption distances (2.24 Å [63]) than PEN (2.34 Å [9]). The adsorption distance of the fluorine atoms of F4PEN on Cu(111), however, was 3.40 Å, and thus even higher than that of the PFP fluorine atoms on the same substrate (3.08 Å [9]).

The similar adsorption distances on Ag(111) and the almost planar adsorption geometry could explain the similar vacuum level shifts (around 0.5 eV) upon monolayer formation of the three molecules (Figure 3): In the absence of notable organic–metal interactions, the interface dipole is mainly due to the pushback effect, and its magnitude is determined by the adsorption distance [83,84]. In all cases, the vacuum level shift saturated at a nominal thickness of 4 Å. This thickness thus represented an almost closed monolayer coverage, and subsequently deposited molecules grew predominantly in multilayers (and not on possibly uncovered substrate patches).

The almost identical HOMO positions were unexpected and in contrast to the monolayers of PEN and PFP on graphite, with a likewise lying-down orientation and large differences in the HOMO positions [11,25,26]. In general, for a strong interfacial coupling and charge transfer, the resonance structure of the adsorbate in the monolayer can be notably different from that in multilayers [75,85-87]. For the specific case of the pentacene derivatives on Ag(111), strong coupling was not observed. However, the interaction of PEN with Ag(111) was termed “soft chemisorption” [51], and by a closer look at the PEN monolayer spectrum in Figure 3a, a faint peak close to E_F (marked with an asterisk) could be ascribed to a charge transfer from the substrate [28]. The transport gap of PEN is 2.20 eV [88]. Similar transport gaps can be expected for PFP and F4PEN, which puts the Fermi level rather close to the LUMO. Moreover, in the vicinity of a metal surface, the gap has been found to decrease, and the molecular energy levels become broadened [1,89,90], which is expected to promote the charge transfer to the LUMO [7,8].

The positions of the HOMO levels of molecular monolayers on metal substrates depend also on the magnitude of the above mentioned screening effect [10,72,89] or, more generally, on the electronic polarization of the charged molecules on the surfaces. In addition to the substrate contribution, interactions with neighboring molecules, which have an electrostatic and an induction contribution, have to be taken into account [11,44]. Induction interactions are always stabilizing the photohole and should–given the same coverage–lead to similar shifts for PEN, F4PEN and PFP. As mentioned in the introduction, the electrostatic contribution depends on intramolecular quadrupole moments and has, due to the strong polar character of the C–F bonds, opposite signs for PEN and PFP [11]. Electrostatic

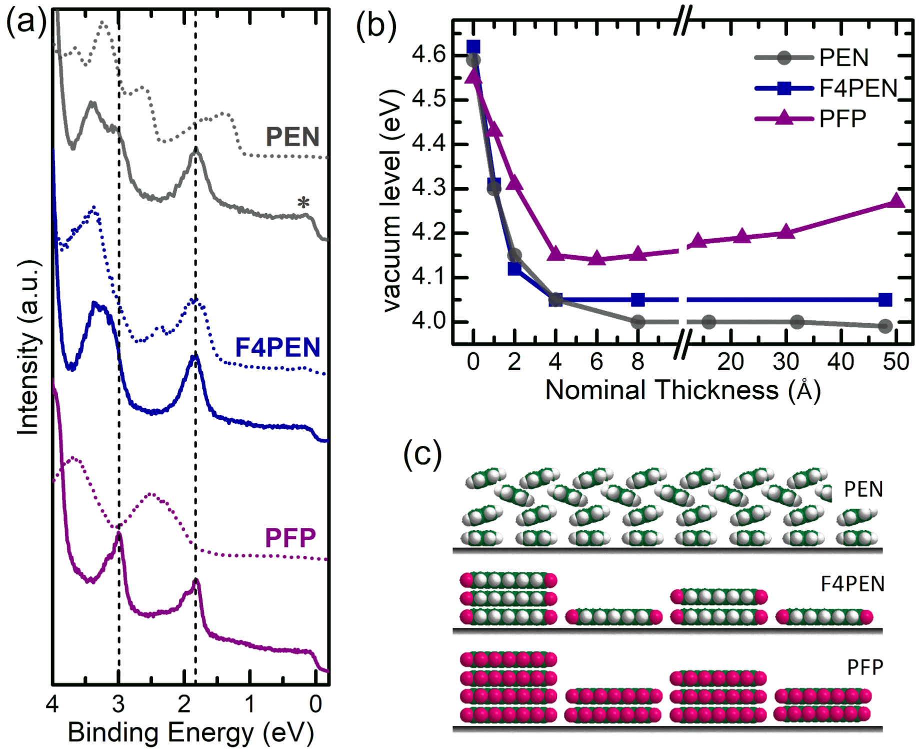

Figure 3: (a) Valence band spectra for (fluorinated) pentacene in (sub)monolayer (solid lines) and multilayer (dotted lines) thin films on Ag(111). (b) Evolution of the vacuum level of (fluorinated) pentacene with increasing thickness on Ag(111). The PEN and PFP data in (a) and (b) is taken from [28,50]. (c) Hypothetical growth modes of (fluorinated) pentacene on Ag(111) on profile view, with the C atoms in green, the F atoms in red and the H atoms in grey. Note, that PEN (F4PEN and PFP) is viewed along the short (long) molecular axis. A more detailed discussion on the F4PEN adsorption geometry on Ag(111) based on the analysis of the f_H values can be found in Supporting Information File 1, Figure S6.

potential maps of PEN, F4PEN and PFP in the gas phase can be found in [46]. In general, hydrogen atoms bear a minimum, and fluorine atoms a maximum of the electron density, i.e., the quadrupole moments of F4PEN along the molecular short and long axes have opposite signs, while they have the same signs for PEN and PFP, respectively. Without precise knowledge of the F4PEN monolayer structure, the electronic polarization cannot be calculated, but it is reasonable to assume that the interplay of substrate, induction and electrostatic contributions resulted in the observed identical HOMO level position in all three monolayers.

For an in-depth discussion of the multilayer electronic structure, for which the valence electron spectra were strikingly different (Figure 3a), knowledge about the morphology and the molecular orientation was indispensable [91-94]. As mentioned above, multilayers of PEN show a herringbone arrangement on virtually all substrates [47,56-59], and for commonly prepared vacuum-sublimed thin films on metals, the long molecular axis is parallel to the substrate [95-97]. Indeed, for the PEN multilayers on Ag(111), the HOMO-derived peak measured by partly angle-averaging UPS exhibited the typical shape of crystalline PEN in a herringbone arrangement [28,98-100]. The shift of the HOMO onset to lower BE could be explained by the reduced IE of PEN thin films consisting of tilted instead of lying molecules [28,29]. PFP, in contrast, exhibits π-stacking on various substrates [18,56]. The X-ray scattering data shown in Supporting Information File 1, Figure S7 confirmed this ordering motif for the Ag(111) surface. The almost symmetric shape of the PFP HOMO in multilayers on Ag(111) resembled that of likewise π-stacked organic multilayer thin films [101-103]. The shift to higher BE could, in part, be attributed to the screening effect [50], and the broadening could be ascribed to the intermolecular band dispersion [18]. The multilayer structure of F4PEN on Ag(111) is unknown, but the comparison of photoelectron spectroscopy data with that of PEN and PFP hinted at π-stacking: For F4PEN, a herringbone arrangement involving an inclination of the molecular short axis would expose the C–H bonds (and not the C–F polar bonds) to the surface. This case would be in analogy to PEN, and a shift of the HOMO towards a lower BE should be expected, which was, however, not observed. π-stacking, on the other hand, could explain the photoelectron spectroscopy data: The rigid shifts in UPS and XPS were due to screening by the substrate; the valence electron peak between the HOMO and the HOMO−1 for multilayer coverage had almost the same BE as the HOMO in PFP multilayers.

Conclusion

In conclusion, in the monolayer regime on Ag(111), (partial) fluorination of pentacene did not notably affect the adsorption geometry and the energy level alignment. This finding was most likely due to the interplay of the substrate, induction and electrostatic contributions to the solid state polarization, i.e., a mutual compensation of different mechanisms. Our results show that the rationale of "decoupling by fluorination" required a threshold of organic–metal interaction strength, as can be seen by the monolayers of PEN, F4PEN and PFP on Cu(111), which were indeed distinctively different [9,63]. Moreover, the strong intramolecular polar C–F bond had an eminent impact on the multilayer structure of the pentacene derivatives on Ag(111), which were π-stacked for PFP and F4PEN, whereas PEN adopted a herringbone arrangement. For PFP this could be ascribed to attractive quadrupole interactions between adjacent PFP molecules [18,56], and this seemed to be the case for partial fluorination as well. The differences in thin film structure were also reflected in the electronic structures, which were distinctively different in multilayers on Ag(111). Our results highlight that even for weak organic–metal interaction, the fluorine substitution significantly affects the organic thin film growth beyond the first layer as well as the multilayer electronic structure.

Experimental

F4PEN was synthesized following an established procedure [60] and vacuum-sublimed on clean metal surfaces (prepared by repeated Ar^+ ion sputtering and annealing cycles [up to 550 °C]), with deposition rates of about 0.5 Å/min. The film mass thickness was monitored with a quartz crystal microbalance (QCM) near the sample, and a nominal thickness of 4 Å is close to monolayer coverage. The high-resolution XPS (HR-XPS) and normal-incidence XSW (NIXSW) experiments were performed at beamline I09 at Diamond Light Source (DLS, UK) using both the soft (110–1100 eV) and hard (2.1–18 keV) X-ray beams [104,105]. Sample preparation and measurements were performed in situ under ultrahigh vacuum (UHV) conditions. The analysis chamber (base pressure: 3×10^{-10} mbar) contained a VG Scienta EW4000 HAXPES hemispherical photoelectron analyzer, which was mounted at 90° relative to the incident X-ray beam. The reflectivity and photoelectron core level spectra of all elements were recorded at different photon energies E (31 data sets) within a ±3 eV interval around the normal-incidence Bragg energy E_{Bragg} (2630 eV) of Ag(111). The photoelectron yield Y_{P} $(E - E_{\mathrm{Bragg}})$ and the reflectivity were modeled taking into account the experimental geometry and the nondipole corrections associated with it [82]. For HR-XPS, the photon energy was 800 eV, and the angle between the incoming beam and the substrate normal was 60°. Thickness-dependent UPS and XPS experiments were carried out at Soochow University in an ultrahigh vacuum system consisting of three interconnected chambers (base pressure: 3×10^{-10} mbar) for substrate preparation, thin film evaporation and analysis. LEED was performed using a Micro-Channel-Plate LEED (OCI BDL800IR-MCP). Photoelectron spectroscopy experiments were performed using a SPECS PHOIBOS 150 analyzer and monochromatized He I radiation (21.22 eV) and the monochromatized Al Kα line (1486.6 eV) for UPS and XPS, respectively. For UPS, the energy resolution was 80 meV, and the angle between the incident beam and the sample surface was fixed to 40°. The spectra were collected at photoelectron take-off angles of 45°, with an acceptance angle of ±12°. A sketch of the measurement geometry can be found in Reference [28]. The XPS and UPS valence band spectra were plotted with respect to E_{F}. In the plots of the secondary electron region of UPS (measured in normal emission), the energy scale was corrected by the applied bias voltage (−3 V) and the analyzer work function. Thus, the position of the SECO corresponds to the vacuum level (VL) with respect to E_{F}. All organic thin film preparation steps and all measurements were performed at room temperature (295 K).

Supporting Information

Comparison of low- and high-coverage F4PEN on Ag(111), both HR-XPS and XSW results, full spectra of coverage-dependent XPS results, C 1s and F 1s core levels, full UPS survey spectra, XRD measurement and analysis of PFP on Ag(111) and a set of XSW measurements.

Supporting Information File 1

Additional experimental data.
[https://www.beilstein-journals.org/bjnano/content/supplementary/2190-4286-11-120-S1.pdf]

Acknowledgements

The authors thank the Diamond Light Source for access to beamline I09, and the staff, in particular D. A. Duncan, for excellent support during the beamtime.

Funding

This work was financially supported in part by the National Key R&D Program of China (Grant No. 2017YFA0205002), the 111 Project of the Chinese State Administration of Foreign Experts Affairs, the Collaborative Innovation Center of Suzhou Nano Science & Technology (NANO-CIC) and the Soochow University-Western University Joint Center for Synchrotron Radiation Research. Q. W. gratefully acknowledges financial support from the China Scholarship Council (CSC No. 201706920041).

ORCID® iDs

Qi Wang - https://orcid.org/0000-0002-9777-3637
Antoni Franco-Cañellas - https://orcid.org/0000-0001-7767-9611
Holger F. Bettinger - https://orcid.org/0000-0001-5223-662X
Frank Schreiber - https://orcid.org/0000-0003-3659-6718
Alexander Gerlach - https://orcid.org/0000-0003-1787-1868
Steffen Duhm - https://orcid.org/0000-0002-5099-5929

References

1. Fahlman, M.; Fabiano, S.; Gueskine, V.; Simon, D.; Berggren, M.; Crispin, X. *Nat. Rev. Mater.* **2019,** *4,* 627–650. doi:10.1038/s41578-019-0127-y
2. Nakano, K.; Tajima, K. *Adv. Mater. (Weinheim, Ger.)* **2017,** *29,* 1603269. doi:10.1002/adma.201603269
3. Zojer, E.; Taucher, T. C.; Hofmann, O. T. *Adv. Mater. Interfaces* **2019,** *6,* 1900581. doi:10.1002/admi.201900581
4. Schwarze, M.; Tress, W.; Beyer, B.; Gao, F.; Scholz, R.; Poelking, C.; Ortstein, K.; Günther, A. A.; Kasemann, D.; Andrienko, D.; Leo, K. *Science* **2016,** *352,* 1446–1449. doi:10.1126/science.aaf0590
5. Heimel, G.; Salzmann, I.; Duhm, S.; Koch, N. *Chem. Mater.* **2011,** *23,* 359–377. doi:10.1021/cm1021257
6. Schwarze, M.; Schellhammer, K. S.; Ortstein, K.; Benduhn, J.; Gaul, C.; Hinderhofer, A.; Perdigón Toro, L.; Scholz, R.; Kublitski, J.; Roland, S.; Lau, M.; Poelking, C.; Andrienko, D.; Cuniberti, G.; Schreiber, F.; Neher, D.; Vandewal, K.; Ortmann, F.; Leo, K. *Nat. Commun.* **2019,** *10,* 2466. doi:10.1038/s41467-019-10435-2
7. Oehzelt, M.; Koch, N.; Heimel, G. *Nat. Commun.* **2014,** *5,* 4174. doi:10.1038/ncomms5174
8. Yang, J.-P.; Bussolotti, F.; Kera, S.; Ueno, N. *J. Phys. D: Appl. Phys.* **2017,** *50,* 423002. doi:10.1088/1361-6463/aa840f
9. Koch, N.; Gerlach, A.; Duhm, S.; Glowatzki, H.; Heimel, G.; Vollmer, A.; Sakamoto, Y.; Suzuki, T.; Zegenhagen, J.; Rabe, J. P.; Schreiber, F. *J. Am. Chem. Soc.* **2008,** *130,* 7300–7304. doi:10.1021/ja800286k
10. Goiri, E.; Borghetti, P.; El-Sayed, A.; Ortega, J. E.; de Oteyza, D. G. *Adv. Mater. (Weinheim, Ger.)* **2016,** *28,* 1340–1368. doi:10.1002/adma.201503570
11. D'Avino, G.; Duhm, S.; Della Valle, R. G.; Heimel, G.; Oehzelt, M.; Kera, S.; Ueno, N.; Beljonne, D.; Salzmann, I. *Chem. Mater.* **2020,** *32,* 1261–1271. doi:10.1021/acs.chemmater.9b04763
12. Yamane, H.; Gerlach, A.; Duhm, S.; Tanaka, Y.; Hosokai, T.; Mi, Y. Y.; Zegenhagen, J.; Koch, N.; Seki, K.; Schreiber, F. *Phys. Rev. Lett.* **2010,** *105,* 046103. doi:10.1103/physrevlett.105.046103
13. Kleimann, C.; Stadtmüller, B.; Schröder, S.; Kumpf, C. *J. Phys. Chem. C* **2014,** *118,* 1652–1660. doi:10.1021/jp411289j
14. Peisert, H.; Knupfer, M.; Schwieger, T.; Fuentes, G. G.; Olligs, D.; Fink, J.; Schmidt, T. *J. Appl. Phys.* **2003,** *93,* 9683–9692. doi:10.1063/1.1577223
15. Duhm, S.; Bürker, C.; Hosokai, T.; Gerlach, A. Vertical Bonding Distances Impact Organic-Metal Interface Energetics. In *Electronic Processes in Organic Electronics;* Ishii, H.; Kudo, K.; Nakayama, Y., Eds.; Springer: Japan, 2015; pp 89–107. doi:10.1007/978-4-431-55206-2_6
16. Otero, R.; Vázquez de Parga, A. L.; Gallego, J. M. *Surf. Sci. Rep.* **2017,** *72,* 105–145. doi:10.1016/j.surfrep.2017.03.001
17. Willenbockel, M.; Lüftner, D.; Stadtmüller, B.; Koller, G.; Kumpf, C.; Soubatch, S.; Puschnig, P.; Ramsey, M. G.; Tautz, F. S. *Phys. Chem. Chem. Phys.* **2015,** *17,* 1530–1548. doi:10.1039/c4cp04595e
18. Salzmann, I.; Moser, A.; Oehzelt, M.; Breuer, T.; Feng, X.; Juang, Z.-Y.; Nabok, D.; Della Valle, R. G.; Duhm, S.; Heimel, G.; Brillante, A.; Venuti, E.; Bilotti, I.; Christodoulou, C.; Frisch, J.; Puschnig, P.; Draxl, C.; Witte, G.; Müllen, K.; Koch, N. *ACS Nano* **2012,** *6,* 10874–10883. doi:10.1021/nn3042607
19. Jones, A. O. F.; Chattopadhyay, B.; Geerts, Y. H.; Resel, R. *Adv. Funct. Mater.* **2016,** *26,* 2233–2255. doi:10.1002/adfm.201503169
20. Hu, J.; Aghdassi, N.; Bhagat, S.; Garmshausen, Y.; Wang, R.; Koch, N.; Hecht, S.; Duhm, S.; Salzmann, I. *Adv. Mater. Interfaces* **2020,** *7,* 1901707. doi:10.1002/admi.201901707
21. Hofmann, P. E.; Tripp, M. W.; Bischof, D.; Grell, Y.; Schiller, A. L. C.; Breuer, T.; Ivlev, S. I.; Witte, G.; Koert, U. *Angew. Chem., Int. Ed.* **2020,** in press. doi:10.1002/anie.202006489
22. Kim, D. K.; Lubert-Perquel, D.; Heutz, S. *Mater. Horiz.* **2020,** *7,* 289–298. doi:10.1039/c9mh00355j
23. Duva, G.; Mann, A.; Pithan, L.; Beyer, P.; Hagenlocher, J.; Gerlach, A.; Hinderhofer, A.; Schreiber, F. *J. Phys. Chem. Lett.* **2019,** *10,* 1031–1036. doi:10.1021/acs.jpclett.9b00304
24. Sakamoto, Y.; Suzuki, T.; Kobayashi, M.; Gao, Y.; Fukai, Y.; Inoue, Y.; Sato, F.; Tokito, S. *J. Am. Chem. Soc.* **2004,** *126,* 8138–8140. doi:10.1021/ja0476258
25. Yamane, H.; Nagamatsu, S.; Fukagawa, H.; Kera, S.; Friedlein, R.; Okudaira, K. K.; Ueno, N. *Phys. Rev. B* **2005,** *72,* 153412. doi:10.1103/physrevb.72.153412
26. Kera, S.; Hosoumi, S.; Sato, K.; Fukagawa, H.; Nagamatsu, S.-i.; Sakamoto, Y.; Suzuki, T.; Huang, H.; Chen, W.; Wee, A. T. S.; Coropceanu, V.; Ueno, N. *J. Phys. Chem. C* **2013,** *117,* 22428–22437. doi:10.1021/jp4032089
27. Salzmann, I.; Duhm, S.; Heimel, G.; Oehzelt, M.; Kniprath, R.; Johnson, R. L.; Rabe, J. P.; Koch, N. *J. Am. Chem. Soc.* **2008,** *130,* 12870–12871. doi:10.1021/ja804793a
28. Lu, M.-C.; Wang, R.-B.; Yang, A.; Duhm, S. *J. Phys.: Condens. Matter* **2016,** *28,* 094005. doi:10.1088/0953-8984/28/9/094005
29. Koch, N.; Vollmer, A.; Duhm, S.; Sakamoto, Y.; Suzuki, T. *Adv. Mater. (Weinheim, Ger.)* **2007,** *19,* 112–116. doi:10.1002/adma.200601825
30. Gall, J.; Zhang, L.; Fu, X.; Zeppenfeld, P.; Sun, L. D. *Phys. Rev. B* **2017,** *96,* 125424. doi:10.1103/physrevb.96.125424
31. Dougherty, D. B.; Jin, W.; Cullen, W. G.; Reutt-Robey, J. E.; Robey, S. W. *J. Phys. Chem. C* **2008,** *112,* 20334–20339. doi:10.1021/jp804682v
32. Yang, X.; Egger, L.; Fuchsberger, J.; Unzog, M.; Lüftner, D.; Hajek, F.; Hurdax, P.; Jugovac, M.; Zamborlini, G.; Feyer, V.; Koller, G.; Puschnig, P.; Tautz, F. S.; Ramsey, M. G.; Soubatch, S. *J. Phys. Chem. Lett.* **2019,** *10,* 6438–6445. doi:10.1021/acs.jpclett.9b02231

33. Kim, V. O.; Broch, K.; Belova, V.; Chen, Y. S.; Gerlach, A.; Schreiber, F.; Tamura, H.; Della Valle, R. G.; D'Avino, G.; Salzmann, I.; Beljonne, D.; Rao, A.; Friend, R. *J. Chem. Phys.* **2019,** *151,* 164706. doi:10.1063/1.5130400
34. Cocchi, C.; Breuer, T.; Witte, G.; Draxl, C. *Phys. Chem. Chem. Phys.* **2018,** *20,* 29724–29736. doi:10.1039/c8cp06384b
35. Shi, X.-Q.; Li, Y.; Van Hove, M. A.; Zhang, R.-Q. *J. Phys. Chem. C* **2012,** *116,* 23603–23607. doi:10.1021/jp310007v
36. Hinderhofer, A.; Heinemeyer, U.; Gerlach, A.; Kowarik, S.; Jacobs, R. M. J.; Sakamoto, Y.; Suzuki, T.; Schreiber, F. *J. Chem. Phys.* **2007,** *127,* 194705. doi:10.1063/1.2786992
37. Duhm, S.; Salzmann, I.; Heimel, G.; Oehzelt, M.; Haase, A.; Johnson, R. L.; Rabe, J. P.; Koch, N. *Appl. Phys. Lett.* **2009,** *94,* 033304. doi:10.1063/1.3073046
38. Coropceanu, V.; Malagoli, M.; da Silva Filho, D. A.; Gruhn, N. E.; Bill, T. G.; Brédas, J. L. *Phys. Rev. Lett.* **2002,** *89,* 275503. doi:10.1103/physrevlett.89.275503
39. Delgado, M. C. R.; Pigg, K. R.; da Silva Filho, D. A.; Gruhn, N. E.; Sakamoto, Y.; Suzuki, T.; Osuna, R. M.; Casado, J.; Hernández, V.; Navarrete, J. T. L.; Martinelli, N. G.; Cornil, J.; Sánchez-Carrera, R. S.; Coropceanu, V.; Brédas, J.-L. *J. Am. Chem. Soc.* **2009,** *131,* 1502–1512. doi:10.1021/ja807528w
40. Sato, N.; Seki, K.; Inokuchi, H. *J. Chem. Soc., Faraday Trans. 2* **1981,** *77,* 1621–1633. doi:10.1039/f29817701621
41. Tsiper, E. V.; Soos, Z. G. *Phys. Rev. B* **2003,** *68,* 085301. doi:10.1103/physrevb.68.085301
42. Neaton, J. B.; Hybertsen, M. S.; Louie, S. G. *Phys. Rev. Lett.* **2006,** *97,* 216405. doi:10.1103/physrevlett.97.216405
43. Yoshida, H.; Yamada, K.; Tsutsumi, J.; Sato, N. *Phys. Rev. B* **2015,** *92,* 075145. doi:10.1103/physrevb.92.075145
44. D'Avino, G.; Muccioli, L.; Castet, F.; Poelking, C.; Andrienko, D.; Soos, Z. G.; Cornil, J.; Beljonne, D. *J. Phys.: Condens. Matter* **2016,** *28,* 433002. doi:10.1088/0953-8984/28/43/433002
45. Duhm, S.; Salzmann, I.; Bröker, B.; Glowatzki, H.; Johnson, R. L.; Koch, N. *Appl. Phys. Lett.* **2009,** *95,* 093305. doi:10.1063/1.3213547
46. Shen, B.; Geiger, T.; Einholz, R.; Reicherter, F.; Schundelmeier, S.; Maichle-Mössmer, C.; Speiser, B.; Bettinger, H. F. *J. Org. Chem.* **2018,** *83,* 3149–3158. doi:10.1021/acs.joc.7b03241
47. Kawai, S.; Pawlak, R.; Glatzel, T.; Meyer, E. *Phys. Rev. B* **2011,** *84,* 085429. doi:10.1103/physrevb.84.085429
48. Ugolotti, A.; Harivyasi, S. S.; Baby, A.; Dominguez, M.; Pinardi, A. L.; López, M. F.; Martín-Gago, J. Á.; Fratesi, G.; Floreano, L.; Brivio, G. P. *J. Phys. Chem. C* **2017,** *121,* 22797–22805. doi:10.1021/acs.jpcc.7b06555
49. Wong, S. L.; Huang, H.; Huang, Y. L.; Wang, Y. Z.; Gao, X. Y.; Suzuki, T.; Chen, W.; Wee, A. T. S. *J. Phys. Chem. C* **2010,** *114,* 9356–9361. doi:10.1021/jp910581b
50. Duhm, S.; Hosoumi, S.; Salzmann, I.; Gerlach, A.; Oehzelt, M.; Wedl, B.; Lee, T.-L.; Schreiber, F.; Koch, N.; Ueno, N.; Kera, S. *Phys. Rev. B* **2010,** *81,* 045418. doi:10.1103/physrevb.81.045418
51. Duhm, S.; Bürker, C.; Niederhausen, J.; Salzmann, I.; Hosokai, T.; Duvernay, J.; Kera, S.; Schreiber, F.; Koch, N.; Ueno, N.; Gerlach, A. *ACS Appl. Mater. Interfaces* **2013,** *5,* 9377–9381. doi:10.1021/am402778u
52. Eremtchenko, M.; Temirov, R.; Bauer, D.; Schaefer, J. A.; Tautz, F. S. *Phys. Rev. B* **2005,** *72,* 115430. doi:10.1103/physrevb.72.115430
53. Lo, Y.-Y.; Chang, J.-H.; Hoffmann, G.; Su, W.-B.; Wu, C.-I.; Chang, C.-S. *Jpn. J. Appl. Phys.* **2013,** *52,* 101601. doi:10.7567/jjap.52.101601
54. Glowatzki, H.; Heimel, G.; Vollmer, A.; Wong, S. L.; Huang, H.; Chen, W.; Wee, A. T. S.; Rabe, J. P.; Koch, N. *J. Phys. Chem. C* **2012,** *116,* 7726–7734. doi:10.1021/jp208582z
55. Bürker, C.; Ferri, N.; Tkatchenko, A.; Gerlach, A.; Niederhausen, J.; Hosokai, T.; Duhm, S.; Zegenhagen, J.; Koch, N.; Schreiber, F. *Phys. Rev. B* **2013,** *87,* 165443. doi:10.1103/physrevb.87.165443
56. Klues, M.; Witte, G. *CrystEngComm* **2018,** *20,* 63–74. doi:10.1039/c7ce01700f
57. Ruiz, R.; Choudhary, D.; Nickel, B.; Toccoli, T.; Chang, K.-C.; Mayer, A. C.; Clancy, P.; Blakely, J. M.; Headrick, R. L.; Iannotta, S.; Malliaras, G. G. *Chem. Mater.* **2004,** *16,* 4497–4508. doi:10.1021/cm049563q
58. Käfer, D.; Ruppel, L.; Witte, G. *Phys. Rev. B* **2007,** *75,* 085309. doi:10.1103/physrevb.75.085309
59. Pachmajer, S.; Jones, A. O. F.; Truger, M.; Röthel, C.; Salzmann, I.; Werzer, O.; Resel, R. *ACS Appl. Mater. Interfaces* **2017,** *9,* 11977–11984. doi:10.1021/acsami.6b15907
60. Bula, R. P.; Oppel, I. M.; Bettinger, H. F. *J. Org. Chem.* **2012,** *77,* 3538–3542. doi:10.1021/jo202450u
61. Geiger, T.; Schundelmeier, S.; Hummel, T.; Ströbele, M.; Leis, W.; Seitz, M.; Zeiser, C.; Moretti, L.; Maiuri, M.; Cerullo, G.; Broch, K.; Vahland, J.; Leo, K.; Maichle-Mössmer, C.; Speiser, B.; Bettinger, H. F. *Chem. – Eur. J.* **2020,** *26,* 3420–3434. doi:10.1002/chem.201905843
62. Savu, S.-A.; Biddau, G.; Pardini, L.; Bula, R.; Bettinger, H. F.; Draxl, C.; Chassé, T.; Casu, M. B. *J. Phys. Chem. C* **2015,** *119,* 12538–12544. doi:10.1021/acs.jpcc.5b03768
63. Franco-Cañellas, A.; Wang, Q.; Broch, K.; Shen, B.; Gerlach, A.; Bettinger, H. F.; Duhm, S.; Schreiber, F. *Phys. Rev. Mater.* **2018,** *2,* 044002. doi:10.1103/physrevmaterials.2.044002
64. Franco-Cañellas, A.; Duhm, S.; Gerlach, A.; Schreiber, F. *Rep. Prog. Phys.* **2020,** *83,* 066501. doi:10.1088/1361-6633/ab7a42
65. van Straaten, G.; Franke, M.; Bocquet, F. C.; Tautz, F. S.; Kumpf, C. *J. Electron Spectrosc. Relat. Phenom.* **2018,** *222,* 106–116. doi:10.1016/j.elspec.2017.07.007
66. Gerlach, A.; Bürker, C.; Hosokai, T.; Schreiber, F. X-Ray Standing Waves and Surfaces X-Ray Scattering Studies of Molecule–Metal Interfaces. In *The Molecule–Metal Interface;* Koch, N.; Ueno, N.; Wee, A. T. S., Eds.; Wiley-VCH: Weinheim, Germany, 2013; pp 153–172. doi:10.1002/9783527653171.ch6
67. Kera, S.; Hosokai, T.; Duhm, S. *J. Phys. Soc. Jpn.* **2018,** *87,* 061008. doi:10.7566/jpsj.87.061008
68. Basagni, A.; Ferrighi, L.; Cattelan, M.; Nicolas, L.; Handrup, K.; Vaghi, L.; Papagni, A.; Sedona, F.; Valentin, C. D.; Agnoli, S.; Sambi, M. *Chem. Commun.* **2015,** *51,* 12593–12596. doi:10.1039/c5cc04317d
69. Zegenhagen, J. Surface Structure Analysis with X-Ray Standing Waves. In *The X-Ray Standing Wave Technique;* Bracco, G.; Holst, B., Eds.; Springer: Berlin, Heidelberg, Germany, 2013; pp 249–275. doi:10.1007/978-3-642-34243-1_9
70. Baskaran, A.; Smereka, P. *J. Appl. Phys.* **2012,** *111,* 044321. doi:10.1063/1.3679068
71. Koch, N. *J. Phys.: Condens. Matter* **2008,** *20,* 184008. doi:10.1088/0953-8984/20/18/184008
72. Hill, I. G.; Mäkinen, A. J.; Kafafi, Z. H. *J. Appl. Phys.* **2000,** *88,* 889–895. doi:10.1063/1.373752
73. Kahn, A.; Koch, N.; Gao, W. *J. Polym. Sci., Part B: Polym. Phys.* **2003,** *41,* 2529–2548. doi:10.1002/polb.10642

74. Crispin, X.; Geskin, V.; Crispin, A.; Cornil, J.; Lazzaroni, R.; Salaneck, W. R.; Brédas, J.-L. *J. Am. Chem. Soc.* **2002,** *124,* 8131–8141. doi:10.1021/ja025673r
75. Chen, M.-T.; Hofmann, O. T.; Gerlach, A.; Bröker, B.; Bürker, C.; Niederhausen, J.; Hosokai, T.; Zegenhagen, J.; Vollmer, A.; Rieger, R.; Müllen, K.; Schreiber, F.; Salzmann, I.; Koch, N.; Zojer, E.; Duhm, S. *J. Phys.: Condens. Matter* **2019,** *31,* 194002. doi:10.1088/1361-648x/ab0171
76. Wang, Q.; Franco-Cañellas, A.; Ji, P.; Bürker, C.; Wang, R.-B.; Broch, K.; Thakur, P. K.; Lee, T.-L.; Zhang, H.; Gerlach, A.; Chi, L.; Duhm, S.; Schreiber, F. *J. Phys. Chem. C* **2018,** *122,* 9480–9490. doi:10.1021/acs.jpcc.8b01529
77. Stadtmüller, B.; Schröder, S.; Kumpf, C. *J. Electron Spectrosc. Relat. Phenom.* **2015,** *204,* 80–91. doi:10.1016/j.elspec.2015.03.003
78. Smoluchowski, R. *Phys. Rev.* **1941,** *60,* 661–674. doi:10.1103/physrev.60.661
79. Koch, N. *ChemPhysChem* **2007,** *8,* 1438–1455. doi:10.1002/cphc.200700177
80. Bagus, P. S.; Staemmler, V.; Wöll, C. *Phys. Rev. Lett.* **2002,** *89,* 096104. doi:10.1103/physrevlett.89.096104
81. Wang, Q.; Franco-Cañellas, A.; Yang, J.; Hausch, J.; Struzek, S.; Chen, M.; Thakur, P. K.; Gerlach, A.; Duhm, S.; Schreiber, F. *ACS Appl. Mater. Interfaces* **2020,** *12,* 14542–14551. doi:10.1021/acsami.9b22812
82. Gerlach, A.; Schreiber, F.; Sellner, S.; Dosch, H.; Vartanyants, I. A.; Cowie, B. C. C.; Lee, T.-L.; Zegenhagen, J. *Phys. Rev. B* **2005,** *71,* 205425. doi:10.1103/physrevb.71.205425
83. Toyoda, K.; Hamada, I.; Lee, K.; Yanagisawa, S.; Morikawa, Y. *J. Chem. Phys.* **2010,** *132,* 134703. doi:10.1063/1.3373389
84. Toyoda, K.; Hamada, I.; Lee, K.; Yanagisawa, S.; Morikawa, Y. *J. Phys. Chem. C* **2011,** *115,* 5767–5772. doi:10.1021/jp1107262
85. Liu, W.; Filimonov, S. N.; Carrasco, J.; Tkatchenko, A. *Nat. Commun.* **2013,** *4,* 2569. doi:10.1038/ncomms3569
86. Hofmann, O. T.; Glowatzki, H.; Bürker, C.; Rangger, G. M.; Bröker, B.; Niederhausen, J.; Hosokai, T.; Salzmann, I.; Blum, R.-P.; Rieger, R.; Vollmer, A.; Rajput, P.; Gerlach, A.; Müllen, K.; Schreiber, F.; Zojer, E.; Koch, N.; Duhm, S. *J. Phys. Chem. C* **2017,** *121,* 24657–24668. doi:10.1021/acs.jpcc.7b08451
87. Heimel, G.; Duhm, S.; Salzmann, I.; Gerlach, A.; Strozecka, A.; Niederhausen, J.; Bürker, C.; Hosokai, T.; Fernandez-Torrente, I.; Schulze, G.; Winkler, S.; Wilke, A.; Schlesinger, R.; Frisch, J.; Bröker, B.; Vollmer, A.; Detlefs, B.; Pflaum, J.; Kera, S.; Franke, K. J.; Ueno, N.; Pascual, J. I.; Schreiber, F.; Koch, N. *Nat. Chem.* **2013,** *5,* 187–194. doi:10.1038/nchem.1572
88. Han, W.; Yoshida, H.; Ueno, N.; Kera, S. *Appl. Phys. Lett.* **2013,** *103,* 123303. doi:10.1063/1.4821445
89. Heimel, G. Introduction to the Theory of Metal/Organic Interfaces. In *The WSPC Reference on Organic Electronics: Organic Semiconductors;* Bredas, J.-L.; Marder, S. R., Eds.; World Scientific, 2016; pp 131–158. doi:10.1142/9789813148598_0005
90. Anderson, P. W. *Phys. Rev.* **1961,** *124,* 41–53. doi:10.1103/physrev.124.41
91. Chen, W.; Qi, D.-C.; Huang, H.; Gao, X.; Wee, A. T. S. *Adv. Funct. Mater.* **2011,** *21,* 410–424. doi:10.1002/adfm.201000902
92. Yonezawa, K.; Hinderhofer, A.; Hosokai, T.; Kato, K.; Makino, R.; Schreiber, F.; Ueno, N.; Kera, S. *Adv. Mater. Interfaces* **2014,** *1,* 1400004. doi:10.1002/admi.201400004
93. Ji, R.-R.; Wang, Q.; Hu, J.-X.; Duhm, S. *Can. J. Chem.* **2017,** *95,* 1130–1134. doi:10.1139/cjc-2017-0021
94. Kera, S.; Yamane, H.; Ueno, N. *Prog. Surf. Sci.* **2009,** *84,* 135–154. doi:10.1016/j.progsurf.2009.03.002
95. Grimm, M.; Metzger, C.; Graus, M.; Jugovac, M.; Zamborlini, G.; Feyer, V.; Schöll, A.; Reinert, F. *Phys. Rev. B* **2018,** *98,* 195412. doi:10.1103/physrevb.98.195412
96. Djuric, T.; Ules, T.; Flesch, H.-G.; Plank, H.; Shen, Q.; Teichert, C.; Resel, R.; Ramsey, M. G. *Cryst. Growth Des.* **2011,** *11,* 1015–1020. doi:10.1021/cg101230j
97. Käfer, D.; Witte, G. *Chem. Phys. Lett.* **2007,** *442,* 376–383. doi:10.1016/j.cplett.2007.06.006
98. Fukagawa, H.; Yamane, H.; Kataoka, T.; Kera, S.; Nakamura, M.; Kudo, K.; Ueno, N. *Phys. Rev. B* **2006,** *73,* 245310. doi:10.1103/physrevb.73.245310
99. Kera, S.; Ueno, N. *J. Electron Spectrosc. Relat. Phenom.* **2015,** *204,* 2–11. doi:10.1016/j.elspec.2015.07.007
100. Yoshida, H.; Sato, N. *Phys. Rev. B* **2008,** *77,* 235205. doi:10.1103/physrevb.77.235205
101. Yamane, H.; Kera, S.; Okudaira, K. K.; Yoshimura, D.; Seki, K.; Ueno, N. *Phys. Rev. B* **2003,** *68,* 033102. doi:10.1103/physrevb.68.033102
102. Aghdassi, N.; Wang, Q.; Ji, R.-R.; Wang, B.; Fan, J.; Duhm, S. *Nanotechnology* **2018,** *29,* 194002. doi:10.1088/1361-6528/aab0c8
103. Kashimoto, Y.; Yonezawa, K.; Meissner, M.; Gruenewald, M.; Ueba, T.; Kera, S.; Forker, R.; Fritz, T.; Yoshida, H. *J. Phys. Chem. C* **2018,** *122,* 12090–12097. doi:10.1021/acs.jpcc.8b02581
104. Bürker, C.; Franco-Cañellas, A.; Broch, K.; Lee, T.-L.; Gerlach, A.; Schreiber, F. *J. Phys. Chem. C* **2014,** *118,* 13659–13666. doi:10.1021/jp503046w
105. Lee, T.-L.; Duncan, D. A. *Synchrotron Radiat. News* **2018,** *31,* 16–22. doi:10.1080/08940886.2018.1483653

License and Terms

The definitive version of this article is the electronic one which can be found at: https://doi.org/10.3762/bjnano.11.120

BEILSTEIN JOURNAL OF NANOTECHNOLOGY

Self-assembly and spectroscopic fingerprints of photoactive pyrenyl tectons on *h*BN/Cu(111)

Domenik M. Zimmermann[1], Knud Seufert[1], Luka Đorđević[2], Tobias Hoh[1], Sushobhan Joshi[1], Tomas Marangoni[3], Davide Bonifazi*[2,4] and Willi Auwärter*[1]

Full Research Paper

Address:
[1]Physics Department E20, Technical University of Munich, James-Franck-Straße 1, D-85748 Garching, Germany, [2]The School of Chemistry, Cardiff University, UK-CF10 3AT Cardiff, United Kingdom, [3]Department of Chemical and Pharmaceutical Sciences, University of Trieste, I-34127 Trieste, Italy and [4]Institute of Organic Chemistry, Faculty of Chemistry, University of Vienna, Währinger Str. 38, 1090 Vienna, Austria

Email:
Davide Bonifazi* - davide.bonifazi@univie.ac.at; Willi Auwärter* - wau@tum.de

* Corresponding author

Keywords:
electronic structure; hexagonal boron nitride; optical properties; pyrene; self-assembly

Beilstein J. Nanotechnol. **2020,** *11,* 1470–1483.
https://doi.org/10.3762/bjnano.11.130

Received: 13 May 2020
Accepted: 03 September 2020
Published: 29 September 2020

This article is part of the thematic issue "Molecular assemblies on surfaces – towards physical and electronic decoupling of organic molecules".

Guest Editor: S. Maier

Abstract

The controlled modification of electronic and photophysical properties of polycyclic aromatic hydrocarbons by chemical functionalization, adsorption on solid supports, and supramolecular organization is the key to optimize the application of these compounds in (opto)electronic devices. Here, we present a multimethod study comprehensively characterizing a family of pyridin-4-ylethynyl-functionalized pyrene derivatives in different environments. UV–vis measurements in toluene solutions revealed absorption at wavelengths consistent with density functional theory (DFT) calculations, while emission experiments showed a high fluorescence quantum yield. Scanning tunneling microscopy (STM) and spectroscopy (STS) measurements of the pyrene derivatives adsorbed on a Cu(111)-supported hexagonal boron nitride (*h*BN) decoupling layer provided access to spatially and energetically resolved molecular electronic states. We demonstrate that the pyrene electronic gap is reduced with an increasing number of substituents. Furthermore, we discuss the influence of template-induced gating and supramolecular organization on the energies of distinct molecular orbitals. The selection of the number and positioning of the pyridyl termini in tetrasubstituted, *trans*- and *cis*-like-disubstituted derivatives governed the self-assembly of the pyrenyl core on the nanostructured *h*BN support, affording dense-packed arrays and intricate porous networks featuring a kagome lattice.

Introduction

Atomic-level control of molecular materials at interfaces is crucial to fully exploit the materials' potential in electronic, optoelectronic, spintronic, and sensing applications [1,2]. Specifically, the effects of adsorption, conformation, and supramolecular organization on the resulting electronic and optical properties of molecular tectons and the respective assemblies must be comprehensively characterized [3-6]. Diverse self-assembly protocols have been extensively explored on metal substrates, and organic–metal interfaces have been analyzed in great detail [7,8]. In many cases, molecule–metal interactions can adversely affect the intrinsic electronic characteristics of molecular adsorbates and quench the optical properties [9-13]. Consequently, recent studies aiming to characterize the relation of adsorption, supramolecular organization, and electronic and optical properties in organic layers relied on bulk insulator supports [14-16]. As a promising alternative to bulk insulators, ultrathin dielectric films can act as decoupling layers but maintain the possibility to perform STM and STS measurements [17]. Atomically-thin *h*BN sheets attracted considerable interest as such spacer layers [18] and can promote site-dependent decoupling and adsorption [19,20], yielding access to optical transitions [21] as well as allowing for orbital-resolved STM imaging [19,21-23]. For instance, *h*BN/Cu(111) [24-27] features a work function template with a moiré superstructure: Depending on the registry of the layer and substrate atoms, the surface is divided in areas of low and high local work function, denoted as "pores" and "wires", respectively [28-31]. In recent years, our group and others used *h*BN/Cu(111) to guide the self-assembly of porphyrins [28,32,33], decouple perylenetetracarboxylic dianhydride (PTCDA) aggregates [34], study interfacial charge transfer in binary phthalocyanine arrays [35], probe vibronic conductance in oligophenylenes [36], and control the charge state of F_{16}CoPc [37]. Studies focusing on the preparation of coordination networks [38], wires of polycyclic aromatic hydrocarbons [39], and graphene patches [40,41] were also performed on *h*BN/Cu(111). However, advanced supramolecular architectures, such as organic porous networks, have not been reported on either *h*BN/Cu(111) or other metal-supported *h*BN monolayers so far, in contrast to graphene [42-44] or bulk *h*BN [14,45,46].

Pyrene derivatives are excellent candidates to study the interplay of functionalization and supramolecular organization as the planar polycyclic aromatic core provides an extended π-system that can be readily substituted at distinct positions [47-54]. With prominent fluorescence properties, pyrene is often considered the "fruitfly of photochemists", and several materials have been prepared for applications in optoelectronic devices and organic electronics [47]. On metal surfaces under ultrahigh vacuum (UHV), unsubstituted [55] as well as functionalized pyrene derivatives [9,48,56-64] were employed as versatile tectons to engineer supramolecular [9,48,55-59,61-64] and covalent architectures [56,58-60,64]. On two-dimensional materials, pyrene serves as an anchor for noncovalent functionalization, e.g., to develop graphene platforms to be used in sensing applications [65-67] and to employ *h*BN monolayers for capturing aromatic organic pollutants [68]. On bulk insulators, it was, for instance, demonstrated how the optical properties of an adsorbed bispyrene derivative relate to the structural order of the assemblies [15].

In this paper, we address the effects of chemical substituents on the electronic and self-assembly properties of pyrene derivatives on a *h*BN/Cu(111) substrate. To this end, pyrenyl derivatives bearing four and two pyridin-4-ylethynyl substituents have been used to steer and control the self-assembly on *h*BN/Cu(111), including the formation of dense-packed arrays and intricate kagome networks. The resulting structures deviate in part from the assemblies previously studied on Ag(111) [48]. Additionally, the *h*BN decoupling layer allows the determination of the electronic properties of the pyrene adsorbates by STM and STS", and the comparison with the gaps estimated by theoretical simulations in vacuum and by UV-vis spectroscopies in solution. Remarkably, the electronic states of the pyrene adsorbates near the Fermi level, probed at the submolecular level via STM and STS, e.g., reveal to be close to the gas-phase-like frontier orbitals.

The electronic landscape of the *h*BN/Cu(111) template induces a periodic modulation of the electronic structure of the pyrene films at the single digit nanometer scale. The on-surface STM/STS experiments, the photophysical characterization in solution, and the DFT modeling (in vacuum and with toluene solvation) evidence a reduction of the molecular gap when proceeding from di- to tetrasubstituted pyrene derivatives, but with effects that are different depending on the chemical surrounding.

Results

Structural and electronic properties in vacuum

The pyrenyl derivatives studied in this work are shown in Figure 1a and have been prepared following previous synthetic protocols [48]. The highest molecular symmetry is given by the tetrasubstituted species **1**, namely 1,3,6,8-tetrakis(pyridin-4-ylethynyl)pyrene. Reducing the number of substituents to two reduces the molecular symmetry, and concomitantly introduces interesting new properties, leading to prochiral *trans*-like-substituted 1,6-bis(pyridin-4-

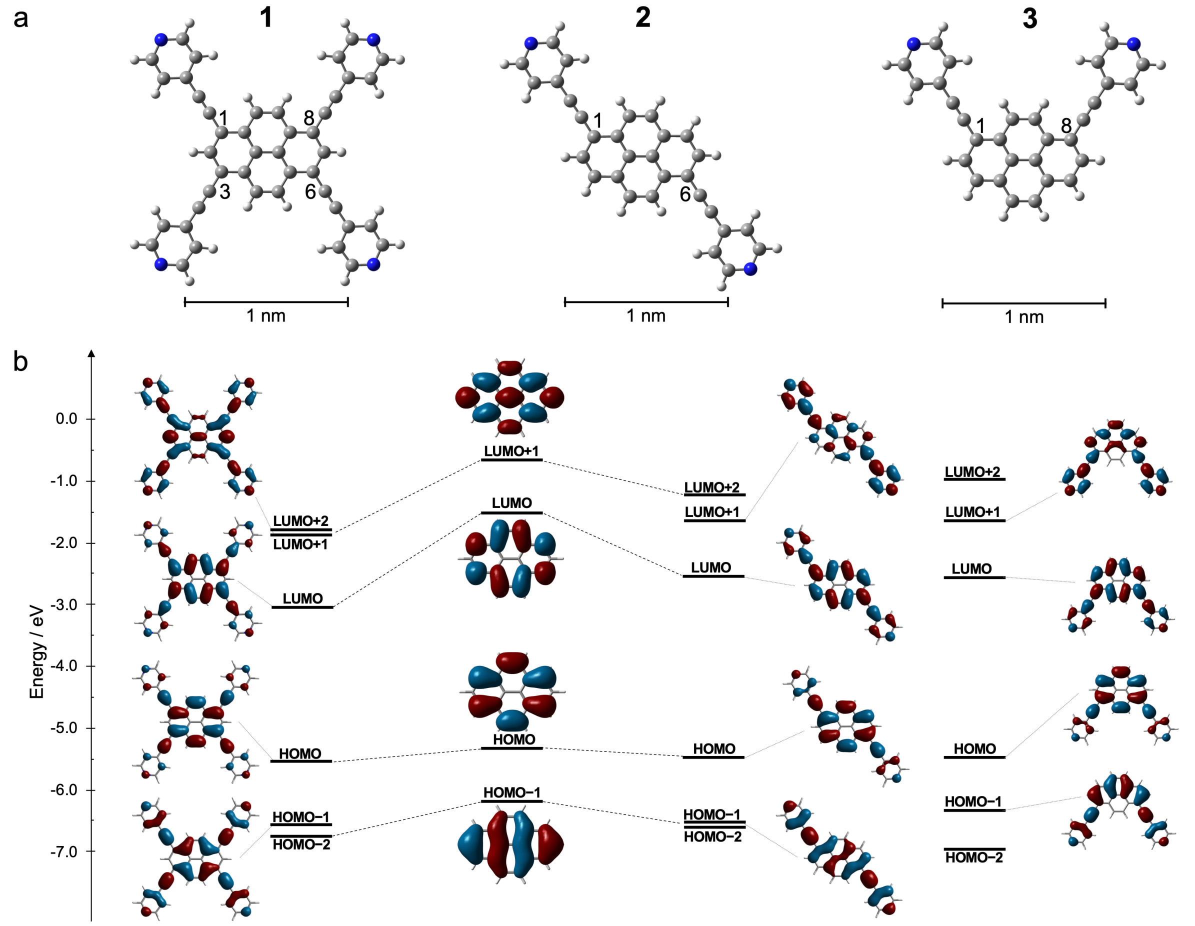

Figure 1: Functionalized pyrene derivatives investigated in this work (DFT-optimized geometries in the gas phase). a) Structure of 1,3,6,8-tetrakis(pyridin-4-ylethynyl)pyrene (**1**, *tetra*), 1,6-bis(pyridin-4-ylethynyl)pyrene (**2**, *trans*-like), and 1,8-bis(pyridine-4-ylethynyl)pyrene (**3**, *cis*-like). Element colors: N (blue), C (grey), H (white). b) Schematic drawing of the frontier Kohn–Sham orbitals for the tetra-, *trans*-like-, and *cis*-like-pyridyl–ethynyl-substituted pyrene derivatives **1**, **2**, and **3**, together with an orbital correlation diagram in comparison to the molecular orbitals (MOs) for pyrene itself, at the B3LYP/6-31G** level of theory.

ylethynyl)pyrene (**2**) and polar *cis*-like-substituted 1,8-bis(pyridin-4-ylethynyl)pyrene (**3**).

To evaluate the effect of the substitution on the electronic properties of the pyrene core, DFT calculations were performed (B3LYP/6-31G** level of theory, in vacuum). The frontier Kohn-Sham orbitals of pyrene and the di- and tetrasubstituted (pyridin-4-ylethynyl)pyrenes **1**, **2**, and **3** are shown in Figure 1b (see also Figures S1–S5, Supporting Information File 1). The computations revealed that the pyrenes have large orbital coefficients at the 1-, 3-, 6-, and 8-positions, with the nodal plane going through the 2- and 7-positions (Figure 1) [69-74]. As a consequence of this spatial distribution, the orbital interactions between the pyrene and the pyridin-4-ylethynyl MOs had a stabilizing effect on the highest occupied (HOMO) and lowest unoccupied molecular orbital (LUMO) energy levels. While the HOMO stabilization played only a small part, it was the considerable lowering of the LUMO energy levels that governed the shrinking of the HOMO–LUMO gap upon the derivatization with pyridin-4-ylethynyl groups. The picture of the orbital interactions was similar in the di- and tetrapyrenyl derivatives, with the HOMO–LUMO gap being influenced mostly by the number of substituents. The molecular gap of the tetrasubstituted pyrene **1** (2.54 eV) became narrower than that of the disubstituted pyrenes **2** and **3** (2.95 eV and 2.94 eV, respectively). This was in accordance with our experimental findings (vide infra) and previous literature reports [70,71,74].

Molecular self-assembly on *h*BN/Cu(111)

Tetrasubstituted pyrene

Depositing the tetrapyridylpyrene derivate **1** onto *h*BN/Cu(111) at room temperature and subsequent cooling to 6 K gave rise to the formation of extended well-ordered islands even in the submonolayer regime (Figure 2). Imaging these islands at specific sample bias voltages simultaneously showed two patterns with distinct periodicities and symmetries. The rectangular

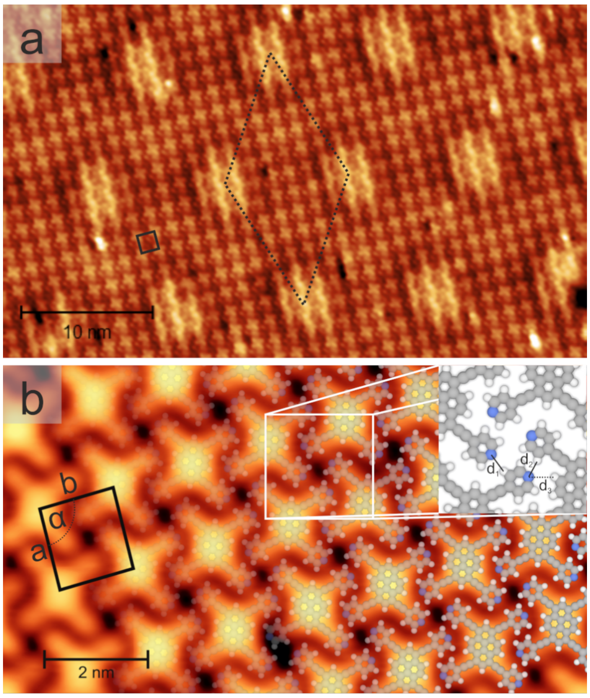

Figure 2: Self-assembly of 1,3,6,8-tetrakis(pyridin-4-ylethynyl)pyrene (**1**, *tetra*) on hBN/Cu(111), as imaged by STM. a) Overview image (2.0 V, 0.1 nA). The moiré pattern of the underlying hBN/Cu(111) caused site-selective gating, as reflected in the hexagonal superlattice in the image (dotted rhombus). b) High-resolution image (0.1 V, 0.2 nA), partially overlaid by structural models. The black tetragon marks the unit cell (lattice vectors *a* and *b*) and the white square highlights the intermolecular interactions (see inset).

lattice of the X-shaped units corresponded to a densely-packed molecular array (black tetragon in Figure 2), with every unit representing one molecule. The quasihexagonal pattern with larger periodicity (dotted rhombus in Figure 2a) reflected a modulation of the molecular electronic structure imposed by the electronically corrugated *h*BN/Cu(111) support, as discussed in detail below [18,28,37,38]. The high-resolution STM data in Figure 2b gives a closer look at the intramolecular features. Along with the pyrene core, imaged as a large, elongated protrusion, four additional lobes contributed to the X-shaped appearance of the molecular units of **1**. Each of these peripheral protrusions was attributed to one pyridin-4-ylethynyl substituent. Atomistic models (see overlays in Figure 2b), reflecting the gas-phase optimized molecular structure, matched the submolecular contrast in the STM images, and thus supported this assignment. Based on this comparison, we ruled out strong adsorption-induced deformations of the molecule and concluded that the pyrene core adsorbed mostly flat, i.e., the π-conjugated core aligned parallel to the *h*BN sheet. This assembly could be described by a nearly rectangular unit cell including one molecule (see black tetragon in Figure 2b, a_{tetra} = 1.63 nm ± 0.05 nm, b_{tetra} = 1.50 nm ± 0.05 nm, and α_{tetra} = 92° ± 2°). Accordingly, the surface molecular density $\rho_{\mathrm{tetra}/h\mathrm{BN}}$ of molecule **1** amounted to 0.41 molecules/nm^2. The molecules interdigitated in both the a_{tetra} and b_{tetra} directions, with two distinct interdigitation arrangements, inducing organizational chirality of the achiral pyrene units [48]. Based on the model of the assembly depicted in Figure 2b, the array was stabilized by intermolecular noncovalent interactions, including N···H bonds. Distinct organizational motifs could be discriminated (see inset of Figure 2b). The terminal N atom of one molecule could either establish H-bonding with a hydrogen atom of an adjacent pyridyl moiety of a neighboring molecule (link labeled d_1 in Figure 2b, projected N···H bond length 0.29 nm ± 0.05 nm) or was positioned in the hydrophobic pocket between the pyridyl group and the pyrene core of an adjacent molecule (see d_2 and d_3).

trans-like-disubstituted pyrene

Figure 3 shows the STM images of the surface after the deposition of the *trans*-like-disubstituted pyrene derivative **2** on *h*BN/Cu(111). The molecules form open porous networks, featuring a kagome lattice architecture with cavities of two distinct sizes and shapes [42,48,75,76]. At the bias voltage used in Figure 3, the substrate-induced contrast modulation (see below Figure 5c) was not observed. The pyrene **2**, being prochiral, becomes chiral upon surface adsorption [61,77,78], and two stereoisomers can equally be formed on the surface.

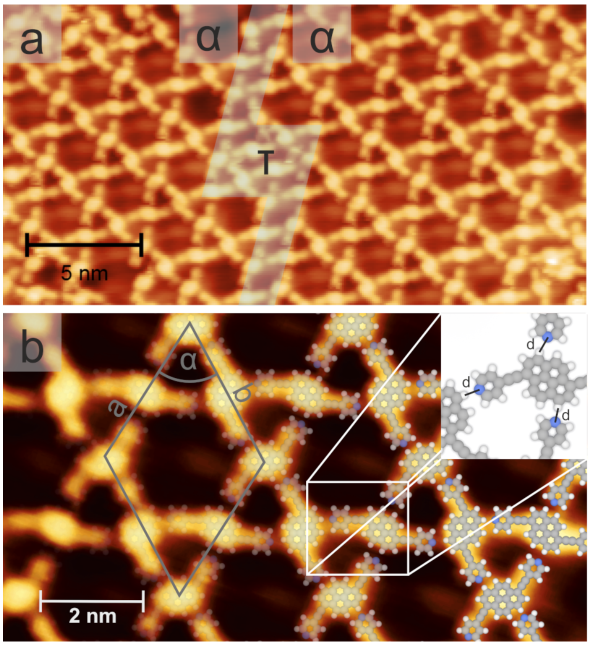

Figure 3: Self-assembly of 1,6-bis(pyridin-4-ylethynyl)pyrene (**2**, *trans*-like) on *h*BN/Cu(111). a) Overview image (1.0 V, 0.1 nA). Two homochiral domains (α) with an open porous kagome structure are connected by a narrow transition region (τ). b) High-resolution STM image (1.0 V, 0.1 nA), partially overlaid by structural models. The grey rhombus shows the unit cell and the white square highlights the intermolecular interactions, represented by the distances *d* in the inset.

Each enantiomer segregates into homochiral domains (α and α‘, see Figure 3 and Figure S6, Supporting Information File 1). The lateral extension of the regular, defect-free arrays is usually rather limited (<30 nm), with the narrow transition regions τ representing dislocations (Figure 3a) or mirror domain boundaries (Figure S6, Supporting Information File 1). STM images resolving individual molecules (Figure 3b) revealed a bright protrusion, attributed to the pyrene core, centered between two peripheral lobes, assigned to the pyridin-4-ylethynyl substituents (see structural models in Figure 3b). The unit cell of the kagome lattice is visualized by the grey rhombus in Figure 3b ($a_{\text{trans}} = b_{\text{trans}} = 3.0$ nm ± 0.07 nm, $\alpha_{\text{trans}} = 60° \pm 2°$) and contains three molecules. The molecular surface density amounted to about 0.38 molecules/nm^2, and thus was lower than that of the derivative **1**. The formation of this kagome network was mediated by the formation of intermolecular H-bonds between the pyridyl ligands and the adjacent pyrene cores, with a projected N···H bond length of 0.21 nm ± 0.05 nm (labeled as *d* in Figure 3b). For each chirality, six distinct rotational orientations of the *trans*-like molecule **2**, separated by 30°, were observed on *h*BN/Cu(111) (not shown). Although rare, coexisting densely packed arrays could be detected near the step edges (see Figure S7, Supporting Information File 1).

cis-like-disubstituted pyrene

The deposition of the *cis*-like-disubstituted pyrene derivative **3** on *h*BN/Cu(111) at submonolayer coverage yielded extended, densely packed islands featuring straight edges. Figure 4a shows an STM image recorded at a bias voltage where both the molecular lattice and the substrate-induced long-range modulation of the electronic structure are resolved (compare to Figure 2a). High-resolution data (Figure 4b) allowed us to discern individual molecules with submolecular features. Each molecule was characterized by three protrusions, which corresponded to the central pyrene and the two peripheral pyridin-4-ylethynyl substituents, respectively. Two oppositely oriented molecules formed an interdigitated dimeric motif (highlighted by the yellow outlines in Figure 4b) that involved N···H interactions between the pyridyl moieties (d_2 = 0.30 nm ± 0.05 nm, inset of Figure 4b). These dimers formed rows, where one N atom of each unit was oriented towards the pyrene core of a neighboring dimer. This noncovalent interaction was described by the distance d_1 (0.28 ± 0.05 nm, inset of Figure 4b). Multiple rows, aligned in parallel, with a well-defined registry, constituted the extended islands. As no pyridinic N atom was directly involved in the interrow interaction, the stabilization of the islands was attributed to van der Waals forces. The straight edges reflected the row structure of the islands (see Figure 4a). The unit cell of the assembly (grey rectangle in Figure 4b, a_{cis} = 2.27 nm ± 0.07 nm, b_{cis} = 1.57 nm ± 0.05 nm, α_{cis} = 90° ± 2°) contained two molecules, resulting in a molecular surface density of 0.56 molecules/nm^2. The dimer of species **3** occured in two interdigitation arrangements [48], giving rise to mirror domains, reflecting organizational chirality. Overall, six distinct rotational orientations of the *cis*-like pyrene molecule **3**, separated by 60°, were observed on *h*BN/Cu(111) (not shown).

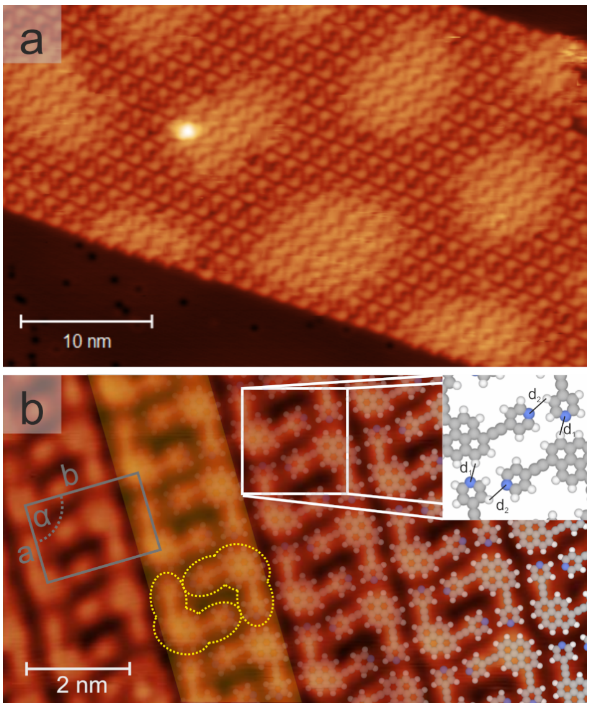

Figure 4: Self-assembly of 1,8-bis(pyridin-4-ylethynyl)pyrene (**3**, *cis*-like) on hBN/Cu(111). a) Overview image (1.38 V, 0.024 nA). Regular islands were formed after rt deposition. Several rows, each containing molecules in two opposite orientations, formed a ribbon-like assembly. The hexagonal moiré pattern of the underlying hBN/Cu(111) was visualized by site-selective gating. b) High-resolution image (1.0 V, 0.27 nA) partially overlaid with the corresponding structural models. The grey rectangle shows the unit cell and the white square highlights the intermolecular bonding of the substituents, schematically represented in the inset. A dimeric motif is marked by the yellow outline, with a dimer row shaded in yellow.

Binary assemblies

The combination of different pyrene derivatives opens pathways to distinct multicomponent assemblies on *h*BN/Cu(111). For example, the sequential deposition of the *cis*-like derivative **3** and the *trans*-like pyrene **2** afforded binary architectures, including regular densely packed arrays and kagome networks hosting the species **3** in the large cavities (Figure S8, Supporting Information File 1).

Scanning tunneling spectroscopic measurements

Next, the electronic structure of the functionalized pyrene derivatives **1–3** on *h*BN/Cu(111) was addressed. Specifically, we performed bias-dependent STM imaging and dI/dV spectroscopy to probe the influence of the substitution, in conjunction with the distinct assemblies, on the molecular electronic states. Additionally, the role of the electronic landscape of the *h*BN/Cu(111) support, inducing a periodic modulation of the pyrene electronic structure via site-selective gating, is highlighted. Figure 5 shows a series of dI/dV spectra recorded above the molecular centers of the pyrene derivative **1** (Figure 5b), **2** (Figure 5d), and **3** (Figure 5f) at different adsorption positions on *h*BN/Cu(111), as indicated by grey markers in the corresponding STM images in Figure 5a, 5c, and 5e, respectively. The spectra of all three compounds revealed well-defined features in the occupied (negative sample bias) and unoccupied (positive sample bias) spectral regions. Tentatively, the characteristic signatures were assigned to the HOMO, LUMO, and LUMO+1.

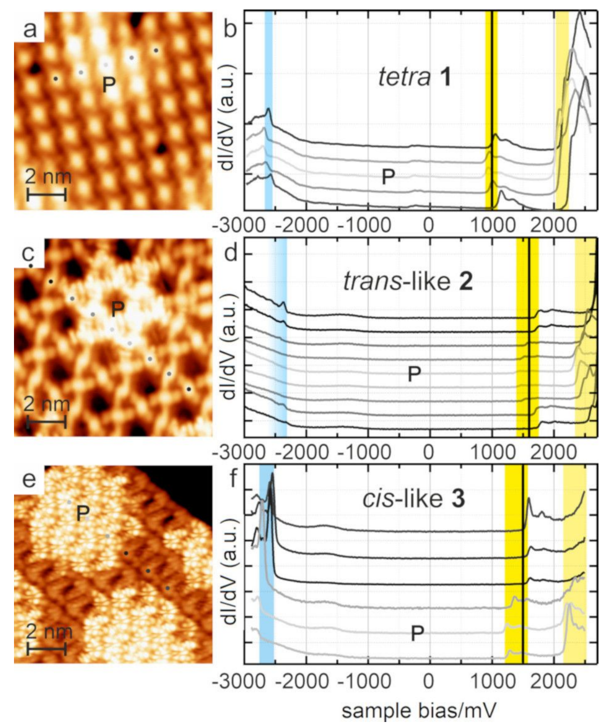

Figure 5: dI/dV signatures of the pyrenes **1–3** on *h*BN/Cu(111) and template-induced gating. a), c), and e) STM images of the *tetra*, *trans*-like, and *cis*-like pyrenes on *h*BN, taken at a sample bias at the onset of an unoccupied MO (a: 1 V, 0.04 nA; c: 1.6 V, 0.2 nA; and e: 1.5 V, 0.1 nA). The bright areas represent the pore regions of the *h*BN/Cu(111) support. b), d), and f) dI/dV spectra recorded on the center of molecules at the position of the grey dots in a), c), and e). The darker the color of the dot and the corresponding spectrum, the larger the lateral distance to the *h*BN pore. HOMO, LUMO, and LUMO+1 are indicated by blue, yellow, and light yellow boxes, respectively. Black vertical lines reflect the sample bias voltage of the corresponding STM image (tip stabilization parameters–b: 0.8 V, 0.25 nA; d: 2.7 V, 0.2 nA; and f: 2.5 V, 0.2 nA).

The colored bars in Figure 5 highlight the energy positions of these frontier orbitals (determined as the bias voltage at the half maximum of the MO leading edge). The observation of well-defined, narrow molecular resonances and large HOMO–LUMO gaps evidenced a reduction of the electronic molecule–support interactions by the *h*BN spacer layer, as previously reported for adsorbates on *h*BN/Cu(111) [28,35-38] and other *h*BN/metal supports [18-20,79,80]. The dI/dV modulations observed within the gap were attributed to the *h*BN/Cu(111) support and tip states, respectively (vide infra).

A closer look at the dI/dV spectra in Figure 5b, 5d, and 5f revealed a site-dependent shift of the molecular resonances (MOs), an effect attributed to site-selective gating by the underlying *h*BN/Cu(111) support. This template featured a moiré pattern with areas of low local work function (pores, P) and high local work function (wires, W) [25,29,30], which was reflected by the molecular level alignment, as measured by dI/dV spectroscopy [28,35-37]. On pore areas, the MOs were shifted downwards (i.e., towards the Fermi level (E_F) for unoccupied states, and away from E_F for occupied states) compared to the wire areas. The grayscale of the spectra in Figure 5 reflect the proximity to a pore, with light grey indicating adsorption on pore areas and dark grey reflecting adsorption on (or near) wire areas. Accordingly, the periodic modulation of the pyrene electronic structure induced by the moiré pattern of the underlying *h*BN/Cu(111) could directly be visualized in STM images recorded at suitable sample bias voltages (see Figure 2a, Figure 4a and Figure 5a, 5c, 5d, as well as Figures S9 and S10, and the movie in Supporting Information File 2). At bias voltages (see vertical black lines in Figure 5b, 5d, and 5f) where a specific MO could only contribute to the tunneling current in the pore areas, a contrast between the pore and the wire areas emerged in the STM images, with the molecules on the pores featuring an increased apparent height and a modified submolecular contrast (vide infra).

Next, the dI/dV signature of the tetrasubstituted pyrene derivative **1** (Figure 5b) was in the focus. A site-dependent shift was evident for all MOs: The LUMO energy ranged from about 0.89 V (P) to 1.11 V (W), revealing a shift of ≈0.22 V, as highlighted by the width of the yellow box in Figure 5b. A similar shift (≈0.23 V) was observed for the LUMO+1. The HOMOs were observed at voltages between −2.54 V (W) and −2.66 V (P, width of the blue box ≈ 0.13 V). Thus, for the species **1**, the spectra revealed STM-derived HOMO–LUMO gaps of 3.64 eV (in the pore areas) and 3.56 eV (in the wire areas). The wire spectrum for the molecule **1** was recorded at a larger distance from the real wire position, as compared to **2** and **3** (see Figure 5a, 5c, and 5e). The voltage-dependent STM contrast and the site-dependent variation of spectral features described above for the derivative **1** was analogously observed for the derivatives **2** and **3** (see blue and yellow boxes in the Figure 5(d and f). However, the MOs occurred at energies characteristic for the three different pyrene species, yielding distinct STS gaps, as summarized in Figure 6a.

Figure 7 shows the high-resolution STM images of the pyrene derivatives **1** and **3** recorded at bias voltages where the MOs were accessible. In contrast to imaging at bias voltages within the HOMO–LUMO gap, where the STM images essentially reflect the molecular shape (Figure 2b, Figure 3b, and Figure 4b) [17], distinct intramolecular features of electronic origin emerged (see also Figure S12, Supporting Information File 1). A comparison to the Kohn–Sham orbitals (see Figure 1) and to the frontier orbitals calculated in the EHT scheme (see insets in Figure 7) revealed striking similarities. For example, the number of antinodes as well as the nodal planes between the experimental images and the calculations were in agreement, strongly suggesting that the STM contrast indeed reflected the MO contributions, corroborating the assignment of spectral features to the HOMOs and the LUMOs. Furthermore, the agreement between the gas-phase calculations and STM data indicated that no charging occurred upon pyrene adsorption on *h*BN/Cu(111) [37].

To complement the on-surface investigations, we measured the optical gap by means of UV–vis spectroscopic characterization in solution (toluene) of the *trans*-like and tetrasubstituted pyrenyl derivatives (Figure 8a and Figure 8b). The *cis*-substituted pyrene **3** showed a lower solubility in solvents such as toluene, and therefore the optical properties could not be measured, although (TD)DFT calculations indicated a similarity to the *trans*-like isomer (Figure S3 and Tables S1–S3, Supporting Information File 1). The absorption spectrum of the

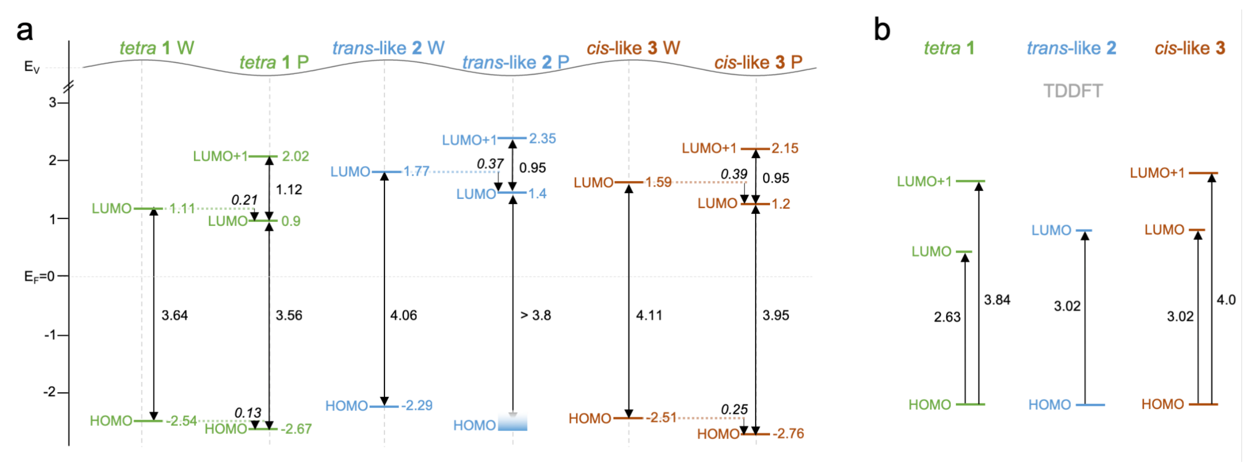

Figure 6: Diagrams summarizing the spectroscopic values determined for the pyrene derivatives **1**–**3**. a) STS data for *h*BN/Cu(111), sketching the energy level alignment (compare to Figure S11, Supporting Information File 1). b) Time-dependent DFT (TDDFT)-calculated excitation energy in explicit solvent reflecting the UV–vis measurements in toluene solution (see Tables S1–S3). The units are in Volt. P: pore area, W: wire area.

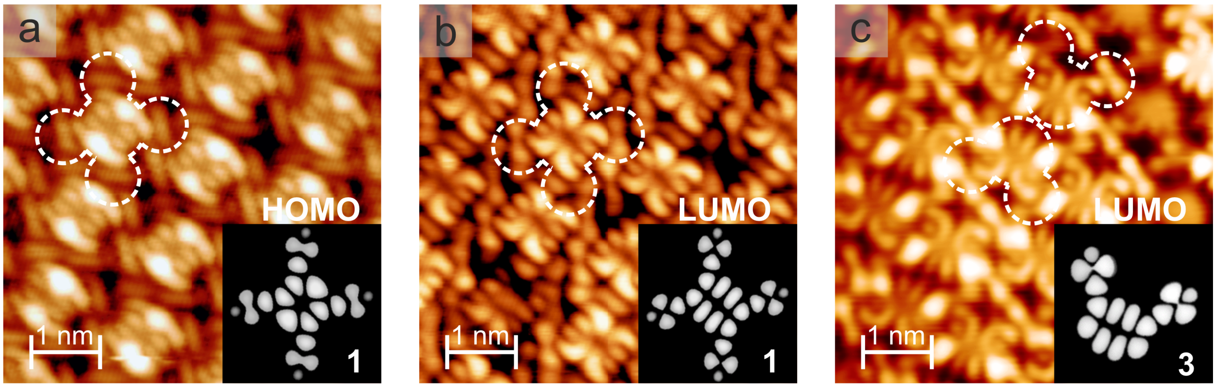

Figure 7: High-resolution STM images revealing the bias-dependent intramolecular contrast of the pyrene derivatives **1** and **3** on *h*BN/Cu(111), recorded with a tip of unknown termination. a) Array of the tetrasubstituted species **1** imaged at a bias voltage of −2.87 V (0.06 nA) and b) at 1.4 V (0.04 nA). c) Assembly of the *cis*-like derivative **3**, imaged at 1.5 V (0.27 nA). The dashed contours highlight the individual molecules. The insets show the EHT-calculated MOs corresponding to the HOMO (a) and the LUMO (b and c) of the free molecule (compare to Figure 2).

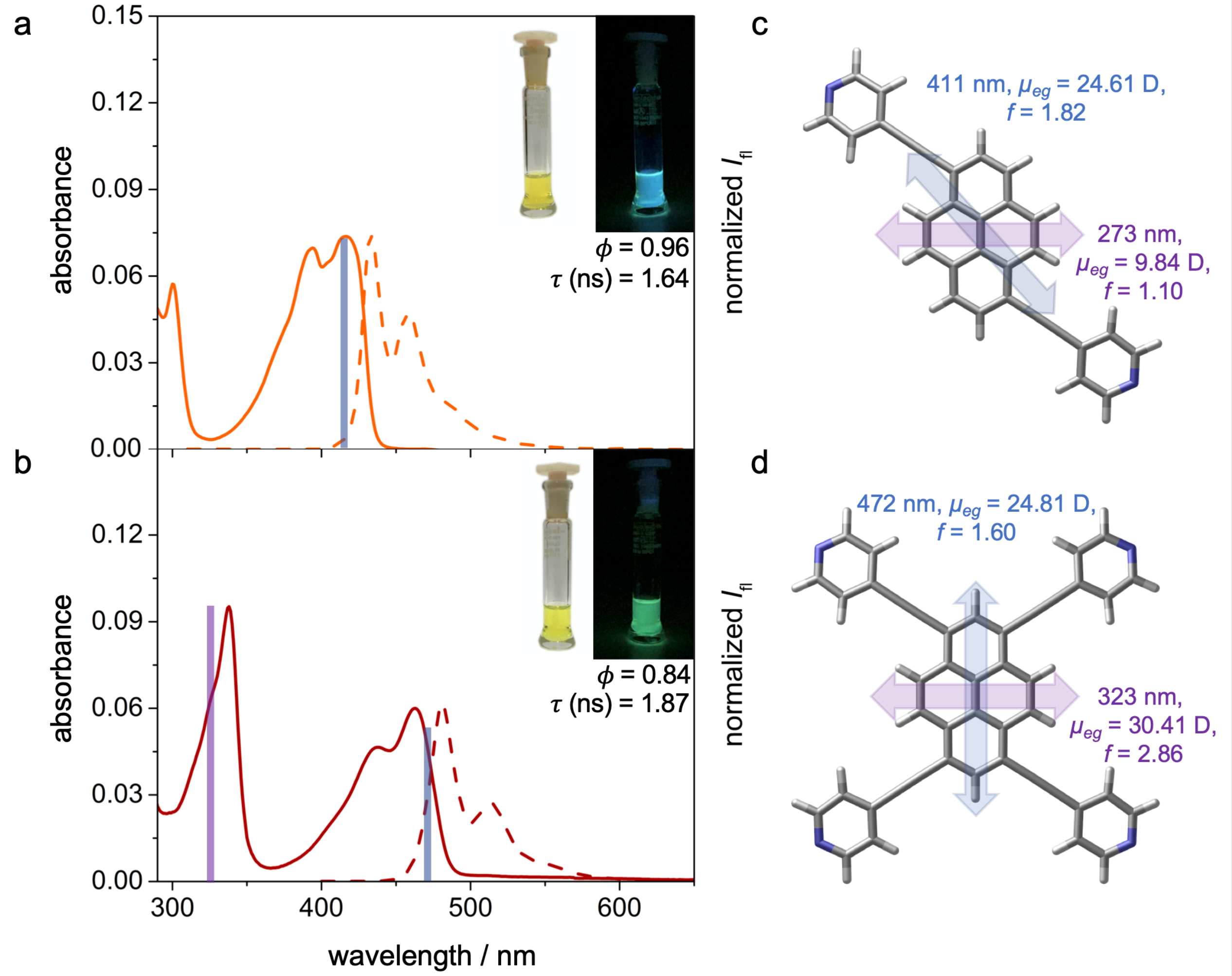

Figure 8: Optical characterization. a) and b) UV–vis absorption (solid line) and emission spectra (dotted line) of the *trans*-like (a, orange line) and tetrasubstituted (b, red line) pyrenyl derivatives in toluene (c = 1.0 × 10^{-6} M) at rt. Insets: photographs of toluene solutions in daylight and upon irradiation with a hand-held UV lamp (λ_{ex} = 365 nm). c) and d) Calculated transitions (blue and purple lines), transition dipole moments (μ_{eg}), and oscillator strengths (f), as determined by TDDFT (CAM-B3LYP, 6-31G**, explicit solvent: toluene).

trans-substituted pyrene **2** showed two main absorption peaks centered at 416 and 394 nm (2.98 and 3.15 eV, respectively), with another lower-absorption transition at a higher energy (300 nm, 4.13 eV). The selective excitation of the low-energy absorption peak lead to a strong emission at 433 and 458 nm (2.86 and 2.71 eV), with a quantum yield of 96% (determined using coumarin 153 in an EtOH solution as a reference). As expected, the tetrasubstituted pyrene **1** showed electronic transitions that were bathochromically shifted to higher wavelengths, with two main bands observed at 463 and 438 nm (2.68 and 2.83 eV) and one at a higher energy at 338 nm (3.67 eV). The excitation of the lowest-energy bands also led to a strong emissive band, centered at 481 and 513 nm (2.58 and 2.42 eV), with a quantum yield of 84%. The same optical transitions seemed to be involved in both the absorption and emission processes, as confirmed by a mirror symmetry of the fluorescent spectral envelope compared to the lowest-energy absorption transitions. Moreover, the small Stokes shifts (17 and 18 nm for the *trans*- and tetrasubstituted pyrene derivatives, respectively) confirmed the fact that for both structures, the ground and excited states were similar, while the matching excitation and absorption spectra pointed at an efficient radiative deactivation of the excited state (Figure S13, Supporting Information File 1) [71].

TDDFT calculations (CAM-B3LYP/6-31G**, toluene CPCM solvation) [69,73] were further performed, and the results are summarized in Figure 8c, Figure 8d, and Tables S1–S3. The main transitions for the *trans*-pyrene seemed to originate from the HOMO→LUMO transition (estimated at λ = 411 nm (3.02 eV), f = 1.82) and the HOMO−1→LUMO/HOMO→LUMO+2 transitions (estimated at λ = 273 nm (4.54 eV), f = 1.10), with the transition dipole moments aligned along the 1- and 6-positions (towards the pyridin-4-ylethynyl termini) and the short molecular axes of the central pyrene core.

On the other hand, the tetrapyrenyl transition dipole moments were aligned along the long and short molecular axes of the pyrene core, with the two main transitions having HOMO→LUMO (estimated at λ = 472 nm (2.63 eV), *f* = 1.60) and HOMO−1→LUMO/HOMO→LUMO+1 contributions (estimated at λ = 323 nm (3.84 eV), *f* = 2.84).

Discussion

Self-assembly

In this section, we will put forward a comparative discussion of the self-assembly of pyridin-4-ylethynyl-functionalized pyrenes on *h*BN/Cu(111) and on Ag(111) [48]. The molecular density of tetrapyridylpyrene **1** in arrays on *h*BN/Cu(111) was higher compared to Ag(111) ($\rho_{\text{tetra}/h\text{BN}}$ = 0.41 molecules/nm^2 vs $\rho_{\text{tetra/Ag}}$ = 0.37 molecules/nm^2). Accordingly, distinct differences were observed in the unit cell dimensions and the intermolecular alignment, even though the N···H interactions contributed to the self-assembly in both cases. At the same time, the intermolecular distance along the unit cell vector *b* was similar on *h*BN/Cu(111) and Ag(111), the separation along the unit cell vector *a* was clearly reduced on *h*BN, reflecting the minimum energy interdigitation configuration, determined by basic molecular mechanics modeling for two modules of **1** in the gas phase. Thus, we tentatively assigned the higher packing density on *h*BN to the reduced site-specific molecule–support interactions. Indeed, distinct registries of the derivative **1** on the Ag(111) atomic lattice were reported [48]. However, additional effects potentially perturbing the intermolecular alignment, such as subtle differences in the pyridine tilt angle (out of the surface plane), could not be excluded based on our experimental observations. The kagome-like porous network architectures formed by the *trans*-like-disubstituted pyrene derivative **2** on *h*BN/Cu(111) and Ag(111) matched within the experimental precision. Accordingly, in contrast to the derivative **1**, no effect of a reduced site-specific molecule–support interaction was discernible for the derivative **2**. Thus, we speculate that the unit cell of an unsupported supramolecular structure, being close to the one observed on *h*BN, can be accommodated on the Ag(111) atomic lattice, where a commensurate structure was reported [48].

The assembly of densely packed islands of the *cis*-like-disubstituted pyrene derivative **3** on *h*BN/Cu(111) at a low coverage was in stark contrast to the formation of extended chains and disordered two-dimensional agglomerates on Ag(111) [48]. The prominent head-to-head coupling motif on Ag(111) was not observed on *h*BN. This corroborated previous assumptions about interactions of the pyridyl termini with Ag surface atoms mediating the chain formation [48]. The interdigitated dimeric motif and the row-like island structure observed on *h*BN/Cu(111), however, matched the findings in the monolayer regime on Ag(111). Accordingly, as for the *trans*-like pyrene **2**, the support played a minor role in the intralayer structure of the extended molecular arrays.

Nonetheless, the results for the pyrenes **1**–**3** on *h*BN/Cu(111) clearly demonstrated that the support did affect the rotational alignment of molecules and assemblies. As discussed for the *cis*- and *trans*-like isomers, the molecules were oriented along specific directions, separated by 60 or 30°, respectively. This suggested that the ethynyl-functionalized pyrene cores were aligned with the high-symmetry directions of the *h*BN/Cu(111) support, and thus yielded only distinct orientations of the supramolecular architectures. Indeed, DFT calculations have predicted the adsorption of the pyrene with the aromatic rings centered above the N-positions of a free-standing *h*BN sheet [81]. Preferred alignments have also been reported for low coverages of PTCDA and MnPc on the strongly corrugated *h*BN/Rh(111) support [21,22,80], with computational modeling showing PTCDA rings positioned above the N sites of a *h*BN flake [14]. In contrast, no preferred orientations have been identified for a hydrocarbon lander molecule (i.e., DBP) on *h*BN/Pt(111) [19].

The formation of extended domains for the pyrene derivatives **1**–**3** on *h*BN/Cu(111) even at a submonolayer coverage was reminiscent of findings for carbonitrile-functionalized porphyrins [38] and quaterphenylenes [36] but contrasted the site-selective adsorption on pore areas reported for TCNQ, porphines, and fluorinated phthalocyanines [28,33,37]. Taken all together, these observations demonstrated that distinct tectons with peripheral recognition moieties can afford the assembly of extended supramolecular architectures also on electronically superstructured *h*BN platforms.

Spectroscopic investigations and determination of the molecular gap

Both the STS studies addressing the adsorbed species on the single-molecule level and the optical spectroscopy in solution confirmed the gap reduction upon increasing the number of pyridin-4-ylethynyl substituents, as predicted by DFT calculations (Figure 6). Within the experimental uncertainty, the STM-derived HOMO–LUMO gap of the disubstituted species **2** and **3** was the same. Interestingly, however, the spectra of the *cis*-like derivative showed a rigid energy shift of ≈0.2 V for all MOs (the LUMO was shifted towards E_F and the HOMO away from E_F), compared to the *trans*-like species. Such a rigid shift can be caused by charges in the molecular layer (biasing nearby molecules) and by local modifications of the work function affecting the interfacial level alignment [9,35,82,83]. As the STM/STS experiments provided no indication of charging, we ruled out a dominating contribution of the former effect.

Instead, we tentatively assigned the rigid MO shift to the differences in the self-assembled structures, namely a densely packed arrangement for the derivative **3** and the porous structure for the derivative **2**. With the *h*BN/Cu(111) work function being modified upon molecular adsorption (Figure S11, Supporting Information File 1), open-porous structures would feature a smaller work function shift compared to densely packed molecular films. In the absence of charge transfer, the work function was assumed to decrease upon the adsorption of pyrenes on *h*BN/Cu(111) [84]. Accordingly, the derivate **3** would experience a lower average local work function than the derivate **2**, resulting in a downward shift of the MOs, as observed in the experiment (Figure 5 and Figure 6). Indeed, the molecular packing effect was corroborated by comparing the MO signatures of the molecule **2** in the porous and densely packed assemblies, respectively. In the latter, the MOs were centered at lower energies, similar to those observed for the densely packed islands of the species **3**. The HOMO–LUMO gap (≈4.1 V) was not considerably affected by the different molecular organization (see Figure S7d, Supporting Information File 1). In contrast to recent reports on F_{16}CoPc/*h*BN/Cu(111) [37] and PTCDA/NaCl/Ag(111) [83], an additional effect of the molecular aggregation and packing density, namely the screening by neighboring molecules, yielding a reduction of the STS-derived HOMO–LUMO gap, did not seem to play a dominant role here. The packing might have also influenced the adsorption geometry (registry, subtle conformational adaption) without manifestation in the experiments.

For all three pyrene derivatives, the calculated energy difference between the HOMO and the LUMO (Figure 1 and Figure S2, Supporting Information File 1) was considerably smaller than the one measured by STS (Figure 6a). This discrepancy was tentatively assigned to an underestimation of the gap by the applied DFT scheme. The energy difference between the calculated ionization potential (IP) and the electron affinity (EA) on the other hand exceeded the STS gap. The STS-derived separation between the LUMO and the LUMO+1 was reduced for the disubstituted species compared to the tetrasubstituted pyrene **1** (see Figure 6). This trend matched the DFT prediction (Figure 1) and was assigned to the stabilization of the LUMO for tetrasubstitution.

The template-induced gating by the electronic landscape of the *h*BN/Cu(111) similarly affected all three pyrene derivatives. The energy shift of the LUMO between the pore and wire areas (0.21 V for **1**, 0. 37 V for **2**, and 0.39 V for **3**, see Figure 6) agree well with the previously reported MO shifts on *h*BN/Cu(111) (ranging from 0.25 to 0.4 V [28,35-37]) and reflect the local work function variation across the moiré pattern [25,29,30]. In a recent study on F_{16}CoPc/*h*BN/Cu(111), we demonstrated that the local work function difference between the pore and wire regions was preserved upon molecular adsorption [37]. Note, that the smaller shift for the molecule **1** was attributed to the larger distance of the respective wire spectrum from the real wire position (vide supra). The shrinking of the HOMO–LUMO gap in the pore areas, consistently observed for the species **1**–**3**, was attributed to the increased molecule–support interactions in the pores [28], where the *h*BN was located closer to the Cu(111) support [29]. Accordingly, no rigid shift of the occupied and unoccupied molecular electronic states occurred, as reflected in the HOMO energy shifts (e.g., 0.25 V for **3**), falling below the LUMO shifts (see Figure 6). Dissimilar responses of distinct MOs to work function variations were previously discussed, e.g., for pentacene on dielectric decoupling layers [23].

The assignment of the dI/dV signature to the MOs was corroborated by resolving the submolecular features in high-resolution STM images at these bias voltages, reflecting the frontier orbitals of the free pyrenes (Figure 7 and Figure S12, Supporting Information File 1). Nonetheless, with additional features observed in the gap of the dI/dV spectra (see Figure 5b, 5d, and 5f), the unambiguity of such an identification needs to be addressed. The step-like increase in the dI/dV signal at ≈−350 meV (Figure 5b) reflected the electronic interface state of *h*BN/Cu(111) [25]. The support also accounted for the steadily increasing background contribution at negative bias voltages exceeding −2V (apparent in all spectra) [28,31,41].

A comparison between the values of the HOMO–LUMO gaps and the excitation energy obtained by STS and UV–vis absorption (see Figure 6) revealed that the optical gap seemed to be smaller than the electronic gap. This was expected due to the intrinsic differences in the measurement process of these gaps [85]. However, studies comparing orbital-resolved STM/STS data to optical gaps are scarce [86]. In addition to this effect, the adsorption and supramolecular organization on *h*BN could sensitively affect the optical transitions [14,16,21]. For example, the fluorescence peak energy of perylene derivatives was reduced considerably (0.3–0.4 eV) upon the adsorption on bulk-like *h*BN [14]. Accordingly, the gaps and excitation energy compiled in Figure 6 did not allow for a direct comparative assessment of the interaction of the pyrene derivatives with the environment on hBN or in solution.

Conclusion

In summary, we characterized the electronic and photophysical properties as well as the self-assembly abilities of a family of functionalized pyrenes bearing four and two pyridin-4-ylethynyl substituents. Specifically, UV–vis spectroscopic investigations in toluene solution and the dI/dV measurements at the vacuum/

solid interface showed that the electronic and optical gaps could be engineered by the number of substituents. This agrees with the DFT computations predicting a gap reduction when proceeding from unsubstituted pyrene cores to di- and tetrasubstituted derivatives. Applying an atomically thin *h*BN sheet as decoupling layer, the electronic structure of the pyrene derivatives was probed at the submolecular level, visualizing an MO-like contrast and evidencing effects of supramolecular organization. Importantly, three distinct molecular resonances could be detected, and the response to template-induced gating revealed weak molecule–support interactions. The STM data showed an electronic patterning of the pyrene films with periodicities in the single digit nanometer range. Furthermore, we provide a first case study for the self-assembly of advanced porous structures on *h*BN monolayers, introducing a chiral kagome-like architecture. These results gave unprecedented information on the spatially and energetically resolved molecular states of a photoactive polycyclic aromatic hydrocarbon on a solid support and highlight the potential to engineer interfacial electronic and optoelectronic properties by molecular design and surface organization.

Experimental

STM and STS

All scanning-probe experiments were performed in a custom-designed UHV system hosting a CreaTec low-temperature STM (CreaTec Fischer & Co. GmbH, createc.de) and providing a base pressure below 1×10^{-9} mbar. The monocrystalline Cu(111) substrate was cleaned by repeated Ar^+ sputtering cycles at an energy of 800–1000 eV, followed by annealing at 1070 K. Monolayer *h*BN was grown via chemical vapor deposition using borazine ($(HBNH)_3$, Katchem spol s.r.o, www.katchem.cz), following a protocol described previously [25]. Subsequently, a submonolayer coverage of the pyrene modules was deposited by organic molecular beam epitaxy from thoroughly degassed quartz crucibles held at 450–500 K. During deposition, the Cu(111) surface was kept at rt, and the pressure remained below 2×10^{-9} mbar. The STM images were acquired in constant current mode, with the sample being held at ≈6 K using electrochemically etched W tips. In the figure captions, voltages refer to the bias voltage applied to the sample. Differential conductance (dI/dV) spectra were recorded using the lock-in technique (f = 969 Hz, V_{rms}= 18 mV). Reducing the tip-sample distance by increasing the current by a factor of five for the pyrene derivative **1** had no significant effect on the measured gap. Very broad spectral features (e.g., the peaks around −1.43 V in Figure 5d and −1.65 V in Figure 5f) that did not shift considerably with the lateral position of the spectrum were attributed to the tip states and not to the pyrene-related molecular resonances.

Photophysical investigations

The toluene solutions of the *trans*- and tetrasubstituted pyrenes (ACS spectroscopic grade, Sigma-Aldrich) were subjected to sonication and heating cycles, and then left to cool to rt before recording the absorption and emission spectra. Absorption spectra were recorded using air-equilibrated solutions at rt, with an Agilent Cary 5000 UV–vis spectrophotometer using quartz cells with a path length of 1.0 cm. Emission spectra were recorded on an Agilent Cary Eclipse fluorescence spectrofluorometer. Emission lifetime measurements were performed on a JobinYvon-Horiba FluoroHub single-photon-counting module, using nano-LED-pulsed sources at 295 or 372 nm. The quantum yield measurements were performed using the relative determination, with coumarin 153 (C153, $\phi = 0.53$ in ethanol) as the standard (st) [87]. The fluorescence quantum yields were then calculated according to Equation 1:

$$\phi_x = \phi_{st} \cdot \frac{I_x}{I_{st}} \cdot \frac{\eta_x^2}{\eta_{st}^2} \tag{1}$$

Therein, I is the measured integrated fluorescence emission intensity, η is the refractive index of the solvent, and ϕ is the quantum yield.

Computational methods

DFT calculations were performed using the Gaussian 09 (Revision D.01) program package [88]. The starting geometries were obtained from molecular mechanics or semiempirical models, followed by DFT geometry optimizations on unconstrained C_1 symmetry. Geometry optimizations were followed by frequency calculations on the optimized structures, which confirmed the existence of minima. DFT calculations were performed using the hybrid functional B3LYP [89-91], with the 6-31G(d,p) basis set. Electronic transitions (up to 10 states) were calculated by means of TDDFT [92] using the CAM-B3LYP [93] functional in combination with the 6-31G(d,p) basis set [73]. The conductor-like polarizable continuum model (CPCM) was used to introduce nonspecific solvation effects. The spectra were generated either with GaussView 5 [94] or GaussSum [95], assuming a half-width of 0.15 eV for proper simulation. The IP and EA were determined as the vertical energy difference between the neutral molecule and the cation/anionic forms, respectively, following Equation 2 and Equation 3 [96]:

$$IP = E_{cation} - E_{neutral} \tag{2}$$

$$EA = E_{neutral} - E_{anion} \tag{3}$$

The resulting values (in eV) were: tetrasubstituted pyrene **1**: IP = 6.49, EA = 2.14; *trans*-like pyrene **2**: IP = 6.58, EA = 1.50; and *cis*-like pyrene **3**: IP = 6.58, EA = 1.48.

Supporting Information

Supporting Information File 1

Additional computational results (including electronic transitions, electrostatic potential, Cartesian coordinates of optimized structures) and additional STM data (including bias-dependent imaging series and bicomponent assemblies).
[https://www.beilstein-journals.org/bjnano/content/supplementary/2190-4286-11-130-S1.pdf]

Supporting Information File 2

STM image sequence with increasing bias voltage covering the LUMO and LUMO+1 spectral regions.
[https://www.beilstein-journals.org/bjnano/content/supplementary/2190-4286-11-130-S2.mp4]

Acknowledgements

We thank Alexander Riss for fruitful discussions.

Funding

This work was supported by the European Research Council (ERC) Consolidator Grant NanoSurfs (No. 615233). D. B. gratefully acknowledges the EU through the ERC Starting Grant “COLORLANDS” and MC-RISE “INFUSION” projects, the MIUR through the FIRB (“SUPRACARBON”), and the School of Chemistry at Cardiff University for financial support. W. A. acknowledges funding by the Deutsche Forschungsgemeinschaft (DFG) via a Heisenberg professorship.

ORCID® iDs

Knud Seufert - https://orcid.org/0000-0002-4111-0965
Luka Đorđević - https://orcid.org/0000-0002-8346-7110
Tobias Hoh - https://orcid.org/0000-0002-1391-6347
Davide Bonifazi - https://orcid.org/0000-0001-5717-0121
Willi Auwärter - https://orcid.org/0000-0001-9452-4662

References

1. Grill, L.; Hecht, S. *Nat. Chem.* **2020,** *12,* 115–130. doi:10.1038/s41557-019-0392-9
2. Cinchetti, M.; Dediu, V. A.; Hueso, L. E. *Nat. Mater.* **2017,** *16,* 507–515. doi:10.1038/nmat4902
3. Bonifazi, D.; Mohnani, S.; Llanes-Pallas, A. *Chem. – Eur. J.* **2009,** *15,* 7004–7025. doi:10.1002/chem.200900900
4. Carloni, L.-E.; Bezzu, C. G.; Bonifazi, D. *Chem. – Eur. J.* **2019,** *25,* 16179–16200. doi:10.1002/chem.201902576
5. Goronzy, D. P.; Ebrahimi, M.; Rosei, F.; Arramel; Fang, Y.; De Feyter, S.; Tait, S. L.; Wang, C.; Beton, P. H.; Wee, A. T. S.; Weiss, P. S.; Perepichka, D. F. *ACS Nano* **2018,** *12,* 7445–7481. doi:10.1021/acsnano.8b03513
6. Hollerer, M.; Lüftner, D.; Hurdax, P.; Ules, T.; Soubatch, S.; Tautz, F. S.; Koller, G.; Puschnig, P.; Sterrer, M.; Ramsey, M. G. *ACS Nano* **2017,** *11,* 6252–6260. doi:10.1021/acsnano.7b02449
7. Barth, J. V. *Annu. Rev. Phys. Chem.* **2007,** *58,* 375–407. doi:10.1146/annurev.physchem.56.092503.141259
8. Cahen, D.; Kahn, A.; Umbach, E. *Mater. Today* **2005,** *8,* 32–41. doi:10.1016/s1369-7021(05)70985-8
9. Della Pia, A.; Riello, M.; Floris, A.; Stassen, D.; Jones, T. S.; Bonifazi, D.; De Vita, A.; Costantini, G. *ACS Nano* **2014,** *8,* 12356–12364. doi:10.1021/nn505063w
10. Gebauer, W.; Langner, A.; Schneider, M.; Sokolowski, M.; Umbach, E. *Phys. Rev. B* **2004,** *69,* 155431. doi:10.1103/physrevb.69.155431
11. Forker, R.; Kasemann, D.; Dienel, T.; Wagner, C.; Franke, R.; Müllen, K.; Fritz, T. *Adv. Mater. (Weinheim, Ger.)* **2008,** *20,* 4450–4454. doi:10.1002/adma.200801112
12. Dienel, T.; Proehl, H.; Forker, R.; Leo, K.; Fritz, T. *J. Phys. Chem. C* **2008,** *112,* 9056–9060. doi:10.1021/jp709718t
13. Zamborlini, G.; Lüftner, D.; Feng, Z.; Kollmann, B.; Puschnig, P.; Dri, C.; Panighel, M.; Di Santo, G.; Goldoni, A.; Comelli, G.; Jugovac, M.; Feyer, V.; Schneider, C. M. *Nat. Commun.* **2017,** *8,* 1949. doi:10.1038/s41467-017-01480-w
14. Kerfoot, J.; Korolkov, V. V.; Nizovtsev, A. S.; Jones, R.; Taniguchi, T.; Watanabe, K.; Lesanovsky, I.; Olmos, B.; Besley, N. A.; Besley, E.; Beton, P. H. *J. Chem. Phys.* **2018,** *149,* 054701. doi:10.1063/1.5041418
15. Bocquet, F.; Nony, L.; Para, F.; Luangprasert, P.; Naubron, J.-V.; Loppacher, C.; Leoni, T.; Thomas, A.; Ranguis, A.; d'Aléo, A.; Fages, F.; Becker, C. *Phys. Rev. B* **2018,** *97,* 235434. doi:10.1103/physrevb.97.235434
16. Alkhamisi, M.; Korolkov, V. V.; Nizovtsev, A. S.; Kerfoot, J.; Taniguchi, T.; Watanabe, K.; Besley, N. A.; Besley, E.; Beton, P. H. *Chem. Commun.* **2018,** *54,* 12021–12024. doi:10.1039/c8cc06304d
17. Repp, J.; Meyer, G.; Stojković, S. M.; Gourdon, A.; Joachim, C. *Phys. Rev. Lett.* **2005,** *94,* 026803. doi:10.1103/physrevlett.94.026803
18. Auwärter, W. *Surf. Sci. Rep.* **2019,** *74,* 1–95. doi:10.1016/j.surfrep.2018.10.001
19. Mehler, A.; Néel, N.; Kröger, J. *J. Vac. Sci. Technol., A* **2019,** *37,* 061404. doi:10.1116/1.5125486
20. Schulz, F.; Drost, R.; Hämäläinen, S. K.; Liljeroth, P. *ACS Nano* **2013,** *7,* 11121–11128. doi:10.1021/nn404840h
21. Forker, R.; Dienel, T.; Krause, A.; Gruenewald, M.; Meissner, M.; Kirchhuebel, T.; Gröning, O.; Fritz, T. *Phys. Rev. B* **2016,** *93,* 165426. doi:10.1103/physrevb.93.165426
22. Iannuzzi, M.; Tran, F.; Widmer, R.; Dienel, T.; Radican, K.; Ding, Y.; Hutter, J.; Gröning, O. *Phys. Chem. Chem. Phys.* **2014,** *16,* 12374–12384. doi:10.1039/c4cp01466a
23. Koslowski, S.; Rosenblatt, D.; Kabakchiev, A.; Kuhnke, K.; Kern, K.; Schlickum, U. *Beilstein J. Nanotechnol.* **2017,** *8,* 1388–1395. doi:10.3762/bjnano.8.140
24. Preobrajenski, A. B.; Vinogradov, A. S.; Mårtensson, N. *Surf. Sci.* **2005,** *582,* 21–30. doi:10.1016/j.susc.2005.02.047
25. Joshi, S.; Ecija, D.; Koitz, R.; Iannuzzi, M.; Seitsonen, A. P.; Hutter, J.; Sachdev, H.; Vijayaraghavan, S.; Bischoff, F.; Seufert, K.; Barth, J. V.; Auwärter, W. *Nano Lett.* **2012,** *12,* 5821–5828. doi:10.1021/nl303170m

26. Brülke, C.; Heepenstrick, T.; Humberg, N.; Krieger, I.; Sokolowski, M.; Weiß, S.; Tautz, F. S.; Soubatch, S. *J. Phys. Chem. C* **2017,** *121,* 23964–23973. doi:10.1021/acs.jpcc.7b06107
27. Hwang, B.; Kwon, J.; Lee, M.; Lim, S. J.; Jeon, S.; Kim, S.; Ham, U.; Song, Y. J.; Kuk, Y. *Curr. Appl. Phys.* **2013,** *13,* 1365–1369. doi:10.1016/j.cap.2013.04.018
28. Joshi, S.; Bischoff, F.; Koitz, R.; Ecija, D.; Seufert, K.; Seitsonen, A. P.; Hutter, J.; Diller, K.; Urgel, J. I.; Sachdev, H.; Barth, J. V.; Auwärter, W. *ACS Nano* **2014,** *8,* 430–442. doi:10.1021/nn406024m
29. Schwarz, M.; Riss, A.; Garnica, M.; Ducke, J.; Deimel, P. S.; Duncan, D. A.; Thakur, P. K.; Lee, T.-L.; Seitsonen, A. P.; Barth, J. V.; Allegretti, F.; Auwärter, W. *ACS Nano* **2017,** *11,* 9151–9161. doi:10.1021/acsnano.7b04022
30. Zhang, Q.; Yu, J.; Ebert, P.; Zhang, C.; Pan, C.-R.; Chou, M.-Y.; Shih, C.-K.; Zeng, C.; Yuan, S. *ACS Nano* **2018,** *12,* 9355–9362. doi:10.1021/acsnano.8b04444
31. Li, Q.; Zou, X.; Liu, M.; Sun, J.; Gao, Y.; Qi, Y.; Zhou, X.; Yakobson, B. I.; Zhang, Y.; Liu, Z. *Nano Lett.* **2015,** *15,* 5804–5810. doi:10.1021/acs.nanolett.5b01852
32. Ducke, J.; Riss, A.; Pérez Paz, A.; Seufert, K.; Schwarz, M.; Garnica, M.; Rubio, A.; Auwärter, W. *ACS Nano* **2018,** *12,* 2677–2684. doi:10.1021/acsnano.7b08887
33. Schwarz, M.; Duncan, D. A.; Garnica, M.; Ducke, J.; Deimel, P. S.; Thakur, P. K.; Lee, T.-L.; Allegretti, F.; Auwärter, W. *Nanoscale* **2018,** *10,* 21971–21977. doi:10.1039/c8nr06387g
34. Brülke, C.; Heepenstrick, T.; Krieger, I.; Wolff, B.; Yang, X.; Shamsaddinlou, A.; Weiß, S.; Bocquet, F. C.; Tautz, F. S.; Soubatch, S.; Sokolowski, M. *Phys. Rev. B* **2019,** *99,* 121404. doi:10.1103/physrevb.99.121404
35. Tan, A.; Zhang, P. P. *Phys. Chem. Chem. Phys.* **2019,** *21,* 26146–26153. doi:10.1039/c9cp04853g
36. Palma, C.-A.; Joshi, S.; Hoh, T.; Ecija, D.; Barth, J. V.; Auwärter, W. *Nano Lett.* **2015,** *15,* 2242–2248. doi:10.1021/nl503956p
37. Pörtner, M.; Wei, Y.; Riss, A.; Seufert, K.; Garnica, M.; Barth, J. V.; Seitsonen, A. P.; Diekhöner, L.; Auwärter, W. *Adv. Mater. Interfaces* **2020,** *7,* 2000080. doi:10.1002/admi.202000080
38. Urgel, J. I.; Schwarz, M.; Garnica, M.; Stassen, D.; Bonifazi, D.; Ecija, D.; Barth, J. V.; Auwärter, W. *J. Am. Chem. Soc.* **2015,** *137,* 2420–2423. doi:10.1021/ja511611r
39. Riss, A.; Richter, M.; Paz, A. P.; Wang, X.-Y.; Raju, R.; He, Y.; Ducke, J.; Corral, E.; Wuttke, M.; Seufert, K.; Garnica, M.; Rubio, A.; Barth, J. V.; Narita, A.; Müllen, K.; Berger, R.; Feng, X.; Palma, C.-A.; Auwärter, W. *Nat. Commun.* **2020,** *11,* 1490. doi:10.1038/s41467-020-15210-2
40. Hwang, B.; Hwang, J.; Yoon, J. K.; Lim, S.; Kim, S.; Lee, M.; Kwon, J. H.; Baek, H.; Sung, D.; Kim, G.; Hong, S.; Ihm, J.; Stroscio, J. A.; Kuk, Y. *Sci. Rep.* **2016,** *6,* 31160. doi:10.1038/srep31160
41. Roth, S.; Matsui, F.; Greber, T.; Osterwalder, J. *Nano Lett.* **2013,** *13,* 2668–2675. doi:10.1021/nl400815w
42. Mao, J.; Zhang, H.; Jiang, Y.; Pan, Y.; Gao, M.; Xiao, W.; Gao, H.-J. *J. Am. Chem. Soc.* **2009,** *131,* 14136–14137. doi:10.1021/ja904907z
43. Maccariello, D.; Garnica, M.; Niño, M. A.; Navío, C.; Perna, P.; Barja, S.; Vázquez de Parga, A. L.; Miranda, R. *Chem. Mater.* **2014,** *26,* 2883–2890. doi:10.1021/cm5005467
44. Kumar, A.; Banerjee, K.; Liljeroth, P. *Nanotechnology* **2017,** *28,* 082001. doi:10.1088/1361-6528/aa564f
45. Korolkov, V. V.; Svatek, S. A.; Allen, S.; Roberts, C. J.; Tendler, S. J. B.; Taniguchi, T.; Watanabe, K.; Champness, N. R.; Beton, P. H. *Chem. Commun.* **2014,** *50,* 8882–8885. doi:10.1039/c4cc03720k
46. Korolkov, V. V.; Baldoni, M.; Watanabe, K.; Taniguchi, T.; Besley, E.; Beton, P. H. *Nat. Chem.* **2017,** *9,* 1191–1197. doi:10.1038/nchem.2824
47. Figueira-Duarte, T. M.; Müllen, K. *Chem. Rev.* **2011,** *111,* 7260–7314. doi:10.1021/cr100428a
48. Kaposi, T.; Joshi, S.; Hoh, T.; Wiengarten, A.; Seufert, K.; Paszkiewicz, M.; Klappenberger, F.; Ecija, D.; Đorđević, L.; Marangoni, T.; Bonifazi, D.; Barth, J. V.; Auwärter, W. *ACS Nano* **2016,** *10,* 7665–7674. doi:10.1021/acsnano.6b02989
49. Casas-Solvas, J. M.; Howgego, J. D.; Davis, A. P. *Org. Biomol. Chem.* **2014,** *12,* 212–232. doi:10.1039/c3ob41993b
50. Cirera, B.; Đorđević, L.; Otero, R.; Gallego, J. M.; Bonifazi, D.; Miranda, R.; Ecija, D. *Chem. Commun.* **2016,** *52,* 11227–11230. doi:10.1039/c6cc04874a
51. Đorđević, L.; Valentini, C.; Demitri, N.; Mézière, C.; Allain, M.; Sallé, M.; Folli, A.; Murphy, D.; Mañas-Valero, S.; Coronado, E.; Bonifazi, D. *Angew. Chem., Int. Ed.* **2020,** *59,* 4106–4114. doi:10.1002/anie.201914025
52. Đorđević, L.; Marangoni, T.; Liu, M.; De Zorzi, R.; Geremia, S.; Minoia, A.; Lazzaroni, R.; Ishida, Y.; Bonifazi, D. *ChemPlusChem* **2019,** *84,* 1270–1278. doi:10.1002/cplu.201800623
53. Llanes-Pallas, A.; Palma, C.-A.; Piot, L.; Belbakra, A.; Listorti, A.; Prato, M.; Samori, P.; Armaroli, N.; Bonifazi, D. *J. Am. Chem. Soc.* **2009,** *131,* 509–520. doi:10.1021/ja807530m
54. Gonzalez-Rodriguez, E.; Abdo, M. A.; dos Passos Gomes, G.; Ayad, S.; White, F. D.; Tsvetkov, N. P.; Hanson, K.; Alabugin, I. V. *J. Am. Chem. Soc.* **2020,** *142,* 8352–8366. doi:10.1021/jacs.0c01856
55. Schleicher, S.; Borca, B.; Rawson, J.; Matthes, F.; Bürgler, D. E.; Kögerler, P.; Schneider, C. M. *Phys. Status Solidi B* **2018,** *255,* 1800235. doi:10.1002/pssb.201800235
56. Liu, X.; Du, Y.; Timmer, A.; Mönig, H.; Wan, X.; Huang, X.; Ji, Q.; Kan, E.; Ariga, K.; Hill, J. P.; Fuchs, H.; Kong, H. *J. Phys. Chem. C* **2019,** *123,* 16281–16287. doi:10.1021/acs.jpcc.9b04060
57. Lischka, M.; Fritton, M.; Eichhorn, J.; Vyas, V. S.; Strunskus, T.; Lotsch, B. V.; Björk, J.; Heckl, W. M.; Lackinger, M. *J. Phys. Chem. C* **2018,** *122,* 5967–5977. doi:10.1021/acs.jpcc.7b10403
58. Jiang, L.; Papageorgiou, A. C.; Oh, S. C.; Sağlam, Ö.; Reichert, J.; Duncan, D. A.; Zhang, Y.-Q.; Klappenberger, F.; Guo, Y.; Allegretti, F.; More, S.; Bhosale, R.; Mateo-Alonso, A.; Barth, J. V. *ACS Nano* **2016,** *10,* 1033–1041. doi:10.1021/acsnano.5b06340
59. Hu, J.; Hu, J.; Zhang, Z.; Shen, K.; Liang, Z.; Zhang, H.; Tian, Q.; Wang, P.; Jiang, Z.; Huang, H.; Wells, J. W.; Song, F. *Appl. Surf. Sci.* **2020,** *513,* 145797. doi:10.1016/j.apsusc.2020.145797
60. Sun, Q.; Gröning, O.; Overbeck, J.; Braun, O.; Perrin, M. L.; Borin Barin, G.; El Abbassi, M.; Eimre, K.; Ditler, E.; Daniels, C.; Meunier, V.; Pignedoli, C. A.; Calame, M.; Fasel, R.; Ruffieux, P. *Adv. Mater. (Weinheim, Ger.)* **2020,** *32,* 1906054. doi:10.1002/adma.201906054
61. France, C. B.; Parkinson, B. A. *J. Am. Chem. Soc.* **2003,** *125,* 12712–12713. doi:10.1021/ja037056o
62. Pham, T. A.; Song, F.; Nguyen, M.-T.; Stöhr, M. *Chem. Commun.* **2014,** *50,* 14089–14092. doi:10.1039/c4cc02753a
63. Zhao, H.; Zhang, S.; Li, S.; Song, X.; Liu, W.; Liu, B.; Dong, M. *RSC Adv.* **2015,** *5,* 103316–103320. doi:10.1039/c5ra20316c
64. Pham, T. A.; Song, F.; Nguyen, M.-T.; Li, Z.; Studener, F.; Stöhr, M. *Chem. – Eur. J.* **2016,** *22,* 5937–5944. doi:10.1002/chem.201504946

65. Xu, Y.; Bai, H.; Lu, G.; Li, C.; Shi, G. *J. Am. Chem. Soc.* **2008,** *130,* 5856–5857. doi:10.1021/ja800745y
66. Han, Y.; Li, H.; Jafri, S. H. M.; Ossipov, D.; Hilborn, J.; Leifer, K. *Appl. Surf. Sci.* **2020,** *510,* 145409. doi:10.1016/j.apsusc.2020.145409
67. Singh, M.; Holzinger, M.; Tabrizian, M.; Winters, S.; Berner, N. C.; Cosnier, S.; Duesberg, G. S. *J. Am. Chem. Soc.* **2015,** *137,* 2800–2803. doi:10.1021/ja511512m
68. Chen, X.; Jia, S.; Ding, N.; Shi, J.; Wang, Z. *Environ. Sci.: Nano* **2016,** *3,* 1493–1503. doi:10.1039/c6en00378h
69. Kurata, R.; Ito, A.; Gon, M.; Tanaka, K.; Chujo, Y. *J. Org. Chem.* **2017,** *82,* 5111–5121. doi:10.1021/acs.joc.7b00315
70. Maeda, H.; Maeda, T.; Mizuno, K.; Fujimoto, K.; Shimizu, H.; Inouye, M. *Chem. – Eur. J.* **2006,** *12,* 824–831. doi:10.1002/chem.200500638
71. Diring, S.; Camerel, F.; Donnio, B.; Dintzer, T.; Toffanin, S.; Capelli, R.; Muccini, M.; Ziessel, R. *J. Am. Chem. Soc.* **2009,** *131,* 18177–18185. doi:10.1021/ja908061q
72. Crawford, A. G.; Dwyer, A. D.; Liu, Z.; Steffen, A.; Beeby, A.; Palsson, L.-O.; Tozer, D. J.; Marder, T. B. *J. Am. Chem. Soc.* **2011,** *133,* 13349–13362. doi:10.1021/ja2006862
73. Ji, L.; Edkins, R. M.; Lorbach, A.; Krummenacher, I.; Brückner, C.; Eichhorn, A.; Braunschweig, H.; Engels, B.; Low, P. J.; Marder, T. B. *J. Am. Chem. Soc.* **2015,** *137,* 6750–6753. doi:10.1021/jacs.5b03805
74. Lee, Y. O.; Pradhan, T.; Yoo, S.; Kim, T. H.; Kim, J.; Kim, J. S. *J. Org. Chem.* **2012,** *77,* 11007–11013. doi:10.1021/jo3010974
75. Furukawa, S.; Uji-i, H.; Tahara, K.; Ichikawa, T.; Sonoda, M.; De Schryver, F. C.; Tobe, Y.; De Feyter, S. *J. Am. Chem. Soc.* **2006,** *128,* 3502–3503. doi:10.1021/ja0583362
76. Schlickum, U.; Decker, R.; Klappenberger, F.; Zoppellaro, G.; Klyatskaya, S.; Auwärter, W.; Neppl, S.; Kern, K.; Brune, H.; Ruben, M.; Barth, J. V. *J. Am. Chem. Soc.* **2008,** *130,* 11778–11782. doi:10.1021/ja8028119
77. Ernst, K.-H. *Phys. Status Solidi B* **2012,** *249,* 2057–2088. doi:10.1002/pssb.201248188
78. Zaera, F. *Chem. Soc. Rev.* **2017,** *46,* 7374–7398. doi:10.1039/c7cs00367f
79. Erler, P.; Schmitt, P.; Barth, N.; Irmler, A.; Bouvron, S.; Huhn, T.; Groth, U.; Pauly, F.; Gragnaniello, L.; Fonin, M. *Nano Lett.* **2015,** *15,* 4546–4552. doi:10.1021/acs.nanolett.5b01120
80. Liu, L.; Dienel, T.; Widmer, R.; Gröning, O. *ACS Nano* **2015,** *9,* 10125–10132. doi:10.1021/acsnano.5b03741
81. Dappe, Y. J.; Andersen, M.; Balog, R.; Hornekær, L.; Bouju, X. *Phys. Rev. B* **2015,** *91,* 045427. doi:10.1103/physrevb.91.045427
82. Borghetti, P.; El-Sayed, A.; Goiri, E.; Rogero, C.; Lobo-Checa, J.; Floreano, L.; Ortega, J. E.; de Oteyza, D. G. *ACS Nano* **2014,** *8,* 12786–12795. doi:10.1021/nn5060333
83. Cochrane, K. A.; Schiffrin, A.; Roussy, T. S.; Capsoni, M.; Burke, S. A. *Nat. Commun.* **2015,** *6,* 8312. doi:10.1038/ncomms9312
84. Bokdam, M.; Khomyakov, P. A.; Brocks, G.; Zhong, Z.; Kelly, P. J. *Nano Lett.* **2011,** *11,* 4631–4635. doi:10.1021/nl202131q
85. Kirchhuebel, T.; Monti, O. L. A.; Munakata, T.; Kera, S.; Forker, R.; Fritz, T. *Phys. Chem. Chem. Phys.* **2019,** *21,* 12730–12747. doi:10.1039/c8cp07318j
86. Sanning, J.; Ewen, P. R.; Stegemann, L.; Schmidt, J.; Daniliuc, C. G.; Koch, T.; Doltsinis, N. L.; Wegner, D.; Strassert, C. A. *Angew. Chem., Int. Ed.* **2015,** *54,* 786–791. doi:10.1002/anie.201407439
87. Würth, C.; Grabolle, M.; Pauli, J.; Spieles, M.; Resch-Genger, U. *Nat. Protoc.* **2013,** *8,* 1535–1550. doi:10.1038/nprot.2013.087
88. *Gaussian 09,* Revision D.01; Gaussian, Inc.: Wallingford, CT, 2016.
89. Becke, A. D. *Phys. Rev. A* **1988,** *38,* 3098–3100. doi:10.1103/physreva.38.3098
90. Lee, C.; Yang, W.; Parr, R. G. *Phys. Rev. B* **1988,** *37,* 785–789. doi:10.1103/physrevb.37.785
91. Becke, A. D. *J. Chem. Phys.* **1993,** *98,* 5648–5652. doi:10.1063/1.464913
92. Adamo, C.; Jacquemin, D. *Chem. Soc. Rev.* **2013,** *42,* 845–856. doi:10.1039/c2cs35394f
93. Yanai, T.; Tew, D. P.; Handy, N. C. *Chem. Phys. Lett.* **2004,** *393,* 51–57. doi:10.1016/j.cplett.2004.06.011
94. *GaussView,* Version 5; Gaussian, Inc.: Wallingford, CT, 2016.
95. O'boyle, N. M.; Tenderholt, A. L.; Langner, K. M. *J. Comput. Chem.* **2008,** *29,* 839–845. doi:10.1002/jcc.20823
96. Zhao, X.; Xiong, Y.; Ma, J.; Yuan, Z. *J. Phys. Chem. A* **2016,** *120,* 7554–7560. doi:10.1021/acs.jpca.6b07552

License and Terms

The definitive version of this article is the electronic one which can be found at:
https://doi.org/10.3762/bjnano.11.130

BEILSTEIN JOURNAL OF NANOTECHNOLOGY

Controlling the electronic and physical coupling on dielectric thin films

Philipp Hurdax[1], Michael Hollerer[1], Larissa Egger[1], Georg Koller[1], Xiaosheng Yang[2,3,4], Anja Haags[2,3,4], Serguei Soubatch[2,3], Frank Stefan Tautz[2,3,4], Mathias Richter[5], Alexander Gottwald[5], Peter Puschnig[1], Martin Sterrer[1] and Michael G. Ramsey*[1]

Full Research Paper

Open Access

Address:
[1]Institute of Physics, University of Graz, NAWI Graz, Universitätsplatz 5, 8010 Graz, Austria, [2]Peter Grünberg Institute (PGI-3), Forschungszentrum Jülich, 52425 Jülich, Germany, [3]Jülich Aachen Research Alliance (JARA), Fundamentals of Future Information Technology, 52425 Jülich, Germany, [4]Experimentalphysik IV A, RWTH Aachen University, 52074 Aachen, Germany and [5]Physikalisch-Technische Bundesanstalt (PTB), 10587 Berlin, Germany

Email:
Michael G. Ramsey* - michael.ramsey@uni-graz.at

* Corresponding author

Keywords:
decoupling; integer charge transfer; organic films; *para*-sexiphenyl; thin dielectric film

Beilstein J. Nanotechnol. **2020,** *11,* 1492–1503.
https://doi.org/10.3762/bjnano.11.132

Received: 29 May 2020
Accepted: 25 August 2020
Published: 01 October 2020

This article is part of the thematic issue "Molecular assemblies on surfaces – towards physical and electronic decoupling of organic molecules".

Guest Editor: M. Stöhr

Abstract

Ultrathin dielectric/insulating films on metals are often used as decoupling layers to allow for the study of the electronic properties of adsorbed molecules without electronic interference from the underlying metal substrate. However, the presence of such decoupling layers may effectively change the electron donating properties of the substrate, for example, by lowering its work function and thus enhancing the charging of the molecular adsorbate layer through electron tunneling. Here, an experimental study of the charging of *para*-sexiphenyl (6P) on ultrathin MgO(100) films supported on Ag(100) is reported. By deliberately changing the work function of the MgO(100)/Ag(100) system, it is shown that the charge transfer (electronic coupling) into the 6P molecules can be controlled, and 6P monolayers with uncharged molecules (Schottky–Mott regime) and charged and uncharged molecules (Fermi level pinning regime) can be obtained. Furthermore, it was found that charge transfer and temperature strongly influence the orientation, conformation, and wetting behavior (physical coupling) of the 6P layers on the MgO(100) thin films.

Introduction

Since the first scanning tunneling microscope (STM) imaging of the highest occupied molecular orbital (HOMO) and the lowest unoccupied molecular orbital (LUMO) of pentacene (5A) on NaCl/Cu(111) was performed [1], the concept of decoupling molecules from metal substrates with large bandgap dielectric films has become widely accepted. Although such systems have become a rich field of research, particularly in the scanning probe microscopy community, it is often forgotten that the wide bandgap insulating layer is not a sufficient condition for decoupling. Although it reduces wave function overlap with the substrate, it can in fact promote charge transfer via tunneling. The determining factor is the energy level alignment of the frontier orbitals of the adsorbate relative to the Fermi level (E_F) of the underlying metal [2,3]. As dielectric films can significantly reduce the work function, principally due to Pauli repulsion (pushback) at the metal interface, adsorbates of sufficiently high electron affinity (EA) will become negatively charged via tunneling from the underlying metal. This was predicted by Pacchioni et al. [4-6] and either inferred or observed for adsorbates ranging from metal atoms [7,8] and small molecules [9,10] to larger π-conjugated molecules [11-13].

This phenomenon has been comprehensively analyzed for 5A on epitaxial MgO(100)/Ag(100), in which orbital-resolved STM and photoemission tomography (PT) have enabled the quantification of both the charge on individual molecules and the number of charged molecules in the 5A monolayer (ML) [14]. For 5A MLs on regularly grown epitaxial MgO(100) films, all molecules appear to be charged. Orbital-resolved STM reveals the LUMO both above and below the Fermi level, with a large gap between a singly occupied molecular orbital (SOMO) and a singly unoccupied molecular orbital (SUMO). In addition, PT confirms an integer charge transfer, which would be expected to result from tunneling [15]. However, using the ability to tune the MgO(100)/Ag(100) work function after MgO film growth (Φ_{MgO}) by changing the composition at the dielectric–metal interface without changing its surface [16-19], it has been recently shown that two distinct adsorption regimes exist [20]. On films with a high Φ_{MgO}, all molecules in the ML remain neutral, whereas on a low-Φ_{MgO} substrate, charge transfer is observed. In the former (the "vacuum level alignment" regime) the molecules are electronically decoupled, while in the latter, the electronic levels are tied to the Fermi level of the underlying Ag(100). The equilibration process for this "Fermi level pinning regime" has been realized by the proportion of charged and neutral molecules coexisting in the first monolayer, as schematically illustrated in Figure 1. In this work function regime, ranging from all the molecules being charged to no molecules being charged, the molecular ML is characterized by a constant pinning work function (Φ_{pin}). The critical substrate work function (Φ_{crit}) for the charge transfer is given by the condition $\Phi_{\mathrm{MgO}} = \Phi_{\mathrm{pin}}$. On the macroscopic level, the simple relationships between the density of the integer charged molecules, the dielectric thickness (d_{diel}), and the change in the work function upon adsorption of the molecules ($\Delta\Phi = \Phi_{\mathrm{mol}} - \Phi_{\mathrm{MgO}}$, where Φ_{mol} is the final work function after adsorption of the molecules) is very well described by electrostatics with a simple capacitor model given by

$$\Delta\Phi = \frac{\sigma\left(d_{\mathrm{diel}} + d_0\right)}{\varepsilon_0\varepsilon_{\mathrm{r}}} = \frac{\sigma d_{\mathrm{cs}}}{\varepsilon_0\varepsilon_{\mathrm{r}}}, \tag{1}$$

where σ is the average charge density in the molecular film, ε_{r} is the dielectric constant of the thin film, and d_{cs} is the distance between the charge in the molecule and its image charge in the metal (i.e., the charge separation distance).

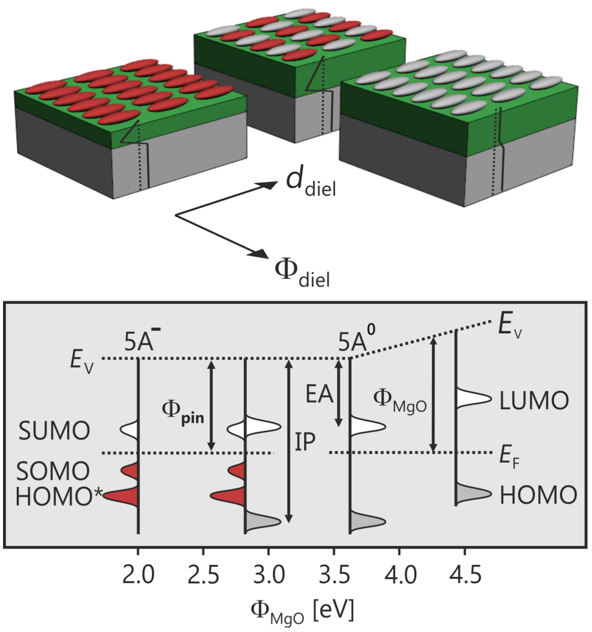

Figure 1: Molecular level schematic of integer charge transfer across dielectric films. Top: The ratio of integer charged (red) and neutral (gray) molecules is determined by the work function of the substrate after dielectric film growth (Φ_{diel}) and the dielectric film thickness (d_{diel}), according to the capacitor model. Bottom: Energy level alignment for charged $5A^-$ and neutral $5A^0$ on MgO(100)/Ag(100) from the Fermi level pinning to the vacuum level alignment regime. HOMO* refers to orbitals of charged molecules.

In this report, we demonstrate the robustness of the conclusions drawn from the 5A study by considering *para*-sexiphenyl (6P, $C_{36}H_{26}$). In contrast to 5A, 6P is geometrically more flexible, more specifically, it is nonplanar in the gas phase and has a relatively low electron affinity. On the pristine Ag(100) substrate, 6P simply physisorbs with no evidence of LUMO hybridization, which remains unoccupied [21]. It will be shown that the introduction of the dielectric interlayer can lead to integer charge transfer and electrostatic coupling to this otherwise passive metal surface. Unlike the 5A case, Φ_{crit} for the charge transfer is not equal to the Φ_{pin} for 6P. This is understood in terms of conformational changes in the 6P and the enhanced physical coupling to the substrate induced by the charge transfer. Finally, the charging effect on the thermal dynamics and the stability of the 6P monolayer are considered.

Results and Discussion

Ambivalent behavior of 6P on regularly prepared MgO(100)/Ag(100) thin films

Figure 2 shows STM images of four 6P/MgO(100)/Ag(100) preparations for MgO films with a thickness of 2 ML (Figure 2a, Figure 2b) and 3 ML (Figure 2c, Figure 2d), and 6P coverage ranging from sub-ML (Figure 2a) and close-to-monolayer (Figure 2b, Figure 2c) to 2 ML (Figure 2d). STM shows 6P molecules arranged in ordered monolayer islands (Figure 2b, Figure 2c), with their long axes aligned parallel to each other and parallel to the substrate surface. This is typical for 6P on atomically clean and ordered substrates obtained from bulk oxides to metal substrates [21-25]. In the submonolayer coverage regime (Figure 2a), we find molecules with different orientations coexisting on the surface. Their long axes are aligned along the principal crystallographic directions [001]/[010] and [011]. In the monolayer regime, molecules align either along [001]/[010] (Figure 2b) or [011] (Figure 2c), while in Figure 2d, where multilayer islands of up to three layers high are present, the molecules in the domains are rotated by 18° with respect to [011]. Note that on some MgO preparations, severe island growth was observed, while on others it was less pronounced.

Generally, the molecules appear as rod-like features in STM. A pronounced six-lobe structure with a slight zig-zag appearance is seen in some of the molecules in Figure 2a. This structure is even more evident in the molecules forming the ordered island in Figure 2c. These may be associated with the six phenyl rings of the 6P molecule presenting a twisted conformation. In the gas phase, 6P naturally occurs with a torsional angle of 35° between its phenyl rings [26]. The observation of such a twist on MgO(100)/Ag(100) suggests that the interaction between the 6P molecules and MgO is very weak. In addition, next to the 6P molecules with a zig-zag appearance, there are other molecules with 6 lobes, but in a linear arrangement (Figure 2a). A possible explanation for this observation is the charging-induced planarization of 6P. For comparison, on the pristine Ag(100) substrate, planar 6P molecules are observed in the submonolayer regime despite the lack of any charge transfer, as evi-

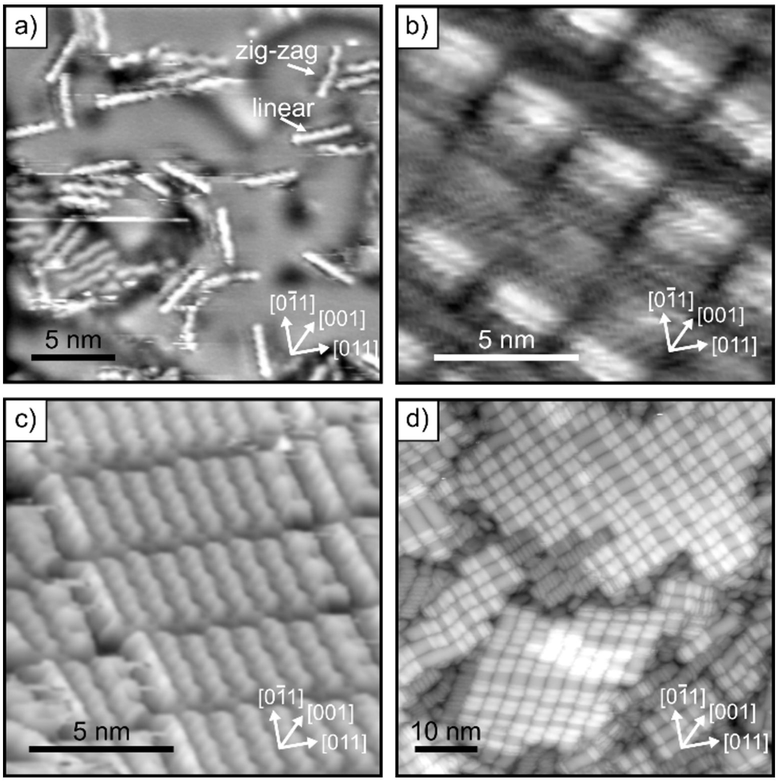

Figure 2: STM images of 6P deposited on (a,b) 2 ML MgO(100)/Ag(100) and (c,d) 3 ML MgO(100)/Ag(100). (a) Individual 6P molecules, $T_{\mathrm{dep,6P}}$ = −193 °C, size: 25 nm × 25 nm, U_b = +0.4 V, i_t = 25 pA; (b,c) 6P monolayer islands, $T_{\mathrm{dep,6P}}$ = 30 °C, size: 13 nm × 13 nm, U_b = +1.4 V, i_t = 16 pA (b) and U_b = −0.08 V, i_t = 140 pA (c). (d) Multilayer 6P islands, $T_{\mathrm{dep,6P}}$ = 30 °C, size: 60 nm × 60 nm, U_b = +1.7 V, i_t = 30 pA. All STM images were recorded at 80 K.

denced by the absence of an emission from the LUMO in photoemission tomography [21]. This implies that the van der Waals interaction with the metal is sufficient to planarize the molecule. From the STM images shown here of 6P on the MgO(100)/Ag(100) films it is not possible to provide an unambiguous assignment of charged and uncharged molecules, since the orbital resolution has not been achieved in this system. However, the existence of two different 6P appearances (Figure 2a) and monolayer orientations (Figure 2b, Figure 2c) might be related to different charge states of the molecules on the surface.

The images of orbitals of molecules adsorbed on surfaces can also be obtained from the angular intensity distribution in valence band photoemission experiments via PT [27]. When the photoelectron emission angle is converted to momentum, the resulting momentum maps approximately reflect the square of the Fourier transform of the real space orbitals (i.e., the momentum maps image the orbital in the reciprocal space). PT experiments conducted on 6P monolayers on MgO(100)/Ag(100) revealed that films prepared under nominally identical conditions could yield apparently contradicting results. On some preparations, no molecular emissions were observed in the MgO bandgap, whereas on others, distinctive features appeared in the gap at 0.5 and 2.5 eV below the Fermi level. The momentum maps of these molecular emissions (Figure 3) can be unambiguously assigned to the orbitals and the geometry of the molecules from which they are emitted [28]. The experimental maps in Figure 3a and Figure 3b are in very good agreement with the simulations of the HOMO and LUMO for 6P having two orthogonal orientations. The observation of the LUMO emission clearly shows that charge transfer has occurred.

The azimuthal orientations of the molecules can be derived by comparing the orientations of the molecular emission patterns to the orientation of the emission pattern from the Ag(100) substrate or from the crystal surface unit cell inferred from low energy electron diffraction (LEED) experiments. This comparison shows that all charged molecules have their long axes aligned 45° with respect to the close-packed atomic rows of the substrate (i.e., along the [001]/[010] azimuths) in agreement with the orientation of the molecules obtained via STM in Figure 2b.

Significantly, the theoretical maps shown in Figure 3 are for flat lying planar molecules. The photoemission tomography technique is very sensitive to any out-of-plane tilt or twist in 6P [29-32]. A nonzero torsional angle leads to orbital periodicity doubling in the real space and orbital periodicity halving in the reciprocal space [23]. It can therefore be concluded that, while neutral molecules can have a twist in different orientations on

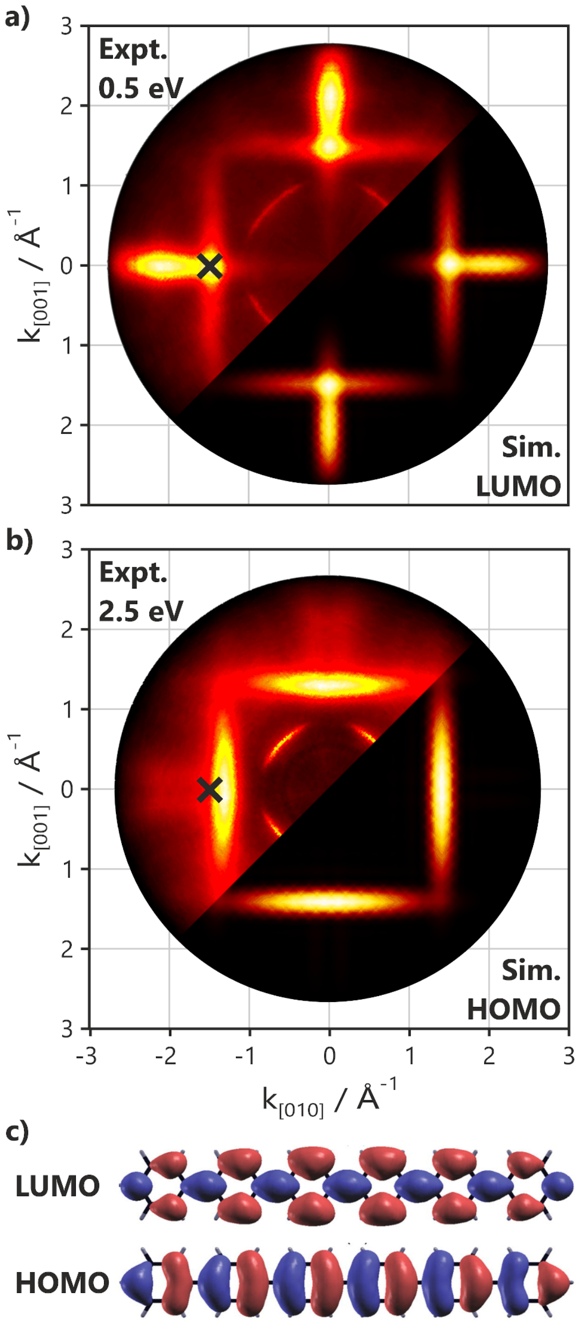

Figure 3: Photoemission momentum maps of 6P on MgO(100)/Ag(100) at energies of (a) 0.5 eV and (b) 2.5 eV below E_F, measured with a photon energy of 35 eV and at an incidence angle of 40°. The experimental maps (top left of a and b) are shown in comparison to the maps calculated from the density functional theory orbitals (c) for two orthogonally oriented planar 6P molecules of the LUMO (bottom right of a) and the HOMO (bottom right of b). The geometry for the maximum LUMO intensity used in the following angle-resolved ultraviolet photoemission spectroscopy experiments is marked with crosses. Deviations from the simulations for isolated molecules are a result of MgO and Ag(100) sp-band emissions. Films of 6P were grown and measured at room temperature.

the MgO surface, the molecules that have experienced charge transfer are planarized. Therefore, they lose the 35° torsional angle between their phenyl rings and align exclusively along [001]/[010]. It should be noted that the occupation of the LUMO is predicted to reduce the torsional angle in the molecule, given that it has a bonding character with respect to the phenyl rings (see Figure 3c) [33]. However, this is not a sufficient condition for planarization. Density functional theory (DFT) calculations for the isolated molecule indicate that the torsional angle changes from 35 to only 20° upon the formation of the anion. Presumably, the electrostatic interaction of the charged molecules with the substrate completes the planarization.

In summary these results suggest that MgO films prepared under nominally identical conditions can result in either charged or uncharged molecules. While uncharged molecules retain the torsional angle between their phenyl rings, the charge transfer is accompanied by a change in the orientation of the molecules and they become planar. In the following subsection, the critical role of the work function for charging and its influence on the surface wetting capability of the molecules will be highlighted.

Work function control of electronic coupling

Figure 4 displays angle-resolved ultraviolet photoemission spectroscopy (ARUPS) scans after the 6P molecules were submitted to the same saturation exposure on the same 2 ML MgO(100) film. The initial work function, Φ_{MgO}, was tuned to different values. Figure 4a shows wide scans in normal emission, where the MgO valence band dominates at an energy between 9 and 4 eV below E_{F}.

For Φ_{MgO} greater than 2.8 eV, there is only a minor decrease in the work function (<0.1 eV) and only a small attenuation in the MgO emissions of approximately 15% compared to the clean substrate, suggesting that only a small fraction of the surface is covered with molecules and 3D islands are formed. For Φ_{MgO} below 2.8 eV, the results change completely. They show the onset of significant substrate attenuation, changes in the spectral lineshape, and an increase in the work function upon 6P deposition. The attenuation behavior suggests that the molecules fully wet the surface only for Φ_{MgO} below 2.65 eV, where a 60% reduction in the MgO intensity is observed. The increase of the work function indicates a charge transfer to 6P. The charge transfer is observed directly by the presence of a LUMO emission seen at high emission angles in Figure 4a. Magnified scans of the MgO bandgap region in the geometry of maximum LUMO emission intensity, indicated by the crosses in Figure 3, are displayed in Figure 4b. For Φ_{MgO} greater than 2.8 eV, no significant orbital emissions are found in the gap, implying that no charged molecules are present on the surface. For Φ_{MgO} below 2.8 eV, molecular emissions arise at 2.52 and 0.55 eV with respect to E_{F}. Their photoemission energies and angular

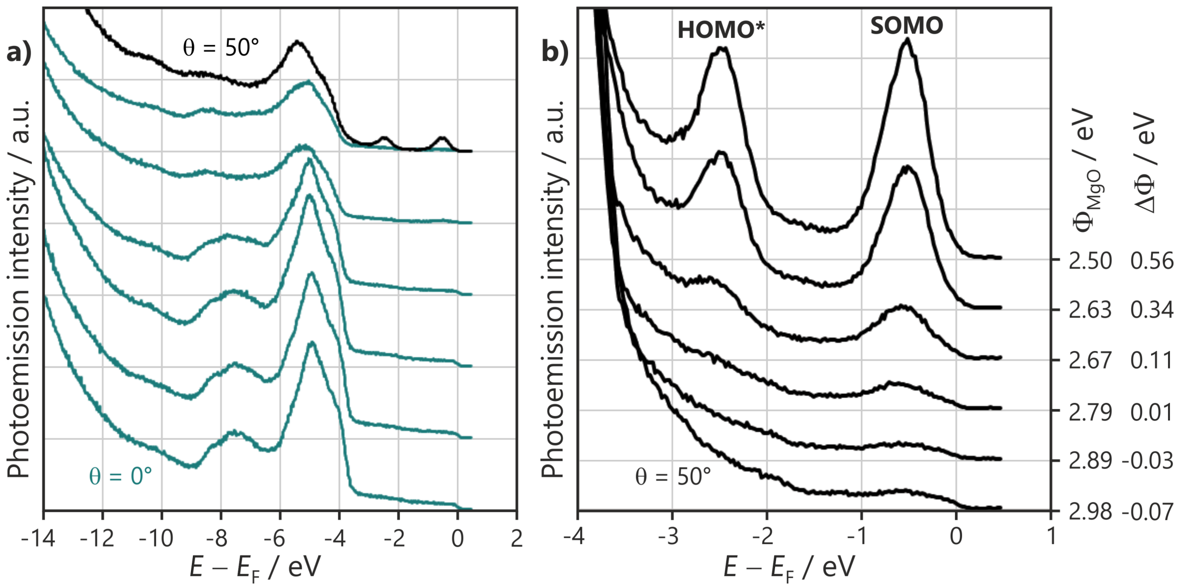

Figure 4: He I ARUPS spectra for different preparations with the same saturation exposure of 6P (4 Å) on the same 2 ML MgO film tuned to different work functions. Φ_{MgO} values and the change in Φ induced on 6P exposure (ΔΦ) are given on the right. (a) Wide scans at normal emission (θ = 0°) emphasizing the MgO emission region. The black curve shows the ARUPS spectrum measured at θ = 50° in the [001] azimuth, where the 6P HOMO* and SOMO emissions in the MgO bandgap region are prominent. (b) Magnification of the HOMO* and SOMO emissions in the MgO bandgap at θ = 50°.

distributions agree with the photoemission tomography of the HOMO and LUMO of the planar 6P seen in Figure 3. Note that the emissions in the MgO bandgap are due to the orbitals of charged molecules and will be referred to as HOMO* and SOMO henceforth. Neutral molecules are difficult to observe directly via ARUPS, as their HOMO emission lies below the gap in the region of intense MgO emissions (Figure 5a). The HOMO* and SOMO intensities increase with decreasing Φ_{MgO}, indicating an increase in the number of charged molecules. Thus, $\Phi_{\mathrm{MgO}} = 2.8$ eV is the critical work function value, below which charge transfer into 6P molecules occurs. The extreme sensitivity to Φ_{MgO} shown in Figure 4 explains the apparently ambivalent results obtained from STM and photoemission tomography in the previous section, as the accepted procedure for growing epitaxial MgO(100) films on Ag(100) [19,34] produces a scatter of the Φ_{MgO} values on either side of the critical work function ($\Phi_{\mathrm{crit}} = 2.8$ eV).

Figure 5 shows the evolution of the ARUPS spectra with an increasing 6P dose on an MgO(100) film with $\Phi_{\mathrm{MgO}} = 2.58$ eV (i.e., below Φ_{crit}). In the MgO valence band region (Figure 5a), gradual changes can be observed. In the MgO bandgap region (magnified in Figure 5b), the intensities of the HOMO* and SOMO increase and reach their maximum value at a 6P dose between 1 and 1.5 Å. The increase in the molecular emission features is accompanied by an increase in the work function ($\Delta\Phi$, values listed on the right). The dose corresponding to a full 6P monolayer is estimated to be approximately 2.8 Å from the attenuation behavior of the valence band of the underlying MgO. The fact that the molecular emissions and Φ saturate well before the completion of the ML suggests that a significant number of neutral molecules are also present in the ML on this specific MgO film. A close inspection of Figure 5a shows that the HOMO of the neutral molecules can be seen at ≈3.6 eV.

In previous research, the charge transfer to 5A on MgO(100)/Ag(100) was quantified by comparing ARUPS data to predictions made by PT, yielding a LUMO occupation of 1 electron [14]. Following the same approach for 6P, the ratio between the HOMO* and the SOMO maximum intensity values is predicted to be 0.57 for a singly occupied LUMO. The various 6P preparations yielded intensity ratio values ranging from 0.60–0.75, suggesting a LUMO occupation of 1.0 to 1.3 electrons. This is consistent with single integer charge transfer, expected for tunneling, when uncertainties in the theoretical description of the photoemission intensities of the simple plane-wave final-state approximation and in the experimental determination of the peak areas are considered.

The capacitor model and the interlayer dielectric constant

The behavior observed in the ARUPS series of Figure 4 and Figure 5 is consistent with the predictions from the capacitor model expressed in Equation 1. Figure 6a depicts the relationship between the SOMO intensity (I_{SOMO}) and the work function change induced by molecule adsorption ($\Delta\Phi$), obtained

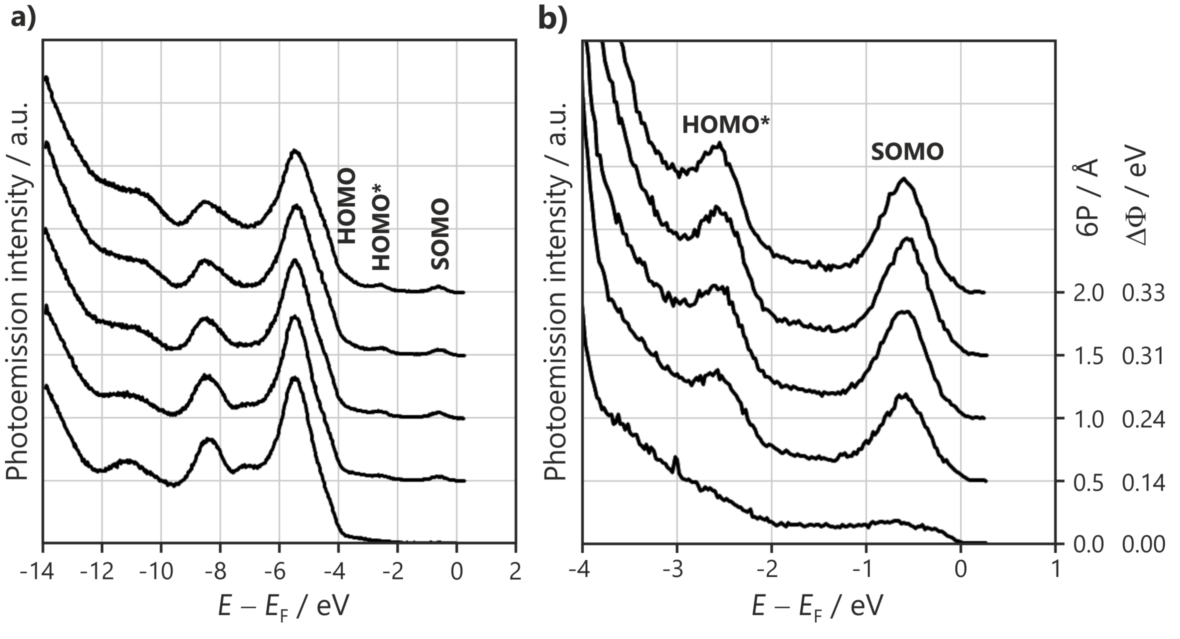

Figure 5: He I ARUPS spectra for a 6P dosing series on 2 ML MgO(100)/Ag(100) ($\Phi_{\mathrm{MgO}} = 2.58$ eV) recorded at a takeoff angle of 50° in the [001] azimuth. (a) Full scan and (b) magnification of the molecular emissions in the MgO bandgap. 6P exposure and change in the work function upon deposition are indicated on the right.

from the series of 6P saturation doses on MgO films with different Φ_{MgO} values. The linear proportionality between I_{SOMO} and $\Delta\Phi$ agrees with the capacitor model [20], considering that I_{SOMO} reflects the number of integer charged molecules in the monolayer and thus the charge density (σ) on the surface.

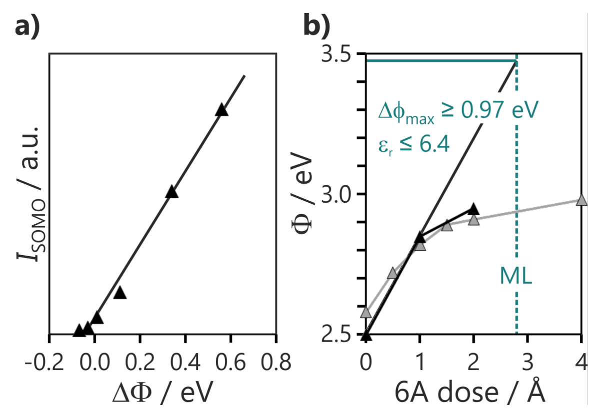

Figure 6: (a) Relation between integrated SOMO intensity and work function change induced by molecule adsorption on MgO(100)/Ag(100) ($\Delta\Phi$) after tuning Φ_{MgO} to slightly different values. (b) Work function versus 6P dose for two different initial work functions. The dose corresponding to a full ML is indicated by the dashed line.

For the capacitor model to be predictive and quantitative for ultrathin decoupling layers, a realistic value for their dielectric constant (ε_r) is required. This can be estimated from a molecular dosing series, such as in Figure 5. Figure 6b shows the increase of Φ with an increasing 6P dose for two different MgO films with $\Phi_{MgO} < \Phi_{crit}$ values. Initially, Φ increases rapidly with 6P exposure since all molecules become charged. The curve then flattens out as Φ approaches Φ_{pin} and additional molecules remain neutral. This is reached at an exposure of ≈1.4 Å, which is half of the amount required to complete the ML. It can be concluded that on these films there is a 50/50 mix of charged and neutral molecules in the completed monolayer.

Assuming all molecules are charged at low exposure, the ε_r value can be estimated from the initial slope ($\Delta\Phi/\sigma$) in Figure 6b, according to:

$$\varepsilon_r = \frac{\sigma}{\Delta\Phi}\frac{d_{cs}}{\varepsilon_0} \qquad (2)$$

In order to determine the charge density, the knowledge of the density of charged molecules in the monolayer is required. In the case of pentacene, this could be reliably measured with STM, as 5A monolayers with all molecules charged could be produced. The LEED image for 6P films on MgO(100)/Ag(100) with a high proportion of charged molecules showed faint superstructure spots, which suggest a later molecular spacing of 6.6 Å. The van der Waals dimensions of 6P (6.7 × 27.2 Å) [26] are close to the unit cell (6.35 × 27.47 Å) which is commensurate with MgO(100). The area of this unit cell corresponds to a molecular footprint of 173 Å^2 and gives an upper bound of 6.4 for ε_r. The ordered structure in the STM image of Figure 2b, where molecules do not show a zig-zag structure and are oriented along [11] (like the charged molecules in PT), is consistent with this lateral spacing. However, this structure suggests a slightly longer length of 31 Å for the long unit cell vector. This value yields a molecular area of 197 Å^2 and an ε_r of 5.7. This estimate is in agreement with the values for ε_r (between 5 and 6) obtained for 5A/MgO(100)/Ag(100) using two different approaches and MgO thickness values ranging from 2 to 8 ML [20]. This suggests that the effective ε_r for MgO thin films is significantly smaller than the bulk value of 9.9 [35].

Critical and pinning work functions

The rather abrupt changes over a narrow work function range observed for both the charge transfer and wetting behavior for 6P are in contrast with the 5A system. In the latter, the number of charged molecules increases gradually with Φ_{MgO} below the critical work function, and a wetting ML is always present, whether or not the charge transfer occurs. Due to the critical role of the work function for charge transfer, it is convenient to plot the work function after saturating the surface with molecules (Φ_{mol}) as a function of Φ_{MgO}. This is shown in Figure 7 for both 5A and 6P on 2 ML MgO(100)/Ag(100). For the 5A case, the regimes of vacuum level alignment and Fermi level pinning are clearly expressed: In the vacuum level alignment regime, there is no charge transfer and the final work function closely follows the Schottky–Mott rule in which $\Phi_{mol} = \Phi_{MgO}$ (the 45° line in Figure 7), albeit with a slight reduction in Φ due to Pauli repulsion (pushback). The Fermi level pinning is characterized by a constant final work function, Φ_{pin}, and an increase in the number of charged molecules with decreasing Φ_{MgO}. The number of charged molecules is determined by the potential needed to raise Φ to Φ_{pin} values, whereupon no further charge transfer can occur. It is quite intuitive that Φ_{pin} equals the critical work function for the onset of charge transfer, Φ_{crit}.

However, surprisingly, this is not the case for 6P as shown in red in Figure 7. For high Φ_{MgO} values, again Φ_{mol} is essentially equal to Φ_{MgO}. The critical work function for the charge transfer (i.e., the point where Φ_{mol} increases above the 45° line) is approximately 2.8 eV. This is significantly lower than the value for 5A, which is expected due to the lower EA of 6P (theoretical values of 2.39 eV and 1.45 eV, respectively, using the B3LYP functional). However, unlike for 5A, as Φ_{MgO} decreases further, Φ_{mol} does not remain constant but increases above Φ_{crit}. This reflects the rapid increase in the number of charged molecules observed in Figure 4. Only for

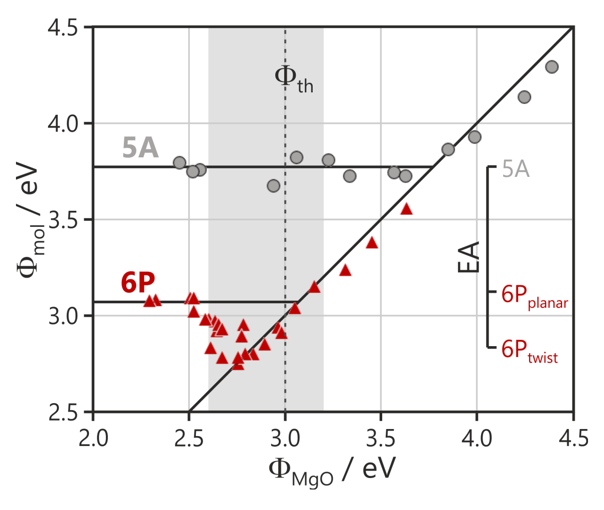

Figure 7: The work function after the deposition of a saturating dose of 5A (grey) and 6P (red) (Φ_{mol}) as a function of the initial work function of a clean MgO(100)/Ag(100) substrate (Φ_{MgO}). The line with a slope of unity expresses the Schottky–Mott limit of the vacuum level alignment ($\Phi_{mol} = \Phi_{MgO}$). The horizontal lines correspond to the pinning work functions of 5A and 6P on 2 ML MgO films on Ag(100). The dashed line indicates the theoretical work function for a stoichiometric MgO–Ag(100) interface [36], and the shaded gray area indicates the most typical range of work functions obtained with MgO film growth under nominally identical conditions. The inserted scale shows the theoretical gas-phase electron affinities for 5A, twisted 6P, and planar 6P and it has been shifted to align the EA of 5A with the measured pinning work function for 5A.

$\Phi_{MgO} \leq 2.5$ eV the final work function adopts a constant value of 3.07 eV, which is the pinning work function of 6P on 2 ML MgO(100)/Ag(100). Thus, for 6P, Φ_{pin} is 0.3 eV higher than Φ_{crit}.

We suggest that this difference is related to the conformational change of 6P upon charging. Φ_{crit} derives from the electron affinity of the neutral, twisted molecule, while Φ_{pin} derives from the EA of the planar molecule. The planarization of the molecule will lead to greater orbital overlap between the phenyl rings. This will cause an increase in the energy spread of the π bands, resulting in a decrease in the ionization potential and an increase in the electron affinity. Gas phase DFT calculations show that the EA of planar 6P (1.74 eV) is indeed 0.3 eV higher than the EA of twisted 6P (1.45 eV). This is in close agreement with the measured difference between Φ_{pin} and Φ_{crit} seen in Figure 7, while only a negligible difference in molecular surface dipole is expected between twisted and planar molecules [37]. It should be noted that this alone cannot explain that, depending on the initial work function, either Φ_{crit} or Φ_{pin} is the decisive work function for charge transfer.

In order to better understand the transition between the two regimes, an alternative representation of the data from Figure 7 is given in Figure 8a. In the latter, the work function change upon 6P deposition as a function of the substrate work function, for various 6P films on a number of different 2 ML MgO films is plotted. This is displayed in comparison to the 6P surface coverage, which is expressed by a wetting parameter in Figure 8b. The wetting parameter reflects the combined effects of the intensity of all molecular emissions and the suppression of substrate emissions (see Experimental section). The small wetting parameter in the vacuum level alignment regime confirms that molecules do not wet the surface, indicating a low molecule–substrate interaction and 3D island formation.

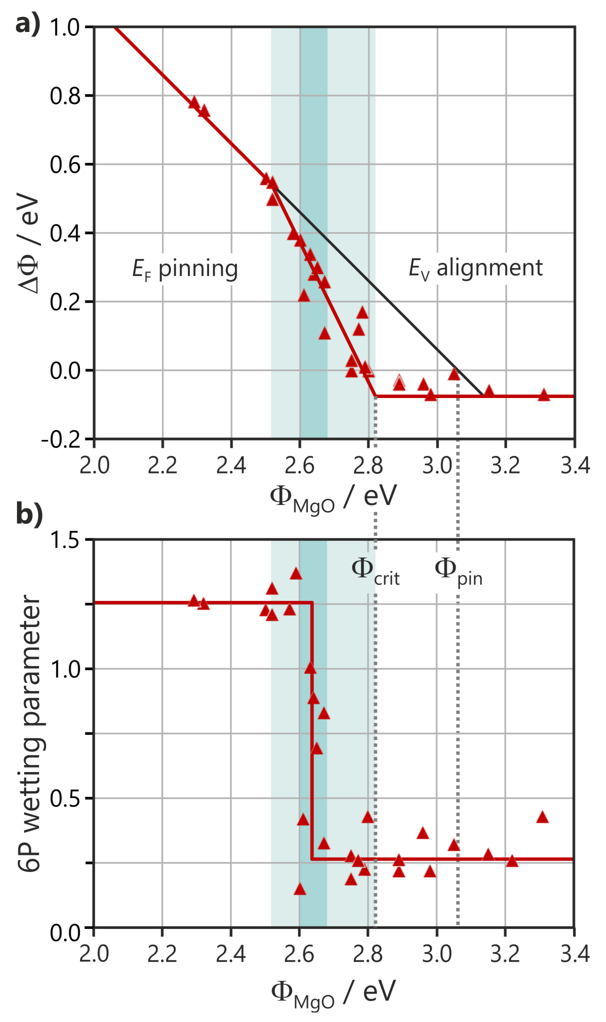

Figure 8: Changes in the charge transfer and wetting behavior of 6P on MgO(100)/Ag(100) as a function of Φ_{MgO}. (a) Work function change induced by 6P as an indicator of charge transfer. The black 45° line corresponds to a constant final work function and expresses the behavior when $\Phi_{pin} = \Phi_{crit}$. (b) Wetting parameter as an indicator of the fraction of the substrate covered by 6P.

For Φ_{MgO} values between Φ_{crit} and 2.52 eV, Figure 8a exhibits a steep rise in $\Delta\Phi$ and, therefore, in the number of charged molecules. However, the wetting indicated in Figure 8b remains low, until Φ_{MgO} reaches approximately 2.64 eV, where an

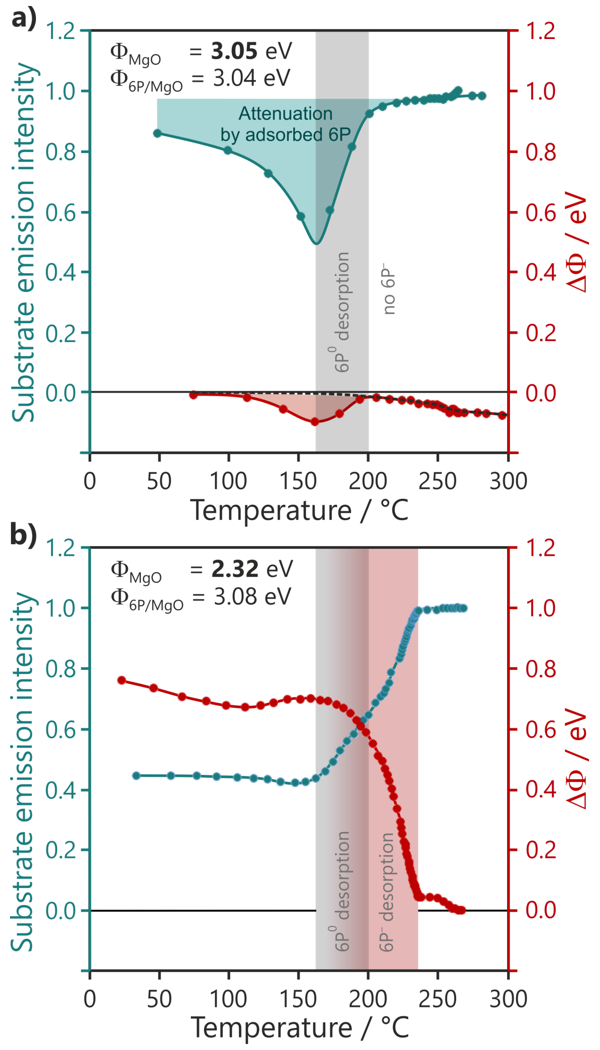

Figure 9: Thermal stability of 6P films (4 Å) on 2 ML of MgO with work functions (a) above and (b) below the critical work function. The blue curves depict the normalized photoemission intensity of the MgO valence band relative to the intensity after 6P film desorption. The red curves depict the change in work function relative to the pristine MgO film work functions, Φ_{MgO}.

abrupt discontinuous transition to high wetting occurs. We propose that the critical factor for this phase transition is the density of charged molecules present on the surface. The planarization and electrostatic interaction of the charged molecules with the substrate can be expected to reduce the mobility of the charged molecules. These charged molecules will in turn restrict the free motion of the neutral molecules and, at a critical density, immobilize and reorient them. This wetting transition occurs when 30% of the molecules are charged, as estimated from $\Delta\Phi$ in the capacitor model, while the final Φ_{pin} is established after 60% of the molecules are charged.

The effect of charge transfer and physical coupling on thermal stability

We now turn to the role of charge transfer on the physical coupling by considering the thermal stability of the molecular film. This is considered in Figure 9a and Figure 9b for a 6P deposit of 4 Å on two 2 ML thick MgO films for Φ_{MgO} values above (Figure 9a) and below (Figure 9b) the critical work function for charge transfer. The graphs show the intensity of the substrate photoemission signal (MgO valence band peak intensity in normal emission) and the response of the work function while increasing the temperature. For the high Φ_{MgO} film case, where the ARUPS results show no charged molecules on the surface, the temperature increase leads first to an apparently counterintuitive decrease in substrate intensity until the temperature reaches approximately 160 °C. This is followed by an abrupt increase in intensity until the temperature reaches 200 °C. At that point, since the intensity has almost returned to its value prior to the 6P deposition, all the molecules can be considered to be desorbed from the surface. This behavior is mirrored in the work function, which first decreases and then, at 160 °C, increases, returning to its original value by 200 °C. The initial substrate intensity suggests that, at room temperature, only approximately 20% of the surface is covered by molecules, implying that 3D islanding occurs. The temperature increase liberates molecules from the islands and allows them to wet the MgO surface. Right before their desorption at 160 °C, the attenuation of the substrate emission signal suggests a complete surface coverage. The temperature-induced wetting of the surface with neutral molecules is reflected in the pushback-induced lowering of Φ by ≈ -0.1 eV.

The desorption behavior on the low Φ_{MgO} film, with up to 80% of the molecules charged according to the capacitor model (Figure 9b), is quite different. The initial substrate attenuation confirms that the molecules wet the surface at room temperature. There is no significant change in this attenuation until the temperature reaches 160 °C. At that point, the substrate intensity increases as the molecules begin to desorb from the surface. From Figure 9a, we already know that this is the desorption temperature of neutral molecules. However, on this MgO film, desorption continues well beyond 200 °C, and the substrate intensity returns to the value corresponding to the clean substrate at 230 °C. It stands to reason that this further increase in the substrate intensity between 200 and 230 °C is caused by the desorption of the initially charged molecules. This is confirmed by the behavior of the work function in Figure 9b, which shows a concomitant strong decrease in this temperature range. This higher desorption temperature of the charged molecules relative to the neutral molecules can be expected due the electrostatic interaction of the charged molecule with its image charge. It may therefore seem surprising that the onset of the work function decrease and, therefore, the desorption of charged molecules happens already within the desorption regime of the neutral molecules. This might be explained by the spontaneous discharging as a result of the thermal energy distribution, enabling desorption as a neutral molecule.

Conclusion

While charged 6P molecules could not be unambiguously identified by STM, valence band photoemission measurements allowed for their clear observation. Moreover, PT and ARUPS allowed the orientation and number of charged molecules to be quantified. The number of charged molecules and the determination if a given molecule was charged or not were found to be extremely sensitive to the precise work function of the particular MgO(100)/Ag(100) film preparation. This was investigated systematically by tuning the work function of a MgO(100)/Ag(100) film to values around the critical work function for integer charge transfer to 6P molecules. The simple relationship observed between the number of charged molecules and the work function change on the molecular adsorption proves that the charge transfer is governed by simple electrostatics. This confirms the conclusions drawn from a recent study with pentacene [20] and suggests that the ε_r of thin dielectrics may be significantly different from the values of their bulk counterparts (e.g., the ε_r of the MgO film presented here is approximately half the value of bulk MgO).

In contrast to pentacene, 6P is a geometrically flexible molecule. The charge transfer to 6P leads to both conformational and orientational changes and has a profound influence on the wetting and thermal stability of the 6P films. Upon anion formation, the molecule is planarized and orients exclusively along the [001] azimuth due to its electrostatic bond to the substrate. The presence of charged molecules hinders the mobility of the twisted neutral molecules [38]; therefore, when approximately 30% of the molecules are charged, a transition occurs and the neutral molecules also wet the surface. The conformational change induced by charge transfer leads to the final pinning work function being higher than the critical work function, as the latter is related to the electron affinity of the neutral twisted molecule, while the former is associated with the EA of the planar conformation. Increasing MgO thickness decreases the EA due to reduced polarization [20]. The Φ_{crit} is reduced to such a low value that systematic thickness-dependent studies of charge transfer to 6P could not be performed.

On dielectric interlayers, a simple measurement of the work function before and after the adsorbate overlayer growth is perhaps the most telling result with regard to electronic and physical coupling. If there is only a small reduction of Φ, then the system is in the vacuum level alignment regime and there is no charge transfer. If there is any significant change in Φ, then the system is in the Fermi level pinning regime with equilibrium achieved by a balance between charged and neutral adsorbates in the first monolayer. An increase in Φ, as in the examples here, implies a charge transfer from the underlying substrate to the LUMO while a decrease in Φ would indicate integer charge transfer from the HOMO to the substrate. The mode of charge transfer is primarily determined by the electron affinity and ionization potential levels and their relation to the Fermi level of the substrates. This is set by the dielectric/substrate work function.

It is important to emphasize that once in the Fermi level pinning regime, both charged and neutral species will co-exist on the dielectric. This has not been recognized until now because many of the standard techniques cannot easily distinguish between charged and neutral species. For reasonably large molecules with delocalized frontier orbitals, the integer charge is spread over many atoms and the resulting chemical shift will be too small to be seen with X-ray photoelectron spectroscopy [20]. Similarly, the LEED technique will probably not be sensitive to the charge state per se, although differences in the molecular orientation and in the long-range order might occur. With a thorough analysis and molecular orbital resolution, it should be possible to distinguish them with scanning probe techniques. Generally, however, studies with orbital resolution tend to focus on very low coverages, where only charged species will be present.

Experimental

All experiments were performed under ultrahigh vacuum (UHV) conditions with a base pressure of $\leq 3 \times 10^{-10}$ mbar. The Ag(100) crystal was cleaned by cycles of Ar^+ sputtering and annealing at 500 °C. MgO(100) films were grown by Mg evaporation in an oxygen environment. The Mg fluxes used were on the order of 1 Å/min as monitored by a quartz microbalance. The MgO deposition was done at a temperature of 270 °C and at an O_2 pressure of 10^{-6} mbar, followed by slow cooling (approximately 2.5 °C/min). This is the accepted procedure that provides epitaxial MgO(100) films with high structural quality [19,34]. One ML of MgO is defined as a single atomic layer (i.e., half a unit cell of crystalline bulk MgO), corresponding to a thickness of 2.105 Å. Work functions, measured from the secondary electron cutoff in the photoemission, could be reduced by annealing in UHV or further Mg exposure while annealing. The work function could be increased by O_2 exposure (5×10^{-7}–2×10^{-4} mbar) at moderate temperatures. Monitoring the work function during this post-preparation allowed for a close control of this parameter. *para*-Sexiphenyl (6P) was deposited at a rate of 0.8–3 Å/min at RT. When the 6P exposure is given in Angstroms, this refers to the microbalance reading with a density of 1 g/cm^3. After conducting the ARUPS measurements on 6P/MgO(100)/Ag(100), 6P was desorbed from the substrate by flashing to 250 °C. Then, the work function of the substrate was modified as desired for the next 6P preparation. This allowed the experiments to be performed on a MgO film with the exact same thickness but with different work functions.

The photoemission tomography experiments were conducted at the Metrology Light Source insertion device beamline of the Physikalisch-Technische Bundesanstalt using the toroidal electron spectrometer. The ARUPS experiments were performed with a small hemispherical sector electron analyzer mounted on a goniometer (VG-ADES400) with a He I discharge lamp as photon source. Details of the PT and ARUPS setups as well as the identification of molecular orbitals can be found in work by Hollerer et al. [14]. The intensity values of the molecular photoemission features were determined by subtracting the background, measured prior to the adsorption, from the molecules and determining the area of the peak measured in the direction of the maximum emission intensity. At the He I of 21.22 eV, these were at 50° and 45° with respect to the surface normal along the [001] azimuthal direction for the LUMO and the HOMO, respectively.

The wetting parameter quantifies the spectral changes reflecting the wetting of 6P. It is calculated from the intensity of the MgO valence band peak prior to/after 6P deposition ($I_{\mathrm{MgO}}/I_{\mathrm{MgO}'}$) and the corresponding intensities ($I_{\mathrm{6P}}/I_{\mathrm{6P}'}$) in the energy range (between 14 eV and 6 eV below E_{F}, normal emission) where the emission of the 6P sigma-orbitals is found, as

$$\frac{I_{\mathrm{MgO}}}{I_{\mathrm{MgO}}{}'}\frac{I_{\mathrm{6P}}{}'}{I_{\mathrm{6P}}}-1.$$

To assess the desorption dynamics, the samples were heated manually by a filament behind the crystal at a very low heating rate of approximately 0.1 °C/s (on average).

STM measurements were performed at −193 °C with a Createc low-temperature STM using electrochemically etched tungsten tips. The bias voltage was applied to the sample.

Acknowledgements

We would like to thank Hendrik Kaser (PTB, Germany) and John Riley (La Trobe University, Australia) for their technical support.

Funding

This work was funded by the Austrian Science Fund (FWF) (projects P27649-N20, P27427-N20 and I 3731) and the Deutsche Forschungsgemeinschaft (DFG) (projects Po 2226/2-1 and Ri 804/8-1).

ORCID® iDs

Georg Koller - https://orcid.org/0000-0001-7741-2394
Xiaosheng Yang - https://orcid.org/0000-0002-7632-0401
Anja Haags - https://orcid.org/0000-0001-9117-8805
Serguei Soubatch - https://orcid.org/0000-0002-1455-0260
Alexander Gottwald - https://orcid.org/0000-0003-2810-7419
Peter Puschnig - https://orcid.org/0000-0002-8057-7795
Martin Sterrer - https://orcid.org/0000-0001-9089-9061
Michael G. Ramsey - https://orcid.org/0000-0003-0523-1994

References

1. Repp, J.; Meyer, G.; Stojković, S. M.; Gourdon, A.; Joachim, C. *Phys. Rev. Lett.* **2005,** *94,* 026803. doi:10.1103/physrevlett.94.026803
2. Wu, S. W.; Ogawa, N.; Nazin, G. V.; Ho, W. *J. Phys. Chem. C* **2008,** *112,* 5241–5244. doi:10.1021/jp7114548
3. Swart, I.; Sonnleitner, T.; Repp, J. *Nano Lett.* **2011,** *11,* 1580–1584. doi:10.1021/nl104452x
4. Pacchioni, G.; Giordano, L.; Baistrocchi, M. *Phys. Rev. Lett.* **2005,** *94,* 226104. doi:10.1103/physrevlett.94.226104
5. Giordano, L.; Baistrocchi, M.; Pacchioni, G. *Phys. Rev. B* **2005,** *72,* 115403. doi:10.1103/physrevb.72.115403
6. Giordano, L.; Pacchioni, G. *Phys. Chem. Chem. Phys.* **2006,** *8,* 3335–3341. doi:10.1039/b604288k
7. Sterrer, M.; Risse, T.; Heyde, M.; Rust, H.-P.; Freund, H.-J. *Phys. Rev. Lett.* **2007,** *98,* 206103. doi:10.1103/physrevlett.98.206103
8. Sterrer, M.; Risse, T.; Martinez Pozzoni, U.; Giordano, L.; Heyde, M.; Rust, H.-P.; Pacchioni, G.; Freund, H.-J. *Phys. Rev. Lett.* **2007,** *98,* 096107. doi:10.1103/physrevlett.98.096107
9. Gonchar, A.; Risse, T.; Freund, H. J.; Giordano, L.; Di Valentin, C.; Pacchioni, G. *Angew. Chem., Int. Ed.* **2011,** *50,* 2635–2638. doi:10.1002/anie.201005729
10. Starr, D. E.; Weis, C.; Yamamoto, S.; Nilsson, A.; Bluhm, H. *J. Phys. Chem. C* **2009,** *113,* 7355–7363. doi:10.1021/jp900410v
11. Schulz, F.; Drost, R.; Hämäläinen, S. K.; Liljeroth, P. *ACS Nano* **2013,** *7,* 11121–11128. doi:10.1021/nn404840h
12. Wang, H.; Amsalem, P.; Heimel, G.; Salzmann, I.; Koch, N.; Oehzelt, M. *Adv. Mater. (Weinheim, Ger.)* **2014,** *26,* 925–930. doi:10.1002/adma.201303467
13. Yang, X.; Krieger, I.; Lüftner, D.; Weiß, S.; Heepenstrick, T.; Hollerer, M.; Hurdax, P.; Koller, G.; Sokolowski, M.; Puschnig, P.; Ramsey, M. G.; Tautz, F. S.; Soubatch, S. *Chem. Commun.* **2018,** *54,* 9039–9042. doi:10.1039/c8cc03334j
14. Hollerer, M.; Lüftner, D.; Hurdax, P.; Ules, T.; Soubatch, S.; Tautz, F. S.; Koller, G.; Puschnig, P.; Sterrer, M.; Ramsey, M. G. *ACS Nano* **2017,** *11,* 6252–6260. doi:10.1021/acsnano.7b02449
15. Hofmann, O. T.; Rinke, P.; Scheffler, M.; Heimel, G. *ACS Nano* **2015,** *9,* 5391–5404. doi:10.1021/acsnano.5b01164
16. Cho, S. B.; Yun, K.-H.; Yoo, D. S.; Ahn, K.; Chung, Y.-C. *Thin Solid Films* **2013,** *544,* 541–544. doi:10.1016/j.tsf.2012.12.072
17. Jaouen, T.; Aebi, P.; Tricot, S.; Delhaye, G.; Lépine, B.; Sebilleau, D.; Jézéquel, G.; Schieffer, P. *Phys. Rev. B* **2014,** *90,* 125433. doi:10.1103/physrevb.90.125433
18. Jaouen, T.; Tricot, S.; Delhaye, G.; Lépine, B.; Sébilleau, D.; Jézéquel, G.; Schieffer, P. *Phys. Rev. Lett.* **2013,** *111,* 027601. doi:10.1103/physrevlett.111.027601
19. Pal, J.; Smerieri, M.; Celasco, E.; Savio, L.; Vattuone, L.; Ferrando, R.; Tosoni, S.; Giordano, L.; Pacchioni, G.; Rocca, M. *J. Phys. Chem. C* **2014,** *118,* 26091–26102. doi:10.1021/jp507718n

20. Hurdax, P.; Hollerer, M.; Puschnig, P.; Lüftner, D.; Egger, L.; Ramsey, M. G.; Sterrer, M. *Adv. Mater. Interfaces* **2020,** *7,* 2000592. doi:10.1002/admi.202000592
21. Hollerer, M.; Pachmajer, S.; Lüftner, D.; Butej, B.; Reinisch, E.-M.; Puschnig, P.; Koller, G.; Ramsey, M. G.; Sterrer, M. *Surf. Sci.* **2018,** *678,* 149–156. doi:10.1016/j.susc.2018.04.017
22. Koller, G.; Berkebile, S.; Krenn, J. R.; Tzvetkov, G.; Hlawacek, G.; Lengyel, O.; Netzer, F. P.; Teichert, C.; Resel, R.; Ramsey, M. G. *Adv. Mater. (Weinheim, Ger.)* **2004,** *16,* 2159–2162. doi:10.1002/adma.200400276
23. Koller, G.; Berkebile, S.; Oehzelt, M.; Puschnig, P.; Ambrosch-Draxl, C.; Netzer, F. P.; Ramsey, M. G. *Science* **2007,** *317,* 351–355. doi:10.1126/science.1143239
24. Oehzelt, M.; Grill, L.; Berkebile, S.; Koller, G.; Netzer, F. P.; Ramsey, M. G. *ChemPhysChem* **2007,** *8,* 1707–1712. doi:10.1002/cphc.200700357
25. Wagner, M.; Berkebile, S.; Netzer, F. P.; Ramsey, M. G. *ACS Nano* **2015,** *9,* 12070–12078. doi:10.1021/acsnano.5b05013
26. Baker, K. N.; Fratini, A. V.; Resch, T.; Knachel, H. C.; Adams, W. W.; Socci, E. P.; Farmer, B. L. *Polymer* **1993,** *34,* 1571–1587. doi:10.1016/0032-3861(93)90313-y
27. Puschnig, P.; Ramsey, M. G. Photoemission Tomography: Valence Band Photoemission as a Quantitative Method for Investigating Molecular Films. In *Encyclopedia of Interfacial Chemistry;* Wandelt, K., Ed.; Elsevier: Amsterdam, Netherlands, 2018; pp 380–391. doi:10.1016/b978-0-12-409547-2.13782-5
28. Puschnig, P.; Berkebile, S.; Fleming, A. J.; Koller, G.; Emtsev, K.; Seyller, T.; Riley, J. D.; Ambrosch-Draxl, C.; Netzer, F. P.; Ramsey, M. G. *Science* **2009,** *326,* 702–706. doi:10.1126/science.1176105
29. Berkebile, S.; Koller, G.; Fleming, A. J.; Puschnig, P.; Ambrosch-Draxl, C.; Emtsev, K.; Seyller, T.; Riley, J.; Ramsey, M. G. *J. Electron Spectrosc. Relat. Phenom.* **2009,** *174,* 22–27. doi:10.1016/j.elspec.2009.04.001
30. Grimm, M.; Metzger, C.; Graus, M.; Jugovac, M.; Zamborlini, G.; Feyer, V.; Schöll, A.; Reinert, F. *Phys. Rev. B* **2018,** *98,* 195412. doi:10.1103/physrevb.98.195412
31. Reinisch, E. M.; Puschnig, P.; Ules, T.; Ramsey, M. G.; Koller, G. *Phys. Rev. B* **2016,** *93,* 155438. doi:10.1103/physrevb.93.155438
32. Reinisch, E. M.; Ules, T.; Puschnig, P.; Berkebile, S.; Ostler, M.; Seyller, T.; Ramsey, M. G.; Koller, G. *New J. Phys.* **2014,** *16,* 023011. doi:10.1088/1367-2630/16/2/023011
33. Brédas, J. L.; Thémans, B.; Fripiat, J. G.; André, J. M.; Chance, R. R. *Phys. Rev. B* **1984,** *29,* 6761–6773. doi:10.1103/physrevb.29.6761
34. Pal, J.; Smerieri, M.; Celasco, E.; Savio, L.; Vattuone, L.; Rocca, M. *Phys. Rev. Lett.* **2014,** *112,* 126102. doi:10.1103/physrevlett.112.126102
35. Subramanian, M. A.; Shannon, R. D.; Chai, B. H. T.; Abraham, M. M.; Wintersgill, M. C. *Phys. Chem. Miner.* **1989,** *16,* 741–746. doi:10.1007/bf00209695
36. Prada, S.; Martinez, U.; Pacchioni, G. *Phys. Rev. B* **2008,** *78,* 235423. doi:10.1103/physrevb.78.235423
37. Heimel, G.; Salzmann, I.; Duhm, S.; Rabe, J. P.; Koch, N. *Adv. Funct. Mater.* **2009,** *19,* 3874–3879. doi:10.1002/adfm.200901025
38. Hla, S.-W.; Braun, K.-F.; Wassermann, B.; Rieder, K.-H. *Phys. Rev. Lett.* **2004,** *93,* 208302. doi:10.1103/physrevlett.93.208302

License and Terms

The definitive version of this article is the electronic one which can be found at:
https://doi.org/10.3762/bjnano.11.132

BEILSTEIN JOURNAL OF NANOTECHNOLOGY

Adsorption and self-assembly of porphyrins on ultrathin CoO films on Ir(100)

Feifei Xiang, Tobias Schmitt, Marco Raschmann and M. Alexander Schneider[*]

Full Research Paper

Open Access

Address:
Solid State Physics, Friedrich-Alexander-Universität
Erlangen-Nürnberg (FAU), 91058 Erlangen, Germany

Email:
M. Alexander Schneider[*] - alexander.schneider@fau.de

* Corresponding author

Keywords:
adsorption energy; molecular rotors; porphyrins; self-assembly;
transition metal oxides

Beilstein J. Nanotechnol. **2020,** *11,* 1516–1524.
https://doi.org/10.3762/bjnano.11.134

Received: 31 May 2020
Accepted: 22 September 2020
Published: 05 October 2020

This article is part of the thematic issue "Molecular assemblies on surfaces – towards physical and electronic decoupling of organic molecules".

Guest Editor: S. Maier

Abstract

Porphyrins represent a versatile class of molecules, the adsorption behavior of which on solid surfaces is of fundamental interest due to a variety of potential applications. We investigate here the molecule–molecule and molecule–substrate interaction of Co-5,15-diphenylporphyrin (Co-DPP) and 2*H*-tetrakis(*p*-cyanophenyl)porphyrin (2H-TCNP) on one bilayer (1BL) and two bilayer (2BL) thick cobalt oxide films on Ir(100) by scanning tunneling microscopy (STM) and density functional theory (DFT). The two substrates differ greatly with respect to their structural and potential-energy landscape corrugation with immediate consequences for adsorption and self-assembly of the molecules studied. On both films, an effective electronic decoupling from the metal substrate is achieved. However, on the 1BL film, Co-DPP molecules are sufficiently mobile at 300 K and coalesce to self-assembled molecular islands when cooled to 80 K despite their rather weak intermolecular interaction. In contrast, on the 2BL film, due to the rather flat potential landscape, molecular rotation is thermally activated, which effectively prevents self-assembly. The situation is different for 2H-TCNPP, which, due to the additional functional anchoring groups, does not self-assemble on the 1BL film but forms self-assembled compact islands on the 2BL film. The findings demonstrate the guiding effect of the cobalt oxide films of different thickness and the effect of functional surface anchoring.

Introduction

Due to their variability with respect to functionalization and corresponding potential applications, porphyrins represent a fascinating class of molecules the properties of which at inorganic interfaces still have to be fully understood [1]. The investigation of adsorption properties and structures using surface science methods has been very successful in recent decades, but it mainly focused on metal or semi-metal surfaces. The research revealed numerous ways to steer self-assembly and on-surface reactions by a careful choice of functionalization and substrates [2]. Despite its importance for applications, the investigation of the structure and binding of porphyrins on semiconducting and, notably, metal oxide surfaces remains scarce [3-13]. We chose here to investigate two different porphyrins on thin films of cobalt(II) oxide (CoO). Cobalt(II) oxide not only is a semi-conducting oxide, it is also an anti-ferromagnet due to electron correlation effects and it shows catalytic activity [14-17]. As a thin film grown on Ir(100), the oxide is of extremely high quality [18-20] avoiding the complexity that arises from atomic-scale defects in bulk materials [5-8]. The atomic structure of these films has been investigated in detail by diffraction methods [18-21]. The corresponding data ensures reproducibility of the cobalt oxide preparation and meaningful computer-based substrate modeling.

Functionalization of porphyrins may introduce new properties of the molecular adlayer, for example, by introducing elements that allow for strong anchoring [8,10-13]. This may, however, counteract the possibility to form ordered layers when, due to the enhanced molecule–substrate interaction, the molecules become immobile or the functional groups used as anchors cannot give rise to intermolecular forces anymore. The molecules employed in this study, Co-5,15-diphenylporphyrin (Co-DPP) and 2*H*-tetrakis(*p*-cyanophenyl)porphyrin (2H-TCNPP), are representatives with which this important hierarchy of interaction energies may be studied. While Co-DPP anchors mainly through its central metal atom and provides rather weak intermolecular interaction via its phenyl substituents, 2H-TCNPP may use its cyanophenyl groups for either coupling to the substrate or for providing relatively strong molecule–molecule interactions. The two molecules have been investigated on metal surfaces. It was shown that free-base (2H) or metalated DPP molecules assemble in two-dimensional or linear structures on metal surfaces [22,23] and that on-surface dehydrogenative polymerization reactions may be induced [24]. DPP molecules interact via the phenyl rings and the molecular macrocycle. In contrast, 2H-TCNPP is found to either form metal-organic networks or structures that, depending on the substrate, are stabilized by hydrogen bonding or dipolar coupling via its cyano groups [10,25,26]. This is similar to findings for other cyano-functionalized molecules [27-30]. The aim of this paper is to find the adsorption geometry of the two molecules, to demonstrate electronic decoupling from the supporting Ir substrate, and to reveal the relevant energetic hierarchy that may lead to self-assembly on the particular oxide surfaces.

Experimental

All experiments were performed in ultra-high vacuum (UHV) at a base pressure of 8×10^{-11} mbar. STM images were taken using a custom-built low-temperature UHV STM operated at liquid-nitrogen temperature (80 K). We used etched tungsten tips and the bias voltage is the potential of the sample with respect to the tip. Co-DPP (**1**, PorphyChem SAS, 98% purity, Figure 1a) and 2H-TCNPP (**2**, Porphyrin Systems, 97% purity, Figure 1b) were evaporated from a graphite crucible effusion cell. Co-DPP was evaporated at a measured cell temperature of 540 K and 2H-TCNPP at 640 K, which resulted in a molecular deposition rate of 0.04 and 0.06 $\mathrm{nm^{-2} \cdot min^{-1}}$. Both molecules were carefully outgassed for 2 to 5 h prior to deposition at ±10 K of the evaporation temperature.

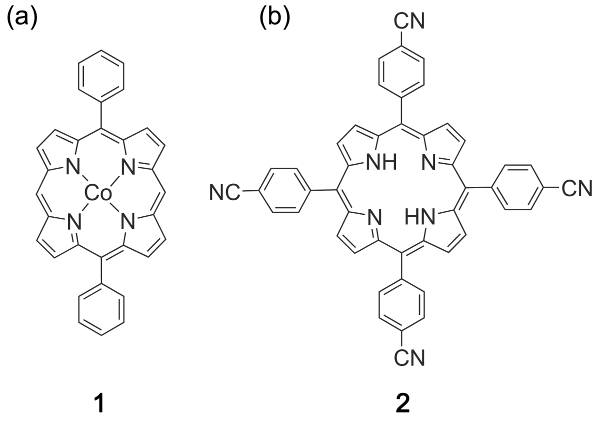

Figure 1: Chemical structure of (a) Co-DPP (**1**) and (b) 2H-TCNPP (**2**).

CoO was prepared on an Ir(100) single crystal surface cleaned by ion sputtering and annealing. The Ir(100)-(1 × 1) surface was prepared according to [31]. We employ thin films of two distinct thicknesses, which we state in bilayers, derived from the Co–O bilayer of a rock salt CoO(111) crystal. Cobalt was evaporated from a metal rod using an e-beam evaporator. A one-bilayer (1BL) or a two-bilayer (2BL) film were obtained by depositing 0.9 ML or 1.8 ML, respectively, of cobalt on the Ir(100)-(1 × 1) at 320 K substrate temperature followed by annealing in 2×10^{-9} mbar O_2 at 520 K. To improve ordering, the films were flash-heated to 670 K in UHV. The cleanliness, quality and thickness of the prepared substrates was verified by comparison to low-energy electron diffraction intensity data of earlier studies [18,20].

A 1BL CoO(111) film exhibits a corrugated, slightly distorted cobalt oxide bilayer (Figure 2a,b). It forms a one-dimensional moiré on the Ir(100) surface with perfect row matching resulting in a superstructure between $c(8 \times 2)$ and $c(10 \times 2)$ with respect to the Ir(100) surface lattice [20]. While the cobalt ions bind directly to the iridium substrate, there is a considerable buckling of 100 pm of the oxygen atoms. The 2BL CoO(111) film is structurally much flatter with a surface corrugation of only 20 pm [18] (Figure 2c,d). From the structural analysis of thicker CoO(111) films we imply that the surface is oxygen-terminated and shows a wurtzite-type of surface termination [19]. This has been confirmed by surface X-ray diffraction analysis of the 2BL film [21]. Although the 2BL film is structurally close to a $c(10 \times 2)$ surface structure it may be considered as a flat, quasi-hexagonal layer with lattice parameter $a_{\text{2BL CoO}}$ = 3.0–3.1 Å [18]. STM images of both films show the positions of the oxygen atoms as bright protrusions [20].

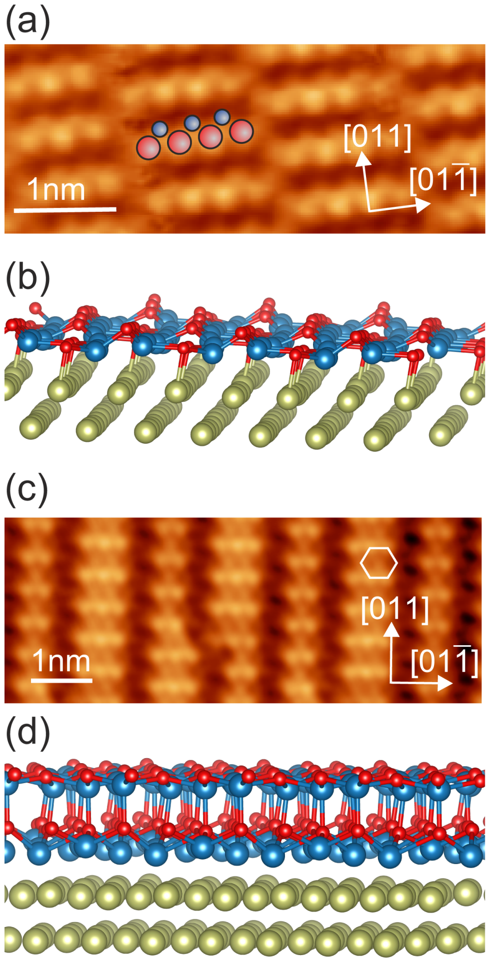

Figure 2: (a) STM image of the 1BL CoO film on Ir(100) with a corrugation of 100 pm and (b) side view of the relaxed film structure from a DFT calculation viewed approximately along the $[01\bar{1}]$ direction of Ir(100). (c) STM image of the 2BL CoO with a corrugation of 20 pm and (d) side view of the film structure. In both cases the terminating oxygen atoms are imaged by STM. They form a quasi-hexagonal pattern in (c). Note that the color scaling of (c) is enhanced with respect to (a). The different corrugations of the cobalt oxide films are also reproduced by the calculations. Cobalt, oxygen, and iridium are represented by blue, red, and yellow balls respectively. In (a) and (c) the crystallographic axes of the Ir(100) substrate are shown. Imaging parameters: (a) U = 0.1 V, I = 0.1 nA; (b) U = 0.5 V, I = 0.5 nA.

Computational Methods

Non-magnetic ab initio calculations were performed using the Vienna Ab-initio Simulation Package (VASP) [32] employing the PBE-PAW general gradient approximation [33]. To account for dispersion forces the zero damping DFT-D3 correction of Grimme et al. was used [34]. Slabs were constructed from two layers of iridium and one or two bilayers of cobalt oxide. For the iridium lattice the relaxed DFT-D3 parameter (a = 3.835 Å) was used. The lateral size was eight $c(10 \times 2)$ unit cells for the 1BL system (27.1 × 21.7 Å^2) and eight $c(8 \times 2)$ unit cells as approximation for the 2BL system ((21.7 Å)^2). These cell sizes ensured that the distance between repeated images of the molecules was always larger than 4.1 Å in any molecular orientation. The slabs were separated by approximately 12 Å of vacuum (measured from the topmost atom of the adsorbed molecule), resulting in a third cell dimension of 23 Å and 25 Å, respectively. For structural relaxation all molecular atoms were allowed to relax. Only in the case of **1**, the central Co atom was kept fixed laterally at a position guided by the analysis of our experimental STM images of **1** and by our results on Co phthalocyanine [35]. For the 1BL system, only the bottom Ir layer was kept fixed. For the 2BL calculations, the bare substrate was relaxed first, keeping the bottom Ir layer fixed. During subsequent adsorption studies the molecule and the first CoO bilayer were allowed to relax. Calculations were carried out with an energy cutoff of 400 eV and at the gamma point only, all structures were relaxed until forces were smaller than 0.1 eV/Å. STM simulations were performed employing the Tersoff–Hamann approximation [36]. The projected density of states (PDOS) was calculated using the same parameters. To compare the molecular PDOS on the oxide to that on the bare Ir(100), Co-DPP was put on a bridge site on three layers of Ir. The molecule and two layers of Ir were allowed to relax but no further search for the lowest-energy configuration was carried out.

Results

Figure 3 demonstrates the different situations encountered after depositing **1** or **2** on the ultra-thin 1BL CoO film. To activate surface diffusion of the molecules, a temperature of 300–320 K was applied to both systems either by keeping the substrate at that temperature during deposition or by short time (5 min) annealing. Either choice of thermal treatment resulted in the same molecular structures. Higher temperatures could not be applied to **2** without changing the appearance of the molecules. This is attributed to metalation of the free-base porphyrin with Co ions [12,13]. Both molecules adsorb flat-lying on the cobalt oxide film. While **1** forms compact well-ordered islands even at low molecular coverage (Figure 3a), **2** tends to agglomerate into small groups in which neither long-range order nor a preferred binding motive can be detected (Figure 3b). This latter observation remains true for larger coverages at which the size of such agglomerates is increased. The situation for **2** is comparable to adsorption properties observed on Cu(111) when metal-organic coordination is not activated [10]. However, different to

Cu(111), even annealing to 420 K – and, in consequence, metalating – does not improve the molecular ordering of **2** on 1BL CoO. Further heating cannot be applied since oxidation of the molecules sets in.

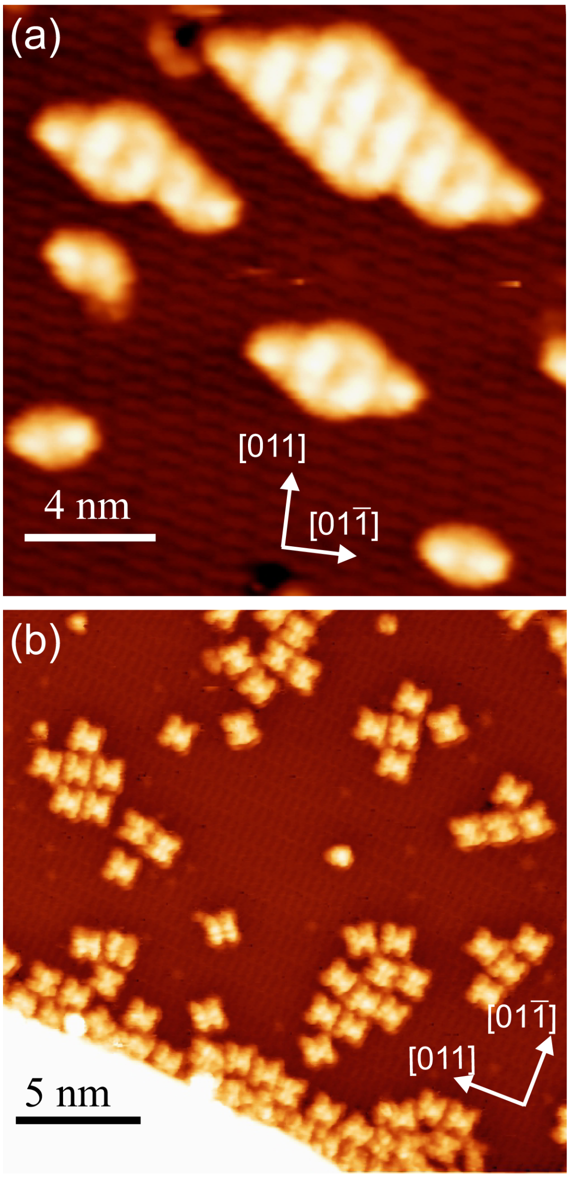

Figure 3: Low coverage of (a) **1** and (b) **2** deposited on 1BL CoO on Ir(100). **1** was deposited at 220 K substrate temperature and annealed to 300 K while for **2** the substrate temperature during deposition was 320 K. Imaging parameters (a) U = −1.6 V, I = 0.35 nA, apparent molecular height Δz = 3.7 Å; (b) U = 2.0 V, I = 0.30 nA, Δz = 3.3 Å.

The self-assembled structures of **1** may be identified in detail with the help of bias-dependent STM imaging, which allows for an unambiguous identification of single molecules in the structure (Figure 4). The resulting commensurate assembly pattern is indicated by pairs of molecules. While in Figure 4a and Figure 4c the phenyl group becomes dominant in the STM images, it is almost invisible in Figure 4b and a homogeneous contrast develops in Figure 4d. Such compact assemblies were previously observed for the case of the non-metalated 2H-DPP compound on Ag(110) [24] and on Au(111) [22], but, for example, not on Cu(111) [23]. For the assembly on 1BL CoO, the distance between the phenyl rings is a little larger than $2a_{\mathrm{Ir}}$ = 5.4 Å, which indicates that this cannot provide a substantial attractive interaction. A distance of approx. 3 Å is found between a phenyl group and the macrocycle of a neighboring molecule in the assemblies of Figure 3a and Figure 4. This could provide an attractive interaction between the involved aromatic systems. Similar values are found on the metal surfaces. The details of these compact structures on different substrates are therefore regulated by the substrate lattice. Furthermore, similar to what is observed for many metal substrates, the central metal ion of the molecule is not imaged as a protrusion on CoO for tunneling bias voltages of ±2.0 V around the Fermi energy.

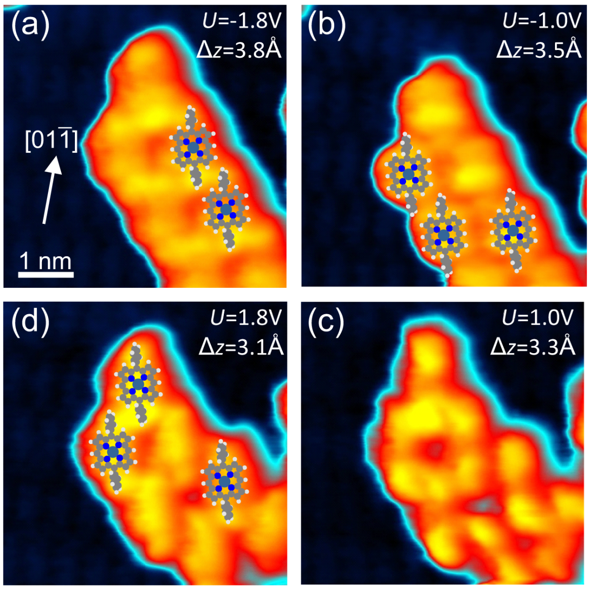

Figure 4: (a–d) Sequence of voltage-dependent STM images of a self-assembled island of **1** on 1BL of CoO. (a) and (b) represent filled-state images while (c) and (d) are empty-state images. The tunneling current for all images was I = 0.35 nA. The apparent molecular height is indicated in the panels. All images have the same lateral scale and orientation (see (a)), the color scale is non-linear for better visibility. Due to unwanted tip–molecule interactions the assembly changed between (b) and (c).

In Figure 5 we analyze the behavior of **1** on the 2BL CoO film. Imaging of **1** proved difficult at liquid-nitrogen temperatures since the molecules are easily pulled by the STM tip even at junction resistances of R_T = 10 GΩ. When molecules remain in place, they are imaged as round doughnut-like objects with four positions along the ring, which are imaged brighter (Figure 5a).

By manipulating the molecules with the STM tip, we almost never detected a defect in the oxide layer at which the molecules might have been pinned. Only if molecules come close to each other or are trapped by a defect does the former dumbbell shape reappear proving that no change of the molecular structure has taken place (Figure 5b). Hence, the round appearance of the molecules is due to a rotational motion much faster than the imaging speed of the STM, which is in the millisecond regime. The STM images, therefore, represent time averages of the motion of the molecule. The positions where the ring is imaged brighter corresponds to positions that the molecule is more likely to be found in. Such a rotation around a central axis perpendicular to the surface has previously been observed for variety of molecules [37-39]. Many metal phthalocyanines have been shown to rotate on metal surfaces [40-43], but notably also a modified Co phthalocyanine on Si(100) [44].

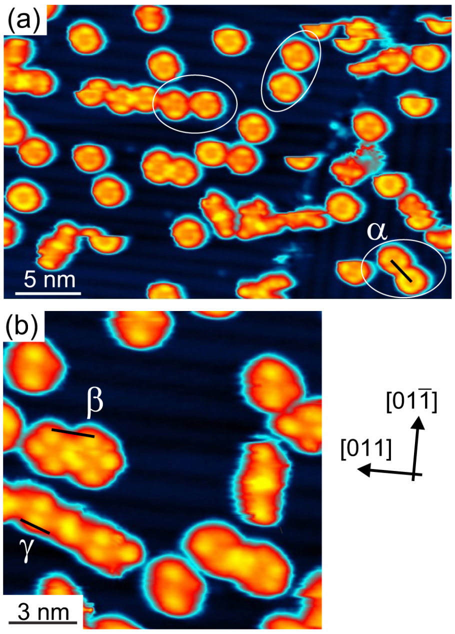

Figure 5: (a) **1** on 2BL CoO deposited at 200 K and imaged at 80 K. The molecules appear as round features unless close to a neighboring molecule or substrate defect. This indicates that **1** rotates around its central Co ion at time scales that are fast with respect to the STM scanning time of a few milliseconds. The STM image represents a time average and shows that the potential landscape of the rotating molecule has two minima with an angle of approximately 90° between each other. The intermolecular distance of the encircled pairs indicated by the black bar at one of them is α = 2.6 nm or larger. (b) Detail of the intermolecular interaction. In close proximity the interaction between neighboring molecules stops the rotation. While the pair β still rotates, molecules γ are stationary. The distances are β = 1.9 nm and γ = 1.5 nm. Imaging parameters U = 1.8 V , I = 0.15 nA, apparent molecular height Δz = 3.3 Å. (Color scale is non-linear for better visibility.)

Molecules sometimes come close enough to each other or can be manipulated such that the rotational motion first gets modified due to the interaction between the phenyl rings of the molecule and finally stops. At a molecule–molecule distance of 2.6 nm and larger (encircled in white in Figure 5a), the appearance in STM of a molecule is not, or only slightly, modified by its neighbors. At a distance of 1.9 nm (β in Figure 5b) the configuration where the molecules attach in a chain-like fashion is slightly more probable, that is, it is imaged brighter in STM. However, the bond still breaks and the molecule may rotate or swing between its various orientations. Only if the intermolecular distance is reduced further to 1.5 nm (γ in Figure 5b) the molecules eventually assemble in stable chain-like structures. It can be expected that such structures will form at larger molecular coverage due to steric blocking of the rotational motion. We propose that the rotating molecular state at temperatures of 80 K and above prevents the molecules from locking into a compact self-assembled layer at low coverage. When stationary molecules with a rotational potential barrier larger than the diffusion barrier self-assemble, the intermolecular forces guide the molecules to diffuse into a state of low-energy at an appropriate bonding distance. This is, for example, observed at low coverage of 2H-DPP on Cu(111) [23]. When, as it appears here, the diffusion and the rotational barrier are of equal magnitude, the intermolecular forces cannot exert their directional influence on the diffusive motion of the molecules since the directional intermolecular bond always “swings open”. Increasing the annealing temperature does not help to form supramolecular structures at low coverage. At 300 K, all molecules will attach to defects or move to 1BL CoO areas present in the film.

In contrast, **2** forms compact islands on the 2BL film when the molecules are deposited at approx. 300 K or when the system is annealed to that temperature (Figure 6a). The appearance of **2** on the 2BL film is very similar to that on Ag(111) and allows for an identification of individual molecules in the compact structures [10]. Different superstructures are observed, which also differ in the type of intermolecular interactions. The structure marked by a white rectangle in Figure 6a, shown in detail in Figure 6b, contains two bonding motifs. The first is the dipolar interaction of CN groups of neighboring molecules that are oriented parallel to each other. This bond mediates the interaction along the vertical direction in Figure 6b. The second is a hydrogen bond between a CN group and the macrocycle of a molecule nearby (along the horizontal direction in Figure 6b). A structural analysis of Figure 6b reveals a $\begin{pmatrix} 6 & 2 \\ 1 & 6 \end{pmatrix}$ superstructure with respect to the quasi-hexagonal structure of the CoO 2BL film (red rectangle in Figure 6b). Arranging **2** in its gas phase configuration within this cell, we find that the CN groups of the dipolar bond have a distance of 0.4 nm and that the hydrogen bond has a length of 0.3 nm between the N atom and the closest H atom of the macrocycle. Expecting some distortions of the molecule on the surface, this is well in the range of dipolar and hydrogen bond distances [25,30,45]. From the molecular orien-

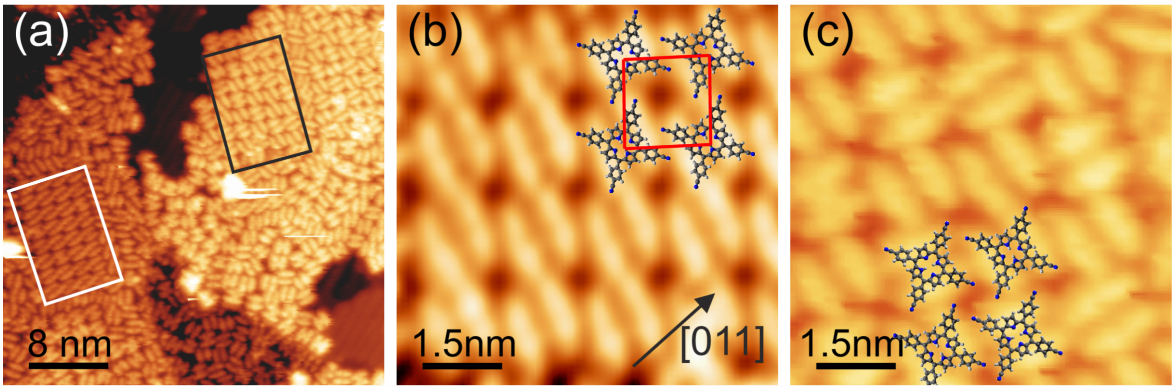

Figure 6: (a) **2** on 2BL CoO deposited at 300 K and imaged at 80 K. The molecules assemble into compact ordered islands with different interaction patterns. (b) Detailed view of the area in (a) marked in white and suggested arrangement of **2** within the unit cell (red). Here, dipolar interactions and hydrogen bridge bonds are observed. (c) The same as (b) but for the area marked in black. Here, only hydrogen bridge bonds are active. Imaging parameters U = 3.0 V, I = 0.1 nA, apparent molecular height Δz = 3.1 Å.

tation of the assembly marked by the black rectangle in Figure 6a, shown in detail in Figure 6c, it becomes apparent that the dipolar interaction is missing. From that we conclude that the two types of interaction are of almost equal strength, and hence also other compact formations observed display different patterns of these bond types. A similar delicate balance of the interaction strength between functionalized porphyrins has also been observed on metal surfaces [27].

Discussion

To gain insight into the reasons behind the experimental findings, DFT calculations were performed. Both, **1** and **2** were structurally relaxed on the 1BL CoO film in order to find the adsorption geometry. The lowest-energy configurations of **1** are shown in Figure 7a,b. We find that the central Co atom of **1** forms a strong bond with one of the O atoms of the substrate (Figure 7b). The Co–O bond length is 1.92 Å and the bonding O is lifted from its original position by 0.2 Å. This is essentially identical to the situation found for Co phthalocyanine on the same surface [35]. The only difference is that the Co atom of **1** stays in the plane of the porpyhrin macrocycle. For Co phthalocyanine, we observe lateral and vertical distortions of up to 0.25 Å of the CoO substrate layer upon adsorption of **1**. However, the repulsive interaction between the two phenyl rings and the surface causes the molecule macrocycle to bend considerably. The largest surface height difference between carbon atoms of the macrocycle amounts to 0.8 Å. The calculated adsorption energy is $E_{\text{ads}} = -(E_{\text{total}} - E_{\text{CoDPP}} - E_{\text{CoO/Ir}}) = 2.7$ eV. The corresponding STM simulation (Figure 7a, inset) agrees well with the symmetric dumbbell appearance in the experimental images.

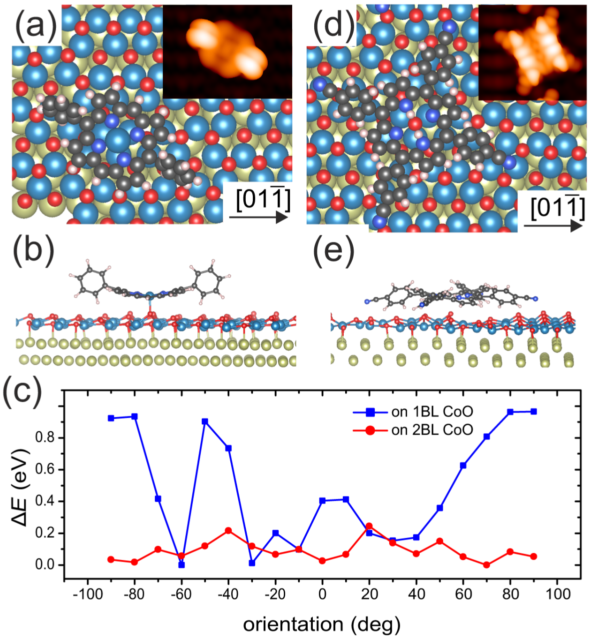

Figure 7: (a,b) Top and side view, respectively, of the relaxed structure of **1** on 1BL CoO according to our DFT calculations. (c) Calculated total energy difference of **1** as a function of the molecular orientation on CoO ultrathin films. Significant rotational barriers of 0.9 eV exist on the 1BL film, while on the 2BL film the activation energy of rotational motion is below 200 meV. The orientation is given as the angle of the molecular axis with respect to the [01$\bar{1}$] direction of the Ir(100) surface. (d, e) Top and side view, respectively, of **2** on 1BL CoO. Insets in (a) and (d) are STM-DFT simulations at bias voltages of −1.6 V and +2.0 V, that is, the voltages at which the images of, respectively, Figure 3a and Figure 3b.

We also calculated the relaxed structure of **1** on 2BL CoO, where the molecule adopts a ruffled configuration [46]. We find that the maximum surface height difference between carbon atoms of the macrocycle now amounts to only 0.5 Å while the bond length of the Co atom of **1** to the surface oxygen is now 3.0 Å. This means the distance between the molecule and the surface corresponds closely to the sum of the van der Waals radii of carbon and oxygen (3.2 Å). The binding energy is reduced to E_{ads} = 1.55 eV. It was attempted to find a local energy minimum in an adsorption state much closer to the surface but the calculation returned to the weakly bound state. This much weaker binding and larger molecule–surface distance also manifests itself in greatly different energy barriers with respect to the rotation of the molecule on the surface. To this end, we calculated the total energy for different orientations of **1** on 1BL and 2BL CoO (Figure 7c). The orientation is given as the angle between the molecular axis (defined by the phenyl groups) and the $[01\bar{1}]$ direction of the Ir substrate. While **1** on 1BL experiences barriers up to 0.9 eV, which effectively hinder rotation at 80 K, on 2BL the potential landscape is rather flat, with two maxima representing barriers of only approx. 200 meV.

The configuration of **2** on 1BL CoO is shown in Figure 7d,e. The molecule adopts a saddle-shape configuration. Due to the absence of molecular self-assembly on the 1BL film, it was suspected that the cyanophenyl rings would form bonds to the substrate. Extensive tests were performed to ensure that the found configuration captures the interaction with the substrate correctly. We started (due to simplicity) with a relaxation based on the configuration of **1** with the central Co atom replaced by two H atoms and two cyano groups attached to the phenyl rings of **1**, that is, a 2*H*-dicyanophenylporphyrin. Upon relaxation the macrocycle flattened and the cyanophenyl rings reduced their tilts from the almost orthogonal configuration towards a 45° tilting angle. This indicated an energy gain upon flattening of the molecule and allows for an interaction between the cyano group and the substrate. Consequently, we tested the relaxation of **2** in several attempts starting with configurations where the phenyl rings were bent such that a bond between the cyano group and a Co ion of the substrate could be formed. However, the structure always relaxed into a state in which the N–Co distance exceeded 3.1 Å. While the STM simulation of that configuration shown in Figure 7d matches well with some of the molecules depicted in Figure 3b, it cannot be excluded that **2** assumes different configurations on the 1BL film that are not captured by the present state of modeling. Nevertheless, the weak bending of the phenyl rings (approx. 5°) indicates a molecule–substrate interaction that is absent in the case of **1**. We note that the superstructure formed by **2** on 2BL CoO (Figure 6) is not commensurate to the 1BL film. Hence, the partial engagement of the cyano groups in a surface bond may weaken the intermolecular forces and thereby strengthen the regulating influence of the substrate lattice. In consequence, the formation of any commensurate or incommensurate self-assembly structure is prevented on 1BL CoO.

Finally, to investigate the degree of electronic decoupling, in Figure 8 we compare the PDOS for the free molecule of **1** and its adsorbed state on 1BL, 2BL CoO, and on Ir(100). The PDOS on Ir(100) shows significant broadening of the molecular orbitals due to a strong hybridization with the Ir 5d and 6s states. In contrast, this hybridization is absent for the 1BL and 2BL CoO system. On 1BL CoO there is a strong hybridization of the molecular Co d orbitals with the states of the substrate. Consequently, significant changes are observed. However, already for the N atoms that are bound to the molecular Co atom this influence is reduced considerably. The comparison of the PDOS of the free molecule with that adsorbed on 2BL CoO shows that the Co PDOS is the same as that of the free molecule, indicating a weak hybridization of the Co center atom with the substrate. The remaining deviations between the N and C PDOS of **1** adsorbed on 1BL or 2BL CoO and that of the free molecule are difficult to interpret. They are surely a sign of weak hybridization with the CoO film, maybe in combination with an influence of the different molecular conformations.

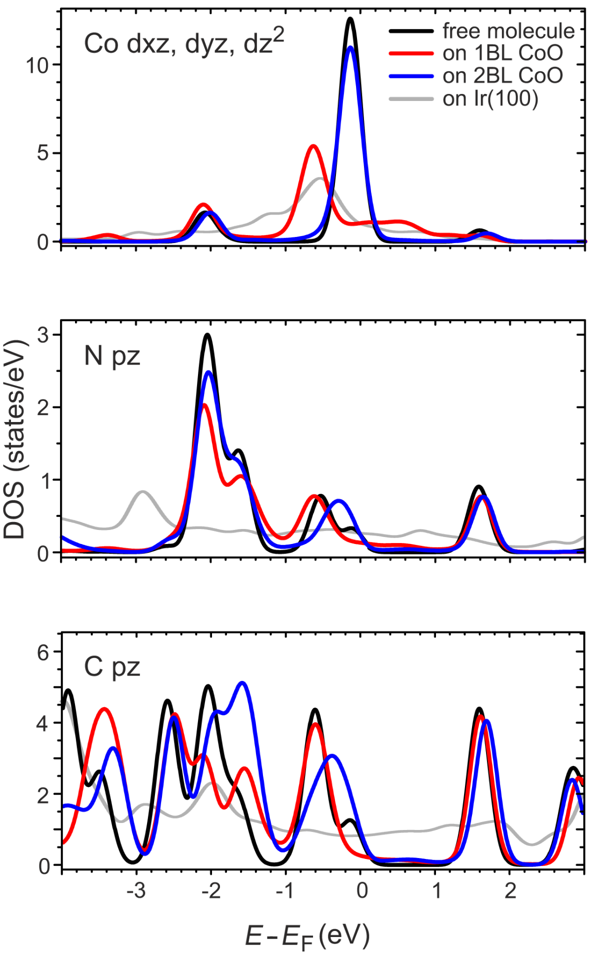

Figure 8: Calculated projected density of states (PDOS) near the Fermi energy of molecular orbitals with components parallel to the surface normal.

We interpret these findings as a demonstration that the oxide effectively decouples the molecules from the metal substrate and that their electronic structure remains almost undisturbed when adsorbing on the CoO films. Certainly, due to the neglect of spin and correlation in the calculations, the true PDOS will deviate and conclusions have to be drawn with care. However, the work function of CoO is, with 5.85 eV (1BL) and 6.01 eV (2BL) [47], significantly higher than that of most metals. Following the arguments of Yang et al. [48], a charge transfer into unoccupied molecular orbitals is not expected and one can therefore consider the molecules not only to be physically but also electronically decoupled from the metal substrate at least for a CoO thickness exceeding 1BL.

Conclusion

We investigated in detail the adsorption behavior of a non-functionalized, metalated phenylporpyhrin (Co-DPP, **1**) and a cyano-functionalized, non-metalated phenylporpyhrin (2H-TCNPP, **2**) on cobalt oxide CoO(111) films in the ultrathin limit of one and two bilayer thickness. It is found that the molecule–substrate interaction decreases with increasing cobalt oxide thickness. Nevertheless, dispersion forces constitute a considerable binding potential, which keeps the molecules in a flat adsorption geometry. With respect to self-assembly of the molecules it is found that in the case of Co-DPP on the one-bilayer cobalt oxide film compact self-assembled islands are formed. This is due to the potential landscape provided by the ultrathin film, which supports the self-assembly despite the rather weak intermolecular interaction mediated by the phenyl groups. The surface influence is absent or considerably weaker when two bilayer films are deposited. Here, the Co-DPP rotate at temperatures of 80 K and higher, effectively preventing self-assembly. Conversely, the corrugation of the potential-energy landscape for the cyano-functionalized porphyrin prevents self-assembly on the one bilayer film, but the strong intermolecular interaction creates compact islands on the smoother two bilayer film. Calculations of the projected density of states of **1** on the bare metal and on the oxide layers demonstrate that also a high degree of electronic decoupling from the metal substrate is achieved at the cost of only weak hybridization with the oxide. The work therefore shows that the subtle interplay within the hierarchy of energies leading to self-assembly is also active on oxide surfaces and that the oxygen-terminated CoO(111) surface can be used as a decoupling layer for molecular studies.

Funding

This work was funded by the Deutsche Forschungsgemeinschaft (DFG) within the research unit FOR 1878 ”Functional molecular structures on complex oxide surfaces” (*fun*COS). M.A.S gratefully acknowledges support and supply of CPU time by the ”Regionales Rechenzentrum Erlangen (RRZE)”.

ORCID® iDs

Feifei Xiang - https://orcid.org/0000-0002-4930-5919
M. Alexander Schneider - https://orcid.org/0000-0002-8607-3301

References

1. Auwärter, W.; Écija, D.; Klappenberger, F.; Barth, J. V. *Nat. Chem.* **2015,** *7,* 105–120. doi:10.1038/nchem.2159
2. Gottfried, J. M. *Surf. Sci. Rep.* **2015,** *70,* 259–379. doi:10.1016/j.surfrep.2015.04.001
3. Rangan, S.; Coh, S.; Bartynski, R. A.; Chitre, K. P.; Galoppini, E.; Jaye, C.; Fischer, D. *J. Phys. Chem. C* **2012,** *116,* 23921–23930. doi:10.1021/jp307454y
4. Köbl, J.; Wang, T.; Wang, C.; Drost, M.; Tu, F.; Xu, Q.; Ju, H.; Wechsler, D.; Franke, M.; Pan, H.; Marbach, H.; Steinrück, H.-P.; Zhu, J.; Lytken, O. *ChemistrySelect* **2016,** *1,* 6103–6105. doi:10.1002/slct.201601398
5. Schneider, J.; Kollhoff, F.; Schindler, T.; Bichlmaier, S.; Bernardi, J.; Unruh, T.; Libuda, J.; Berger, T.; Diwald, O. *J. Phys. Chem. C* **2016,** *120,* 26879–26888. doi:10.1021/acs.jpcc.6b08956
6. Prauzner-Bechcicki, J. S.; Zajac, L.; Olszowski, P.; Jöhr, R.; Hinaut, A.; Glatzel, T.; Such, B.; Meyer, E.; Szymonski, M. *Beilstein J. Nanotechnol.* **2016,** *7,* 1642–1653. doi:10.3762/bjnano.7.156
7. Olszowski, P.; Zajac, L.; Godlewski, S.; Such, B.; Pawlak, R.; Hinaut, A.; Jöhr, R.; Glatzel, T.; Meyer, E.; Szymonski, M. *Beilstein J. Nanotechnol.* **2017,** *8,* 99–107. doi:10.3762/bjnano.8.11
8. Jöhr, R.; Hinaut, A.; Pawlak, R.; Zajac, Ł.; Olszowski, P.; Such, B.; Glatzel, T.; Zhang, J.; Muntwiler, M.; Bergkamp, J. J.; Mateo, L.-M.; Decurtins, S.; Liu, S.-X.; Meyer, E. *J. Chem. Phys.* **2017,** *146,* 184704. doi:10.1063/1.4982936
9. Werner, K.; Mohr, S.; Schwarz, M.; Xu, T.; Amende, M.; Döpper, T.; Görling, A.; Libuda, J. *J. Phys. Chem. Lett.* **2016,** *7,* 555–560. doi:10.1021/acs.jpclett.5b02784
10. Lepper, M.; Schmitt, T.; Gurrath, M.; Raschmann, M.; Zhang, L.; Stark, M.; Hölzel, H.; Jux, N.; Meyer, B.; Schneider, M. A.; Steinrück, H.-P.; Marbach, H. *J. Phys. Chem. C* **2017,** *121,* 26361–26371. doi:10.1021/acs.jpcc.7b08382
11. Lepper, M.; Köbl, J.; Schmitt, T.; Gurrath, M.; de Siervo, A.; Schneider, M. A.; Steinrück, H.-P.; Meyer, B.; Marbach, H.; Hieringer, W. *Chem. Commun.* **2017,** *53,* 8207–8210. doi:10.1039/c7cc04182a
12. Wechsler, D.; Fernández, C. C.; Tariq, Q.; Tsud, N.; Prince, K. C.; Williams, F. J.; Steinrück, H.-P.; Lytken, O. *Chem. – Eur. J.* **2019,** *25,* 13197–13201. doi:10.1002/chem.201902680
13. Wähler, T.; Schuster, R.; Libuda, J. *Chem. – Eur. J.* **2020,** *26,* 12445–12453. doi:10.1002/chem.202001331
14. Zhang, M.; de Respinis, M.; Frei, H. *Nat. Chem.* **2014,** *6,* 362–367. doi:10.1038/nchem.1874
15. Walton, A. S.; Fester, J.; Bajdich, M.; Arman, M. A.; Osiecki, J.; Knudsen, J.; Vojvodic, A.; Lauritsen, J. V. *ACS Nano* **2015,** *9,* 2445–2453. doi:10.1021/acsnano.5b00158
16. Natile, M. M.; Glisenti, A. *Chem. Mater.* **2002,** *14,* 3090–3099. doi:10.1021/cm0211150
17. Gao, S.; Lin, Y.; Jiao, X.; Sun, Y.; Luo, Q.; Zhang, W.; Li, D.; Yang, J.; Xie, Y. *Nature* **2016,** *529,* 68–71. doi:10.1038/nature16455
18. Giovanardi, C.; Hammer, L.; Heinz, K. *Phys. Rev. B* **2006,** *74,* 125429. doi:10.1103/physrevb.74.125429

19. Meyer, W.; Hock, D.; Biedermann, K.; Gubo, M.; Müller, S.; Hammer, L.; Heinz, K. *Phys. Rev. Lett.* **2008,** *101,* 016103. doi:10.1103/physrevlett.101.016103
20. Tröppner, C.; Schmitt, T.; Reuschl, M.; Hammer, L.; Schneider, M. A.; Mittendorfer, F.; Redinger, J.; Podloucky, R.; Weinert, M. *Phys. Rev. B* **2012,** *86,* 235407. doi:10.1103/physrevb.86.235407
21. Roy, S.; Meyerheim, H. L.; Mohseni, K.; Tian, Z.; Sander, D.; Hoffmann, M.; Adeagbo, W.; Ernst, A.; Hergert, W.; Felici, R.; Kirschner, J. *Phys. Rev. B* **2014,** *89,* 165428. doi:10.1103/physrevb.89.165428
22. Xiang, F.; Li, C.; Wang, Z.; Liu, X.; Jiang, D.; Leng, X.; Ling, J.; Wang, L. *Surf. Sci.* **2015,** *633,* 46–52. doi:10.1016/j.susc.2014.11.021
23. Xiang, F.; Gemeinhardt, A.; Schneider, M. A. *ACS Nano* **2018,** *12,* 1203–1210. doi:10.1021/acsnano.7b06998
24. Xiang, F.; Lu, Y.; Wang, Z.; Ju, H.; Di Filippo, G.; Li, C.; Liu, X.; Leng, X.; Zhu, J.; Wang, L.; Schneider, M. A. *J. Phys. Chem. C* **2019,** *123,* 23007–23013. doi:10.1021/acs.jpcc.9b06025
25. Wood, P. A.; Borwick, S. J.; Watkin, D. J.; Motherwell, W. D. S.; Allen, F. H. *Acta Crystallogr., Sect. B: Struct. Sci.* **2008,** *64,* 393–396. doi:10.1107/s0108768108010239
26. Baker Cortés, B. D.; Schmidt, N.; Enache, M.; Stöhr, M. *J. Phys. Chem. C* **2019,** *123,* 19681–19687. doi:10.1021/acs.jpcc.9b05055
27. Yokoyama, T.; Yokoyama, S.; Kamikado, T.; Okuno, Y.; Mashiko, S. *Nature* **2001,** *413,* 619–621. doi:10.1038/35098059
28. Schlickum, U.; Decker, R.; Klappenberger, F.; Zoppellaro, G.; Klyatskaya, S.; Auwärter, W.; Neppl, S.; Kern, K.; Brune, H.; Ruben, M.; Barth, J. V. *J. Am. Chem. Soc.* **2008,** *130,* 11778–11782. doi:10.1021/ja8028119
29. Stöhr, M.; Boz, S.; Schär, M.; Nguyen, M.-T.; Pignedoli, C. A.; Passerone, D.; Schweizer, W. B.; Thilgen, C.; Jung, T. A.; Diederich, F. *Angew. Chem., Int. Ed.* **2011,** *50,* 9982–9986. doi:10.1002/anie.201102627
30. Gottardi, S.; Müller, K.; Moreno-López, J. C.; Yildirim, H.; Meinhardt, U.; Kivala, M.; Kara, A.; Stöhr, M. *Adv. Mater. Interfaces* **2014,** *1,* 1300025. doi:10.1002/admi.201300025
31. Heinz, K.; Schmidt, G.; Hammer, L.; Müller, K. *Phys. Rev. B* **1985,** *32,* 6214–6221. doi:10.1103/physrevb.32.6214
32. Kresse, G.; Furthmüller, J. *Phys. Rev. B* **1996,** *54,* 11169–11186. doi:10.1103/physrevb.54.11169
33. Perdew, J. P.; Burke, K.; Ernzerhof, M. *Phys. Rev. Lett.* **1996,** *77,* 3865–3868. doi:10.1103/physrevlett.77.3865
34. Grimme, S.; Antony, J.; Ehrlich, S.; Krieg, H. *J. Chem. Phys.* **2010,** *132,* 154104. doi:10.1063/1.3382344
35. Schmitt, T.; Ferstl, P.; Hammer, L.; Schneider, M. A.; Redinger, J. *J. Phys. Chem. C* **2017,** *121,* 2889–2895. doi:10.1021/acs.jpcc.6b12337
36. Tersoff, J.; Hamann, D. R. *Phys. Rev. B* **1985,** *31,* 805–813. doi:10.1103/physrevb.31.805
37. Gimzewski, J. K.; Joachim, C.; Schlittler, R. R.; Langlais, V.; Tang, H.; Johannsen, I. *Science* **1998,** *281,* 531–533. doi:10.1126/science.281.5376.531
38. Zhong, D.; Blömker, T.; Wedeking, K.; Chi, L.; Erker, G.; Fuchs, H. *Nano Lett.* **2009,** *9,* 4387–4391. doi:10.1021/nl902670k
39. Kottas, G. S.; Clarke, L. I.; Horinek, D.; Michl, J. *Chem. Rev.* **2005,** *105,* 1281–1376. doi:10.1021/cr0300993
40. Gao, L.; Liu, Q.; Zhang, Y. Y.; Jiang, N.; Zhang, H. G.; Cheng, Z. H.; Qiu, W. F.; Du, S. X.; Liu, Y. Q.; Hofer, W. A.; Gao, H.-J. *Phys. Rev. Lett.* **2008,** *101,* 197209. doi:10.1103/physrevlett.101.197209
41. Wu, T.; Liu, L.; Zhang, Y.; Wang, Y.; Shen, Z.; Li, N.; Berndt, R.; Hou, S.; Wang, Y. *Chem. Commun.* **2020,** *56,* 968–971. doi:10.1039/c9cc07440f
42. Lu, H.-L.; Cao, Y.; Qi, J.; Bakker, A.; Strassert, C. A.; Lin, X.; Ernst, K.-H.; Du, S.; Fuchs, H.; Gao, H.-J. *Nano Lett.* **2018,** *18,* 4704–4709. doi:10.1021/acs.nanolett.8b01019
43. Tu, Y.-B.; Tao, M.-L.; Sun, K.; Ni, C.; Xie, F.; Wang, J.-Z. *RSC Adv.* **2017,** *7,* 34262–34266. doi:10.1039/c7ra05611g
44. Hersam, M. C.; Guisinger, N. P.; Lyding, J. W. *Nanotechnology* **2000,** *11,* 70–76. doi:10.1088/0957-4484/11/2/306
45. Steiner, T. *Angew. Chem., Int. Ed.* **2002,** *41,* 48–76. doi:10.1002/1521-3773(20020104)41:1<48::aid-anie48>3.0.co;2-u
46. Zhang, Q.; Zheng, X.; Kuang, G.; Wang, W.; Zhu, L.; Pang, R.; Shi, X.; Shang, X.; Huang, X.; Liu, P. N.; Lin, N. *J. Phys. Chem. Lett.* **2017,** *8,* 1241–1247. doi:10.1021/acs.jpclett.7b00007
47. Otto, S.; Fauster, T. *J. Phys.: Condens. Matter* **2016,** *28,* 055001. doi:10.1088/0953-8984/28/5/055001
48. Yang, X.; Krieger, I.; Lüftner, D.; Weiß, S.; Heepenstrick, T.; Hollerer, M.; Hurdax, P.; Koller, G.; Sokolowski, M.; Puschnig, P.; Ramsey, M. G.; Tautz, F. S.; Soubatch, S. *Chem. Commun.* **2018,** *54,* 9039–9042. doi:10.1039/c8cc03334j

License and Terms

BEILSTEIN JOURNAL OF NANOTECHNOLOGY

Detecting stable adsorbates of (1*S*)-camphor on Cu(111) with Bayesian optimization

Jari Järvi[*], Patrick Rinke and Milica Todorović

Full Research Paper

Open Access

Address:
Department of Applied Physics, Aalto University, P.O. Box 11100,
00076 Aalto, Espoo, Finland

Email:
Jari Järvi[*] - jari.jarvi@aalto.fi

[*] Corresponding author

Keywords:
Bayesian optimization; camphor; Cu(111); density-functional theory;
electronic structure; organic surface adsorbates; physical chemistry;
structure search; surface science

Beilstein J. Nanotechnol. **2020,** *11,* 1577–1589.
https://doi.org/10.3762/bjnano.11.140

Received: 14 May 2020
Accepted: 16 September 2020
Published: 19 October 2020

This article is part of the thematic issue "Molecular assemblies on surfaces – towards physical and electronic decoupling of organic molecules".

Guest Editor: S. Maier

Abstract

Identifying the atomic structure of organic–inorganic interfaces is challenging with current research tools. Interpreting the structure of complex molecular adsorbates from microscopy images can be difficult, and using atomistic simulations to find the most stable structures is limited to partial exploration of the potential energy surface due to the high-dimensional phase space. In this study, we present the recently developed Bayesian Optimization Structure Search (BOSS) method as an efficient solution for identifying the structure of non-planar adsorbates. We apply BOSS with density-functional theory simulations to detect the stable adsorbate structures of (1*S*)-camphor on the Cu(111) surface. We identify the optimal structure among eight unique types of stable adsorbates, in which camphor chemisorbs via oxygen (global minimum) or physisorbs via hydrocarbons to the Cu(111) surface. This study demonstrates that new cross-disciplinary tools, such as BOSS, facilitate the description of complex surface structures and their properties, and ultimately allow us to tune the functionality of advanced materials.

Introduction

Current frontier technologies are increasingly based on advanced functional materials, which are often blends of organic and inorganic components. For example, in search for renewable energy solutions, hybrid perovskites are currently the best candidate to replace silicon in our solar cells [1]. In medicine, hybrid materials have been studied extensively for applications in tissue engineering [2] and drug delivery [3]. To optimize the functional properties of these materials, we need detailed knowledge of their atomic structure. Of particular interest is the hybrid interface, which has a central role in defining the electronic properties of the material.

Assemblies of organic molecules on surfaces have been studied experimentally, for example with X-ray diffraction [4,5], scanning tunneling microscopy [6-8] and atomic force microscopy (AFM) [9-11]. These methods have a considerable resolution in imaging planar surface structures, but interpreting images of bulky three-dimensional molecules on surfaces can be difficult, which prevents an accurate structure determination. In such cases, computations can help in detecting the most stable structures.

With atomistic simulations, we can determine the optimal structures by computing the potential energy surface (PES). We can identify stable structures in the minima of the PES and evaluate their mobility via the associated energy barriers. The most stable structure, that is the most probable structure in nature, corresponds to the global minimum of the PES. For its reliable identification, we must explore the PES thoroughly.

Calculating the full PES for complex hybrid materials requires either (i) fast energy computations, or (ii) an advanced method of constructing the complete PES with a small number of energy points. Classical force-field potentials are fast to compute, but they cannot accurately model hybrid materials, in which atomic interactions often feature a mixture of covalent and dispersive bonding, with charge transfer and polarization effects. Instead, we must employ quantum mechanical methods, such as density-functional theory (DFT) [12,13], for electronically accurate energy sampling. Regarding hybrid materials, this makes a thorough exploration of the PES prohibitively expensive with conventional phase-space exploration methods, such as minima hopping [14], Monte Carlo methods [15], or metadynamics [16], which typically require calculating thousands of energy points on the PES.

Traditionally, stable structures have been identified by initializing the minima search with estimated low-energy structures, based on chemical intuition [17,18], thus narrowing down the search space. With hybrid materials, however, this intuition is difficult to apply and can lead to biased or incorrect results. For example, with only partial knowledge of the PES, a metastable local minimum energy structure could easily be misinterpreted as the most stable global minimum.

Recently, Gaussian processes (GPs) [19] and Bayesian optimization (BO) [20] have been applied in modeling the PES to identify structures with minimum energy. GP regression has been used for example in local structure optimization [21], in finding minimum energy paths [22], and in predicting specific materials properties, such as melting temperature [23] or elasticity [24]. BO has been applied in detecting molecular conformers [25] and adsorbate structures [26,27], in identifying stable molecular compounds [28], and in discovering materials with low thermal hysteresis [29] or thermal conductivity [30]. Typically, previous studies have employed customized material-specific models, using, for example, a coarse-grained search space with discrete molecular configurations, or predetermined GP hyperparameters, at the cost of generality of the method.

In this work, we show that the recently developed Bayesian Optimization Structure Search (BOSS) machine learning method [31-34] provides a solution to the structure search conundrum. With BOSS, we adopt the aforementioned approach (ii) and construct the complete PES using a small number of energy points. To demonstrate the capabilities of BOSS, we apply it with DFT to the adsorption of (1*S*)-camphor ($C_{10}H_{16}O$, hereafter shortened as camphor) on the Cu(111) surface. Camphor is an exemplary case of a bulky molecule, which is difficult to image with microscopy. AFM experiments [35] have revealed various different conformers of camphor on Cu(111), which makes it ideal for benchmarking the BOSS method.

Our objective is to detect the stable adsorbate structures of camphor on Cu(111). With BOSS, we build a surrogate model of the PES of adsorption and data-mine this PES to identify the stable structures in its minima. We converge the model for a reliable detection of all the PES minima, not only the global energy minimum. We estimate the mobility of the adsorbates from the energy barriers extracted from the surrogate PES and analyze the electronic structure of each adsorbate. Our results provide insight into the adsorption of complex organic molecules on metallic substrates and pave the way to more complex studies of hybrid monolayer formation and hybrid interfaces.

In the following sections, we first introduce our computational methods for adsorbate structure identification with BOSS, the first-principles calculations, and their application on detecting the stable adsorbates of camphor on Cu(111). We then present our results, discuss our findings, and conclude the analysis.

Computational Methods

Adsorbate structure identification

BOSS is a machine learning method that accelerates structure search via strategic sampling of the PES. With given initial data, BOSS builds the most probable surrogate model of the PES, refines it iteratively with active learning, and identifies the stable structures in the minima of the PES. In this work, we apply BOSS with DFT for accurate sampling of the energy points. In the following, we introduce the four-step process (Figure 1) of structure detection with BOSS and DFT, in analogy to [31]. We construct the surrogate model of the PES by sampling the adsorption energies with DFT (I). We then identify the stable structures by extracting the local minima of the PES (II) and verify them with full structural relaxation with DFT (III). We analyze the relaxed structures (IV) regarding their stability and mobility via the energy barriers on the PES, and investigate their electronic properties with DFT.

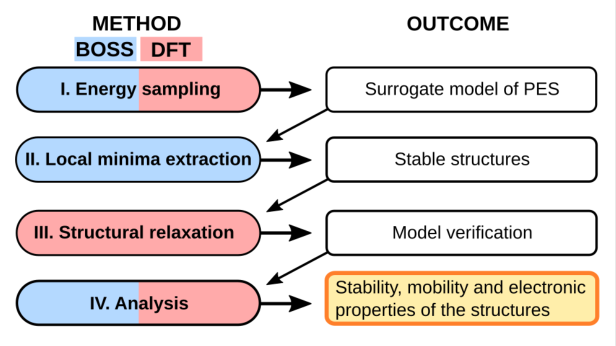

Figure 1: Structure search with BOSS (blue) and DFT (red). (I) The PES is sampled with BOSS by calculating energies of atomic configurations with DFT to obtain the surrogate model of the PES. (II) BOSS identifies the stable structures in the minima of the PES. (III) The stable structures are confirmed with full relaxation with DFT, after which (IV) their mobility and adsorption properties are analyzed via the corresponding energy barriers and electronic structure.

Bayesian Optimization Structure Search

With the atomic structures and their corresponding energies, BOSS constructs a surrogate model of the PES. We define the atomic structures using chemical building blocks [36], which are natural rigid components of the structure, for example, rigid molecules, functional groups, or a surface slab. The PES is then defined in the phase space resulting from the remaining degrees of freedom, for example the relative translation and/or rotation of building blocks.

BOSS refines the PES model iteratively with active learning using BO (Figure 2a). We here only sketch the search principle and refer the interested reader to a more in-depth presentation and to the theoretical foundation in [19,31,37]. BO is a two-step process, in which data is first fitted with a GP distribution over functions using Bayesian regression. With the resulting surrogate model (Figure 2b), BOSS then determines the next sampling point using an acquisition function.

In the surrogate model, the posterior mean is the most probable model of the predicted function (here the PES). The posterior variance describes the uncertainty of the model in less explored areas. It therefore vanishes at the known data points.

The next sampling point is determined using the exploratory Lower Confidence Bound (eLCB) [38] acquisition function, which balances exploitation against exploration. In exploitation, BO refines the model by acquiring the next point near the currently predicted global minimum. In exploration, the next acquisition is made at the point of maximum posterior variance, exploring less visited areas. In this study, we converge the PES model with respect to the coordinates and energy of all the minima, not only the global energy minimum.

Local minima and barrier extraction

Once the PES is converged, we data-mine the surrogate model. We extract the lowest energy minima, which we equate with the lowest-energy adsorbate structures. The minima are detected using the built-in local minima search functionality of BOSS. The search is performed with minimizers, which apply the limited-memory Broyden–Fletcher–Goldfarb–Shanno (L-BFGS) [39] optimization algorithm. The minimizers start in different regions of the PES and traverse the landscape, following the gradients to locate the minima.

The confidence of the surrogate model in different regions of the PES is quantified via the standard deviation (σ^B), which is the square root of the posterior variance in the GP model (Figure 2b). With the standard deviation, we evaluate the confidence of the surrogate model in the identified minima. Furthermore, we evaluate the accuracy of the model by computing the energy of each identified minima structure with DFT (E^D) and

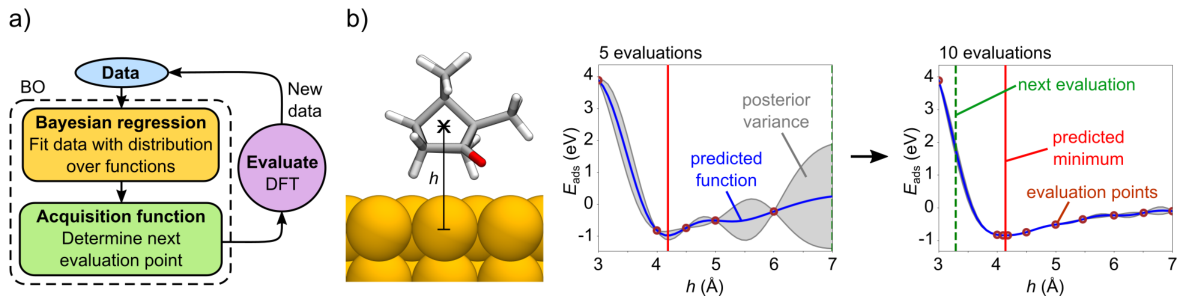

Figure 2: BOSS workflow and example performance. (a) Basic principle of the BOSS method, in which Bayesian optimization (BO) is applied iteratively with DFT to build a surrogate model of the PES. (b) 1D example of the iterative process, in which the adsorption energy E_{ads} of camphor on Cu(111) is predicted as a function of height *h* of the molecule from the surface. The predicted adsorption height is converged in five energy evaluations to within 0.1 Å. After ten evaluations, the posterior variance, which describes the uncertainty of the model, has become vanishingly small throughout the search region.

compare it to the corresponding energy in the surrogate model (E^{B}).

The BOSS PES also provides access to energy barriers, with which we can estimate the mobilities of our identified adsorbate structures. BOSS provides post-processing tools to locate the lowest energy barriers between two minima in the PES with the nudged elastic band (NEB) method. Since we compute the PES with the building block approximation and not in the space of all atomic degrees of freedom, these energy barriers are only upper limits to the true barriers. However, even qualitative accuracy in barrier evaluations suffices to identify the least mobile structures, which are the best candidates when compared to experimentally observed structures. We will return to energy barriers and our way of estimating them in the Results section, after we have introduced the camphor/Cu(111) system in more detail.

Structural relaxation and analysis

We verify the identified structures against a full DFT structure relaxation. In this, we remove the building block approximation and allow unrestricted motion of all atoms according to the interatomic forces in DFT. We then quantify and analyze the structural changes in the relaxation with respect to the atomic coordinates and the energy change ($\Delta E_{\mathrm{R}}^{\mathrm{D}}$) for each structure.

To validate the building block approximation, we evaluate the changes in the internal geometry of the building blocks after releasing them in the relaxation. For this, we calculate the average root-mean-square deviation of the atomic positions and the mean deviation of bond lengths, comparing the structures before and after the relaxation.

We furthermore investigate the electronic structure of the stable adsorbates by analyzing their partial density of states (DOS) and the charge distribution with the Mulliken analysis of partial charges [40].

Camphor on Cu(111)

We study the adsorption of camphor on the Cu(111) surface using two building blocks: (i) the global minimum camphor conformer and (ii) the Cu(111) surface slab. With BOSS, we first identify the global minimum camphor conformer without the Cu(111) surface with a 3D search of methyl group rotations (Figure 3a). We normalize the lengths and angles of the C–H bonds in the three methyl groups by setting them to identical values, based on their average lengths and angles (see Supporting Information File 1). With this, we obtain an ideal camphor geometry with three identical minima in the methyl group rotation (i.e., 120° periodicity). We then study the rotation of the methyl groups in the ranges $\theta, \varphi, \omega \in [-60, 60]°$.

With the identified global minimum conformer, we study the adsorption of camphor on Cu(111) with respect to molecular orientation and location. We define the PES of adsorption in a 6D phase space with three rotational angles (α, β, γ) and three translational directions (x, y, z), which correspond to the Cu lattice directions [10−1], [−12−1] and [111], respectively (Figure 3b). The adsorption height of the molecule (z) is defined with respect to the center point of rotation (Figure 3b), which is the middle point of the line connecting two C atoms at the sides of the rigid cage of camphor. We investigate the orientation of the molecule with full 360° rotation of all angles, in the range $(\alpha, \beta, \gamma) \in [-180, 180]°$. The search range in the x–y plane of the Cu(111) surface is $(x,y) \in [-0.5, 0.5]$ (Figure 3c), defined in fractional unit cell coordinates, which corresponds to lattice vectors $[a', b'] = [2.57, 4.45]$ Å.

Before we embarked on the full 6D camphor-on-Cu(111) search, we first scanned the system with several low-dimen-

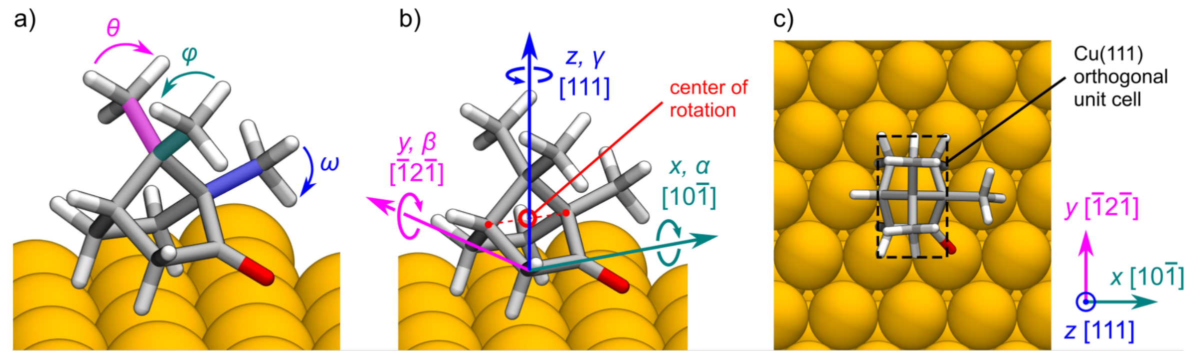

Figure 3: Degrees of freedom for the minimum energy search. (a) Three methyl group rotation angles θ, φ and ω of camphor in the 3D conformer search with BOSS. (b) Three translational directions (x, y, z) and three rotation angles (α, β, γ) of camphor in the 6D search for stable adsorbate structures. The center of rotation is the middle point between the two carbon atoms, highlighted in red. (c) Orthogonal unit cell of Cu(111), which is the search range in x and y directions.

sional searches. Such low-dimensional searches (e.g., 1D variation of the adsorption height or 2D scans of molecular registry on the surface) permit us to relatively quickly explore the behavior of the system. We use them to find appropriate limits for the search dimensions (e.g., maximum and minimum height over the surface). Additionally, low-dimensional simulations help us to assess the contributions from rotational and translational degrees of freedom separately, to estimate the expected number of local minima and their approximate values, and to develop qualitative checks for expected energy landscapes (e.g., reflecting surface symmetries). The computational effort associated with these preparatory simulations is recycled, since all points sampled in reduced dimensions later serve as input in the 6D study. We note that analysis of low-dimensional simulations only provides us with qualitative insight into surface adsorption. Quantitative conclusions on the stable structures can only be drawn from a full 6D search.

With BOSS, we perform three low-dimensional searches, in which we study the adsorption of camphor on Cu(111) as a function of its (i) adsorption height (1D), (ii) orientation (3D), and (iii) adsorption site (2D). First, we investigate the height of the molecule with a 1D search (Figure 2b) to determine a suitable height for the rotational search. Based on the resulting energy curve we estimate the optimal height at which we avoid high-energy peaks in all molecular orientations, and conduct the 3D rotational search. We then set the molecule in the observed minimum energy orientation (Figure 4b) and perform a 2D search of the adsorption site within the orthogonal unit cell of the Cu(111) surface (Figure 3c). With the acquired knowledge of the energy ranges, we then determine the optimal height range of the molecule for the 6D search.

We perform a 6D search with combined degrees of freedom to identify the stable adsorbate structures of camphor on Cu(111). The search is initialized using the previously acquired energy points from the low-dimensional studies. We multiply the number of initial energy points by applying the twofold translational symmetry in the orthogonal unit cell and the threefold rotational symmetry of the Cu(111) surface at the top site. With BOSS, we acquire new energy points and converge the 6D PES with respect to the energy and coordinates of the identified local minima (details provided in Supporting Information File 1).

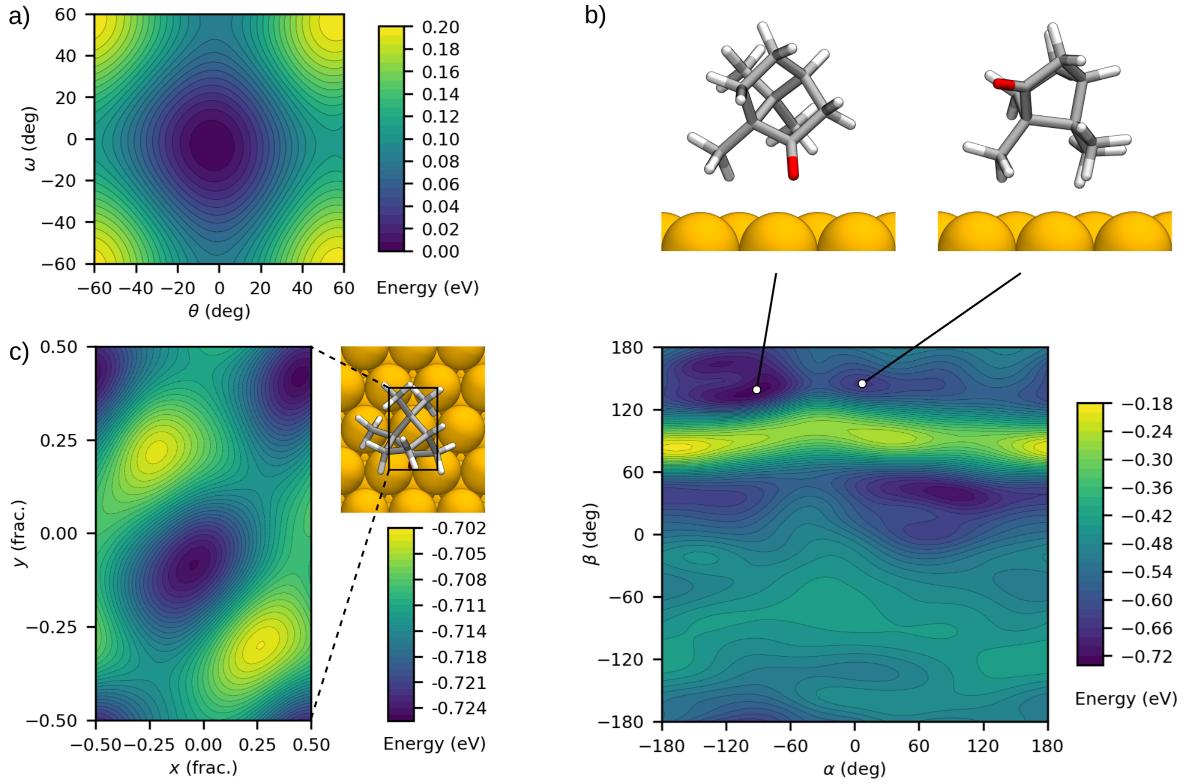

Figure 4: Energy landscapes from preparatory BOSS simulations. (a) θ–ω 2D cross section of the 3D PES in the camphor conformer search, featuring a single minimum and an energy barrier of 0.1 eV for methyl group rotation. (b) α–β 2D cross section of the 3D PES in the search for adsorption orientation of camphor on Cu(111). The landscape features multiple local minima and a higher-energy region at β ≈ 90°. (c) PES of the 2D translational *x*–*y* search of the adsorption site of camphor on Cu(111). The landscape has two identical minima, which agree with the translational symmetry in the orthogonal unit cell.

The electronic structure of the stable adsorbates is analyzed with the partial DOS and the Mulliken analysis of partial charges. We compare the partial DOS of the adsorbed camphor to the highest occupied and lowest unoccupied molecular orbitals (HOMO and LUMO, respectively) of an isolated camphor molecule. In the Mulliken analysis, we calculate the sum of partial atomic charges per element in the adsorbed camphor and compare them to the corresponding charge distribution of an isolated molecule. With this analysis, we study the effect of adsorption on the electronic structure of camphor in the identified stable structures.

First-principles calculations

We use density-functional theory to calculate the adsorption energy of camphor on Cu(111) in the BOSS runs, to relax the predicted stable structures and to analyze the electronic structure of the stable adsorbates. We apply the all-electron, numeric atom-centered orbital code FHI-aims [41-43] with the Perdew–Burke–Ernzerhof (PBE) exchange–correlation functional [44]. PBE is augmented with van der Waals (vdW) corrections employing the vdW$^{\text{surf}}$ parametrization [45] of the Tkatchenko–Scheffler method [46]. Previous work found that PBE + vdW$^{\text{surf}}$ adequately describes organic molecules on metal surfaces [45,47,48].

Our converged settings employ tier-1 basis sets with light grid settings and a Γ-centered 3 × 2 × 1 *k*-point mesh with a $(6 \times 4)\sqrt{3}$ supercell model. We apply relativistic corrections with the zero-order regular approximation [49] and Gaussian broadening of 0.1 eV of the electronic states. The total energy is converged within 10^{-6} eV in the self-consistency cycle and the structures are relaxed below a maximum force component of 10^{-2} eV/Å.

We model the Cu substrate with a Cu(111) slab of four atomic layers and $(6 \times 4)\sqrt{3}$ orthogonal unit cells (192 atoms, lattice vectors $[a, b, c]$ = [15.41, 17.79, 56.29] Å). The lattice constant of Cu is set to 3.632 Å, which we obtain from relaxed bulk Cu, in agreement with reference studies [50,51]. We construct the four-layer Cu slab by fixing the two bottom layers to their optimal layer separation (d_{34} = 2.097 Å, corresponding to bulk Cu). The two top layers are then relaxed, which results in a reduced layer separation (d_{12} = 2.076 Å, d_{23} = 2.081 Å), in agreement with previous calculations [52]. We apply this Cu slab model as a building block in the subsequent study of camphor adsorption.

Our other building block is the global minimum conformer of camphor, which we add onto the Cu slab model. The $(6 \times 4)\sqrt{3}$ supercell provides a good approximation of a single molecule on the surface, with an average lateral separation of 10 Å between the periodic images of camphor and 50 Å separation between the periodic Cu(111) slabs.

The adsorption energy E_{ads} is calculated as

$$E_{\text{ads}} = E_{\text{tot}} - \left(E_{\text{Cu}} + E_{\text{cam}}\right), \tag{1}$$

in which E_{tot} is the total energy of the camphor/Cu(111) system, E_{Cu} is the energy of the relaxed Cu slab, and E_{cam} is the energy of an isolated camphor molecule.

Results

Camphor conformer search

We analyzed the camphor conformers with a 3D BOSS search of the methyl group rotations. The energy landscape (Figure 4a), converged in 20 evaluations, features a single global energy minimum at (θ, φ, ω) = (−3, 7, −3)°, and an energy barrier of 0.1 eV for the rotation of the methyl groups. Given this barrier, the rotation of the methyl groups Δφ away from the global minimum is expected to be small at room temperature. The Arrhenius law predicts that in 50% of the molecules $\Delta\varphi < 10°$, and in 70% $\Delta\varphi < 15°$. Camphor is likely to be found in a conformation very close to the global minimum geometry. We thus take the identified conformer as a building block in the following adsorption study. Any further structural deformations are accounted for at a later stage with full DFT relaxation.

Qualitative insight into adsorption of camphor on Cu(111)

Before conducting a full 6D search, we carried out several low-dimensional searches to develop a feeling for the behavior of camphor on Cu(111). First, we performed a 1D search in the *z* direction, then a 3D rotational search in (α, β, γ), and finally a 2D translational search in the *x*–*y* plane.

We learned about the adsorption height range of camphor on Cu(111) from a 1D BOSS search (Figure 2b) within the limits $z \in [3, 7]$ Å (other variables were set to $(x, y, \alpha, \beta, \gamma)$ = (0, 0, 0, 0, 0)). The predicted minimum of the adsorption energy converged in five evaluations and is found at −0.847 eV at a height z = 4.14 Å. The energy curve has a strong dispersive character and the repulsive energy increases rapidly as the molecule approaches the surface below 4 Å.

For the 3D rotational study, we placed the molecule into a fixed position at (x, y, z) = (0, 0, 5) Å to avoid close contact between the molecule and the surface. Molecular placement at the top site (above a Cu atom) here allows us to curtail the γ range to [−60, 60]°. The resulting PES (Figure 4b) converged in 115 evaluations and contains many features associated with different reactive sites of camphor. The higher energy band at $\beta \approx 90°$ corresponds to the closest approach of the molecule to the surface (via methyl group ω in Figure 3a). The multiple minima and strong barriers imply that camphor may adsorb on Cu(111) in various stable orientations. We explored the structures associated with the most favourable minima to infer the binding mechanisms. As shown in Figure 4b, we found that both charge-withdrawing O and neutral methyl groups face the surface, suggesting that both chemical and dispersive bonding can be expected in the full 6D search.

The 2D search in the x–y plane allowed us to compute the translational energy landscape for camphor. We set the molecule to the global minimum orientation $(\alpha, \beta, \gamma) = (-84, 143, 3)°$ from the previous rotational search, at $z = 5$ Å. The PES (Figure 4c) converged in 20 evaluations and features two identical minima at $(x, y) = (-0.05, -0.08)$ and $(0.45, 0.42)$ in fractional coordinates of the unit cell. These correspond to the translational symmetry of the Cu(111) surface in the orthogonal unit cell. We conclude that our model fitting is qualitatively correct even when the landscapes are very flat, as with this choice of parameters. The flat energy landscapes indicate that rotational degrees of freedom may influence adsorption more than translational ones, but this is best verified in 6D.

Based on the low-dimensional studies, we expect to find multiple stable adsorbate structures in the 6D search, with varying molecular orientations and both chemical and dispersive bonding. Given the observed energy ranges, we conclude that the optimal search range for the height of the molecule in the 6D search is $z \in [4, 7]$ Å. The range is sufficiently broad to include all the minima and avoids high-energy peaks in the closest approach of the molecule to the surface.

Predicted stable adsorbates

For the 6D search of stable adsorbates, we employed the 492 previously acquired energy points from the low-dimensional studies. These points were then multiplied according to the translational and rotational symmetries of the Cu(111) surface, which resulted in 986 initial energy points for the 6D search. We converged the 6D PES (details provided in Supporting Information File 1) by acquiring 197 new points, for which we also applied the symmetries. The surrogate model of the 6D PES was then constructed with 1380 energy points.

In the minima of the PES, we identified eight unique stable structures with predicted adsorption energies (E^{B}) in the range $[-0.961, -0.634]$ eV (Figure 5a and Table 1). We have classified the structures with respect to the bonding species closest to the surface in the adsorbed camphor, namely oxygen (class Ox) and hydrogen (class Hy). The standard deviation of the adsorption energy (σ^{B}) in the surrogate PES is 0.019 eV in the global minimum and 0.025 eV on average over all minima (Table 1), which shows low uncertainty of the model in these points. The energies of the identified structures, calculated with DFT (E^{D}) are in the range $[-0.933, -0.631]$ eV, in close agreement with the predicted energies.

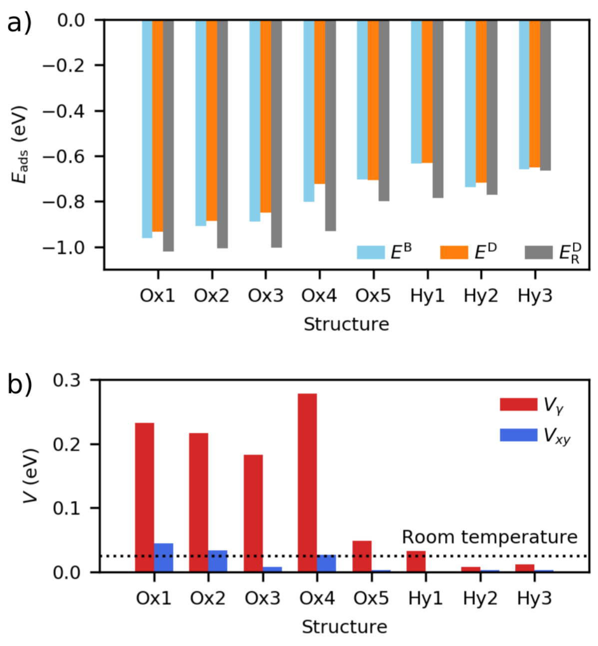

Figure 5: Energetics of adsorption and mobility for surface adsorbates. (a) Adsorption energies (E_{ads}) of the stable adsorbates predicted by BOSS (E^{B}), their true values calculated with DFT (E^{D}) and the adsorption energies of the relaxed structures ($E^{\mathrm{D}}_{\mathrm{R}}$). (b) Energy barriers ($V$) for γ rotation (V_{γ}) and x–y translation (V_{xy}), in comparison with thermal energy at room temperature.

Relaxed structures

We verified the stable structures by performing full DFT relaxations (Figure 6a,b). In the relaxation, we observed an average decrease of −0.11 eV from the E^{D} energies (Figure 5a and Table 1). We found that in class Ox structures, 80% of the binding energy is due to dispersion whereas in class Hy structures the binding energy is purely dispersive.

The structural changes in the relaxation were analyzed by comparing the location and orientation of the molecule before and after the relaxation. We observed the relaxed structures to be almost identical with the initial ones. The average change in the location of the molecule, over all structures, is $(\overline{\Delta x}, \overline{\Delta y}, \overline{\Delta z}) = (0.13, 0.09, 0.19)$ Å and in the orientation $(\overline{\Delta\alpha}, \overline{\Delta\beta}, \overline{\Delta\gamma}) = (6.1, 5.8, 2.5)°$. The structural changes in the Cu slab are minimal. The changes in the internal geometry of camphor in the relaxation, after removing the building block

Table 1: Adsorption energies of the stable adsorbates, predicted by BOSS (E^B), and their standard deviation in the surrogate model of the 6D PES (σ^B). Adsorption energies calculated with DFT (E^D) and their difference from the predicted energies (ΔE^D). Energy after relaxation (E^D_R), and energy change in the relaxation (ΔE^D_R). Predicted energy barriers of γ rotation (V_γ) and *x*–*y* translation (V_{xy}).

	E^B (eV)	σ^B (eV)	E^D (eV)	ΔE^D (eV)	E^D_R (eV)	ΔE^D_R (eV)	V_γ (eV)	V_{xy} (eV)
Ox1	−0.961	0.019	−0.933	+0.028	−1.022	−0.089	0.232	0.045
Ox2	−0.910	0.013	−0.885	+0.025	−1.008	−0.123	0.216	0.034
Ox3	−0.889	0.027	−0.850	+0.039	−1.005	−0.155	0.183	0.008
Ox4	−0.803	0.032	−0.723	+0.079	−0.932	−0.209	0.278	0.027
Ox5	−0.704	0.016	−0.706	−0.002	−0.800	−0.094	0.048	0.003
Hy1	−0.634	0.021	−0.631	+0.003	−0.784	−0.154	0.033	0.001
Hy2	−0.737	0.041	−0.719	+0.019	−0.772	−0.053	0.008	0.003
Hy3	−0.658	0.027	−0.652	+0.005	−0.664	−0.012	0.012	0.003

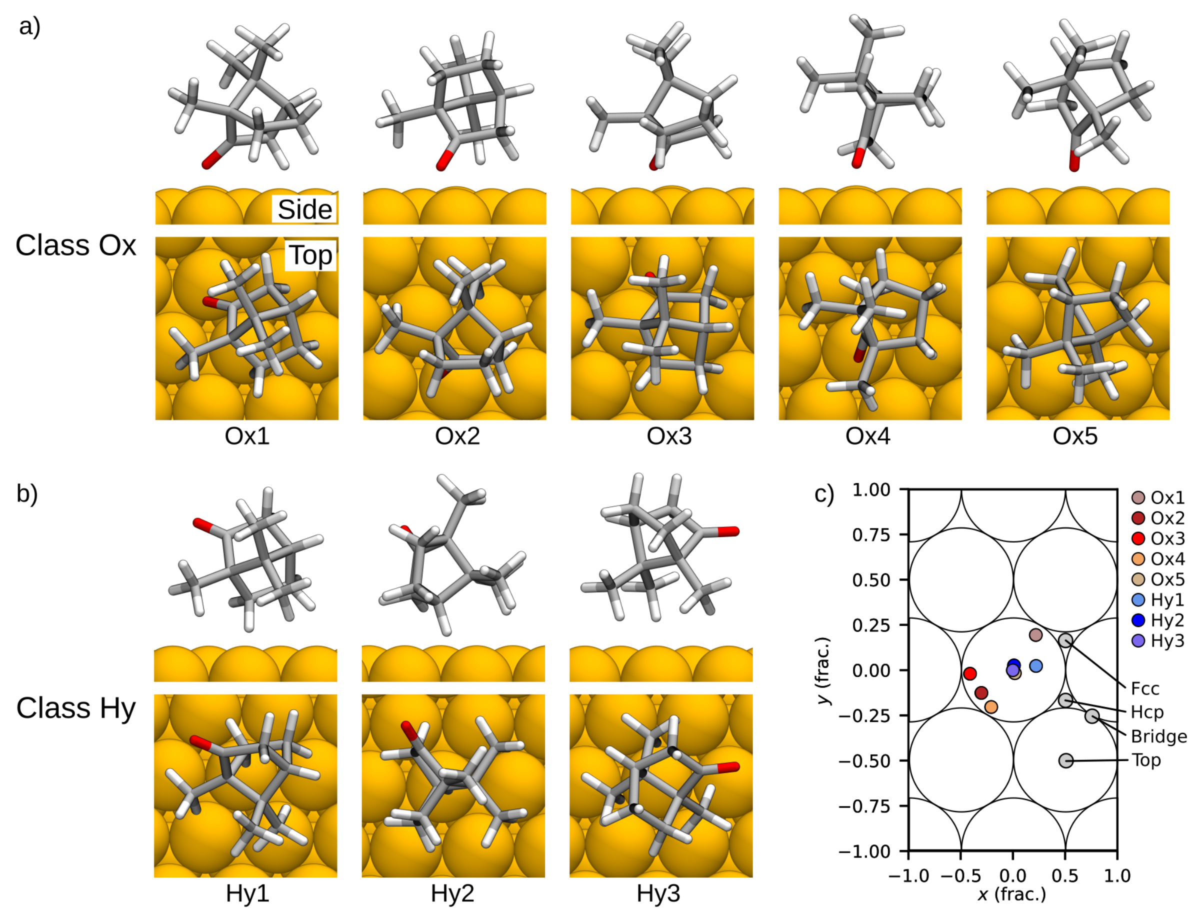

Figure 6: Relaxed stable adsorbate structures of camphor on Cu(111) in the 6D search, showing (a) chemisorption of the molecule via oxygen (class Ox) and (b) physisorption via hydrogen (class Hy). (c) Adsorption site of camphor in the relaxed structures (center of the molecule) and the high-symmetry points of the Cu(111) surface.

approximation, were evaluated using the average root-mean-square deviation of the atomic positions and the mean deviation of bond lengths, which are 0.13 Å and 0.003 Å, respectively, on average over all structures (see Supporting Information File 1 for structure-specific data).

We analyzed the adsorption site of camphor in the relaxed structures (Figure 6c) with respect to the center of the molecule (Figure 3b). The adsorption sites show a notable difference between the two classes. Class Hy structures (in particular Hy2 and Hy3) prefer to adsorb close to the top site, whereas class Ox structures feature more variance in their location. Three of the class Ox structures (Ox1, Ox3, and Ox4) adsorb near the bridge site and Ox5 is close to the top site.

To estimate the mobility of camphor molecules on the surface, we inspect translational and rotational barriers. The translational energy barriers were computed using 2D *x*–*y* cross sections (grid of 100 × 100 points) of the predicted 6D PES, as described in the Computational Methods section. For the γ rotation barriers, we extracted 1D γ energy profiles from the 6D PES but found them overly smooth and free of features expected for an asymmetric molecule rotating on the Cu(111) surface. We concluded the upper limits for γ rotation to be too inaccurate and analyze the γ energy barriers using the fully relaxed structures of local minima geometries. For each mininimum type, we rotated camphor in-place (center point of rotation in Figure 3b) and computed the rotational energy profile with a 1D BOSS search (converged in 15 evaluations). While this approach is still approximate, the resulting energy profiles exhibit features that correctly reflect surface symmetry and provide us with a better estimate of the barriers without investing time and computational expense into NEB calculations.

The predicted energy barriers of γ rotation and *x*–*y* translation (Figure 5b and Table 1) are in the range [0.008, 0.278] and [0.001, 0.045] eV, respectively. The barriers are highest in class Ox structures, specifically in structures Ox1–Ox4, with a notable difference to class Hy. When we take into account the standard deviation of the adsorption energy in the surrogate model (Table 1), the smallest energy barriers (of the order of 0.01 eV and below) are practically zero. This indicates free rotation of structures Hy2 and Hy3, and free diffusion of structures Ox3, Ox5, and Hy1–Hy3, even at low temperatures.

Electronic structure

We analyzed the charge distribution of the stable adsorbates with the Mulliken analysis of partial charges and investigated their partial DOS to study the effect of adsorption on the electronic structure. The Mulliken analysis of partial charges in the relaxed structures (Figure 7a and Table 2), in comparison to the charge distribution of an isolated camphor molecule, shows electron transfer from the adsorbed camphor molecule to the Cu substrate. The electron transfer is highest in class Ox structures, in which the O atom of camphor is close to the Cu surface. The average partial charge of camphor (Δ*q*) is +0.21 *e* (elementary charge, *e* = |e^-|) in class Ox structures and +0.10 *e* in class Hy structures. In class Ox structures, the main contribution to the positive charge comes from hydrogen (H) atoms, with O as the second notable contributor. In class Hy structures, the positive charge of camphor originates predominantly from H atoms.

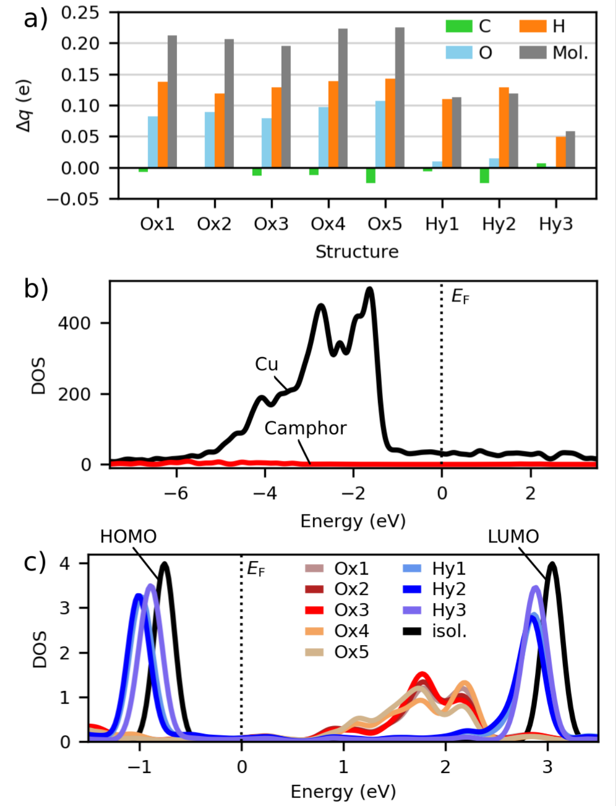

Figure 7: Electronic properties of different camphor adsorbates. (a) The sum of partial charges (Δ*q*) in the adsorbed camphor in the relaxed structures. (b) DOS of Cu and camphor in structure Ox1, and (c) DOS of camphor in the relaxed structures and in an isolated molecule.

Table 2: The sum of partial charges of C, O, and H in an adsorbed camphor molecule (Δq_C, Δq_O, and Δq_H, respectively) and the total partial charge of the camphor molecule (Δ*q*).

	Δq_C (*e*)	Δq_O (*e*)	Δq_H (*e*)	Δ*q* (*e*)
Ox1	−0.01	+0.08	+0.14	+0.21
Ox2	−0.00	+0.09	+0.12	+0.21
Ox3	−0.01	+0.08	+0.13	+0.20
Ox4	−0.01	+0.10	+0.14	+0.22
Ox5	−0.02	+0.11	+0.14	+0.23
Hy1	−0.01	+0.01	+0.11	+0.11
Hy2	−0.03	+0.01	+0.13	+0.12
Hy3	+0.01	+0.00	+0.05	+0.06

In the partial DOS of the relaxed structures (Figure 7b,c), we analyze the electronic states of the adsorbed camphor close to the Fermi level. The partial DOS of class Ox structures features hybridization of the electronic states, in comparison to the HOMO and LUMO of an isolated camphor. The hybridization implies chemical bonding between the molecule and the substrate in class Ox. Conversely, in class Hy, the electronic states resemble the HOMO and LUMO of an isolated camphor molecule and are at −1.0 and 2.9 eV, respectively, with an energy gap of 3.9 eV. This indicates physisorption between the molecule and the substrate in class Hy.

Discussion

With the low-dimensional studies of molecular translation (1D and 2D) and rotation (3D), we obtained a qualitative description of the adsorption properties of camphor on Cu(111). We gained insight into the estimated adsorption height of the molecule and acquired the ranges of adsorption energy with respect to molecular orientation and the adsorption site. The rotational energy landscape with multiple local minima suggests that camphor can adsorb on Cu(111) in various stable orientations. From the low-dimensional analysis, we obtained the required knowledge to determine the optimal search range for the height of the molecule in the subsequent 6D study.

In the relaxation of the identified structures, we observed minor changes in the molecular orientation, the adsorption site, and the adsorption energy. This effectively confirms the accuracy of the surrogate model of the 6D PES. Negligible changes in the internal structure of camphor and the Cu slab in the relaxation validates the building block approximation in this study.

The eight stable adsorbate structures extracted from the 6D search feature notable differences between the class Ox and class Hy structures, specifically, regarding their adsorption energy, adsorption site, energy barriers, and the electronic structure. Class Ox adsorbates have the highest adsorption energies and high energy barriers of molecular mobility. In class Ox structures, the preferred adsorption site is near the bridge site, so that the O atom can point sideways to bond with the Cu atom. In class Hy structures, methyl groups avoid the top site, so the molecule centers there, and the methyl groups point sideways. The DOS of class Ox structures feature hybridization of the electronic states and the electron transfer from the molecule to the substrate is significantly larger than in class Hy structures, with the largest contribution per atom from O. This indicates chemisorption of camphor via O to the Cu substrate. Conversely, in class Hy structures we observed the characteristics of physisorption. Class Hy structures have systematically lower adsorption energies, energy barriers, and electron transfer to the substrate, and their DOS resembles the HOMO and LUMO of an isolated molecule. These findings are supported by the vdW contributions in the adsorption energy, which show 80% dispersive bonding in class Ox structures and fully dispersive adsorption in class Hy structures.

To verify the identified stable structures, we can compare them to adsorbates observed in experiments. The adsorption of camphor on Cu(111) has been studied experimentally with AFM by Alldritt and co-workers [35]. In their images, they have observed various different adsorbate structures, which shows that camphor can adsorb on Cu(111) in multiple stable configurations. In the experiments, camphor molecules were deposited onto the Cu surface at 20 K temperature and the imaging was done at 5 K. When the surface is annealed to the imaging temperature, we expect the deposited molecules to obtain the global minimum conformer geometry, which corresponds to the camphor building block in this study. Based on the estimated energy barriers of molecular mobility in this study, we conclude that the experiments likely feature chemisorbed camphor molecules from class Ox. In particular, the structures Ox1–Ox4, which have the highest barriers, are the most likely candidates for static adsorbates. They also have the highest adsorption energies, which makes them the most probable structures to be observed. Conversely, class Hy structures, which have lower adsorption energies and low energy barriers for molecular mobility, are less likely to be imaged in experiments. A more detailed comparison between BOSS and AFM will be reported in [53].

We highlight the computational efficiency of global structure search with BOSS by comparing the number of required DFT calculations to a conventional structure search. The best candidates for the minimum-energy structures can be first estimated using chemical intuition and then relaxed with DFT to identify the stable structures. With camphor on Cu(111), we can search for the stable adsorbates by placing the molecule on each of the four high-symmetry points of the Cu surface (Figure 6c) and investigate, for example, ten different molecular orientations at each of the adsorption sites. We estimate that the relaxation of the structures requires on average 40 calculation steps per structure. With this method, the estimated computational cost would be 1600 DFT calculations. Still, this amounts to exploring only a small portion of the PES and does not guarantee a reliable identification of the global minimum energy structure.

With BOSS, we identified the stable structures of camphor on Cu(111) with 892 DFT calculations (689 to construct the surrogate model of the 6D PES, and 203 to relax the eight structures). Relaxation of the predicted stable structures in the local minima of the PES was fast (25 relaxation steps per structure on average) due to their low initial energy. With the PES model, we were able to reliably identify not only all the minima, but also the associated energy barriers of molecular mobility. This comparison highlights the benefits of the BOSS approach, which are, in particular, (i) computational efficiency, (ii) reliable identification of the most stable structures, and (iii) energy barriers readily obtained with the surrogate model of the PES.

Conclusion

In this study, we have demonstrated the efficiency of BOSS in global structure search with complex molecular adsorbates. We have shown the accuracy of the constructed surrogate model of the PES, in comparison with adsorption energies of stable structures calculated with DFT. As a benchmark system, we have analyzed the adsorption of a camphor molecule on the Cu(111) surface with respect to molecular translation and rotation. With BOSS, we constructed a surrogate model of the 6D PES of adsorption and identified its minima, in which we detected the most stable structure (global minimum) and seven other stable structures (local minima).

We classified our stable structures into two classes, that is, Ox and Hy, with respect to the bonding species in the adsorbed camphor. The differences between the two classes were further categorized by the trends in the adsorption energies and the energy barriers of molecular motion. By analyzing the electronic structure of the stable adsorbates, we concluded that in the most stable structures (class Ox), camphor chemisorbs to the Cu surface via O bonding. Our results imply that class Ox structures are viable candidates for static camphor adsorbates observed in AFM experiments.

By combining machine learning with DFT, BOSS provides a novel method for a reliable structure identification via the surrogate model of the PES. With the complete PES, we obtain chemical insight into numerous materials properties (e.g., the stable adsorbate structures and their mobility) in one go, without prior presumptions about the material. Our approach eliminates the human bias present in conventional structure search, in which the optimal structures are commonly estimated using chemical intuition. Efficient and unbiased structure search methods, such as BOSS, facilitate the study of complex hybrid interface structures. The acquired knowledge can be applied in the precision engineering of interface structures in functional materials to optimize their advantageous properties.

Supporting Information

Supporting information features camphor geometry in global minimum conformer search, convergence of the 6D surrogate model, and coordinates of camphor in the predicted and relaxed stable structures.

Supporting Information File 1

Camphor global minimum conformer, convergence of the 6D model, and coordinates of camphor.
[https://www.beilstein-journals.org/bjnano/content/supplementary/2190-4286-11-140-S1.pdf]

Acknowledgements

The authors wish to acknowledge CSC – IT Center for Science, Finland, and the Aalto Science-IT project for generous computational resources. An award of computer time was provided by the Innovative and Novel Computational Impact on Theory and Experiment (INCITE) program. This research used resources of the Argonne Leadership Computing Facility, which is a DOE Office of Science User Facility supported under Contract DE-AC02-06CH11357.

Funding

This work has received funding from the Academy of Finland via the Artificial Intelligence for Microscopic Structure Search (AIMSS) project No. 316601 and the Flagship programme: Finnish Center for Artificial Intelligence FCAI, and from the Emil Aaltonen Foundation.

ORCID® iDs

Jari Järvi - https://orcid.org/0000-0003-3727-5887
Patrick Rinke - https://orcid.org/0000-0003-1898-723X
Milica Todorović - https://orcid.org/0000-0003-0028-0105

Preprint

A non-peer-reviewed version of this article has been previously published as a preprint: https://arxiv.org/abs/2002.05598

References

1. Snaith, H. J. *Nat. Mater.* **2018,** *17,* 372–376. doi:10.1038/s41563-018-0071-z
2. Terzaki, K.; Kissamitaki, M.; Skarmoutsou, A.; Fotakis, C.; Charitidis, C. A.; Farsari, M.; Vamvakaki, M.; Chatzinikolaidou, M. *J. Biomed. Mater. Res., Part A* **2013,** *101A,* 2283–2294. doi:10.1002/jbm.a.34516
3. Contessotto, L.; Ghedini, E.; Pinna, F.; Signoretto, M.; Cerrato, G.; Crocellà, V. *Chem. – Eur. J.* **2009,** *15,* 12043–12049. doi:10.1002/chem.200900603
4. Farronato, M.; Bidermane, I.; Lüder, J.; Bouvet, M.; Vlad, A.; Jones, A.; Simbrunner, J.; Resel, R.; Brena, B.; Prévot, G.; Witkowski, N. *J. Phys. Chem. C* **2018,** *122,* 26480–26488. doi:10.1021/acs.jpcc.8b08462
5. Wang, L.; Bian, J.; Lu, L.; Liang, Z.; Zhang, D.; Yang, B.; Li, L.; Lu, G.; Yang, Y. *J. Mater. Chem. C* **2020,** *8,* 3527–3535. doi:10.1039/c9tc06739f
6. Kühnle, A. *Curr. Opin. Colloid Interface Sci.* **2009,** *14,* 157–168. doi:10.1016/j.cocis.2008.01.001
7. Kumar, A.; Banerjee, K.; Dvorak, M.; Schulz, F.; Harju, A.; Rinke, P.; Liljeroth, P. *ACS Nano* **2017,** *11,* 4960–4968. doi:10.1021/acsnano.7b01599
8. Tian, G.; Shen, Y.; He, B.; Yu, Z.; Song, F.; Lu, Y.; Wang, P.; Gao, Y.; Huang, H. *Surf. Sci.* **2017,** *665,* 89–95. doi:10.1016/j.susc.2017.08.008
9. Wold, D. J.; Haag, R.; Rampi, M. A.; Frisbie, C. D. *J. Phys. Chem. B* **2002,** *106,* 2813–2816. doi:10.1021/jp013476t
10. Mönig, H.; Amirjalayer, S.; Timmer, A.; Hu, Z.; Liu, L.; Díaz Arado, O.; Cnudde, M.; Strassert, C. A.; Ji, W.; Rohlfing, M.; Fuchs, H. *Nat. Nanotechnol.* **2018,** *13,* 371–375. doi:10.1038/s41565-018-0104-4

11. Zint, S.; Ebeling, D.; Schlöder, T.; Ahles, S.; Mollenhauer, D.; Wegner, H. A.; Schirmeisen, A. *ACS Nano* **2017,** *11,* 4183–4190. doi:10.1021/acsnano.7b01109
12. Hohenberg, P.; Kohn, W. *Phys. Rev.* **1964,** *136,* B864–B871. doi:10.1103/physrev.136.b864
13. Kohn, W.; Sham, L. J. *Phys. Rev.* **1965,** *140,* A1133–A1138. doi:10.1103/physrev.140.a1133
14. Goedecker, S. *J. Chem. Phys.* **2004,** *120,* 9911–9917. doi:10.1063/1.1724816
15. Li, F.; Liu, Y.; Wang, L.; Zhao, J.; Chen, Z. *Theor. Chem. Acc.* **2012,** *131,* 1163. doi:10.1007/s00214-012-1163-5
16. Laio, A.; Parrinello, M. *Proc. Natl. Acad. Sci. U. S. A.* **2002,** *99,* 12562–12566. doi:10.1073/pnas.202427399
17. Obersteiner, V.; Scherbela, M.; Hörmann, L.; Wegner, D.; Hofmann, O. T. *Nano Lett.* **2017,** *17,* 4453–4460. doi:10.1021/acs.nanolett.7b01637
18. Packwood, D. M.; Han, P.; Hitosugi, T. *Nat. Commun.* **2017,** *8,* 14463. doi:10.1038/ncomms14463
19. Rasmussen, C. E.; Williams, C. K. I. *Gaussian Processes for Machine Learning;* Adaptive Computation and Machine Learning; The MIT Press: Cambridge, MA, USA, 2005. doi:10.7551/mitpress/3206.001.0001
20. Shahriari, B.; Swersky, K.; Wang, Z.; Adams, R. P.; de Freitas, N. *Proc. IEEE* **2016,** *104,* 148–175. doi:10.1109/jproc.2015.2494218
21. Garijo del Río, E.; Mortensen, J. J.; Jacobsen, K. W. *Phys. Rev. B* **2019,** *100,* 104103. doi:10.1103/physrevb.100.104103
22. Koistinen, O.-P.; Dagbjartsdóttir, F. B.; Ásgeirsson, V.; Vehtari, A.; Jónsson, H. *J. Chem. Phys.* **2017,** *147,* 152720. doi:10.1063/1.4986787
23. Seko, A.; Maekawa, T.; Tsuda, K.; Tanaka, I. *Phys. Rev. B* **2014,** *89,* 054303. doi:10.1103/physrevb.89.054303
24. Balachandran, P. V.; Xue, D.; Theiler, J.; Hogden, J.; Lookman, T. *Sci. Rep.* **2016,** *6,* 19660. doi:10.1038/srep19660
25. Chan, L.; Hutchison, G. R.; Morris, G. M. *J. Cheminf.* **2019,** *11,* 32. doi:10.1186/s13321-019-0354-7
26. Packwood, D. M.; Hitosugi, T. *Appl. Phys. Express* **2017,** *10,* 065502. doi:10.7567/apex.10.065502
27. Carr, S.; Garnett, R.; Lo, C. BASC: Applying Bayesian Optimization to the Search for Global Minima on Potential Energy Surfaces. In *Proceedings of Machine Learning Research,* June 20–22, 2016; Balcan, M. F.; Weinberger, K. Q., Eds.; PMLR: New York, New York, USA, 2016; pp 898–907.
28. Jørgensen, M. S.; Larsen, U. F.; Jacobsen, K. W.; Hammer, B. *J. Phys. Chem. A* **2018,** *122,* 1504–1509. doi:10.1021/acs.jpca.8b00160
29. Xue, D.; Balachandran, P. V.; Hogden, J.; Theiler, J.; Xue, D.; Lookman, T. *Nat. Commun.* **2016,** *7,* 11241. doi:10.1038/ncomms11241
30. Seko, A.; Togo, A.; Hayashi, H.; Tsuda, K.; Chaput, L.; Tanaka, I. *Phys. Rev. Lett.* **2015,** *115,* 205901. doi:10.1103/physrevlett.115.205901
31. Todorović, M.; Gutmann, M. U.; Corander, J.; Rinke, P. *npj Comput. Mater.* **2019,** *5,* 35. doi:10.1038/s41524-019-0175-2
32. Egger, A. T.; Hörmann, L.; Jeindl, A.; Scherbela, M.; Obersteiner, V.; Todorović, M.; Rinke, P.; Hofmann, O. T. *Adv. Sci.* **2020,** *7,* 2000992. doi:10.1002/advs.202000992
33. Fang, L.; Makkonen, E.; Todorović, M.; Rinke, P.; Chen, X. *arXiv* **2020,** No. 2006.15006.
34. BOSS code repository. https://gitlab.com/cest-group/boss (accessed March 13, 2020).
35. Alldritt, B.; Hapala, P.; Oinonen, N.; Urtev, F.; Krejci, O.; Federici Canova, F.; Kannala, J.; Schulz, F.; Liljeroth, P.; Foster, A. S. *Sci. Adv.* **2020,** *6,* eaay6913. doi:10.1126/sciadv.aay6913
36. Oganov, A. R.; Glass, C. W. *J. Chem. Phys.* **2006,** *124,* 244704. doi:10.1063/1.2210932
37. Gutmann, M. U.; Corander, J. *J. Mach. Learn. Res.* **2016,** *17,* 4256–4302.
38. Brochu, E.; Cora, V. M.; de Freitas, N. *arXiv* **2010,** No. 1012.2599.
39. Byrd, R. H.; Lu, P.; Nocedal, J.; Zhu, C. *SIAM J. Sci. Comput.* **1995,** *16,* 1190–1208. doi:10.1137/0916069
40. Mulliken, R. S. *J. Chem. Phys.* **1955,** *23,* 1833–1840. doi:10.1063/1.1740588
41. Blum, V.; Gehrke, R.; Hanke, F.; Havu, P.; Havu, V.; Ren, X.; Reuter, K.; Scheffler, M. *Comput. Phys. Commun.* **2009,** *180,* 2175–2196. doi:10.1016/j.cpc.2009.06.022
42. Havu, V.; Blum, V.; Havu, P.; Scheffler, M. *J. Comput. Phys.* **2009,** *228,* 8367–8379. doi:10.1016/j.jcp.2009.08.008
43. Ren, X.; Rinke, P.; Blum, V.; Wieferink, J.; Tkatchenko, A.; Sanfilippo, A.; Reuter, K.; Scheffler, M. *New J. Phys.* **2012,** *14,* 053020. doi:10.1088/1367-2630/14/5/053020
44. Perdew, J. P.; Burke, K.; Ernzerhof, M. *Phys. Rev. Lett.* **1996,** *77,* 3865–3868. doi:10.1103/physrevlett.77.3865
45. Ruiz, V. G.; Liu, W.; Tkatchenko, A. *Phys. Rev. B* **2016,** *93,* 035118. doi:10.1103/physrevb.93.035118
46. Tkatchenko, A.; Scheffler, M. *Phys. Rev. Lett.* **2009,** *102,* 073005. doi:10.1103/physrevlett.102.073005
47. Hofmann, O. T.; Atalla, V.; Moll, N.; Rinke, P.; Scheffler, M. *New J. Phys.* **2013,** *15,* 123028. doi:10.1088/1367-2630/15/12/123028
48. Ruiz, V. G.; Liu, W.; Zojer, E.; Scheffler, M.; Tkatchenko, A. *Phys. Rev. Lett.* **2012,** *108,* 146103. doi:10.1103/physrevlett.108.146103
49. van Lenthe, E.; Baerends, E. J.; Snijders, J. G. *J. Chem. Phys.* **1993,** *99,* 4597–4610. doi:10.1063/1.466059
50. Haas, P.; Tran, F.; Blaha, P. *Phys. Rev. B* **2009,** *79,* 085104. doi:10.1103/physrevb.79.085104
51. Liu, W.; Ruiz, V. G.; Zhang, G.-X.; Santra, B.; Ren, X.; Scheffler, M.; Tkatchenko, A. *New J. Phys.* **2013,** *15,* 053046. doi:10.1088/1367-2630/15/5/053046
52. Stroppa, A.; Termentzidis, K.; Paier, J.; Kresse, G.; Hafner, J. *Phys. Rev. B* **2007,** *76,* 195440. doi:10.1103/physrevb.76.195440
53. Järvi, J.; Alldritt, B.; Krejčí, O.; Todorović, M.; Liljeroth, P.; Rinke, P. *Res. Square* **2020**. doi:10.21203/rs.3.rs-50783/v1

License and Terms

The definitive version of this article is the electronic one which can be found at:
https://doi.org/10.3762/bjnano.11.140

BEILSTEIN JOURNAL OF NANOTECHNOLOGY

PTCDA adsorption on CaF_2 thin films

Philipp Rahe

Full Research Paper

Open Access

Address:
Fachbereich Physik, Universität Osnabrück, Barbarastrasse 7,
49076 Osnabrück, Germany

Email:
Philipp Rahe - prahe@uni-osnabrueck.de

Keywords:
calcium difluoride; decoupling; insulating thin film; 3,4,9,10-perylene tetracarboxylic dianhydride (PTCDA); scanning tunnelling microscopy

Beilstein J. Nanotechnol. **2020,** *11,* 1615–1622.
https://doi.org/10.3762/bjnano.11.144

Received: 27 June 2020
Accepted: 13 October 2020
Published: 26 October 2020

This article is part of the thematic issue "Molecular assemblies on surfaces – towards physical and electronic decoupling of organic molecules".

Guest Editor: S. Maier

Abstract

Thin insulating films are commonly employed for the electronic decoupling of molecules as they enable a preservation of the intrinsic molecular electronic functionality. Here, the molecular properties of 3,4,9,10-perylene tetracarboxylic dianhydride (PTCDA) adsorbed on insulating CaF_2 thin films that were grown on Si(111) surfaces are studied. Scanning tunnelling microscopy is used to compare the properties of PTCDA molecules adsorbed on a partly CaF_1-covered Si(111) surface with deposition on thicker CaF_2/CaF_1/Si(111) films. The identification of mostly single molecules on the CaF_1/Si(111) interface layer is explained by the presence of atomic-size defects within this layer. Geometry-optimisation calculations using density functional theory reveal a geometry on CaF_2(111) of nearly flat-lying PTCDA molecules with two oxygen atoms displaced towards calcium surface ions. This geometry is in agreement with the experimental observations.

Introduction

The study of molecular adsorption on thin insulating films is motivated by the possibility to investigate and utilise molecular properties in their largely undisturbed state [1]. Molecule–thin film insulator interfaces are additionally of central importance in modern applications, for example as a critical component in organic thin-film transistors [2]. However, and despite the success of using thin insulating NaCl films for molecular decoupling [3], it is now understood that ultrathin layers are often not sufficient to truly insulate a molecular assembly. To name two examples, the conductivity through a NaCl bilayer still dominates the conductivity along a molecular wire [4] and only the usage of thick NaCl films has enabled charge stability of single molecules [5].

A particularly well-studied case of surface-specific molecular properties is the adsorption of 3,4,9,10-perylene tetracarboxylic dianhydride (PTCDA) on metal [6-12], semiconductor [13], and insulator surfaces [14-19], as well as the deposition on conducting surfaces covered by insulating thin films [20-24] or two-dimensional materials [25]. It is also noteworthy that PTCDA on bulk NaCl(001) surfaces shows long-range order with a dewetting transition at a certain coverage [18], while experiments using NaCl thin films on Cu(111) revealed an absence of long-range order with molecules rather bound to step edges [22]. Explanations for this different behaviour include the slight difference in the lattice constants of bulk and thin-film NaCl and the extension of the metallic state across the thin film. A difference in the molecular adsorption properties on insulating thin films of varying thickness has also been found for PTCDA molecules on partially KBr-covered Ag(111) surfaces [24] as well as for cyanoporphyrin molecules on KBr-covered Cu(111) surfaces [26].

Here, the understanding of molecular adsorption on insulating thin films is extended by studying an insulator-on-semiconductor system, namely CaF_2 thin films grown on Si(111) surfaces, with PTCDA as the probe molecule. In particular, the adsorption properties of PTCDA on CaF_2/CaF_1/Si(111), CaF_1/Si(111), as well as Si(111)-(7 × 7) surfaces are experimentally investigated by high-resolution scanning tunnelling microscopy (STM) and the adsorption geometry on a $CaF_2(111)$ slab is theoretically modelled using density functional theory (DFT). A prominent difference of the molecular properties on the different surface areas is the presence of mostly single molecules in CaF_1/Si(111) regions, while ultrasmall molecular assemblies are experimentally observed on thicker CaF_2 films. A rather flat-lying geometry is found from geometry-optimisation calculations of a single PTCDA molecule on a CaF_2 slab using DFT, whereby an interaction between two carbonyl oxygen atoms and two surface calcium ions leads to a slight deformation of the PTCDA molecule.

Methods

Sample preparation and STM experiments were performed under ultrahigh-vacuum conditions. Highly B-doped p-type Si(111) samples (Institute of Electronic Materials Technology, Warsaw, Poland) were used as substrates. The (7 × 7) reconstruction was formed by flash cycles and the (7 × 7) surface quality was checked by STM imaging.

CaF_2 material (cleanliness 99.9%, Alfa Aesar, Kandel, Germany) was deposited from an e-beam evaporator (type EFM3T, Focus GmbH, Huenstetten, Germany) on silicon samples held at about 600 °C by direct-current heating. Further details on the sample preparation and CaF_2/Si(111) surface properties can be found in [27-29]. PTCDA molecules were deposited from custom-built Knudsen cells heated to 290–300 °C. Samples were held at room temperature during deposition unless noted otherwise. STM data were acquired at 77 or 5 K using a ScientaOmicron qPlus LT AFM/STM operated by a MATRIX controller and an atom-tracking system [30]. Image data were acquired in constant-current or constant-height mode while applying a sample bias U_b. Gwyddion [31] was used for the image data analysis.

Density functional theory calculations were performed using cp2k (http://www.cp2k.org) [32] and parameters similar to previous calculations were chosen [33]. The MOLOPT short-range basis sets of double-ζ quality [34,35], mixed Gaussian and plane waves, GTH potentials [36], the PBE GGA functional [37], the Γ point sampling, the Grimme DFT-D3 dispersion correction [38], and a basis-set superposition-error corrected calculation of the adsorption energies using the counterpoise method [39] were used. Geometry-optimisation calculations were performed for a single PTCDA molecule adsorbed on a (6 × 6) slab with a thickness of three CaF_2 triple layers. The lowest triple layer was held fixed. A tolerance of 10^{-4} Ha/Bohr was used.

Results and Discussion

PTCDA adsorption was studied by STM after deposition on partly CaF_1-covered Si(111)-(7 × 7) and CaF_2/CaF_1/Si(111) surfaces. Representative overview images acquired at 77 K on the three different surfaces areas are reproduced in Figure 1a–c. In agreement with an earlier study [13] of PTCDA on Si(111)-(7 × 7), molecules bind in various geometries to the pristine silicon surface as apparent from Figure 1a. Among these

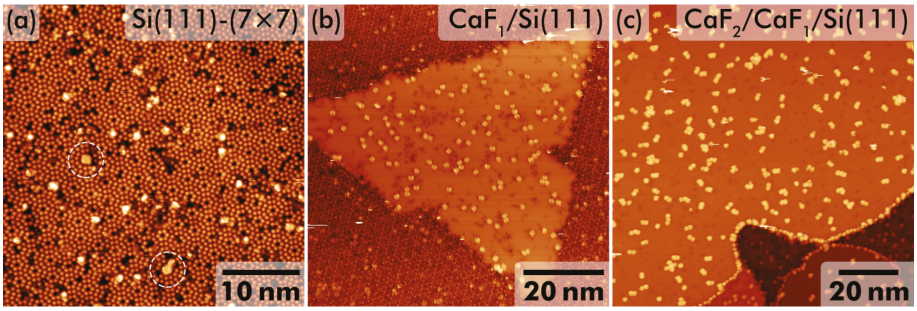

Figure 1: STM images of PTCDA molecules on (a) Si(111)-(7 × 7), (b) partly CaF_1-covered Si(111), and (c) CaF_2/CaF_1/Si(111) surface areas. Imaging parameters: (a) dynamic STM, U_b = 3.0 V, I_t = 50 pA; (b) STM, U_b = −3.0 V, I_t = 50 pA; (c) U_b = −3.0 V, I_t = 50 pA.

geometries, a distinguished adsorption position on top of the (7 × 7) corner hole stands out. Two examples are marked by white ellipses in Figure 1a.

The growth of ordered CaF_2 films on Si(111) requires the formation of a CaF_1 interface layer as the first step. This interface layer is generated by an interface reaction between CaF_2 and the silicon surface [28,29], where surface temperatures around 600 °C during deposition facilitate the dissociation of CaF_2 to CaF_1 and F. The dissociated fluorine atoms mostly desorb from the surface, likely in the form of Si_xF molecules [28,29]. Thicker CaF_2 layers can then be grown stoichiometrically on the interface layer by successive CaF_2 deposition. The CaF_1/Si(111) surface has a (1 × 1) termination after etching the Si(111)-(7 × 7) reconstruction.

After PTCDA deposition, individual double-lobe features are apparent in STM at negative sample bias on the CaF_1/Si(111) areas (see also Figure 1b), in addition to the dark spots that were identified before as single atomic-size defects within the CaF_1 interface layer [27]. Each of these double-lobe features is tentatively assigned to a single PTCDA molecule. In contrast, very small assemblies formed by a few bright protrusions are observed on CaF_2 surface areas, see Figure 1c. In these data, a single protrusion is again assigned to an individual PTCDA molecule. Neither long-range order nor extended island formation is apparent in any surface area.

Examples of imaging individual PTCDA molecules with STM are shown in Figure 2. The images of the cornerhole geometry on Si(111) taken at negative (Figure 2a) and positive (Figure 2d) sample bias both resemble the previously observed contrast for PTCDA at a cornerhole position at negative sample bias [13], where the molecule appears in the form of a central ring surrounded by two bright, elongated lobes. The previously observed striped structure measured at positive sample bias of +0.4 V [13] was not found as imaging was not stable at small bias in the present experiments.

On the CaF_1 interface layer, a double-lobe feature (see also Figure 1b) is the prevalently observed shape of PTCDA, similar to the coffee bean-like shape measured by STM on KCl(001)/Ag(001) [21] or on KBr(001)/InSb(001) [23] thin films. A similar pattern was also observed in STM imaging of PTCDA/Ag(111) with an s-tip at a bias between −0.4 and −0.5 V [12] and explained by strong domination of the LUMO. In contrast, imaging at larger tip–sample distance and the according loss of sensitivity to intramolecular features was given as an explanation for the prevalently observed double-lobe feature on KCl(001)/Ag(001) [21]. The experiments are in agree-

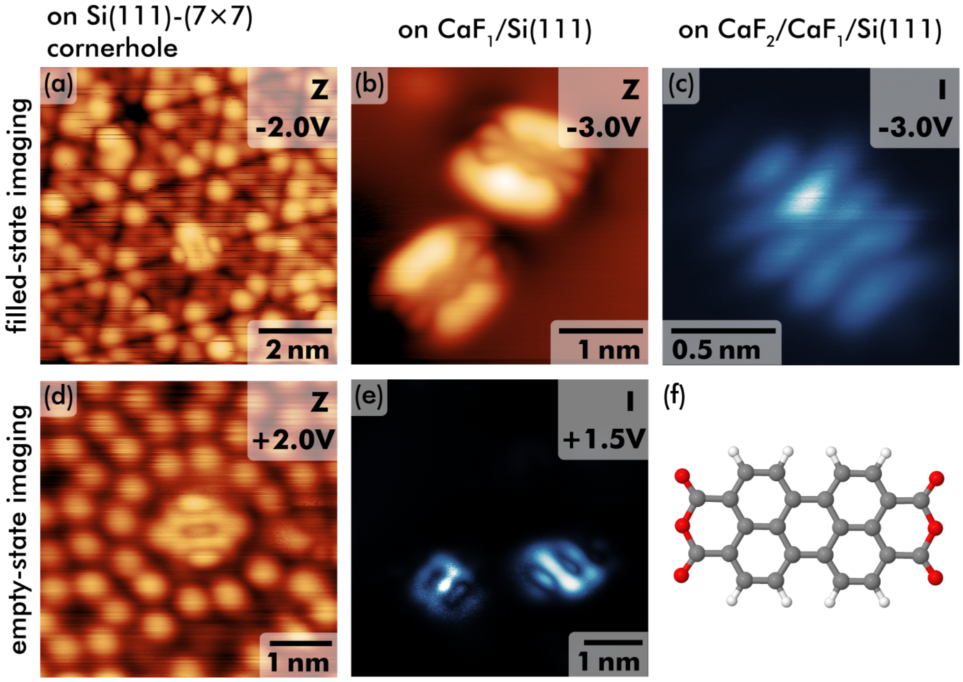

Figure 2: STM images of individual PTCDA molecules on different surface areas. Imaging of PTCDA on a Si(111)-(7 × 7) cornerhole position at (a) negative and (d) positive sample bias (sample bias indicated in the upper right corner). (b) Topography-mode image at negative bias and (e) constant-height mode imaging at positive bias of PTCDA on a CaF_1/Si(111) surface area. (c) Example of imaging PTCDA on a CaF_2/CaF_1/Si(111) multilayer in constant-height mode. (f) Model drawing of a single PTCDA molecule (black: carbon, white: hydrogen, red: oxygen atoms).

ment with these findings as the substructure between the two double lobes (see Figure 2b) was only apparent in very few cases; most data only reveal two bright lobes. Molecules were often manipulated and tip changes occurred when reducing the tip–sample distance for improving the STM contrast. The substructure enclosed by the double lobes is reminiscent of the LUMO charge density distribution [10], yet, at negative sample bias. Possible reasons include a non-negligible electronic coupling across the ultrathin film, coupling to defects within the CaF_1 layer, or charge transfer into the LUMO. Imaging at a positive sample bias of +1.5 V was performed in constant-height mode as the reduced sample conductivity at positive bias impeded operation in constant-current mode. Still, conductivity through PTCDA molecules is also observed at this bias voltage with an orbital structure in Figure 2e that is different from the filled-state image in Figure 2b. One example of a constant-height STM image acquired at a negative sample bias of −3 V on the $CaF_2/CaF_1Si(111)$ thick film is shown in Figure 2c and reveals a striped structure of the PTCDA molecule. However, as the molecular appearance was different depending on the molecule and tip state, it is not discussed here in further detail.

The STM data in Figure 1 and Figure 2 suggest preferred adsorption orientations of PTCDA in CaF_1 and CaF_2 areas. A detailed statistical analysis is shown in Figure 3a, where the orientation along the double-lobe shape (i.e., along the long molecular axis, see also white dashed line in Figure 3c) was measured with respect to a CaF_2 $\langle\bar{1}\bar{1}2\rangle$ direction from more than 1000 molecules in a total of 10 images. The CaF_2 directions were determined from filled-state imaging of the (7 × 7) reconstruction [27]. Due to the type-B epitaxy of CaF_2 on Si(111) at the chosen growth parameters, the CaF_2 $[\bar{1}\bar{1}2]$ direc-

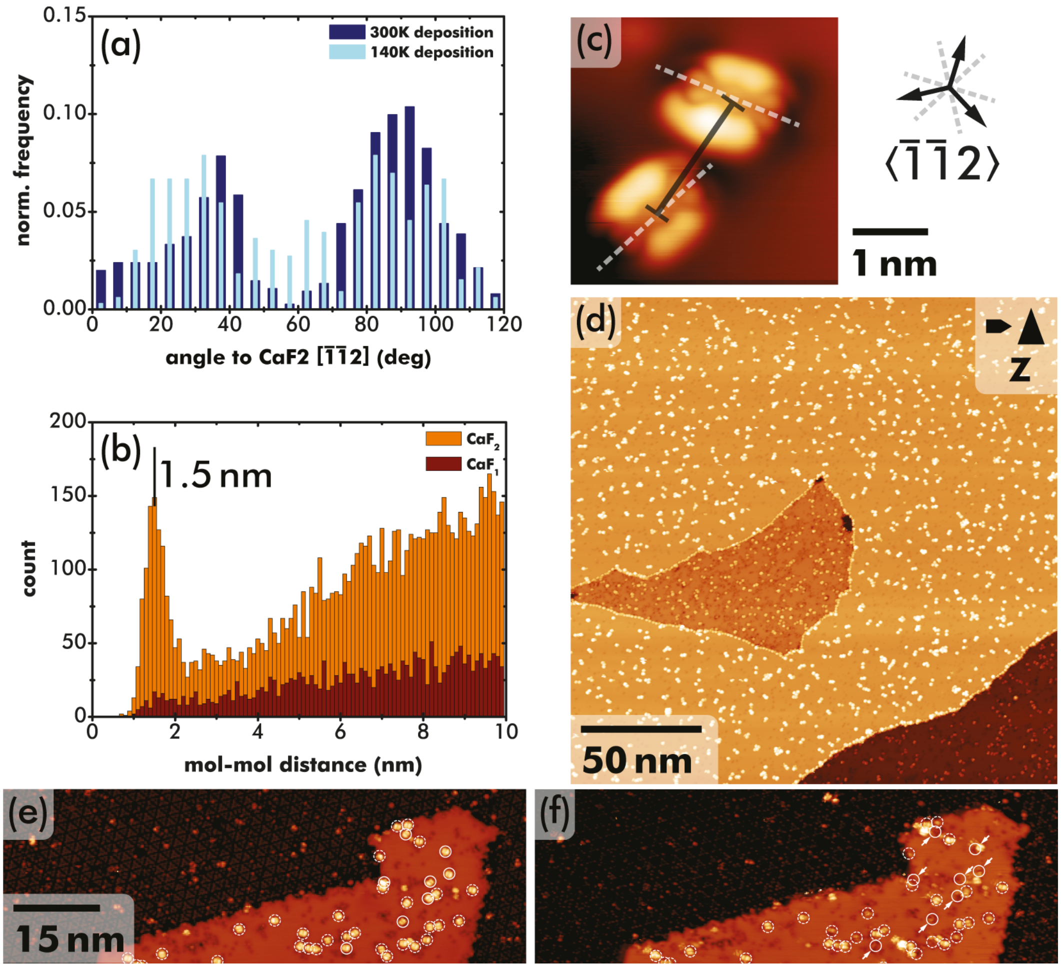

Figure 3: Statistical analysis of (a) the double-lobe orientation on the CaF_1 layer and (b) the nearest-neighbour distance on CaF_1 and CaF_2/CaF_1 areas. The orientation is determined by the angle between the CaF_2 $[\bar{1}\bar{1}2]$ direction and the axis through the double-lobe structure, see white lines in (c). Nearest-neighbour distances are determined by the molecule–molecule distance measured from centre to centre, see black marker in (c). The topography image in (d) presenting PTCDA on a mixed CaF_2 and $CaF_1/Si(111)$ surface is used for the statistical analysis in (b). STM data acquired on a $CaF_1/Si(111)$ surface area (e) before and (f) after accidental removal of single PTCDA molecules by the STM tip. Stationary molecules are marked by dashed white circles, removed molecules by solid circles and arrows in (f).

tion is identical to the Si $[11\bar{2}]$ direction that was determined from STM images. Three equivalent CaF_2 $\langle\bar{1}\bar{1}2\rangle$ directions are depicted at the right of the exemplary image in Figure 3c. The statistical analysis was performed on two sample sets whereby the PTCDA molecules were deposited either on a sample held at room temperature (total of about 750 molecules) or with the sample support cooled by liquid nitrogen (more than 300 molecules). As apparent from the height distribution in Figure 3a, there is a strong tendency for PTCDA molecules to align under angles of about ±30° with respect to a CaF_2 $\langle\bar{1}\bar{1}2\rangle$ direction, especially after deposition on samples held at room temperature. The width of the peaks is attributed to uncertainties of the angle measurement and the asymmetry to a statistical artefact. However, it is also noteworthy that the intermediate minimum in the distribution is less pronounced in measurements performed after PTCDA deposition on cooled samples, which suggests an increased barrier at the estimated sample temperature of 140 K to arrive in the optimum adsorption geometry.

A second statistical analysis was performed for the nearest-neighbour distances between nearby PTCDA molecules on CaF_1/Si(111) and CaF_2/CaF_1/Si(111) areas from measuring the pairwise molecular separations of a total of about 400 (1600) molecules on the CaF_1 (CaF_2) area in the STM image in Figure 3d. The distances were measured as the centre–centre separation, illustrated by the black line in Figure 3c. In agreement with the visual impression from the overview images in Figure 1b and Figure 1c, a preference for a centre–centre distance of about 1.5 nm is found for the CaF_2/CaF_1/Si(111) areas, while no clear preference is apparent from the distribution on the CaF_1/Si(111) interface layer areas. As the surface lattice periodicities are identical for the interface and subsequent layers due to the extremely small mismatch between the silicon and CaF_2 lattice constants [28], the absence of nearby PTCDA molecules on CaF_1 areas can rather be explained by nucleation at defects present in the interface layer. This is substantiated by data in Figure 3e and Figure 3f, where defects in the interface layer are imaged at positions where molecules were accidentally removed in the STM scans between the two images. These positions are marked by solid white circles and arrows in Figure 3f, while stationary molecules are marked by white dashed circles in both panels. Defects are imaged in STM as black depressions although they are of atomic size [27]. In contrast, the CaF_2 surfaces are mostly defect-free.

The PTCDA adsorption geometry was further investigated by using density functional theory-based calculations. Geometry-optimisation was performed for a total of seven starting geometries with flat-lying PTCDA molecules positioned under different angles and at various lateral positions on the three-layered, (6 × 6) CaF_2(111) slab (only the top layer is shown in Figure 4). Five starting geometries relaxed into the same final geometry

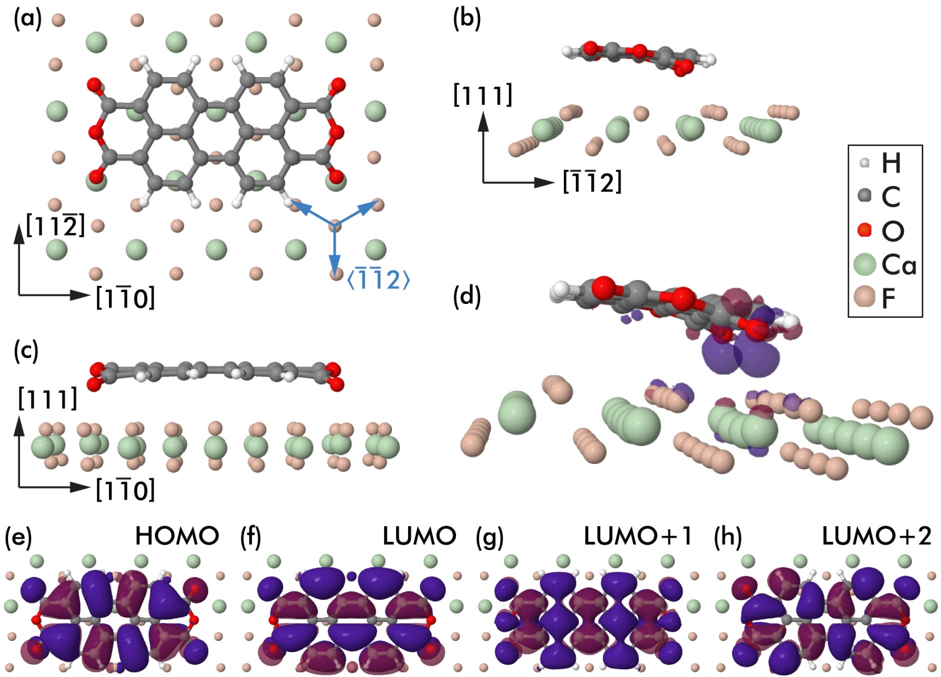

Figure 4: Geometry-optimised adsorption geometry of a single PTCDA molecule on a CaF_2(111) slap in (a) top view and (b,c) side views. (d) Perspective view of the geometry with isosurfaces at −0.01 e/Å^3 (red) and 0.01 e/Å^3 (blue) of the electron density difference $\Delta\rho$ included. (e–h) Isosurfaces of the molecular orbitals HOMO, LUMO, LUMO+1 and LUMO+2 of the PTCDA/CaF_2(111) system.

shown in Figure 4 and two geometries were trapped in local minima of the energy landscape and are, thus, not further discussed here. The geometry in Figure 4 with a BSSE-corrected binding energy of −1.66 eV is assessed to be the optimum adsorption geometry for a single PTCDA molecule on a $CaF_2(111)$ surface. In this geometry, the PTCDA molecule is aligned with the long axis along the $[1\bar{1}0]$ direction, which corresponds to an alignment with an angle of 30° off a CaF_2 $\langle\bar{1}\bar{1}2\rangle$ direction (directions are included for clarity in Figure 4a). This orientation is in full agreement with the experimental observation in Figure 3a, where maxima in the orientation histogram were found at angles of about 30° off the $\langle\bar{1}\bar{1}2\rangle$ directions.

The PTCDA molecule is in a nearly flat-lying geometry, with the exception that two of the four carbonyl oxygen atoms are displaced out of the PTCDA plane towards a surface calcium ion. An attraction between the molecular oxygen and surface calcium atoms is suggested from an oxygen–calcium distance of about 2.8 Å. Note that this distance is larger than 2.4 Å recently found for the oxygen–calcium distance of a carboxylic acid moiety of a ferrocene derivative that binds vertically to $CaF_2(111)$ [33]. The oxygen displacement does not occur on the other side of the molecule where the carbonyl oxygen atoms are located on top of the lower-lying surface fluorine atoms. Thus, the larger O–Ca distance for PTCDA/$CaF_2(111)$ is likely the result of an interplay between the carbonyl oxygen–calcium attraction and the repulsion between the other oxygen atoms and the surface fluorine atoms, as well as the resulting deformation of the PTCDA molecule.

Figure 4d presents a perspective view of the optimum adsorption geometry, including isosurfaces at ±0.01 $e/Å^3$ of the electron density difference $\Delta\rho = \rho_{full} - \rho_{slab} - \rho_{PTCDA}$. This difference was calculated as a difference between the electron densities of the full (ρ_{full}), CaF_2 slab (ρ_{slab}), and PTCDA gas phase (ρ_{PTCDA}) systems. The main finding is electron accumulation below the carbonyl oxygen atoms, in agreement with the attractive interaction with the surface calcium atom already identified before from the oxygen displacement.

Isosurfaces of the molecular orbital densities of the highest occupied molecular orbital (HOMO) as well as the three lowest unoccupied molecular orbitals (LUMO, LUMO+1, and LUMO+2) as calculated with cp2k for the PTCDA/$CaF_2(111)$ system are depicted in Figure 4e–h. The orbital shapes largely resemble earlier calculations of a flat PTCDA molecule in the gas phase [10], although the LUMO+1 and LUMO+2 states are here separated by about 0.1 eV and found in different order (in agreement with a previous study [10], a smaller LUMO+1/LUMO+2 energetic separation was calculated for the gas-phase molecule). The dominant contribution of the orbitals to the data shown in Figure 2 is deferred from the orbital shape: The filled-state image (Figure 2b) on the CaF_1 thin film is of strong LUMO character, whereas the filled-state image (Figure 2c) on the CaF_2/CaF_1 area has similarities with the HOMO structure. The empty-state image on the thin film (Figure 2e) reveals a pattern that reminds of the LUMO+1 orbital shape, which supports the earlier suggestion that the molecular levels on the interface layer are shifted with respect to the gas-phase molecule.

A slightly deformed adsorption geometry including a small tilt of the molecule with respect to the surface plane is furthermore in agreement with the experimental observation of a slight asymmetry in the imaged lobe height, see for example Figure 2b where one of the lobes is imaged higher than the other. Last, the optimum adsorption geometry suggests a cause for the absence of long-range order: Extended PTCDA structures, such as the brickwall or the herringbone pattern, are not compatible with the three-fold rotational symmetry and the surface lattice dimensions. The adsorption geometry seems to especially block the common hydrogen bond motif between PTCDA molecules.

Conclusion

Adsorption properties of PTCDA molecules on Si(111)-(7 × 7), CaF_1/Si(111), and CaF_2/CaF_1/Si(111) surface areas were studied by STM at low temperatures. Single molecules were identified on the CaF_1/Si(111) interface layer while ultrasmall molecular assemblies were found on the CaF_2/CaF_1/Si(111) areas. The presence of mostly single PTCDA molecules in CaF_1 regions is rationalised by nucleation at defects present within the CaF_1 interface layer. In contrast, the CaF_2/CaF_1 layer is mostly defect-free. A statistical analysis revealed a preferred molecular orientation of the long molecular axis along a CaF_2 $\langle 1\bar{1}0\rangle$ direction, in full agreement with the DFT-calculated optimum adsorption geometry. The DFT-based analysis furthermore revealed a nearly flat-lying molecular adsorption geometry with a downward displacement of two carbonyl oxygen atoms. Based on an analysis of the electron density difference, these atoms are attracted towards the surface calcium ions. A comparison of calculated molecular orbital shapes with the experimental STM data suggests a strong influence of the LUMO in filled-state STM imaging on the CaF_1 interface layer. Instead, the absence of long-range order on the CaF_2 films is explained by a mismatch of the common PTCDA motifs with the CaF_2 surface structure.

Acknowledgements

The author is most thankful to Philip Moriarty (University of Nottingham, UK) for supporting the experimental work and for most helpful comments on the data analysis as well as the manuscript.

Funding

Financial support from the People Programme (Marie Curie Actions) of the European Union's Seventh Framework Programme (FP7/2007-2013) under Research Executive Agency (REA) Grant No. 628439 and by the German Research Foundation (DFG) via grant RA2832/1-1 are gratefully acknowledged. Computing time was granted by the University of Osnabrück via DFG project 239246210.

References

1. Repp, J.; Meyer, G.; Stojković, S. M.; Gourdon, A.; Joachim, C. *Phys. Rev. Lett.* **2005,** *94,* 026803. doi:10.1103/physrevlett.94.026803
2. Yang, T.; Wu, Q.; Dai, F.; Huang, K.; Xu, H.; Liu, C.; Chen, C.; Hu, S.; Liang, X.; Liu, X.; Noh, Y.-Y.; Liu, C. *Adv. Funct. Mater.* **2020,** *30,* 1903889. doi:10.1002/adfm.201903889
3. Repp, J.; Meyer, G. *Appl. Phys. A: Mater. Sci. Process.* **2006,** *85,* 399–406. doi:10.1007/s00339-006-3703-0
4. Bombis, C.; Ample, F.; Lafferentz, L.; Yu, H.; Hecht, S.; Joachim, C.; Grill, L. *Angew. Chem., Int. Ed.* **2009,** *48,* 9966–9970. doi:10.1002/anie.200904645
5. Fatayer, S.; Schuler, B.; Steurer, W.; Scivetti, I.; Repp, J.; Gross, L.; Persson, M.; Meyer, G. *Nat. Nanotechnol.* **2018,** *13,* 376–380. doi:10.1038/s41565-018-0087-1
6. Ziroff, J.; Forster, F.; Schöll, A.; Puschnig, P.; Reinert, F. *Phys. Rev. Lett.* **2010,** *104,* 233004. doi:10.1103/physrevlett.104.233004
7. Tautz, F. S. *Prog. Surf. Sci.* **2007,** *82,* 479–520. doi:10.1016/j.progsurf.2007.09.001
8. Romaner, L.; Nabok, D.; Puschnig, P.; Zojer, E.; Ambrosch-Draxl, C. *New J. Phys.* **2009,** *11,* 053010. doi:10.1088/1367-2630/11/5/053010
9. Duhm, S.; Gerlach, A.; Salzmann, I.; Bröker, B.; Johnson, R. L.; Schreiber, F.; Koch, N. *Org. Electron.* **2008,** *9,* 111–118. doi:10.1016/j.orgel.2007.10.004
10. Rohlfing, M.; Temirov, R.; Tautz, F. S. *Phys. Rev. B* **2007,** *76,* 115421. doi:10.1103/physrevb.76.115421
11. Eremtchenko, M.; Schaefer, J. A.; Tautz, F. S. *Nature* **2003,** *425,* 602–605. doi:10.1038/nature01901
12. Kraft, A.; Temirov, R.; Henze, S. K. M.; Soubatch, S.; Rohlfing, M.; Tautz, F. S. *Phys. Rev. B* **2006,** *74,* 041402. doi:10.1103/physrevb.74.041402
13. Nicoara, N.; Paz, Ó.; Méndez, J.; Baró, A. M.; Soler, J. M.; Gómez-Rodríguez, J. M. *Phys. Rev. B* **2010,** *82,* 075402. doi:10.1103/physrevb.82.075402
14. Kunstmann, T.; Schlarb, A.; Fendrich, M.; Wagner, T.; Möller, R.; Hoffmann, R. *Phys. Rev. B* **2005,** *71,* 121403. doi:10.1103/physrevb.71.121403
15. Jia, Q.; Hu, Z.-X.; Ji, W.; Burke, S. A.; Gao, H.-J.; Grütter, P.; Guo, H. *Phys. Chem. Chem. Phys.* **2016,** *18,* 11008–11016. doi:10.1039/c5cp07999c
16. Aldahhak, H.; Schmidt, W. G.; Rauls, E. *Surf. Sci.* **2013,** *617,* 242–248. doi:10.1016/j.susc.2013.08.003
17. Dienel, T.; Loppacher, C.; Mannsfeld, S. C. B.; Forker, R.; Fritz, T. *Adv. Mater. (Weinheim, Ger.)* **2008,** *20,* 959–963. doi:10.1002/adma.200701684
18. Burke, S. A.; Ji, W.; Mativetsky, J. M.; Topple, J. M.; Fostner, S.; Gao, H.-J.; Guo, H.; Grütter, P. *Phys. Rev. Lett.* **2008,** *100,* 186104. doi:10.1103/physrevlett.100.186104
19. Burke, S. A.; Topple, J. M.; Grütter, P. *J. Phys.: Condens. Matter* **2009,** *21,* 423101. doi:10.1088/0953-8984/21/42/423101
20. Cochrane, K. A.; Schiffrin, A.; Roussy, T. S.; Capsoni, M.; Burke, S. A. *Nat. Commun.* **2015,** *6,* 8312. doi:10.1038/ncomms9312
21. Guo, Q.; Paulheim, A.; Sokolowski, M.; Aldahhak, H.; Rauls, E.; Schmidt, W. G. *J. Phys. Chem. C* **2014,** *118,* 29911–29918. doi:10.1021/jp509663s
22. Karacuban, H.; Koch, S.; Fendrich, M.; Wagner, T.; Möller, R. *Nanotechnology* **2011,** *22,* 295305. doi:10.1088/0957-4484/22/29/295305
23. Such, B.; Goryl, G.; Godlewski, S.; Kolodziej, J. J.; Szymonski, M. *Nanotechnology* **2008,** *19,* 475705. doi:10.1088/0957-4484/19/47/475705
24. Loppacher, C.; Zerweck, U.; Eng, L. M.; Gemming, S.; Seifert, G.; Olbrich, C.; Morawetz, K.; Schreiber, M. *Nanotechnology* **2006,** *17,* 1568–1573. doi:10.1088/0957-4484/17/6/006
25. Martínez-Galera, A. J.; Nicoara, N.; Martínez, J. I.; Dappe, Y. J.; Ortega, J.; Gómez-Rodríguez, J. M. *J. Phys. Chem. C* **2014,** *118,* 12782–12788. doi:10.1021/jp500768y
26. Glatzel, T.; Zimmerli, L.; Kawai, S.; Meyer, E.; Fendt, L.-A.; Diederich, F. *Beilstein J. Nanotechnol.* **2011,** *2,* 34–39. doi:10.3762/bjnano.2.4
27. Rahe, P.; Smith, E. F.; Wollschläger, J.; Moriarty, P. J. *Phys. Rev. B* **2018,** *97,* 125418. doi:10.1103/physrevb.97.125418
28. Olmstead, M. A. Heteroepitaxy of Disparate Materials: From Chemisorption to Epitaxy in CaF2/Si(111). In *Thin Films: Heteroepitaxial Systems;* Liu, W. K.; Santos, M. B., Eds.; Series on Directions in Condensed Matter Physics, Vol. 15; World Scientific: Singapore, 1999; pp 211–266. doi:10.1142/9789812816511_0005
29. Wollschläger, J. Resonant Tunneling Devices Based on Epitaxial Insulator-Semiconductor Structures: Growth and Characterisation of CaF2 Films on Si(111). In *Recent Research Developments in Applied Physics;* Pandalai, S., Ed.; Transworld Research Network: Trivandrum, India, 2002; Vol. 5-II, pp 621–695.
30. Rahe, P.; Schütte, J.; Schniederberend, W.; Reichling, M.; Abe, M.; Sugimoto, Y.; Kühnle, A. *Rev. Sci. Instrum.* **2011,** *82,* 063704. doi:10.1063/1.3600453
31. Nečas, D.; Klapetek, P. *Cent. Eur. J. Phys.* **2012,** *10,* 181–188. doi:10.2478/s11534-011-0096-2
32. Hutter, J.; Iannuzzi, M.; Schiffmann, F.; VandeVondele, J. *Wiley Interdiscip. Rev.: Comput. Mol. Sci.* **2014,** *4,* 15–25. doi:10.1002/wcms.1159
33. Laflör, L.; Schlage, F. A.; Kantorovich, L.; Moriarty, P. J.; Reichling, M.; Rahe, P. *J. Phys. Chem. C* **2020,** *124,* 9900–9907. doi:10.1021/acs.jpcc.0c00115
34. VandeVondele, J.; Hutter, J. *J. Chem. Phys.* **2007,** *127,* 114105. doi:10.1063/1.2770708
35. Lippert, G.; Hutter, J.; Parrinello, M. *Theor. Chem. Acc.* **1999,** *103,* 124–140. doi:10.1007/s002140050523
36. Krack, M. *Theor. Chem. Acc.* **2005,** *114,* 145–152. doi:10.1007/s00214-005-0655-y
37. Perdew, J. P.; Burke, K.; Ernzerhof, M. *Phys. Rev. Lett.* **1996,** *77,* 3865–3868. doi:10.1103/physrevlett.77.3865
38. Grimme, S.; Antony, J.; Ehrlich, S.; Krieg, H. *J. Chem. Phys.* **2010,** *132,* 154104. doi:10.1063/1.3382344
39. Boys, S. F.; Bernardi, F. *Mol. Phys.* **1970,** *19,* 553–566. doi:10.1080/00268977000101561

License and Terms

BEILSTEIN JOURNAL OF NANOTECHNOLOGY

The influence of an interfacial hBN layer on the fluorescence of an organic molecule

Christine Brülke, Oliver Bauer and Moritz M. Sokolowski*

Full Research Paper
Open Access

Address:
Institut für Physikalische und Theoretische Chemie, Universität Bonn, Wegelerstr. 12, 53115 Bonn

Email:
Moritz M. Sokolowski* - sokolowski@pc.uni-bonn.de

* Corresponding author

Keywords:
decoupling; fluorescence; hexagonal boron nitride; 3,4,9,10-perylene tetracarboxylic dianhydride (PTCDA); Raman spectroscopy

Beilstein J. Nanotechnol. **2020,** *11,* 1663–1684.
https://doi.org/10.3762/bjnano.11.149

Received: 29 May 2020
Accepted: 09 October 2020
Published: 03 November 2020

This article is part of the thematic issue "Molecular assemblies on surfaces – towards physical and electronic decoupling of organic molecules".

Guest Editor: M. Stöhr

Abstract

We investigated the ability of a single layer of hexagonal boron nitride (hBN) to decouple the excited state of the organic molecule 3,4,9,10-perylene tetracarboxylic dianhydride (PTCDA) from the supporting Cu(111) surface by Raman and fluorescence (FL) spectroscopy. The Raman fingerprint-type spectrum of PTCDA served as a monitor for the presence of molecules on the surface. Several broad and weak FL lines between 18,150 and 18,450 cm^{-1} can be detected, already from the first monolayer onward. In contrast, FL from PTCDA on a bare Cu(111) surface is present only from the second PTCDA layer onward. Hence, a single layer of hBN decouples PTCDA from the metal substrate to an extent that a weak radiative FL decay of the optical excitation can occur. The different FL lines can be ascribed to different environments of the adsorption sites, namely molecules adsorbed at surface defects, in large ordered domains, and located in the second layer.

Introduction

In recent years, two-dimensional materials (2DMs) have been established as a highly interesting field of studies, both in regard to their fundamental physical properties as well as their potential for technical applications [1]. Specifically, the use of 2DMs in layered heterostructures has been promoted [2,3]. Here, one challenge lies in the understanding of not only the processes in the individual materials, but also of those that occur at the interfaces between layers of different materials. Advantageously, some 2DMs can be grown directly on metal substrates by chemical vapor deposition [2]. This is, for example, exploited when a 2DM interfacial layer is inserted between the metallic electrode and a functional organic layer of an organic electronic device, such as an organic light emitting diode [3]. The purpose of the interfacial layer is to achieve a separation or “decoupling” of the two adjacent layers. Here, the term decoupling refers to the spatial separation of the electronic states of the molecules and those of the underlying metal, which leads to unperturbed molecular properties [4]. A scientifically relevant question is to which extent decoupling of the organic molecules from a metal electrode is achieved when a 2DM layer in the limit of a single interfacial layer, for example, a monolayer of hexagonal boron nitride (hBN), is used.

Such a decoupling is achieved when the wave functions of the metal are spatially separated from those of the molecule leading to a reduced overlap. The overlap of molecular and metallic wave functions has, in particular, an impact on excited molecular states. For fluorescent molecules, this is observed as a strongly reduced quantum yield of the fluorescence (FL) due to non-radiant decay processes via the metal states. This phenomenon is generally referred to as "quenching" [5]. When the decoupling is not efficient, a fast and non-radiative decay of the excitation of the molecule via the metallic states prevails. Therefore, the probing of the FL of a molecule located at the outer surface of a 2DM layer grown on a metal characterizes the degree of electronic coupling of the molecular and metallic states.

For completeness, we note that quenching of an electronic excitation of a molecule in the first layers on a metal surface can be the result of interfacial charge transfer (CT) [5] or of energy transfer [6]. Here, CT is in our focus since energy transfer, although additionally present, varies less abruptly on the scale of single layers [7]. A simple energy diagram of the CT process of a fluorescent molecule across interfaces is depicted in Figure 1. As an example, we use the sample system of this work, namely, 3,4,9,10-perylene tetracarboxylic dianhydride (PTCDA) on a layer of hBN on Cu(111). Here, we consider an S_1 excitation which involves mainly a HOMO/LUMO (highest occupied and lowest unoccupied molecular orbital) electronic excitation. Rapid CT leads to a delocalization of the excited electron from the LUMO into unoccupied metallic states and/or a filling of the HOMO by an electron from the metal. We note that the HOMO and LUMO for the chemisorbed molecule differ from those of the gas phase molecule. Thus, the LUMO that is drawn in Figure 1a is not identical to the LUMO in the gas phase. For a second molecular layer, even without significant overlap of the wave functions of metal and molecule, quenching is also possible, because the CT may occur from the second layer to the metal via states in the first layer [5].

In principle, the hybridization of molecular and metallic states and the dynamical CT in the excited state can be probed by photoemission spectroscopy (PES). In particular, core hole clock spectroscopy has been used to measure the time constant of dynamical CT in the valence band states as a function of the lifetime of the core hole, which is typically of the order of 10^{-14} s [8,9]. However, this technique is insensitive to a CT process of a considerably longer time constant. A technique for detecting CT processes with a longer time constant is FL spectroscopy, in which the CT process competes with the radiative fluorescent decay of the excitation. It constitutes an alternative and non-radiative decay channel for the excited state. Typically, the FL lifetime of the excited state S_1 is of the order of ca. 10^{-9} s [5]. Hence, a CT process with a time constant that is not significantly larger will reduce the FL yield (see Figure 1). Thus, even a very small overlap of states becomes evident in the experiment as it causes a reduction of the FL yield (i.e., quenching). The degree of quenching may vary and, hence, lead to different branching ratios between the radiative and non-radiative channels. In order to obtain high FL yields of molecules on metallic substrates, thin interfacial films of consider-

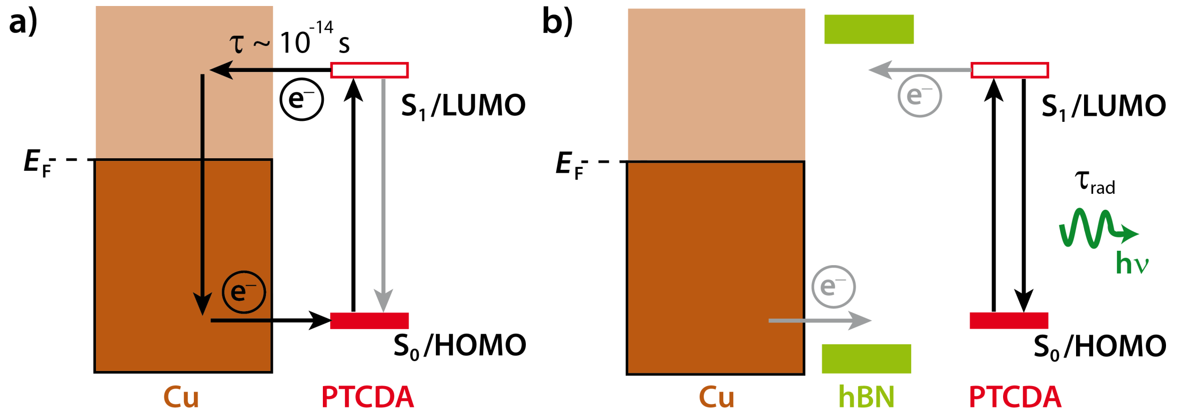

Figure 1: (a) Schematic diagram of the radiative and non-radiative decay processes of an optical excitation of a PTCDA molecule at the interface to a Cu surface via charge transfer. Metallic and molecular electronic states are indicated in brown and red, respectively. The radiative decay of the excitation (gray arrow) is quenched. (b) A decoupling layer of hBN (green) suppresses the overlap of the Cu and PTCDA wave functions. This reduces the charge transfer such that the excitation decays under emission of a photon (green arrow).

able thickness (5–10 monolayers) of alkali halides have been used in our lab [10]. In contrast, experiments on the light emission from molecules induced by scanning tunneling microscopy (STM-LE) required thin alkali halide films of two monolayers thickness in order to support tunneling [11-13].

A single layer or films of hBN are attractive for decoupling a molecule from an underlying metal substrate as hBN exhibits a wide bandgap of 5.9 eV [14]. Perspectively, it could also provide a substrate for STM-LE experiments. Furthermore, it is of interest due to its mechanical [15], chemical [16], and thermal [17] stability, the easy synthesis of hBN monolayers on Cu foils for usage in devices [18], and, finally, the wide structural variety of hBN monolayers depending on the underlying metal substrate [19].

To investigate the decoupling of an organic molecule from a metal substrate by a monolayer of hBN we chose PTCDA and the Cu(111) surface. PTCDA serves as a planar model molecule for investigations of organic layers on surfaces [20-23]. Monolayers of hBN on Cu(111) have been investigated by several groups and are, hence, rather well understood [24-29]. In particular, we found that hBN on Cu(111) forms a flat layer at a relatively large vertical distance from the Cu(111) top layer of 3.24 Å using an X-ray standing-waves analysis [30]. This large distance is, in principle, in agreement with the results reported independently by Schwarz and co-workers [31]. Large distances of the molecule with respect to the hBN and the metal interface are expected to be beneficial for the decoupling because the metal wave functions decrease exponentially into the vacuum.

We have previously shown that the bonding situation between PTCDA and hBN/Cu(111) is weak and physisorptive [32] as opposed to the chemisorptive bond between PTCDA and Cu(111) [33]. Ultraviolet photoelectron spectroscopy (UPS) experiments showed that on the Cu(111) surface the chemical bonding leads to a filling of the LUMO [33]. In contrast, on hBN/Cu(111), the differential energies of the PTCDA orbitals remain unaltered in comparison to those of PTCDA in the gas phase, which points to a more physisorptive bonding to the hBN/Cu(111) surface [32]. The HOMO of PTCDA is found at ca. 2.6 eV [32]. Hence, we can expect that both the LUMO and the HOMO are placed within the bandgap of hBN, as indicated in Figure 1b. This is in agreement with the findings by Martínez-Galera et al. for PTCDA/hBN/Rh(110) [34]. From scanning tunneling spectroscopy (STS) experiments, the authors concluded that the coupling is only weak. They deduced further that the CT (in the ground state) between molecule and substrate, if present at all, is small. These differences between PTCDA/hBN/Cu(111) and PTCDA/Cu(111) are also mirrored by their vertical molecular structures. The hybridization of the electronic states of PTCDA and Cu leads to a distortion of the molecule where the oxygen atoms are pushed away from the substrate and out of the molecular plane [35]. On hBN/Cu(111), the molecule remains essentially flat and at a very large vertical distance from the hBN layer of 3.37 Å [32]. In contrast, on Cu(111) the vertical distance of the perylene core from the Cu(111) surface is only 2.66 Å [35]. This again points to a difference in the bonding character on the two surfaces.

Several studies have probed the influence of the adsorption on metal-supported hBN layers on the electronic structure of large organic molecules, namely their frontier orbitals, by PES [36] or STS [37,38]. However, to the best of our knowledge, there have been no studies on the FL of monolayers of molecules on metal-supported hBN layers, yet. Kerfoot et al. [22] studied the FL of PTCDA and perylene-3,4,9,10-tetracarboxylic-3,4,9,10-diimide (PTCDI) on an exfoliated hBN monolayer that was transferred onto SiO_2. Forker et al. [23] investigated the optical absorption properties of PTCDA on hBN/Rh(111) and hBN/Pt(111).

Here, we report a direct comparison of FL spectra of PTCDA/hBN/Cu(111) and PTCDA/Cu(111), which allows for a relative determination of the efficiency of the hBN layer to decouple the excited states of PTCDA from Cu(111). For PTCDA on Ag(111) and Au(111) [39], it has been shown that FL can only be observed from the second and third molecular layer onward. The excitation of the first layers is completely quenched by the metal substrates as described above. In UPS experiments, a partial filling of the LUMO of PTCDA was found on Ag(111), but not on Au(111) [33]. Thus, the quenching on Ag(111) is directly understood by the static charge transfer seen in UPS. The quenching on Au(111), not as evident from UPS, demonstrates the sensitivity of FL spectroscopy to an overlap of wave functions of excited states. Accordingly, the same behavior as on Ag(111) can be expected on Cu(111), where a filling of the LUMO has been found, too [33]. In addition, for multilayer PTCDA films we can compare the first, interfacial PTCDA layer with a hBN layer regarding their abilities to decouple the next PTCDA layer from the Cu(111) substrate.

In this contribution, we will discuss Raman modes and several different FL lines of PTCDA that were observed on both hBN/Cu(111) and Cu(111). For an effective comparison, the structures and the growth modes of the PTCDA layers are relevant. Details of the structural investigation of the two surfaces, including low-energy electron diffraction (LEED) patterns, are given in Appendix A. Since the interpretation of the optical data requires this knowledge, we summarize some details ahead here. PTCDA forms ordered structures and follows a layer-by-layer growth for at least the first three layers on Cu(111) and the first two layers on hBN/Cu(111). We are able to distinguish PTCDA/hBN/Cu(111) from PTCDA/Cu(111), as well as the monolayer and multilayers of PTCDA on Cu(111) and hBN/Cu(111) by differences in the respective LEED patterns.

Experimental

All experiments were carried out in an ultrahigh-vacuum chamber with a base pressure of 2.3×10^{-10} mbar. The Cu(111) sample could be heated up to 1100 K via a tungsten filament and electron bombardment and cooled down to 20 K by using liquid helium.

The hBN layer was grown by dosing the precursor borazine $[(HBNH)_3]$ into the chamber while the sample was held at 1010 K. Borazine was purchased from Katchem spol. s r. o., Czech Republic (http://www.katchem.cz). It was kept in a glass tube connected to the chamber via a dosing valve at constantly −5 °C. Prior to the hBN preparation, it was cleaned by three cycles of freezing the liquid borazine using liquid N_2 and pumping away the gas phase above the frozen borazine. The composition of the gas phase in the borazine source was monitored by a quadrupole mass spectrometer (QMS). It was considered suitable for hBN preparation when the signals for H_2 (a product of the decomposition of borazine that is known to occur even when stored at low temperatures, m/z 2) and borazine (m/z 80) showed a ratio of approximately 1:1.

The clean Cu(111) surface was prepared by consecutive steps of sputtering for 30 min with Ar^+ ions (1000 eV, 4 µA) and annealing at 1010 K for 30 min. After the last sputtering cycle, the Cu(111) sample was heated to 1010 K and ca. 2000 L borazine were dosed (1.5×10^{-6} mbar via the background for 30 min) onto the sample held at 1010 K. After stopping the borazine dosing, the sample was cooled down with $1\ \mathrm{K \cdot s^{-1}}$. The structural quality of the bare Cu(111) surface, the hBN layers, and the PTCDA layers was checked by LEED. We used a SPA-LEED instrument as described in [30]. An additional annealing step between the last sputter cycle and the borazine deposition was omitted here in order to prevent segregation of chemical impurities from the Cu bulk to the surface, which we otherwise occasionally observed as additional LEED spots. The criteria for a good hBN layer were a sharp continuous ring of intensity with a radius that is 2% larger than the distance of the first-order Cu spots from the specular spot and the appearance of a clear star-like pattern of satellites around the specular spot caused by multiple electron scattering as reported in [30].

PTCDA was evaporated from a glass crucible. The molecular flux was also monitored by the QMS at m/z 392, which corresponds to the mass of the non-fractured PTCDA molecule. The flux was typically one monolayer per minute. During deposition, the sample was held at a constant temperature. PTCDA layers on Cu(111) were prepared by keeping the sample at a temperature of either 20 or 300 K during deposition. PTCDA layers on hBN/Cu(111) were prepared by deposition at a sample temperature of 20 K and subsequent annealing. The sample was annealed in iterative steps of heating, holding at a constant temperature for 3 min, and cooling down again to 20 K for a measurement. The annealing temperatures were in the range of 100–400 K and are specified below. In the following, one monolayer (ML) of PTCDA refers to a single layer of close-packed, flat-lying PTCDA molecules. After every experiment, the exact coverage was determined by a thermally programmed desorption (TPD) experiment with a margin of error of ±0.05 ML. The calibration for PTCDA/hBN/Cu(111) was derived from the TPD data shown in [32]. Since the packing densities of PTCDA on hBN/Cu(111) and on Cu(111) are within a few percent of each other (see Appendix A), this calibration is also valid for PTCDA/Cu(111) within the noted margin of error.

For the optical experiments, the sample was transferred into a glass tube, standing out from the end of the chamber. In the glass tube, the sample was illuminated by a focused laser beam at an incident angle of approximately 45° with respect to the surface normal. The diameter of the laser spot on the sample was about 0.5 mm. The fluorescence and Raman scattered light from the sample was collected and parallelized by an achromatic lens and focused by a second achromatic lens onto the entrance slit of the spectrometer. The spectrometer (Acton, Spectra Pro 2300i, $f = 0.3$ m) was operated with three different gratings (300, 600, and 1200 grooves per millimeter, yielding a resolution of 48, 24, and 12 $\mathrm{cm^{-1}}$, respectively). It was equipped with a nitrogen-cooled CCD camera, operated at −110 °C. In order to block external stray light from entering the spectrometer, the glass tube, the lenses and the entrance slit of the spectrometer were enclosed by a black box. If not specified otherwise, we used an optically pumped cw semiconductor laser (Coherent Sapphire LP UBB CDRH) with a wavelength of 458 nm (photon energy of 2.698 eV or 21,816 $\mathrm{cm^{-1}}$) and $P = 50$ mW. To block the laser light from entering the spectrometer, a long-pass filter (cut-off at 475 nm) was positioned in front of the entrance slit of the spectrometer. All spectra were recorded at a sample temperature of 20 K with an exposure time of 2 s, 50 accumulations, and a slit width of the spectrometer of 0.1 mm.

Results and Discussion

1 Overview of the spectra

Figure 2 shows overview spectra of 1.55 ML PTCDA on Cu(111) (red spectrum) and 0.50 ML PTCDA on hBN/Cu(111) (blue spectrum). PTCDA on Cu(111) was deposited at a sample temperature of 300 K and the LEED pattern confirmed the formation of a second layer (see Appendix A). PTCDA on hBN/Cu(111) was deposited at a sample temperature of 20 K and subsequently annealed at 300 K. The FL spectrum shown here is identical to the FL spectrum of PTCDA deposited at a sample temperature of 300 K, which showed the LEED pattern in Figure 8b (see below in Appendix A), revealing an ordered structure. Hence, we conclude that the blue FL spectrum shown in Figure 2, which is, as it will become clear, relevant for the comparison with PTCDA/Cu(111), also stems from an ordered PTCDA layer on hBN/Cu(111).

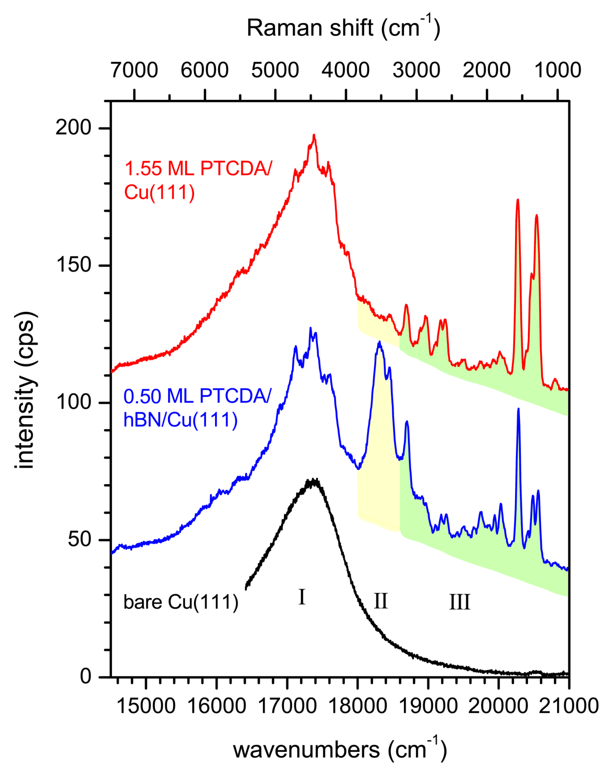

Figure 2: Overview spectra of 1.55 ML PTCDA on Cu(111) (red), of 0.50 ML PTCDA on hBN/Cu(111) (blue), and of the clean Cu(111) surface (black). For preparation details, see text. We distinguish three regions I, II, and III. The sharp lines marked in green are Raman modes (region III). The features marked in yellow are assigned to fluorescence (region II). The broadest feature on the low-energy side is due to defect luminescence of the Cu substrate (region I). All spectra were measured at 20 K using a grating with 300 grooves per millimeter. The spectra are shifted vertically for clarity.

For the discussion of the spectra, we consider three regions (I–III). At first glance, two of these regions appear qualitatively rather equal for both substrates: On the low-energy side below 18,000 cm^{-1} (region I) a broad luminescence can be observed and on the high-energy side above 18,600 cm^{-1} (region III), there is a set of sharp peaks. However, the two spectra differ significantly between 18,000 and 18,600 cm^{-1} (region II) due to broad FL peaks (highlighted in yellow) present for hBN/Cu(111), but absent for PTCDA/Cu(111).

We tentatively assign the broad peak in region I to a radiative decay of interband transitions from the Cu substrate, as it can also be observed on the clean substrates (Cu(111) and hBN/Cu(111)) before PTCDA deposition when all other features are absent (see Figure 2, black spectrum). An enhancement of radiative interband transitions has been reported for Cu nanoparticles [40]. We thus speculate that surface defects (protrusions) play a role here. This is in agreement with our observation that the intensity of this “defect luminescence” in region I depends on the exact position of the spot of the excitation light on the sample. It will not be in the focus of this work. The sharp peaks in region III are identified as Raman lines from PTCDA (highlighted in green). The Raman lines were additionally identified by using a dye laser with tunable wavelength [20] (497–507 nm). These peaks shift according to the wavelength of the laser (see Appendix B). Notably, some Raman peaks are superposed in the region of the defect luminescence of the Cu(111) surface (region I), too.

2 Raman modes

First, we will discuss the Raman lines. The peaks in the spectrum between 21,000 and 18,600 cm^{-1} in Figure 2 exhibit Raman shifts that correspond to the energies of the vibrational modes of PTCDA adsorbed on surfaces observed before [41,42]. The vibronic modes of PTCDA that can be observed in Raman spectroscopy are A_g, B_{1g}, B_{2g}, and B_{3g} modes, with the most prominent modes being A_g modes between 1,250 and 1,650 cm^{-1} [41-43]. The spectral positions of most of these modes are about constant for PTCDA adsorbed on different substrates [41] or for different film thicknesses [42]. An interesting exception was observed for PTCDA on Ag(111) [42] for the breathing mode of the central carbon ring at ca. 1,300 cm^{-1}. In the following, we will refer to it as ring breathing (RB) mode. On Ag(111), two different adsorption states of PTCDA were observed. Both states are bonded chemisorptively to the surface [44]. The RB mode of PTCDA deposited at a low temperature (LT) of 180 K exhibits a Raman shift of 1,310 cm^{-1}. This is higher in energy by 13 cm^{-1} compared to the Raman shift (1,297 cm^{-1}) for the RB mode of a layer at room temperature (RT) [42]. The special role of this RB mode will be discussed in further detail below.

2.1 Surface-enhanced Raman scattering

The fact that the Raman modes of a small quantity of molecules can be observed here at all is attributed to surface-enhanced Raman scattering (SERS) [45]. This effect is most commonly observed on rough surfaces of noble metals [45] or at metal nanostructures [46], and it is utilized in surface-enhanced

Raman spectroscopy [47]. There are two explanations for it, namely, a chemical mechanism and an electromagnetic mechanism, which is thought to be the dominant contribution to the enhancement. The chemical mechanism is related to the specific chemical surface bonding of the investigated system. At its heart, a CT between the molecule and the substrate occurs due to the chemisorptive bonding, which leads to a change in the polarizability of the molecule and thus to an enhancement of the Raman signal. It is also possible that electronic excitations of the adsorbed molecule allow for a resonance Raman effect, which causes an additional enhancement [46]. According to the electromagnetic mechanism, on a rough surface, surface plasmon polaritons (SPPs) can also be excited by the incident light. The surface plasmons are located in the vicinity of surface defects, such as protrusions. The field enhancement at these defects leads to an enhancement of the Raman scattering [48]. Subsequently, the scattered light can be enhanced in the same manner. The electromagnetic mechanism may be responsible for an enhancement of the signal by a factor of 10^5–10^6 [48]. The contribution of the chemical mechanism is generally much smaller, causing an enhancement by a factor of not more than 10^2–10^3 [46].

Recently, hBN has gained interest as a SERS substrate [49]. In a comparative study on 2DMs on SiO_2 it was shown that hBN had an enhancement effect on the Raman modes of adsorbed copper phthalocyanine molecules [50]. The effect was explained by the polar character of the B–N bonds, which induced a dipole in the adsorbed molecule. The resulting interfacial dipole–dipole interactions are thought to have a similar effect on the polarizability of the adsorbed molecule as a CT.

Regarding the Raman enhancement effect of a noble metal surface, we mention a recent study by Stallberg et al. [39], which investigated optical spectra of PTCDA on Ag(111) and Au(111). They found Raman modes of PTCDA on the Au(111) surface, but not on the Ag(111) surface. This observation was discussed in view of the different energies of the SPPs of the two surfaces. Stallberg et al. used photon energies of 2.37 eV on Au(111) and 2.43 eV on Ag(111) and concluded that only the SPP of Au(111) located at $E_{\mathrm{SPP}}^{\mathrm{Au}} = 2.5$ eV can resonantly interact with the incident light, leading to an enhancement of the Raman modes. The SPP on the Ag(111) surface has an energy of $E_{\mathrm{SPP}}^{\mathrm{Ag}} = 3.7$ eV. Hence, a resonance was considered less probable, yielding no enhancement of Raman modes. This model should evidently encompass that the coupling to the SPPs requires a rough surface or local protrusions on the surface due to defects that break the translational symmetry. For comparison, we note that the energy of the SPP of Cu(111), which is calculated from the condition $-\mathrm{Im}(\varepsilon^{-1}) = \varepsilon_2 / (\varepsilon_1^2 + \varepsilon_2^2)$ [51] using the dielectric functions given in [52], is obtained at a value of $E_{\mathrm{SPP}}^{\mathrm{Cu}} = 2.3$ eV. Our excitation energy was 2.698 eV. From our experiment we have indeed evidence that SERS is related to surface defects. This will be discussed in Section 2.3.

2.2 Raman modes of PTCDA on hBN/Cu(111) and Cu(111)

Figure 3a and Figure 3b show region III of the spectra of PTCDA on hBN/Cu(111) and Cu(111) for Raman shifts of 1,240 to 1,660 cm^{-1} in detail. All Raman shifts are also summarized in Table 1. Some values are given as averages for different coverages as no trends as a function of the coverage were found (see caption). First, we discuss spectra of PTCDA on hBN/Cu(111) and Cu(111), which were both stable under annealing at 300 K (cf. Figure 3a) and, hence, represent the final state. Kinetic effects do not play a role here. In Section 2.2.2, we focus on temperature-dependent effects (cf. Figure 3b).

2.2.1 The final state – 300 K spectra: Figure 3a shows Raman modes of PTCDA/hBN/Cu(111) after deposition at 20 K and subsequent annealing at 300 K (blue), and of PTCDA/Cu(111) after deposition at 300 K (red). The positions of the Raman modes of 1 ML PTCDA/Ag(111) measured by Schneider and Wagner [42,53], which was deposited at a sample temperature of 400 K, are indicated by green vertical bars for comparison. It is apparent from Figure 3a that the modes of PTCDA/hBN/Cu(111) are systematically shifted to smaller energies by about 7 cm^{-1} compared to PTCDA/Cu(111). In contrast, the modes of PTCDA/Ag(111) [53] agree well with the modes of PTCDA/Cu(111) within 0.3%. An exception is the RB mode. This mode will be discussed separately below. The shift of the other modes to higher vibrational energies seen in comparison of hBN/Cu(111) and the metal surfaces Cu(111) and Ag(111) can be linked to the different bonding of PTCDA to the surfaces. In UPS experiments [33], a chemisorptive interaction of the metal surfaces with the PTCDA molecule was found, leading to a (partial) filling of the former LUMO on Ag(111) and Cu(111). On PTCDA/hBN/Cu(111), no such chemisorptive bonding was observed in UPS [32]. We suppose that the energy of the vibrational modes recorded here are influenced by molecule–substrate interactions. The chemisorptive bond to the metal surface makes the intermolecular bonds harder, which causes the respective vibrational modes to increase in energy. For Raman shifts below 1,500 cm^{-1}, this interpretation is also supported by the closer agreement of the Raman modes on hBN/Cu(111) with those measured for PTCDA single crystals [55] (see Table 1). However, for modes above 1,570 cm^{-1}, the situation is reversed and not yet understood.

As mentioned before, the significance of the RB mode has been reported for PTCDA/Ag(111) [53]. The energy of this mode in-

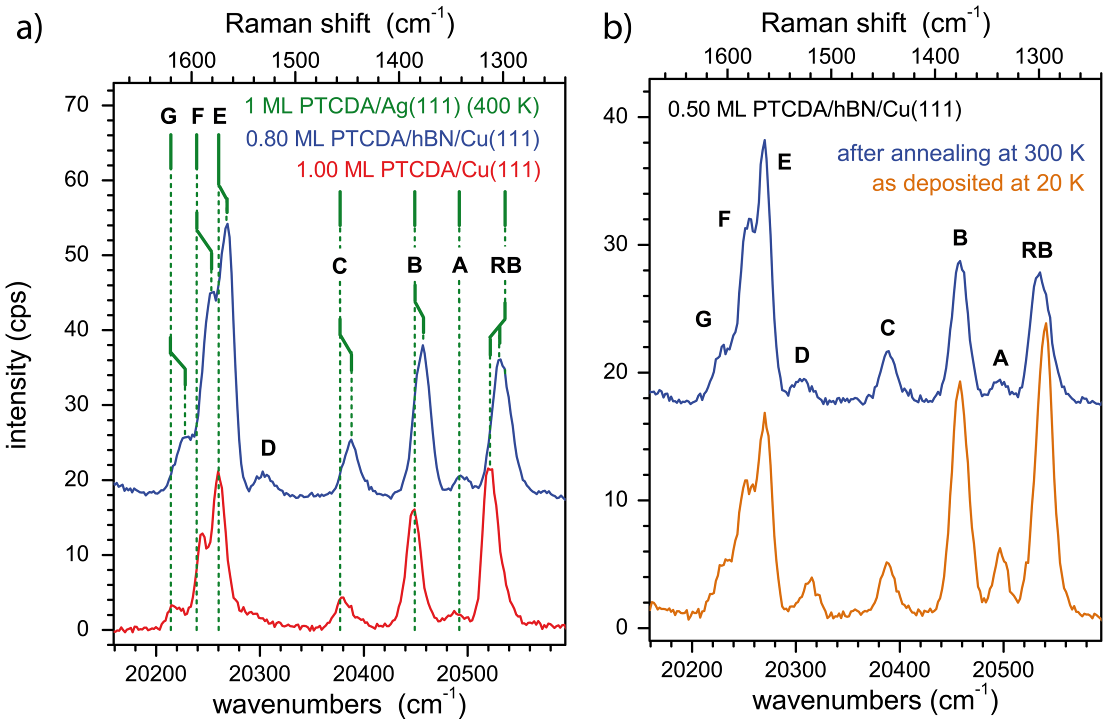

Figure 3: Zoom-in on the high-energy region (III) of the spectra. (a) 0.80 ML PTCDA/hBN/Cu(111) after deposition at 20 K and subsequent annealing at 300 K (blue) and 1.00 ML PTCDA/Cu(111) after deposition at 300 K (red). The positions of the Raman modes of 1 ML PTCDA/Ag(111) [53] are indicated in green. (b) 0.50 ML PTCDA/hBN/Cu(111) after deposition at 20 K (orange) and after subsequent annealing at 300 K (blue). All spectra were measured at 20 K using a grating with 1200 grooves per millimeter. Labels of the peaks refer to Table 1, the peaks H–K are not shown here.

Table 1: Raman shifts (in cm^{-1}) of PTCDA on hBN/Cu(111) and Cu(111), prepared at sample temperatures T_S (for details on the preparation, see text). Data were measured at 20 K. The values for PTCDA/hBN/Cu(111) are averaged for different film thicknesses (eight datasets with coverages between 0.05 and 0.80 ML for both 20 and 300 K). The error margins given are the standard deviation. The values for PTCDA/Cu(111) refer to coverages of 1.20 ML for T_S = 20 K and 1.00 ML for T_S = 300 K. For comparison, the Raman shifts of 1 ML PTCDA/Ag(111) measured by Schneider et al. [53], the vibrational energies of PTCDA/KCl/Ag(100) measured by Paulheim et al. in FL experiments [54], and the Raman shifts of the PTCDA single crystal measured by Tenne et al. [55] are listed. The ring breathing (RB) mode of the central carbon ring of PTCDA is the only mode that changes as a function of film thickness. The values for the RB mode of multilayers (RB$_{\text{multi}}$) refer to 5.10 ML and 8.20 ML PTCDA/hBN/Cu(111) (averaged values), 3.44 ML PTCDA/Cu(111) for T_S = 20 K, 2.55 ML PTCDA/Cu(111) for T_S = 300 K, and 60 ML PTCDA/Ag(111) [53]. The modes of PTCDA/Cu(111) with T_S = 20 K are intrinsically very small and often not observed. Those modes are listed as “n.o.”.

mode	hBN/Cu(111)	hBN/Cu(111)	Cu(111)	Cu(111)	Ag(111) [53]	KCl [54]	PTCDA single crystal [55][a]
T_S	20 K	300 K	20 K	300 K	400 K	<20 K	
RB$_{\text{mono}}$	1296.7 ± 1.6	1301.2 ± 1.7	1304.0	1312.9	1298	1288	—
RB$_{\text{multi}}$	1301.8 ± 3.8	1309.8 ± 3.1	1300.0	1309.5	1309	—	1302.3
A	1339.4 ± 1.5	1339.2 ± 1.2	n.o.	1346.5	1342	1332	1335.0
B	1378.0 ± 1.0	1377.5 ± 1.5	1383.8	1386.0	1385	1368	1375.4/1383.6
C	1447.8 ± 1.5	1447.4 ± 1.7	n.o.	1454.6	1457	1446	1451.0
D	1522.4 ± 2.1	1529.4 ± 0.7	n.o.	n.o.	—	1523	—
E	1566.6 ± 1.9	1567.9 ± 2.5	1571.4	1574.0	1574	1564	1570.6
F	1582.7 ± 3.7	1582.3 ± 2.0	n.o.	1589.6	1595	1584	1589.1
G	1606.7 ± 1.7	1607.3 ± 2.0	n.o.	1616.2	1620	—	1615.0
H	1674.3 ± 0.7	1673.3 ± 2.4	n.o.	n.o.	—	—	—
I	1757.8 ± 1.8	1758.0 ± 1.7	n.o.	1764.3	—	—	—
J	1795.0 ± 1.3	1796.2 ± 2.2	n.o.	n.o.	—	—	1783.0
K	1820.4 ± 1.2	1825.9 ± 1.3	n.o.	1833.7	—	—	—

[a] Only the upper Davydov components are listed.

creases for PTCDA on different substrates, going from KCl films on Ag(100) (1,288 cm^{-1}, derived from FL spectra) [54], to Ag(111) (1,298 cm^{-1}) [53], hBN/Cu(111) (1,301 cm^{-1}, derived from FL spectra), and Cu(111) (1,313 cm^{-1}, derived from FL spectra), contrary to the other modes. This trend neither conforms with the strength of the (chemisorptive) bond to the substrate surface [33], nor with the bonding distance, or the amount of molecular distortion [32,35,56,57]. However, in some way it reflects the change in the distortion motif of the PTCDA molecule. On KCl/Ag(100), the PTCDA molecule is bend like an arch with all of the oxygen atoms pulled towards the surface [57]. On Ag(111), the molecule is saddle-shaped with only the carboxylic oxygen atoms pulled downwards out of the molecular plane towards the surface [56]. On Cu(111), the opposite is found. The oxygen atoms are pushed away from the surface, upwards out of the molecular plane, leading to a boat shape [35]. On hBN/Cu(111), the PTCDA molecule is nearly undistorted and hence planar [32]. It was surmised that the PTCDA molecule is bonded to the Ag(111) surface (and the KCl surface [57]) via the carboxylic oxygen atoms, while on Cu(111), the bonding proceeds primarily via the perylene core [58]. We hence suggest that the bonding via the perylene core on Cu(111) leads to a reduced flexibility of the intramolecular bonds of the core (including the central carbon ring), which causes the higher Raman shift of the RB mode. The flat, saddle-, and arch-like shapes of the molecule on hBN/Cu(111), Ag(111), and KCl/Ag(100) lead to smaller Raman shifts of the RB mode of 12 cm^{-1}, 15 cm^{-1}, and 25 cm^{-1}, respectively. The special sensitivity of the RB mode to the interfacial bonding was also seen in high-resolution electron loss spectra [59].

We also compare with PTCDA multilayers. The Raman shifts of the multilayers was found at similar energies on all three substrates, that is, at 1,309.8 cm^{-1} for multilayers of PTCDA/hBN/Cu(111), at 1,309.5 cm^{-1} for 2.55 ML PTCDA/Cu(111), and at 1,309 cm^{-1} for 60 ML PTCDA/Ag(111) [53]. This is in agreement with an identical interaction between the PTCDA multilayers as it is expected. The energy of the RB mode for the multilayers is between that of the monolayer on hBN/Cu(111) (1,301.2 cm^{-1}) and the monolayer on Cu(111) (1,312.9 cm^{-1}). Actually, it is rather close to the value seen on Cu(111) within 3 cm^{-1} (see Table 1). This may indicate that intermolecular interactions between adjacent layers in a multilayer also have a significant impact on the vibrational properties and cannot be neglected. We note that these values are slightly larger than those measured for PTCDA single crystals [55] or thick films [43].

2.2.2 Temperature induced changes in the Raman spectra: The unique behavior of the RB mode can also be seen in its dependency on the preparation temperature both for PTCDA/hBN/Cu(111) and PTCDA/Cu(111). We compare spectra recorded directly after deposition at 20 K with those after annealing at 300 K (on hBN/Cu(111)) (Figure 3b) or with those after deposition at 300 K (on Cu(111)) (spectra not shown). For PTCDA deposited onto Cu(111) at 20 K, no Raman peaks could be observed at all in the sub-monolayer regime, and even for multilayers, the intensities of the Raman modes did not exceed two counts per second. (These are the modes given in Table 1.) At higher temperatures, the RB mode shifts to higher energies by 4 and 9 cm^{-1} for PTCDA on hBN/Cu(111) and Cu(111), respectively; the other modes remain unchanged (±0.4%, cf. Table 1).

This reflects the situation of PTCDA/Ag(111) [42] where the only significant temperature-dependent shift (by 10 cm^{-1}) was also observed for the RB mode. In that study, the shift of the RB mode was originally attributed to be of chemical origin due to different bonding to the Ag(111) substrate present only in the monolayer but not for the multilayers. However, this interpretation appears less possible for the monolayers considered here. Hence, we recall a later study [56] that revealed the existence of a chemisorbed LT state of the monolayer in which the PTCDA molecule is positioned at a similar distance (±5%, regarding the perylene core) from the surface as the RT state but is significantly more distorted than the RT state (maximum height difference of atoms of 0.31 Å compared to 0.20 Å) [56]. In addition, the LT state is present as a disordered phase, while the RT state forms highly ordered domains [44]. This is accompanied by a change in the valence band structure as seen, for example, in UPS [44]. Thus, instead of a multilayer/monolayer effect, the above described differences in the Raman shifts may also be caused by the intermolecular interactions and a modification in the interfacial bonding in the ordered domains of the RT state, which form upon annealing at room temperature. We propose that, in particular, the effect of intermolecular interactions is also relevant for the monolayer of PTCDA on hBN/Cu(111), whereas on Cu(111) concomitant changes in the interfacial bonding may play a role, too. The increased temperature induces the formation of ordered domains (observed in LEED). The intermolecular interactions in the domains then cause a change in the structure and charge distribution within the molecule. This in turn increases the vibrational energies, in particular of the RB mode located on the perylene core.

2.3 The role of surface defects for SERS

For both PTCDA/hBN/Cu(111) and PTCDA/Cu(111), the overall intensities of the Raman modes are of the same order, which implies that both surfaces cause a similar degree of Raman enhancement. However, we refrain from making a statement about the SERS effectiveness of hBN on Cu(111) for the following reason: In our experiments, the Raman intensities on either hBN/Cu(111) or Cu(111) were both found to be highly dependent on the exact position of the incident laser beam on the sample (varying by a factor of up to ca. 7). This indicates that the specific local surface quality, for example, the surface roughness at the spot where the Raman scattering occurred, influences the intensity of the Raman modes. Hence, we cannot draw quantitative conclusions here. Nevertheless, we gain some insight into this aspect from an experiment we conducted at low temperatures, which we describe in the following.

As mentioned in the previous section, in the sub-monolayer regime of PTCDA/Cu(111) deposited at 20 K no Raman peaks could be observed at all, and even for multilayers their intensities were very small (spectra not shown). For PTCDA on hBN/Cu(111) the situation is drastically different. Figure 3b shows the Raman modes of PTCDA (0.50 ML) after deposition at 20 K (orange) and after subsequent annealing at 300 K (blue). For both preparations, the Raman modes are clearly present and of a similar intensity.

We discuss two possible explanations for these different kinds of behavior after deposition at 20 K: (i) The dipole–dipole interaction between hBN and PTCDA enhances the Raman signal. In this process, the underlying copper would not be involved [50]. (ii) The Raman modes of PTCDA are strongly enhanced at specific adsorption sites, which we refer to as “hot spots”. On Cu(111), the molecules can reach these hot spots only by temperature-induced diffusion. Whereas, after deposition at 20 K, the molecules stay statistically distributed on the surface, and only a small fraction is located at these sites where the SERS effect occurs. On hBN/Cu(111), the significantly smaller interaction between PTCDA and the hBN surface compared to Cu(111) and a consequently smaller corrugation of the bonding potential lead to a much higher mobility, which allows for a diffusion to the hot spots even at low temperatures of 20 K.

We propose the second interpretation to be relevant. Our arguments are the following: Firstly, we have shown in a previous work [32] that the interaction between PTCDA and hBN/Cu(111) is of a physisorptive nature, which makes a strong SERS effect due to dipole–dipole interactions at the interface [50] unlikely. Secondly, the strong dependence of the Raman intensity on the sample position (see above) conforms with the interpretation of a SERS effect related to local hot spots. However, the details of the related adsorption sites remains unclear.

Since the SERS effect is primarily observed on rough/nanostructured rather than on flat metal surfaces [45], the SERS effect is expected to be larger for molecules located in proximity to surface defects. Thus, at surface positions with a higher defect density, the Raman intensities are expected to be higher. The relevance of the defect density in the present case is corroborated by our observation that at positions where the Raman intensity was high, the defect luminescence of the substrate (see region I in Figure 2) was also higher. In a theoretical study, García-Vidal and Pendry investigated the enhancement due to the SERS effect as a function of the roughness on a surface [48]. They found that on an inhomogeneously rough surface, the Raman spectrum is dominated by the enhanced signals from molecules located at features that exhibit a maximum in roughness. We can support this interpretation by results from a previous experiment. We observed by light microscopy that Ag(100) samples that had been prepared in a similar manner as the Cu(111) surface used here and that yielded a high-quality LEED pattern indicating the presence of long-range ordered and large, defect-free terraces, actually show variations in their surface morphology on a micrometer scale [60]. We propose that the defect-rich regions exhibit a large step density due to impurities and/or grain boundaries. Consequently, we assume that the hot spots are related to an inhomogeneous mesoscopic roughness of the Cu(111) surface, which is remnant after sputtering and annealing.

In conclusion, the Raman lines of PTCDA/hBN/Cu(111) and PTCDA/Cu(111) observed between 18,600 and 21,000 cm^{-1} are in accordance with the characteristic fingerprint of the molecule. They can be used as a monitor for its presence on the surfaces. Coverages cannot be determined quantitatively from the intensities of the Raman modes, since these depend on the sample positions, which we assign to a correlation with the local roughness due to structural defects of the surface. Note that we systematically did not observe the characteristic Raman line of hBN at approximately 1,370 cm^{-1} that was observed for hBN on SiO_2/Si [61], on Cu foils [62], and on other metal foils [63,64] for our samples of hBN/Cu(111). This is an obvious discrepancy, which we cannot explain based on our current data. It may, however, be related to the specific interface between hBN and the single crystalline Cu substrate.

3 Fluorescence

3.1 PTCDA/hBN/Cu(111)

We turn to the FL, which can be observed in region II of Figure 2, between 18,000 and 18,600 cm^{-1}. We note ahead that we did not observe vibronic bands related to the FL peaks as it is the case, for example, for PTCDA on KCl [65].

First, we consider which experimental conditions led to the observation of FL peaks. Figure 4a shows a zoom-in on region II of the spectrum of 0.60 ML PTCDA on hBN/Cu(111) as deposited at a sample temperature of 20 K, and after a series of subsequent annealing steps at temperatures between 100 and 400 K. The peak on the high-energy side of the spectrum (marked in green and labeled "R") is a Raman mode. This mode has also been observed for PTCDA/Ag(111) [53]. Furthermore, its change in intensity as a function of the annealing temperature agreed with that of other Raman modes. The behavior of the two other peaks depicted in Figure 4a (marked in yellow and pink) was quantitatively different. We assign these peaks to the FL of PTCDA molecules and will refer to them as FL_A (at ca. 18,450 cm^{-1}) and FL_B (at ca. 18,300 cm^{-1}). Both peaks appear after annealing at temperatures above ca. 200 K (FL_A) and ca. 280 K (FL_B).

We take this finding as an indication that the FL of PTCDA on hBN/Cu(111) depends on the structural order of the molecules on the surface that is established by annealing. We explain the existence of two FL peaks by the presence of two structurally different "phases" of PTCDA. Since all optical measurements were carried out at a sample temperature of 20 K, the temperature-induced structural ordering upon annealing that led to the FL peaks is irreversible. The broad FL peaks are superimposed with several sharp Raman lines, which lead to modulations of the peaks. There are two important differences between the FL_A and FL_B peaks: FL_B is significantly broader than FL_A (by a factor of ca. three, which we will discuss in detail in the Section Final Discussion). In addition, the intensity of FL_A saturates, while that of FL_B does not. Notably, the intensity of FL_A saturates upon annealing at 280 K, which is the temperature that is required for FL_B to be observed at all. This behavior was found for layers within a range of sub-monolayer coverages (between 0.10 and 0.80 ML).

For further insight, we refer to a temperature-dependent series of spectra at a higher coverage of 1.55 ML PTCDA on hBN/Cu(111), shown in Figure 4b. We observe the same Raman line as for the 0.60 ML spectrum, as well as FL_A and FL_B. However, there are a few important differences compared to the spectra in Figure 4a: (i) FL_A can be observed in the spectrum immediately after deposition at 20 K; (ii) FL_B appears in the spectrum already after annealing at 200 K (not at 280 K); and (iii) additional FL intensity at lower energies (ca. 18,150 cm^{-1}) appears, which we assign to a third peak FL_C. The appearance of FL_A at low temperatures leads us to the conclusion that the attributed "phase A" of PTCDA/hBN/Cu(111) forms directly at higher coverages, while at lower coverages its formation requires annealing. Hence, we assign FL_A to PTCDA molecules at surface defects. In a sub-monolayer, the molecules can reach these defects via diffusion, which has to be temperature-induced. For a higher coverage, the sites at defects are already populated during the deposition, even at low temperatures. A saturation of the sites at defects leads to the observed intensity saturation of the corresponding FL_A peak. We note in this context that the surface defects connected to FL_A are not identical to the hot spots mentioned above, which support the SERS

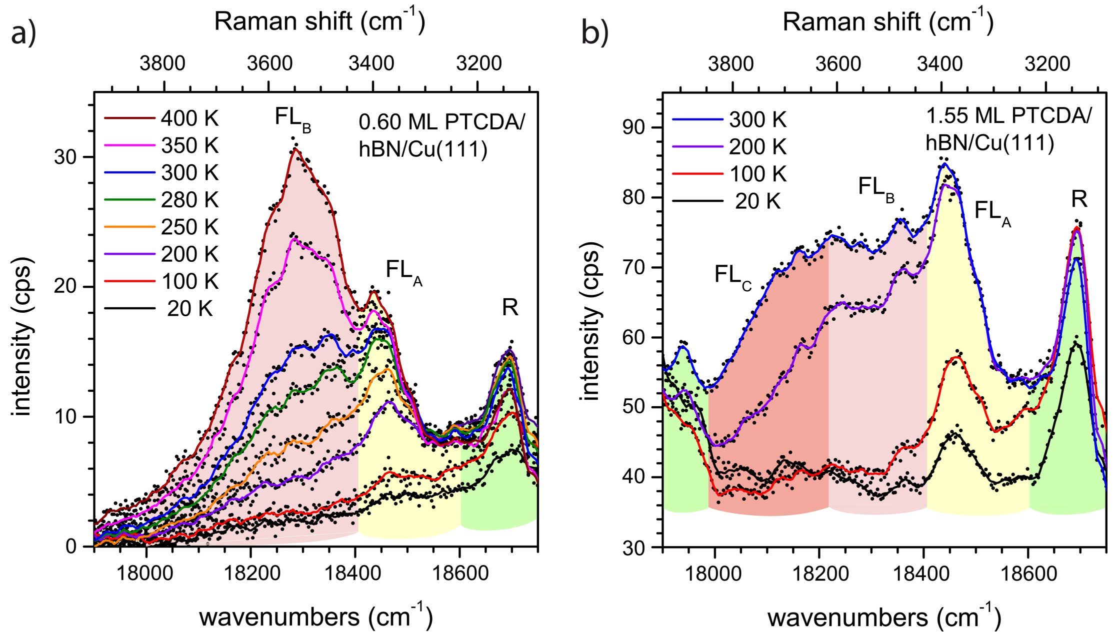

Figure 4: Fluorescence spectra of (a) 0.60 ML PTCDA and (b) 1.55 ML PTCDA on hBN/Cu(111) as deposited at 20 K (black) and subsequently annealed at different temperatures. Raman modes are highlighted in green, FL peaks FL_A, FL_B, and FL_C are highlighted in yellow, pink, and red, respectively. The spectrum of the clean surface was subtracted as a background. Spectra are smoothed (lines, original data as dots). All spectra were measured at 20 K using a grating with 600 grooves per millimeter.

effect, as we will discuss below. After the saturation of the defects, the temperature-induced formation of a second "phase B" occurs leading to the peak FL_B.

We also observed the FL_B peak on hBN/Cu(111) after deposition at 300 K for coverages of 1–3 ML. For all these experiments, we observed the LEED pattern that is characteristic of ordered domains of PTCDA/hBN/Cu(111) (see Appendix A). Thus, we conclude that FL_B stems from these ordered PTCDA domains in the first layer on hBN. The formation of ordered domains is not possible at a sample temperature of 20 K during deposition. It requires a certain threshold temperature (ca. 280 K). This explains why FL_B can only be observed after annealing or deposition at or above this temperature.

The energetic difference between FL_A and FL_B amounts to ca. 150 cm^{-1}. We compare this to the energetic shift reported by Forker et al. who investigated PTCDA on hBN/Rh(111) [23]. They found that PTCDA molecules on hBN/Rh(111) are trapped in the pores of the hBN superstructure, which leads to isolated monomers on the surface. Annealing leads to the formation of ordered domains and a redshift of the spectrum by 223 cm^{-1} (27.6 meV) [23]. The molecules trapped in pores on hBN/Rh(111) can be compared with isolated molecules located at defects on hBN/Cu(111). However, please note that we do not consider trapped PTCDA molecules but isolated molecules to be the origin of FL_A. This will be discussed in further detail in Section 3.3 in relation with further information from FL experiments. An energetic shift of the same order has also been observed for the FL of isolated molecules and that of ordered domains of PTCDA on NaCl [10]. Here, two different structures of ordered domains of PTCDA were observed (a herringbone and a quadratic structure) the S_0/S_1 transitions of which are redshifted relative to the isolated molecules by 560 cm^{-1} and 300 cm^{-1}, respectively.

For a comparison of FL_B of PTCDA domains on hBN/Cu(111) at 18,300 cm^{-1}, we refer to optical data taken for ordered monolayers of PTCDA on a monolayer of hBN grown on other substrates. The respective values are given in Table 2. Note that only PTCDA/hBN/SiO_2 was investigated by FL spectroscopy while for PTCDA/hBN/Pt(111) and PTCDA/hBN/Rh(111) absorption spectra were measured. We cannot explain the differences of the S_0/S_1 transition energies, yet. However, we observe a trend of higher transition energies from hBN/SiO_2 to hBN/Cu(111) to hBN/Pt(111) to hBN/Rh(111). This is the direction of increasing interactions between the hBN layer and the supporting metal substrate, as indicated by the increasing amplitude of the buckling of the hBN layers [30,66]. We note that Forker et al. [23] could exclude a dominant role of the dielectric properties of the metal substrates for the transition energies.

The peak FL_C (cf. Figure 4b) shows the same behavior as FL_B at a coverage of 1.55 ML. It is as broad as FL_B and appears after annealing at 200 K. However, it is not present at a coverage of 0.60 ML. Thus, it does not stem from PTCDA directly adsorbed on hBN, but from ordered PTCDA domains in a second layer. However, this is different from the FL emission (Y), which is present in bulk-like PTCDA layers and was reported, for example, in [67]. Indeed, we observed the broad Y line and its vibronic progression Y' for higher coverages of 4–5 ML at 15,950 and 14,700 cm^{-1}, respectively. This is in agreement with the line positions measured in [67] within 50 cm^{-1} and 300 cm^{-1}, respectively.

In summary, for PTCDA/hBN/Cu(111) three FL peaks can be observed. FL_A (ca. 18,450 cm^{-1}) is present in the first layer and stems from molecules at surface defects. To enable the molecules to reach these defects, a temperature-induced diffusion is necessary at sub-monolayer coverage. FL_B (ca. 18,300 cm^{-1}) stems from ordered domains in the first PTCDA layer. It can only form under deposition at a sample temperature above ca. 280 K, or after annealing at this temperature. FL_C (ca. 18,150 cm^{-1}) is assigned to the FL from ordered PTCDA domains in the second or higher layers.

3.2 Comparison with PTCDA/Cu(111)

Figure 5a shows the FL spectra of PTCDA/hBN/Cu(111), prepared by deposition at 20 K and subsequent annealing at 300 K and of PTCDA/Cu(111), prepared by deposition at 300 K, both with varying coverages. We will list the important observations

Table 2: Spectral positions of the S_0/S_1 transition of PTCDA domains in the first monolayer on hBN on SiO_2 [22], Cu(111), Pt(111) [23], and Rh(111) [23]. PTCDA on hBN/SiO_2 and on hBN/Cu(111) were investigated using FL spectroscopy. The results for PTCDA on hBN/Pt(111) and hBN/Rh(111) were gained in absorption experiments.

hBN/SiO_2 [22]	hBN/Cu(111)	hBN/Pt(111) [23]	hBN/Rh(111) [23]
2.234 eV 18,060 cm^{-1}	2.26 eV 18,300 cm^{-1}	2.31 eV 18,700 cm^{-1}	2.38 eV 19,200 cm^{-1}

for these spectra: (i) There is no fluorescence at all for a full monolayer of PTCDA on bare Cu(111) while on hBN/Cu(111) FL can be observed for a coverage as low as 0.10 ML. (ii) In the second monolayer of PTCDA on bare Cu(111), an FL peak appears at 18,450 cm^{-1}, which corresponds to FL$_A$. (iii) In the third PTCDA layer on Cu(111), there is an FL peak at

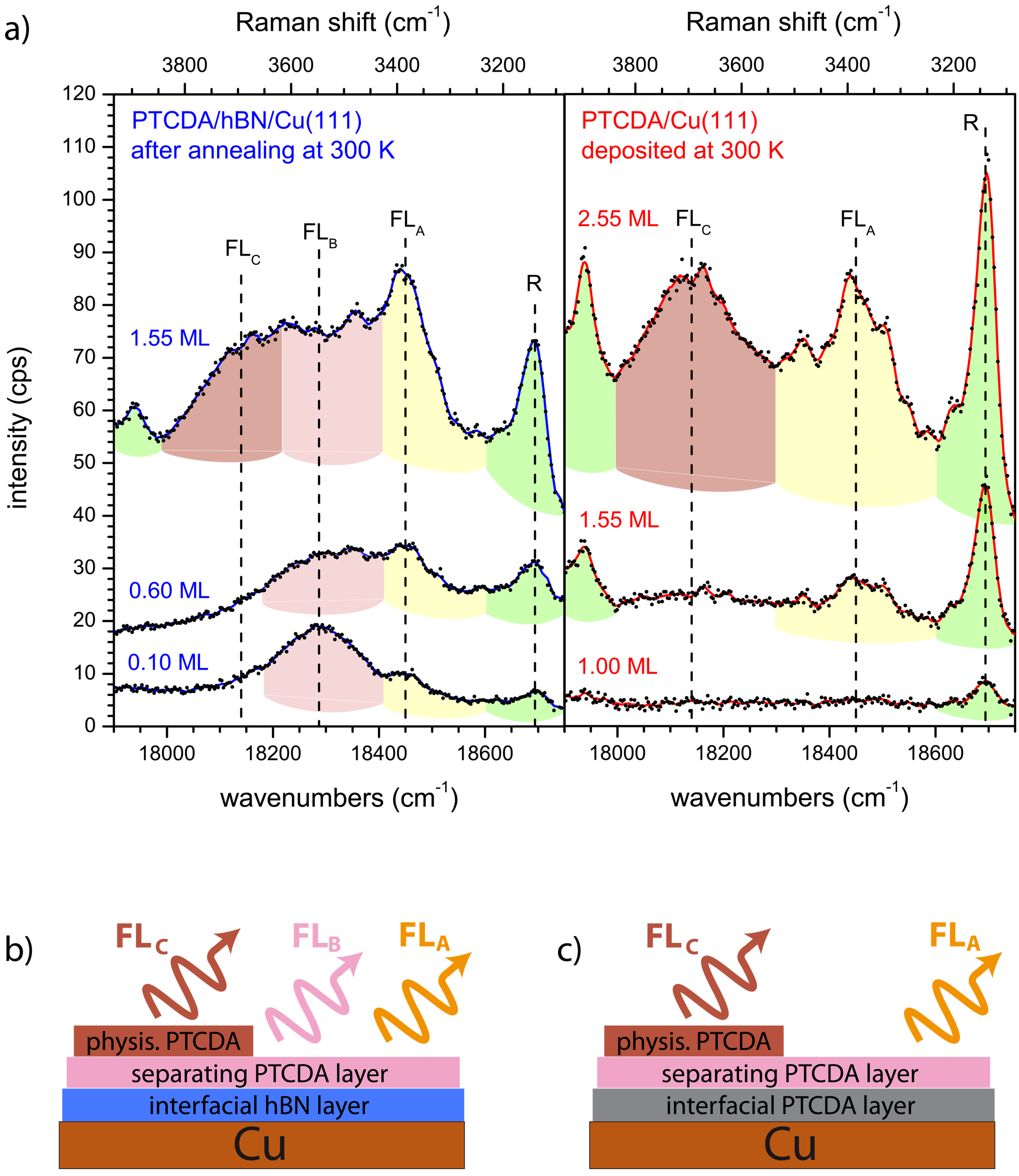

Figure 5: (a) Fluorescence spectra of PTCDA on hBN/Cu(111) (left, blue spectra, prepared by deposition at 20 K and subsequent annealing at 300 K) and PTCDA/Cu(111) (right, red spectra, prepared by deposition at 300 K). Raman intensities are highlighted in green; FL peaks FL$_A$, FL$_B$, and FL$_C$ are highlighted in yellow, pink, and red, respectively. There is no FL from ordered domains in the first or second layers of PTCDA/Cu(111), but from the first layer of PTCDA/hBN/Cu(111). Spectra are smoothed (lines) and vertically shifted (original data as dots). Spectra of the clean substrates were subtracted as background. All spectra were measured at 20 K using a grating with 600 grooves per millimeter. (b) Schematic representations of 2 ML PTCDA/hBN/Cu(111) and (c) 3 ML PTCDA/Cu(111) and the FL signals observed from these layers. The FL from the first PTCDA layer on Cu is quenched (gray). The interfacial hBN layer (blue) and the interfacial chemisorbed PTCDA layer (gray) decouple the fluorescing molecules from the metal. Defect-mediated FL (FL$_A$) is emitted from the separating PTCDA layer (pink) in both cases, FL$_C$ originates from the physisorbed PTCDA layer (red). Only for PTCDA/hBN/Cu(111) FL occurs from PTCDA domains in the separating layer (FL$_B$). For details on the different PTCDA layers, see text.

18,150 cm^{-1}, which is the position of FL$_C$ observed for 1.55 ML PTCDA/hBN/Cu(111). (iv) FL$_B$ is not observed at all for PTCDA/Cu(111). The absence of FL$_B$ on Cu(111) is understood as we have assigned it to PTCDA domains on hBN/Cu(111). The other three observations have to be explained.

Ad (i): The absence of any FL of 1.00 ML PTCDA on Cu(111) confirms the complete quenching of the molecular excitation in the first layer on a metal surface as has previously been observed for the Ag(111) [5,39] and the Au(111) [39] surfaces. Ad (ii): For PTCDA/Cu(111), a sufficient decoupling to allow some FL is achieved for the second layer (1.55 ML). Thus, FL$_A$ can be observed, which we assigned to FL from molecules at defects on the hBN/Cu(111) surface. It is remarkable that the PTCDA molecules have to interact with defects in order to fluoresce, and that the same kind of FL can be observed on both substrates. For PTCDA on Cu(111), as on hBN/Cu(111), a temperature-induced process is necessary to observe FL$_A$ as PTCDA on Cu deposited at 20 K shows no FL at all (not shown). Only for PTCDA deposited at 300 K on Cu(111), we can observe the spectra shown in Figure 5. As stated in the previous section, we assume a temperature-induced diffusion process to surface defects where the PTCDA molecules are then able to fluoresce. The nature of these defects will be discussed in the next Section 3.3. Ad (iii): From our LEED experiments (see Appendix A) we know that PTCDA on Cu(111) grows layer-by-layer in the first three layers. Thus, we can assign the peak FL$_C$, which appears in the third layer, to FL from ordered PTCDA domains adsorbed on top of two completed PTCDA layers. As we will discuss now, this is in accordance with the observation of FL$_C$ from the second layer of PTCDA/hBN/Cu(111). We summarize our observations with the schematic layer models that are given in Figure 5b,c. In both cases an interfacial layer that is adsorbed on the Cu(111) surface exists. This layer decouples PTCDA molecules in higher layers, which leads to FL from these layers. The interfacial layer is either a layer of hBN or a monolayer of chemisorbed PTCDA. The next layer in both cases is formed by ordered PTCDA domains that show FL$_A$, likely from molecules at defects. In the case of PTCDA on hBN/Cu(111), an additional FL$_B$ from ordered domains is present. We call this first PTCDA layer a separating layer. In the TPD spectrum of PTCDA/hBN/Cu(111), the desorption peak of the separating layer can be distinguished from that of the multilayers (however, no separated peak for the second layer is observed) [32]. On Cu(111), the first (interfacial) layer does not desorb at all, and in the TPD spectrum, the second (separating) layer is also distinct from the multilayers [68]. The multilayers (both on hBN/Cu(111) and Cu(111)) are likely physisorbed and include the layers from the second and third layer onward. The ordered PTCDA domains in these layers are the origin of FL$_C$.

Our findings are in accord with the conclusions by Stallberg et al. who measured photoluminescence spectra of PTCDA on Ag(111) and Au(111) [39]. From coverages of 1.8 ML on Ag(111) and 2.2 ML on Au(111) onward they observed FL peaks at 17,000 cm^{-1} and 17,300 cm^{-1} (denoted by M in [39]). These were assigned to PTCDA layers separated from the metal substrate by the first interfacial PTCDA layer. This M line was distinct from that of the bulk-like FL emission from thick films, which was found at 15,000 cm^{-1} (Y line) and 13,700 cm^{-1} (E line). The M line was observed even for multilayers, co-existing with the bulk emission. Similarly, for PTCDA/Cu(111), we observed the Y line and its vibronic progression Y' of the multilayer FL for a coverage of 4.60 ML at 16,100 cm^{-1} and 14,750 cm^{-1}, respectively, while FL$_A$ and FL$_C$ were still present (not shown). The Y line was assigned to the 0–0 transition of the PTCDA bulk phase [67]. Thus, the co-existence of the Y line and FL$_A$ and FL$_C$ is consistent with the formation of bulk-like clusters at a coverage of 4.60 ML. Likewise, on hBN/Cu(111), we observed the Y and Y' lines for coverages from about 4–5 ML onward (see Section 3.1) in parallel with FL$_A$, FL$_B$, and FL$_C$. This confirms, in accordance with our LEED data, that at least two complete layers of PTCDA form on both surfaces under the given preparation conditions.

3.3 FL at defect positions

As stated above, we assign FL$_A$ to molecules adsorbed at surface defects. Since FL$_A$ can be observed for PTCDA/hBN/Cu(111) and PTCDA/Cu(111), we assume the same kind of defects has to be present on both surfaces. We propose that these defects are different to the metallic "hot spots" supporting SERS because FL$_A$ is shifted in energy, which is less expected for coupling to metallic protrusions. An alternative origin of these defects could be the presence of carbon containing species due to segregation from the Cu bulk. Although this interpretation is speculative, we give some background in order to aid subsequent research. When the Cu(111) crystal was annealed at a temperature above 1050 K and for a period of time longer than 30 min, we observed an additional superstructure in LEED. Although we cannot identify these segregations unambiguously, we assume carbon segregation as carbon is known to form highly ordered nanostructures on Cu(111) [69]. Indeed, we adjusted our preparation by reducing the temperature to 1010 K during borazine deposition and omitting the annealing step under vacuum before borazine deposition to avoid this segregation (see Experimental section). However, we cannot exclude a small and randomly distributed residual amount of segregated carbon species since these would be invisible in LEED. We indeed found that samples showing segregated carbon in LEED do not allow for the formation of the hBN layer. Presumably, due to the extended carbon coverage, there is not enough bare Cu surface left for supporting the catalytic growth of hBN. Accordingly, on a surface with a small amount of carbon, growth defects in the hBN layer at positions where carbon is present may be expected. Thus, we consider carbon species in direct contact with the bare Cu that lead to similar or even identical defects on both surfaces (hBN/Cu(111) and bare Cu(111)), which, in turn, promote identical FL signals of PTCDA molecules. Note that these carbon-related defects are different from the defects that cause the SERS effect. The hot spots that lead to an enhancement of Raman signals are caused by structural defects of the Cu crystal, such as surface roughness, and not by a different chemical species.

Besides FL_A, no further FL can be observed for 1.55 ML PTCDA/Cu(111) despite the fact that the LEED pattern shows well-resolved spots of ordered domains. The absence of FL from these ordered domains indicates that a single PTCDA monolayer on Cu(111) cannot decouple PTCDA in the second layer from the metal surface sufficiently enough for FL to occur. Thus, the observation of only FL_A for a coverage of 1.55 ML leads to the conclusion that the defects at which the fluorescing molecules are adsorbed also have a decoupling effect. This corroborates our deduction that the defects cannot be Cu ad-atoms.

We would like to reiterate that we exclude the possibility that the FL_A of PTCDA on hBN/Cu(111) stems from molecules trapped in the "moirons" of the hBN layer [24]. Studies on hBN/Cu(111) have shown a trapping of large organic molecules in the moirons of the electronic superstructure of hBN/Cu(111) at low molecular coverages [38]. At larger coverages, the entire surface was found to be homogeneously filled with molecules. Yet, they still showed site-dependent alterations in their electronic structure, namely a shift of the molecular frontier orbitals [38]. However, we propose that the situation of PTCDA on hBN/Cu(111) is different. First of all, as stated above, FL_A is also observed for PTCDA on Cu(111), which clearly excludes trapped PTCDA molecules on hBN as a possible origin for FL_A. Furthermore, our own STM investigations showed no signs of a preferential occupation of the moirons on the hBN/Cu(111) surface by PTCDA [32]. Also, holes in the hBN layer that would allow for a direct contact between the molecules and the bare Cu(111) surface can be excluded as the origin for FL_A because the FL of PTCDA molecules in direct contact with the metal would be fully quenched.

4 Final discussion

We found that two layers of PTCDA are necessary to decouple PTCDA molecules from the Cu(111) surface in order to observe FL from ordered domains in the third layer. The same effect can be achieved by only one single layer of hBN. On hBN/Cu(111), two FL components (FL_A and FL_B) are present for the first PTCDA layer, while a third one (FL_C) can only be observed from the second layer onward. On Cu(111), the FL from the first PTCDA layer is completely quenched. FL_A and FL_C are observed only from the second and third layer onward, respectively. FL_A is assigned to a defect-related FL, while both FL_B and FL_C are assigned to ordered PTCDA domains. We can exclude bulk-like crystallites on top of the monolayer as the origin of the FL_B and FL_C peaks by the following arguments: (i) The LEED patterns of PTCDA on hBN/Cu(111) and on Cu(111) identify the formation of long-range ordered structures in the second layer. (ii) LEED investigations (see Appendix A) and TPD experiments [32,68] show that PTCDA/Cu(111) and PTCDA/hBN/Cu(111) form at least three or two complete layers, respectively. (iii) The spectral positions of FL_B and FL_C are unambiguously distinct from the Y and Y' peaks of the FL of the PTCDA bulk.

We return to the question of CT across the hBN layer posed in the Introduction section. Our results indicate that the hBN layer is able to suppress the CT such that FL is observed. However, this suppression is not complete because the FL intensity is very low. In comparison to the FL of PTCDA observed on thin KCl films, we reckon that the FL on hBN/Cu(111) is smaller by a factor of ca. 10^4 [70]. However, hBN should not be dismissed as a decoupling layer altogether. In an analogue experiment, we measured the FL spectrum of 5,10,15,20-tetraphenylbisbenz[5,6]indeno[1,2,3-*cd*:1',2',3'-*lm*]perylene (DBP) on hBN/Cu(111) (not shown). (For the chemical formula and optical properties of DBP, refer to the work by Rouillé et al. [71].) Here, we observed FL at sub-monolayer coverage [72]. The FL intensity was larger by a factor of ca. 10^2 compared to the FL intensity of PTCDA on hBN/Cu(111). This can be explained by the fact that DBP is a lander-type molecule. It exhibits four peripheral phenyl groups, which function as spacers between the molecular backbone and the surface [71]. This presumably, in addition to the hBN layer and a weak interaction, supports the suppression of the CT process and allows for a higher FL intensity.

We further discuss the widths of the FL peaks on Cu(111) and hBN/Cu(111) in some detail. The large width of the FL peaks may partly be caused by disorder in the molecular domains or by a very small lifetime of the excited state. Since our LEED experiments showed the formation of ordered PTCDA domains, we assume that the main contribution for the line broadening is due to a reduced FL lifetime, τ_{FL}, and that contributions from disorder and dephasing can be neglected [73,74]. Thus, the value of τ_{FL} measured from the full width at half maximum (FWHM) of the FL peaks on the frequency scale according to FWHM = $1/2\pi\tau_{FL}$ yields a lower limit for the lifetime of the excited states. Because of the small FL yield we can assign τ_{FL}

in good order to the time constant of the CT process. Hence, τ_{FL} gives quantitative information about the efficiency of the decoupling from the metal interface. Figure 6 representatively shows region II of the optical spectra of 0.60 ML PTCDA/hBN/Cu(111) and 2.55 ML PTCDA/Cu(111). Both spectra show FL_A and FL from ordered domains as either FL_B or FL_C, respectively. The FL peaks and the Raman modes were fitted with sets of Lorentzians. The widths and positions of the narrower Raman lines were fixed during the fits. The fits were thus robust concerning the determination of the FWHM of the FL peaks. The lifetimes derived from these fits are given in Table 3. All of them are of a similar size and of the order of 10^{-14} s. Thus, we can understand why we did not observe final-state effects in the photoemission spectra (i.e., UPS) of PTCDA/hBN/Cu(111) due to CT across the interface, that is, the signature of uncoupled molecules [32], albeit the FL experiments demonstrate that some coupling to the underlying Cu(111) surface is present. The reason is that the time constant of this coupling is only of the same order as the time constant of the photoemission process. Therefore, it has only a small or negligible impact on the spectra. These small lifetimes are in agreement with the findings by Stallberg et al. [39], who showed that the lifetimes of the excited states of PTCDA in the second layer on Ag(111) and in the third layer on Au(111) are smaller than an upper value of 4×10^{-12} s, which was given by the time resolution for their experiment. The small lifetimes also explain why the FL intensities were so low with respect to those measured, for example, for an ordered monolayer of PTCDA/KCl/Ag(100) [65].

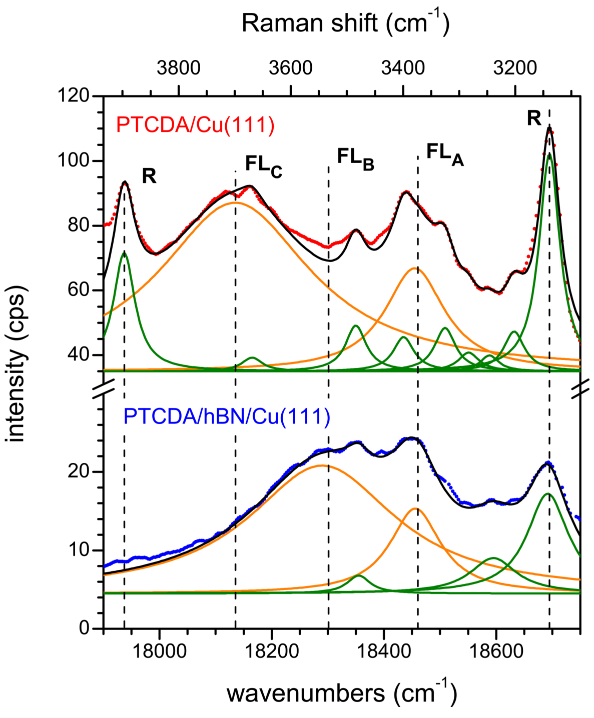

Figure 6: Fluorescence spectra of 0.60 ML PTCDA/hBN/Cu(111) (blue, bottom) and 2.55 ML PTCDA/Cu(111) (red, top). Original data (dots) are smoothed and shifted vertically. Both spectra were fitted using Lorentzian functions for the FL peaks (orange lines) and the most important Raman modes (green lines). Cumulative fits shown in black. Spectra of the clean substrates were subtracted as a background (cf. Figure 5). All spectra were measured at 20 K using a grating with 600 grooves per millimeter.

Both the small FL intensities and the short lifetime of the excited state of PTCDA on hBN/Cu(111) show that, at least for this molecule, a single hBN layer is not sufficient to completely decouple the electronic states of the molecule and the metal. While the static CT related to the interfacial bonding is suppressed, as demonstrated by UPS [32], it is still significant for the excited state. A similar observation has been made for tetracene molecules on thin insulating layers of AlO_x on $Ni_3Al(111)$ [75]. Here, too, the luminescence was found to be quenched despite the large bandgap of AlO_x (6.5 eV) and the weak interactions at the interface due to a CT between overlapping π orbitals and the electronic states of the metal.

Conclusion

We have measured the fluorescence of PTCDA on hBN/Cu(111) and Cu(111) to determine the efficiency of the electronic decoupling of PTCDA from the Cu substrate by a single hBN layer. The observation of Raman lines served as a monitor for the presence of PTCDA on the surface. In addition, LEED patterns show the formation of ordered structures and a layer-by-layer growth for at least the first two layers on hBN/Cu(111) and the first three layers on Cu(111).

Table 3: Spectral positions of the FL peaks observed for PTCDA/hBN/Cu(111) and PTCDA/Cu(111), the species the FL peaks originate from, the FWHM of the FL peaks, and the lifetimes τ_{FL} of the respective excited states. Defect FL and physisorbed PTCDA apply for both PTCDA/hBN/Cu(111) and PTCDA/Cu(111).

	FL_A	FL_B	FL_C
FL peak position	18,450 cm^{-1}	18,300 cm^{-1}	18,150 cm^{-1}
assignment	defect related FL	PTCDA/hBN	physisorbed PTCDA
FWHM	(120 ± 10) cm^{-1}	(320 ± 16) cm^{-1}	(330 ± 15) cm^{-1}
τ_{FL}	$(4.4 \pm 0.3) \times 10^{-14}$ s	$(1.7 \pm 0.1) \times 10^{-14}$ s	$(1.6 \pm 0.1) \times 10^{-14}$ s

The intensities of the Raman lines do not scale with the coverage, neither on hBN/Cu(111), nor on Cu(111). This clearly shows that additional aspects of the sample system, likely defects of the Cu substrate, play a role. We summarize the underlying mechanisms under the SERS effect. The small but discernibly different chemical shifts of Raman modes on the two surfaces are explained by the molecule–substrate interactions and specific bonding geometries of the molecule to the surface.

On both substrates, a broad fluorescence at ca. 18,450 cm^{-1} can be observed, which is identified as FL from molecules interacting with surface defects. This can be observed both for the first PTCDA layer on hBN/Cu(111) and the second layer of PTCDA on Cu(111). FL from the first PTCDA layer on Cu(111) is not observed. In contrast, the first PTCDA layer on hBN/Cu(111) already shows a weak FL from ordered domains at ca. 18,300 cm^{-1}.

On bare Cu(111), two interfacial layers of PTCDA are required to achieve an equivalent decoupling of the third layer as one layer of hBN on Cu(111) for the first PTCDA layer. The third layer on Cu(111) shows FL at ca. 18,150 cm^{-1}. This FL can be also observed in the second PTCDA layer on hBN/Cu(111) and is attributed in both cases to domains of physisorbed PTCDA on a separating PTCDA layer that forms on either the hBN layer or the first chemisorbed interfacial PTCDA monolayer on Cu(111).

While the charge transfer between PTCDA molecules and metal is sufficiently suppressed by a single hBN layer such that a weak fluorescence is observed, this suppression is limited. We estimate a lifetime of the excited state of ca. 10^{-14} s, which explains the very small fluorescence intensities. As a result, we find that a single layer of hBN on Cu(111) is able to decouple PTCDA molecules from the metal surface in so far as to prevent a total quenching of the fluorescence of the first molecular layer. However, a competing non-radiative channel for the decay of the excited state of the molecule remains as some charge transfer with a time constant of 10^{-14} s^{-1} is still possible. Thus, while a single layer of hBN provides a more efficient decoupling of a PTCDA layer from the Cu(111) surface than the first PTCDA layer itself, its efficiency is limited.

Appendix A: Structural Investigations

Here, we present the structural investigations of monolayer PTCDA on hBN/Cu(111) and Cu(111) by LEED.

The structure of PTCDA/Cu(111)

We begin with a summary of earlier reported results. At RT, PTCDA on the Cu(111) surface follows a layer-by-layer growth mode for the first three layers [76]. The obtained films remain unchanged under annealing at 530 K. From the fourth layer onward, the formation of nanocrystals begins. In TPD spectra, the desorption of the multilayer can be distinguished from the desorption of the second layer [68]. A desorption of the first layer was not observed due to a chemisorptive bonding to the Cu(111) surface. An STM study on the PTCDA monolayer on Cu(111) was published by Wagner et al. [77]. The authors reported two co-existing PTCDA phases, both displaying the characteristic herringbone arrangement, one commensurate, the other commensurate only in higher order.

In our experiments, PTCDA layers on Cu(111) were always grown at a sample temperature of 300 K. Experiments conducted in two different UHV chambers with different deposition rates resulted in identical LEED patterns. All LEED measurements were performed at 100 K.

Figure 7a shows the LEED pattern of a complete monolayer PTCDA/Cu(111) with sharp diffraction spots. The spots marked in dark red are explained by one single phase (α). Additionally, a second phase (β, marked in green in Figure 7) is present. From the relative spot intensities, the α phase is considered as the majority phase. The monolayer LEED pattern is fully explained by the α and β phases with no systematic differences between the LEED pattern and the simulation. There are systematic extinctions of all $\{h0\}$ and $\{0k\}$ spots for which h and k are odd. This points to the presence of glide planes in both phases. The structural parameters, which can be determined from the LEED pattern with small margins of error (ca. 5%), are given in Table 4. The first columns of the superstructure matrices of the α phase and the β phase exhibit elements that are integer numbers (within the margins of error). This means that both phases exhibit on-line-coincidence (OLC) [78] with the Cu(111) surface.

Both phases (α and β) exhibit a rectangular unit cell and belong to the *p*2*gg* space group. The differences between the two are the azimuthal orientations of the unit cell vectors relative to the Cu(111) surface vectors and the packing densities. The unit cell of the α phase is more closely aligned with the Cu surface vector $\mathbf{a}_1$ (2.5°) compared to the β phase (10.3°). Furthermore, the molecules in the β phase are slightly more densely packed than in the α phase ($A_\alpha = 103\% \times A_\beta$, cf. Table 4).

The most prominent feature of the LEED pattern is the characteristic arrangement of spots forming a “double triangle” (marked by a red box in Figure 7a). This is well known for the rectangular unit cell of PTCDA molecules forming the typical herringbone motif [80,81] that can also be found in the (102) plane of the bulk material [82]. In contrast to other coinage

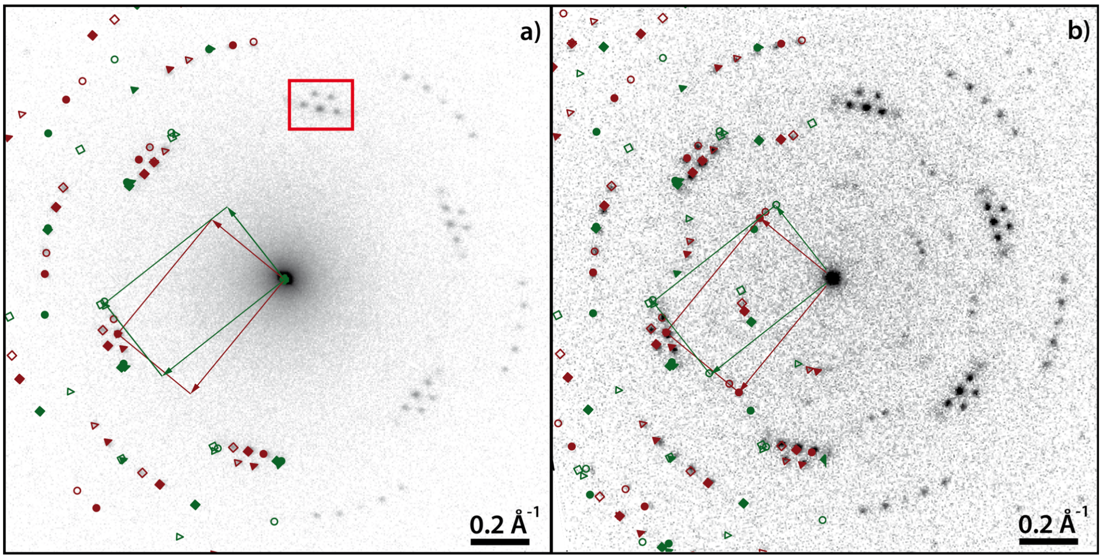

Figure 7: LEED pattern of (a) 1 ML PTCDA/Cu(111) and (b) 1.55 ML PTCDA/Cu(111) deposited at 300 K. On the left-hand side, the LEED patterns are superimposed with the corresponding simulations. Different colors refer to different PTCDA phases (dark red: α phase, green: β phase) and different symbols refer to different symmetry equivalent domains of a specific phase. The LEED patterns differ in the diffraction spots {*h*0} and {0*k*} for which *h* and *k* are odd. They are present in (b), but extinct in (a). The red box in (a) highlights the characteristic double-triangle arrangement of spots of the herringbone structure of PTCDA on surfaces. The LEED patterns were recorded at an electron energy of 77.6 eV and at a sample temperature of 100 K.

Table 4: Structural results of PTCDA/Cu(111) according to the structure model proposed by Wagner et al. [77] (phase '1' and '2') and as determined from our LEED experiments (α phase and β phase) and of PTCDA/hBN/Cu(111). The vectors of the unit cells, $\mathbf{b}_1$ and $\mathbf{b}_2$, the angle β between the two, and the areas of the unit cells, *A*, are given. ϕ is the enclosed angle between the vector $\mathbf{b}_1$ and the substrate lattice vector, $\mathbf{a}_1$. ρ is the packing density of the molecules. Additionally, the superstructure matrices, **M**, are given. The matrix for PTCDA/hBN/Cu(111) refers to the Cu(111) surface at 100 K. We note that the parameters of phase '1' and '2' are derived from the (higher-order) commensurate structure models given in [77] and slightly deviate from the experimental STM results (within error margins). The error for β is the experimental error of the STM data. The matrices given for phase '1' and '2' differ from those reported by Wagner et al. [77] because they refer to a symmetry-equivalent domain according to the rules given in [79].

	Cu(111) - phase '1' [77]	Cu(111) - phase '2' [77]
$\mathbf{b}_1$ (Å)	12.8(3)	13.4(1)
$\mathbf{b}_2$ (Å)	22.1(3)	22.0(1)
β (°)	90(5)	92(5)
A (Å^2)	283(10)	295(3)
ϕ (°)	0	11
ρ (molecules Å^{-2})	7.07 × 10^{-3}	6.78 × 10^{-3}
M	$\begin{pmatrix} 5 & 0 \\ 5 & 10 \end{pmatrix}$	$\begin{pmatrix} 5.75 & 1.25 \\ 3.40 & 9.80 \end{pmatrix}$

	Cu(111) - α phase	Cu(111) - β phase	hBN/Cu(111)
$\mathbf{b}_1$ (Å)	12.4(2)	11.8(2)	12.07(3)
$\mathbf{b}_2$ (Å)	19.5(3)	19.9(5)	19.33(9)
β (°)	90.0(9)	90.0(13)	90(3)
A (Å^2)	242(7)	235(10)	233(2)
ϕ (°)	2.5(7)	10.3(10)	9(1)
ρ (molecules Å^{-2})	8.26 × 10^{-3}	8.51 × 10^{-3}	8.85 × 10^{-3}
M	$\begin{pmatrix} 4.98(9) & 0.25(7) \\ 4.06(11) & 8.79(15) \end{pmatrix}$	$\begin{pmatrix} 5.01(8) & 0.95(9) \\ 3.03(15) & 8.82(20) \end{pmatrix}$	$\begin{pmatrix} 5.12(5) & 0.9(1) \\ 3.0(3) & 8.64(9) \end{pmatrix}$

metal substrates, however, where two separate triangles consisting of six diffraction spots are observed [80,83]. Here, the {11} and {20} spots coincide, leading to two triangles that are characteristically corner-connected by one spot.

The PTCDA β phase on Cu(111) found in LEED bears significant similarity to the structure '2' proposed by Wagner and co-workers [77]. Using the same rules for the matrix notations [79] for all structures shows that the matrix elements of structure '2' and of the β phase found in our work differ only slightly (only one entry differs by more than 13%). The orientations of the unit cell vector $\mathbf{b}_1$ with respect to the substrate is identical for both structures within ±1.6° (cf. Table 4). Hence, we propose that the β phase possibly corresponds to structure '2' by Wagner, although a difference in the size of the unit cell remains. Structure '1' given by Wagner, however, was not observed in our LEED experiments and differs from our α phase. Furthermore, the packing densities found for the α phase and the β phase agree well (within 2.5%) with those of the (102) planes of the PTCDA bulk phases (8.40×10^{-3} and 8.32×10^{-3} molecules Å^{-2}, respectively [82]), while the densities in structures '1' and '2' differ more significantly from these (by 14% and 21%). These differences may possibly be due to a difference in the substrate quality or preparation conditions in the two studies.

We now turn to PTCDA coverages above 1 ML. Both monolayer phases of PTCDA on Cu(111) (α and β) exist in parallel from the (sub-)monolayer to the multilayer regime. Additional deposition of PTCDA up to a coverage of 3 ML leads to additional weak spots in the LEED pattern (see Figure 7b). They can also be explained by the two PTCDA phases identified above. The spots that appear at distances of 0.3–0.6 Å^{-1} from the specular spot correspond to $\{h0\}$ and $\{0k\}$ spots of the α phase and the β phase for which h and k are odd and which were extinct before. No spot shifts as a function of the coverage were found. This may have two reasons. Either the molecules form only a single wetting layer on which additional molecules form clusters, or the higher layers adapt the same structure as the first layer without mismatch. Two observations point to the latter case: The intensity of the adsorbate diffraction spots increases with coverage while the relative intensity of the specular spot decreases. In addition, the {10} and {01} spots become detectable, which means that the glide planes of the adsorbate structure vanish. The glide lines in the space group $p2gg$ of the PTCDA unit cell only exist if the underlying Cu(111) surface is not taken into account. For the first monolayer, this may be the case because the small periodicity of the Cu atoms compared to the PTCDA periodicity is not "felt" by the electrons scattered by a single PTCDA layer. For a second PTCDA layer, however, the periodicities in this layer and in the underlying monolayer are identical. Both layers are shifted laterally against each other [82], which breaks the glide plane symmetry. Thus, the LEED data indicate the growth of at least two or even more complete layers of PTCDA on Cu(111). This is in accordance with the results reported in [68,76].

In summary, our LEED investigations show that PTCDA on Cu(111) forms two co-existing phases, both of them displaying on-line-coincidence to the surface with a herringbone arrangement of the molecules. Both are observed from the (sub-)monolayer regime to at least the beginning of the growth of the third layer. The adsorbate forms at least two complete layers before clusters form.

PTCDA on hBN/Cu(111)

Figure 8 shows LEED patterns of PTCDA/hBN/Cu(111) at a coverage of 2 ± 0.5 ML (Figure 8a,c) and 0.8 ± 0.2 ML (Figure 8b). All structures were grown at a sample temperature of 260 K and a deposition rate of 1 ML/min. They were observed in two different UHV chambers. LEED measurements were performed at 110 K. Note that the LEED pattern in Figure 8a has previously been published in [32]. In that study, we attributed this LEED pattern to a pure monolayer of PTCDA on hBN/Cu(111). Further analysis now leads us to the conclusion that the LEED pattern stems from a slightly higher coverage. This will be discussed in further detail below. Nonetheless, our findings presented in [32] still hold.

Commonly, two kinds of LEED patterns were observed for PTCDA/hBN/Cu(111) and were found from the sub-monolayer to the multilayer regime. The observable pattern, and thus the PTCDA structure that formed, did not depend on the PTCDA coverage, but rather on the quality of the hBN layer. The azimuthally smeared out intensity in Figure 8b,c (which was most commonly observed) points to an azimuthal disorder of the PTCDA domains on hBN/Cu(111), both in the first and in higher layers. In some cases, LEED patterns such as that given in Figure 8a were observed, which shows spots that are exceptionally not smeared out azimuthally. The radii of the rings in Figure 8b,c match the distances of the spots from the specular spot in Figure 8a.

We attribute the higher azimuthal order, which manifests in the more discrete spots, to a lower-quality hBN layer with defects or uncovered areas of Cu(111). Both may allow a pinning of PTCDA molecules to the Cu(111) surface. These molecules function as growth nuclei for PTCDA domains and determine the azimuthal orientation of these domains. Evidence for this interpretation is given by the fact that the orientation of the PTCDA domains on hBN/Cu(111) is in agreement with the orientation of PTCDA domains in the β phase on Cu(111) (within

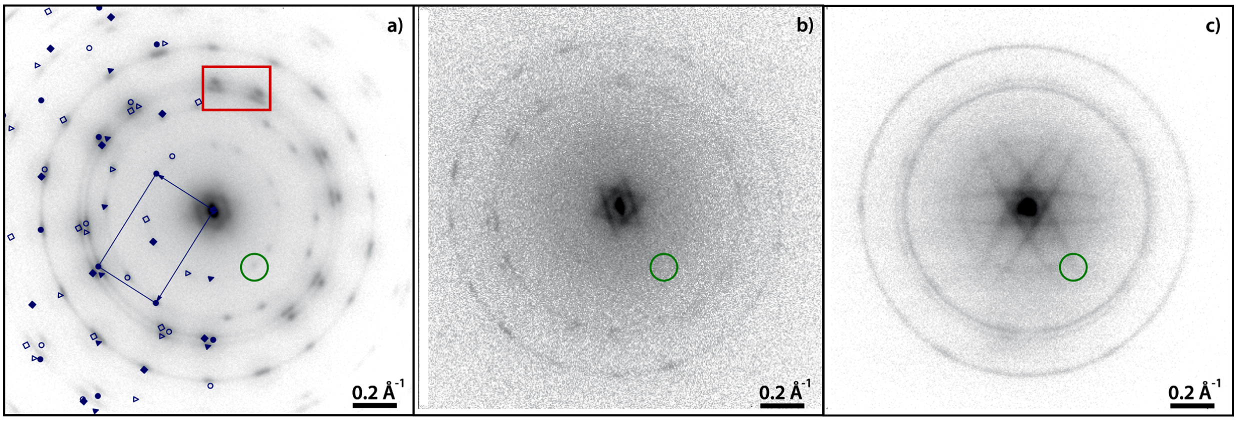

Figure 8: LEED pattern of PTCDA layers on hBN/Cu(111). (a) LEED pattern of 2 ± 0.5 ML PTCDA/hBN/Cu(111). The intensities of the LEED spots are azimuthally smeared out. The maxima in the ring intensities indicate the presence of azimuthally ordered domains. The left half of the LEED pattern is superimposed with the corresponding simulation. Different symbols refer to different symmetrically equivalent domains. This is the same LEED pattern as the one shown in [32], which we originally interpreted as a monolayer. More detailed analysis shows now that the second PTCDA layer has started to form (see main text). The red box highlights the characteristic double-triangle arrangement of spots of the herringbone structure of PTCDA on surfaces. The green ring marks a {10} diffraction spot. (b) LEED pattern of 0.8 ± 0.2 ML PTCDA/hBN/Cu(111). The LEED intensity is homogeneously distributed in rings around the specular spot. The radii of the rings match the distances of the spots in (a) from the specular spot. The green ring marks the same position as in (a). However, the rings corresponding to spot positions of $\{h0\}$ and $\{0k\}$ for which h or k are odd are extinct. (c) LEED pattern of 2 ± 0.5 ML PTCDA/hBN/Cu(111). The LEED intensity is homogeneously distributed in rings around the specular spot as in (b). At this higher coverage, the first-order PTCDA spots are no longer extinct. At the position of the green circle, a faint homogeneous ring can hence be observed. All LEED patterns were recorded at an electron energy of 31 ± 1 eV and at a sample temperature of 110 K.

the error margins, cf. Table 4). The comparison to PTCDA/Cu(111) shows that the β phase has a higher structural resemblance with PTCDA/hBN/Cu(111) than the majority α phase, not only with regard to the orientation, but also to the size of the unit cell (with a deviation of 0.85% of the areas of the unit cells of PTCDA/hBN/Cu(111) and the β phase).

However, in general, PTCDA domains on hBN/Cu(111) have no intrinsically preferred orientation. In Figure 8b and Figure 8c, near the specular spot, a star-like pattern caused by multiple scattering of electrons on hBN/Cu(111) [30] can be observed. Its sharpness points to the high quality of the hBN layer that leads to the homogeneous distribution of the azimuthal orientation of the PTCDA domains.

The discrete spots in Figure 8a support the determination of the structural parameters (cf. Table 4). The similarity of this LEED pattern to those of other PTCDA structures on surfaces is obvious. This includes the double-triangle arrangement of spots (marked by a red box), which makes the structural difference of PTCDA on Cu(111) and on hBN/Cu(111) apparent. Here, the double triangle is formed by six spots leading to two separated triangles. (On Cu(111), these are connected at their corners.) The structure is incommensurate to the hBN layer, and also to the underlying Cu(111) surface. This is in accordance with a weak corrugation of the PTCDA/hBN interaction potential. The LEED pattern points to an arrangement of the molecules in the herringbone motif, as on Cu(111) [77] and other substrates [80,83]. This was also seen in STM measurements [32].

A comparison between the LEED pattern of the first PTCDA layer on hBN/Cu(111) (Figure 8b) with those of higher PTCDA layers (Figure 8a,c) shows that the diffraction spots $\{h0\}$ and $\{0k\}$ for which h or k are odd are extinct for the monolayer, but appear in the second layer. In Figure 8a, a discrete {10} spot is marked by a green circle. In Figure 8c, a line of a continuous ring that corresponds to the {10} spots of PTCDA is seen in the same circle. In Figure 8b, however, there is no intensity at this position in the LEED pattern. The same discussion on the extinction as for PTCDA/Cu(111) applies here (see Section “The structure of PTCDA/Cu(111)”). Furthermore, the distance of the diffraction spots from the specular spot does not change with increasing coverage. This indicates the same layer-by-layer growth mode of PTCDA on both Cu(111) and hBN/Cu(111).

In summary, monolayers of PTCDA/Cu(111) and PTCDA/hBN/Cu(111), despite their structural similarity, can be distinguished by their LEED patterns on the basis of two crucial features. On Cu(111), the “double triangle” is formed by five spots, making it a corner-connected double triangle, while on hBN/Cu(111) six spots form two distinct triangles. Furthermore, the azimuthal smearing of the spots of PTCDA on hBN/

Cu(111) is specific. Additionally, LEED allows the identification of a second PTCDA layer on Cu(111) and hBN/Cu(111) due to the appearance of additional spots, which are absent in the monolayers for symmetry reasons.

Appendix B: Additional optical spectra

Here, additional optical spectra that were referred to in the main text are shown. As mentioned in Section 3.1, the Raman lines in region III of the optical spectra were identified using a dye laser with a tunable wavelength. The Raman lines shift according to the wavelength of the laser. Figure 9 shows spectra recorded with wavelengths between 497 and 507 nm as a function of the Raman shift. Here, all Raman peaks stay at the same energies as expected. Notably, the intensities of the Raman modes change as a function of wavelength. The highest intensities are observed for 458 nm, exceeding the intensities for 502.66 nm (the highest in Figure 9) by a factor of seven.

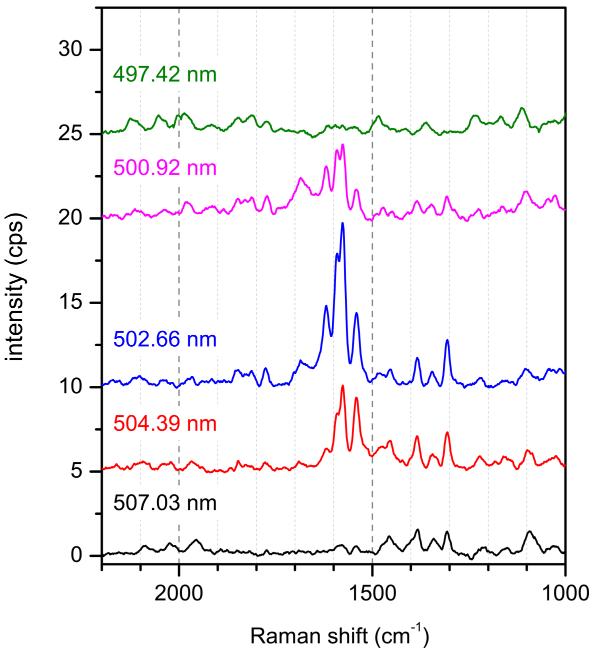

Figure 9: Raman modes of 0.90 ML PTCDA on hBN/Cu(111), measured with a dye laser with tunable wavelength (497–507 nm). Data are smoothed and shifted vertically after subtraction of a background. All spectra were measured at 20 K using a grating with 1200 grooves per millimeter.

In Section 3.1, we stated that PTCDA deposited on hBN/Cu(111) at a sample temperature of 300 K leads to the same FL as PTCDA deposited at 20 K and subsequently annealed at 300 K. Figure 10 shows spectra from PTCDA/hBN/Cu(111) prepared according to either recipe. In both cases, FL_A and FL_B are present.

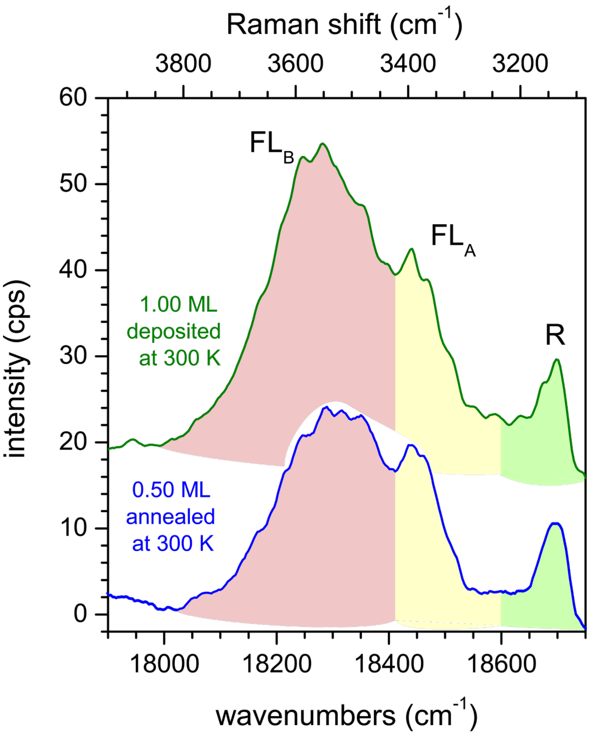

Figure 10: FL spectra of 0.50 ML PTCDA on hBN/Cu(111), deposited at 20 K and subsequently annealed at 300 K (blue, c.f Figure 2) and 1.00 ML PTCDA on hBN/Cu(111), deposited at 300 K (green). Data are smoothed and shifted vertically after subtraction of a background. All spectra were measured at 20 K using a grating with 600 grooves per millimeter.

Acknowledgements

We wish to acknowledge C. Marquardt, M. Scheuermann, and B. Wolff for experimental support and E. LeMoal and V. Wagner for helpful discussions.

References

1. Xu, M.; Liang, T.; Shi, M.; Chen, H. *Chem. Rev.* **2013,** *113,* 3766–3798. doi:10.1021/cr300263a
2. Tan, C.; Cao, X.; Wu, X.-J.; He, Q.; Yang, J.; Zhang, X.; Chen, J.; Zhao, W.; Han, S.; Nam, G.-H.; Sindoro, M.; Zhang, H. *Chem. Rev.* **2017,** *117,* 6225–6331. doi:10.1021/acs.chemrev.6b00558
3. Novoselov, K. S.; Mishchenko, A.; Carvalho, A.; Castro Neto, A. H. *Science* **2016,** *353,* aac9439. doi:10.1126/science.aac9439
4. Yang, X.; Krieger, I.; Lüftner, D.; Weiß, S.; Heepenstrick, T.; Hollerer, M.; Hurdax, P.; Koller, G.; Sokolowski, M.; Puschnig, P.; Ramsey, M. G.; Tautz, F. S.; Soubatch, S. *Chem. Commun.* **2018,** *54,* 9039–9042. doi:10.1039/c8cc03334j
5. Gebauer, W.; Langner, A.; Schneider, M.; Sokolowski, M.; Umbach, E. *Phys. Rev. B* **2004,** *69,* 155431. doi:10.1103/physrevb.69.155431
6. Chance, R. R.; Prock, A.; Silbey, R. Molecular Fluorescence and Energy Transfer Near Interfaces. In *Advances in Chemical Physics;* Prigogine, I.; Rice, S. A., Eds.; John Wiley & Sons, Ltd, 1978; Vol. 37, pp 1–65. doi:10.1002/9780470142561.ch1

7. Campion, A.; Gallo, A. R.; Harris, C. B.; Robota, H. J.; Whitmore, P. M. *Chem. Phys. Lett.* **1980,** *73,* 447–450. doi:10.1016/0009-2614(80)80692-0
8. Neppl, S.; Bauer, U.; Menzel, D.; Feulner, P.; Shaporenko, A.; Zharnikov, M.; Kao, P.; Allara, D. L. *Chem. Phys. Lett.* **2007,** *447,* 227–231. doi:10.1016/j.cplett.2007.09.013
9. Kao, P.; Neppl, S.; Feulner, P.; Allara, D. L.; Zharnikov, M. *J. Phys. Chem. C* **2010,** *114,* 13766–13773. doi:10.1021/jp1042816
10. Müller, M.; Le Moal, E.; Scholz, R.; Sokolowski, M. *Phys. Rev. B* **2011,** *83,* 241203. doi:10.1103/physrevb.83.241203
11. Luo, Y.; Chen, G.; Zhang, Y.; Zhang, L.; Yu, Y.; Kong, F.; Tian, X.; Zhang, Y.; Shan, C.; Luo, Y.; Yang, J.; Sandoghdar, V.; Dong, Z.; Hou, J. G. *Phys. Rev. Lett.* **2019,** *122,* 233901. doi:10.1103/physrevlett.122.233901
12. Imada, H.; Miwa, K.; Imai-Imada, M.; Kawahara, S.; Kimura, K.; Kim, Y. *Phys. Rev. Lett.* **2017,** *119,* 013901. doi:10.1103/physrevlett.119.013901
13. Kimura, K.; Miwa, K.; Imada, H.; Imai-Imada, M.; Kawahara, S.; Takeya, J.; Kawai, M.; Galperin, M.; Kim, Y. *Nature* **2019,** *570,* 210–213. doi:10.1038/s41586-019-1284-2
14. Watanabe, K.; Taniguchi, T.; Kanda, H. *Nat. Mater.* **2004,** *3,* 404–409. doi:10.1038/nmat1134
15. Falin, A.; Cai, Q.; Santos, E. J. G.; Scullion, D.; Qian, D.; Zhang, R.; Yang, Z.; Huang, S.; Watanabe, K.; Taniguchi, T.; Barnett, M. R.; Chen, Y.; Ruoff, R. S.; Li, L. H. *Nat. Commun.* **2017,** *8,* 15815. doi:10.1038/ncomms15815
16. Mahvash, F.; Eissa, S.; Bordjiba, T.; Tavares, A. C.; Szkopek, T.; Siaj, M. *Sci. Rep.* **2017,** *7,* 42139. doi:10.1038/srep42139
17. Li, L. H.; Cervenka, J.; Watanabe, K.; Taniguchi, T.; Chen, Y. *ACS Nano* **2014,** *8,* 1457–1462. doi:10.1021/nn500059s
18. Lee, K. H.; Shin, H.-J.; Lee, J.; Lee, I.-y.; Kim, G.-H.; Choi, J.-Y.; Kim, S.-W. *Nano Lett.* **2012,** *12,* 714–718. doi:10.1021/nl203635v
19. Auwärter, W. *Surf. Sci. Rep.* **2019,** *74,* 1–95. doi:10.1016/j.surfrep.2018.10.001
20. Paulheim, A.; Marquardt, C.; Aldahhak, H.; Rauls, E.; Schmidt, W. G.; Sokolowski, M. *J. Phys. Chem. C* **2016,** *120,* 11926–11937. doi:10.1021/acs.jpcc.6b01956
21. Eisfeld, A.; Marquardt, C.; Paulheim, A.; Sokolowski, M. *Phys. Rev. Lett.* **2017,** *119,* 097402. doi:10.1103/physrevlett.119.097402
22. Kerfoot, J.; Korolkov, V. V.; Nizovtsev, A. S.; Jones, R.; Taniguchi, T.; Watanabe, K.; Lesanovsky, I.; Olmos, B.; Besley, N. A.; Besley, E.; Beton, P. H. *J. Chem. Phys.* **2018,** *149,* 054701. doi:10.1063/1.5041418
23. Forker, R.; Dienel, T.; Krause, A.; Gruenewald, M.; Meissner, M.; Kirchhuebel, T.; Gröning, O.; Fritz, T. *Phys. Rev. B* **2016,** *93,* 165426. doi:10.1103/physrevb.93.165426
24. Joshi, S.; Ecija, D.; Koitz, R.; Iannuzzi, M.; Seitsonen, A. P.; Hutter, J.; Sachdev, H.; Vijayaraghavan, S.; Bischoff, F.; Seufert, K.; Barth, J. V.; Auwärter, W. *Nano Lett.* **2012,** *12,* 5821–5828. doi:10.1021/nl303170m
25. Koitz, R.; Seitsonen, A. P.; Iannuzzi, M.; Hutter, J. *Nanoscale* **2013,** *5,* 5589. doi:10.1039/c3nr00709j
26. Hite, J. K.; Robinson, Z. R.; Eddy, C. R., Jr.; Feigelson, B. N. *ACS Appl. Mater. Interfaces* **2015,** *7,* 15200–15205. doi:10.1021/acsami.5b00723
27. Preobrajenski, A. B.; Vinogradov, A. S.; Mårtensson, N. *Surf. Sci.* **2005,** *582,* 21–30. doi:10.1016/j.susc.2005.02.047
28. Lyalin, A.; Nakayama, A.; Uosaki, K.; Taketsugu, T. *Top. Catal.* **2014,** *57,* 1032–1041. doi:10.1007/s11244-014-0267-7
29. Lin, S.; Huang, J.; Gao, X. *Phys. Chem. Chem. Phys.* **2015,** *17,* 22097–22105. doi:10.1039/c5cp03027g
30. Brülke, C.; Heepenstrick, T.; Humberg, N.; Krieger, I.; Sokolowski, M.; Weiß, S.; Tautz, F. S.; Soubatch, S. *J. Phys. Chem. C* **2017,** *121,* 23964–23973. doi:10.1021/acs.jpcc.7b06107
31. Schwarz, M.; Riss, A.; Garnica, M.; Ducke, J.; Deimel, P. S.; Duncan, D. A.; Thakur, P. K.; Lee, T.-L.; Seitsonen, A. P.; Barth, J. V.; Allegretti, F.; Auwärter, W. *ACS Nano* **2017,** *11,* 9151–9161. doi:10.1021/acsnano.7b04022
32. Brülke, C.; Heepenstrick, T.; Krieger, I.; Wolff, B.; Yang, X.; Shamsaddinlou, A.; Weiß, S.; Bocquet, F. C.; Tautz, F. S.; Soubatch, S.; Sokolowski, M. *Phys. Rev. B* **2019,** *99,* 121404. doi:10.1103/physrevb.99.121404
33. Duhm, S.; Gerlach, A.; Salzmann, I.; Bröker, B.; Johnson, R. L.; Schreiber, F.; Koch, N. *Org. Electron.* **2008,** *9,* 111–118. doi:10.1016/j.orgel.2007.10.004
34. Martínez-Galera, A. J.; Gómez-Rodríguez, J. M. *J. Phys. Chem. C* **2019,** *123,* 1866–1873. doi:10.1021/acs.jpcc.8b10810
35. Gerlach, A.; Sellner, S.; Schreiber, F.; Koch, N.; Zegenhagen, J. *Phys. Rev. B* **2007,** *75,* 045401. doi:10.1103/physrevb.75.045401
36. Ng, M. L.; Preobrajenski, A. B.; Zakharov, A. A.; Vinogradov, A. S.; Krasnikov, S. A.; Cafolla, A. A.; Mårtensson, N. *Phys. Rev. B* **2010,** *81,* 115449. doi:10.1103/physrevb.81.115449
37. Koslowski, S.; Rosenblatt, D.; Kabakchiev, A.; Kuhnke, K.; Kern, K.; Schlickum, U. *Beilstein J. Nanotechnol.* **2017,** *8,* 1388–1395. doi:10.3762/bjnano.8.140
38. Joshi, S.; Bischoff, F.; Koitz, R.; Ecija, D.; Seufert, K.; Seitsonen, A. P.; Hutter, J.; Diller, K.; Urgel, J. I.; Sachdev, H.; Barth, J. V.; Auwärter, W. *ACS Nano* **2014,** *8,* 430–442. doi:10.1021/nn406024m
39. Stallberg, K.; Namgalies, A.; Höfer, U. *Phys. Rev. B* **2019,** *99,* 125410. doi:10.1103/physrevb.99.125410
40. Yeshchenko, O. A.; Bondarchuk, I. S.; Losytskyy, M. Y. *J. Appl. Phys.* **2014,** *116,* 054309. doi:10.1063/1.4892432
41. Kaiser, R.; Friedrich, M.; Schmitz-Hübsch, T.; Sellam, F.; Kampen, T. U.; Leo, K.; Zahn, D. R. T. *Fresenius' J. Anal. Chem.* **1999,** *363,* 189–192. doi:10.1007/s002160051169
42. Wagner, V. *Phys. Status Solidi A* **2001,** *188,* 1297–1305. doi:10.1002/1521-396x(200112)188:4<1297::aid-pssa1297>3.0.co;2-x
43. Scholz, R.; Kobitski, A. Y.; Kampen, T. U.; Schreiber, M.; Zahn, D. R. T.; Jungnickel, G.; Elstner, M.; Sternberg, M.; Frauenheim, T. *Phys. Rev. B* **2000,** *61,* 13659–13669. doi:10.1103/physrevb.61.13659
44. Kilian, L.; Hauschild, A.; Temirov, R.; Soubatch, S.; Schöll, A.; Bendounan, A.; Reinert, F.; Lee, T.-L.; Tautz, F. S.; Sokolowski, M.; Umbach, E. *Phys. Rev. Lett.* **2008,** *100,* 136103. doi:10.1103/physrevlett.100.136103
45. Otto, A.; Mrozek, I.; Grabhorn, H.; Akemann, W. *J. Phys.: Condens. Matter* **1992,** *4,* 1143–1212. doi:10.1088/0953-8984/4/5/001
46. Schlücker, S. *Angew. Chem., Int. Ed.* **2014,** *53,* 4756–4795. doi:10.1002/anie.201205748
47. Cialla, D.; März, A.; Böhme, R.; Theil, F.; Weber, K.; Schmitt, M.; Popp, J. *Anal. Bioanal. Chem.* **2012,** *403,* 27–54. doi:10.1007/s00216-011-5631-x
48. García-Vidal, F. J.; Pendry, J. B. *Phys. Rev. Lett.* **1996,** *77,* 1163–1166. doi:10.1103/physrevlett.77.1163
49. Xia, M. *Coatings* **2018,** *8,* 137. doi:10.3390/coatings8040137
50. Ling, X.; Fang, W.; Lee, Y.-H.; Araujo, P. T.; Zhang, X.; Rodriguez-Nieva, J. F.; Lin, Y.; Zhang, J.; Kong, J.; Dresselhaus, M. S. *Nano Lett.* **2014,** *14,* 3033–3040. doi:10.1021/nl404610c

51. Ehrenreich, H.; Philipp, H. R. *Phys. Rev.* **1962,** *128,* 1622–1629. doi:10.1103/physrev.128.1622
52. Babar, S.; Weaver, J. H. *Appl. Opt.* **2015,** *54,* 477. doi:10.1364/ao.54.000477
53. Schneider, M. Vibronische und optische Eigenschaften ultradünner organischer Filme am Beispiel PTCDA/Ag(111). Ph.D. Thesis, Universität Würzburg, Würzburg, 2002.
54. Paulheim, A.; Marquardt, C.; Sokolowski, M.; Hochheim, M.; Bredow, T.; Aldahhak, H.; Rauls, E.; Schmidt, W. G. *Phys. Chem. Chem. Phys.* **2016,** *18,* 32891–32902. doi:10.1039/c6cp05661j
55. Tenne, D. A.; Park, S.; Kampen, T. U.; Das, A.; Scholz, R.; Zahn, D. R. T. *Phys. Rev. B* **2000,** *61,* 14564–14569. doi:10.1103/physrevb.61.14564
56. Hauschild, A.; Temirov, R.; Soubatch, S.; Bauer, O.; Schöll, A.; Cowie, B. C. C.; Lee, T.-L.; Tautz, F. S.; Sokolowski, M. *Phys. Rev. B* **2010,** *81,* 125432. doi:10.1103/physrevb.81.125432
57. Hochheim, M.; Paulheim, A.; Sokolowski, M.; Bredow, T. *J. Phys. Chem. C* **2016,** *120,* 24240–24249. doi:10.1021/acs.jpcc.6b08540
58. Bauer, O. Surface bonding of a functionalized aromatic molecule: Adsorption configurations of PTCDA on coinage metal surfaces. Ph.D. Thesis, Universität Bonn, Bonn, 2014.
59. Tautz, F. S.; Eremtchenko, M.; Schaefer, J. A.; Sokolowski, M.; Shklover, V.; Umbach, E. *Phys. Rev. B* **2002,** *65,* 125405. doi:10.1103/physrevb.65.125405
60. Marquardt, C.; Paulheim, A.; Rohbohm, N.; Merkel, R.; Sokolowski, M. *Rev. Sci. Instrum.* **2017,** *88,* 083702. doi:10.1063/1.4997953
61. Gorbachev, R. V.; Riaz, I.; Nair, R. R.; Jalil, R.; Britnell, L.; Belle, B. D.; Hill, E. W.; Novoselov, K. S.; Watanabe, K.; Taniguchi, T.; Geim, A. K.; Blake, P. *Small* **2011,** *7,* 465–468. doi:10.1002/smll.201001628
62. Bresnehan, M. S.; Hollander, M. J.; Wetherington, M.; LaBella, M.; Trumbull, K. A.; Cavalero, R.; Snyder, D. W.; Robinson, J. A. *ACS Nano* **2012,** *6,* 5234–5241. doi:10.1021/nn300996t
63. Nakhaie, S.; Wofford, J. M.; Schumann, T.; Jahn, U.; Ramsteiner, M.; Hanke, M.; Lopes, J. M. J.; Riechert, H. *Appl. Phys. Lett.* **2015,** *106,* 213108. doi:10.1063/1.4921921
64. Xu, Z.; Tian, H.; Khanaki, A.; Zheng, R.; Suja, M.; Liu, J. *Sci. Rep.* **2017,** *7,* 43100. doi:10.1038/srep43100
65. Müller, M.; Paulheim, A.; Eisfeld, A.; Sokolowski, M. *J. Chem. Phys.* **2013,** *139,* 044302. doi:10.1063/1.4813521
66. Preobrajenski, A. B.; Nesterov, M. A.; Ng, M. L.; Vinogradov, A. S.; Mårtensson, N. *Chem. Phys. Lett.* **2007,** *446,* 119–123. doi:10.1016/j.cplett.2007.08.028
67. Schneider, M.; Umbach, E.; Sokolowski, M. *Chem. Phys.* **2006,** *325,* 185–192. doi:10.1016/j.chemphys.2005.08.059
68. Wagner, T.; Karacuban, H.; Möller, R. *Surf. Sci.* **2009,** *603,* 482–490. doi:10.1016/j.susc.2008.12.007
69. Han, Q.; Shan, H.; Deng, J.; Zhao, A.; Wang, B.; Hou, J. G. *Nanoscale* **2014,** *6,* 7934–7939. doi:10.1039/c4nr00017j
70. Wolff, B. Determination of the desorption energy of PTCDA on hBN/Cu(111) by thermal desorption spectroscopy. Master's Thesis, Universität Bonn, Bonn, 2019.
71. Rouillé, G.; Kirchhuebel, T.; Rink, M.; Gruenewald, M.; Kröger, J.; Forker, R.; Fritz, T. *Phys. Chem. Chem. Phys.* **2015,** *17,* 30404–30416. doi:10.1039/c5cp03761a
72. Wolff, B. Dynamics of Open Quantum Systems. Master's Thesis, Universität Bonn, Bonn, 2019.
73. Valeur, B. *Molecular Fluorescence,* 1st ed.; Wiley-VCH: Weinheim, Germany, 2002.
74. Ambrose, W. P.; Basché, T.; Moerner, W. E. *J. Chem. Phys.* **1991,** *95,* 7150–7163. doi:10.1063/1.461392
75. Langner, A.; Su, Y.; Sokolowski, M. *Phys. Rev. B* **2006,** *74,* 045428. doi:10.1103/physrevb.74.045428
76. Wagner, T.; Bannani, A.; Bobisch, C.; Karacuban, H.; Stöhr, M.; Gabriel, M.; Möller, R. *Org. Electron.* **2004,** *5,* 35–43. doi:10.1016/j.orgel.2003.12.001
77. Wagner, T.; Bannani, A.; Bobisch, C.; Karacuban, H.; Möller, R. *J. Phys.: Condens. Matter* **2007,** *19,* 056009. doi:10.1088/0953-8984/19/5/056009
78. Forker, R.; Meissner, M.; Fritz, T. *Soft Matter* **2017,** *13,* 1748–1758. doi:10.1039/c6sm02688e
79. Barlow, S. M.; Raval, R. *Surf. Sci. Rep.* **2003,** *50,* 201–341. doi:10.1016/s0167-5729(03)00015-3
80. Glöckler, K.; Seidel, C.; Soukopp, A.; Sokolowski, M.; Umbach, E.; Böhringer, M.; Berndt, R.; Schneider, W.-D. *Surf. Sci.* **1998,** *405,* 1–20. doi:10.1016/s0039-6028(97)00888-1
81. Kilian, L.; Umbach, E.; Sokolowski, M. *Surf. Sci.* **2006,** *600,* 2633–2643. doi:10.1016/j.susc.2006.03.049
82. Ogawa, T.; Kuwamoto, K.; Isoda, S.; Kobayashi, T.; Karl, N. *Acta Crystallogr., Sect. B: Struct. Sci.* **1999,** *55,* 123–130. doi:10.1107/s0108768198009872
83. Mannsfeld, S.; Toerker, M.; Schmitz-Hübsch, T.; Sellam, F.; Fritz, T.; Leo, K. *Org. Electron.* **2001,** *2,* 121–134. doi:10.1016/s1566-1199(01)00018-0

License and Terms

The definitive version of this article is the electronic one which can be found at:
https://doi.org/10.3762/bjnano.11.149

BEILSTEIN JOURNAL OF NANOTECHNOLOGY

Extended iron phthalocyanine islands self-assembled on a Ge(001):H surface

Rafal Zuzak, Marek Szymonski and Szymon Godlewski*

Full Research Paper

Open Access

Address:
Centre for Nanometer-Scale Science and Advanced Materials, NANOSAM, Faculty of Physics, Astronomy, and Applied Computer Science, Jagiellonian University, Łojasiewicza 11, PL 30-348 Kraków, Poland

Email:
Szymon Godlewski* - szymon.godlewski@uj.edu.pl

* Corresponding author

Keywords:
hydrogenated semiconductor; iron phthalocyanine (FePc); scanning tunneling microscopy; self-assembly

Beilstein J. Nanotechnol. **2021,** *12,* 232–241.
https://doi.org/10.3762/bjnano.12.19

Received: 31 July 2020
Accepted: 19 February 2021
Published: 05 March 2021

This article is part of the thematic issue "Molecular assemblies on surfaces – towards physical and electronic decoupling of organic molecules".

Guest Editor: S. Maier

Abstract

Self-assembly of iron(II) phthalocyanine (FePc) molecules on a Ge(001):H surface results in monolayer islands extending over hundreds of nanometers and comprising upright-oriented entities. Scanning tunneling spectroscopy reveals a transport gap of 2.70 eV in agreement with other reports regarding isolated FePc molecules. Detailed analysis of single FePc molecules trapped at surface defects indicates that the molecules stay intact upon adsorption and can be manipulated away from surface defects onto a perfectly hydrogenated surface. This allows for their isolation from the germanium surface.

Introduction

The development of molecular circuitry requires the preparation of nanostructures isolated from the influence of the underlying substrate. This is of crucial importance for atomic and single-molecule prototypes, but holds also for layered materials. Single-molecule prototypes or molecular nanostructures are often prepared on metals, which usually provide a sufficiently low diffusion barrier for efficient self-assembly and simultaneously allow for in-depth analysis through atomically precise tools from the family of scanning probe microscopes [1-3]. At the same time, however, metallic substrates usually influence the properties of adsorbed molecular species, leading to hybridization, charge transfer, or screening at the interface [4-6]. Also, metallic surfaces may provide relatively weak binding, dominated by van der Waals interactions [7], but the lack of a gap results in broadening and shifting of the molecular resonances. In recent years, it has been proposed to add a buffer layer between the metallic substrate and the molecules of interest [8,9]. This approach allows for the decoupling of the molecules or molecular nanoarchitectures from the metallic substrate and, thus, helps to retain the originally designed properties.

Different insulating films have already been applied, ranging from ionic salts such as NaCl [8,9], KCl [10,11], or KBr [12], through oxide [13] or nitride [14] layers to molecular wetting layers [15] and two-dimensional materials, such as graphene [16,17], hBN [11,18], or even organic layers [19]. Recently, it has been proposed that a monolayer of transition metal dichalcogenides, for example, MoS_2, may play a similar role [4,20,21].

Similarly, it has been reported that the passivation of semiconducting materials, which removes surface dangling bonds and significantly reduces surface reactivity, may also provide a sufficiently insulating layer for an efficient decoupling of molecular structures from the substrate influence. Among such surfaces, hydrogen-passivated Si(001):H [22,23], Si(111):H [24], and Ge(001):H [25-28] surfaces are most commonly mentioned. Iron phthalocyanines (FePc) have been studied on Si(111):H [24] and it was concluded that the molecules are weakly coupled to the substrate. Interestingly, in another study, it has been reported that FePc molecules deposited at room temperature on Si(111):H serve as sources of single Fe atoms and undergo de-metalation [29]. Importantly, hydrogen-passivated Si/Ge surfaces may also act as platforms for nanostructurization by the atomically precise desorption of individual hydrogen atoms and the creation of unsaturated dangling bonds (DBs) or DB systems with predesigned architecture [30,31]. In such a way, different atomic nanostructures could be fabricated in a controllable manner; artificial molecules [32] or surface logic gates [33] could act as examples. Further, such nanostructures may be applied in hybrid systems to couple organic molecules with the underlying surface in a controlled way [34,35], or even provide pivot points for nanoscale rotors [30]. It is also worth mentioning that bringing into practice newly designed nanoscale circuits might be beneficial especially on Ge or Si surfaces, since those semiconductors are at the foundations of traditional electronics. Finally, hydrogen-passivated semiconductors may also provide sufficient isolation for organic molecules to allow for the growth of molecular crystals. It has been already shown that PTCDA molecules form ordered islands on hydrogen-passivated Si or Ge surfaces [36-39]. For instance, it has been shown that on Ge(001):H those molecules form hexagonal islands composed from flat-lying molecules that are sufficiently decoupled from the underlying semiconductor [36]. Vicinal Si(001):H has been applied in order to achieve control over the growth of molecular columns of CuPc molecules [40].

Metal phthalocyanines exhibit useful physical, chemical, and electronic properties. They are considered as promising candidates for practical applications in (opto)electronics and photovoltaics, for instance, in solar cells or transistors [24,41,42]. Moreover, they are ideal candidates to study the influence of the interaction between the central metal atom and the surrounding ligands on the overall properties. Commonly, metal phthalocyanines and their derivatives have been investigated on crystalline metal surfaces [43-57]. However, the need to electronically decouple organic moieties from the underlying substrates directed the attention towards insulators and/or semiconductors. Metal phthalocyanines on semiconducting TiO_2 surfaces have been frequently studied in the context of a future application in photovoltaics [58,59]. A few of the phthalocyanines with different central metal atoms exhibit magnetic properties [60] and thus attract growing attention.

Having this in mind, we have sublimed FePc molecules on a Ge(001):H surface and studied the formation of molecular nanoislands. Our STM data indicate that FePc molecules stay intact upon adsorption. While single molecules are trapped at surface defects and could be manipulated with the STM tip away from the defects onto the perfectly hydrogenated Ge(001):H surface, the major fraction of the molecules could be found within single-layer islands extending surprisingly far over distances reaching hundreds of nanometers. Within these islands FePc molecules adopt an upright orientation, which is characteristic for substrates weekly interacting with metal phthalocyanines. Our combined scanning tunneling microscopy (STM) and scanning tunneling spectroscopy (STS) measurements indicate that the FePc molecules stay intact upon adsorption on the Ge(001):H surface. The gap measured with STS matches well independently recorded data for weekly coupled FePc molecules. Also, it is in good agreement with optical measurements, indicating a week coupling of FePc located within the islands with the Ge(001):H surface.

Results and Discussion

Ge(001):H surface

The Ge(001):H surface exhibits (2 × 1) reconstruction with dimer rows running along the [110]/[1−10] directions. In fact, the hydrogenation is never perfect and some surface defects could be identified within the surface [61-65]. These are mainly single or double hydrogen vacancies. This means that within a Ge dimer either one hydrogen atom is missing, this is called a single dangling bond (DB), or the dimer lacks both hydrogen atoms and the so-called dangling bond dimer (DBD) is formed. A typical STM appearance of the Ge(001):H surface with the above atomic-scale defects is shown in Figure 1.

Molecular islands of FePc on Ge(001):H

After deposition of FePc molecules onto a Ge(001):H surface at room temperature, we observe single molecules distributed over the surface, as well as extended molecular islands, as shown in Figure 2. Interestingly, the recorded islands partly extend over several hundreds of nanometers, crossing several terrace steps

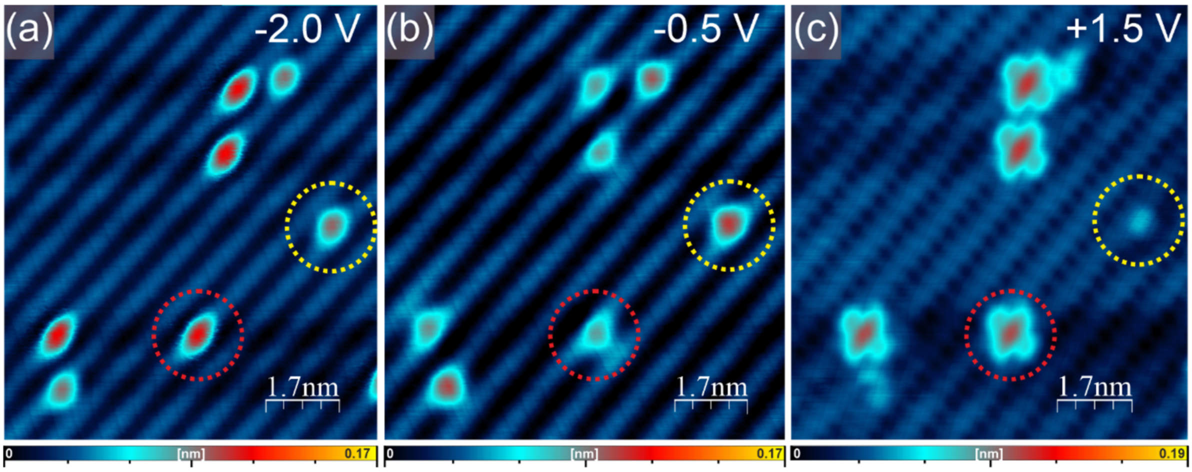

Figure 1: Typical STM appearance of a Ge(001):H surface with atomic-scale defects. (a, b) Filled- and (c) empty-state STM images. The yellow dashed circles indicate a single DB, while the red circles mark a DBD. In panel (c), the characteristic “butterfly” image of the DBD is shown. Imaging conditions: bias voltage −2.0 V (a), −0.5 V (b) and +1.5 V (c); tunneling current: 2 pA.

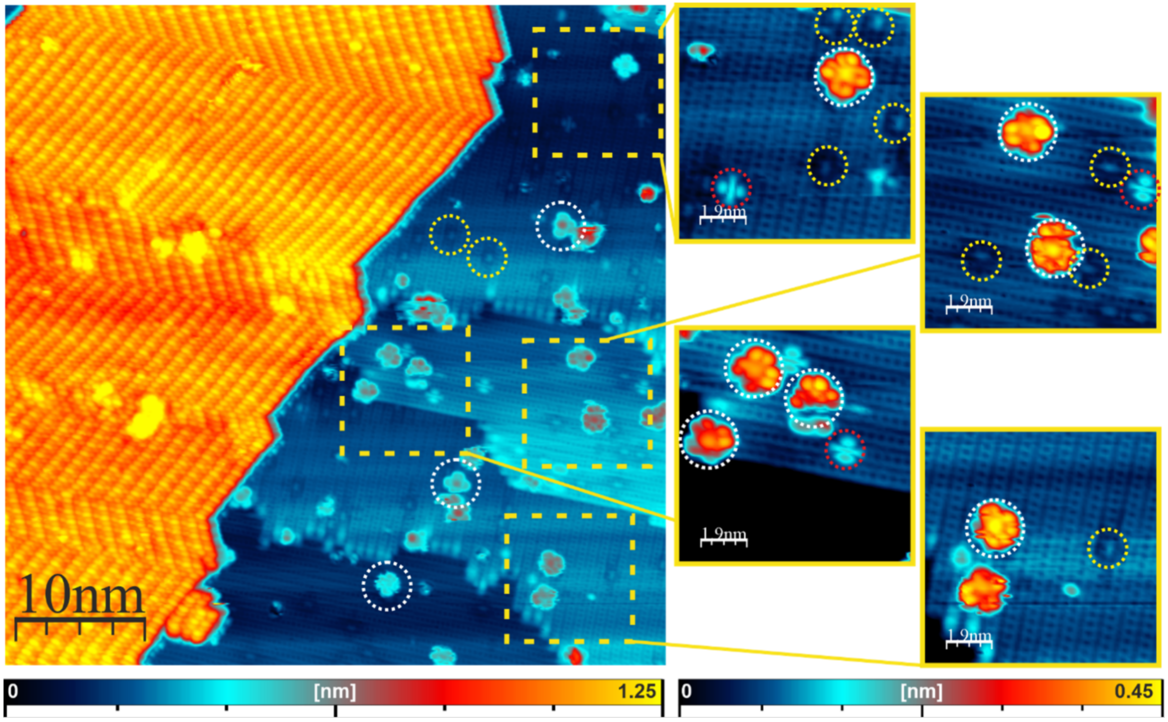

Figure 2: Empty-state STM image of individual FePc molecules and an extended molecular island self-assembled on Ge(001):H. White circles mark individual FePc molecules trapped at surface defects. Yellow circles mark single DBs with a clearly discernible dark halo surrounding them due to single electron charging. Red circles indicate isolated DBDs exhibiting the characteristic “butterfly” appearance. Imaging conditions: bias voltage +2 V, tunneling current 50 pA.

without losing integrity, as shown in Supporting Information File 1, Figure S7. Taking into account the above atomic-scale defects and our previous experiments with other organic molecules [35], we may expect that single FePc molecules on the surface are trapped at surface defects, although the formation of molecular islands hints at a sufficient mobility of the molecules on the Ge(001):H surface. In a previously reported case of starphenes on Ge(001):H, the molecules passivated all DBDs when a sufficient amount of molecules was deposited onto the surface [34]. In contrast to that, we can distinguish unoccupied

DBs and DBDs in the vicinity of largely extended molecular islands in case of FePc molecules. This is shown in Figure 2, where single DBs and DBDs are marked, respectively, by yellow and red dotted circles. A number of single FePc molecules, which adopt a flat-lying configuration, could be found on the terraces; for clarity these molecules are marked by white dashed circles.

We begin with the analysis of the molecular islands. First we note that in the case of smaller islands, a slight shift of the FePc island with respect to the underlying Ge(001):H substrate can be seen during scanning; this is shown by a white arrow in Figure 3a. Interestingly, a close inspection of the Ge(001):H surface surrounding the island shows no signs of any discontinuity of the STM appearance. This makes the modification of

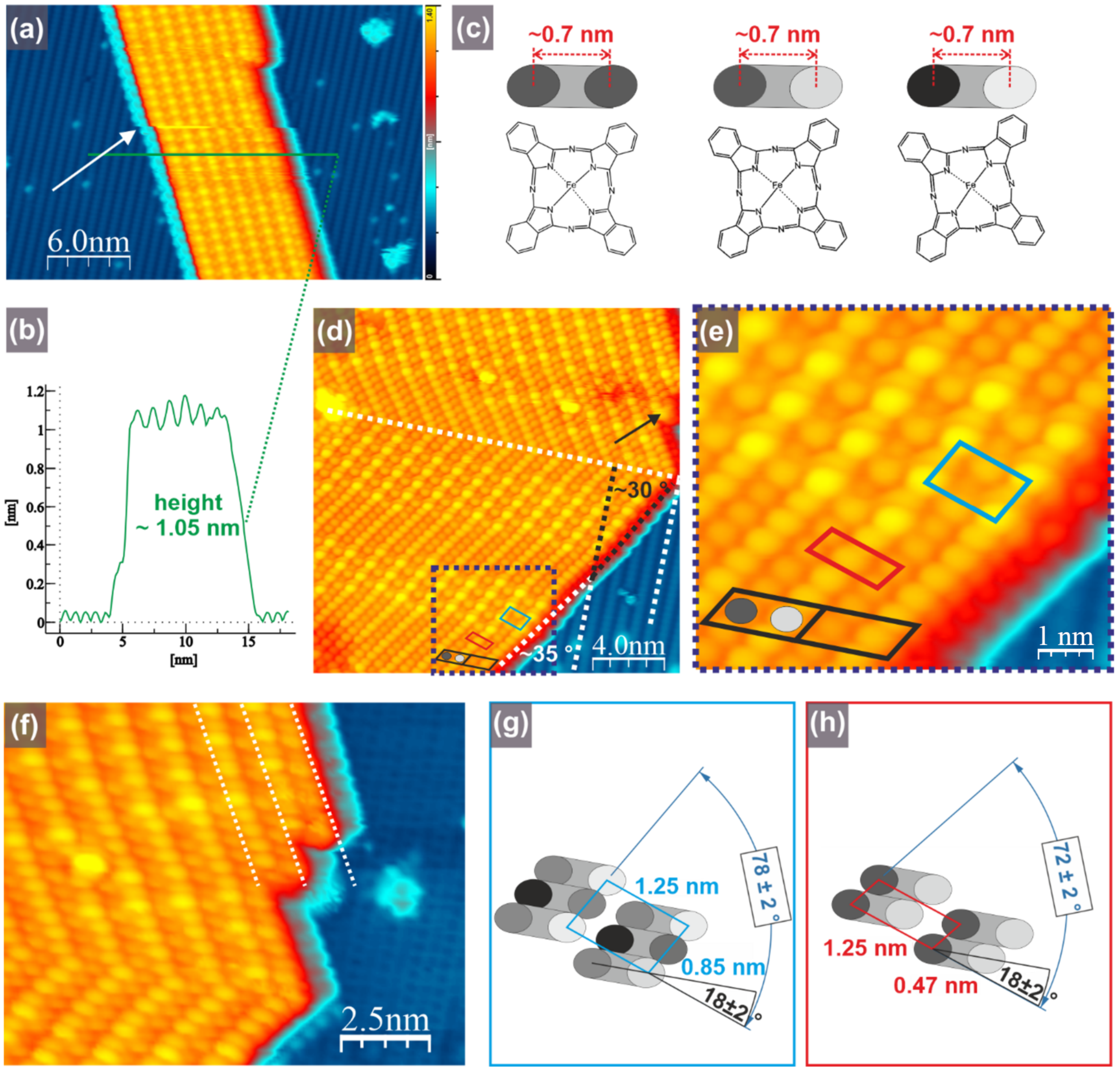

Figure 3: FePc island on a Ge(001):H surface. (a) Filled-state STM image of the island. The white arrow indicates the discontinuity of the FePc island image. (b) Height profile of the FePc island measured along the green line in (a). The apparent height of the island reaches approximately 1.05 nm, which indicates the upright orientation of FePc molecules within the island. (c) Structural scheme of FePc (bottom) with schematic appearance of the STM contrast for upright-oriented molecules within the islands (top view). The differently shaded lobes mimic the contrast variation of the STM appearance due to a slight rotation of the molecules. (d) High-resolution STM image of the CuPc island with clearly visible different domains. One white dashed line indicates the direction of surface-reconstructed rows, while the second white line divides the FePc island into two parts, in which molecular columns are oriented along mirrored directions. Black parallelograms indicate anticipated images of single FePc molecules. Red and blue parallelograms show repeated units of two different domains. The black arrow indicates the place where the island is expanded by one additional FePc column. (e) Magnification of the area marked by a violet dashed rectangle in (d) with unit cells and assignment of the STM appearance of FePc molecules within the island. (f) STM image of the island with clearly noticeable side extension composed of two rows of lobes indicated by the dashed white lines. (g, h) Simplified structural models of different domains indicated in (d) and (e). The variation of lobe contrast mimics differences in the STM contrast. STM imaging conditions: bias voltage −2 V (a, e), tunneling current 100 pA (a, d, e, f).

the STM tip apex unlikely and points to the fact that the observed shift may originate from a real shift of the island on the Ge(001):H surface. This observation indicates a weak interaction between the island and the surface and also a low barrier for island displacement. Further, from the analysis of the apparent height of the molecular island, an upright orientation of the molecules can be inferred. Such a behavior has been frequently reported for substrates on which the interaction between the molecules and the surface is weak. This leads to a dominant role of molecule–molecule interactions and the formation of molecular crystals. In case of phthalocyanines, the upright orientation has been reported, for example, for CuPc on a layer of C_{60} [66] and for CuPc on top of the CuPc wetting layer on TiO_2 [67]. As indicated in Figure 3b, the STM-measured height of the molecular island reaches approximately 1.05 nm. This is in good agreement with previous reports indicating the STM height of an upright-oriented phthalocyanines to be in the range from 1.10 nm [66] to 1.16 nm [67]. This is much more than a layer of flat-lying molecules, exhibiting an STM height below 0.8 nm [66], and more than the range of 0.3–0.4 nm for single FePc molecules in the present study. In the case of CuPc on TiO_2 [67], the formation of upright-oriented molecules within assemblies has been achieved by annealing. Here, we obtain islands composed of upright-standing molecules already at room temperature, which indicates a dominant role of intermolecular forces compared to interactions between molecules and hydrogenated surface.

In order to analyze in more detail the properties of the FePc islands, we consider now high-resolution imaging analysis. Already within the STM image in Figure 3a, we can notice lobes that differ in their apparent height. The separation between differently bright nearest neighboring lobes, which reaches approximately 0.7 nm, suggests that they originate from the same molecule. We can introduce a tentative model of the imaging, which assumes that the two unevenly bright lobes correspond to the two outer benzene rings of the same molecule. This is shown schematically in Figure 3c, where the upper panels show schematically the STM top view. The two lobes originating from the very same molecule are colored in different shades of gray. The intensity of the color corresponds schematically to the apparent height of the recorded STM image and, thus, mimic the real height of the specific part of the molecule, that is, the outer benzene ring. This is indicated in the lower part of Figure 3c, where the two outer benzene rings of upright-oriented FePc molecules are always located exactly underneath the corresponding lobes. The actual height of the STM images corresponding to certain benzene rings may arise from a slight rotation of the FePc molecules along the axis perpendicular to the molecular plane, as indicated in Figure 3c. It may also be the effect of a slight variation of the vertical component of the molecule position. However, this does not seem sufficient to provide complete information about the structure of the FePc island. Therefore, in order to obtain more information about the island structure, we consider the image displayed in Figure 3d and the magnification in Figure 3e. Within the image in Figure 3d, the dashed white line indicates the island domain boundary, which is perpendicular to the surface reconstruction rows. The STM image of the molecular island is composed of lobes that are not equally bright. The separation of the neighboring lobes along the dashed white line located at the domain boundary (i.e., across surface reconstruction rows) reaches approximately 0.7 nm, as described above. Close inspection of the island edge at the position marked by the black arrow indicates that the extension of the island is associated with the appearance of two lines of additional lobes. The effect is even better visualized in Figure 3f, where two additional columns of FePc molecules are marked by dashed white lines. This has been repeatedly observed and therefore we can conclude that the island extension is always associated with the appearance of two rows of lobes. Thus, it seems reasonable to assume that the two lobes originate from a single molecule, in accordance with the tentative model of imaging shown in Figure 3c.

For clarity, the anticipated appearance of a single molecule is marked in Figure 3e by a black parallelogram and the two unevenly bright lobes, which are mimicked by two differently colored lobes in Figure 3c. We can notice that the structure of the part of the island located above the white dashed line is almost a mirror image of the part below. We have written "almost" because within both parts of the island one can clearly notice the presence of two subtly different substructures. Their repeating units are highlighted in red and blue in Figure 3e and the corresponding dimensions and angles can be found in Figure 3g and Figure 3h, respectively. The proposed molecule arrangement is indicated by the superimposed anticipated STM images of the molecules containing two lobes for each molecule. While in the "red" structure the neighboring molecules adopt identical orientation and form columns running at approximately 35° with respect to the Ge(001):H surface pattern, the molecules in the "blue" structure form columns at an angle of approximately 30° with respect to the Ge(001):H surface reconstruction rows and exhibit an additional ad-structure. This additional modification comes from the fact that only every second molecule within the row is imaged identically brightly. We mimic this effect by coloring the corresponding STM lobes in different shades of gray in Figure 3g and Figure 3h. In reality, as explained above, this may correspond to a slight rotation along the axis perpendicular to the FePc molecule plane resulting in a non-equal height of the two outer benzene rings, as visualized in Figure 3c. We note here that the uneven brightness of the molecules may also correspond to a slight and periodic variation of the location vertical component of the neighboring FePc molecules. Effectively, the proposed "blue" unit cell is almost twice as large as the "red" one, as a result of the additional contrast modulation described above. In both structures the plane of the FePc molecule is rotated by approximately 18° with respect to the unit cell vector, as visualized in Figure 3g and Figure 3h.

At this point, it is worth mentioning that the observed structure does not correspond to any known FePc crystal phase. This indicates the influence of the substrate–molecule interactions on the crystal formation in the monolayer. The bulk α-FePc phase is characterized by columns within which the separation between the centers of the nearest FePc molecules reaches approximately 3.79 Å [68]. While the neighboring columns contain molecules rotated in opposite directions, the separation between every second column is reported to be 23.9 Å. The β phase is characterized by a slightly larger rotation angle of the molecules within columns, thus resulting in a larger separation between the centers of the nearest neighboring molecules, which reaches 4.79 Å. This is accompanied by a slightly decreased column separation of 19.6 Å for every second column [68]. Nevertheless, our proposed model provides comparable molecule–molecule separations of 4.25 Å and 4.7 Å for the "blue" and "red" structures, respectively. The transversal separation of the columns reaches approximately 1.25 nm, which is slightly more than half of the reported values for the α and β phases. However, our model suggests identical rotation within neighboring columns and, therefore, shall correspond to the half of the unit cells of the α and the β phase. While the majority of phthalocyanines exhibits alternate rotation of the molecules within neighboring columns, there are examples of structures, in which the molecules are rotated uniformly, that is, CuPc on a wetting layer on TiO_2 [67]. For clarity, the simplified schematic drawings of the α and β phases and our models are shown in Figure 4.

In order to acquire information on the electronic properties of the FePc molecules within the islands on the Ge(001):H we have performed STS measurements. Figure 5 shows a single-point spectrum recorded on the FePc island. For clarity, the inset indicates the lateral position of the STM tip during measurements. Within the data we can clearly notice the presence of narrow resonances centered at approximately −1.34 V and +1.36 V, which are separated by a flat part of the spectrum associated with the bandgap of the FePc island. The gap reaches approximately 2.7 eV, which correlates well with the recently reported data for FePc on graphene where the molecules were decoupled from the substrate [17]. Therefore, our results suggest that the FePc islands are well isolated electronically from the influence of the underlying germanium by the passivating hydrogen layer. This is in line with previous reports

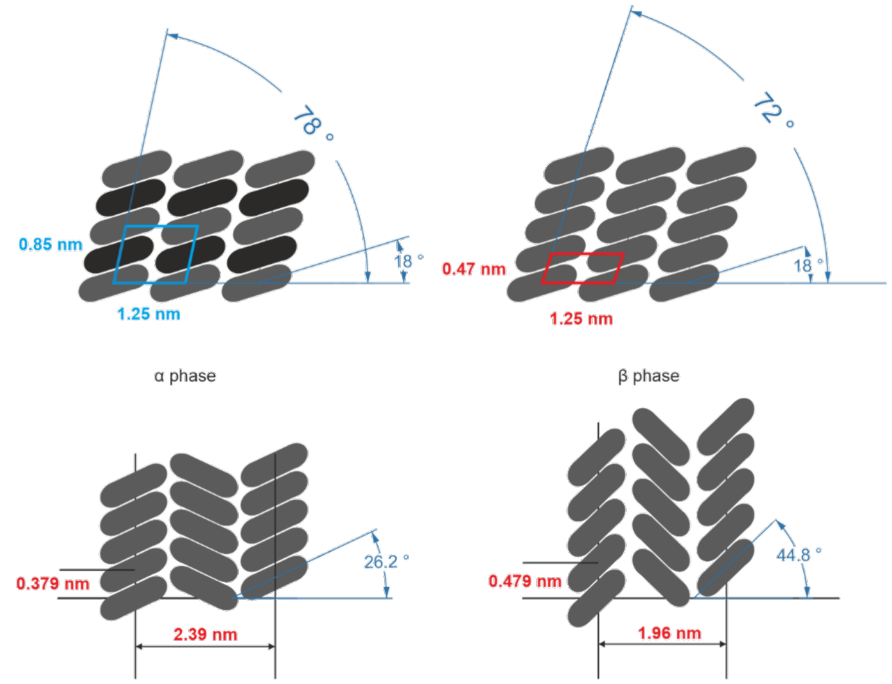

Figure 4: Schematic illustration of the two observed FePc islands on Ge(001):H (top) along with the molecular columns in the α and β phases of FePc (bottom). Images show top views. The differently colored molecules in the "blue" model correspond to molecules differently visualized in STM measurements.

showing that other organic compounds are well decoupled from the surface by hydrogen, unless they are contacted with the underlying semiconductor through atomic-scale defects, that is, DBs or DBDs [25].

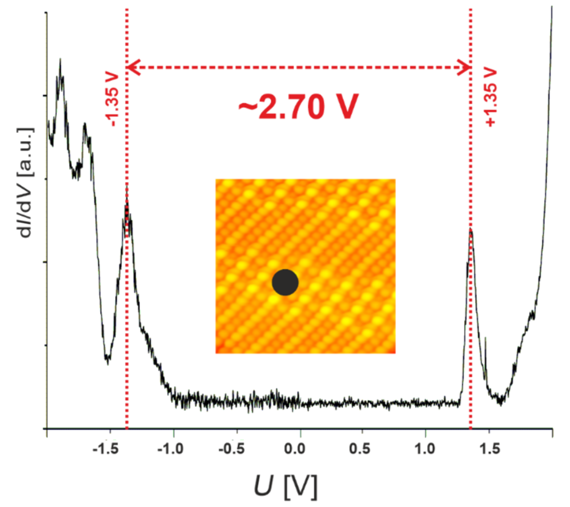

Figure 5: A single-point STS spectrum acquired on a FePc island. The gap measured with STS reaches approximately 2.70 eV, the dot in the inset shows the lateral position of the tip during STS measurements.

Manipulation of single FePc molecules

It is worth noting that the STM appearance of the individual flat-lying FePc molecules is different from that of the molecules in the FePc island. This finding suggests that the molecules are probably trapped at some surface defects and that the interaction is responsible for the modification of the STM-recorded contrast. One can also note that some molecules are clearly unstable during STM imaging. This makes the identification of the FePc molecules uncertain. In order to unambiguously identify single molecules, a single molecule manipulated and moved onto a perfectly hydrogenated Ge(001):H surface. This is shown in Figure 6. Figure 6a shows a few phthalocyanine molecules on the Ge(001):H surface that are trapped at defects and are unstable during STM measurements. This is manifested by their fuzzy appearance. Dynamic behavior of other organic molecules trapped at dangling bonds has been already reported. The DBD located underneath a starphene molecule could, for instance, act as a pivot point of a molecular rotor [30]. The FePc molecule of interest is marked by a dashed white circle in Figure 6. Figure 6b shows the actual moment of unintentional manipulation when the molecule marked by the dashed circle suddenly appeared on a perfectly hydrogenated Ge(001):H surface area. This could be inferred from that fact that the image shows the molecule only in the upper part of the scan, whereas the lower part of the topography presents the perfectly hydrogenated Ge(001):H surface. In a consecutive scan, shown in Figure 6c, the FePc molecule exhibits the typical symmetric appearance. The STM image of the molecule consists of one central lobe located at the anticipated position of the metal atom, which is surrounded by eight lobes. Such an appearance is characteristic for metal phthalocyanines that are isolated from the influence of the substrate, as already shown for FePc on Si(111):H [24] or on graphene [17]. We note here that the image corresponds well to previously reported images acquired at voltages below the values at which resonances on a central atom or the ligands are recorded [24]. The above findings indicate that the FePc molecules stay intact upon deposition on the Ge(001):H surface and that they are decoupled from the germanium substrate by the passivating hydrogen layer. Moreover, the manipulation event allows for the identification of the anchoring sites for the FePc molecules visible within Figure 6a. As visible in Figure 6, the manipulation described above is not the only modification recorded in the scanned area. We can notice two other molecules located in the central part of Figure 6a, which are displaced during scanning and disappear in Figure 6b,c. A comparison of Figure 6a and Figure 6b indicates that all three abovementioned FePc molecules were initially located on defects appearing as narrow bright features in the central part of the Ge(001):H surface reconstruction row. These defects are marked by red dashed circles in Figure 6b,c. A close inspection shows that they exactly resemble DBDs presented in the filled-state STM image in Figure 1a. This allows us to draw the conclusion that the FePc molecules recorded in Figure 6a were immobilized by DBDs. It is worth noting that the preferred localization of polycyclic molecules on DBDs on Ge(001):H has already been reported for starphenes [25,30,34] and tribiphyenylenes [35].

The appearance of the single FePc molecules described above and the fact that we did not record any means of Fe intercalation point to the adsorption of intact molecules. In contrast, on the Si(111):H surface, FePc molecules are reported to lose their central metal atom at room temperature [29].

Conclusion

We have demonstrated that FePc molecules deposited on a Ge(001):H surface at room temperature self-assemble into extended monolayer islands comprising upright-oriented FePc molecules. The STS data recorded on the islands indicated a transport gap of approximately 2.70 eV, which is in good agreement with previously reported values for isolated molecules. Since the Ge(001):H surface contains atomic-scale defects, a fraction of FePc molecules was found flat-lying and immobilized at these defects. Such molecules could be displaced laterally by means of STM manipulation and placed onto a perfectly hydrogenated Ge(001):H surface, which provided sufficient isolation from the underlying germanium substrate. Based on high-resolution STM images, we have proposed a simplified

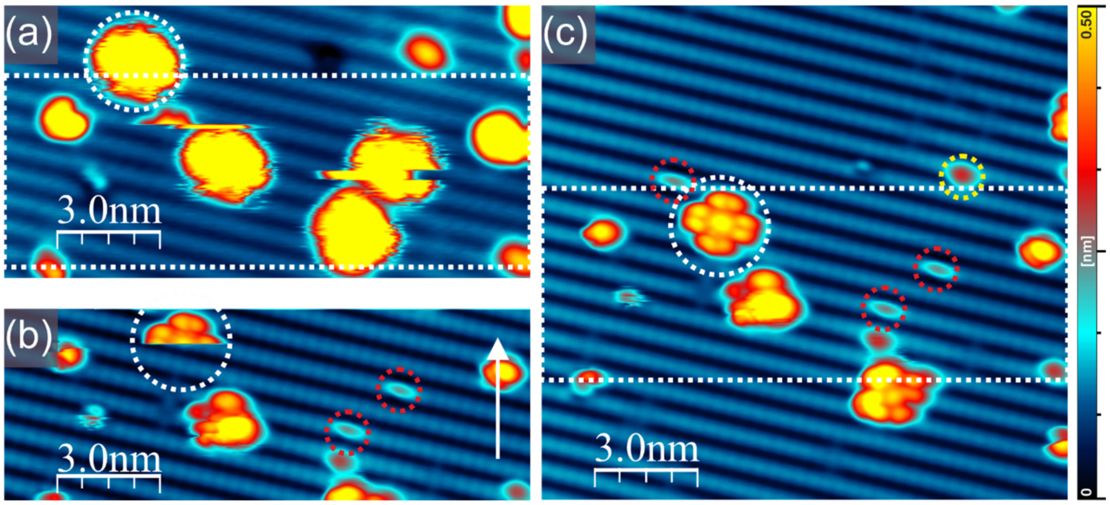

Figure 6: Single FePc molecules trapped at surface defects on a Ge(001):H surface. The white dashed circles indicate the molecule of interest. Molecules visualized in panel (a) are unstable and appear as fuzzy features with clearly discernible lateral displacement events. (a, b) The molecule marked by a white circle is removed from the defect and placed onto a perfectly hydrogenated area. Panel (b) shows the appearance of the molecule during upward scanning. The slow scan direction is marked by a white arrow on the right. (c) High-resolution STM image. The molecule marked by a white circle is located on a perfectly hydrogenated Ge(001):H surface and exhibits the typical appearance of isolated FePc molecules. Different atomic-scale surface defects that can be discerned are marked by dashed circles (i.e., a single DB (yellow) and DBDs (red)). The white dashed rectangles in (a) and (c) indicate the area visualized in (b). Imaging conditions: bias voltage −2.0 V; tunneling current 30 pA.

model of the layer structure, which resembles molecular columns present in phthalocyanine crystals.

Experimental

The whole experiment was performed in an UHV system equipped with a low-temperature STM manufactured by Omicron Nanotechnology GmbH. The Ge samples used in the experiments were cut from undoped wafers (TBL Kelpin crystals, n-type, 45 Ω·cm). After insertion into the UHV system the samples were sputtered and annealed for 15 min (Ar^+, 600 eV, 1020 K). The Ge sample was hydrogenated using a custom-built hydrogen cracker following the procedure described in [61]. Deposition of the FePc molecules (Sigma-Aldrich, purity > 99%) was performed from a Knudsen cell manufactured by Kentax. During evaporation the crucible temperature was kept at 330 °C. All STM/STS experiments were performed at liquid helium temperature (ca. 4.5 K) with electrochemically etched Pt–Ir tips used as probes. FePc molecules were evaporated at room temperature.

Supporting Information

Supporting Information File 1

Additional information on single DB charge state switching on Ge(001):H.
[https://www.beilstein-journals.org/bjnano/content/supplementary/2190-4286-12-19-S1.pdf]

Funding

We acknowledge financial support from the National Science Center, Poland (2019/35/B/ST5/02666) and the EU project PAMS (610446). The STM experiments were carried out using equipment purchased with financial support from the European Regional Development Fund within the framework of the Polish Innovation Economy Operational Program (contract no. POIG.02.01.00-12-023/08). R. Z. acknowledges support received from the National Science Center, Poland (2017/24/T/ST5/00262).

ORCID® iDs

Rafal Zuzak - https://orcid.org/0000-0001-6617-591X
Marek Szymonski - https://orcid.org/0000-0002-3442-0543
Szymon Godlewski - https://orcid.org/0000-0002-8515-1566

References

1. Gross, L.; Mohn, F.; Moll, N.; Liljeroth, P.; Meyer, G. *Science* **2009,** *325,* 1110–1114. doi:10.1126/science.1176210
2. Binnig, G.; Rohrer, H.; Gerber, C.; Weibel, E. *Phys. Rev. Lett.* **1982,** *49,* 57–61. doi:10.1103/physrevlett.49.57
3. Binnig, G.; Rohrer, H. *Surf. Sci.* **1983,** *126,* 236–244. doi:10.1016/0039-6028(83)90716-1
4. Yousofnejad, A.; Reecht, G.; Krane, N.; Lotze, C.; Franke, K. J. *Beilstein J. Nanotechnol.* **2020,** *11,* 1062–1071. doi:10.3762/bjnano.11.91
5. Lu, X.; Grobis, M.; Khoo, K. H.; Louie, S. G.; Crommie, M. F. *Phys. Rev. B* **2004,** *70,* 115418. doi:10.1103/physrevb.70.115418
6. Thygesen, K. S.; Rubio, A. *Phys. Rev. Lett.* **2009,** *102,* 046802. doi:10.1103/physrevlett.102.046802

7. Zuzak, R.; Dorel, R.; Krawiec, M.; Such, B.; Kolmer, M.; Szymonski, M.; Echavarren, A. M.; Godlewski, S. *ACS Nano* **2017,** *11,* 9321–9329. doi:10.1021/acsnano.7b04728
8. Gross, L.; Moll, N.; Mohn, F.; Curioni, A.; Meyer, G.; Hanke, F.; Persson, M. *Phys. Rev. Lett.* **2011,** *107,* 086101. doi:10.1103/physrevlett.107.086101
9. Repp, J.; Meyer, G.; Stojković, S. M.; Gourdon, A.; Joachim, C. *Phys. Rev. Lett.* **2005,** *94,* 026803. doi:10.1103/physrevlett.94.026803
10. Schulz, F.; Drost, R.; Hämäläinen, S. K.; Liljeroth, P. *ACS Nano* **2013,** *7,* 11121–11128. doi:10.1021/nn404840h
11. Koslowski, S.; Rosenblatt, D.; Kabakchiev, A.; Kuhnke, K.; Kern, K.; Schlickum, U. *Beilstein J. Nanotechnol.* **2017,** *8,* 1388–1395. doi:10.3762/bjnano.8.140
12. Godlewski, S.; Goryl, G.; Kolodziej, J. J.; Szymonski, M. *Appl. Surf. Sci.* **2010,** *256,* 3746–3752. doi:10.1016/j.apsusc.2010.01.018
13. Naitoh, Y.; Rosei, F.; Gourdon, A.; Lægsgaard, E.; Stensgaard, I.; Joachim, C.; Besenbacher, F. *J. Phys. Chem. C* **2008,** *112,* 16118–16122. doi:10.1021/jp8053197
14. Hirjibehedin, C. F.; Lutz, C. P.; Heinrich, A. J. *Science* **2006,** *312,* 1021–1024. doi:10.1126/science.1125398
15. Palmgren, P.; Yu, S.; Hennies, F.; Nilson, K.; Åkermark, B.; Göthelid, M. *J. Chem. Phys.* **2008,** *129,* 074707. doi:10.1063/1.2969081
16. Riss, A.; Wickenburg, S.; Tan, L. Z.; Tsai, H.-Z.; Kim, Y.; Lu, J.; Bradley, A. J.; Ugeda, M. M.; Meaker, K. L.; Watanabe, K.; Taniguchi, T.; Zettl, A.; Fischer, F. R.; Louie, S. G.; Crommie, M. F. *ACS Nano* **2014,** *8,* 5395–5401. doi:10.1021/nn501459v
17. de la Torre, B.; Švec, M.; Hapala, P.; Redondo, J.; Krejčí, O.; Lo, R.; Manna, D.; Sarmah, A.; Nachtigallová, D.; Tuček, J.; Błoński, P.; Otyepka, M.; Zbořil, R.; Hobza, P.; Jelínek, P. *Nat. Commun.* **2018,** *9,* 2831. doi:10.1038/s41467-018-05163-y
18. Pörtner, M.; Wei, Y.; Riss, A.; Seufert, K.; Garnica, M.; Barth, J. V.; Seitsonen, A. P.; Diekhöner, L.; Auwärter, W. *Adv. Mater. (Weinheim, Ger.)* **2020,** *7,* 2000080. doi:10.1002/admi.202000080
19. Deimel, P. S.; Feulner, P.; Barth, J. V.; Allegretti, F. *Phys. Chem. Chem. Phys.* **2019,** *21,* 10992–11003. doi:10.1039/c9cp01583c
20. Reecht, G.; Krane, N.; Lotze, C.; Zhang, L.; Briseno, A. L.; Franke, K. J. *Phys. Rev. Lett.* **2020,** *124,* 116804. doi:10.1103/physrevlett.124.116804
21. Krane, N.; Lotze, C.; Reecht, G.; Zhang, L.; Briseno, A. L.; Franke, K. J. *ACS Nano* **2018,** *12,* 11698–11703. doi:10.1021/acsnano.8b07414
22. Croshaw, J.; Dienel, T.; Huff, T.; Wolkow, R. *Beilstein J. Nanotechnol.* **2020,** *11,* 1346–1360. doi:10.3762/bjnano.11.119
23. Bellec, A.; Ample, F.; Riedel, D.; Dujardin, G.; Joachim, C. *Nano Lett.* **2009,** *9,* 144–147. doi:10.1021/nl802688g
24. Gruyters, M.; Pingel, T.; Gopakumar, T. G.; Néel, N.; Schütt, C.; Köhler, F.; Herges, R.; Berndt, R. *J. Phys. Chem. C* **2012,** *116,* 20882–20886. doi:10.1021/jp3058433
25. Godlewski, S.; Kolmer, M.; Kawai, H.; Such, B.; Zuzak, R.; Saeys, M.; de Mendoza, P.; Echavarren, A. M.; Joachim, C.; Szymonski, M. *ACS Nano* **2013,** *7,* 10105–10111. doi:10.1021/nn404254y
26. Olszowski, P.; Zapotoczny, B.; Prauzner-Bechcicki, J. S.; Vilas-Varela, M.; Pérez, D.; Guitián, E.; Peña, D.; Szymonski, M. *J. Phys. Chem. C* **2015,** *119,* 27478–27482. doi:10.1021/acs.jpcc.5b08883
27. Ahmad Zebari, A. A.; Kolmer, M.; Prauzner-Bechcicki, J. S. *Beilstein J. Nanotechnol.* **2013,** *4,* 927–932. doi:10.3762/bjnano.4.104
28. Engelund, M.; Papior, N.; Brandimarte, P.; Frederiksen, T.; Garcia-Lekue, A.; Sánchez-Portal, D. *J. Phys. Chem. C* **2016,** *120,* 20303–20309. doi:10.1021/acs.jpcc.6b04540
29. Gruyters, M.; Pingel, T.; Berndt, R. *Phys. Rev. B* **2013,** *87,* 165405. doi:10.1103/physrevb.87.165405
30. Godlewski, S.; Kawai, H.; Kolmer, M.; Zuzak, R.; Echavarren, A. M.; Joachim, C.; Szymonski, M.; Saeys, M. *ACS Nano* **2016,** *10,* 8499–8507. doi:10.1021/acsnano.6b03590
31. Baseer Haider, M.; Pitters, J. L.; DiLabio, G. A.; Livadaru, L.; Mutus, J. Y.; Wolkow, R. A. *Phys. Rev. Lett.* **2009,** *102,* 046805. doi:10.1103/physrevlett.102.046805
32. Wyrick, J.; Wang, X.; Namboodiri, P.; Schmucker, S. W.; Kashid, R. V.; Silver, R. M. *Nano Lett.* **2018,** *18,* 7502–7508. doi:10.1021/acs.nanolett.8b02919
33. Kolmer, M.; Zuzak, R.; Dridi, G.; Godlewski, S.; Joachim, C.; Szymonski, M. *Nanoscale* **2015,** *7,* 12325–12330. doi:10.1039/c5nr01912e
34. Godlewski, S.; Kawai, H.; Engelund, M.; Kolmer, M.; Zuzak, R.; Garcia-Lekue, A.; Novell-Leruth, G.; Echavarren, A. M.; Sanchez-Portal, D.; Joachim, C.; Saeys, M. *Phys. Chem. Chem. Phys.* **2016,** *18,* 16757–16765. doi:10.1039/c6cp02346k
35. Godlewski, S.; Engelund, M.; Peña, D.; Zuzak, R.; Kawai, H.; Kolmer, M.; Caeiro, J.; Guitián, E.; Vollhardt, K. P. C.; Sánchez-Portal, D.; Szymonski, M.; Pérez, D. *Phys. Chem. Chem. Phys.* **2018,** *20,* 11037–11046. doi:10.1039/c8cp01094c
36. Ahmad Zebari, A. A.; Kolmer, M.; Prauzner-Bechcicki, J. S. *Appl. Surf. Sci.* **2015,** *332,* 403–408. doi:10.1016/j.apsusc.2015.01.173
37. Chen, Q.; Rada, T.; Bitzer, T.; Richardson, N. V. *Surf. Sci.* **2003,** *547,* 385–393. doi:10.1016/j.susc.2003.10.021
38. Sazaki, G.; Fujino, T.; Sadowski, J. T.; Usami, N.; Ujihara, T.; Fujiwara, K.; Takahashi, Y.; Matsubara, E.; Sakurai, T.; Nakajima, K. *J. Cryst. Growth* **2004,** *262,* 196–201. doi:10.1016/j.jcrysgro.2003.08.080
39. Vaurette, F.; Nys, J. P.; Grandidier, B.; Priester, C.; Stievenard, D. *Phys. Rev. B* **2007,** *75,* 235435. doi:10.1103/physrevb.75.235435
40. Nakamura, M.; Matsunobe, T.; Tokumoto, H. *J. Appl. Phys.* **2001,** *89,* 7860–7865. doi:10.1063/1.1373700
41. Zeis, R.; Siegrist, T.; Kloc, C. *Appl. Phys. Lett.* **2005,** ***86,*** 022103. doi:10.1063/1.1849438
42. Cheng, Z.; Du, S.; Guo, W.; Gao, L.; Deng, Z.; Jiang, N.; Guo, H.; Tang, H.; Gao, H.-J. *Nano Res.* **2011,** *4,* 523–530. doi:10.1007/s12274-011-0108-y
43. Komeda, T.; Isshiki, H.; Liu, J. *Sci. Technol. Adv. Mater.* **2010,** *11,* 054602. doi:10.1088/1468-6996/11/5/054602
44. Wang, X.; Cai, Z.-F.; Wang, Y.-Q.; Feng, Y.-C.; Yan, H.-J.; Wang, D.; Wan, L.-J. *Angew. Chem., Int. Ed.* **2020,** *132,* 16232–16237. doi:10.1002/ange.202005242
45. Lu, X.; Hipps, K. W. *J. Phys. Chem. B* **1997,** *101,* 5391–5396. doi:10.1021/jp9707448
46. Fan, Q.; Luy, J.-N.; Liebold, M.; Greulich, K.; Zugermeier, M.; Sundermeyer, J.; Tonner, R.; Gottfried, J. M. *Nat. Commun.* **2019,** *10,* 5049. doi:10.1038/s41467-019-13030-7
47. Lu, X.; Hipps, K. W.; Wang, X. D.; Mazur, U. *J. Am. Chem. Soc.* **1996,** *118,* 7197–7202. doi:10.1021/ja960874e
48. Wang, Y.; Wu, K.; Kröger, J.; Berndt, R. *AIP Adv.* **2012,** *2,* 041402. doi:10.1063/1.4773458
49. Sk, R.; Deshpande, A. *Mol. Syst. Des. Eng.* **2019,** *4,* 471–483. doi:10.1039/c9me00014c

50. Bouju, X.; Mattioli, C.; Franc, G.; Pujol, A.; Gourdon, A. *Chem. Rev.* **2017,** *117,* 1407–1444. doi:10.1021/acs.chemrev.6b00389
51. Goiri, E.; Borghetti, P.; El-Sayed, A.; Ortega, J. E.; de Oteyza, D. G. *Adv. Mater. (Weinheim, Ger.)* **2016,** *28,* 1340–1368. doi:10.1002/adma.201503570
52. Gottfried, J. M. *Surf. Sci. Rep.* **2015,** *70,* 259–379. doi:10.1016/j.surfrep.2015.04.001
53. Bao, D.-L.; Zhang, Y.-Y.; Du, S.; Pantelides, S. T.; Gao, H.-J. *J. Phys. Chem. C* **2018,** *122,* 6678–6683. doi:10.1021/acs.jpcc.8b00086
54. Snezhkova, O.; Bischoff, F.; He, Y.; Wiengarten, A.; Chaudhary, S.; Johansson, N.; Schulte, K.; Knudsen, J.; Barth, J. V.; Seufert, K.; Auwärter, W.; Schnadt, J. *J. Chem. Phys.* **2016,** *144,* 094702. doi:10.1063/1.4942121
55. Barth, J. V. *Annu. Rev. Phys. Chem.* **2007,** *58,* 375–407. doi:10.1146/annurev.physchem.56.092503.141259
56. Sabik, A.; Mazur, P.; Gołek, F.; Trembulowicz, A.; Antczak, G. *J. Chem. Phys.* **2018,** *149,* 144702. doi:10.1063/1.5050377
57. Tang, C. W. *Appl. Phys. Lett.* **1986,** *48,* 183–185. doi:10.1063/1.96937
58. Bodek, L.; Engelund, M.; Cebrat, A.; Such, B. *Beilstein J. Nanotechnol.* **2020,** *11,* 821–828. doi:10.3762/bjnano.11.67
59. Bodek, L.; Cebrat, A.; Piatkowski, P.; Such, B. *J. Phys. Chem. C* **2019,** *123,* 9209–9216. doi:10.1021/acs.jpcc.9b01043
60. Bartolomé, J.; Monton, C.; Schuller, I. K. Magnetism of Metal Phthalocyanines. In *Molecular Magnets;* Bartolome, S. J.; Luis, F.; Fernández, J. F., Eds.; Springer-Verlag : Berlin, Heidelberg, 2014; pp 221–245. doi:10.1007/978-3-642-40609-6
61. Kolmer, M.; Godlewski, S.; Kawai, H.; Such, B.; Krok, F.; Saeys, M.; Joachim, C.; Szymonski, M. *Phys. Rev. B* **2012,** *86,* 125307. doi:10.1103/physrevb.86.125307
62. Godlewski, S.; Kolmer, M.; Lis, J.; Zuzak, R.; Such, B.; Gren, W.; Szymonski, M.; Kantorovich, L. *Phys. Rev. B* **2015,** *92,* 115403. doi:10.1103/physrevb.92.115403
63. Livadaru, L.; Pitters, J.; Taucer, M.; Wolkow, R. A. *Phys. Rev. B* **2011,** *84,* 205416. doi:10.1103/physrevb.84.205416
64. Engelund, M.; Godlewski, S.; Kolmer, M.; Zuzak, R.; Such, B.; Frederiksen, T.; Szymonski, M.; Sánchez-Portal, D. *Phys. Chem. Chem. Phys.* **2016,** *18,* 19309–19317. doi:10.1039/c6cp04031d
65. Godlewski, S.; Kolmer, M.; Engelund, M.; Kawai, H.; Zuzak, R.; Garcia-Lekue, A.; Saeys, M.; Echavarren, A. M.; Joachim, C.; Sanchez-Portal, D.; Szymonski, M. *Phys. Chem. Chem. Phys.* **2016,** *18,* 3854–3861. doi:10.1039/c5cp07307c
66. Huang, H.; Chen, W.; Chen, S.; Qi, D. C.; Gao, X. Y.; Wee, A. T. S. *Appl. Phys. Lett.* **2009,** *94,* 163304. doi:10.1063/1.3122940
67. Godlewski, S.; Tekiel, A.; Prauzner-Bechcicki, J. S.; Budzioch, J.; Szymonski, M. *ChemPhysChem* **2010,** *11,* 1863–1866. doi:10.1002/cphc.201000165
68. O'Rourke, J. K.; Brooks, J. S.; Bell, N. A.; Cawley, J.; Thorpe, S. C. *Sens. Actuators, B* **1993,** *14,* 690–692. doi:10.1016/0925-4005(93)85146-2

License and Terms